POLITECNICO DI TORINO
Repository ISTITUZIONALE

Building Simulation Applications BSA 2022 - Proceedings of 5th IBPSA-Italy conference

Original
Building Simulation Applications BSA 2022 - Proceedings of 5th IBPSA-Italy conference / Pernigotto, Giovanni; Patuzzi, Francesco; Prada, Alessandro; Corrado, Vincenzo; Gasparella, Andrea. - ELETTRONICO. - (2023), pp. 1-540. [10.13124/9788860461919]

Availability:
This version is available at: 11583/2980215 since: 2023-07-13T14:29:31Z

Publisher:
Bozen-Bolzano University Press

Published
DOI:10.13124/9788860461919

Terms of use:

This article is made available under terms and conditions as specified in the corresponding bibliographic description in the repository

Publisher copyright

(Article begins on next page)

27 April 2024

Estimated Versus Actual Heating Energy Use of Residential Buildings

Matthias Schuss – TU Wien, Vienna, Austria – matthias.schuss@tuwien.ac.at
Martin Fleischhacker – Vienna, Austria – martin2fleischhacker@gmail.com
Ardeshir Mahdavi – TU Wien, Vienna, Austria – amahdavi@tuwien.ac.at

Abstract

The energy demand of buildings plays an important role with regard to energy conservation objectives as well as reduction of greenhouse gas emission. The well-established building energy certificates provide essential information concerning the thermal quality and resulting energy demands of buildings in general. Hence, related Austrian regulations and standards specify a demand-orientated calculation method based on construction and material data together with standardized usage profiles, as well as a location-related weather data set. This method is also applied in the case of existing buildings, which differs from some other European countries, where certificates represent real energy usage and provide a comparison with similar buildings in terms of construction period and usage. However, it is not guaranteed that an energy demand certificate according to Austrian standards is able to represent the actual energy use of existing buildings, a circumstance that is typically referred to as 'energy performance gap'. In this context, we conducted a comprehensive comparison of real energy consumption and the certificate-based energy demand predictions for a number of buildings located in and around the city of Vienna, Austria. Specifically, 15 residential building complexes with nearly 1400 units were selected, involving a large variety of building construction dates and their thermal quality. The buildings were analyzed in detail based on historic energy consumption data from 2011 to 2017. The paper provides an overview of the real energy performance together with a detailed analysis of the discrepancies between actual energy use and certificate-based estimations. Generally speaking, the buildings with a higher energy standard and lower demand displayed higher discrepancies (expressed in terms of relative deviations) than older buildings with higher energy demand.

1. Introduction

Over the past decades, increasing efforts have been made to reduce energy consumption in all sectors. The building sector requires an average of 40 % of the total energy demand of the European Union (EU, 2010). Great saving potentials were identified for buildings and this resulted in extensive energy efficiency measures. As a result, not only new buildings are now better insulated, but also the existing building stock is to be significantly improved with necessary thermal retrofitting measures. Other additional tools for higher energy efficiency are better building systems that could contribute to further reduction of the energy requirements of the buildings. But how effective are these measures and how much can energy consumption actually be reduced?

In Austria, the Energy Performance Certificate Submission Act of 2012 mandates the following: "... the obligation of the seller or inventor to present and hand over an energy certificate to the buyer or existing customer when selling or in-stocking a building or object of use, as well as the obligation to provide certain indicators on the energy quality of the building ...)" (EAVG, 2012).

The basic idea of an energy certificate lies in the possibility of verifiability of the energy demand and better estimation of running costs. Furthermore, this is expected to influence the market prices according to the thermal quality and the predicted future energy needs and costs. Hence, an energy certificate should not be merely a project description with vague information about the energy demand and thermal quality to fulfil the requirements defined by law. Rather, it should act as a purchase or sales argument and should motivate owners to improve the energy performance. In this context, the present contribution examines the validity of energy

certificates based on information from a set of building complexes.

2. Method

Recorded energy usage data of nearly 1400 apartments over a period of seven years (2011 to 2017) was analyzed with focus on the verifiability of the energy demand as entailed in the building energy certificates. To this end, energy consumption data from annual accounting bills were collected and compared with certificates to assess differences between the predicted and the real energy usage both at the building complex level and at the level of individual units. An initial quality check of the available data showed that 12 complexes with a total of 1043 units could be used for a detailed comparison between the estimated heating demands and the real energy usage.

3. Used Building Sampling

The building sample consists of a total of 15 complexes with nearly 1400 units, as shown in Table 1. From the schematic drawings of the cubature, it is the fact that the sampling includes different types of building complexes with single buildings as well as blocks of attached buildings may be seen. The buildings are mainly located in the city of Vienna (see Fig. 1). Buildings referred to as BH and KF are close to near to the border of the Vienna municipality, whereas AS is near Wiener Neustadt (approximately 45 km from Vienna).

Table 2 shows the variety of the buildings in terms of construction and size. Detailed information about the number of units, the building class, the heated and total area, as well as the ratio of volume and area are also included in the overview. The buildings are sorted from high to low energy demand with energy labels from C to A+. Buildings with limited data that show accounting units (relative dimensionless fraction of energy use) instead of kWh in the reporting bills are marked in red.

Table 1 – Overview of building sample, including the object code, number of units, and illustration of cubature

Object	Units/flats	Cubature
AL	28	
JB	46	
ZS	231	
UZ	23	
FM	47	
DP	148	
RA	41	
KE	324	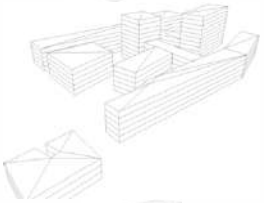
VG	52	
AS	45	
AB	108	
KT	90	
KF	47	
BH	73	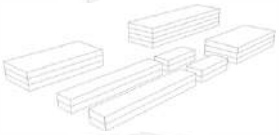
KW	45	

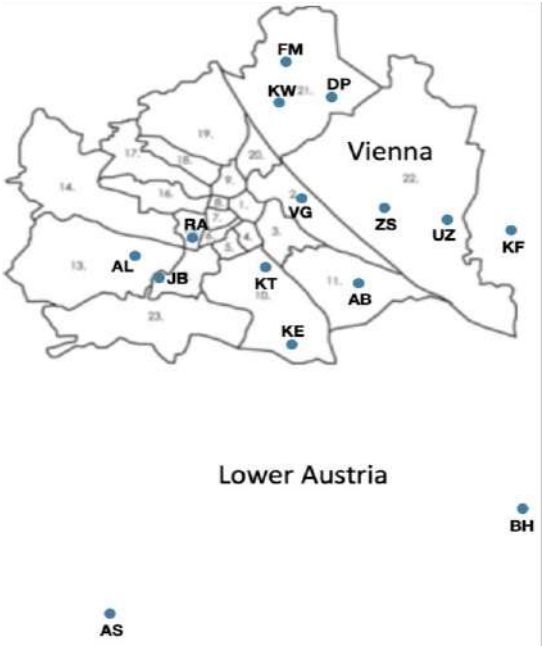

Fig. 1 – Location of the analyzed building complexes

The energy class variety of the analyzed 15 complexes included buildings from C to A++ in a range of 11 to 57 kWh/(m² a) as mentioned in Table 2 and illustrated in Fig. 2.

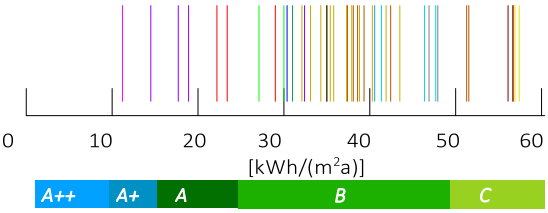

Fig. 2 – Distribution of certificate-based heating demand prediction and the building energy efficiency label from the analyzed building complexes

4. Heating Degree Days and Data Normalization

The calculation of the building energy certificate values depends on the location and its climate conditions and shows a strong dependence on the magnitude of local heating degree days (HDD). Standardized values for the different climate regions and altitudes of buildings in Austria are specified in the related OIB-RL6 regulation (OIB, 2015). The values of heating degree days are calculated as the difference between the room air temperature, which is specified as 20 °C, and the outside temperature, if it is below 12 °C. When calculating the number of heating degree days in a year, all days with daily average outside temperatures below 12 °C are specified as heating days and are considered in the calculation.

The general trend for calculated annual heating degree days for Vienna (Fig. 2), based on real temperature data from the public weather station at "Hohe Warte" (ZAMG, 2018), shows, with 2295.1 K d, the lowest value of heating degree days for 2014 and the highest value of 2940.4 K d for 2015. The mean value of 2720.4 K d is significantly lower than the standard defined value (3355 K d) for "Wien Döbling" as documented in the OIB-RL6 regulation. Hence, the recoded energy usage of the sample buildings could be expected to be significantly lower for these years when compared with the values in the certificates. The analyzed weather data showed, for the study period (2011 to 2017), approximately 19 percent lower heating degree days for Vienna.

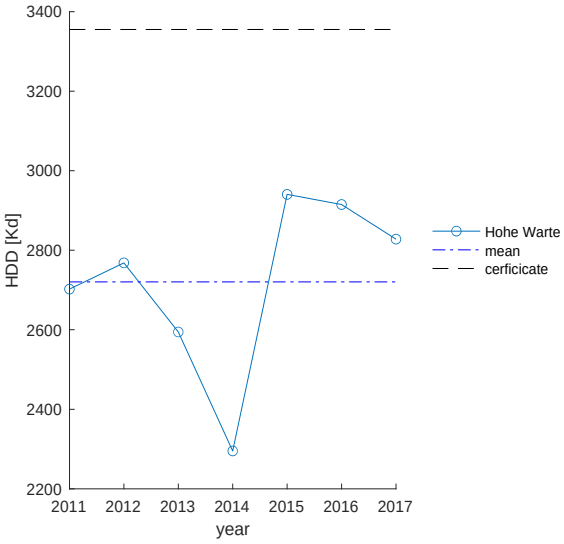

Fig. 3 – Heating degree days for the years 2011 to 2017 based on measurements from the ZAMG weather station ("Hohe Warte") in Vienna

In the following analysis, an HDD-normalization of the data was performed with a yearly factor considering the HHD-difference, and increases the yearly energy usage accordingly. Due to the proximity to Vienna (same climate zone), a separate evaluation of heating degree days in Lower Austria was not considered.

5. Results of Energy Usage Evaluation

In total, 15 residential building complexes with nearly 1400 units were evaluated on the basis of energy consumption data over a period of seven years (2011-2017). For twelve of the complexes with nearly 1050 units, a detailed comparison between the heating demand displayed in the certificate and the recorded heating energy usage was performed with a detailed discussion of the variety. The remaining three other complexes with data showing cost profiles as accounting units are limited in their analyzing possibilities and resulted in an analysis of the variation only.

5.1 Total Energy Consumption for Heating, Ventilation and Hot Water Production

The trends of the total annual energy consumption for heating, ventilation and hot water production (Fig. 4) shows, as expected, a general correlation with the variation of the real heating degree days as presented before.

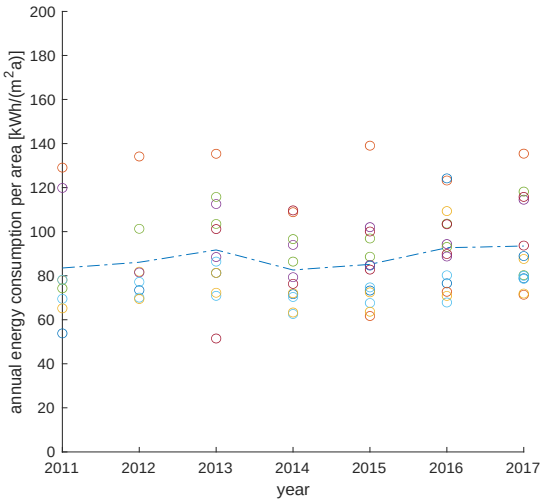

Fig. 4 – Total annual energy consumption for heating, ventilation, and hot water production recorded in the years 2011 to 2017

Fig. 5 illustrates the variation of annual total energy usage for the years 2011 to 2017. As expected, some of the complexes (KE and KF) show a much higher variation than the others. This could be partly explained with energy partly used for hot water preparation, which generally does not depend on the heating degree days, but depends rather on user behavior.

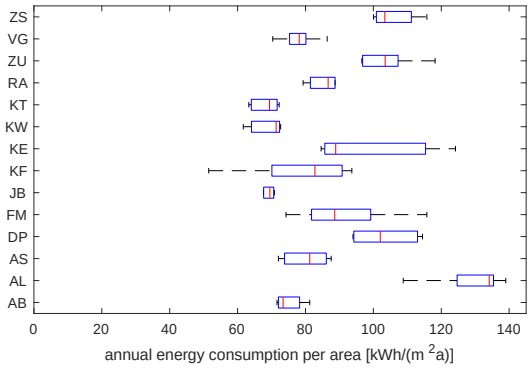

Fig. 5 – Distribution of the total annual energy consumption for heating, ventilation, and hot water production recorded in the years 2011 to 2017

5.2 Energy Demand vs Real Energy Consumption Used for Room Heating

A detailed comparison of the certificate-based energy demand for heating and the real measurements from the year 2011 to 2017 recorded by individual submeters for each unit was possible for 12 of the 15 complexes. An initial comparison of HDD-normalized annual average energy usage for heating (40 buildings and 1043 units) showed much higher usage than expected (Fig. 6). Note that not even a single building in the sample was performing equally or better than estimated in the certificate. A more detailed evaluation of the data was carried out to identify possible tendencies in relation to the building class in the certificate. Fig. 7 shows the variation of the annual HDD-normalized energy usage for heating sorted from high (at the top) to low heating energy demands (marked with blue X in the plot).

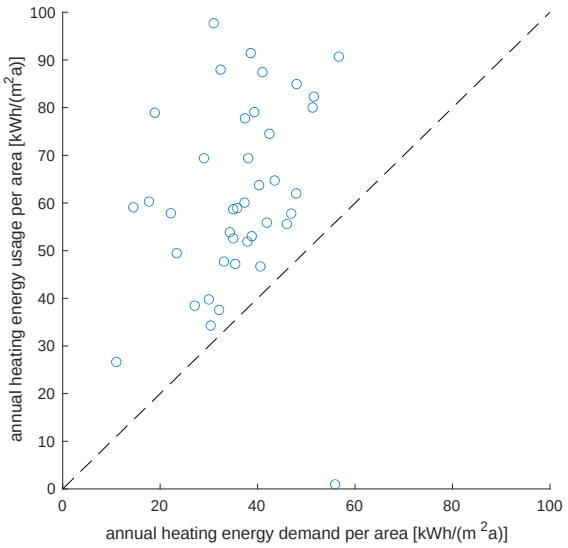

Fig. 6 – Annual certificate-based energy demand versus average annual HDD-normalized energy usage for heating recorded in the years 2011 to 2017

It may be seen that not all instances have a similar variety over time, suggesting a possible role of other influencing parameters other than the outside temperature and the related HDD influence.

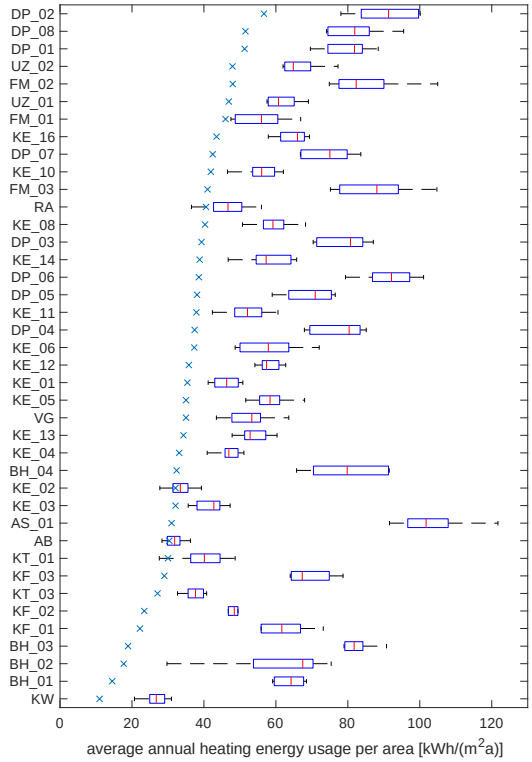

Fig. 7 – Distribution of building average (2011 to 2017) HDD-normalized annual heating energy usage together with the certificate-based heating demand (marked with a blue x)

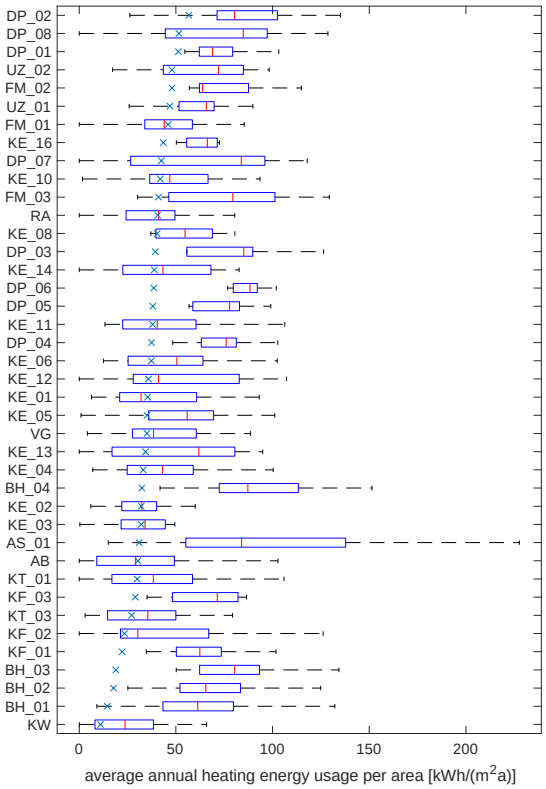

Fig. 8 – Distribution of units' HDD-normalized annual heating energy usage in the year 2016 together with the certificate-based heating demand (marked with a blue x)

Especially in the high-rated buildings (according to certificates), such as AS_01, KF_03, KF_01, BH_03, BH_02 and BH_01, rather high measured energy use values can be observed. A closer look into the variation of the units' HDD-normalized annual heating energy usage was carried out for the year 2016 and is presented in Fig. 7. It may be seen that the variation between the units is very large and could be thought of as having been caused by the occupants' influence. Again, high-ranked buildings display a wide variation. The buildings KW, BH_01, BH_02, BH_03, and BH_04 with a controlled ventilation system show much higher and wider distributed values than expected. These buildings were designed as passive houses. Hence, it could have been expected that the ventilation system would significantly reduce the heating energy use. For three complexes and the respective 9 buildings, a detailed comparison was not possible, but the variation of the energy usage documented with the related accounting units of the annual bills was analyzed in a similar way as above. Fig. 9 shows a similar variety of the units' HDD-normalized annual heating energy usage in groups of

accounting units for each sampling object as for the rest of the building sample.

The main task of the study was to examine the validity of energy certificates and to evaluate how future energy usage and running costs can be predicted. The recorded data of the real energy usage in the years 2011 to 2017 for sampled buildings suggest that the real energy usage for heating is significantly higher.

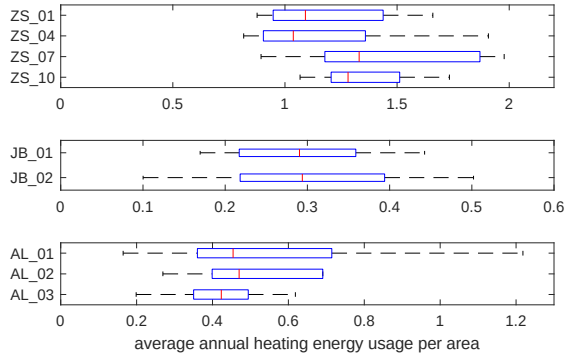

Fig. 9 – Distribution of units' HDD-normalized annual heating energy usage for buildings with heating usage data in accounting units only in the year 2016

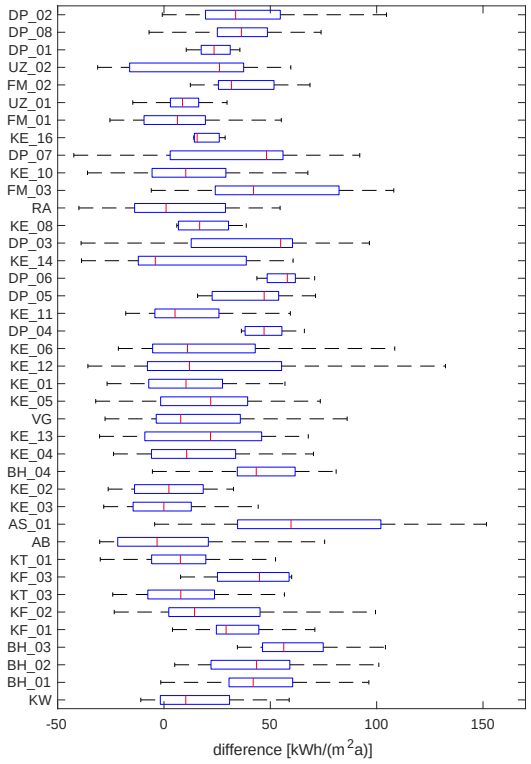

Fig. 10 – Difference distribution of unit average (2011 to 2017) HDD-normalized annual heating energy usage and the certificate-based heating demand

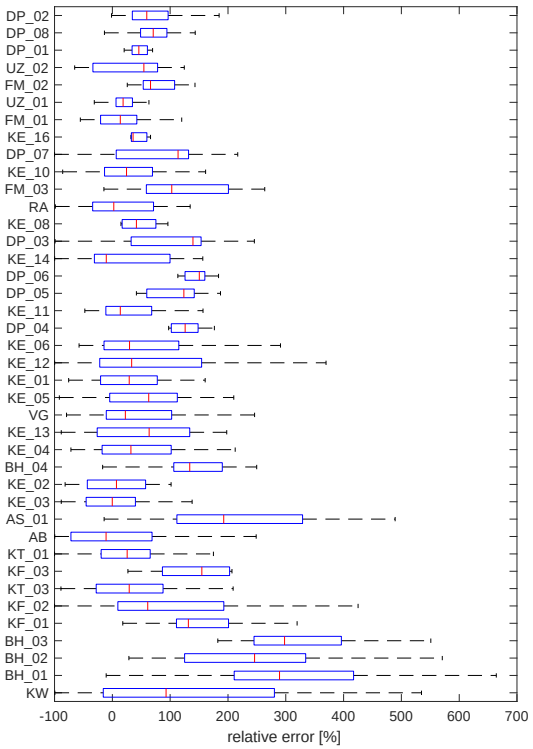

Fig. 11 – Relative error distribution of unit average (2011 to 2017) HDD-normalized annual heating energy usage and the certificate-based heating demand

Fig. 10 illustrates this for example with overview of the unit average (2011 to 2017) HDD-normalized annual heating energy usage and the certificate-based heating demand. It is clearly visible that especially the higher rated buildings at the bottom show similar or, in some cases higher, differences to the predicted heating demand. The unsatisfactory performance of those buildings is even more visible in the calculation of a relative error to the heating demand, as illustrated in Fig. 11.

6. Conclusion

The evaluation of energy consumption data (years 2011 to 2017) from 15 residential building complexes with nearly 1400 units facilitated an examination of the reliability of energy certificates in view of the prediction of building future energy use and related costs. The available data showed much higher energy consumption when compared with the values in energy certificates. This could be shown for the total energy use for heating, domestic hot water, and ventilation in cases with controlled ventilation,

as well as for the heating energy usage itself.
Buildings with higher thermal standards showed in relative terms a larger energy performance gap when compared with buildings with lower energy certificate ratings. This may be a consequence of the high potential for the influence of building occupants in total energy use.

Acknowledgement

This contribution was only possible with support by EBG Hausverwaltung and the provision of the building description documents of the residential properties examined. In addition, the accounting companies concerned, ISTA and TECHEM, facilitated this study with the preparation and provision of the detailed billing data.

References

EU. 2010 "Directive 2010/31/EU". European Union L 153/13 18.6.2010

EAVG 2012. „Bundesgesetz über die Pflicht zur Vorlage eines Energieausweises beim Verkauf und bei der In-Bestand-Gabe von Gebäuden und Nutzungsobjekten BGBl. I Nr. 27/2012

OIB. 2015. "OIB-Richtlinie 6: Energieeinsparung und Wärmeschutz". Österreichisches Institut für Bautechnik. OIB-330.6-009/15.

ZAMG. 2018. „Tagesauswertung Lufttemperatur Wien Hohe Warte, 2011-2017". Zentralanstalt für Meteorologie und Geodynamik. Accessed 25.09.2018. https://www.zamg.ac.at/cms/de/klima/klimauebersichten/jahrbuch

Polyamide Waste Thermal and Acoustic Properties: Experimental and Numerical Investigation on Possible Reuse for Indoor Comfort Improvement

Manuela Neri – University of Brescia, Italy – manuela.neri@unibs.it
Eva Cuerva – Universitat Politècnica de Catalunya, Italy – eva.cuerva@upc.edu
Alfredo Zabaleta – Universitat Politècnica de Catalunya, Spain – alfredo.guardo-zabaleta@upc.edu
Pablo Pujadas – Universitat Politècnica de Catalunya; Spain – pablo.pujadas@upc.edu
Elisa Levi – University of Brescia; Italy – elisa.levi@unibs.it
Ondrej Sikula – Brno University of Technology, Czech Republic – sikula.o@vutbr.cz

Abstract

Referring to the circular economy model, end-of-life household materials (EoLHM), such as packaging and clothes, could be converted into building elements with thermal and acoustic properties; for example, they could be converted into panels to be installed indoors for building refurbishment. Given the high availability almost anywhere, panels made of EoLHM would represent an alternative to commercial insulating materials that, even though relatively cheap, cannot be afforded by disadvantaged people. This paper presents a multidisciplinary analysis aimed at the characterization of polyamide 6.6, obtained as a waste from the production of non-surgical face masks. The research focuses on the thermal and acoustic properties of the material. The properties have been determined experimentally through the guarded hot plate method hot and the impedance tube technique. Then, the influence of the panel's position on the indoor operative temperature and the reverberation time has been analyzed through numerical simulations. Results show that, from the thermal and acoustic point of view, this waste is suitable for the realization of building panels, and the performance depends on the density and the thickness of the material. However, aspects such as fire resistance and the containment of the material need further investigation.

1. Introduction

Living in dwellings characterized by inadequate indoor temperature and poor air quality is called "energy poverty", a condition affecting 1 in 3 Europeans, and linked to 100000 premature deaths each year (European Parliament and Council of the European Union, 2018; González-Eguino, 2015). People living in disadvantaged contexts cannot refurbish their dwellings because of the relatively high price of commercial insulating materials. By 2030, the United Nations aim to make cities inclusive, safe, resilient, and sustainable, and to promote the circular economy model (Carnemolla et al., 2021; United Nations, 2015).

An alternative to commercial insulating materials is insulating elements realized by reusing end-of-life household materials (EoLHM) such as packaging and clothes. In the literature, several studies investigated the properties of EoLHM, but a comprehensive and systematic analysis is still missing (Drochytka et al., 2017; Ibrahim & Meawad, 2018; Kudzal et al., 2018; Mansour & Ali, 2015; Neri et al., 2021a and 2021b; Secchi et al., 2015).

The aim of this paper is the thermal and acoustic characterization of polyamide 6.6 waste (henceforth polyamide) obtained from the production of non-surgical face masks. Firstly, polyamide's thermal and acoustic properties have been determined experimentally. Then, the improvement of the building's indoor condition due to the installation of panels made of polyamide has been assessed through numerical simulations. These panels are intended installed indoors to allow for easy and fast building refurbishment interventions and also by unskilled people.

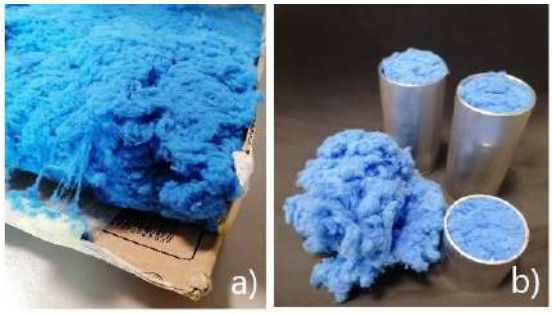

Fig. 1 – Test specimens for the thermal test a), and for acoustic tests b). For the thermal test, the material has been confined in a cardboard case. For the acoustic tests, the material in the samples was contained between two glass tissue discs to ensure that the front surface was normal to the axis of the tube

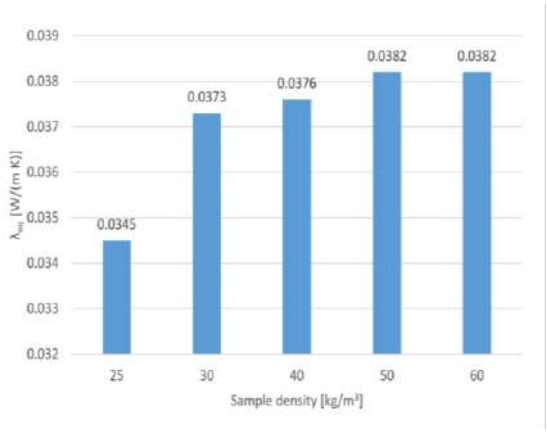

Fig. 2 – Measured equivalent thermal conductivity of polyamide

Indoor comfort embraces several aspects, such as thermal and acoustic comfort, which are the two aspects analyzed in this paper. Under steady-state conditions, heat transfer through a wall is described by the relationship:

$$q = A \cdot \Delta T / (\Sigma (s/\lambda)) \quad (1)$$

where q is the heat flux through the wall, A, s, λ are the surface, thickness, and thermal conductivity of the wall. ΔT is the difference in temperature measured on the panel surfaces. Conversely, under unsteady conditions, the heat flux q depends also on the wall heat capacity and position of the layers. In this study, the thermal conductivity of samples realized with polyamide at different densities has been measured employing the hot plate method with the guard ring.

When dealing with indoor acoustic comfort, one of the aspects to be evaluated is the reverberation time TR, which is related to the indoor sound quality in terms of echo effect and, consequently, vocal message intelligibility. Optimal TR values depend on the ambient' intended use, and reference values are specified in the UNI 11367 (UNI, 2010). TR is the time lapse in which the sound energy density decreases by 60 dB. It is determined by suddenly switching off a sound source and measuring the sound energy level variation. TR can be estimated according to the Sabins formula:

$$TR=0.16\ V/S \quad (2)$$

where V is the volume of the room, and S is the room sound absorption. The term S is defined as $S=\Sigma(\alpha \cdot A)$, where A is the surface extension, and α is the sound absorption coefficient of the room surfaces.

The sound energy balance on a surface impinged by sound power leads to:

$$1=\eta+\tau+\alpha \quad (3)$$

where η is the sound reflection coefficient, τ is the sound transmission coefficient, and α is the sound absorption coefficient.

Generally, for porous material such as the one investigated in this paper, the higher the density, the lower α, while the greater the thickness, the higher α. The sound absorption coefficient for a hard-backed element is defined as:

$$\alpha=1-|TL|^2 \quad (4)$$

where TL is the sound transmission loss, that is generally determined experimentally and is a function of τ according to:

$$TL=10 \cdot \log10(1/\tau) \quad (5)$$

In this paper, the sound absorption coefficient α and transmission loss TL have been determined by means of the impedance tube technique. This technique is suitable for R&D analysis but considers only waves that impinge the sample surface normally.

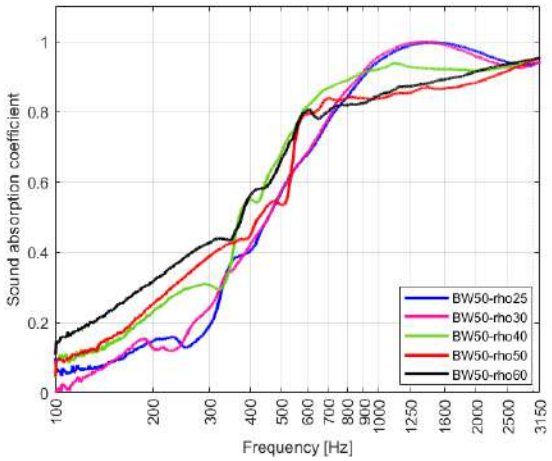

Fig. 3 – Sound absorption coefficient of the 50-mm-thick samples

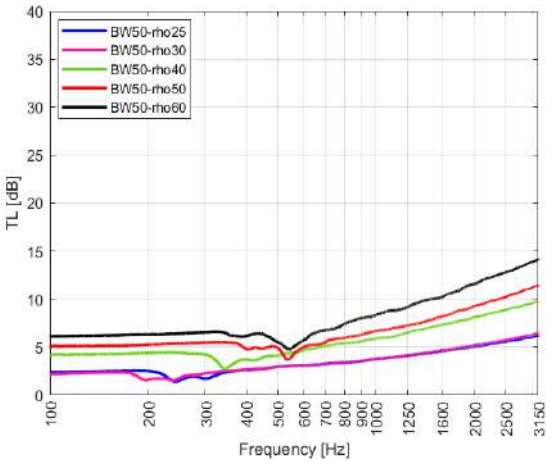

Fig. 5 – Sound transmission loss of the 50-mm-thick samples

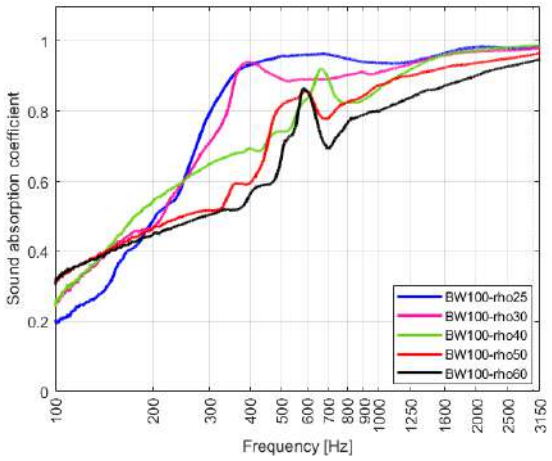

Fig. 4 – Sound absorption coefficient of the 100-mm-thick samples

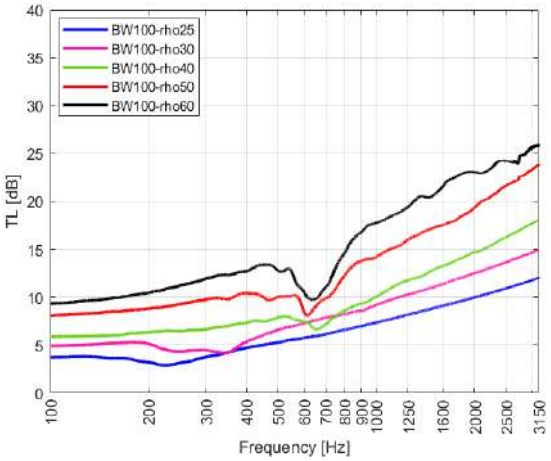

Fig. 6 – Sound transmission loss of the 100-mm-thick samples

2. Experimental Campaign

Since polyamide is a soft and porous material (see Fig. 1), its density depends on the packing degree, which is an important aspect in view of panel self-realization. To evaluate this aspect, the equivalent thermal conductivity λ_{eq} as a function of the density has been determined through the guarded hot plate method.

The test consisted in measuring the heat flow q obtained under a predefined temperature difference ΔT, and λ_{eq} is determined as:

$$\lambda_{eq} = (q \cdot s) / (A \cdot \Delta T) \quad (6)$$

where A and s are the surface and thickness of the same. Results are shown in Fig. 2.

Samples of different densities have been realized and tested in the impedance tube apparatus to determine the polyamide sound absorption coefficient α, and the sound transmission loss TL. The test apparatus consists of two tubes 4.6 cm in diameter connected to a test sample holder. Two microphones are placed on either side of the specimen (45 mm from each other). A source emitting a pink noise is placed at one end of the tube. A multi-channel Fast Fourier Transform (FFT) analyzer acquires the signals captured by the microphones.

The pressure and particle velocity of the travelling and reflected waves are determined by a MATLAB script implemented according to the E2611 ASTM standard (ASTM E2611, 2019). To assess the influence of the specimen's thickness, samples 50-mm and 100-mm thick have been realized and tested. The frequency range is between 100 Hz and 3150 Hz, according to the characteristics of the test apparatus.

Fig. 7 – The real case study, a classroom in the Raval neighbourhood in Barcelona: **a**) façade, **b**) interior with furniture, **c**) view from the balcony, and **d**) view of the opposite building

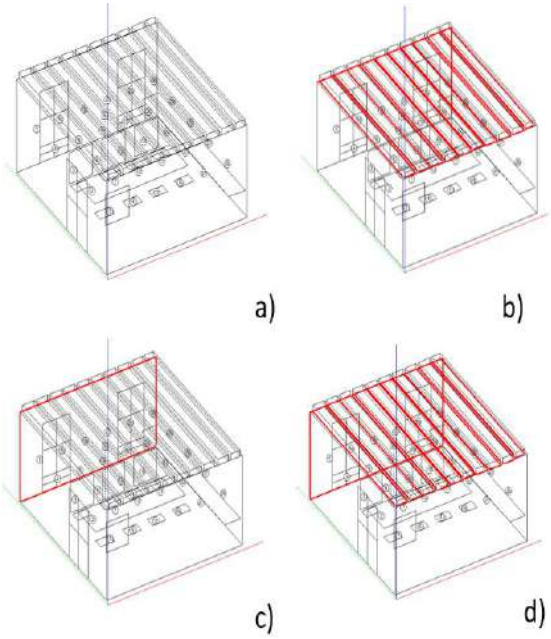

Fig. 8 – Scenarios considered in the numerical analysis: **a)** current configuration without panels (*Case00*), **b)** panels installed on the ceiling (*Case01*), **c)** panels installed indoors on the façade (*Case02*), **d)** panels installed indoors on both the façade and the ceiling (*Case03*)

Table 1 – Wall layers set in the numerical model defined with Energy+

Structure	Layer 1	Layer 2	Layer 3	Layer 4
Roof	T	XPS	HR	P
Internal wall	P	DIW	P	
Facade	P	DIW	P	
Basement	CLS_B	CLS_S	CLSM	T
Floor	P	HF	CLSM	T
Ceiling	T	CLSM	HF	P

Table 2 – Material properties set in the numerical model defined with Energy+

Material	s [m]	λ [W/(m K)]	ϱ [kg/m^3]	c [kJ/(kg K)]
Plaster	0.015	0.8	1600	1
Hollow bricks_R	0.5	0.24	800	1
Hollow bricks_F	0.3	0.24	800	1
CLS_S	0.1	0.9	1800	0.88
Dolomite_IW	0.15	1.75	2872	0.91
XPS	0.08	0.035	30	1.5
Tiles	0.01	0.208	530	1
CLS_M	0.05	1.1	1000	0.88
Dolomite_F	0.35	1.75	2872	0.91
CLS_B	0.3	2.4	2400	1

The lower and the upper working frequencies are determined according to:

$$fu<0.586 * c_{air}/d \quad (7)$$

$$d<0.586* c_{air}/fu \quad (8)$$

where c_{air} is the sound speed in the tube, and d is the tube diameter. Results are shown in Fig. 3 - 6.

3. Numerical Simulations

To assess how the panel made of polyamide and installed indoors on the walls and the ceiling affects indoor conditions, an acoustic and a thermal numerical model were set. Two open-source software solutions, Energy+ and Ramsete, were used.

In the numerical simulations, the panel is 10-cm thick, made of polyamide at 25 kg/m³ confined between two glass veil layers.

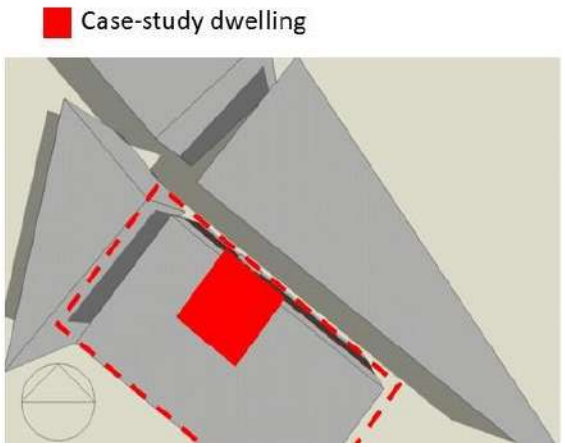

Fig. 9 – Model defined in Energy+. The building is modelled as a single thermal zone which includes another thermal zone related to the classroom. The other buildings participate in the shading effect

The models represent a classroom in the Raval neighborhood in Barcelona (see Fig. 7), where thermal and acoustic measurements were taken. The classroom is on the second floor of a building and is 5.1 x 5.8 x 3.0 m in dimension. The façade is 17 m² with two windows 2.6 x 1.1 m in dimensions. The ceiling is a typical Catalan structure with 30-cm-wide vaults. In the acoustic model (see Fig. 8), also the furniture is modeled, as it may affect the sound wave reflection and, in turn, the reverberation time.
Materials properties are listed in Tab. 1 and Tab. 2: some properties have been hypothesized, while the building owner provided others. The material vapor diffusion factor equal to 180 was chosen. The polyamide vapor diffusion factor equal to 1.254 according to CIBSE Guide A (CISBE, 2015) was chosen. The occupancy level is 0.38 persons/m², and air natural infiltration is considered.
Numerical simulations were performed for different scenarios in which the panel's position varied according to Fig. 8. Scenario *Case00* is representative of the current configuration without pan els. In contrast, panels are installed in the other scenarios: the panels are placed in the ceiling vaults in *Case01*, on the façade in *Case02*, and on both the ceiling and façade in *Case03*. The wall surface covered with panels varies according to the scenario: 29 m² for *Case01*, 17 m² for *Case02*, and 47 m² for *Case03*.

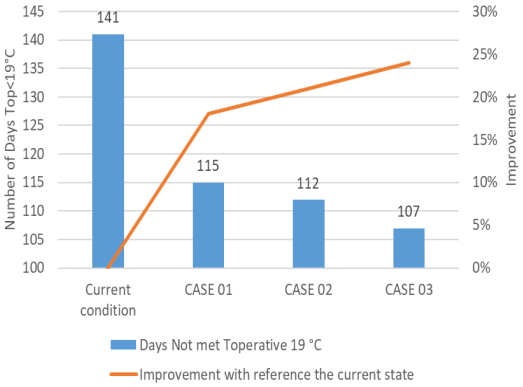

Fig 10 – Number of days when the indoor temperature is lower than 19°C, and improvement of the indoor operative temperature as a function of the panels' position. The panels are intended installed indoors

The model defined in Energy+ includes the building where the classroom is located (considered as two thermal zones) and the surrounding buildings that contribute to shading (see Fig.9). Results in Fig. 10 show the number of days when the indoor temperature is lower than 19 °C, and a heating system would be necessary to maintain an adequate indoor temperature.

Ramsete software is based on the Pyramid Tracing algorithm, and it can analyze problems in large enclosures or outdoors. It considers specular reflections over sound-absorbing surfaces. In the acoustic model, an omnidirectional sound speaker and 30 sound receivers uniformly distributed in the room have been set. In the acoustic analysis, polyamide is considered confined between two layers of glass veil - a very light material that does not affect the thermal and acoustic properties of the panel. Material-sound-absorbing coefficients are reported in Tab. 3, and they have been selected from the database of the software. For polyamide experimental data presented in this paper has been used.

In the classroom, acoustic tests were performed according to the ISO 16283-3:2016 standard (ISO 16283:2016) through the loudspeaker method. The indoor sound pressure level wasmeasured by a sound pressure meter LD-831-C fulfilling the standard IEC 60942 (IEC 60942:2017). Experimental data were used to verify whether the numerical model can predict the acoustic conditions in the

classroom correctly. Measured and estimated reverberation time *TR* are shown in Fig. 11, while the reverberation time estimated for the different panels' positions is reported in Fig. 12.

Table 3 – Sound absorption coefficients α of the materials set in the numerical model defined with Ramsete. Polyamide sound absorption coefficients relate to incident sound waves only

Material	31 Hz	63 Hz	125 Hz	250 Hz	500 Hz	1 kHz	2 kHz	4 kHz
Plaster (walls)	0.01	0.01	0.01	0.01	0.01	0.02	0.02	0.02
Window - slighlty open	0.4	0.8	0.8	0.8	0.8	0.8	0.9	0.99
Glass (windows)	0.21	0.42	0.35	0.25	0.18	0.12	0.07	0.04
Floor	0.02	0.03	0.03	0.03	0.04	0.04	0.04	0.04
Wood (window)	0.06	0.12	0.17	0.2	0.21	0.22	0.18	0.12
Painted wood (ceiling)	0.06	0.11	0.11	0.12	0.12	0.12	0.1	0.1
Plaster on wood (ceiling)	0.02	0.03	0.04	0.05	0.06	0.07	0.07	0.06
Chairs	0.08	0.1	0.15	0.74	0.82	0.9	0.9	0.78
Polyam.- 25 kg/m^3 - 10 cm	0.03	0.1	0.26	0.62	0.96	0.94	0.98	0.9

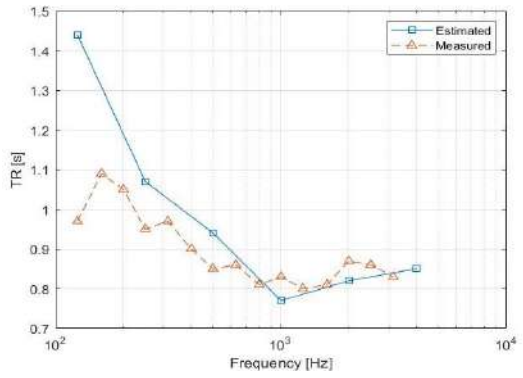

Fig. 11 – Comparison between estimated and measured reverberation time *TR* in the test case in Barcelona

4. Discussion

Through the analysis of experimental and numerical data, an assessment of whether polyamide is suitable for the realization of panels destined for building refurbishment was performed.

4.1 Experimental Results

Fig. 2 shows the measured equivalent thermal conductivity of polyamide as a function of density. Density does not affect the material's thermal properties significantly, and measured values are comparable to those of commercial insulation materials such as mineral wool. However, the best performance was shown by the lightest panel.

According to Fig. 3 and Fig. 4, density affects the material's acoustic properties in the low-middle frequency range. The typical trend for porous materials, with low values at low frequencies and high values in the high-frequency range, is detected. According to Fig. 3, lower sound absorption coefficients are measured for higher density values; indeed, compact wool behaves as a stiff spring that reflects the sound energy. Fig. 4 refers to samples 10-cm thick and shows an overall performance improvement in the low-frequency region for all the tested samples thanks to the greater thickness. Fig. 5 and Fig. 6 show the sound transmission loss *TL* results. In Fig. 5, all five samples feature a similar trend, and higher panel density entails lower *TL*: high-density samples reflect the sound energy backwards, thus reducing the sound transmitted component.

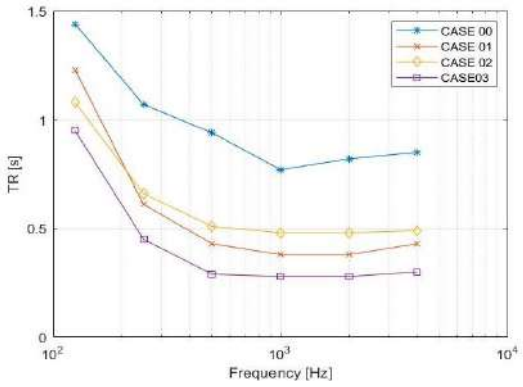

Fig. 12 – Reverberation time *TR* estimated in the different scenarios for the test case in Barcelona

In Fig. 6, the sound absorption performance is better throughout the entire frequency range thanks to the sample thickness of 100 mm, and the five plots are more distant from each other.

4.2 Numerical Results

As regards the numerical analysis, Fig. 10 shows that the presence of panels installed indoors improves the operative temperature. The number of days when the indoor operative temperature is

lower than 19 °C decreases depending on the panel position. When considering panels installed only on a surface, i.e., *CASE01* and *CASE02*, the best condition is represented by the panel installed on the façade; indeed, this is the only wall facing the external environment. The more significant improvement belongs to scenario *CASE03* with panels installed on both the façade and the ceiling, and this is an expected result since a wider surface is treated. However, a weak point is possible water condensation in the wall, and this requires the installation of a vapor barrier.

As the numerical and measured results in Fig. 11 are comparable, the numerical model defined in Ramsete can be used to design interventions for improving indoor acoustic comfort. Fig. 12 shows that when the panels are installed indoors, *TR* is lower than 0.62 s, which corresponds to the optimal reverberation time for environments destined for speech and sports activities suggested by the UNI 11367 (UNI, 2010). The greatest improvement is detected between 200 and 1200 Hz, where *TR* reduces by 0.5 s. Results are comparable for *CASE01* and *CASE02*, but panels installed on the ceiling are more effective at low frequency, while the panel on the internal surface of the façade is more effective in the middle-high frequency range. The best improvement is detected for *CASE03*, with panels installed both on walls and ceiling, and it is coherent with the theory. However, sound-absorption improvement is expected when considering polyamide properties for diffuse sound, but this data is obtainable only by tests performed in the sound reverberation room.

5. Conclusion

The study investigated experimentally and numerically the thermal and acoustic properties of polyamide 6.6. Experimental results have shown that polyamide has interesting properties, which are comparable to commercial insulating materials. Therefore, it could be used for realizing building elements. Results show that density influences sound properties significantly: low-density panels show better thermal insulation (λ_{eq} between 0.034 and 0.0382 W/(m K)) and sound insulation properties (α higher than 0.9 for frequency higher than 400 Hz), while high-density panels show better sound insulation properties which depend also on thickness.

Numerical results show that the panels when installed indoors on the walls and ceiling increase the indoor operative temperature in winter and reduce the reverberation time. Therefore, this material is suitable for building thermal and acoustic refurbishment. However, further analysis is needed to evaluate the thermal performance in summer, sound performance related to the diffuse sound field, material containment, and fire resistance.

Acknowledgement

The contribution has been supported by TAČR NCK CAMEB nr. TN01000056/06, and by the Department of Mechanical and Industrial Engineering of the University of Brescia through the MetATer PRD project.

Nomenclature

A	surface (m^2)
c	specific heat (J/(kg K))
c_{air}	sound speed in air (m/s)
d	distance between microphones (m)
f_l	lower working frequency (Hz)
FFT	Fast Fourier Transform
f_u	upper working frequency (Hz)
q	heat flux (W)
R	thermal resistance (m^2K/W)
s	thickness (m)
S	total absorption surface (m^2)
T	temperature (°C)
TL	sound transmission loss (-)
Top	indoor operative temperature (°C)
TR	reverberation time (s)
V	volume (m^3)
α	sound absorption coefficient (-)
λ	thermal conductivity (W/(m K))
λ_{eq}	equivalent thermal conductivity (W/(m K))
η	sound reflection coefficient (-)
ϱ	density (kg/m^3)
τ	sound transmission coefficient (-)

References

ASTM. 2019. "ASTM E2611 Standard Test Method for Normal Incidence Determination of Porous Material Acoustical Properties Based on the Transfer Matrix Method."

BSI. 2016. "BS EN ISO 16283-3:2016 Acoustics — Field measurement of sound insulation in buildings and of building elements — Part 3: Façade sound insulation."

Carnemolla, P; S. Robinson, and K. Lay. 2021. "Towards inclusive cities and social sustainability: A scoping review of initiatives to support the inclusion of people with intellectual disability in civic and social activities." *City, Culture and Society* 25: 100398. doi: https://doi.org/10.1016/j.ccs.2021.100398

CIBSE. 2015. "CIBSE - Guide A - Environmental design."

Drochytka, R., M. Dvorakova, and J. Hodna. 2017. "Performance Evaluation and Research of Alternative Thermal Insulation Based on Waste Polyester Fibers." *Procedia Engineering* 195: 236–243. doi: https://doi.org/10.1016/j.proeng.2017.04.549

González-Eguino, M. 2015. "Energy poverty: An overview." *Renewable and Sustainable Energy Reviews* 47: 377-385. doi: https://doi.org/10.1016/j.rser.2015.03.013

Ibrahim, S., and A. Meawad. 2018. "Assessment of waste packaging glass bottles as supplementary cementitious materials." *Construction and Building Materials* 182: 451–458. doi: https://doi.org/10.1016/j.conbuildmat.2018.06.119

IEC. 2017. "IEC 60942:2017 - Electroacoustics – Sound calibrators"

Kudzal, A., S. Pliestic, D. Filipovic, I. Kovacev, K. Copec, Z. Janjecic, and D. Bedekovic. 2018. "Mechanical properties of ten-egg boxes made of different materials." *Journal of Food Science and Technology* 55: 1325–1330. doi: https://doi.org/10.1007/s13197-018-3043-z

Mansour, A., and S. Ali. 2015. "Reusing waste plastic bottles as an alternative sustainable building material." *Energy for Sustainable Development* 24: 79–85. doi: https://doi.org/10.1016/j.esd.2014.11.001

Neri, M., M. Pilotelli, M. Traversi, E. Levi, E. A. Piana, M. Bannò, E. Cuerva, P. Pujadas, and A. Guardo. 2021a. "Conversion of end-of-life household materials into building insulating low-cost solutions for the development of vulnerable contexts: Review and outlook towards a circular and sustainable economy." *Sustainability* 13(8): 4397. doi: https://doi.org/10.3390/su13084397

Neri, M., E. Levi, E. Cuerva, F. Pardo-Bosch, A. G. Zabaleta, and P. Pujadas. 2021b. "Sound absorbing and insulating low-cost panels from end-of-life household materials for the development of vulnerable contexts in circular economy perspective." *Applied Sciences* 11(12): 5372. doi: https://doi.org/10.3390/app11125372

Polyamide 6.6 characteristics. Available at https://designerdata.nl/materials/plastics/thermo-plastics/polyamide-6.6. Accessed on the 15th of April 2022.

Secchi, S., F. Asdrubali, G. Cellai, E. Nannipieri, A. Rotili, and I. Vannucchi. 2015. "Experimental and environmental analysis of new sound-absorbing and insulating elements in recycled cardboard." *Journal of Building Engineering* 5: 1–12. doi: https://doi.org/10.1016/j.jobe.2015.10.005

United Nations. 2015. "Transforming Our World: The 2030 Agenda for Sustainable Development."

UNI. 2010. "UNI 11367:2010 Acoustic classification of building units - procedure for evaluation and verification in situ."

Assessment of Demand-Side Management on the Performance of a Single-Dwelling Mechanical Ventilation Plus Radiant Floor System

Paolo Bonato – Eurac Research, Italy – paolo.bonato@eurac.edu
Anton Soppelsa – Eurac Research, Italy – anton.soppelsa@eurac.edu
Marta Avantaggiato – Eurotherm, Italy – marta.avantaggiato@eurotherm.info
Roberto Fedrizzi – Eurac Research, Italy – roberto.fedrizzi@eurac.edu

Abstract

This paper focuses on the profitability of demand-side management strategies developed for a single-dwelling mechanical ventilation plus radiant floor system. Energy savings and comfort indicators are quantified for a number of control options, including demand-controlled ventilation and temperature setbacks. The assessment is based on numerical energy simulations conducted in TRNSYS for the climate of Bolzano (Italy). To perform the simulations, numerical models of the energy system and the reference dwelling were developed. Based on the analysed climate and building, it was found that demand-side management strategies can have a significant impact on the energy consumption and time distribution of energy loads: demand control ventilation allows the achievement of consistent energy savings in the electrical consumption of the fans (up to 37 %), whereas the use of an adaptive dehumidification setpoint can lead to savings within the range of 10 % in summer electrical consumption. The use of non-occupancy temperature setbacks does not show a significant impact on the annual thermal demand, although the time pattern of the loads is considerably affected, with a cascade effect on the performance of the air-to-water heat pump. The use of the climatic curve parameters at the generator allows an improvement of the electrical performance of the heat pump, increasing the SCOP of more than 20 %.

1. Introduction

The smart management of heating, ventilation and air conditioning systems is an active area of research, as new controls are developed to reduce energy consumption and improve occupant hygrothermal comfort. Innovative solutions are moving on from simple strategies, providing an excess of ventilation to deal with poor or no information available on occupation, to providing just enough ventilation to fulfil comfort needs, thus avoiding waste of thermal and electric energy. This trend is favored by the availability of incrementally cheaper sensors and control hardware (Araújo et al., 2020), allowing for a detailed monitoring of the operation conditions and control of system components.

This paper investigates the impact of different control strategies on the performance of a single-dwelling mechanical ventilation and radiant floor system in the context of multi-family houses in Bolzano (Italy). Although a vast literature already exists on the topic of optimization of HVAC operational parameters (Gholamzadehmir et al., 2020; Selmat et al., 2020), this paper aims to contribute by providing a fresh perspective, since:

- it focuses on management strategies that could be easily adopted by using sensors and control hardware already on the market;
- it focuses on the growing sector of renovated buildings, where the use of mechanical ventilation and heat pumps is becoming a wide-spread solution;
- the impact of single-control choices are analysed considering not only the energy domain, but also IAQ and thermal comfort;
- the performances of a real ventilation unit are measured in the laboratory and used to calibrate the numerical model to provide more reliable results.

This study was performed as part of the FESR project NewAir, which hosted the development of an innovative mechanical ventilation unit with dehumidification.

2. Methodology

To assess the energy and comfort signatures of the controls presented in the following, annual energy numerical simulations were performed with dynamic energy simulation software (TRNSYS (Klein et al., 1979)), coupled with a plug-in (TRNFLOW) modeling airflows and pollutant transport. Numerical models are elaborated accordingly after the following steps:

- Development of the thermal model of a renovated flat including a heat-pump-based energy system and radiant floors;
- Development and calibration of the numerical model of a ventilation based on the performance of a prototype tested in the laboratory.

Concerning Key Performance Indicators, the impact of single control strategies is assessed based on a set of indicators, which are (I) heat pump thermal energy generation, (II) heat pump electricity consumption, (III) electricity consumption of fans and refrigerant cycle in the ventilation unit, (IV) overheating / undercooling for thermal comfort and (V) occupancy hours distribution by CO_2 concentration classes according to (EN 16798-1, 2019).

Table 1 – CO_2 concentration thresholds for IAQ (EN 16798-1, 2019)

Class	Living room [ppm]	Bedroom [ppm]
1	< 950	< 780
2	950 < CO_2 < 1200	780 < CO_2 < 950
3	1200 < CO_2 <1750	950 < CO_2 < 1250
4	> 1750	> 1250

2.1 Reference Thermal Zone

The dwelling studied in this work is located in a multi-family house in Bolzano (Italy) and has a heated floor area equal to about 68 m². The apartment is divided into a living room, two bedrooms, a kitchen, a bathroom and a corridor.

The thermal model of the dwelling is divided into six different thermal zones (one per room), each containing an air node. Table 2 lists the main parameters of such a model. The occupancy profile is developed based on a three-state model: a person can be "away" or "at home and sleeping" or "at home and active". Depending on the occupancy status, different generation rates for internal gains (metabolism, use of appliances and lighting) and CO_2 emission are considered.

Table 2 – Thermal model parameters

Properties of building assemblies		
Glass, g-value	0.63	-
Glass, U-value	0.81	W/(m²K)
Window frame, U-value	0.93	W/(m²K)
External walls, U-value	0.35	W/(m²K)
Ventilation and infiltrations		
Design ventilation rate	0.75	ach
Infiltration rate at 50 Pa	1.5	ach
Internal gains and occupancy rate		
Occupants "home and active" (1.2 met (SIA, 2015)), latent gains	0.0153	g/s/pers
Occupants "home and active" (1.2 met (SIA, 2015)), sensible gains	76	W/pers
Appliances installed power (standby consumption: 10 %) (SIA, 2015)	10	W/m²
Lighting installed power (SIA, 2015)	2.7	W/m²
Crowding index	0.044	pers/m²
Full occupancy	3	pers
Thermostat settings		
Air temperature - Space heating	21	°C
Air temperature - Space cooling	25	°C
CO_2 transport model		
CO_2 generation, occupants "home and active" (based on (Persily & De Jonge, 2017))	0.009039	g/s/pers
CO_2 generation, occupants "home and sleeping" (based on (Persily & De Jonge, 2017))	0.007123	g/s/pers
Outdoor CO_2 concentration	400	ppm
Radiant floors		
Winter performance (room at 20 °C, water inlet at 30 °C, DT = 5 K)	36	W/m²
Summer performance (room at 26 °C, water inlet at 16 °C, DT = 5 K)	30	W/m²
Air-to-water heat pump		
COP (A7/W35)	4.17	-
EER (A35/W7)	3.02	-

The energy system is based on a 3 kW air-to-water reversible heat pump, which is able to work at partial loads in the range of 40-100 % compressor

speed. For the sake of simplicity, it is assumed that domestic hot water is prepared with an additional heat generator. The heat pump numerical model is based on the performance map of a commercial product, including multiple air temperatures, water temperatures and compressor speeds. The space heating and cooling network is composed of the heat pump, a small thermal buffer and a radiant floor system. It is assumed that the thermal plant is activated without any restriction on the time of the day, and that the heating season spans the 1st of October to the 15th of April. It is assumed that sensors are installed in all rooms, except for the corridor and bathroom, to monitor temperature, humidity and CO_2 level. The radiant floor works both in heating and cooling working modes. The water loops in living room and bedrooms are managed based on the local temperature measures, whereas the ones in the kitchen and bathroom are controlled based on the living room temperature reading and can provide only heating. The supply temperature to the radiant floors is regulated based on the climatic curves shown in Fig. 1, whereas the water flow rate is governed in each loop by on-off valves activated when the air temperature thresholds are exceeded.

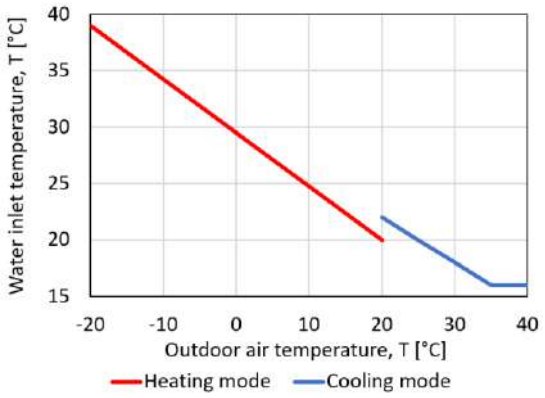

Fig. 1 – Climatic curves applied to the radiant floor system

An annual dataset of climate data was generated from the Meteonorm database for the locality of Bolzano (Italy). This dataset contains hourly values of climatic variables, such as convective air temperature and humidity, solar irradiation and intensity of wind for a typical meteorological year.

2.2 Mechanical Ventilation Unit

In the FESR project "NewAir", a single-dwelling mechanical ventilation unit was developed to supply fresh air, provide dehumidification during summertime and support the distribution of space heating/cooling thermal power. This unit is double flow and integrates a high-efficiency heat recovery unit, a water-to-air heat exchanger, as well as a refrigerant cycle that is used for dehumidification. In more detail, the condenser and the evaporator of the refrigerant cycle are crossed by the supply airflow and a pre-cooling coil is also activated whenever dehumidification is required. Two dampers regulate the heat recovery bypass and the amount of indoor air that is circulated.

The numerical model of the ventilation unit consists of multiple TRNSYS Types, each simulating an energy component of the ventilation unit. Selected parameters were tuned to replicate the performance of the ventilation unit developed in the NewAir project as closely as possible. More specifically, the data sources for the calibration process were:

- Laboratory measures for (1) external pressure - airflow rate - electrical consumption curves, (2) thermal efficiency of the bypass to the heat recovery and (3) dehumidification capacity;
- Online calculators and datasheets from manufacturers for the thermal performances of heat recovery and water coil.

Table 3 lists the maximum airflow rates and the fan consumption in different working modes, derived assuming external pressure losses equal to 100 Pa at 200 m^3/h.

Table 3 – Working modes of the ventilation unit

Working mode	Fresh air [m^3/h]	Circulated air [m^3/h]	Supply air [m^3/h]	Fan cons. [W]
Renewal	140	-	140	110
Circulation	-	200	200	75
Renewal and circulation	100	100	200	124

The ventilation unit is connected to the different indoor spaces by three separate aeraulic networks (supply air, return air and air circulation air), as shown in Fig. 2. The airflow is split among living room and bedrooms based on the floor area.

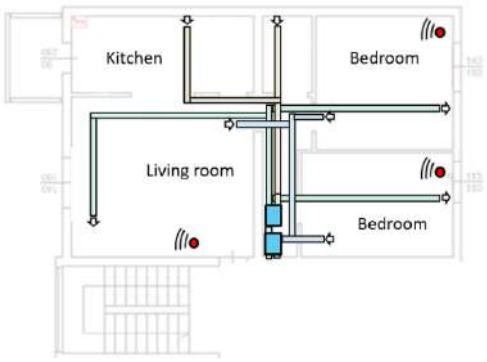

Fig. 2 – Schematic of the aeraulic networks in the apartment. Return air in orange, supply air in green, air circulation in blue

2.3 Demand-Side Management

The demand-side management of energy systems aims at optimizing the use of energy by acting on the consumption picture, that is, on energy use, energy quality or load time-patterns. In the context of a single-dwelling mechanical ventilation plus radiant floor system, this study quantifies the effects of the following control management strategies designed to reduce energy waste:

- Implementation of demand-controlled ventilation (DCV) (Emmerich & Persily, 2001), that is, the modulation of the fresh air intake to meet the ventilation demand of the zone. In this work, multiple options are compared: (1) occupancy-based DCV strategy, where the control hardware is reactive to human presence through, for example, PIR sensors or geofencing, and triggers air renewal at nominal airflow rate when the apartment is occupied; (2) CO_2-based DCV strategy, where the fresh air intake is modulated based on the CO_2 concentration. In this case, the system can work in on-off mode based on a single hysteresis, but could also implement a multistep or a proportional control. In the case of multiple CO_2 sensors, the most critical reading is considered for the fresh airflow calculations. Fig. 4 shows the selected CO_2-based DCV strategies and the related CO_2 thresholds, which were identified based on (EN 16798-1, 2019) limits for IAQ Category I.
- Use of moving thresholds to trigger the dehumidification function of the ventilation unit during the cooling season. A constant relative humidity threshold is a common way of managing dehumidification units, but an alternative solution could be dividing the goals of guaranteeing comfort conditions to occupants and avoiding condensation over the radiant floors. To assess such a strategy, a comparison is performed between a baseline scenario (constant setpoint equal to 55 % relative humidity) and an advanced scenario where multiple movable thresholds are implemented: (1) a limit of 60 % relative humidity and 12 g/kg absolute humidity is applied when the dwelling is occupied to guarantee acceptable comfort (Class II comfort according to (EN 16798-1, 2019); (2) a limit in absolute humidity is applied to avoid condensation based on the working conditions of the radiant floors (i.e., temperature at the inlet of the radiant system). When multiple criteria apply at the same time, the strictest threshold is considered.
- Use of moving thermostat temperature setpoints. A 2 K setback is applied to the air temperature thresholds in two separate circumstances, that is, when the apartment is not occupied (non-occupancy setback) or between 23:00 and 06:00 (night setback). To demonstrate, Fig. 4 shows the air temperature setpoints for a single day.

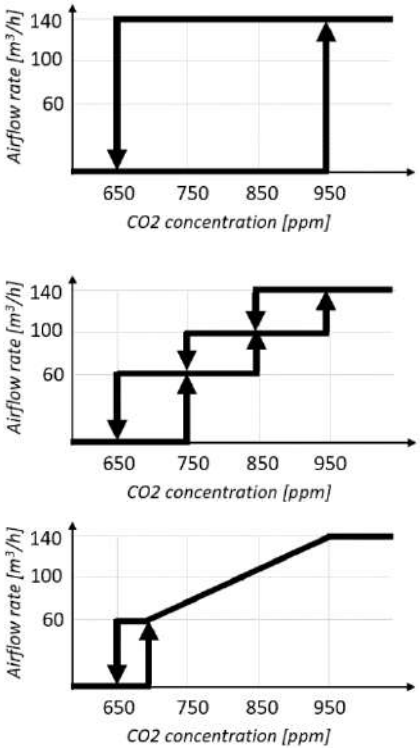

Fig. 3 – CO_2-based DCV with on-off hysteresis (top), multistep modulation (middle) and proportional modulation (bottom)

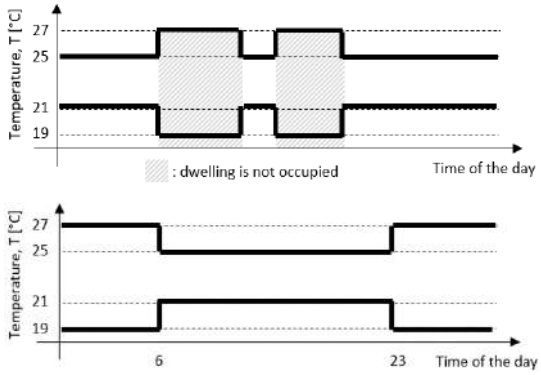

Fig. 4 – Temperature setpoints with non-occupancy setbacks (top) and night setbacks (bottom)

- The implementation of the climatic curve parameters directly to the heat pump rather than to the radiant collectors during wintertime is to produce heat at the required temperature and to avoid a pointless reduction in the heat quality with thermostatic valves. The efficiency of heat pumps is indeed correlated to the temperature level of the water in the condenser, with higher Coefficients of Performance (COPs) at lower water temperatures.

3. Results and Discussion

This section presents the numerical results of the energy simulations divided by analyzed strategy.

3.1 Demand-Controlled Ventilation

Several DCV strategies are compared with a baseline where air renewal is always active. Table 4 reports the numerical results for different scenarios. The air quality is medium-high in all simulated cases. Slightly worse results are found for DCV strategies based on CO_2 concentration, but also in this case, C1 and C2 categories are vastly more populated than C3 and C4. Space heating and cooling thermal demands show limited variations, with higher heating demand and lower cooling demand at higher air change rates. During wintertime, the effect of the additional heat losses due to overventilation is indeed limited by the high-efficiency heat recovery unit. During summertime, higher air change rate may provide at times some benefit in removing the excess heat from indoor spaces, thus reducing the active cooling load. A more evident impact is registered on dehumidification, since the removal of indoor-generated humidity is also influenced by the hygienic air change. DCV strategies are indeed linked to an increase in the consumption of the refrigerant cycle in the range of 11 % to 20 % with respect to the baseline. The electrical consumption of the fans is reduced in the range of -17 % to -38 % in the DCV scenarios, as a result of the lower air volumes exchanged throughout the year. The best- performing DCV strategies are the ones based on CO_2 concentration, since CO_2 generation is dependent on the number and the activity of occupants and thus the air change can be more sharply adapted to the effective demand for air change. Among CO_2-based strategies, no significant difference is found between multistep and proportional control, whereas the on-off strategy is outperformed, as it cannot modulate the airflow and thus is less flexible than the others. Neither overheating nor undercooling issues are found in any of the tested scenarios. The annual HVAC electrical consumption is reduced by DCV between -6 % and -13 % compared with the baseline, but it has to be noted that the advantages of such strategies may vary significantly depending on the occupancy patterns of spaces (IEA, 1997).

Table 4 – Numerical results for scenarios (1) baseline, (2) DCV based on occupancy, (3) DCV CO_2 based with on-off hysteresis, (4) multistep modulation and (5) proportional modulation

	Annual energy demand						CO_2 classes			
	Q_{heat}	Q_{cool}	W_{fan}	W_{rf}	W_{hp}	W_{tot}	C1	C2	C3	C4
	kWh	kWh	kWh	kWh	kWh	kWh	%	%	%	%
1	3333	1515	942	186	1425	2553	44	40	16	0
2	3333	1519	778	207	1423	2408	44	40	17	0
3	3320	1547	674	233	1424	2331	40	42	18	0
4	3316	1535	587	229	1417	2232	38	42	20	0
5	3318	1529	591	224	1416	2231	38	43	19	0

3.2 Moving Thresholds for Dehumidification

Fig. 5 shows the numerical results of the energy simulations for the cooling season: the use of mobile thresholds is compared with a baseline with a constant humidity setpoint equal to 55 % relative humidity. As may be seen, the use of moving thresholds allows the achievement of significant energy savings (about -13 % total electrical consumption). The

impact is not limited to the refrigerant cycle consumption (-40 %), but extends to fan consumption (-4 %) and active cooling demand (-9 %).

The active dehumidification triggers the "renewal and circulation" mode of the ventilation unit, which provides higher airflow rates to maximise the dehumidification effect, but also increases the fan consumption. Dehumidification is also linked to the active cooling load, since before entering the refrigerant cycle, the supply airflow is pre-cooled by a water coil as described above, thus generating a thermal load for the heat pump. The lower electrical consumption of refrigerant cycle, fan and heat pump points to a less frequent use of active dehumidification. No significant difference is found in terms of air quality and thermal comfort. It has to be noted that the working conditions of the radiant floor, and thus the humidity threshold for active dehumidification, will depend on the intensity of the cooling load. In this sense, more challenging conditions for the radiant floor during summertime will represent a smaller possibility of achieving savings by using a movable setpoint.

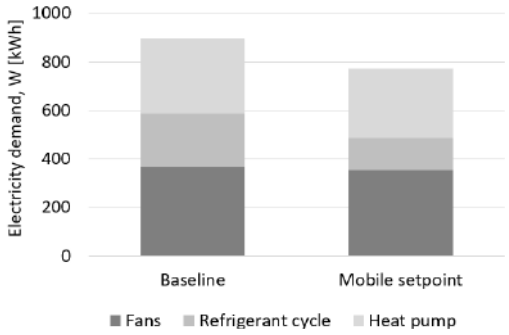

Fig. 5 – Electrical consumption during the cooling season

3.3 Non-Occupancy and Night Temperature Setback

The use of temperature setbacks is assessed by comparing a baseline scenario where the setpoints remain unvaried to the use of a 2 K setback during non-occupancy periods or during night-time. In the non-occupancy scenario, the setback is applied every time the dwelling is empty, which is equal to about 19 % percent of the year, or 1680 hours/year, divided into events that are mostly 1 to 4 hours long for the studied occupancy schedule. The night setback is applied for about 29 % of the year, or 2555 hours/year, in events that are each 7 hours long.

Fig. 6 and Fig. 7 show the monthly thermal energy demand and the percentage variation of heat performance indicators SCOP and SEER with respect to the baseline. As may be seen, the use of the temperature setback leads only to a limited reduction of the thermal demand (in the range of -1 % to -5 % on an annual basis), likely due to the fact that the setback is applied only for limited periods (especially in the non-occupancy scenario) and the thermal losses of the building are minimized by fair envelope properties and low ventilation/infiltration heat losses. The annual electricity consumption of the heat pump is reduced by a factor of -3 % in the non-occupancy setback scenario, and -12 % in the night setback scenario. This is only partially connected to the reduction of the thermal load, since the performance of the heat pump is also affected by the setbacks, as shown in Fig. 6. More specifically, the use of non-occupancy setbacks leads to better SEER during summertime, whereas the use of the night setback leads to higher SCOPs in winter and lower SEERs in summer.

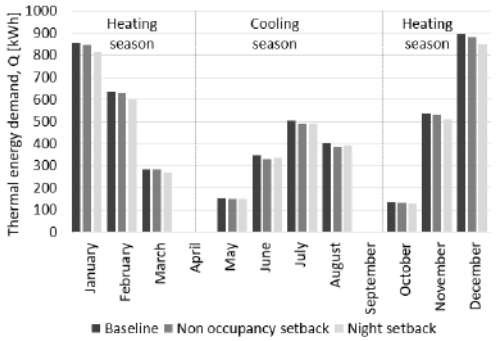

Fig. 6 – Monthly thermal energy demand

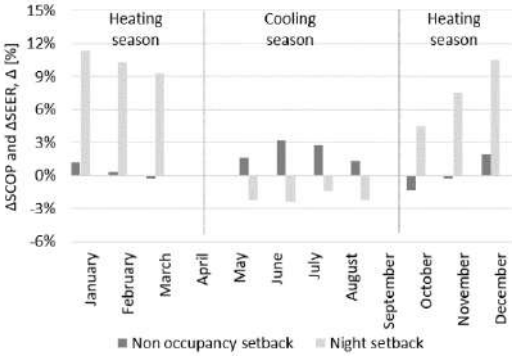

Fig. 7 – SCOP and SEER variation in setback scenarios

To better understand the underlying causes, the hourly daily averages of the thermal energy produced by the heat pump in heating and cooling are

shown in Fig. 8 for the months of January and July. Even though the thermal loads do not significantly vary in absolute terms, as discussed above, the use of setbacks causes a massive impact on the time patterns of thermal energy generation. In the non-occupancy setback scenario, the load profile tends to differ from the baseline during the daytime when occupants are mostly away and a peak in energy demand is registered at around 18-20 h around the time when the dwelling is be occupied again.

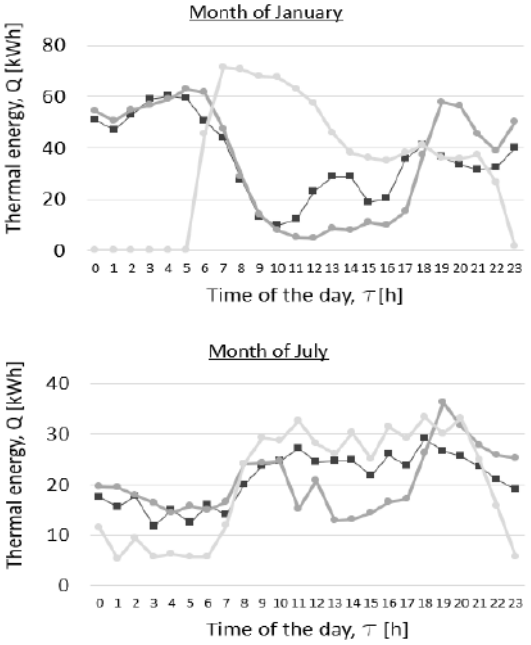

Fig. 8 – Hourly averages of heat pump energy generation

As expected, the use of night setback leads to lower thermal loads during the night, but most of the energy is then delivered during the daytime. The variation of the time patterns for energy generation has quite a significant effect on the air-to-water heat pump performances, since the external air temperature varies throughout the day, with generally higher temperatures during the day (better COPs and worse EERs) and lower temperatures during the night (lower COPs and higher EERs).

Thermal comfort is maintained at all times, although it is found that, when setbacks are applied, air heating/cooling is called on to support the radiant floor, which has a slower response to changing temperature setpoints due to the thermal capacity of the screed.

3.4 Implementation of Climatic Curve at the Generator

A baseline scenario, where the heat pump produces warm water at 40 °C and a thermostatic valve controls the inlet temperature to the radiant floors, is compared with an advanced scenario, where the climatic curve is implemented directly at the heat pump to avoid depreciation of the heat quality.

Table 5 – Performances in baseline and advanced scenarios

Description	Q_{heat}	W_{hp}	SCOP	
	kWh	kWh	-	Δ %
Baseline	3315	1150	2.88	-
Advanced	3226	863	3.74	23 %

As shown in Table 5, the thermal load in the baseline is higher, mostly due to the more intense thermal losses from the water distribution system (about +100 kWh/y). It is also found that applying the climatic curve at the generator leads to a significant improvement in the electrical performances of the heat pump, with a SCOP increasing from 2.9 to 3.7, about +23 % percentage improvement. This is due to the better working conditions of the heat pump, which is not required to produce water at 40 °C, but can profit from a lower-temperature energy demand. It is, however, remarked that state-of-the-art heat pumps can usually offer some form of climatic control. In this case, the simulation results simply reflect the importance of selecting the most appropriate climatic curve based on type of terminals and energy performance of the dwelling to avoid energy waste.

4. Conclusions

This paper presents a study on the performance of different demand-side management strategies applied to a ventilation system plus radiant floor system in the climate of Bolzano.

Based on the analyzed building and climate, the implementation of DCV strategies shows good potential for reducing the electrical consumption of fans (up to -38 %) without worsening the indoor air quality. Space heating and cooling thermal demand are not significantly affected, whereas a moderate impact is registered on dehumidification. It is found

that the use of moving setpoints could be a valid strategy to adapt the operation of the dehumidification system to the dehumidification load and reduce the summer energy consumption (-10 % for the studied conditions). The use of non-occupancy or night setbacks does not lead to significantly different annual energy demands, but a considerable impact is found on the time distribution of the thermal loads, with a cascade effect on the performance of the heat pump. More specifically, night setbacks allow the thermal loads to be shifted to the daytime, with a positive effect on the winter performances of the heat pump and a negative effect in summer. Finally, the implementation of a climatic curve at heat pump level allows the achievement of lower heat losses from the distribution system and a significant improvement in the heat pump performance. Overall, it was found that air change, thermal load and dehumidification are interconnected: changes in the control strategies looking at one domain at the time may lead to suboptimal solutions. In addition, it was found that the performance of the heat pump is massively influenced by the controls of the heating/cooling emission system and that there are options for load shifting that could be synergically exploited by photovoltaics. Far-reaching integrated control logics that can better capture the overall impact of single-control choices to reach one or multiple goals are to be implemented to achieve significant energy savings, while preserving optimal comfort conditions. Future studies will focus on the use of Model Predictive Control (MPC) based on forecasted weather conditions and dwelling loads.

Acknowledgement

The research presented in this paper is supported by funding from the European Regional Development Fund, through the operational programme POR FESR 2014-2020 of the Province of Bolzano, under the project number FESR 1116, named: NEW-AIR - Nuovo approccio per una qualità degli ambienti interni energeticamente efficiente: ricerca e aziende fanno sistema in Alto Adige.

Nomenclature

Symbols

HVAC	Heating, Ventilation and Conditioning
IAQ	Indoor Air Quality
Q	Thermal energy demand, [kWh]
SCOP	Seasonal Coefficient of Performance, [-]
SEER	Seasonal Energy Efficiency Ratio, [-]
W	Electricity consumption, [kWh]

Subscripts/Superscripts

cool	referred to cooling energy
fan	referred to the fans
heat	referred to heating energy
hp	referred to the heat pump system
rf	referred to refrigerant cycle

References

Araújo, T., L. Silva, and A. Moreira. 2020. "Evaluation of Low-Cost Sensors for Weather and Carbon Dioxide Monitoring in Internet of Things Context." *Internet of Things* 1(2): 286-308. https://doi.org/10.3390/iot1020017

CEN. 2019. *EN 16798-1. 2019. Energy performance of buildings - Ventilation for buildings - Part 1.*

Emmerich, S., and A. K. Persily. 2001. "State-of-the-art Review of CO2 Demand Controlled Ventilation Technology and Application." *NISTIR* 6729.

Gholamzadehmir, M., C. Del Pero, S. Buffa, R. Fedrizzi, and N. Aste. 2020. "Adaptive-predictive control strategy for HVAC systems in smart buildings - A review." *Sustainable Cities and Society* 65. https://doi.org/10.1016/j.scs.2020.102480

IEA, International Energy Agency. 1997. "A summary of IEA Annex 18 - Demand Controlled Ventilating Systems"

Klein, S. A., et al. 1979. "TRNSYS 17, transient system simulation program." University of Wisconsin, WI, USA, www.trnsys.com

Persily, A., and L. De Jonge. 2017. "Carbon dioxide generation rates for building occupants." *Indoor air* 27(5): 868-879. https://doi.org/10.1111/ina.12383

Selmat, H., M. F. Haniff, Z. M. Sharif, S. M. Attaran, F. M. Sakri, and M. Al'Hapis Bin Abdul Razak. 2020. "Review on HVAC System Optimization Towards Energy Saving Building Operation." *International Energy Journal* 20(3): 345-358.

SIA. 2015. *SIA 2024: Raumnutzungsdaten für die Energie- und Gebäudetechnik.*

Passive Design Strategies for the Improvement of Summer Indoor Comfort Conditions in Lightweight Steel-Framed Buildings

Nicola Callegaro – University of Trento, Italy – nicola.callegaro@unitn.it
Max Wieser – University of Trento, Italy – max.wieser@unitn.it
Giovanni Manzini – Cogi S.r.l, Italy – lorenzo.manzini@cogi.info
Ivan Kharlamov – Altai State University, Russia – kharlamov-1948@mail.ru
Rossano Albatici – University of Trento, Italy – rossano.albatici@unitn.it

Abstract

The market for lightweight construction systems is growing rapidly due to their potential in terms of prefabrication, ease of transportation and assembly. However, given their thermophysical properties, these types of structures present a limited thermal capacity that may reduce their performance in terms of comfort and energy consumption during the hot seasons. The present paper, through a series of computational fluid dynamics (CFD) simulations, offers a numerical assessment of the performance of an existing lightweight steel-framed building selected as a case study. The data required to perform the simulations are collected with a deep monitoring campaign and the building is analysed in its current state (actual conditions of use) and after the application of simulated passive cooling strategies. The role of natural ventilation, both day and night, is explored by investigating different opening/closing configurations of external windows and internal doors. Moreover, the positive effects of surface thermal mass and shading systems are numerically validated. The results, although limited to a specific context of analysis, show that, with appropriate adaptation strategies, even in lightweight buildings, occupants can achieve adequate levels of comfort, thus reducing the need for cooling. A combined and weighted use of passive solutions results in a reduction of about 3 °C in the average daily indoor temperature. Ventilation at night and solar shading during the day make a steel-framed building as comfortable as a massive one, both with regard to the internal surface temperature of the building components and to the discomfort indices. Changing the mass of the interior cladding of a wall, ceiling or floor, for example, from plasterboard to cement board, is another effective cooling strategy.

1. Introduction

Reducing costs, increasing speed, and minimizing risks have always been the main objectives of the construction industry. Buildings are therefore increasingly made up of standardized and performance-guaranteed components, both considering the systems and the envelope. The market for lightweight steel-framed building systems (LSF) has thus greatly increased over the last few decades, especially in low-rise residential buildings. Several advantages have driven their spread: ease and speed of on-site installation, low weight combined with high mechanical strength, large potential for recycling and reuse, easy prefabrication, flexibility of use for different architectural retrofit purposes, economy in transportation and handling, resistance to moisture and insect attack (Soares et al., 2017).

However, lightweight structures, particularly steel-framed ones, can contribute towards reducing building energy and indoor comfort performance during hot seasons (Lomas & Porritt, 2016) due to steel's high thermal conductivity and lightness (Santos, 2017). This represents a significant challenge, since with the increase in average annual temperature and the continuous growth of electricity demand, particularly of the residential sector, summer air conditioning has had a very significant influence on the overall energy consumption of buildings (Santamouris, 2016).

However, the use of additional thermal mass and high values of internal areal heat capacity can minimize peak heating and cooling loads in lightweight buildings (Di Perna et al., 2011; Kuczyński & Staszczuk, 2020; Rodrigues et al., 2013), especial-

ly when coupled with natural or mechanical ventilation (Yang & Li, 2008). CFD simulation is considered the most valuable tool for designing, verifying, and predicting the indoor thermal comfort level in relation to these aspects. Through this type of simulation, Mora-Pérez et al. (2017) explain the benefits of combined use of mechanical and natural ventilation to maximize comfort and reduce energy consumption. Much attention is often paid to the influence of the specific building component. Deng et al. (2017) discuss in depth the impact of window length, aspect ratio, height above the ground, window opening angle and fly screen porosity on the airflow pattern inside residential buildings. Aryal and Leephakpreeda (2015) emphasize how interior partitions significantly change perceived thermal comfort and the resulting energy consumption for heating and cooling, while Hajdukiewicz et al. (2013) focus on highly-glazed façades in meeting rooms. Few articles simultaneously address different cooling passive strategies through CFD simulation, and the study of lightweight structures, such as steel-framed, is still limited in this field.

In this paper we investigate the effectiveness of lightweight steel-framed structures to ensure, through the implementation of passive design and use strategies, high levels of indoor comfort during the hot season. Through CFD simulation, the paper explores the ways in which natural ventilation, wall heat capacity and external shadings can reduce indoor temperatures and improve comfort. Different windows and door opening/closing patterns are compared at (a) different external wind speeds and (b) the ability of windows shadings to mitigate temperature peaks is evaluated. The behavior of (c) different wall surface claddings with changed weight is also investigated and, finally, a comparison (d) is made between the starting lightweight structure (steel-frame with external insulation), the same structure with the implementation of the aforementioned passive strategies, an insulated reinforced concrete massive structure and an insulated brick structure. Simulations are performed on a case study built in 2018 in Barnaul (RU), southwestern Siberia, and monitored for two years. The continental climate of the area has a high seasonal temperature range with lows of -35 °C in winter and highs of +35 °C in the hot season. The summer behavior of the building was examined, taking into account these particular extreme environmental conditions which, however, due to climate change, will also be increasingly common in less severe climates (IPCC, 2021).

2. Materials and Methods

In this section, the case study, methodology and simulation tools, as well as the parameters monitored, are presented. In addition, the characteristics and the boundary conditions of the simulation model, the different passive strategies implemented, and the output variables analysed in Section 3 are described in depth.

2.1 The Case Study

The case study is a single-storey residential building realized, as regards the structural design, with panels made of cold-bent steel profiles (Fig. 1a-1b). The building is about 80 square meters and is divided into entrance, living room-kitchen, bathroom, boiler room and two bedrooms (Fig. 2). An insulated ceiling divides the living space from the pitched roof, made of sandwich panels. The heating system is powered by gas condensation boiler, and a controlled mechanical ventilation ensures the indoor-outdoor air exchange.

Fig. 1 – The building during (a) and at the end of the construction phase (b). Picture by Giovanni Manzini, 2019

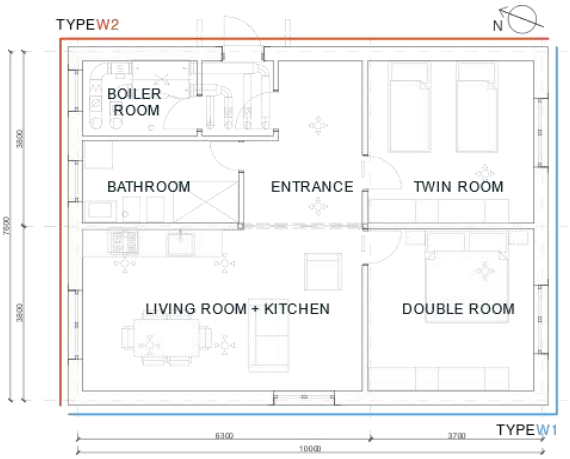

Fig. 2 – Horizontal section of the building

Table 1 – Thermophysical properties of the wall W1

Layers (int. to ext.)	s [cm]	λ [W/(m K)]	ϱ [kg/m³]	c [J/(kg K)]
Plasterboard	2.5	0.2	800	836.8
Insulated Counter-Wall	7	0.072	101.24	1024.3
Glass wool	8	0.035	35	1030
Plasterboard	1.25	0.2	800	836.8
SteelMAX® Structure + insulation	10	0.067	143.78	1022.6
Cement board	1.25	0.35	1150	836.8

Table 2 – Thermophysical properties of the wall W2

Layers (int. to ext.)	s [cm]	λ [W/(m K)]	ϱ [kg/m³]	c [J/(kg K)]
Plasterboard	2.5	0.2	800	836.8
Insulated Counter-Wall	5	0.068	101.2	1024.2
Glass wool	5	0.035	35	1030
Plasterboard	1.25	0.2	800	836.8
SteelMAX® Structure + insulation	10	0.067	143.78	1022.6
Cement board	1.25	0.35	1150	836.8
EPS insulation	5	0.038	21	1260

The building has two different external walls (Tables 1-2, Fig. 2) to test in-situ, through monitoring data, the energy performance of two akin solutions. Table 3 describes the thermal properties of the main building components.

The building is equipped with energy and environmental sensors to monitor its behavior 24 hours a day. The monitored parameters are:

- temperature, relative humidity, and CO2 of all indoor environments.
- surface and internal temperatures of walls, ceiling, floor.
- inlet and outlet temperature of the controlled mechanical ventilation machine.
- energy consumption.
- external environmental conditions (temperature, humidity, wind speed and direction, solar radiation).

The data monitored provided the necessary information to set the boundary conditions for the simulation model.

2.2 The Simulation Model

Computational fluid dynamics (CFD) is a branch of fluid mechanics that analyses and solves problems involving fluid flows using numerical analysis and data structures (Lomax et al., 2013). CFD analysis involves the simultaneous calculation of temperature and velocity domains, flows and pressures, considering the interaction between these variables. The great advantage of this type of simulation, compared to simplified empirical formulae, is the three-dimensional representation of the results. Properly setting the calculation grid and cell size, which have a significant impact on the calculation time and memory demands, as well as on the accuracy of the results, is a key prerequisite for the robustness of the CFD simulation. The minimum size of the cells is determined according to the specific problem to be analysed: for this case study, the volume of a single calculation cell is 8 cm^3 (2x2x2 cm). The number of cells also depends on the calculation domain. In order to include the effect of wind, which is essential for assessing the benefits of natural ventilation, a larger calculation domain than the building envelope is required, which may lead to a higher calculation effort.

Table 3 – Thermal properties of the building components

	W1 Walls	W2 Walls	Ceiling	Ground floor
Thickness [cm]	30	30	43	45
Thermal transmittance [W/m²K]	0.194	0.186	0.27	0.31
Decrement factor [-]	0.59	0.32	0.07	-
Time lag [h]	6.68	8.8	14.2	-
Internal areal heat capacity [kJ/m²K]	22.4	20.9	38.2	-
Periodic thermal transmittance [W/m²K]	0.114	0.06	0.019	-

The domain must be large enough not to bias the result and is typically expressed as a function of the building size. In accordance with Etheridge (2011), the following domains have been evaluated:

- Domain A: this coincides with the internal surface of the envelope. Boundary conditions at the inlets and outlets must be specified to run the simulation
- Domain B: external domain. The supply flow rate is determined as part of the simulation for this type of domain, which has dimensions that are normally twice those of the envelope. This means that the boundary conditions are different, and problems of convergence can arise.
- Domain C: the external flow to the inlet is included in the calculation. This requires extending the domain by an order of magnitude larger than the envelope.
- Domain D (used in the calculation): CFD boundary conditions for internal flows are generated using CFD data for the external flow.

Domain type D used in the case study simulation is a volume of 260 m³ (10.3x7.8x3.25 m) with boundaries that coincide with the internal walls. Based on a calculation previously carried out with an enlarged domain (type C: size of the domain is five times the size of the building), CFD allows wind velocity and air pressure along the building surface to be calculated. This choice reduces computational effort and, at the same time, enables the wind effects to be adequately considered. As regards the turbulence model for the calculation, the k-epsilon model was applied. The simulation model is built in Flovent®, proprietary software from Mentor Graphics®. For any other specifications regarding the methodology or the theory underlying the calculation, please refer to (Mentor Graphics Corporation, 2018).

2.3 Cooling Passive Strategies

2.3.1 Daytime natural ventilation

The transient simulation investigated the daily behavior of the building to the variation of the external climatic conditions, by focusing the analysis on the 48 hottest hours of the summer (3rd-4th of July). The set time step is 1 hour. Several monitor points were defined at different heights and in different rooms. The initial boundary conditions were set according to the data measured on site (Tab. 4). At first, an average wind velocity of 1.3 m/s in a north-westerly to south-easterly direction was considered, equal to the average wind speed measured in situ on that day. Then, extreme conditions of no wind and strong wind (0 and 5 m/s) were set to verify the reliability of the results and the magnitude of the wind.

Table 4 – Simulation boundary conditions

	Min	Max	Mean
Hourly outdoor temperature [°C] (see also Fig. 7c)	13.6	32.2	23.1
Solar radiation [W/m²]		873 (at 12.30 PM)	
Starting indoor temperature [°C]		25	

Several combinations are simulated (Tab. 5) with different window opening/closing schemes (Fig. 3). The daytime period is considered to start at 4 AM and end at 9 AM. In this case, it was considered that night ventilation was not feasible for other reasons (e.g., safety, noise, security).

Table 5 – Daytime natural ventilation: simulation cases

Sim.	Int. doors	Awning Windows	Hopper Windows	Wind
0	Closed	-	-	-
D10	Closed	-	F1, F2, F4, F5, F6	1.3 m/s
D11	Closed	-	F1, F2, F4, F5, F6	0 m/s
D12	Closed	-	F1, F2, F4, F5, F6	5 m/s
D13	Opened	-	F1, F2, F4, F5, F6	1.3 m/s
D14	Opened	-	F1, F2, F4, F5, F6	0 m/s
D15	Opened	-	F1, F2, F4, F5, F6	5 m/s
D20	Closed	F1, F2, F4	F5, F6	1.3 m/s
D21	Closed	F1, F2, F4	F5, F6	0 m/s
D22	Closed	F1, F2, F4	F5, F6	5 m/s
D23	Opened	F1, F2, F4	F5, F6	1.3 m/s
D24	Opened	F1, F2, F4	F5, F6	0 m/s
D25	Opened	F1, F2, F4	F5, F6	5 m/s

Fig. 3 – Windows nomenclature (a). Awning window example (b); hopper window example (c). https://blog.jonnew.com/assets/windows/types.jpg

For this and all simulations described in the next subsections, the output control variables are:

- Indoor temperature
- Internal wall surface temperature
- Predicted mean vote (PMV) (UNI, 2006)
- Predicted Percentage of Dissatisfied (PPD) (UNI, 2006)

Regarding PMV and PPD, to facilitate the calculation, some conditions were assumed to be constants:

- standing activity (1.2 met).
- summer clothing (0.5 clo).
- a relative humidity of 50 %.

The focus of the research was the thermal performance of the building. No acoustic and/or lighting comfort requirements were considered.

2.3.2 Nighttime cooling ventilation

The reduction of surface temperature of the walls, floor, and roof as a result of opening windows at night was explored by running a dynamic simulation. The role of various external window and internal door closing/opening techniques was examined. The night period is considered to start at 9 PM and end at 4 AM. The boundary conditions for temperature and solar radiation are the same as those shown in Table 4. The different combinations are listed in Table 6.

Table 6 – Nighttime cooling ventilation: simulation cases

Sim.	Int. doors	Awning Windows	Hopper Windows	Wind
0	Closed	-	-	-
N10	Closed	-	F1, F2, F4, F5, F6	0.5 m/s
N11	Closed	-	F1, F2, F4, F5, F6	0 m/s
N12	Closed	-	F1, F2, F4, F5, F6	5 m/s
N13	Opened	-	F1, F2, F4, F5, F6	0.5 m/s
N14	Opened	-	F1, F2, F4, F5, F6	0 m/s
N15	Opened	-	F1, F2, F4, F5, F6	5 m/s
N20	Closed	F1, F2, F4	F5, F6	0.5 m/s
N21	Closed	F1, F2, F4	F5, F6	0 m/s
N22	Closed	F1, F2, F4	F5, F6	5 m/s
N23	Opened	F1, F2, F4	F5, F6	0.5 m/s
N24	Opened	F1, F2, F4	F5, F6	0 m/s
N25	Opened	F1, F2, F4	F5, F6	5 m/s

2.3.3 Influence of thermal mass

To evaluate the effect of the surface thermal mass (UNI, 2017), three different simulations were carried out by varying the internal finishing layer, from plasterboard to cement board to plaster (Table 7).

- Sim n° 0: original case study.
- Sim n° M1: the internal plasterboard is replaced by 2 panels of cement board.

- Sim n° M2: the internal plasterboard is replaced by 3 panels of cement board.
- Sim n° M3: the internal plasterboard is replaced by 2cm of plaster (the air layer in the ceiling is thus eliminated).

The reduction of the surface temperature of the walls, floor, and roof due to the material replacement was studied, as well as the comfort (PMV/ PPD) and the reduction of the internal temperature peaks during the day. The dynamic analysis was carried out on two days with conditions similar to those shown in Table 4. The effects were evaluated on the second day of the analysis.

Table 7 – Thermal mass influence: simulation cases

	Internal areal heat capacity [kJ/(m²K)]		
Sim.	**North Walls**	**South Walls**	**Ceiling**
0	20.9	22.4	38.2
M1	33	34.6	43.9
M2	42.2	43.6	49.8
M3	33.3	34.3	52.2

2.3.4 Final comparison

The best cases from the previous 3 analyses were combined to obtain a best practice (case a). This was compared with the original building (case b) and with the same building modifying the load-bearing structure from insulated steel-frame (λ=0.58 W/(m K), ρ=100 kg/m^3) to reinforced concrete (λ=1.4 W/(m K), ρ=2300 kg/m^3 - case c) to brick (λ=0.35 W/(m K), ρ=700 kg/m^3 - case d). A further comparison was made by optimizing "case i" by adding windows external shading (case e). This was simulated by reducing the solar heat gain coefficient of window glass by 85 % when the windows are closed.

3. Results and Discussion

As regards natural daytime ventilation, with reference to the simulations from D10 to D15 shown in Table 5, the most cooled surfaces are the floor (massive element), followed by the leeward external walls, the internal partitions and, finally, the windward walls and the roof (Fig. 4). The cooling rate is similar for the different configurations. In simulation D15 (strong wind and open internal doors), the greatest benefits are found in terms of reduction of indoor temperature and surface temperature (about 3 °C), but the indoor air velocities lead to unacceptable levels of discomfort. The considerations are similar for simulations D20 to D25 (awning windows). It is worth noting that the results are very dependent on the boundary conditions and are mainly useful for comparison. Simulations D10 and D20, which are, in Fig. 4, compared with the base case, reveal that a proper window opening strategy during the daytime, with appropriate outdoor environmental conditions, can reduce the daily average surface temperature of the building components by approximately 2 °C during a typical summer day.

In the case of nighttime natural ventilation combined with an accurate opening strategy for windows and internal doors, it is possible to reduce the temperature of the internal surfaces of the building by up to 7 °C (Fig. 5). Different natural ventilation strategies lead to different results. The analysis shows that cross ventilation, enabled by the opening of the inner doors, produces a 1 °C reduction in the internal temperature compared with single side ventilation. The combination of curtains and hopper windows (SimN23) is most effective in cooling the air volume near the floor area (Fig. 5), which could positively affect comfort conditions of a person lying at rest.

As regards the analysis performed by modifying the wall and roof cladding surfaces (Fig. 6), it can be stated that:

- in the M1 case study, with the replacement of plasterboard by cement board, the reduction of the average internal temperature is about 1°C during the daytime
- the 3 fibrocement panels(M2), which are, in any case, not easy to install from a technical point of view, so were considered only as a theoretical comparison, would guarantee a temperature reduction of 3 °C, with excellent benefits also in terms of PMV and PPD

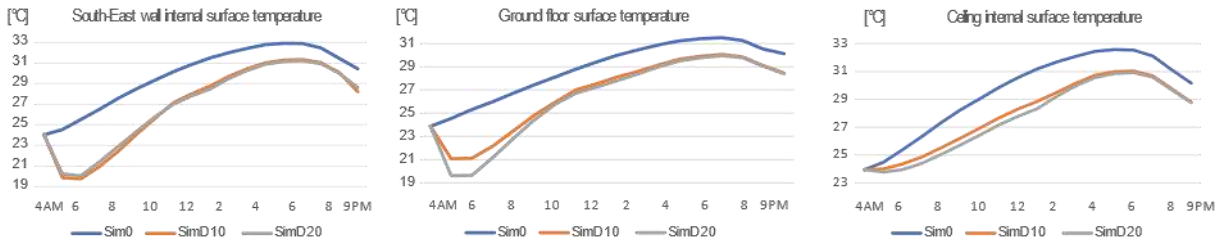

Fig. 4 – Daytime natural ventilation simulations results: internal surface temperatures of different building components (4th of July)

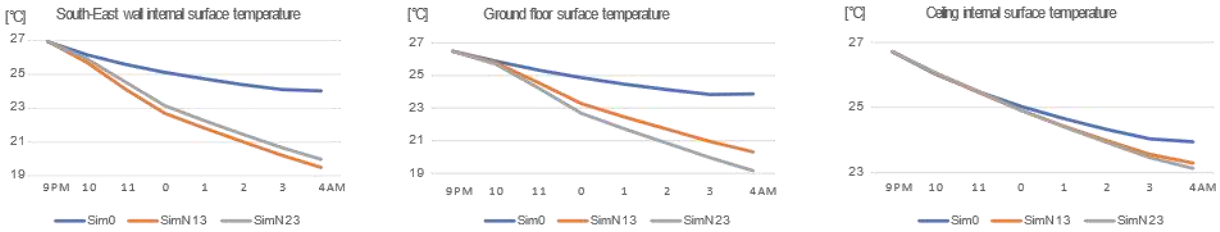

Fig. 5 – Nighttime natural ventilation simulations results: internal surface temperatures of different building components (4th of July)

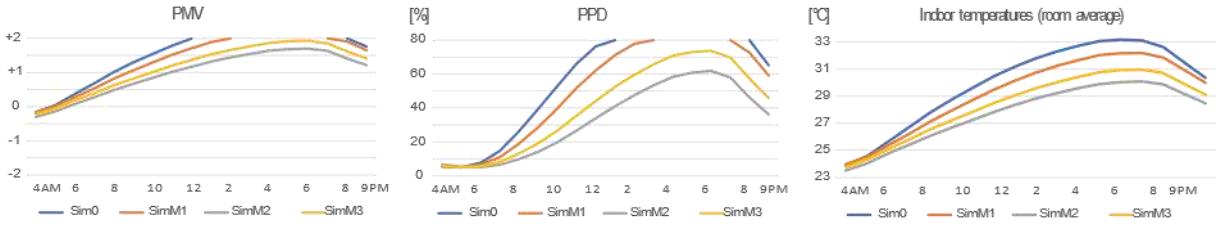

Fig. 6 – Thermal mass simulations results: PMV (a), PPD (b) and indoor temperature (c) trends (4th of July)

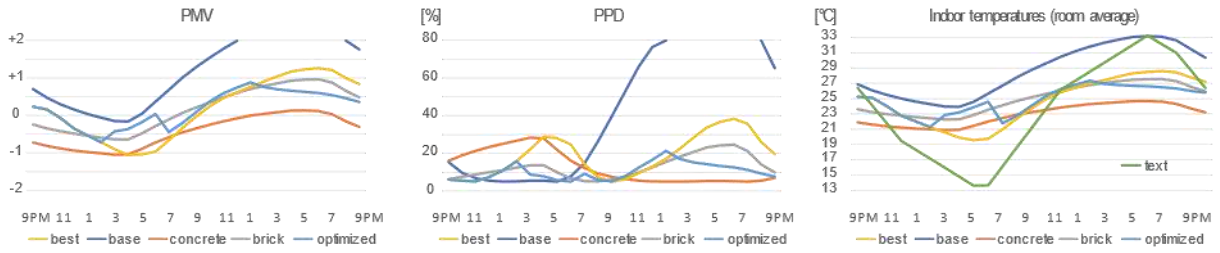

Fig. 7 – Final comparison results: PMV (a), PPD (b) and temperature (c) trends (3rd-4th of July)

- plaster would certainly be more efficient than plasterboard (M3), with a reduction of about 2.2 °C in the average internal temperature.

This positive effect also affects internal surface temperatures for all building components, thus increasing the indoor mean radiant temperature. Therefore, in the M2 case, the percentage reduction of PPD is over 20 %.

Fig. 7 compares data from the on-site monitoring system (base) with simulations described in Section 2.3.4. Massive/Solid constructions (concrete and brick) prove to be effective in softening outdoor temperature peaks, as noted in the literature. However, the combination of multiple passive cooling strategies (best), including a well-planned window opening strategy and heavier interior surface cladding materials, can positively reduce the risk of overheating even in steel-framed constructions.

The "optimized" case, which simulates the presence of a shading system through the reduction of the window solar heat gain coefficient, demonstrates how it is possible to achieve a more-than-acceptable level of comfort in light structures even in summer. Please note that the plots in Fig. 7 represent a 24-hour zoom on a simulation conducted over multiple days. For this reason, the initial indoor temperature conditions do not reflect those described in Table 4.

2. Conclusion

This work, starting from the monitoring of a real case study, provides a numerical evaluation of the indoor thermal comfort achieved in residential buildings during summer by applying passive cooling strategies. The focus is on lightweight steel-framed buildings, where, as the literature has frequently highlighted, overheating is still a big issue. Different strategies were tested through CFD simulations: from natural day and night ventilation to the implementation of different interior surface finishing materials, from different window opening configurations to external shading systems.

Based on the achieved results the paper confirms that:

- it is possible to adjust the nighttime discomfort level (too cold or too hot temperatures) by natural ventilation. It is necessary to find a compromise between the need to cool the envelope components and the internal ambient temperature, which strongly depend on the strategy adopted and, more generally, on the external temperature, wind speed and direction. Acoustic and lighting comfort issues should also be considered.
- the most effective strategy to regulate the daytime discomfort level is to shade window surfaces.
- daytime ventilation, in the analyzed conditions, produce limited effects. It is highly influenced by outdoor environmental condition trends, solar radiation, and sun exposure.
- by simply replacing the internal surface layer, without modifying the load-bearing structure, the internal areal heat capacity of the walls can be increased with positive effects on thermal comfort.

In this paper, monitoring data were exclusively used to set the boundary conditions for the simulation model. In the future, the implemented monitoring system will make it feasible to compare simulation findings with on-site measurements, calibrate the model, and put the recommended strategies into practice, involving building users. Further analysis will be required to evaluate the achieved results at different times of the year and with other building types.

Acknowledgement

This work was realized within the IsolMAX project funded by Cogi Srl - Italy and supported by the Operative Program FESR 2014-2020 of the Autonomous Province of Trento. The authors would like to thank the architect Basilio Guerra of Enerconsult Srl – Brescia (Italy) for his valuable contribution towards the monitoring campaign, and to remember the surveyor Mario Guidotti, head of the project, who recently passed away.

References

Aryal, P., and T. Leephakpreeda. 2015. "CFD Analysis on Thermal Comfort and Energy Consumption Effected by Partitions in Air-Conditioned Building." *Energy Procedia* 79: 183–188. doi: https://doi.org/10.1016/J.EGYPRO.2015.11.459

Deng, X., P. Cooper, Z. Ma, and G. Kokogiannakis. 2017. "Numerical analysis of indoor thermal com-fort in a cross-ventilated space with top-hung windows." *Energy Procedia* 121: 222–229. doi: https://doi.org/10.1016/J.EGYPRO.2017.08.021

Di Perna, C., F. Stazi, A. U. Casalena, and M. D'Orazio. 2011. "Influence of the internal inertia of the building envelope on summertime comfort in buildings with high internal heat loads." *Energy and Buildings* 43(1): 200–206. doi: https://doi.org/10.1016/J.ENBUILD.2010.09.007

Etheridge, D. 2011. *Natural Ventilation of Build-ings: Theory, Measurement and Design*. Wiley.

Hajdukiewicz, M., M. Geron, and M. M. Keane. 2013. "Calibrated CFD simulation to evaluate thermal comfort in a highly-glazed naturally ventilated room." *Building and Environment* 70: 73–89. doi: https://doi.org/10.1016/J.BUILDENV.2013.08.020

IPCC. 2021. *Climate Change 2021: The Physical Science Basis. Contribution of Working Group I to the Sixth Assessment Report of the Intergovernmental Panel on Climate Change*. Cambridge University Press.

Kuczyński, T., and A. Staszczuk. 2020. "Experimental study of the influence of thermal mass on thermal comfort and cooling energy demand in residential buildings." *Energy* 195: 116984. doi: https://doi.org/10.1016/J.ENERGY.2020.116984

Lomas, K. J., and S. M. Porritt. 2016. "Overheating in buildings: lessons from research." *Building Research & Information* 45(1–2): 1–18. doi: https://doi.org/10.1080/09613218.2017.1256136

Lomax, H., T. H. Pulliam, and D. W. Zingg. 2013. *Fundamentals of Computational Fluid Dynamics*. Springer Berlin Heidelberg.

Mentor Graphics Corporation. 2018. *FloVENT ® Background Theory Reference Guide v.12.2.* www.mentor.com

Mora-Pérez, M., I. Guillen-Guillamón, P. A. López-Jiménez. 2017. "A CFD study for evaluating the effects of natural ventilation on indoor comfort conditions." *AIMS Environmental Science* 4(2): 289–309. doi: https://doi.org/10.3934/ENVIRONSCI.2017.2.289

Rodrigues, L. T., M. Gillott, and D. Tetlow. 2013. "Summer overheating potential in a low-energy steel frame house in future climate scenarios." *Sustainable Cities and Society* 7: 1–15. doi: https://doi.org/10.1016/J.SCS.2012.03.004

Santamouris, M. 2016. "Cooling the buildings – past, present and future." *Energy and Buildings* 128: 617–638. doi: https://doi.org/10.1016/J.ENBUILD.2016.07.034

Santos, P. 2017. "Energy Efficiency of Lightweight Steel-Framed Buildings." *Energy Efficient Buildings*. doi: https://doi.org/10.5772/66136

Soares, N., P. Santos, H. Gervásio, J. J. Costa, and L. Simões da Silva. 2017. "Energy efficiency and ther-mal performance of lightweight steel-framed (LSF) construction: A review." *Renewable and Sustainable Energy Reviews* 78, 194–209. doi: https://doi.org/10.1016/J.RSER.2017.04.066

UNI. 2017. *UNI EN ISO 13786:2017 - Thermal performance of building components - Dynamic thermal characteristics - Calculation methods.*

UNI. 2006. *UNI EN ISO 7730:2006 - Ergonomics of the thermal environment - Analytical determination and interpretation of thermal comfort using calculation of the PMV and PPD indices and local thermal comfort criteria.*

Yang, L., and Y. Li. 2008. "Cooling load reduction by using thermal mass and night ventilation." *Energy and Buildings* 40(11): 2052–2058. doi: https://doi.org/10.1016/J.ENBUILD.2008.05.014

Energetic Optimisation of the Domestic Hot Water System in a Residential Building by Means of Dynamic Simulations

Paolo Valdiserri – University of Bologna, Italy – paolo.valdiserri@unibo.it
Aminhossein Jahanbin – University of Bologna, Italy – aminhossein.jahanbin@unibo.it
Giovanni Semprini – University of Bologna, Italy – giovanni.semprini@unibo.it

Abstract

The present study deals with the energetic optimisation of Domestic Hot Water (DHW) system in a residential building located in Catania, Italy. Each dwelling is equipped with a specific decentralised tank with an internal heat exchanger which is connected to a 2-pipe hot water network system for tank charging. The technical water is produced by an Electrical Heat Pump (EHP) coupled to a central storage tank. The energy performance analysis of the DHW model is evaluated by means of dynamic simulations under three different scenarios of charging the decentralised storage tanks by circulating pump unit: Pump activated during daytime, activated twice a day, and activated three times per day. The results obtained allow an evaluation of the DHW consumption profile, temperature variation in central storage and decentralised tanks, and the annual electrical/thermal energy analysis. The results indicate that the activation of the circulating pump during the day leads to an achievement of the highest amount of thermal energy, as well as having minimum temperature oscillation in both central storage and decentralised tanks. However, these advantages are at the cost of consuming much more electrical energy by the heat pump and up to 29 % higher emissions of CO_2. The best scenario in terms of energy-saving and CO_2 emission is the case in which the circulating pump works twice a day, consuming annually 5,832 kWh less electrical energy, compared to the case of an activated pump during the day.

1. Introduction

In recent years, research on the reduction of energy use in buildings has focused primarily on the reduction of space heating/cooling and ventilation needs. At the same time, present knowledge and understanding of energy use for Domestic Hot Water (DHW) production seem to be insufficient. The energy used for DHW production currently accounts for approximately 15–40% of the total energy needed in dwellings, and this proportion is likely to be augmented as the energy used for space heating keeps decreasing. Studies available in the literature indicate that the energy efficiency of DHW systems is surprisingly low and that a significant amount of heat is lost from the hot water before it reaches the draw-off points (Pomianowski et al., 2020). The efficiency of the DHW production and distribution varies to a significant extent from case to case due to the large scattering of key parameters in the system, such as plumbing layout, insulation level of pipework, pipe dimension and location, size of storage tank, and time-dependency of DHW consumption profile (Lutz, 2005; Marini et al., 2015; Valdiserri, 2018).

Space heating and DHW production in existing buildings require water at high temperatures (50-70 °C). Traditional 1st generation gas boilers or district heating networks generally have low efficiency and require high primary energy consumption. Furthermore, a higher thermal loss occurs in traditional DHW centralised systems of large buildings where, typically, a recirculating network from the central storage tank to individual dwellings works at high temperatures 24 hours/day. Nowadays, heat pumps are widely used for space heating purposes in buildings thanks to the high Coefficient of Performance (COP), and for the possibility of utilising renewable energy sources. Meanwhile, storage systems play an important role in order to reduce peak energy demand and increase the efficiency of whole production systems.

For these reasons, the concept developed in the e-

SAFE project (Evola et al., 2021) appoints a central role to heat storage systems, in order to develop innovative technologies that enable effective integration and communication in heating/cooling as well as domestic hot water production. The e-SAFE project defines a control strategy that ensures the supply of hot water produced by the heat pump to individual apartments, optimising the direct use of the electricity produced by the on-site PV system during daytime periods.

In this context, the present study aims to evaluate the energy performance of the proposed model for DHW in the e-SAFE project under three different scenarios of charging the decentralised tanks by circulating pump unit: activated pump during daytime, activated twice a day, and activated three times per day. In order to find the best strategy, by means of dynamic simulations, the DHW consumption profile, technical water flow rate, and annual thermal and electrical energy consumptions are analyzed within three different charging periods. The findings of the present study are expected to provide an insight for the energetic optimisation of DHW systems.

2. DHW System Description

In the e-SAFE project, a specific system for producing DHW was designed for a residential building of 10 dwellings (5 floors) with 32 persons, located in Catania, Italy. As shown in Fig.1, each dwelling is equipped with a specific decentralised wall-mounted tank with an internal heating coil (heat exchanger) which is connected to a 2-pipe hot water network system for tank charging. The technical water is produced by an Electrical Heat Pump (EHP) coupled to a central storage tank. The technical water is supplied to decentralised tanks via the circulating pump unit.

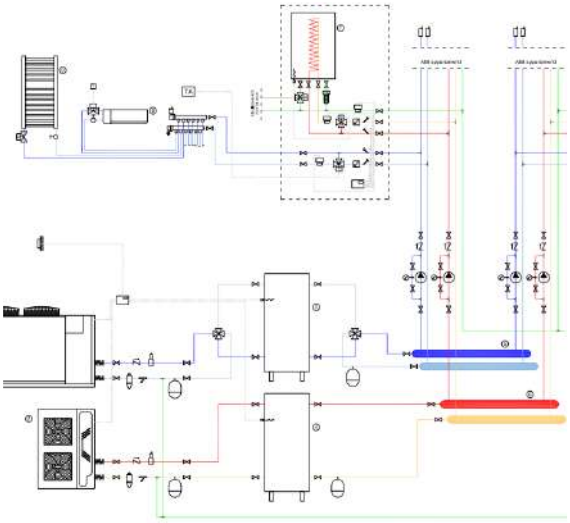

Fig. 1 – Layout of the proposed model for DHW system (the heating/cooling system is not considered in this paper)

The distribution network can be used only for the charging of DHW storage tanks or, in some contexts, can work at low temperature for heating purposes. In both cases, the network (2-pipe water loop) works at high temperature only during charging periods for few hours a day, resulting in lower heat losses in the piping network compared with traditional centralised DHW production, where a recirculating loop at high temperature works 24 hours/day.

3. Dynamic Simulation Model

The energy performance of DHW network is investigated by means of a dynamic simulation model implemented through TRNSYS software. The central storage tank (Type 60g) has a volume of 1500 l, height of 2.4 m and loss coefficient of 0.7 W/(m²K), with a temperature set point of 65 °C. Each apartment was equipped with a plug-and-play decentralised hot water storage system (wall-mounted) with a volume of 140 l. The decentralised tank (Type 534-coiled) consisted of two inlet and two outlet flow ports; on one side, an inlet port for the aqueduct and an outlet port for the DHW; on the other side, an inlet and outlet for the technical water flowing through the heat exchanger. The coiled heat exchanger inside the tank with tube diameter of 0.025 m and loss coefficient of 1.4 W/(m²K) had a total length of 17.8 m with coil diameter and coil pitch equal to 0.145 m and 0.35

m, respectively. The temperature setpoint for the decentralised tank was equal to 55 °C. An ON/OFF controller (Type 2) was employed for both central storage and decentralised tanks in order to regulate the setpoint temperatures in the range of ± 2.5 °C.
The technical water is supplied to the decentralised tanks by two circulating pumps (Type 743), i.e., each pump for five apartments, with the power of 200 W and a constant mass flow rate of 300 kg/h. The energy performance of the DHW model was evaluated under three different scenarios for charging the decentralised tank by circulating pump unit, namely activated pump during the daytime, activated twice a day, and activated three times per day. Table 1 reports the time slots in which the circulating pump is activated.

Table 1 – Operational time slots of the circulating pump

	1 Slot (Continuous)	2 Slots	3 Slots
Operational time slots of pump	06 – 22	08 – 10 & 15 – 18	06 – 08 & 15 – 17 & 20 – 22

The domestic hot water needs were regulated on the basis of the number of people in each apartment, the mean seasonal consumption, and the daily (hourly) consumption profile. In order to model the DHW consumption, a MATLAB code was developed and linked to the TRNSYS model by introducing a NORMRND function, i.e., random samples from a normal (Gaussian) distribution, in order to simulate the daily DHW consumption similar to the real condition.
The MATLAB code reads the number of residents in each apartment from the TRNSYS, and then, at each time step, returns a value as a consumption, simulated on the basis of seasonal and daily (hourly) profile. According to the literature data, the mean daily DHW consumption for each person was considered equal to 45 l, varying slightly in each season. Furthermore, in the daily consumption profile, it was assumed that peaks of the daily consumption profile occur in the early morning between 06 and 10 (45 % of total daily consumption) as well as in the evening between 18 and 22 (25 % of total daily consumption).

4. Results and Discussion

The profile of hot water consumption during a day for three different apartments is illustrated in Fig. 2. The selected apartments are those with the minimum, intermediate and maximum number of residents, namely 1, 3, and 5 persons. It is evident from the figure that peak consumption in each apartment is in the early morning and evening, as described in the previous section. While the peak consumption rate in the apartment with 5 persons reaches 53.9 kg/h, it hardly exceeds 9.5 kg/h in the apartment with 1 person. The trend of DHW request shows the role of virtual user, namely the MATLAB code, in random consumption of DHW in predefined ranges, on the basis of number of persons and daily profile slots. Elaboration of the annual consumption for each apartment implies that the mean daily consumption of hot water for apartments with 1, 3 and 5 person(s) is equal to 43.9, 135.7 and 217.4 l (kg), respectively.

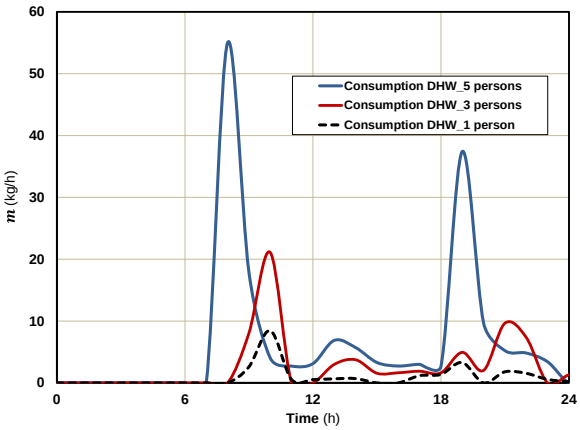

Fig. 2 – The profile of daily hot water consumption in three apartments with 1, 3 and 5 residents

The daily variation in temperature of the central storage and decentralised tank triggered by consuming hot water for different operational time slots is demonstrated in Fig. 3. The considered decentralised tank here is that of the apartment with intermediate number of residents, namely 3 persons. The figure shows that the temperature of decentralised tank increases versus set-point (57.5 °C) in defined working hours of the circulating pump, which feeds the hot water from central storage into the heat exchanger of decentralised tank, and as soon as it discharges the hot water by users (see Fig. 2), its temperature starts to decrease.

It is evident from the figure that reducing the working hours of the circulating pump results in more drastic oscillating in temperature of both central storage and decentralised tank. However, this variation in central storage is less significant compared with the internal tank. While the tank temperature in daytime activated mode (1 slot) does not drop below 37 °C, it reaches 20 °C and 29 °C in 2 and 3 operational time slots, respectively.

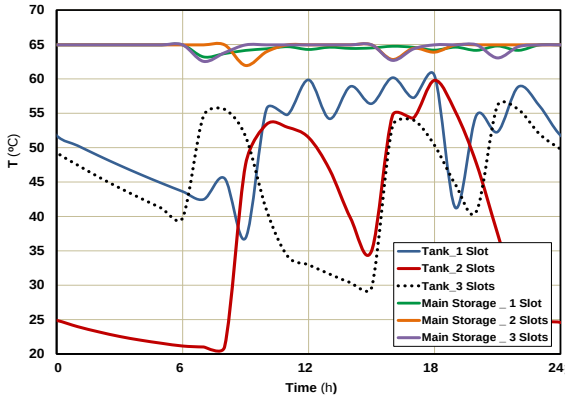

Fig. 3 – The temperature variation in central (main) storage and decentralised tank (of a dwelling with 3 persons) for different activation times of the circulating pump

A comparison between the results of Figs. 2 and 3 allows two points to be concluded. A short activetion time of the circulating pump causes the risk of having a low-temperature DHW when there is a request out of operational time slots, particularly for apartments with larger number of residents. Another issue to be addressed is the advantage of matching the activation time of the circulating pump with hours in which there is the peak of DHW consumption, according to the profiles in Fig. 2.

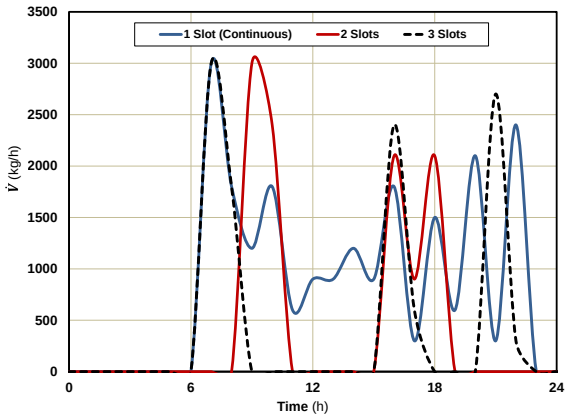

Fig. 4 – Daily total mass flow rate of technical water for different activation times of the circulating pump

Fig. 4 shows the daily total mass flow rate of technical water circulating from the central storage to each apartment's tank, for different working time slots. The figure shows that the flow rate of technical water during the early morning period reaches the highest rate, namely 3000 kg/h, in all operational time slots, implying the hot water demand by all apartments (Fig. 2). Moreover, the figure indicates that, when the circulating pump is in daily activated mode, namely available on request between 06 and 22 h, the flow rate of technical water does not reach zero during the day, due to receiving the hot water request by at least an apartment. On the other hand, the mass flow rate of technical water for 2 and 3 slots daily charging is mostly equal to zero, except for predefined working hours. A comparison between results shows that the total daily mass flow rate of technical water in continuous mode (1 slot) is up to two times higher than that in 2 times activated per day. Indeed, the possibility of charging tanks during the day (1 slot) leads to maintaining the temperature of tanks and, consequently, the DHW as high as possible. Nonetheless, it is shown in the following that this higher temperature will be at the cost of consuming much higher electrical energy, as well as the emission of CO_2.

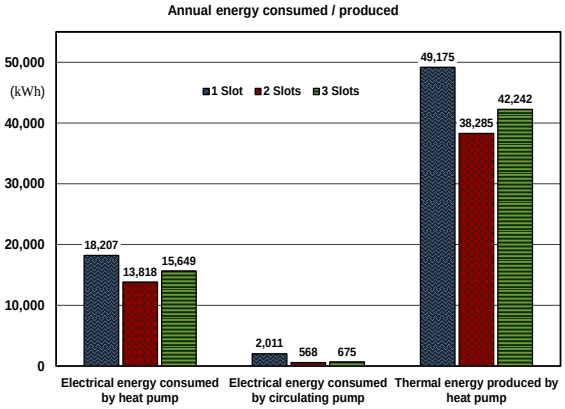

Fig. 5 – A comparison between annual energy consumed/ produced in various activation time slots of the circulating pump

The charts in Fig. 5 compare the annual amount of electrical energy consumed by the heat pump and circulating pump, as well as the thermal energy produced by the heat pump for different operational time slots of the pump. The figure shows that employing a continuous daytime operation of

circulating pump (1 slot) leads to much higher electrical energy consumption of both the heat pump and circulating pump, compared with 2 and 3 slot operations; the total electrical energy consumed by the continuous operation is 5,832 and 3,894 kWh higher than that in 2 and 3 time slot operations, respectively. On the other hand, when the circulating pump is activated during the day (1 slot), the heat pump produces annually about 50,000 kWh thermal energy for DHW production, which is far higher than other scenarios.

Table 2 – A comparison between annual electrical consumption, mean COP of heat pump and CO_2 emission for different activation time slots of the circulating pump

	1 Slot	**2 Slots**	**3 Slots**
Total electrical energy consumed (kWh)	20218	14386	16324
Mean annual COP	2.69	2.77	2.71
CO_2 emission (kg)	9098.1	6473.5	7345.7

Table 2 reports values of the total electrical energy consumed, mean annual COP of heat pump, and amount of CO_2 emission by different scenarios considered for charging the tanks. The table shows that the mean annual COP of the heat pump is slightly improved when the internal tanks charge only two times per day. Considering the mean value of 0.45 kg emission of CO_2 for producing 1 kW of electricity, according to the literature data, the continuous charging of tanks (1 slot) causes 9098 kg emission of CO_2, which is 29 % and 19 % larger than 2- and 3-times charging modes.

5. Conclusions

In the present study, the energetic optimisation of the Domestic Hot Water (DHW) in a residential building was investigated by means of a dynamic simulation model developed in TRNSYS software linked to a MATLAB code. In the proposed model for the DHW system, the technical water was produced by an Electrical Heat Pump (EHP) coupled to a central storage tank. Each dwelling was equipped with a specific decentralised tank with an internal heat exchanger, which was connected to a 2-pipe hot water network system for tank charging. The energy performance of the DHW model was evaluated under three different scenarios for charging internal tanks by circulating pump unit, namely activated pump during daytime, twice a day, and three times per day.

The results obtained by dynamic simulations allowed an evaluation of the DHW consumption, temperature variation in central storage and internal tanks, the flow rate of technical water, and annual electrical/thermal energy consumption analysis. The results showed that employing the daily activated circulating pump has the advantage of achieving the highest amount of thermal energy, as well as having minimum temperature oscillation in both central storage and decentralised tanks. However, these advantages were at the cost of consuming much more electrical energy and up to 29 % higher emission of CO_2. The best scenario in terms of energy saving and CO_2 emission was when the circulating pump was working twice a day consuming annually 5,832 kWh less electrical energy compared to when the pump was activated during the day.

Acknowledgement

This paper was carried out in the framework of the "Energy and seismic affordable renovation solutions" (e-SAFE) project, which received funding from the European Union's Horizon 2020 research and innovation programme under grant agreement No. 893135.

References

Evola, G., G. Margani., V Costanzo, C Tardo, E. M. Marino, G Semprini, R. Tomasi, C. Halmdienst, and B. Voortman. 2021. "The e-SAFE energy and seismic renovation solutions for the European building stock: Main features and requirements." *Journal of Physics: Conference Series* 2069(1): 012224. doi: https://doi.org/10.1088/1742-6596/2069/1/012224

Lutz, J. 2005. *Estimating Energy and Water Losses in Residential Hot Water Distribution Systems*. Lawrence Berkeley National Laboratory.

Marini, D., R. Buswell, and C. Hopfe. 2015. "Estimating waste heat from domestic hot water systems in UK dwellings." In *Proceedings of Building Simulation 2015*, Hyderabad, India. https://doi.org/10.1111/hex.12279

Pomianowski, M. Z., H. Johra, A. Marszal-Pomianowska, and C. Zhang. 2020. "Sustainable and energy-efficient domestic hot water systems: A review." *Renewable and Sustainable Energy Reviews* 128: 109900. doi: https://doi.org/10.1016/j.rser.2020.109900

Valdiserri, P. 2018. "Evaluation and control of thermal losses and solar fraction in a hot water solar system." *International Journal of Low-Carbon Technologies* 13(3): 260–265. doi: https://doi.org/10.1093/ijlct/cty025

Assessing the Climate Resilience of Passive Cooling Solutions for Italian Residential Buildings

Mamak P.Tootkaboni – Politecnico di Torino, Italy – mamak.ptootkaboni@polito.it
Ilaria Ballarini – Politecnico di Torino, Italy – ilaria.ballarini@polito.it
Vincenzo Corrado – Politecnico di Torino, Italy – vincenzo.corrado@polito.it

Abstract

One of the most significant repercussions of greenhouse gas concentration increase has been the global rise in temperature, resulting in drastic changes in the climate. According to this background, buildings are not only contributing to climate change, but they are also being affected by it, as climate change will raise the risk of overheating and cooling demand in buildings. Therefore, assessing and communicating resilient cooling and overheating protection solutions is inexorable. This paper aims to analyse the energy efficiency and climate resiliency of three passive cooling solutions for Italian residential buildings in future climates. Simulations have been performed using EnergyPlus for the pre-retrofitted condition (without insulation and conventional heating and cooling systems) and the retrofitted building (with insulation and a reversible heat pump for heating and cooling). Results show that buildings will be subject to an increase in cooling loads, electrical energy consumption for cooling, and overheating risk due to climate change. The ultra-selective double-glazed window is found to be more climate-resilient in comparison with roller blind and cool roof tiles. Besides, combining these three cooling technologies can guarantee the best future energy performance for each period. However, the overheating risk during the power outage still exists, especially for the post-retrofitted building. These findings have significant implications for understanding how analyzing multiple factors is essential to guarantee the climate resilience of cooling systems in a holistic way.

1. Introduction

Each of the last four decades since 1980 has been successively warmer than the preceding decade. According to the latest Assessment Report (6th A.R.) of the Intergovernmental Panel on Climate Change (IPCC), the concentration of greenhouse gases (GHG) in the atmosphere has continued to increase since 2011 (measurements in IPCC 5th A.R.) (Masson-Delmotte et al., 2021). Considering the fact that global CO_2 emissions from the building sector increased by 50 % from 1990 to 2019, making it the main contributor to GHG emissions, its impact on intensifying climate change is undeniable (Cabeza et al., 2022). Furthermore, climate change is already impacting many weather and climate extremes in all world regions. Due to methodological advances and new data sets, evidence of observed changes in climate-related hazards, such as heatwaves, has increased since the 5th A.R. (Symon, 2013). In this case, buildings are not only responsible for climate change but are highly affected by it. Accordingly, many published studies worldwide suggest a shift in building energy performance due to the impacts of climate change. For instance, Wan et al. (2012) analysed the heating and cooling energy use of an office building in different Chinese cities and reported an increase in cooling energy consumption of up to 24.2 %, implying a shift towards higher electricity demand. In the U.S. context, Shen (2017) demonstrated a rise in cooling energy use and a drop in heating energy use for office and residential buildings in four American cities. In addition, the inconsistency of energy use in residential buildings located in cold and hot regions of the U.S. is expected to decrease due to the impact of climate change. In Canada, an increase in cooling demand by up to 126 % and a decrease in heating demand by up to 33 % were predicted for several urban regions by Berardi & Jafarpur (2020).

Besides the expected changes in energy needs, the overheating risk will also become a challenge in the future. For example, in southern regions of the U.K., overheating is expected to create a cooling problem for a third of the year, as Peacock et al. (2010) suggested. In the same vein, Dino & Akgül (2019) examined a typical mid-rise residential building in four different cities in Turkey, and found that inhabitants would experience overheating, particularly in naturally ventilated houses. In addition, other studies demonstrated that such changes in energy needs, and overheating risk are also predicted for retrofitted and energy-efficient buildings. In other words, due to the changing climate, meeting nearly zero-energy building (NZEB) requirements may not necessarily guarantee the energy performance and indoor environmental quality of buildings in the future. For example, as Tabatabaei Sameni et al. (2015) suggested, thermal discomfort during the cooling season is foreseen for 72 % of analysed social housing flats − built to Passivhaus standards − due to the impact of climate change. Attia & Gobin (2020) looked at a Belgian reference example of the NZEB and found that there would be overheating up to +43.5 % at the end of the century. In another study, Da Guarda et al. (2020) examined the influence of climate change on zero-energy buildings in 2020 (2011 to 2040), 2050 (2041 to 2070), and 2080 (2071 to 2100). It has been proved that energy consumption will rise, so further dimensioning of renewable energy installations is required to achieve zero net energy balance. Taken together, these studies suggest that to maintain energy efficiency, sustainability, and climate resilience of buildings over time, an assessment of the performance of energy-efficient buildings using future weather data is essential.

This paper is a part of research carried out in collaboration with the International Energy Agency (IEA) Energy in Buildings and Communities Programme (E.B.C) Annex 80 "Resilient Cooling of Buildings". This project develops, assesses, and communicates strategies for resilient cooling and overheating protection (Annex 80 IEA EBC, 2018). After creating reliable future weather data for Rome, the resilience of three passive cooling technologies was investigated using thermal comfort and energy performance metrics to assess and develop the adaptation and mitigation framework on a regional scale.

2. Materials and Methods

2.1 Generation of Future Weather Data

In synergy with the IEA-Annex 80 Weather Data Task Group, future typical meteorological years were created for Rome during the first step.

For this purpose, Regional Climate Models (GERICS-REMO 2015, MPI-M-MPI-ESM-LR) from Euro-CORDEX on a 0.11° grid in rotative coordinates (equivalent to a 12.5 km grid) were used. In detail, G.C.M.s (Global Climate Models) are mathematical models for forecasting climate change providing information on a global scale with a spatial resolution of 150–600 km (Symon, 2013). Since climate change effects and related weather extremes at the local level will not be considered using these models, they are not appropriate for energy simulations on the building scale. Therefore, it is necessary to downscale the models to applicable spatial (less than 100 km) and temporal resolution (less than monthly value). The dynamical technique employs regional climate models (R.C.M.s) to obtain finer spatial and temporal climate information; this is one of the downscaling methodologies. R.C.M.s can better capture the geographical and temporal variability of the local climate and provide physically consistent datasets (Soares et al., 2012). As mentioned above, this study employs the GERICS-REMO-2015 as the R.C.M. In addition, since being well-supported by the IPCC report on climate model evaluation (Flato et al., 2014), the MPI-M-MPI-ESM-LR is the study's driving model. Besides, the data source is the EURO-CORDEX entry point through the Earth System Grid Federation (ESGF) for the Europe domain on a 0.11° grid, in rotative coordinates (equivalent to a 12.5 km grid). NetCDF4, which is a file format for storing multi-dimensional scientific data, is the accessible format for this source. The hourly climatic data for Rome Fiumicino airport was extracted using the Cordex Data Extractor program, which enables the discovery of the data point on the grid closest to the

specified latitude and longitude. These climatic data were extracted by adapting the RCP 8,5 (Representative Concentration Pathway) scenario from IPCC 5th A.R. for the 2041-2060 (2050s) and 2081-2100 (2080s) periods. These scenarios were the latest available projections of future climate at the time of the study.

Accordingly, the EN ISO 15927-4 (2005) methodology was applied to construct the future typical meteorological year from the 20 years of climatic data. This international standard addresses the selection of appropriate meteorological data for the assessment of the long- term mean energy use for heating and cooling. Twelve Best Months were picked by comparing the Cumulative Distribution Function of the single and reference years using the Finkelstein-Schafer (F.S.) statistics (Finkelstein & Schafer, 1971). This method was selected for this study because it includes the global solar irradiance, relative humidity, dry-bulb air temperature, and wind speed. The best representative 12 months were then employed to construct the T.M.Y. Historical (2001-2020), future medium-term (2041-2060), and future long-term (2081-2100) are the T.M.Y.s referred to in this study. Despite not being adjusted for bias, the results are reliable; since a relative comparison is applied in this study, and for confronting different technologies, this kind of future weather data is acceptable.

2.2 Cooling Strategies

In IEA EBC Annex 80, four categories of cooling strategies were created according to their approaches to cooling people or the indoor environment. They include strategies aimed at: a) reducing heat gains to indoor environments and people indoors, b) removing sensitive heat from indoor environments, c) enhancing personal comfort apart from cooling whole spaces, and d) removing latent heat from indoor environments.

For the present analysis, three cooling solutions were selected from the first category: ultra-selective double-glazed window, external roller blind, and cool roof tiles.

The ultra-selective double-glazed window is a static technology that incorporates low thermal-infrared emittance (low-E) coatings with spectral control to reduce the window heat loss (U-value ≤ 1.8 W/(m^2 K)) and solar heat gain ($g \leq 30$ %), while admitting most daylight ($\tau_v > 60$ %). The external roller blind is a dynamic technology with a low solar transmittance ($\tau_s < 15$ %) that strongly reduces the solar heat gain due to its external position and can be controlled to optimise both thermal and visual comfort and energy demands for heating, cooling and lighting. Cool roof tiles are a static technology that reduces net radiative heat gain at the envelope (solar + thermal infrared radiation) thanks to the high solar reflectance ($\rho_s > 0.30$ for pitched roofs, $\rho_s > 0.65$ for flat roofs).

2.3 Calculation Methods and Performance Indicators

The following three key performance indicators (KPIs) were used for the performance assessment of the selected cooling solutions:

- *HE* [%], i.e., hours of exceedance, which are the number of hours during June, July, and August in which the operative temperature of the zone is greater than the upper limit temperature,
- $EP_{C,nd}$ [kWh/m^2], which is the thermal energy need for space cooling in June, July, and August,
- $E_{el,C}$ [kWh/m^2], which is the electrical energy consumption (from the grid) for cooling in June, July, and August.

The above indicators were chosen from the list of KPIs officially adopted in IEA EBC Annex 80 to represent the summer performance of the building according to the following criteria: a) thermal discomfort in free-floating conditions (absence of cooling or power outage) or in case of power shortage, b) thermal performance of the fabric in cooling operation, and c) energy performance of the building (including HVAC system) in cooling operation.

All the adopted indicators are based on international standards. *HE* accounts for the number of weighted hours exceeding the acceptable range of the indoor operative temperature. For free-floating conditions, the adaptive comfort method is assumed according to the Annex-H of EN ISO 7730, 2005. $EP_{C,nd}$ reflects the basic energy

needs of the building in ideal thermal conditions (uniform and ideally controlled indoor temperature) without interaction with specific technical building systems (EN ISO 52016-1, 2017). $E_{el,C}$ represents the energy delivered to the building for cooling by adding the effect of the energy losses of the cooling system (EN ISO 52000-1, 2017).

2.4 Case Study

With the aim of extending the research outcomes on a broader territorial scale, the case study was selected to be representative of a specific category, i.e., the Italian single-family house built in the period 1946-1960 (Ballarini et al., 2014). Among the Italian existing building categories, the one selected presents the lowest energy performance due to its highest shape factor and uninsulated envelope components (Ballarini et al., 2017). In a recent study (Tootkaboni et al., 2021), this type of building was found to be more sensitive to climate change due to its high shape factor. According to the IEE-TABULA project (Corrado et al., 2012), the building selected is an "archetype" (Fig.1), which means that it is characterised by average dimensional properties (gross heated volume, shape factor, conditioned net floor area, number of floors, number of apartments) of a representative building sample according to statistical analysis.

The main geometric data of the analysed archetype are listed in Table 1. The thermo-physical features of the building envelope components are provided in Table 2, assuming the building type both in the original pre-retrofit situation and in the retrofitted state. This double condition allows an assessment of the effect of the passive cooling strategies both on low energy-efficiency buildings and on already insulated buildings. The *U*-values of the envelope components in the pre-retrofit state refer to typical technologies of the construction period (solid brick masonry and single-glazing windows). The retrofitted state presents components insulated in accordance with the notional reference building for the climatic zone of Rome, as expressed by the Italian energy regulations (M.D 26 June, 2015), which also represents the nearly zero-energy building target. The post-retrofit windows present a low-E double-glazing. In addition, while the original building is not equipped with solar shading devices, these are provided for in the retrofitted building (external wooden Venetian blinds).

As far as the technical building systems are concerned, the building in the pre-retrofit state is equipped with a gas standard boiler and radiators for space heating and a split system for space cooling. In the post-retrofit phase, both heating and cooling are provided by a reversible air-to-water heat pump with fan coils as heat emitters.

Fig. 1 – Archetype of the Italian single-family house built in the period 1946-1960 (Corrado et al., 2012)

Table 1 – Geometric data of the case study

Parameter	Value
Conditioned gross volume, V_g [m³]	584
Conditioned net floor area, A_{fl} [m²]	162
Shape factor, A_{env}/V_g [m⁻¹]	0,73
Window-to-wall ratio, *WWR* [-]	0,09
Number of floors [-]	2
Number of apartments [-]	1

Table 2 – Thermo-physical parameters of the envelope components

Component	Parameter	Pre-retrofit	Post-retrofit
External wall	U [W·m⁻²K⁻¹]	1.48	0.29
	U [W·m⁻²K⁻¹]	1.65	0.26
Roof	α_s [-]	0.75	0.75
	ρ_s [-]	0.25	0.25
Bottom floor	U [W·m⁻²K⁻¹]	2.00	0.29
Windows	U [W·m⁻²K⁻¹]	4.9	1.30
	U [W·m⁻²K⁻¹]	5.7	1.20
Glazing	g [-]	0.85	0.59
	τ_v [-]	0,90	0,80
Shading	τ_s [-]	N/A	0,40
	ρ_s [-]	N/A	0,12

The energy performance of the case study was assessed considering the behavior of a standard user. Hourly profiles of internal heat gains, which include occupants, electric lighting and appliances, and ventilation airflow rates were assumed in accordance with the Italian National Annex draft of the EN 16798-1 technical standard (2020).

A continuous operation mode of the technical building systems was adopted, considering heating and cooling temperature set-points equal to 20 °C and 26 °C, respectively. The heating season is included in the period from 1st November up to 15th April, while the cooling period was assumed for the months of June, July, and August. The operation of the solar shading devices was set in the function of a threshold value of the incident solar irradiance (300 W/m²), in accordance with UNI/TS 11300-1 (2014).

3. Results and Discussion

The results obtained from the simulations are shown in Figs. 2 to 7. The first two refer to the thermal energy need for space cooling ($EP_{C,nd}$) during the months of June, July, and August in 2020, 2050, and 2080. Besides, Figs. 4 and 5 represent the electrical energy consumption (from the grid) for cooling ($E_{el,C}$) during the same period. An increase of up to 75 % for the pre-retrofitted and 35 % for the post-retrofitted case is shown in $EP_{C,nd}$ over time due to climate change. Furthermore, the increase in $E_{el,C}$ is up to 80 % for the pre-retrofitted and 30 % for the post-retrofitted building. For post-retrofitted building, the variations of $EP_{C,nd}$ and $E_{el,C}$ are less than the pre-retrofitted one. It can be argued that the post retrofitted building is less sensitive to the effects of climate change.

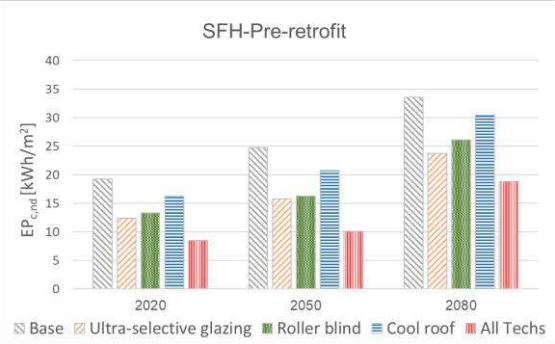

Fig. 2 – Thermal energy need for space cooling (June/July/August) in 2020, 2050, and 2080 for pre-retrofit building

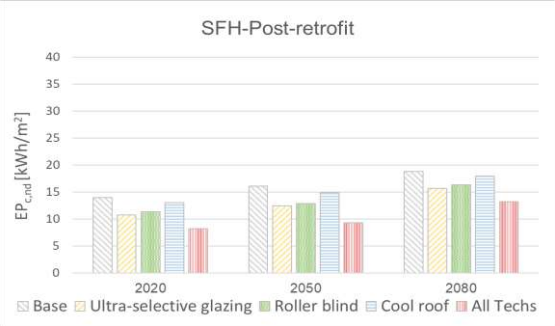

Fig. 3 – Thermal energy need for space cooling (June/July/August) in 2020, 2050, and 2080 for post-retrofit building

The reduction in the $EP_{C,nd}$ and $E_{el,C}$ caused by either of the cooling solutions is more significant in the pre-retrofitted building. In addition, it is shown that the most effective one is ultra-selective glazing in both conditions. The cool roof has a minor effect, as the building has a pitched roof with an attic. This effect is negligible for the electrical energy consumption in the post-retrofitted building in all three periods. If all cooling solutions are applied, the $EP_{C,nd}$ and $E_{el,C}$ can be reduced to the degree that in 2080 they are almost the same as the present base case. This result is valid for both building conditions.

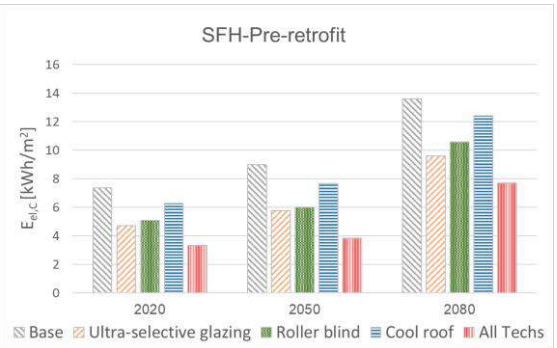

Fig. 4 – Electrical energy consumption (from the grid) for cooling (June/July/August) in 2020, 2050, and 2080 for pre-retrofit building

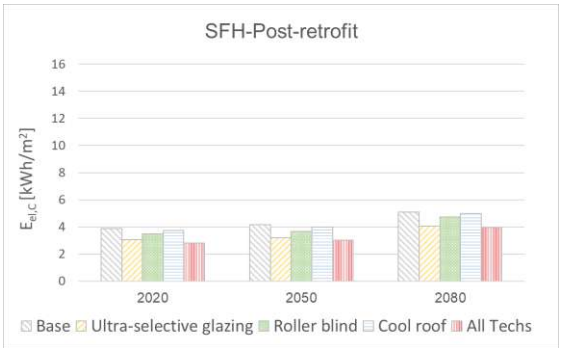

Fig. 5 – Electrical energy consumption (from the grid) for cooling (June/July/August) in 2020, 2050, and 2080 for post-retrofit building

As mentioned earlier, when it comes to the impact of climate change on buildings, it is necessary to take the overheating risk into account. For this purpose, by running free-floating simulations, weighted hours of exceedance for June, July, and August in 2020, 2050, and 2080 are calculated and presented in Figs. 6 and 7. Results report that the weighted hours of exceedance increase due to climate change in both conditions. However, in the post-retrofitted building, occupants will experience overheating equal to 5328 hours in the future scenarios, while this amount reaches a maximum of 2628 hours for the pre-retrofitted building in 2080. This result is due to the unwanted effect of insulation that causes a heat trap in the building in a free-floating regime. The results also show that the cooling solutions can reduce weighted exceedance hours. For the pre-retrofitted building, the effect of ultra-selective glazing and roller blind is almost the same and significantly higher than the cool roof. For post-retrofitted case, ultra-selective glazing has the most significant effect. The effect of the roller blind is diminished in this case since the post-retrofitted building was equipped with a Venetian blind in the base case. By applying all the cooling solutions, weighted hours of exceedance are reduced significantly for both cases. However, the weighted hours of exceedance in the pre-retrofitted building for the worst-case scenario (2080) equal 700 hours, which is much less than the post-retrofitted case (2600 h).

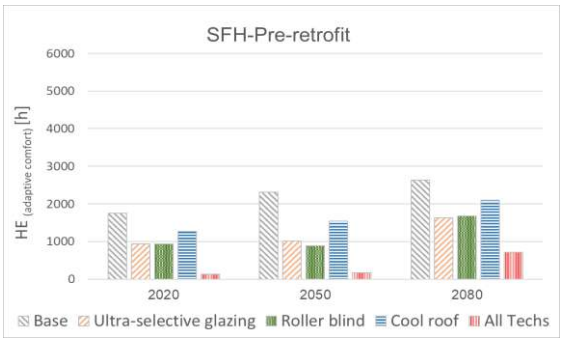

Fig. 6 – Weighted hours of exceedance (June/July/August) in 2020, 2050, and 2080 for pre-retrofit building, in free-floating condition

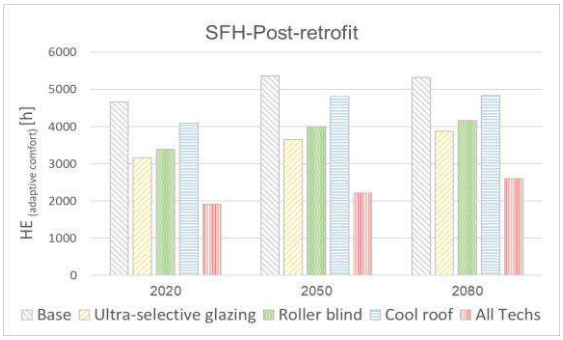

Fig. 7 – Weighted hours of exceedance (June/July/August) in 2020, 2050, and 2080 for post-retrofit building, in free-floating condition

4. Conclusion

The present research aimed to examine the climate resilience of three passive cooling solutions regarding the future performance of Italian residential buildings. To achieve this aim, the impact of the ultra-selective double-glazed window, external roller blind, and cool roof tiles was investigated on the thermal comfort and energy performance of an Italian single-family house built in 1946-1960. Two building conditions (pre-and post-retrofitted) and three periods (2020, 2050, and 2080) were considered. The current study results indicate that, among selected solutions, the ultra-selective double-glazed window has the most significant impact on reducing the effect of climate change on thermal energy needs for space cooling, electrical energy consumption from the grid for cooling, and weighted hours of exceedance in free-floating condition. The findings of this research also revealed that applying all three cooling solutions mentioned could significantly develop

the energy performance of the buildings, so that in the worst-case future scenario (2080), the energy performance will be almost the same as the base case in 2020. This improvement is more considerable for the post-retrofitted building. However, in the absence of electrical energy (free-floating condition), although studied cooling solutions help to reduce the overheating, the risk is still present, specifically for the post-retrofitted building. These findings shed new light on the trade-off between energy efficiency and climate resiliency. In this case, it is necessary to identify cooling solutions that help to mitigate climate change and foster adaptation to it, to ensure both sustainability and climate resilience for the built environment.

Nomenclature

Symbols

A	Area (m^2)
E	Energy consumption (kWh/m^2)
EP	Energy performance (kWh/m^2)
HE	Hours of exceedance (h)
U	Thermal transmittance ($W/(m^2 \cdot K)$)
V	Volume (m^3)
g	Total solar energy transmittance (solar factor) (–)
τ	Transmittance (%)
ρ	Reflectance (%)

Subscripts/Superscripts

C	Space cooling
el	Electrical energy
env	Envelope
fl	Floor
g	Gross
nd	Need
s	Solar
v	Visible

References

Annex 80 IEA EBC. 2018. ''IEA EBC Annex on Resilient Cooling for Residential and Small Commercial Buildings" .Draft Annex Text, pp. 1–13.

Attia, S., and C. Gobin. 2020. "Climate Change Effects on Belgian Households: A Case Study of a Nearly Zero Energy Building." *Energies* 13(20): 5357. doi: https://doi.org/10.3390/en13205357

Ballarini, I., S. P. Corgnati, and V. Corrado. 2014. "Use of reference buildings to assess the energy saving potentials of the residential building stock: The experience of TABULA project. " *Energy policy* 68: 273-284. doi: https://doi.org/10.1016/j.enpol.2014.01.027

Ballarini, I., V. Corrado, F. Madonna, S. Paduos and F. Ravasio. 2017. "Energy refurbishment of the Italian residential building stock: energy and cost analysis through the application of the building typology." *Energy Policy* 105: 148–160. doi: https://doi.org/10.1016/j.enpol.2017.02.026

Berardi, U., and P. Jafarpur. 2020. "Assessing the Impact of Climate Change on Building Heating and Cooling Energy Demand in Canada." *Renewable and Sustainable Energy Reviews* 121: 109681. doi: https://doi.org/10.1016/j.rser.2019.109681

Cabeza, L. F., Q. Bai, P. Bertoldi, J. Kihila, A. F. P. Lucena, É. Mata, S. Mirasgedis, A. Novikova, Y. Saheb, P. Berrill, L. R. Caldas, M. Chàfer, S. Hu, R. Khosla, W. Lamb, D. Vérez, J. Wanemark, and J. Keenan. 2022. "Climate Change 2022, Mitigation of Climate Change. Working Group III contribution to the Sixth Assessment Report of the Intergovernmental Panel on Climate Change." *Climate Change*. https://www.ipcc.ch/report/sixth-assessment-report-working-group-3/

Comitato Termotecnico Italiano. 2020. Technical Commission 241, Doc. (181) Italian National Annex of the EN 16798-1 Technical Standard (Working Draft for Internal Use).

Corrado, V., I. Ballarini, and S. P. Corgnati. 2012. National scientific report on the TABULA activities in Italy. Dipartimento di Energetica, Gruppo di Ricerca TEBE, Politecnico di Torino, Torino, Italy. https://episcope.eu/fileadmin/tabula/public/docs/scientific/IT_TABULA_ScientificReport_POLITO.pdf

Da Guarda, E. L. A., R. M. A. Domingos, S. H. M. Jorge, L. C. Durante, J. C. M. Sanches, M. Leao, and I. J. A. Callejas. 2020. "The influence of

climate change on renewable energy systems designed to achieve zero energy buildings in the present: A case study in the Brazilian Savannah." *Sustainable Cities and Society* 52: 101843. doi: https://doi.org/10.1016/j.scs.2019.101843

Dino, I. G., and C. M. Akgül. 2019. "Impact of Climate Change on the Existing Residential Building Stock in Turkey: An Analysis on Energy Use, Greenhouse Gas Emissions and Occupant Comfort." *Renewable Energy* 141: 828-846. doi: https://doi.org/10.1016/j.renene.2019.03.150

Ente Italiano di Normazione. 2014. *UNI/TS 11300-1. 2014. Energy Performance of Buildings Part 1: Evaluation of Energy Need for Space Heating and Cooling* (in Italian). UNI, Milan, Italy.

European Committee for Standardization. 2005. *EN ISO 7730:2005. Ergonomics of the thermal environment - Analytical determination and interpretation of thermal comfort using calculation of the PMV and PPD indices and local thermal comfort criteria. Annex-H: Long-term evaluation of the general thermal comfort conditions*.

European Committee for Standardization. 2017. *EN ISO 52016-1:2017. Energy performance of buildings -Energy needs for heating and cooling, internal temperatures and sensible and latent heat loads - Part 1: Calculation procedures, 52016–1.*

European Committee for Standardization. 2017. *EN ISO 52000-1:2017.Energy performance of buildings -Overarching EPB assessment -Part 1: General framework and procedures, 52000–1.*

Finkelstein, J. M., and R. E. Schafer. 1971. "Improved goodness-of-fit tests." *Biometrika* 58(3): 641-645. doi: https://doi.org/10.1093/biomet/58.3.641

Flato, G., J. Marotzke, B. Abiodun, P. Braconnot, S. C. Chou, W. Collins, and M. Rummukainen. 2014. "Evaluation of Climate Models. In Climate Change 2013: The Physical Science Basis. Contribution of Working Group I to the Fifth Assessment Report of the Intergovernmental Panel on Climate Change." Cambridge University Press 741–866. doi: https://doi.org10.1017/CBO9781107415324.020

Italian Ministry of Economic Development. 2015. Italian Ministerial Decree 26th June 2015. "Application of energy performance calculation methodologies and specification of prescriptions and minimum requirements."

Masson-Delmotte, V., P. Zhai, A. Pirani, S. L. Connors, C. Péan, S. Berger, N. Caud, Y. Chen, L. Goldfarb, M. I. Gomis, M. Huang, K. Leitzell, E. Lonnoy, J. B. R. Matthews, T. K. Maycock, T. Waterfield, O. Yelekçi, R. Yu, and B. Zhou. 2021. "Summary for Policymakers. The Physical Science Basis. Contribution of Working Group I to the Sixth Assessment Report of the Intergovernmental Panel on Climate Change." *Climate Change*.

Peacock, A. D., D. P. Jenkins, and D. Kane. 2010. "Investigating the Potential of Overheating in UK Dwellings as a Consequence of Extant Climate Change." *Energy Policy* 38(7): 3277-3288. doi: https://doi.org/10.1016/j.enpol.2010.01.021.

Shen, P. 2017. "Impacts of Climate Change on U.S. Building Energy Use by Using Downscaled Hourly Future Weather Data." *Energy and Buildings* 134: 61-70. doi: https://doi.org/10.1016/j.enbuild.2016.09.028

Soares, P. M., R. M. Cardoso, P. Miranda, J. de Medeiros, M. Belo-Pereira, and F. Espirito-Santo. 2012. "WRF high resolution dynamical downscaling of ERA-Interim for Portugal." *Climate dynamics* 39(9): 2497-2522. doi: https://doi.org/10.1007/s00382-012-1315-2

Symon, C. 2013. "Climate Change: Action, Trends and Implications for Business." The IPCC's Fifth Assessment Report.

Sameni, S. M. T., M. Gaterell, A. Montazami, and A. Ahmed. 2015. "Overheating Investigation in UK Social Housing Flats Built to the Passivhaus Standard." *Building and Environment* 92: 222 235. doi: https://doi.org/10.1016/j.buildenv.2015.03.030

Tootkaboni, M. P., I. Ballarini, and V. Corrado. 2021. "Analysing the future energy performance of residential buildings in the most populated Italian climatic zone: A study of climate change impacts." *Energy Reports* 7: 8548-8560. doi: https://doi.org/10.1016/j.egyr.2021.04.012

Wan, K. K., D. H. Li, W. Pan, and J. C. Lam. 2012. "Impact of climate change on building energy use in different climate zones and mitigation and adaptation implications." *Applied Energy* 97: 274-282. doi: https://doi.org/10.1016/j.apenergy.2011.11.048

Ventilation of Residential Buildings in Alpine Region: A Comparison Between Natural, Mechanical, and Mixed-Mode Strategies

Francesca Avella – Eurac Research, Italy – francesca.avella@eurac.edu
Paolo Bonato – Eurac Research, Italy – paolo.bonato@eurac.edu
Annamaria Belleri – Eurac Research, Italy – annamaria.belleri@eurac.edu
Francesco Babich – Eurac Research, Italy – francesco.babich@eurac.edu

Abstract

Many studies have shown how controlled natural ventilation has multiple benefits on the health of people and the buildings in terms of indoor air quality (IAQ) and thermal comfort, as well as on the energy consumption of the building.

However, unfavorable outdoor environmental conditions can limit the use of solely natural ventilation and, for this reason, it is often necessary to resort to mixed-mode ventilation.

The aim of this research is to demonstrate the potential of mixed-mode ventilation strategies in comparison with the performance of controlled natural ventilation and mechanical ventilation applied separately, in the context of a dwelling located in a multi-family house in Bolzano (Italy) during the summer season.

Dynamic simulations were performed, developing a room-by-room coupled thermal and airflow model of the dwelling in TRNSYS and TRNFLOW to characterize its thermal behavior and the natural airflows.

The study analyzes and compares three different scenarios: (1) only controlled natural ventilation (CNV), (2) only mechanical ventilation (MVT), (3) a combination of the two (mixed ventilation strategies, MIX).

In this work, the controlled natural ventilation strategies are designed with a twofold aim, which is (a) to improve the indoor thermal comfort, reducing the overheating risk thanks to ventilative cooling, and (b) to improve IAQ by removing indoor airborne pollutants coming from indoor sources.

The first results show that (a) CNV effectively reduces the overheating risk, also achieving excellent IAQ levels; (b) MVT allows acceptable IAQ conditions and good water vapor removal, while overheating could become an issue in terms of duration and intensity. In addition, there is the electricity consumption associated with MVT; (c) in most cases, mixed ventilation provides excellent performance in terms of IAQ and thermal comfort, compared with the former strategies. Overheating is well managed, and the electrical consumption of MVT is limited.

1. Introduction

Many studies have shown how controlled natural ventilation has multiple benefits on the health of people and buildings in terms of indoor air quality (IAQ) and thermal comfort, as well as on the energy consumption of the building (Belleri et al., 2021; Schulze & Eicker, 2013; Schulze et al., 2018). It also has architectural benefits, as it does not require space for duct network to distribute the air within the building, leaving free use of floor-to-ceiling height (CIBSE, 2005). Furthermore, measures to enhance daylight (such as limited penetration depth and increased floor-to-ceiling height) also favor the use of natural ventilation (Carrilho da Graça & Linden, 2016).

However, unfavorable outdoor environmental conditions can limit the use of solely natural ventilation and, for this reason, it is often necessary to resort to hybrid ventilation systems (Ezzeldin & Rees, 2013; Salcido et al., 2016a), or so-called mixed-mode ventilation. There are many studies that have shown the benefits of combining controlled natural ventilation and mechanical ventilation in terms of indoor environment conditions (Arata & Kawakubo, 2022; Hamdy & Mauro, 2019; Kim & de Dear, 2021; Salcido et al., 2016b), but too little is known about the potential of these strategies applied in the South Tyrolean climate context (northern Italy). These strategies must not only be designed with the aim of maximizing IAQ and

thermal comfort while reducing energy consumption, but should also take into account the climatic conditions, the typological aspects of the building stock and the habits of the occupants.
The aim of this research is to estimate the potential of mixed-mode ventilation strategies in comparison with the performance of controlled natural ventilation and mechanical ventilation applied separately, in the context of a dwelling located in a multi-family house in Bolzano (Italy) during the summer season.

2. Methodology

The case study building presented in this paper consists of a dwelling located in a multi-family house in Bolzano (Italy). It has a net floor area of 54 m² and is occupied by 3 tenants. The model consists of five thermal zones, one for each room of the apartment, i.e., two bedrooms, a living room/kitchen, a bathroom and a small central corridor. Each room, except bathroom and corridor, has only one window. The living area faces south, while the sleeping area faces south and east.
Dynamic simulations and the related analysis were performed, developing a room-by-room coupled thermal and airflow model of the dwelling in TRNSYS and TRNFLOW to characterize its thermal behavior and natural airflows.
We applied the schedules for occupancy, lighting, and electric equipment reported in Wilson et al., 2014, assuming that four occupants are living in the apartment. The total heat gains related to occupants, as well as the CO_2 generation rates, were calculated according to typical metabolic heat generation for domestic activities, namely 1.2 met for occupants in the living area, and 1 met for occupants in the sleeping area. Lighting power density was assumed to be equal to 2.7 W/m². When the rooms are occupied, lights are switched on if beam radiation on the room window surface is below 140 W/m². Electrical equipment power density was assumed to be equal to 8 W/m². If occupants are "sleeping" or "absent", internal loads are considered equal to 2 W/m² (20 % of total installed power); if occupants are "active", internal loads are considered equal to 6 W/m² (60 % of total installed power, considering a coincidence factor of 0.6). Solar shadings are activated if the zone air temperature is above 24 °C and incident solar radiation on the window is above 140 W/m².
The infiltration and ventilation airflows are calculated through the multizone airflow network model coupled to the thermal model through TRNFLOW. The airflow network model includes cracks along the window perimeter and openings at each window and internal door. Fig. 1 also reports a scheme of the airflow network with air nodes, flow paths and flow links. The flow coefficients of the cracks were set in order to have an overall envelope air tightness equal to 0.6 h^{-1} at 50 Pa. No cooling system is considered, but natural ventilation can be activated to provide for ventilative cooling over the warm season. A dual-flow ventilation unit uses supply and return fans to bring fresh air from outside into the living room and bedrooms, and exhausts stale air from the bathroom and kitchen. The ventilation unit is equipped with a high-efficiency passive heat exchanger that allows ventilation thermal losses to be minimized. The heat exchanger can also be bypassed. Each simulation was performed with a timestep of 15 min over the warm season (from May to September). The weather data was generated by Meteonorm using extreme hourly values over a 10-year weather time series for the city of Bolzano. This study analyzes and compares three different scenarios in the climate conditions of Bolzano: (1) only controlled natural ventilation (CNV), (2) only mechanical ventilation (MVT), (3) a combination of the two (mixed ventilation strategies, MIX).

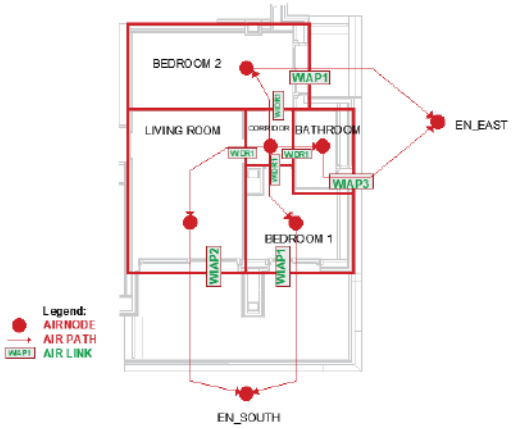

Fig. 1 – Reference building plan, thermal zones, airflow network

2.1 Controlled Natural Ventilation

CNV strategies are designed with a twofold aim, which is (a) to improve the indoor thermal comfort reducing the overheating risk thanks to ventilative cooling, and (b) to improve IAQ by removing indoor airborne pollutants coming from indoor sources.

Two CNV strategies are implemented: a) the single-sided ventilation strategy (CNV-SN) controls the opening and closing of the windows in individual rooms of the apartment independently of the other rooms, while the cross-ventilation strategy (CNV-CR) simultaneously controls multiple rooms. In a real-building application, the opening or closing of the windows could be automated by the application of actuators whose action is guided by algorithms which, based on the internal and external environmental conditions, identify the optimal opening level. The opening or closing of windows is represented in the model by an opening factor, which is a value of between 0 and 1. 0 means total closure and 1 full opening of the window (an opening factor of 0.2 indicates, for instance, a bottom hung window opening) (Table 1). All doors between rooms are assumed to stay half-opened all the time. In order to find the most suitable natural ventilation strategy, internal and external environmental conditions, such as internal temperature and CO_2 concentration, outdoor temperature and relative humidity, are considered in the analysis (Table 2).

Table 1 – Range of window opening factor

Output	Description	Value
WIN_LR	Living room window opening factor	0-1[1]
WIN_BR1	Single bedroom window opening factor	0-1
WIN_BR2	Double bedroom window opening factor	0-1

1 In this study 0.2 is considered because of the vasistas opening mode

Table 2 - Controlled natural ventilation input

Input	Description	Unit of measurement
TAIR_EXT	Convective outside air temperature	°C
HR_EXT	Relative humidity of the outside air	%
TAIR_LR	Convective air temperature in the living room	°C
TAIR_BR1	Convective air temperature in the single bedroom	°C
TAIR_BR2	Convective air temperature in the double bedroom	°C
CO_2_LR	CO_2 concentration in the living room	ppm
CO_2_BR1	CO_2 concentration in the single bedroom	ppm
CO_2_BR2	CO_2 concentration in the double bedroom	ppm

Table 3 – Control parameters for the activation of controlled natural ventilation

Parameter	Description	Default Value
$TAIR_EXT_{min}$	Minimum outdoor temperature	16 °C
HR_EXT_{max}	Minimum relative humidity	85 %
$TAIR_{cmf}$	Convective air temperature for the activation of CNV	25 °C
$CO_2_LR_{min}$	CO_2 concentration limit in the living room	750 ppm
$CO_2_BR1_{min}$	CO_2 concentration limit in the single bedroom	1000 ppm
$CO_2_BR2_{min}$	CO_2 concentration limit in the double bedroom	1000 ppm

Assuming that the apartment is equipped with measurement points of the parameters shown in Table 2, these are compared with the threshold values shown in Table 3.

In Table 4, the control signals are listed, defined as Booleans calculated with logic functions of measured data, control parameters or a combination of other control signals.

Table 4 – Control signals of controlled natural ventilation

Signal	Logic function
Y_SN	SN=1-0
Y_CR	CR=1-0
A	TAIR_EXT > TAIR_EXTmin
R	HR_EXT < HR_EXTmax
G_ZONE	TAIR_EXT < TAIR_ZONE
F_ZONE	TAIR_ZONE > $TAIR_{cmf}$
E_ZONE	CO_2_ZONE > $CO_{2\,min}$[2]
H	MIN(F_LR+F_BR1+F_BR2,1)
L	MIN(G_LR+G_BR1+G_BR2,1)

In Fig. 7 and Fig. 8 the processes that led to the activation of CNV-SN and CNV-CR are summarized. In particular, the activation of the CNV is regulated according to the external environmental conditions (external temperature greater than 16 °C and relative humidity less than 85 %).

2.2 Mechanical Ventilation

A CO_2-based demand-controlled ventilation strategy (DCV) is applied to trigger the operation of the mechanical ventilation unit, which considers the CO_2 concentration threshold value greater than 200 ppm compared with those designed for the activation of the CNV.
More detailed information is reported in Table 5.

Table 5 – MVT properties

Air flow rate per occ [m^3/h]	Specific fan pow. [Wh/m^3][3]	Heat rec. eff	Free cooling mode ON
36	0.28	70 %	TAIR_EXH[4] >23.5 °C TAIR_EXT<TAIR_ZONE TAIR_EXT>16 °C

2.3 Mixed-Mode Ventilation

Mixed-mode ventilation allows the use of CNV and MVT. There are no conditions imposed a priori on the alternative or simultaneous use of the two ventilation techniques, but the control logic settings of both systems prioritize the use of natural ventilation when the outdoor conditions are acceptable. The activation of CNV occurs after an increase of indoor temperature above the reference comfort temperature or for hygienic ventilation needs, while mechanical ventilation intervenes only when the CO_2 concentration exceeds the threshold and natural ventilation is not effective in providing hygienic ventilation rates. In fact, the pollutant concentration thresholds defined for the activation of controlled natural ventilation and mechanical ventilation are different, with lower threshold values for the activation of CNV. From this perspective, it will be possible to encourage the use of natural ventilation compared with mechanical ventilation, reducing electrical consumption. The performance indicators considered in the analysis of the results are summarized in Table 6 and refer to IAQ, thermal comfort and electricity consumption for MVT.

3. Results and Discussion

The study examines and compares three different scenarios: (1) only CNV, (2) only MVT, (3) a combination of the two (mixed ventilation strategies).

2 It refers to CO_2_LRmin - CO_2_BR1min - CO2_BR2min

3 ″SIA-Shop Produkt - 'SIA 2024 / 2015 D - Raumnutzungsdaten Für Energie- Und Gebäudetechnik (Normenwerk => Architekt).'" n.d. Accessed March 31, 2022. http://shop.sia.ch/normenwerk/architekt/sia 2024/d/2015/D/Product.

4 TAIR_EXH = exhaust air temperature

Table 6 – Performance indicators

Symbol	Unit of measurement	Description
N_{on}	h	No. of hours of activation of the CNV and MVT strategies
D_{op}	h	Avg duration of window opening
N_{att}	No	No. of actv. of the window actuators
W_{MVT}	kWh	Electricity consumed by the MVT
$W_{MIX\text{-}SN}$	kWh	Electricity consumed by the MIX-SN
$W_{MIX\text{-}CR}$	kWh	Electricity consumed by theMVT-CN
OH_h	%	% of occ. hours Tair>26 °C (Nicol, 2013)
OH_i	K	Avg. intensity OH during occ. hours
CO_2, $C_{1\text{-}4}$	%	% of occ. hours CO_2 (cat I-IV)[5]
HR, $C_{1\text{-}4}$	%	% of occ. hours HR (cat I-IV)[6]

The results of the simulation model are analyzed in terms of IAQ, thermal comfort and electricity consumption connected to ventilation. Fig. 2 shows the average distribution of occupied hours of the three thermal zones (living room, single bedroom, double bedroom) in the four categories of environmental quality ("CEN/TR 16798-2:2019 Energy Performance of Buildings - Ventilation for Buildings - Part 2: Interpretation of the Requirements in EN 16798-1 - Indoor Environmental Input Parameters for Design and Assessment of Energy Performance of Buildings Addressing Indo" 2019) defined by concentration of CO2 in the thermal zones during the summer period (May-September). As regards CNV, it guarantees excellent levels of IAQ in terms of CO_2 concentration for the greatest number of hours (55 % of occupied hours fall into category I), while, for the remaining part of the time, the IAQ falls in category IV (where Category I corresponds to a high level of expectation, Category II to a medium level). This is probably due to the fact that the activation of the CNV is regulated according to the external environmental conditions (external temperature and relative humidity, see Fig. 7 and Fig. 8), which, if they were not favorable, would not allow the opening of the windows for the correct hygienic replacement.

The optimal results are those obtained from the use of mixed-mode ventilation strategies, able to exploit the potential of natural ventilation strategies and to use MVT as a backup if the activation of natural ventilation is not convenient.

Compared to CNV, MVT guarantees a greater number of occupied hours in which the CO_2 concentration level corresponds to the one required by categories I and II of indoor environmental quality (IEQ).

Focusing on controlled and mixed-mode natural ventilation strategies, Fig. 3 shows the distribution of the activation hours of the strategies in the living room for the summer season by type of ventilation.

Only with controlled natural ventilation strategies are the windows open for about 60 % of the summer hours, while for about 40 % of the hours natural ventilation cannot be activated, despite the need for ventilation, because of unfavorable outdoor conditions. In the case of mixed ventilation, this eventuality is considerably reduced to about 15 % of the total summer hours, thanks to the contribution of mechanical ventilation, which is active for about 30 % of the hours. It is also observed that the number of hours in which both natural and mechanical ventilation are active is very low (about 2 % of the hours).

5 CO_2 categories were defined according to EN16798-1 Annex B assuming 400ppm as the average outdoor concentration ("EN 16798-1:2019 Energy Performance of Buildings - Ventilation for Buildings - Part 1: Indoor Environmental Input Parameters for Design and Assessment of Energy Performance of Buildings Addressing Indoor Air Quality, Thermal Environment, Lighting and Acous" 2019)

6 relative humidity cat. were defined according to EN16798-1 Table I.11

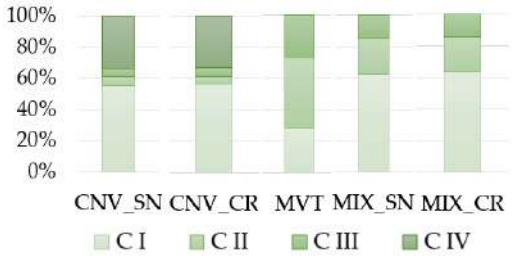

Fig. 2 – Distribution of IAQ categories (C I–C IV) for the CO_2 concentration during the occupied hours considering the five ventilation strategies during the summer period (May-September)

Even if the two control systems do not communicate with each other, their control prevents their simultaneous activation, allowing the two types of ventilation to alternate with each other. In addition, Fig. 4 shows the influence that outdoor temperature and humidity conditions (see Table 3) have on the activation of CNV strategies. As the figure shows, the outdoor temperature is the most critical parameter (higher than 70 % of hours during the summer period), when the outside temperatures are lower and, during the night, they can drop below 16 °C. In general, no significant improvement occurs by activating the CNV-CR strategy, probably due to the fact that air mixing within the apartment was ensured by an open door all the time. As regards the hygrometric results, Fig. 5 shows the distribution of the relative humidity in the four categories of environmental quality during the occupied hours considering all the ventilation scenarios.

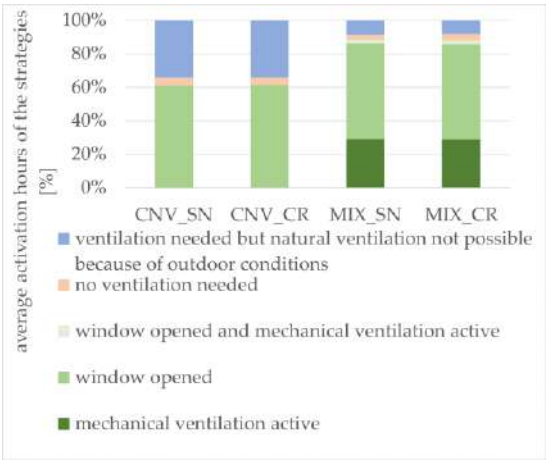

Fig. 3 – Average activation hours of the strategies in the LR during the summer period

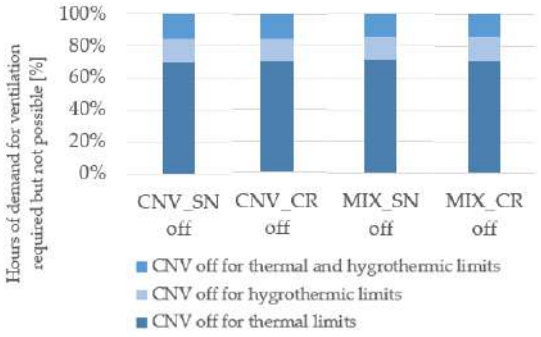

Fig. 4 – LR % of hours in which it is not possible to take advantage of CNV due to the thermal and hygrometric limits imposed on its activation [%]

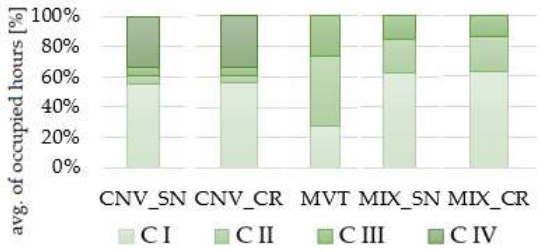

Fig. 5 – Distribution of hygrometric categories (C I – C IV) for the relative humidity assessed during the occupied hours considering the five ventilation strategies during the summer period

In all scenarios, most of the occupied hours fall into category I or II, i.e., with a relative humidity of between 25 % and 60 %. Only the MVT scenario guarantees better results, probably due to the fact that the air intake with MVT is localized in the rooms where there is the greatest generation of water vapor. A percentage of hours greater than 0 % falls into categories III-IV, assuming that unfavorable external conditions do not allow the opening of the windows.

As regard overheating, the graph in Fig. 6 shows the average percentage of occupied hours with overheating risk (reference temperature equal to 26 °C) and the average intensity. As the figure shows, the highest overheating occurs in the MVT case with monthly average overheating hours of 80 % and monthly average intensity of 2.7 °C.

The higher overheating rate in the MVT case is probably due to (1) the presence of the heat recovery unit, which has an undesirable recovery effect even in free cooling mode, (2) the limited air flows moved by the ventilation and finally (3) the lack of forced ventilation control dedicated to ventilative cooling. The scenarios with CNV and MIX strategies show a lower overheating rate, even if lower

percentages of monthly average overheating hours and monthly average overheating intensity are noted in the second case.

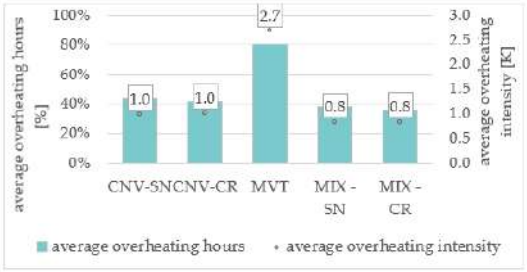

Fig. 6 – Average overheating hours and overheating intensity across all the model zones

As regards electricity consumption, with MVT only this is equal to 75 kWh, MIX-SN to 35 kWh and MIX-CR to 34 kWh. MIX therefore allows a saving of approximately 40 kWh of electricity to be achieved, which corresponds approximately to a reduction of 54 % of electricity consumption for ventilation compared with the case of MVT only.
In the case of CNV, during the cooling season, it is relatively lower than MVT, since the only energy use is for opening and closing the windows.

4. Conclusion

The aim of this research is to demonstrate the potential of mixed-mode ventilation strategies in comparison with the performance of CNV and MVT (without free-cooling option) applied separately, in the context of a dwelling located in a multi-family house in Bolzano (Italy) during the summer season.
This study analyzes and compares three different scenarios in the climate conditions of Bolzano during the cooling season: (1) only CNV, (2) only MVT, (3) a combination of the two (mixed-mode ventilation strategies).
The main results show that CNV and MIX allow a reduction in the overheating risk and an excellent level of IAQ to be achieved, although inadequate outdoor conditions may prevent window opening. MVT allows acceptable IAQ and humidity levels. However, overheating can occur up to 80 % of the time over the summer period due to: (1) the presence of the heat recovery unit, which has an undesirable recovery effect, even in free cooling mode, (2) the limited amount of air flows moved by the ventilation machine and (3) the lack of a forced ventilation control for the ventilative cooling. MIX provides excellent performance in terms of IAQ and overheating control, compared to the former strategies. The lower use of MVT makes it possible to achieve a saving of approximately 40 kWh of electricity for the summer season, which corresponds approximately to a reduction of 54 % of electricity consumption for ventilation compared with the case of MVT only. As shown in the system activation trends, the greater use of natural ventilation corresponds with less frequent use of mechanical ventilation, with a very reduced number of hours of simultaneous activation of the two (approximately 2 % of the total hours).
More in-depth analyses will be carried out on overheating to compare strategies in summer conditions, through an adaptive analysis of thermal comfort.

Acknowledgement

This research is supported by funding from the European Regional Development Fund, operational programme POR FESR 2014-2020 of the Province of Bolzano, project number FESR 1116: NEW-AIR - Nuovo approccio per una qualità degli ambienti interni energeticamente efficiente: ricerca e aziende fanno sistema in Alto Adige.

References

Arata, S., and S. Kawakubo. 2022. "Study on Productivity of Office Workers and Power Consumption of Air Conditioners in a Mixed-Mode Ventilation Building during Springtime." *Building and Environment* 214: 108923.

Belleri, A., F. Avella, and F. Babich. 2021 "The Iimpact Of Controlled Natural Ventilation In Residential Buildings." Roomvent 2020.

Carrilho da Graça, G., and P. Linden. 2016. "Ten Questions about Natural Ventilation of Non-Domestic Buildings." *Building and Environment* 107: 263–73. https://doi.org/10.1016/J.BUILDENV.2016.08.007

CEN. 2019a. *CEN/TR 16798-2:2019 Energy Performance of Buildings - Ventilation for Buildings - Part 2: Interpretation of the Requirements in EN 16798-1 - Indoor Environmental Input Parameters for Design and Assessment of Energy Performance of Buildings Addressing Indo.*

CEN. 2019b. *EN 16798-1:2019 Energy Performance of Buildings - Ventilation for Buildings - Part 1: Indoor Environmental Input Parameters for Design and Assessment of Energy Performance of Buildings Addressing Indoor Air Quality, Thermal Environment, Lighting and Acoustics*."

CIBSE. 2005. "CIBSE Applications Manual AM10." *Cibse Am10*, 70.

Ezzeldin, S., and S. J. Rees. 2013. "The Potential for Office Buildings with Mixed-Mode Ventilation and Low Energy Cooling Systems in Arid Climates." *Energy and Buildings* 65: 368–81. doi: https://doi.org/10.1016/j.enbuild.2013.06.004

Hamdy, M., and G. M. Mauro. 2019. "Optimizing Hybrid Ventilation Control Strategies Toward Zero-Cooling Energy Building." *Frontiers in Built Environment* 5. doi: https://doi.org/10.3389/fbuil.2019.00097

Kim, J., and R. de Dear. 2021. "Is Mixed-Mode Ventilation a Comfortable Low-Energy Solution? A Literature Review." *Building and Environment* 205: 108215. https://doi.org/10.1016/J.BUILDENV.2021.108215

Nicol, F. 2013. The Limits of Thermal Comfort: Avoiding Overheating in European Buildings. London: CIBSE. https://www.cibse.org/knowledge/knowledge-items/detail?id=a0q20000008I7f5AAC

Salcido, J.C., A. A. Raheem, and R. R. A. Issa. 2016a. "From Simulation to Monitoring: Evaluating the Potential of Mixed-Mode Ventilation (MMV) Systems for Integrating Natural Ventilation in Office Buildings through a Comprehensive Literature Review." *Energy and Buildings* 127: 1008–18. doi: https://doi.org/10.1016/j.enbuild.2016.06.054

Salcido, J.C., A. A. Raheem, and R. R. A. Issa. 2016b. "From Simulation to Monitoring: Evaluating the Potential of Mixed-Mode Ventilation (MMV) Systems for Integrating Natural Ventilation in Office Buildings through a Comprehensive Literature Review." *Energy and Buildings* 127: 1008–18. doi: https://doi.org/10.1016/J.ENBUILD.2016.06.054

Schulze, T., and U. Eicker. 2013. "Controlled Natural Ventilation for Energy Efficient Buildings." *Energy and Buildings* 56: 221–32. doi: https://doi.org/10.1016/J.ENBUILD.2012.07.044

Schulze, T., D. Gürlich, and U. Eicker. 2018. "Performance Assessment of Controlled Natural Ventilation for Air Quality Control and Passive Cooling in Existing and New Office Type Buildings." *Energy and Buildings* 172: 265–78. doi: https://doi.org/10.1016/J.ENBUILD.2018.03.023

Wilson, E., C. E. Metzger, S. Horowitz, and R. Hendron. 2014. "2014 Building America House Simulation Protocols." www.nrel.gov/publications

Appendix

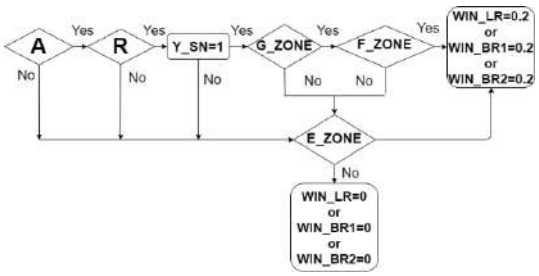

Fig. 7 – CNV-SN

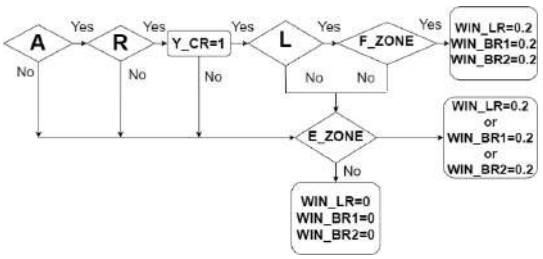

Fig. 8 – CNV-CR

A Comparison Among Three Whole-Building Dynamic Simulation Software and their Applicability to the Indoor Climate Modelling of Historical Buildings

Francesca Frasca – Sapienza University of Rome, Italy – f.frasca@uniroma1.it
Elena Verticchio – Sapienza University of Rome, Italy – elena.verticchio@uniroma1.it
Michele Libralato – University of Udine, Italy – michele.libralato@uniud.it
Paola D'Agaro – University of Udine, Italy – paola.dagaro@uniud.it
Giovanni Cortella – University of Udine, Italy – giovanni.cortella@uniud.it
Anna Maria Siani – Sapienza University of Rome, Italy – annamaria.siani@uniroma1.it
Cristina Cornaro – Università degli Studi di Roma "Tor Vergata", Italy – cornaro@uniroma2.it

Abstract

Building energy simulations are important for assessing the performance of buildings and for designing solutions aimed at reducing energy consumption and carbon emissions. Many software tools perform these simulations, focusing on systems operations and energy losses and gains. When it comes to modelling historical buildings, the simulations could be also used to estimate the risk of damage and decay processes. This paper presents preliminary results based on twelve standardised exercises of increasing complexity for the comparison of microclimate simulations modelled through three whole-building hygrothermal dynamic simulation (BDS) software tools, specifically IDA ICE, WUFI PLUS and ENERGY PLUS. Different to the testing procedures already available, this research focused on the physical variables that are relevant for conservation of historical buildings (i.e., temperature (T) and relative humidity (RH)). Starting from Common Exercise 0 (CE0), seven simulations were customised to capture differences in T values. Then, five building models were specifically conceived to consider some typical features of Historical Buildings (HB0): small window size, heavyweight structures, low insulation of roofs, large volume and free-floating conditions. In the case of CE0, good agreement was found in the simulation of indoor T. In addition, detailed windows reduced the discrepancy in T results compared with the use of simplified windows. In the case of HB0, small windows slightly affected the microclimate simulations regardless of the number of transparent elements and their position. RH variability was driven only by T, as the partial water vapor pressure was affected only by infiltrations through the building. To conclude, the comparison allowed a highlighting of some critical points due to different model implementations, such as weather file timestamp interpretation, window models or irradiation calculations. HB0 models could be used for software and model comparisons, new software testing and training activities.

1. Introduction

Whole-building dynamic simulation (BDS) has been extensively applied over the last decades to study the energy performance of new and existing buildings. BDS can be used as a tool to identify measures aimed at reducing energy consumption and greenhouse gas emissions, as required by the Green Deal to be climate neutral in 2050. In the case of historical buildings, which account for a relevant portion of the total amount of energy consumption (Filippi, 2015) and are part of the cultural heritage, designing efficient and cautious interventions to accomplish the Green Deal goals is a complex matter. In addition, since humidity plays a key role in the different deterioration phenomena affecting materials (making the choice of unique critical thresholds challenging (EN 16893:2018)), simulation can identify the conservation risks of materials triggered by indoor climate conditions (Akkurt et al., 2020; Frasca et al., 2021).
In this context, it was demonstrated that the hygrothermal modeling through BDS can be used advantageously to design solutions for minimizing the energy demand whilst keeping the risk of deterio-

ration low. However, whole set of BDS software needs to accurately model the time behavior of the key hygrothermal variables (e.g., temperature and relative humidity) responsible for degradation on a short and long-term scale. Several commercial BDS software tools are available for hygrothermal modeling. However, since they are based on different numerical methods and parameterizations to solve physical equations, discrepancies may occur in the simulation of indoor climate conditions when the same building is modeled using different BDS software. For this reason, it is worth estimating to what extent the variability among the outputs from different BDS software can affect decision-making on energy (e.g., setup of HVAC systems (Nicolai et al., 2021; Tarantino, 2020)) and conservation issues in real applications (e.g., estimation of climate-induced conservation risks (Frasca et al., 2021; Libralato et al., 2021a)). This evaluation is important, as it offers the chance to provide comparable indoor climate projections regardless of the BDS software in use. This aspect plays a key role when it comes to assessing the impact of the ongoing climate change on material conservation (Campisi & Colajanni, 2021) and the effectiveness of materials for retrofitting/strengthening historical structures. In such a way, the BDS becomes a powerful approach to be applied with the aim of contributing towards meeting global 2030 Sustainable Development Goals (SDGs) in the historical building sector (e.g., definition of adaptation pathways and mitigation strategies against climate change).

This study aimed to compare three commercial whole-BDS software tools (namely EnergyPlus, IDA Indoor Climate and Energy (ICE) and WUFI Plus) frequently validated and commonly used in research activities for the indoor climate modeling of historical buildings (to cite but a few Angelotti et al., 2019; Frasca et al., 2018; Gori et al., 2021; Libralato et al., 2021b). The comparison, based on standardised exercises, was not conceived to identify the most suitable tools for historical buildings modeling, but rather to evaluate the effect on simulations due to the differences in interfaces and modeling approaches. In this contribution, indoor humidity balance considered only the water vapor in/exfiltration through the envelope, to limit the initial uncertainties related to heat and moisture transfer through walls. Further investigations on this topic will be the subject of future studies.

2. Materials and Methods

According to ANSI/ASHRAE 140 Standard, there are three ways to evaluate the accuracy of BDS software tool: empirical validation (comparison with measured data), analytical verification (comparison with a known analytical solution) and comparative testing (the software is compared with itself or to other programs). In this paper, we adopted the comparative testing to estimate the differences among the three BDS software tools. Comparison among BDS software was conceived

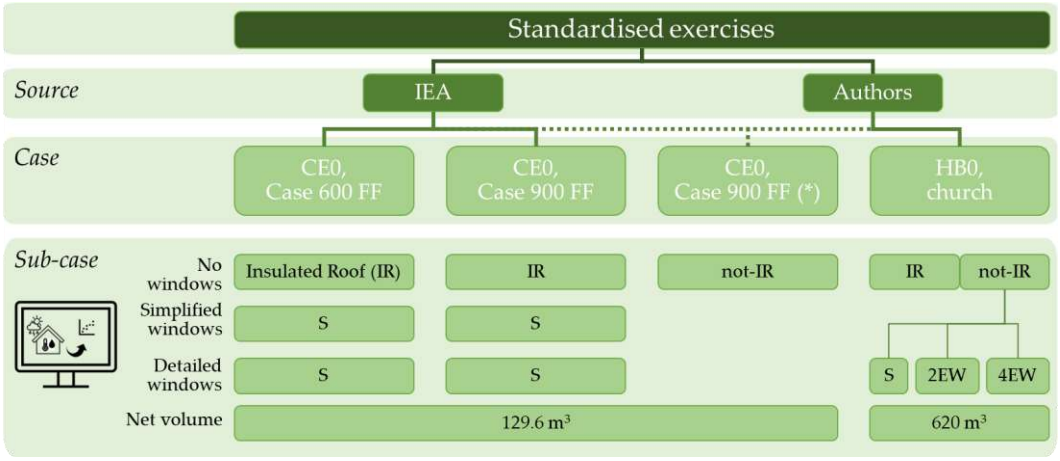

Fig. 1 – Set of simulations based on standardised exercises for the comparative assessment of commercial whole-building dynamic simulation software. CE0: Common Exercise 0; HB0: Historical Building 0; IR: insulated roof; not-IR: not-insulated roof; S: south façade; E: east façade; W: west façade; 2: two windows; 4: four windows

following the schema in Fig. 1. The simulation set consisted of twelve standardised exercises that considered both the BESTEST (Building Energy Simulation TEST) Common Exercise 0 (hereafter called CE0), developed in the framework of the International Energy Agency (IEA), and a historical building (HB0) proposed by the authors. CE0 included seven sub-cases aimed at studying both the influence on simulations of detailed/simplified south-oriented windows as well as the role of a flat insulated/not-insulated roof. HB0, on the other hand, included five sub-cases with a sloping insulated/not-insulated roof and an increasing number of differently oriented windows (South, East-West).

All simulations were run with an initialization period of 31 days and a weather file of data having time steps of 1 hour. All simulations covered one calendar year.

In this study, *.EPW files were used for the weather file. Energy Plus uses the "next hour interpolation scheme", assigning the 1:00 time stamp to the average of the weather file values at hour 0:00 and 1:00. IDA ICE interprets the weather file, assigning the value around the time stamp (average value measured between 30 minutes before and after the time stamp) and the results are reported as the average of the hour preceding the output time stamp. WUFI Plus uses the *.EPW file provided by the user, as it is, starting from hour 01:00 (first observation) and automatically converting radiation and rain (the latter is not included in simulations within this research) in order to consider these loads in accordance with the orientation and the inclination of the individual building component.

IDA ICE climate calculations were based on the "BDFwall" thermal model using a finite differences algorithm of a multi-layer component including wind-dependent bidirectional heat and moisture transport through leaks.

WUFI Plus performed thermal calculations including methods for wind-dependent heat transfer on external surfaces and moisture balance due to in/exfiltration.

In Energy Plus, the heat balance algorithm used is the "Conduction Finite Difference" algorithm, based on the finite difference method. The surface convection algorithm for the external surfaces is the "DOE-2" algorithm, wind-dependent and based on measurements, while for the internal surfaces, constant convection coefficients are used.

In all simulations, a constant air infiltration was set, meaning that no wind-driven air and vapor infiltrations were considered.

2.1 BESTEST Developed in the Framework Of IEA Annex

The CE0 exercise was used to investigate differences in free-floating (FF) simulations among the three BDS software for both lightweight (Case 600) and heavyweight (Case 900) buildings, using the weather at the site of Denver-Stapleton. The FF cases were chosen, as in most historical buildings, active climate control systems are not used. The common exercise adopted was slightly modified to study the features of the BDS software in the simulation of indoor temperature through cases at increasing complexity. All features were retrieved from the Publications and Work Reports available online for the IEA Annex 41 (Rode & Woloszyn, 2007). The influence of solar radiation incident on opaque and transparent surfaces was evaluated modeling the building firstly without windows and, then with windows on the southern façade (U-value = 3.0 $W \cdot m^{-2} \cdot K^{-1}$; hemispherical SHGC = 0.686). Specifically, windows were modeled using both simplified and detailed models available in the BDS software to estimate the influence of the input parameters on the indoor temperature. Windows models differ from the number of input parameters that users can set. In addition, we decided to modify Case 900 FF by replacing the original roof with a not-insulated roof. This case, renamed Case 900 FF (*), was conceived to understand the influence on indoor temperature simulations of not-insulated roof in heavyweight structures (i.e., typical features in historical buildings).

2.2 Standardised Exercise for Historical Building (HB0)

A new standardised exercise for historical buildings (HB0) was proposed by the authors, starting from the average features extracted from the literature on the topic (Akkurt et al., 2020) and from the Italian technical report UNI/TR 11552:2014. All the

cases are considered in free-floating conditions, without internal gains (occupants and other devices) in accordance with CE0.

Fig. 2 shows the 3D geometry of the HB0 model used in the tested sub-cases. Table 1 summarizes some features of the opaque elements in HB0. The simulations are performed using the IWEC weather file for Rome.

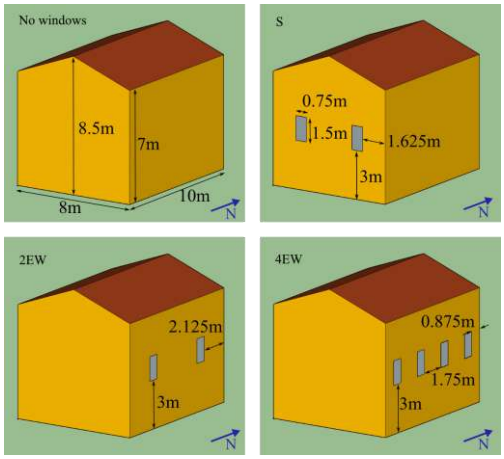

Fig. 2 – 3D sketch of the standardised exercise HB0 used to compare commercial whole-building dynamic simulation software in case of a historical building. Net floor area = 80 m^2; net volume = 620 m^3

U-value of the floor is extremely low in accordance with the BESTest and to avoid the effect of ground modeling on the indoor climate simulation. Windows were modeled as single pane glass with a total transparent area of 0.75×1.5 m^2 without frame and a U-value of 5.5 $W \cdot m^{-2} \cdot K^{-1}$. Five sub-cases were modeled (Fig. 2):

- no transparent elements and insulated roof (hereafter called IR);
- no transparent elements and not-insulated roof (not-IR);
- two windows on south façade (2S);
- two windows on both east and west façades (2EW);
- four windows on both east and west façades (4EW).

The air infiltrations were set to a constant air change of 0.7 h^{-1}, i.e., an average infiltration rate in historical churches (Akkurt et al., 2020). In addition, solar emissivity and absorption of internal/external opaque surfaces were set equal to 0.9 and 0.6, respectively.

2.3 Statistical Analysis

The average of the maximum semi-dispersion (Δ_{max}, i.e., the mean half spread between the smallest and largest number over the simulation period) was used as a synthetic index to compare the variability of hourly microclimate values (i.e., temperature and relative humidity) resulting from the annual simulations modeled by the three BDS software tools. As no reference has been defined so far to estimate agreement between simulations run by different BDS software tools, we decided to use the threshold suggested in (Frasca et al., 2021; Rajčić et al., 2018) for the accuracy assessment of the hygrothermal simulations with respect to microclimate observations: high agreement, if data are within ± 1 °C for T and ± 5 % for RH, good agreement, if data are within ± 3 °C for T and ± 10 % for RH, and poor agreement, if data are beyond ± 3 °C for T and ± 10 % for RH.

Table 1 – Summary of thermo-physical properties of opaque elements in HB0

Building component	**Area**	**U-value**	**Thermal mass**
Unit	[m^2]	[$W \cdot m^{-2} \cdot K^{-1}$]	[$kJ \cdot m^{-2} \cdot K^{-1}$]
External walls	264	0.67	1184
Roof	88	2.48	255
Floor	80	0.04	112

In the case of CE0, the daily evolution of indoor and outdoor temperatures was plotted to assess agreement at a short-term time scale among the three BDS software tools on the coldest and the hottest days of the year of the weather file, respectively.

In the case of HB0, a 3-by-3 matrix of plots was used to analyse the differences in the microclimate outcomes (temperature and partial water vapor pressure). The scatter plots in the matrix allowed a comparison of the outputs between pairs of BDS software (*inter-comparison*). Along the matrix diagonal, stair plots were displayed to study the influence of different HB0 configurations on the microclimate variables within the same BDS software (*intra-comparison*).

3. Results

3.1 BESTEST in IEA Annex (CE0)

Table 2 shows that:

- in the case without windows, temperature simulations were in good agreement both in light- and heavyweight structures;
- the highest variability is associated with the simulations of Case 600 FF with simplified windows;
- the use of detailed windows allowed a reduction in dispersion among simulated indoor T values from 1.4-2.2 °C to 0.9-1.8 °C.

Table 2 – Summary of the maximum semi-dispersion (Δ_{max}) of the hourly temperature values modeled by the three BDS software tools in case of CE0 in free-floating conditions

Case	No windows	Simplified windows	Detailed windows
Case 600 FF	1.0	2.2	1.8
Case 900 FF	0.7	1.4	0.9
Case 900 FF (*)	1.1	-	-

In addition, for both Case 600 FF and Case 900 FF with detailed windows, the modeled minimum annual temperature values (i.e., when the impact of solar radiation is limited) were in accordance with the reference ranges reported in (Rode & Woloszyn, 2007).

On the other hand, lower agreement was observed with the reference ranges in terms of the average and maximum annual temperature values, due to differences in the calculation of solar gains through windows. The first source of discrepancy in the time series of the results is different interpretation of the weather file (WF) due to the different conversion of the time stamp to specific points in time used by the BDS software.

As an example, Figs. 3 and 4 show that the weather file temperatures considered by each software (WF series) have a time shift of at least one hour.

The discrepancy in the WF series influences the simulation of indoor temperatures. Indeed, although highly correlated, T peaks modeled by WUFI Plus and Energy Plus models showed a one-hour delay compared with IDA ICE. This behavior is also affected by differences in the calculation of the wind-driven coefficients of convection and radiation heat transfer, as described in Section 2.

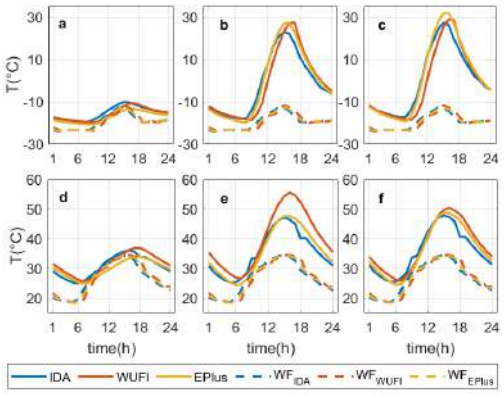

Fig. 3 – Time evolution of temperature on the coldest day (upper panels) and the warmest day (lower panels) in Case 600 FF without windows (a, d), with simplified windows (b, e) and with detailed windows (c, f). The WF series indicates the weather file temperature considered by the software

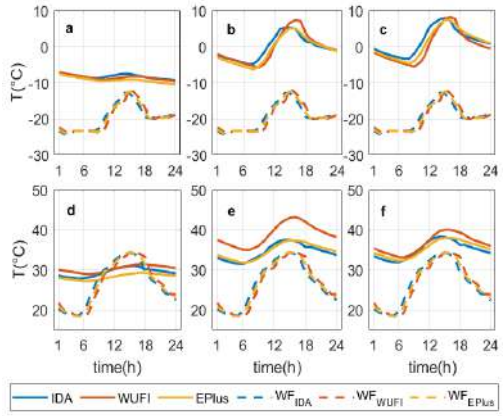

Fig. 4 – Time evolution of temperature on the coldest day (upper panels) and the warmest day (lower panels) in Case 900 FF without windows (a, d), with simplified windows (b, e) and with detailed windows (c, f). The WF series indicate the weather file temperature considered by the software

Moreover, the three BDS software tools calculate the resulting solar radiation incident on surfaces differently, leading to a different indoor heat balance due to the solar net radiative balance. For example, Energy Plus and IDA ICE use the Perez model, but with a different set of coefficients. This effect was evident when comparing the intensity of T peaks in the case of simplified windows models, which seem to be differently reproducing the transparent surface behavior in both Case 600 FF (Fig. 3) and Case 900 FF (Fig. 4).

3.2 Standardised Exercise for Historical Building (HB0)

In the case of HB0, simulations were run using detailed windows.

The values of total annual incident solar radiation on opaque surfaces (walls and roof) were compared to better interpret whether some of the differences in T simulations were ascribable to this contribution (Fig. 5). The smallest differences can be seen for the east side of the roof, as well as for east and west façades. However, specific implementations of the combination of direct and diffuse solar radiation result in different solar gains at each opaque surface. For example, in WUFI Plus, the total annual incident solar radiation is higher on north and lower on south façades than those of the other two BDS software tools. In addition, in IDA ICE, the total annual incident solar radiation on the west side roof is higher not only than that of the other two BDS software but also than that of the east side roof.

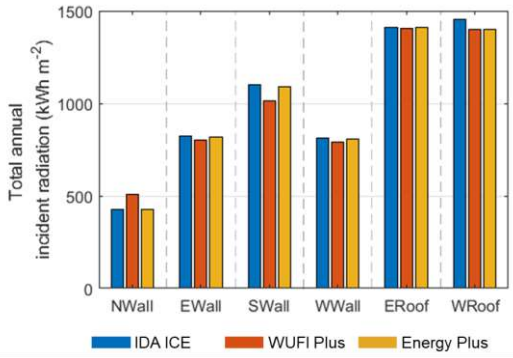

Fig. 5 – Total irradiance incident on opaque elements modeled by the three BDS software for each HB0 case

It was found that T and RH simulations resulting from the three BDS software tools showed good agreement with Δ_{max} ranging between 0.9-1.5 °C for T and 4.9-6.1 % for RH (Table 3).

T simulations modeled by WUFI Plus were on average higher (up to 2 °C) than those modeled by IDA ICE and Energy Plus. For the sake of brevity, only the minimum values were plotted in Fig. 6 as differences in Δ_{max}, for average and maximum values are negligible.

Table 3 – Summary of the maximum semi-dispersion (Δ_{max}) of the hourly temperature (T) and relative humidity (RH) values modelled by the three BDS software in case of HB0 in free-floating conditions

Sub-case	Code	T (°C)	RH (%)
no windows			
insulated roof	HB0_0	0.9	4.1
not-insulated roof	HB0_1	1.5	6.1
two S-windows	HB0_2S	1.4	5.6
two E-W- windows	HB0_2EW	1.4	5.6
four E-W- windows	HB0_4EW	1.4	5.3

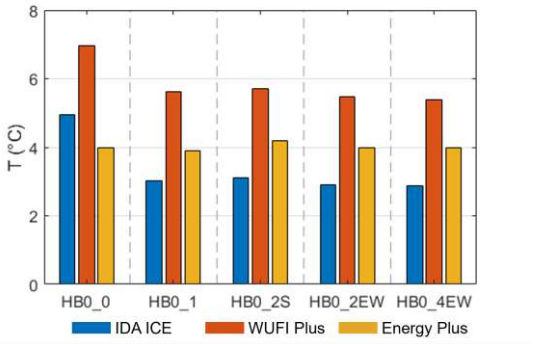

Fig. 6 – Annual minimum temperature values (T) modeled by the three BDS software for each HB0 case

As HB0 differed from Case 900 FF (*) only for the building net volume (Fig. 1), we can assume that differences among the three software tools can be mainly ascribable to the amount of air mass in the calculation. Fig. 7 shows a matrix plot that allows a comprehensive assessment of the differences among HB0 sub-cases (BDS *intra-comparison*, i.e., stair plots along diagonal matrix with the frequency distribution) and among BDS software (*inter-comparison*, scatter plots of paired BDS software).

Looking at the stair plots, transparent elements did not strongly affect T distributions within the same BDS software. In addition, simulations performed by Energy Plus were not sensitive to the insulation on the roof (HB0_0 and HB0_1), as no significant difference in annual T values and distributions was detected (on the contrary, IDA ICE and WUFI Plus simulated lower T values in HB0_0 than those in HB0_1 due to the lower heat transmittance of the roof). Looking at the scatter plots, T simulations resulting from IDA ICE and Energy Plus are scat-

tered around the bisectrix (dashed grey line in Fig. 6), whereas T values simulated by WUFI Plus were usually above the bisectrix in all the sub-cases. If we compare T simulations of WUFI Plus and Energy Plus, it is evident that they were more in agreement in HB0_0 than in the other sub-cases, where T by WUFI Plus were higher than those by Energy Plus. This might be due to differences in the convective heat transfer coefficient in vertical upward flow.

Regarding RH simulations (Table 3), Δ_{max} ranged from between 4.1 % (HB0_0) and 6.1 % (HB0_1), showing good agreement among BDS software. To study the indoor humidity conditions without dependence on T, the partial water vapor pressure (e_v) values were compared in the matrix plot (Fig. 6). Since e_v did not change from one sub-case to another, the differences in RH values were driven only by the difference in T, meaning that moisture exchanges occurred only by infiltration. Although BDS software were able to similarly simulate water vapor saturated conditions, IDA ICE and Energy Plus modeled a higher frequency of saturation conditions (for the sake of brevity, RH plots are not shown).

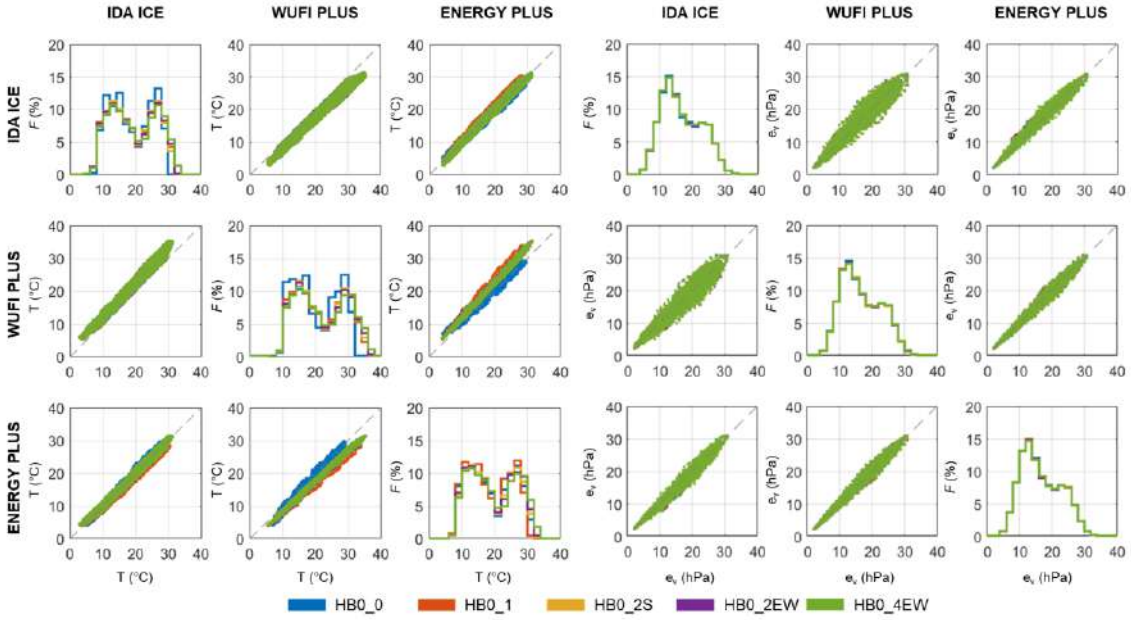

Fig. 7 – Matrix plots of temperature (T) and partial water vapor pressure (e_v) modeled by the BDS software for each HB0 case. Stair plots along the diagonal show the frequency distribution (F)

4. Conclusion

In this paper, a new set of benchmarks for historical building models was presented and used with three BDS software tools with the aim of evaluating the effect on indoor climate simulations related to the differences in their modeling approaches. The benchmarks are designed to represent the characteristics of historical buildings and consist of twelve standardised models, seven of them being a variation of the BESTEST Common Exercise 0 (CE0), while the others are a variation of a single zone historical building (HB0), proposed by the authors. All the buildings are considered in the free-floating condition, without internal gains (occupants and other devices). The results of the comparison of IDA ICE, WUFI Plus and Energy Plus were presented, showing how the benchmark could be used to identify the differences between software.

The variables considered for the comparison are the ones of interest for the conservation of historical buildings, such as indoor air temperature and relative humidity. Incident solar irradiation is also considered for its relevance in the calculations. The maximum semi-dispersion between the time series is used to evaluate the differences between the simulations. Because of their relevance, the time

series of the temperatures of the coldest and the hottest day of the year are compared.

When the benchmark comparison is performed on the three software tools, the results highlighted the differences in the software models and implementations:

- the comparison among the temperature simulations in the case of CE0 showed good agreement in the sub-case without windows both in light- (Case 600 FF) and heavyweight structures (Case 900 FF);
- the addition of the windows increased the variability among the results, with the highest dispersion associated with the Case 600 FF with simplified windows and the lowest with the Case 900 FF with detailed windows;
- in the case of HB0, the annual minimum values of temperature simulated by the BDS software showed low agreement. In general, T simulations modelled by WUFI Plus were on average higher than those modelled by IDA ICE and Energy Plus. These differences are probably ascribable to the amount of air mass considered in the calculation.
- some discrepancies found in the modeled incident solar radiation might have been caused by the different implementations in the BDS software of the combination of direct and diffuse solar radiation resulting in different solar gains at each opaque surface.

These preliminary results provided a basis for two potential future research lines:

- a more detailed comparison of the BDS software, including models of simultaneous heat and moisture transfer through walls, would require an in-depth study of the hygrothermal properties of historical building materials, including also simplified models (Zu et al., 2020);
- a software-independent procedure for the calibration of a hygrothermal model of a historical building should be defined using indoor temperature and relative humidity observations collected in a real context.

Both these research lines could lead to a better interpretation of the energy and indoor climate scenarios through hygrothermal simulation and an increased awareness of the confidence of calibration in the case of historical buildings (Frasca et al., 2019).

Acknowledgement

Frasca F. and Libralato M. acknowledge fellowship funding from MUR (Ministero dell'Università e della Ricerca) under PON "Ricerca e Innovazione" 2014-2020 (D.M. 1062/2021). The research leading to these results has also received funding from the MIUR of Italy within the framework of the PRIN2017 project "The energy flexibility of enhanced heat pumps for the next generation of sustainable buildings (FLEXHEAT)", grant 2017KAAECT. Frasca F. and Siani A.M. thank for the financial support of the conference fee the CollectionCare project (European Union's Horizon 2020 research and innovation programme under grant agreement No 814624).

Nomenclature

Acronyms

BDS	Building Dynamic Simulation
CE0	Common Exercise 0
E	East
e_v	Partial water vapor pressure
HB0	Historical Building 0
IEA	International Energy Agency
IR	Insulated Roof
N	North
S	South
SHGC	Solar Heat Gain Coefficient
U-value	Thermal transmittance
W	West

References

Akkurt, G. G., N. Aste, J. Borderon, A. Buda, M. Calzolari, D. Chung, V. Costanzo, et al. 2020. "Dynamic Thermal and Hygrometric Simulation of Historical Buildings: Critical Factors and Possible Solutions." *Renewable and Sustainable Energy Reviews* 118: 109509. doi: https://doi.org/10.1016/j.rser.2019.109509

Angelotti, A., M. Ballabio, L. Mazzarella, C. Cornaro, G. Parente, F. Frasca, A. Prada, et al. 2019. "Dynamic Simulation of Existing Buildings: Considerations on the Model Calibration." *Building Simulation Conference*

Proceedings 6: 4165–72. doi: https://doi.org/10.26868/25222708.2019.210439

ASHARE. 2007. *ANSI/ASHRAE Standard 140: Standard Method of Test for the Evaluation of Building Energy Analysis Computer Programs*. Atlanta: American Society of Heating, Refrigerating and Air-Conditioning Engineers.

Campisi, T., and S. Colajanni. 2021. "Technological Performances Upgrading and Rehabilitation of Building Heritage inside the Historic Centre of Palermo." *IOP Conference Series: Earth and Environmental Science* 863(1). doi: https://doi.org/10.1088/1755-1315/863/1/012004

CEN. 2018. *EN 16893:2018. Conservation of cultural heritage - Specifications for location, construction and modification of buildings or rooms intended for the storage or use of heritage collections*. European Committee for Standardization (CEN), Brussels, Belgium.

Filippi, M. 2015. "Remarks on the Green Retrofitting of Historic Buildings in Italy." *Energy and Buildings* 95: 15–22. doi: https://doi.org/10.1016/j.enbuild.2014.11.001

Frasca, F., C. Cornaro, and A. M. Siani. 2018. "Performance Assessment of a Heat and Moisture Dynamic Simulation Model in IDA ICE by the Comparison with WUFI Plus." *In IOP Conference Series: Materials Science and Engineering*. doi: https://doi.org/10.1088/1757-899X/364/1/012024

Frasca, F., E. Verticchio, C. Cornaro, and A. M. Siani. 2019. "Optimising Conservation of Artworks, Energy Performance and Thermal Comfort Combining Hygrothermal Dynamic Simulation and On-Site Measurements in Historic Buildings." *In Proceedings of the 16th IBPSA Conference*: 2856–63.

Frasca, F., E. Verticchio, C. Cornaro, and A. M. Siani. 2021. "Performance Assessment of Hygrothermal Modelling for Diagnostics and Conservation in an Italian Historical Church." *Building and Environment* 193: 107672. doi: https://doi.org/10.1016/j.buildenv.2021.107672

Gori, V., S. Efthymiopoulos, X. Tian, J. Dong, and V. Marincioni. 2021. "Assessing the Role of Simulation Tool Selection for the Evaluation of Heat and Moisture Balance in Historic Buildings." *IOP Conference Series: Earth and Environmental Science* 863 (1). doi: https://doi.org/10.1088/1755-1315/863/1/012050

Libralato, M., A. De Angelis, O. Saro, M. Qin, and C. Rode. 2021a. "Effects of Considering Moisture Hysteresis on Wood Decay Risk Simulations of Building Envelopes." *Journal of Building Engineering* 42: 102444. doi: https://doi.org/10.1016/j.jobe.2021.102444

Libralato, M., A. De Angelis, G. Tornello, O. Saro, P. D'agaro, and G. Cortella. 2021b. "Evaluation of Multiyear Weather Data Effects on Hygrothermal Building Energy Simulations Using Wufi Plus." *Energies* 14(21). doi: https://doi.org/10.3390/en14217157

Nicolai, A., S. Hirth, and M. Madjidi. 2021. "SimQuality. A Novel Test Suite for Dynamic Building Energy Simulation Tools." *Proceedings of Building Simulation 2021*. doi: https://doi.org/10.13140/RG.2.2.27833.90725

Rajčić, V., A. Skender, and D. Damjanović. 2018. "An Innovative Methodology of Assessing the Climate Change Impact on Cultural Heritage." *International Journal of Architectural Heritage* 12 (1): 21–35. doi: https://doi.org/10.1080/15583058.2017.1354094

Rode, C., and M. Woloszyn. 2007. "Whole-Building Hygrothermal Modeling in IEA Annex 41." *Proceedings of the 10th ASHRAE conference on Thermal Performance of the Exterior Envelopes of Whole Buildings*.

Tarantino, S. 2020. "Accuracy of Code Compliant Design-Stage Building Energy Performance Simulation Models." *Advancements in Civil Engineering & Technology* 4 (2): 1–17. doi: https://doi.org/10.31031/acet.2020.04.000581

UNI. 2014. *UNI/TR 11552:2014 Standard. Opaque Envelope Components of Buildings - Thermo-Physical Parameters*.

Zu, K., M. Qin, C. Rode, and M. Libralato. 2020. "Development of a Moisture Buffer Value Model (MBM) for Indoor Moisture Prediction." *Applied Thermal Engineering* 171: 115096. doi: https://doi.org/10.1016/j.applthermaleng.2020.115096

QGIS-Based Tools to Evaluate Air Flow Rate by Natural Ventilation in Buildings at Urban Scale

Silvia Santantonio – Politecnico di Torino, Italy – silvia.santantonio@polito.it
Guglielmina Mutani – Politecnico di Torino, Italy – guglielmina.mutani@polito.it

Abstract

Urban-scale evaluations of aerodynamic and morphological parameters allow correction of the wind speed within the urban boundary layer, as the wind profile is strongly influenced by the presence of roughness elements. This can have important implications for defining urban strategies for the reduction of buildings' energy consumption and the improvement of air quality and liveability of outdoor spaces. Among the current models for assessing the air flow rate by natural ventilation in buildings at urban scale, this study aims to define a GIS-based methodology, using existing databases and an open source QGIS plug- in. From a digital surface elevation dataset, and considering prevalent wind directions, the displacement height (z_d) was determined. The wind speed was corrected, applying the logarithmic or turbulent laws of wind profile, respectively, above and below z_d. This method could determine the spatial distribution of wind speed, considering each building façade characteristics and its surroundings. Resulting wind pressure on windward and leeward façades drives the air flow rate inside the buildings. Further developments of this work will improve the air flow modelling in buildings with other tools for applications at urban scale.

1. Introduction

Understanding and modeling the urban local wind environment has been a focus of attention for many researchers, especially in high density urban areas. Here, the heterogeneity of urban morphology, due to the presence of different type of roughness elements, strongly influences local wind performance (Peng et al., 2019). Studying air flow properties has important implications for urban design in terms of energy consumption, outdoor thermal comfort, and air quality, and building energy performance for space heating and cooling (Suszanowicz, 2018). Relations between urban morphology and wind flow can be assessed with different methods: i) field measurements, whose high time and cost limitations mean that they are not suitable for large scale studies; ii) wind tunnel experiments, which constitute the reference dataset, despite operating costs and application limits; iii), Computational Fluid Dynamic (CFD) numerical modellings with high computational requirements (Buccolieri & Hang, 2019); iv) parametric models, mainly based on wind tunnel test or CFD simulations, having a good cost-benefit ratio but limited application field; v) Geographical Information System (GIS) and remote sensing techniques that retrieve roughness parameters based on interactions with buildings' geometries at city-scale, especially at mesoscale (Wong et al., 2010). Into the last group fits the place-based methodology presented in this work: a flexible integration of physical laws of wind phenomena and local characteristics of the urban context, based on the open-source software QGIS and existing databases, already used by urban planners. The study is part of broader research that aims to implement an hourly GIS-based engineering model to assess the energy consumption for the space heating and cooling of residential buildings at urban and district scales (Mutani & Todeschi, 2020; Mutani et al., 2022). The implementation concerns the monthly and hourly detail definition of number of air change per hour (ach) that influences thermal loads by natural ventilation in the building's thermal energy balance, considering the air flow rate for infiltration caused by wind-driven effects. The wind pressure generated on a building façade is evaluated as a function of the vertical and horizontal distribution of wind speed, starting from the characterization of roughness and

built environment characteristics. After a brief description of natural wind profiles in urban areas, this work aims to present some QGIS tools currently available to assess the urban wind field and its relationship with roughness parameters, applying the methodology to a case study.

2. Physical Laws of Wind Profiles

The wind phenomenon is influenced by the surface roughness of the ground and other objects (i.e., buildings, vegetation) that create obstacles to the undisturbed flow. A wind profile is associated with different environmental contexts (i.e., urban, sub-urban, rural areas), describing mathematically the mean wind speed (U_z) as a function of height (z) from the ground. Reference heights individuate boundary layers that limit air flow zones in which different physical laws can be applied.

2.1 Boundary Layers and Heights

In this work, reference was made to an older bibliography for defining wind phenomena, and to a more recent one for applying physical laws. Considering the horizontal scale of wind influence, three scale of interest exist (Oke, 2004): i) the *mesoscale*, where weather and climate are influenced by the whole city; ii) the *local scale*, where landscape features or topography are considered; iii) the *microscale*, where variations occur over very short distances, causing great airflow perturbations around roughness elements. Regarding the vertical scale of wind influence, relevant boundary layers and heights are defined:

- Atmospheric Boundary Layer (ABL)

In the ABL, or Planetary Boundary Layer, which extends up to 1-2 km (Z_{ABL} in Fig.1), the undisturbed wind flow present in upper layers is progressively slowed down due to friction with the ground and roughness elements. In the case of smooth soils (i.e., rural areas) the wind speed reaches upper layers values more quickly than urban areas.

- Urban Boundary Layer (UBL)

The UBL identifies the part of the ABL influenced by the presence of a large city. It is divided into: Mixed Layer (ML), whose upper limits coincide with the height of UBL (Z_i, in Fig.1), and Surface Layer (SL) whose depth is about a tenth of UBL ($Z_{i/10}$, in Fig.1), and which, in turn, is divided into two.

- Internal Sub-Layer (ISL)

In the upper layer of SL, the flow is free of individual wakes associated with roughness elements, and wind can be assumed as a constant flux with a laminar, horizontally homogeneous flow (Re <2000). Here, the wind log law can be applied to determine average wind speed (U_z).

- Roughness Sub-Layer (RSL)

This extends from ground level to the blending height Z_{RSL} (Fig. 1), where effects of individual roughness elements are visible. Airflow perturbation caused by individual surface and obstacles persists for a certain distance until it is mixed with the effect of turbulent eddies. Blending distance depends on the magnitude of the effect, the wind velocity, and the stability of the flux. Minimum $Z_{RSL} = 2 \cdot Z_H$ is suggested by observations in dense urban settings (Oke, 2004); it can vary with density, staggering, and heights of objects.

- Urban Canopy Layer (UCL)

This is equivalent to the mean height Z_H (Fig. 1) of the main roughness elements. To overcome the frictional effect of surface roughness elements, the wind flux loses its momentum: turbulent flows are generated near the surfaces (Re > 4000). Lower wind speed can occur, and turbulent models are required to calculate wind velocity inside urban canyons.

2.2 Aerodynamic Roughness Parameters

At local and micro scale, in the air zone where the flow is free from roughness-element turbulent wakes, two aerodynamic parameters are used to describe the wind speed profile influenced by surface roughness elements (Fig. 1):

- Zero-plane displacement height (z_d)

It is intended as a new "ground level" from which the wind profile originates, after the wind passes over high-density buildings (Lv et al., 2022), and it is used for setting a base for the application of the wind log law (Oke, 2004). According to (Abubaker et al., 2018), it is the depth of still air trapped among the roughness elements.

- Roughness length (z_0)

This is the height above Z_d at which wind velocity becomes zero when the logarithmic wind profile is applied and represents the size of the eddies produced from wind moving over a rough surface (Abubaker et al., 2018). It depends on turbulence intensity and, therefore, on the surface drag.

In urban areas, three flow regimes were classified when aerodynamic parameters are morphometrically determined (Oke, 2004): i) *isolated flow*, where buildings are individual wake generators; ii) *wake interference flow*, where wakes reinforce each other as space between buildings is close; iii) *skimming flow*, where main flow skips over the top of the great density of buildings. The wake interference regime is the one in which the greatest roughness activity can be generated. The building density (λ_P) is very important in cities, where the high variability of roughness height can cause complex surface morphology and turbulent wakes that are challenging to assess.

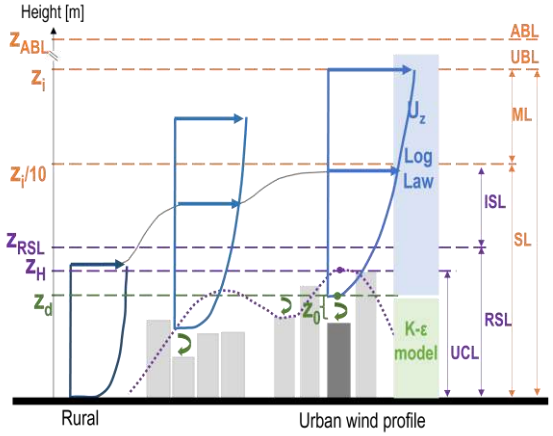

Fig. 1 – Boundary layers and their reference height (y axis) at mesoscale (in orange) and local scale (in purple)

2.3 Wind Profiles Laws at District Scale

In this work, two methods were compared to determine the wind speed (U_z), from measured U_{ref} at reference height (z_{ref}): the *Cp methodology* and *z_d methodology*, whose procedures are schematized in Fig. 2. U_{ref} need to be adjusted considering the wind incident angle (Eq. 1, in Fig. 2) and objects and terrain roughness of the context. For wind fluxes that occur above the displacement height z_d, two wind profiles can be applied.

The power law wind profile is based on empirical assumption for mesoscale application for large heights (30 m < z < 300 m), but it is less accurate when close to the ground. It can be determined according to Eq. 2 (Fig. 2), where V_z is the wind speed at height z [m·s-1], $U_{ref,corr}$ is the adjusted reference wind speed [m·s-1] at height z_{ref}, z_{UBL} is the height of the UBL [m], and ν the terrain roughness coefficient (wind speed profile exponent) [-]. The last two parameters refer to tabular data, determined through empirical assumptions from real measurements or wind tunnel tests. Several references exist in the literature, including the unified terrain roughness categories given by (Choi, 2009). Table 1 reports typical values for roughness parameters for the most used terrain categories.

Table 1 – Referenced roughness parameters for terrain typology

Terrain roughness type	**Z_{UBL} [m]**	**υ [-]**	**Zo [m]**	**Zd [m]**
Level surfaces, grass land	250	0.10	-	-
Flat open country	280	0.14	0.03	0.0
Rolling/level surfaces	300	0.22	0.1	0.0
Heterogeneous surface	330	0.28	-	-
Low density suburban areas	390	0.34	0.5	0.7·z_H
Mid-high density urban areas	450	0.40	1.0	0.8·z_H
Very high density city areas	510	0.45	> 2.0	0.8·z_H

The logarithmic law wind profile allows an approximation of the wind profile at lower boundary condition (z ≤ 200m). Its lower limit of application at urban local scale is identified by z_0 and z_d, according to the logarithmic function of Eq. 3 (Fig. 2), where U_z is the wind speed [m·s^{-1}] at height z, $U_{ref,corr}$ is the corrected wind speed at height z_{ref}, z_d is the zero-plane displacement height [m], and z_0 is the roughness length [m]. At microscale, inside the urban canopy layer, where turbulent fluxes occur at a height z lower than displacement height z_d, the log-law is not valid and turbulent models should be applied. The k-epsilon (k−ϵ) model is the most common model in CFD analyses for simulating the mean flow characteristics for turbulent flow conditions. It belongs to the Reynolds-averaged Navier Stokes (RANS) models that represent an optimal compromise between accuracy and efficiency for microclimate studies in urban environments (Javanroodi et al., 2022).

2.4 Wind Flow at Building Local Scale

Natural ventilation in buildings is driven by pressure differences on building façades by two forces: the stack (or buoyancy) effect and the wind-driven effect. This work focuses on the latter, while in future works, buoyancy will be considered in a multi-zones airflow model to assess ventilation loads in buildings. Wind generates positive pressure and negative pressure on windward and leeward façades, respectively. The surface pressure (P_s, P_v) can be calculated according to Eq.4 or Eq.5 (Fig. 2), respectively, with *Cp* and z_d *methodology*, where ϱ is air density [kg·m^{-3}], V_z (power law) and U_z (log-law) are the adjusted wind speed [m·s^{-1}] and C_p is the pressure coefficient [-]. It is a non-dimensional coefficient estimated according to i) real scale measurements, ii) wind tunnel tests, iii) CFD and iv) parametric models, among which there is *Cpcalc+* software (Chiesa & Grosso, 2019), whose input data are listed in Table 2. Even if the power law application determines a vertical variation of wind velocity at the local urban scale, the C_p allows the distribution of wind speed horizontally and vertically at the scale of interesting points on a building façade with respect to the windward and leeward façade dimensions; it also considers building geometry and orientation, urban density, and roughness characteristic of the surrounding environment. The algorithm used in *Cpcalc+* is based on experimental wind tunnel tests results, considering different typical buildings and urban contexts (e.g., Fracastoro et al., 2001). Limitations of the software concern the scale of the application field (suitable at building scale, not at district-urban scale), and the application range of some parameters, especially the relative building height and the aspect ratios (0.5≤FAR≤4 and 0.5≤SAR≤2).

Table 2 – Input data required by *Cpcalc+* software (https://iris.polito.it/handle/11583/2579969)

Climate data			
Wind speed		Wind direction	
Urban parameter			
Plan Area Density	Surroundings building height		Wind profile exponent
Building Characteristic			
Frontal/Side Aspect Ratio (FAR/SAR)	Building dimension	Building azimuth	Roof slope

2.5 Place-Based Tools and Plug-Ins for Wind Analysis at Urban Scale

In this paragraph, GIS-based tools and a plug-in to assess wind at urban scale are described.

SAGA GIS software presents some useful tools for wind correction at the mesoscale, to consider terrain influence on observed meteorological conditions. In the *Climate and Weather* section, the *Wind Effect Correction* tool allows the scaling factor of the wind effect in determining ABL conditions (e.g., precipitation, cloudiness) to be calibrated. In the *Terrain analysis - Morphometry* section, the *Wind Effect* tool classifies wind exposed and shades area through a dimensionless index, considering terrain elevation and specifying wind data; these tools were created for topo-climatic wind assessments. Existing methods to determine the aerodynamic parameters at urban scale can be grouped into three main classes: i) *reference-based values from field observations,* which provide a wide range of values whose application in complex and heterogenous urban areas has some limitations; ii) *anemometric methods* requiring experimental campaigns, applicable on a limited and non-replicable scale; iii) *morphometric methods* based on the relationships between aerodynamic parameters and roughness elements geometry, described through urban morphological parameters, already used both at mesoscale (Darmanto et al., 2017) and local scale (Badach et al., 2020). This work aims to present z_d *methodology* (Fig. 2), determining z_d and z_0 using the open-source QGIS plug-in Urban Multi-scale Environmental Predictor (UMEP), version 1.6.1 (Lindberg et al. 2016). Among the pre-processing tools, there are the *Urban Morphology- Morphometric Calculator (Grid)* and *(Point*), which only differ in the geometry of the calculation area. Both calculate five morphometric parameters (Table 3, Fig. 3) based on digital surface models (DSM) to calculate the two aerodynamic parameters according to six different methods (Table 4). The required input data are three separate raster files (*geoTIFF)* with the same pixel resolution: DSM, digital elevation model (DEM, only ground elevation), and roughness elements elevation, calculated with the QGIS *Raster calculator tool*, by subtracting the other two rasters (DSM-DEM).

	Cp method	**z_d method**
Software:	CpCalc+	QGIS UMEP plug-in
Input data:	Wind speed (U_{ref}) from a reference height (z_{ref}) of the weather station	
Uref adjustment – wind incident angle (θ)	Eq. 1) $U_{ref.corr} = U_{ref} \cdot \cos(\theta)$ — θ wind incident angle normal to the windward building facade	
Uref adjustment – terrain and object roughness correction:	**Power law wind profile** Eq. 2) $V_z = U_{ref.corr} \cdot (\frac{z_{UBLref}}{z_{ref}})^{v_{ref}} \cdot (\frac{z}{z_{UBL_z}})^{v_z}$ v z_{UBL} - Tabular data - Mesoscale	**Log law wind profile** Eq. 3) $U_z = U_{ref.corr} \cdot \left[\frac{\ln(\frac{z-z_d}{z_0})}{\ln(\frac{z_{ref}-z_d}{z_0})}\right]$ Z_d Z_0 - GIS plug-in - Local scale **Turbulent wind profile** *Uz from correlations of CFD results*
	vertical distribution for each z_n	vertical distribution for each z_n
		horizontal distribution for each grid cell
Pressure coefficient (Cp) calculation:	vertical and horizontal distribution on building facades (from Cpcalc+)	
Surface pressure :	Eq. 4) $Ps\,[Pa] = \frac{1}{2} \cdot \rho \cdot V_z^2 \cdot Cp$	Eq. 5) $Pv\,[Pa] = \frac{1}{2} \cdot \rho \cdot U_z^2$
Limits of the methodology:	• Roughness correction at mesoscale (wide scale) • Roughness correction from tabular data (wide range values) • Application range of some parameters based on experimental tests (0,5 ≤FAR ≤4 and 0,5 ≤SAR ≤2, building height) • Building scale application not suitable for district scale	• Results accuracy strongly affected by the radius of calculation area and size of grid cells (no unified standard for selecting area) • Horizontal distribution of wind speed variation only for heights greater than Zd (above canopy layer)

Fig. 2 – Comparison between the Cp and z_d methodologies for the assessment of surface pressure generated by the wind flow

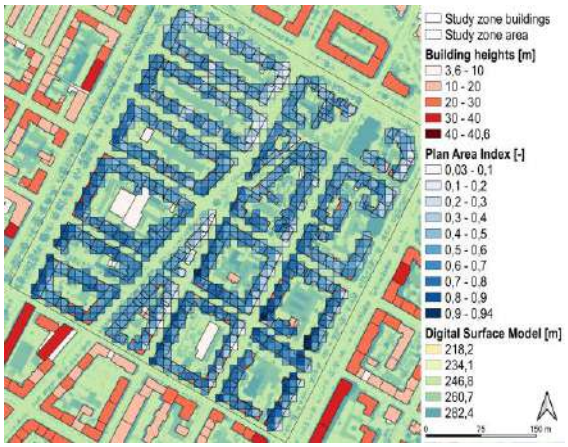

Fig. 3 – Plan area index (λp) within its range (0-1) for a squared cell grid, considering building heights in a selected area

The main setting concerns the extension of the calculation area that will be considered to determine the morphological and aerodynamic parameters, indicating the radius length from the selected point or the centroid of each grid cell. There are no unified standards for the size of calculation area, though it greatly affects the accuracy of results (Lv et al., 2022). In addition, it is possible to specify the wind direction (in degrees, from north - clockwise). The five morphometric parameters calculated in UMEP correspond to some of the most frequently used urban parameters in the urban planning research field; Table 3 reports their definitions. The morphological and aerodynamic parameters can vary according to the analyzed wind direction, allowing more precise results of z_d and z_0, considering the variability of the roughness surfaces (Oke, 2004).

Table 3 – Urban parameters defined in QGIS-UMEP tool

Urban parameter	**Unit**	**Formula**
Plan Area Index	[-]	$\lambda_p = (\sum_{i=1}^{n} Api) / A_T$
Frontal Area Index	[-]	$\lambda_f = (\sum_{i=1}^{n} Afi) / A_T$
Mean Height	[m]	$z_H = (\sum_{i=1}^{n} Hi) / n$
Maximum Height	[m]	$z_{Hmax} = \mathrm{Max}\,(H_i)$
Height variability	[m]	$z_{Hstd} = \sqrt{\frac{1}{n}\sum_{i=1}^{n}(Hi - Z_H)^2}$

The UMEP tool calculates the aerodynamic roughness parameters (z_d, z_0) by applying six different morphometric methods (Kent et al., 2017). For each method, Table 4 reports urban parameters used in the calculation: plan area density (λ_p), frontal area ratio(λ_f), average (z_H) and maximum (z_{Hmax}) buildings height and height variability (z_{Hstd}). In this work, the Kanda method was used (Kanda et al., 2013), as it is more suitable in dense, city-center districts, due to the importance of considering roughness elements' height heterogeneity. The flow chart in Fig. 4 summarizes the *z_d methodology* used to determine the aerodynamic parameters and the proper wind profile with the QGIS UMEP plug-in.

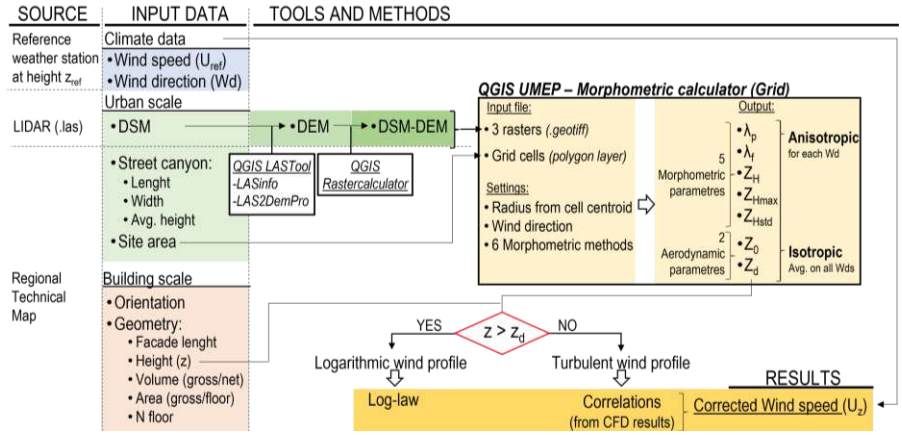

Fig.4 – Flow chart of the z_d methodology based on QGIS-UMEP tools

Table 4 – Morphometric methods included in the UMEP plug-in

Method	Urban Parameter				
	λ_p	λ_f	Z_H	Z_{Hmax}	Z_{Hstd}
Rule of thumb			X		
Raupach		X	X		
Bottema	X	X	X		
Macdonald	X	X	X		
Millward-Hopkins	X	X	X		X
Kanda	X	X	X	X	X

3. Application of the UMEP Tool at District Scale in Turin

The place-based methodology was applied to a central district in the city of Turin (Italy). For an in-depth analysis of case study zone (200 m x 200 m) selection criteria and characteristics, refer to (Mutani et al., 2021). The local monthly prevalent wind is from North-NorthEast and West-SouthWest, with a mean velocity of 1.4 m/s. Table 5 shows main the urban parameters calculated in QGIS to describe the case study area.

Table 5 – Morphological and roughness characteristic of the area

Urban parameter	Unit	Study area
Built Coverage Ratio (BCR)	[-]	0.33
Plan Area Density (PAD)	[-]	1.66
Volume Area Ratio (VAR)	[-]	0.30
Surrounding buildings' height	[m]	19.5
Height of boundary layer (z_{UBL})	[m]	450
Wind speed profile exponent (v)	[-]	0.4
Short urban canyon (L/H)	[m]	≤ 3
Long urban canyon (L/H)	[m]	> 5

For the UMEP tool application, a grid vector polygon was created, with a 5-m-squared grid, and results were assigned to grid cells and related buildings. Three raster files were created, starting from a 1-m resolution surface elevation dataset (DSM). From the centroid of each cell of the grid, a 300m radius study area was set, obtaining, for each cell, 12 different results of morphological and aerodynamic parameters, for 12 wind directions.

4. Results and Discussion

The UMEP tool results are the *anisotropic* and *isotropic* output: the first gives values for each wind direction, the second reports mean values of all wind directions. Fig. 5 shows the isotropic results of the displacement height z_d for the case study zone. The anisotropic results of z_d consider the two prevalent wind directions (N-NE, Fig.6a and W-SW, Fig.6b). Results were assessed at the building scale. According to building heights (z) and floor numbers, for each floor, the wind speed was adjusted applying the log law (if $z > z_d$) or the turbulent motion equation (if $z \leq z_d$). Buildings were classified into those with logarithmic and turbulent wind profile, or only turbulent profile (red and blue points, in Fig. 6a-b, respectively). Figs. 6a-6b show that the buildings for which the log law is valid are those located in urban canyons oriented parallel to the prevailing wind direction. In this work, the wind speed above z_d was calculated applying the log law equation (Eq.3, in Fig.2), while below z_d, it was calculated based on correlations

found from the CFD model results (Javanroodi et al., 2022). Reference was made to a case study with similar urban morphological characteristics (Table 5); linear and exponential correlations were determined for short and long canyons (Fig. 7).

A block of buildings (red rectangle, Fig. 6a) well exposed to the N-NE wind, was selected to assess the surface pressure generated by the wind on the windward façade of buildings, comparing results of the two different methodologies (Fig. 2). Wind speed was corrected applying the power law (*Cp method*) and log law (z_d *method*), at three representative heights for each building in the block (first floor-z_1, average floor-z_2, top floor-z_3) and 30 points on windward block façade (i.e., 1-30).

Fig. 5 – Isotropic result of the displacement height z_d [m].

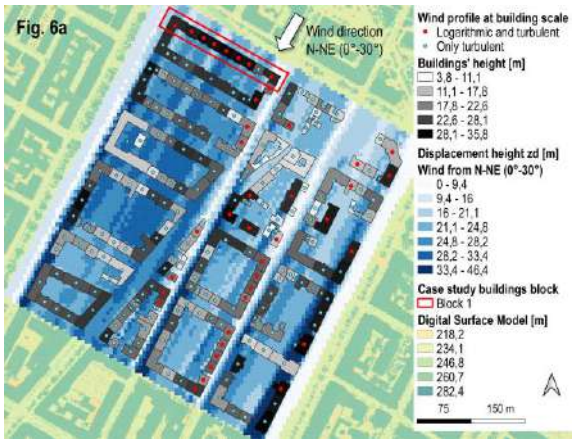

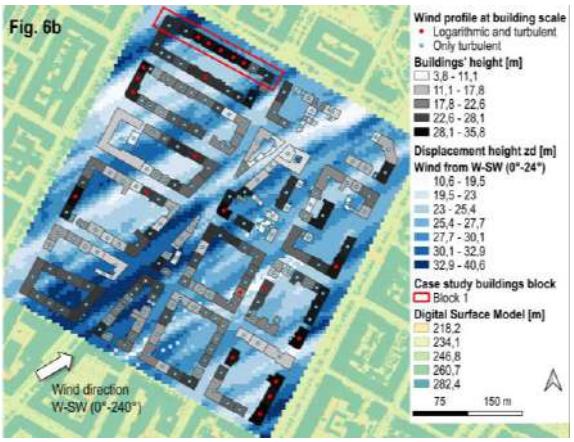

Fig. 6 a,b – Anisotropic result of displacement height z_d, for wind direction N-NE (a) and W-SW (b)

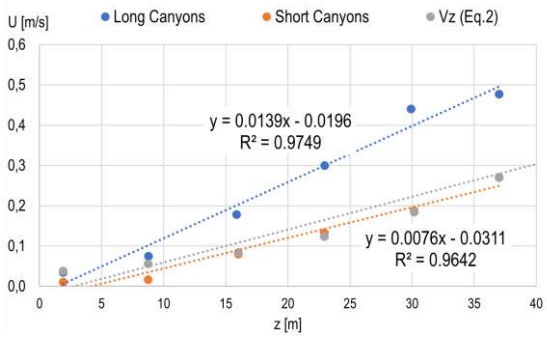

Fig. 7 – Correlations for long (blue) and short (orange) canyons

To horizontally distribute the wind speed along the windward façade, C_p was calculated with the *Cpcalc+*; in the z_d *method*, a value of z_d and z_0 was determined for each cell of the grid, obtaining a different wind velocity for each cell spatially distributed in front of the façades. Considering the three heights of building, Fig. 8 shows results of the surface pressure P_s and P_v, calculated with *Cp-method* and z_d*-method*, respectively.

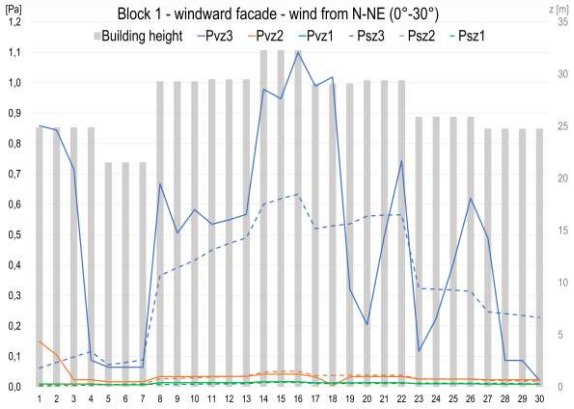

Fig. 8 – Surface pressure calculated with the cp method (Ps, dotted lines) and the zd method (Pv, continuous line)

It can be noticed that, for the height z3 (blue line), above z_d, results of *z_d-method* are more precise than the c*p-method* one when describing variations that occur on façades and that are mainly due to the wind wakes generated from surrounding buildings. The main limit of the c*p-method* concerns its range of application, since the analyzed block exceeds the aspect ratio range (FAR>4). For heights (z_1, z_2), below z_d, surface pressures are very low in both methods, due to the reduced wind speed inside the canyon (Fig. 8).

5. Conclusion and Further Development

This study aims to determine the variation in wind speed at local scale as a function of roughness elements and their effects on the urban context. The model's place-based approach, based on accessible databases and open-source software (QGIS), is applied at neighbourhood scale and it is adaptable to other contexts and urban scales. The methodology presented determines heights of boundary canopy layer (z_d, z_0) to apply the proper wind profile law, in relation to building heights. If compared to the *Cp method*, it can assess horizontal wind speed distribution along building façades, and to calculate surface pressure driving the air flow rate inside buildings. This aspect can be further investigated thanks to the flexibility of GIS place-based methodology. In fact, the novelty of this work lies in the possibility of adapting and integrating new or already existing software into QGIS, in the attempt to calculate the natural ventilation loads with a lumped model for all buildings at urban scale. A recent upgrade of the *CpCalc+* algorithm in a Python script (Chiesa & Grosso, 2019), constitutes an interesting opportunity for methodology implementation. Therefore, different scenarios can be investigated, including exploiting the GIS tool to retrieve all input data at urban scale necessary for Cp calculations, or directly integrating the *CpCalc+* algorithm into a dedicated QGIS plug-in. A simplified parametric model to evaluate wind flows around buildings at urban scale is essential for supporting urban planning in increasing buildings' energy performance and liveability of urban environments.

References

Abubaker, A., I. Kostić, and O. Kostić. 2018. "Numerical modelling of velocity profile parameters of the atmospheric boundary layer simulated in wind tunnels". *IOP CS: Materials Science and Engineering* 393: 012025. doi: https://doi.org/10.1088/1757-899X/393/1/012025

Badach, J., D. Voordeckers, L. Nyka, and M. Van Acker. 2020. "A framework for Air Quality Management Zones - Useful GIS-based tool for urban planning: Case studies in Antwerp and Gdańsk". *Building Environment* 174: 106743. doi: https://doi.org/10.1016/j.buildenv.2020.106743

Buccolieri, R., and J. Hang. 2019. "Recent Advances in Urban Ventilation Assessment and Flow Modelling". *Atmosphere* 10(3). doi: https://doi.org/10.3390/atmos10030144

Chiesa, G., and M. Grosso. 2019. "Python-based calculation tool of wind-pressure coefficients on building envelopes". *JPCS* 1343(1): 012132. doi: https://doi.org/10.1088/1742-6596/1343/1/012132

Choi, E., 2009. "Proposal for Unified Terrain Categories Exposures Velocity Profiles". In 7th APCWE, Vol. VII.

Darmanto, N. S., A. C. G. Varquez, and M. Kanda. 2017. "Urban roughness parameters estimation from globally available datasets for mesoscale modeling in megacities". *Urban Climate* 21: 243–261. doi: https://doi.org/ 10.1016/j.uclim.2017.07.001

Fracastoro, G. V., G. Mutani, M. Perino. 2001. "A simple tool to assess the feasibility of hybrid ventilation systems". In 4th IAQVEC, Vol. III: 1421-1429, Hunan (China). ISBN:962-442-190-0

Javanroodi, K., V. M. Nik, M. G. Giometto, and J.-L. Scartezzini, 2022. "Combining computational fluid dynamics and neural networks to characterize microclimate extremes: Learning the complex interactions between meso-climate and urban morphology". *STE* 829: 154223. doi: https://doi.org/10.1016/j.scitotenv.2022.154223

Kanda, M., A. Inagaki, T. Miyamoto, M. Gryschka, and S. Raasch 2013. "A New Aerodynamic Parametrization for Real Urban Surfaces". *BLM* 148(2): 357–377. doi: https://doi.org/10.1007/s10546-013-9818-x

Kent, C. W., et al., 2017. "Evaluation of Urban Local-Scale Aerodynamic Parameters: Implications for the Vertical Profile of Wind Speed and for Source Areas". *BLM* 164(2): 183–213. doi: https://doi.org/10.1007/s10546-017-0248-z

Lindberg, F., et al., 2018. "Urban Multi-scale Environmental Predictor (UMEP): An integrated tool for city-based climate services". *Environmental Modelling & Software* 99: 70–87. doi: https://doi.org/10.1016/j.envsoft.2017.09.020

Lv, G., et al., 2022. "An urban-scale method for building roofs available wind resource evaluation based on aerodynamic parameters of urban sublayer surfaces". *Sustainable Cities and Society* 80: 103790. doi: https://doi.org/10.1016/j.scs.2022.103790

Mutani, G., and V. Todeschi. 2020. "Building energy modeling at neighborhood scale". *EE* 13 (7): 1353–1386. doi: https://doi.org/10.1007/s12053-020-09882-4

Mutani, G., S. Santantonio, and V. Todeschi, 2021. "Evaluation of ventilation loads in buildings energy modelling at urban scale". In 2021 IEEE 4th CANDO-EPE 37–42. doi: https://doi.org/10.1109/CANDO-EPE54223.2021.9667547

Mutani, G., S. Santantonio, and V. Todeschi, 2022. "Urban-Scale energy models: the relationship between cooling energy demand and urban form". *JPCS* 38th UIT, 2021, Gaeta (Italy).

Oke. T. 2004. "Initial guidance to obtain representative meteorological observations at urban sites. Instruments and observing methods". World Meteorological Organization/TD 1250-81

Peng, Y., Z. Gao, R. Buccolieri, and W. Ding. 2019. "An Investigation of the Quantitative Correlation between Urban Morphology Parameters and Outdoor Ventilation Efficiency Indices". *Atmosphere* 10(1). doi: https://doi.org/10.3390/atmos10010033

Suszanowicz, D. 2018. "Optimisation of Heat Loss through Ventilation for Residential Buildings". *Atmosphere* 9(3). doi: https://doi.org/10.3390/atmos9030095

Wong, M., et al. 2010. "GIS techniques for mapping urban ventilation, using frontal area index and least cost path analysis". *IAPRSS* 38(2):586-591.

Modeling Energy Consumption in a Single-Family House in South Tyrol: Comparison Between Hemp Concrete and Clay Bricks

Silvia Ricciuti – Eurac Research, Italy – silvia.ricciuti@eurac.edu
Irene Lara-Ibeas – Eurac Research, Italy – irene.laraibeas@eurac.edu
Annamaria Belleri – Eurac Research, Italy – annamaria.belleri@eurac.edu
Francesco Babich – Eurac Research, Italy – francesco.babich@eurac.edu

Abstract

The built environment generates nearly 40 % of annual global CO_2 emissions. To reduce these emissions, alternative materials able to store CO_2 have started to be used in the construction sector. In the case of hemp concrete, part of this storage occurs during its service life leading to a potential decrease of indoor CO_2 levels. Assuming that CO_2 is used to control ventilation rates in certain buildings, the use of this material might lead to lower ventilation requirements and, thus, reduced energy consumption. The aim of this work was to develop an energy model including the CO_2 sequestration capability of hemp concrete to estimate the potential energy savings derived from its use in a typical residential building in South Tyrol with CO_2-based demand controlled ventilation. This result was later compared with the energy consumption of the same building made of clay bricks and the influence of air infiltration on indoor CO_2 levels was also evaluated. The results obtained from the simulations showed that indoor CO_2 levels were always lower in the hemp concrete buildings compared to the building made of clay bricks. However, in hemp concrete buildings with high air infiltration rates, the effect of the CO_2 absorption by the hemp concrete wall might be negligible. The energy required for the mechanical ventilation to maintain the CO_2 levels under the 1200 ppm threshold was estimated to be 0.28, 0.02 and 0.01 kWh/(m^2 yr), for the clay brick with low infiltration, hemp concrete houses with low and high air infiltration, respectively. Therefore, the operation of hemp concrete buildings with CO_2-based demand-controlled ventilation may have a slightly lower energy consumption as well as environmental impact than the equivalent clay brick buildings.

1. Introduction

The revised Energy Performance of building directive (EPBD) is reinforcing the need to reduce the energy consumption of buildings with the vision of a decarbonized building stock by 2050. Achieving zero emissions from the existing building stock will require not only increasing energy efficiency and generating 100 % renewable energy, but also reducing the emissions associated with the manufacture of the construction materials, the so-called embodied carbon emissions. Therefore, the construction sector plays a critical role in fighting climate change and a significant shift is required towards the use of more eco-friendly and sustainable materials to meet the European climate-neutral targets. In this context, hemp concrete has been recently adopted as an innovative solution by the building industry to reduce emissions, as this material stores more than 90 % of the carbon dioxide (CO_2) emitted during its production (Jami et al., 2019). Part of this storage occurs during its service life leading to a decrease of indoor CO_2 levels. Given this feature, the use of this material in buildings with CO_2-based demand-controlled ventilation might lead to lower ventilation requirements and a potential reduction of the energy consumption of the building.

Several studies have been conducted to characterize the CO_2 sequestration potential of hemp concrete (Arehart et al., 2020; Jami et al., 2016), most of them being focused on the assessment of its carbon footprint through Life Cycle Assessment (Pretot et al., 2014). However, the influence of CO_2 storage capacity of hemp concrete on the energy consumption of a building made with this material has not been explored so far. Thus, the aim of this research was to

develop an energy model including CO_2 absorption by hemp concrete to estimate the energy savings achievable in a hemp concrete residential building with CO_2-based demand-controlled ventilation and compare them with the energy consumption of the same building made of clay bricks.

2. Methodology

In this study, dynamic thermal simulations were used to evaluate the performance of hemp-based constructions. The thermal transmittance of a hemp concrete wall was calculated based on the data provided by the manufacturer, and experimental measurements were conducted to estimate CO_2 absorption rate of a hemp concrete wall. Then, these experimental data were included in a building energy model created using EnergyPlus to estimate the energy consumption of a hemp concrete building with CO_2-based demand-controlled ventilation. The same model was used to estimate the energy consumption of an identical house made of clay bricks for comparison.

2.1 Modeling

2.1.1 Reference Building

The case study building is representative of typical new single-family houses in the South Tyrol region (northern Italy). This building was chosen as a result of the analysis of a building stock in a valley in South Tyrol obtained from the TABULA project[1] and the guidelines and database of the local energy certification agency called Agenzia per l'Energia Alto Adige-CasaClima.

The case-study building was modeled and simulated with EnergyPlus 9.3.0 (US Department of Energy's (DOE), USA). Each simulation was performed over an entire reference year using an hourly timestep. For the simulations, the city of Bolzano (capital of South Tyrol) was selected and the corresponding weather file was taken from the energy plus weather platform (https://energyplus.net/weather).

2.1.2 Geometry And Construction Type

The geometry of a building has a major impact on the efficiency of the building. In particular, the volume-to-surface ratio determines the relative heat loss on the thermal envelope. In order to partially reduce the heat losses, the building was assumed to be a semi-detached house, as illustrated in Fig. 1. The opaque components of the building are listed in Table 2. These elements were taken from a freely available catalogue (dataholz.eu) which is a catalogue of wood and wood-based materials, building materials, components and component connections for timber construction covering thermal, acoustic, fire and ecological performance levels, released by accredited testing institutes or accepted research institutions.

The case-study building consists of 9 thermal zones: one living room, two bathrooms, three bedrooms and one studio. The building has a net floor area of 124 m^2 and a floor-to-ceiling height of 2.7 m. The east façade was assumed to be adjacent to another similar building (adiabatic).

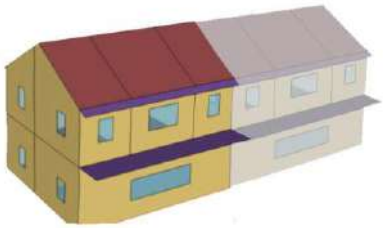

Fig. 1 – Reference case-study building

For the external walls, two typologies were simulated:

- A supporting structure of wood, filled with clay bricks and an external insulation (see Table 1)
- A supporting structure of wood, filled with hemp bricks (see Table 2).

2.1.3 Internal Gains, Heating And Ventilation

The internal gains, heating and ventilation systems were modeled as in previous work (Babich et al., 2020). The key points are as follows:

Schedules for occupancy, lighting and electric equipment set according to the 2014 Building America House Simulation Protocol (Wilson et al., 2014) were applied, as this protocol considers

[1] https://episcope.eu/iee-project/tabula/

disaggregated schedules for living room and bedrooms, as well as for weekdays and weekends.

Table 1 – Brick wall stratigraphy

n.	Material	S [m]	λ [W/(m K)]	P [kg/m³]	c [J/(kg K)]
1	External Plaster	0.015	0.7	1400	1000
2	Insulation	0.16	0.04	18	1450
3	Clay Brick	0.3	0.22	930	1450
4	Interior Plaster	0.015	0.7	1400	1000

Total thickness = 0.49 m
U-value = 0.18 W/(m² K)

The total number of occupants in the house was assumed as being equal to four. Based on typical metabolic heat generation for domestic activities (ASHRAE, 2009), the heat gains related to the occupancy were assumed to be 126 W for a standing relaxed person and 72 W for seated person.

The amount of carbon dioxide generated by a person depends on their activity level. In this model, the activity for the occupants of the living room was assumed to be equal to 1 met (i.e., seated quiet person) and 0.7 met for people occupying the bedroom (i.e., sleeping person). Based on these activity levels, the rate of CO_2 generation was calculated according to Eq. 2 (ASHRAE, 2009):

$$G_{CO_2} = G_{O_2} * RQ = \frac{0.00276 * A_D * M}{(0.23 * RQ + 0.77)} * RQ \qquad (1)$$

Where G_{CO_2} is a CO_2 generation rate per person (L/s); A_D is the Dubois area (m²); RQ is the respiratory quotient (-); and M is the metabolic rate (met).

The heating setpoint was set to 20 °C during the day and a constant setback of 18 °C during the night. The heating system was modeled as an ideal system with infinite heating capacity that supplied conditioned air to the zone, meeting all the load requirement and consuming no energy.

To guarantee acceptable indoor air quality, pollutants must remain below a certain threshold. In this study, only CO_2 was considered and a CO_2 threshold value of 1200 ppm was selected for the activation of the mechanical ventilation based on category 2 (i.e., normal level of expectation, which is the suggested level for residential buildings) of the standard EN 16798-1:2019.

The reference building was intended to represent a typical new residential building of the South Tyrol region. According to the local legislation, air tightness of n_{50} = 1.5 h^{-1} was selected to meet the requirements of CasaClima A and B standard. Additionally, a value of n_{50} = 3 h^{-1} was also simulated to investigate the relevance of the air tightness on the CO_2 absorption capacity of hemp concrete walls.

2.1.4 Carbon Dioxide Sequestration

To model contaminant levels in EnergyPlus, the ZoneAirContaminantBalance object is commonly used. It can be used also to model CO_2 levels, although carbon dioxide is not considered an indoor contaminant. In this object, the outdoor CO_2 concentration was assumed to be equal to 400 ppm. The carbon dioxide sequestration capability of hemp concrete was modeled using a ZoneContaminantSourceAndSink:Carbondioxide object. This object allows the input of carbon dioxide sources or sinks in a zone. To model the hemp concrete walls as a sink, a value of -1 for the design carbon generation rate (m³/s) was set for each room. The design value is modified by the schedule, which was defined based on the experimental measurements conducted in the hemp concrete prototype house.

2.2 Thermal Transmittance Calculation

The thermal transmittance (U value) defines the ability of an element of structure to transmit heat under steady-state conditions (Willoughby, 2002). It is a measure of the quantity of heat that will flow through a given element subjected to a temperature difference on its external surfaces. The measurement of transmittance allows an estimate of the thermal conduction characteristics of vertical and horizontal opaque closures, which are necessary for calculating the heating requirements of buildings and, consequently, energy demands.

The composition of the hemp concrete façade investigated in this work is presented in Table 2. The wall was composed of an external plaster, two rows of hemp bricks of 24 cm each and an internal plaster.

Hemp bricks were composed of a mixture of hemp shives and a lime binder.

The thermal transmittance of a wall was estimated according to the standard UNI EN ISO 6946:2008 based on the thermal transmittance of the different elements of the wall provided by the manufacturer. Knowing the thickness (s_i) and the conductivity (λ_i) of each layer, it is possible to calculate its thermal resistance and then the thermal transmittance (see Eq. 1) of the wall.

$$U = \frac{1}{R} = \frac{1}{R_{si}+\frac{s_i}{\lambda_i}+\frac{s_n}{\lambda_n}+\frac{1}{C}+R_{se}} \qquad (2)$$

Where R_{si} is the internal surface resistance, R_{se} is the external surface resistance and R the total thermal resistance of the wall.

Table 2 – Stratigraphy of the analysed wall

n.	Material	S [m]	λ [W/(m K)]	ϱ [kg/m3]	C [J/(kg K)]
1	External Plaster	0.020	0.7	1400	1000
2	Hemp brick	0.24	0.07	330	1700
3	Hemp brick	0.24	0.07	330	1700
4	Plaster	0.020	0.7	1400	1000
	Total thickness = 0.40 m U-value = 0.18 W/(m² K)				

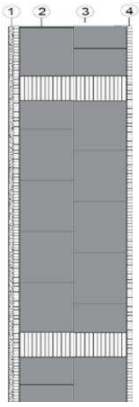

2.3 CO_2 Monitoring

To estimate the CO_2 absorption rate of hemp concrete, CO_2 levels were monitored in a prototype house (see Fig. 2). The interior of the prototype house consisted of a wooden floor and ceiling and hemp concrete walls, whereas the façade was made of wood. In this house, two CO_2 sensors (K30, CO_2 meter, USA) were installed one inside and another outside the house to continuously monitor CO_2 levels from July to October 2021.

Outdoor air is an additional source of CO_2, therefore, the outdoor air supply entering the prototype house should be considered in order to estimate the CO_2 absorption rate of hemp concrete. A blower door test was conducted to determine the number of air exchanges per hour in the prototype house.

Fig. 2 - Prototype house made of hemp concrete and wood

3. Results And Discussion

3.1 Thermal Transmittance

The thermal transmittance calculated according to UNI EN ISO 6946:2008 was equal to 0.18 W/(m² K). This value is lower than the required thermal transmittance by the National standard (Ministero Dello Sviluppo Economico, 2015), which is set at 0.26 W/(m² K) for new buildings in climate zone E, indicating that hemp concrete has high insulation properties.

The same thermal transmittance value was obtained for the modeled clay brick wall, thus the energy consumption related to the heating requirements is expected to be similar in both buildings. However, it is important to mention that the hemp brick wall does not have any thermal insulation layer and hence a lower variety of raw materials is needed for its manufacture. In the case of clay bricks, an insulation layer is required to meet the national standards for new buildings in terms of thermal transmittance. Therefore, besides the energy consumption and CO_2 emissions associated with the manufacturing process of the bricks, an additional amount of resources is needed for the manufacture of the insulation layer, which may potentially increase the environmental impact of the building construction.

3.2 CO_2 Absorption Rate

To estimate the CO_2 absorption rate, the CO_2 levels measured inside the prototype house were analyzed

and the air exchange rate of house was determined. The air exchange rate (n_{50}) per hour in the prototype house determined by the blower door test under a pressure difference of 50 Pa was found to be 7.22 h^{-1}. However, it is important to mention that this value represents the number of air exchanges at a pressure difference of 50 Pa when, at ambient pressure levels, this difference is approximately between 1 and 4 Pa. Therefore, the air exchange rate at 1 Pa was estimated from the air exchange rate at 50 Pa to be equal to 0.57 h^{-1} using the equations proposed in ASHRAE Handbook of Fundamentals.

The CO_2 levels inside the prototype house were analyzed and a repetitive daily pattern was identified over the different weeks of the monitoring campaign as illustrated in Fig. 3. During the morning, the indoor CO_2 concentration was closer to the ambient levels (~400 ppm) and slightly higher (500-750 ppm) when occupants were inside the house. Every evening, when the occupants were gone and the house was closed, CO_2 levels sharply decreased down to 50-100 ppm. As can be seen in the figure, the upper part of the CO_2 concentration curve is linear, but the lower part has the shape of an exponential function indicating that steady-state concentration was reached overnight.

During the monitoring campaign, the different linear intervals (from 400 to 50-100 ppm) of the CO_2 level decreases were analyzed and an average CO_2 concentration variation of -103.2 ppm/h was estimated. This concentration variation was the result of two processes: i) addition of CO_2 coming from the outdoor air due the infiltration in the building and ii) CO_2 absorption by hemp concrete.

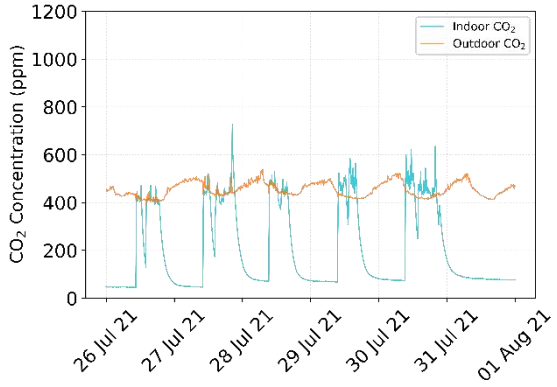

Fig. 3 - CO_2 levels measured inside and outside the prototype

Thus, considering an outdoor CO_2 level of ~400 ppm, an air exchange per hour at 1 Pa of 0.57 h^{-1}, and assuming steady-state conditions in a ventilated space with a uniform CO_2 concentration the average CO_2 absorption rate of hemp concrete was estimated to be equal to 331.2 ppm/h.

3.3 Indoor CO_2 Levels

The simulation was run for the three investigated house configurations. The CO_2 concentrations obtained over a day in the living room are presented in Fig. 4. As it was the most crowded room, the living room was selected to illustrate the effect of hemp concrete walls on indoor CO_2 concentrations. Due to the CO_2 sequestration capability of hemp concrete, the CO_2 levels in the houses made with this material were always lower than in the brick house. Comparing the two hemp concrete houses, the CO_2 trends are very similar, most of the time the levels being slightly lower in the house with a lower infiltration rate. Interestingly, between 8 pm and 3 am, the CO_2 levels were lower in the hemp concrete house with n50 = 3 h^{-1} than in the one with n_{50} = 1.5 h^{-1}. This fact might be explained by the higher infiltration rate, which allowed a faster air renewal and thus contributed to the dilution of the indoor CO_2 concentrations.

According to the results obtained, hemp concrete walls might influence indoor CO_2 levels, however, the impact of this absorptive property on the indoor CO_2 levels strongly depends on the air infiltration rate. In buildings with infiltration rates higher than 3 h^{-1}, the CO_2 sequestrated by the hemp wall might be negligible, as the rate of air renewal is much higher than the absorption rate and thus the indoor CO_2 is evacuated before it can be absorbed by the wall.

3.4 Energy consumption

The energy consumption was estimated for the three house configurations investigated. The main sources of energy consumption were the district heating and the mechanical ventilation. As expected, the energy consumption associated with the heating is very similar for the hemp concrete and the clay brick buildings with a low infiltration rate (see

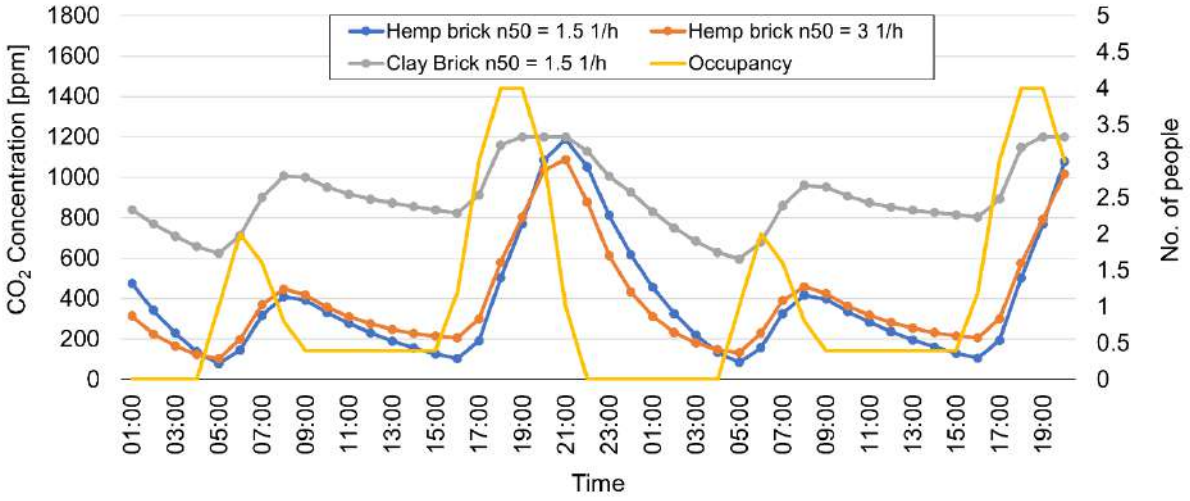

Fig. 4 - CO_2 concentration in the living room of the three investigated configurations

Table 3), as these walls have similar thermal properties. In the case of the hemp concrete building with higher infiltration rate, the energy consumption significantly increased due to the heat losses resulting from the faster air renewal. On the other hand, the energy required to run the mechanical ventilation and maintain the CO_2 levels under the 1200 ppm threshold was estimated to be 0.28, 0.02 and 0.01 kWh/(m² yr), for the clay brick and the hemp concrete houses with low and high air infiltration, respectively. In this case, as clay bricks are not able to sequestrate CO_2, a great difference was observed between the house made of this material and the ones made of hemp concrete, regardless of the air infiltration. However, even if the difference is remarkable, the absolute value is relatively small and might not have a significant impact on the overall energy consumption of the building.

Nonetheless, the energy consumption should be evaluated in context. An increase in the energy consumption also means an increment in greenhouse emissions. To uniformly express the climate impact of different greenhouse gases, the CO_2 equivalent unit is commonly used.

In Italy, the CO_2 emission factors used to convert from energy data to CO_2 equivalents are defined and regularly updated by the Italian National Energy Efficiency Agency ENEA (Agenzia Nazionale Efficienza Energetica). These factors depend on the primary source used to generate electricity and the generation efficiency.

Table 3 - Final energy and mechanical ventilation needed for three different configurations

	Thermal Energy Demand [kWh/(m² yr)]	**Energy Needs for Mechanical Ventilation [kWh/(m² yr)]**
Hemp brick n_{50} = 1.5 h^{-1}	29.55	0.02
Clay brick n_{50} = 1.5 h^{-1}	31.25	0.28
Hemp brick n_{50} = 3 h^{-1}	46.75	0.01

In Bolzano, there is a district heating plant that provides heating from waste incineration. For this type of energy generation, the CO_2 emission factor is 0.17 $kg_{CO2,equi}/kWh_{fin}$. Conversely, the mechanical ventilation requires electrical energy and the CO_2 emission factor for this conversion is equal to 0.46 $kg_{CO2,equi}/kWh_{fin}$ (Istituto Superiore per la Protezione e la Ricerca Ambientale, 2021). Based on these factors, the associated greenhouse emissions were calculated in CO_2 equivalents. As shown in Fig. 5, the emissions produced by the hemp concrete house with lower air infiltration are 8 % and 58 % lower than the ones associated with the clay brick house and the hemp concrete house with higher air

infiltration, respectively. These results indicate that the operation of hemp concrete buildings with CO_2-based demand-controlled ventilation may have a slightly smaller environmental impact than its clay brick counterparts.

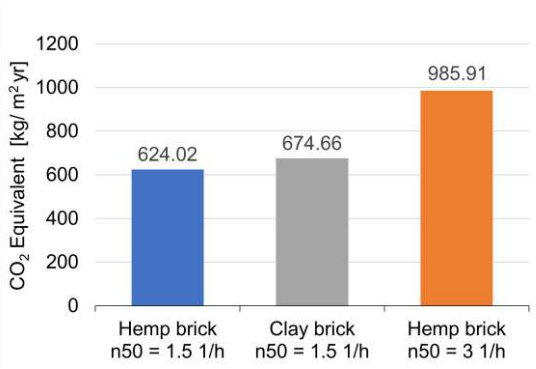

Fig. 5 - CO_2 equivalent emissions for the three different house configurations

4. Conclusion

The research presented in this paper aimed to develop an energy model including the CO_2 absorption by hemp concrete to estimate the potential energy savings achievable in a hemp concrete residential building with CO_2-based demand controlled ventilation and compare them with the energy consumption of the same building made of clay bricks. The key findings are:

- Indoor CO_2 levels in hemp concrete buildings are lower than in clay brick buildings due to the CO_2 sequestration capability of hemp concrete.
- In hemp concrete buildings with high air infiltration rates, the effect of the CO_2 absorption by the hemp concrete wall may be negligible.
- Regardless of the air infiltration, there is a significant difference in the electrical energy required to run the mechanical ventilation and maintain the CO_2 levels under the 1200 ppm threshold between hemp concrete and clay brick houses.
- The operation of hemp concrete buildings with CO_2-based demand-controlled ventilation may have a slightly lower environmental impact than the equivalent clay brick buildings.

4.1 Limitations And Future Work

Estimation of CO_2 absorption rate strongly depends on the temperature, the relative humidity and composition of the hemp concrete. In this study, only one type of hemp concrete was investigated, thus the results obtained can only be considered for hemp concretes with comparable composition. Moreover, CO_2 measurements in the prototype house were conducted from July to October. The data collected during those months were averaged to estimate an average CO_2 absorption rate. However, this time interval does not represent the full year and seasonal variability (i.e., low temperatures during winter) could potentially affect the CO_2 absorption rate. Therefore, the CO_2 absorption rate averaged over the entire year might be slightly different from the estimated value. More studies in which CO_2 is monitored over a longer period including all seasons of the year are needed in order to accurately determine the CO_2 absorption rate of hemp concrete.

Acknowledgement

The research leading to these results has received funding from the European Regional Development Fund POR FESR 2014–2020 of the Province of Bolzano, under Project number 1161, TinyFOP, Tiny FOP MOB - nachhaltige Realexperimente im Bausektor der Zukunft (Tiny FOP MOB - sustainable real-world experiments in the construction sector of the future).

Nomenclature

Symbols

s	Thickness (m)
λ	Thermal Conductivity (W/(m K))
ρ	Density (kg/m^3)
C	Specific heat (J/(kg K))
U	Thermal transmittance (W/(m^2 K))
Ug	Thermal transmittance of glass (W/(m^2 K))
Uf	Thermal transmittance of window frame (W/(m^2 K))

References

Arehart, J. H., W. S. Nelson, and W. V. Srubar. 2020. "On the Theoretical Carbon Storage and Carbon Sequestration Potential of Hempcrete." *Journal of Cleaner Production* 266: 121846. doi: https://doi.org/10.1016/j.jclepro.2020.121846

ASHRAE. 2009. *ASHRAE Handbook: Fundamentals*. American Society of Heating, Refrigeration and Air-Conditioning Engineers.

Babich, F., I. Demanega, F. Avella, and A. Belleri. 2020. "Low Polluting Building Materials and Ventilation for Good Air Quality in Residential Buildings: A Cost–Benefit Study." *Atmosphere* 11(1): 102. doi: https://doi.org/10.3390/atmos11010102

Istituto Superiore per la Protezione e la Ricerca Ambientale. 2021. "Indicatori di efficienza e decarbonizzazione del sistema energetico nazionale e del settore elettrico."

Jami, T., S. R. Karade, and L. P. Singh. 2019. "A Review of the Properties of Hemp Concrete for Green Building Applications." *Journal of Cleaner Production* 239: 117852. doi: https://doi.org/10.1016/j.jclepro.2019.117852

Jami, T., D. Rawtani, and Y. K. Agrawal. 2016. "Hemp Concrete: Carbon-Negative Construction." *Emerging Materials Research* 5(2): 240–47. doi: https://doi.org/10.1680/jemmr.16.00122

Ministero Dello Sviluppo Economico. 2015. "Decreto Interministeriale 26 Giugno 2015-Applicazione Delle Metodologie Di Calcolo Delle Prestazioni Energetiche e Definizione Delle Prescrizioni e Dei Requisiti Minimi Degli Edifici."

Pretot, S., F. Collet, and C. Garnier. 2014. "Life Cycle Assessment of a Hemp Concrete Wall: Impact of Thickness and Coating." *Building and Environment* 72: 223–31. doi: https://doi.org/10.1016/j.buildenv.2013.11.010

Willoughby, J. 2002. "30 - Insulation." In Plant Engineer's Reference Book (Second Edition), edited by D. A. Snow, 30–31. Oxford: Butterworth-Heinemann. doi: https://doi.org/10.1016/B978-075064452-5/50085-7

Wilson, E, C Engebrecht Metzger, S Horowitz, and R Hendron. 2014. "2014 Building America House Simulation Protocols." National Renewable Energy Laboratory.

A Fully Automated and Scalable Approach for Indoor Temperature Forecasting in Buildings Using Artificial Neural Networks

Jakob Bjørnskov – University of Southern Denmark, Denmark – jabj@mmmi.sdu.dk
Muhyiddine Jradi – University of Southern Denmark, Denmark – mjr@mmmi.sdu.dk
Christian Veje – University of Southern Denmark, Denmark – veje@mmmi.sdu.dk

Abstract

Improving the performance of buildings is a core pillar to attaining future energy and environmental goals in different countries, considering that the building sector is a major contributor in terms of both energy consumption and carbon emissions. These ambitious goals and the call for smarter, energy-efficient, and flexible buildings have called for innovative and scalable energy and indoor thermal comfort modeling and prediction approaches. This work presents a fully automated and scalable solution using Artificial Neural Networks to forecast indoor room temperatures in buildings. A case study of an 8500 m² university building in Denmark was considered for testing and evaluating the proposed approach. An extensive dataset was constructed with sensor data from 76 rooms that contain both readings on indoor temperature, CO_2 concentrations, and actuating signals on radiator valves and dampers, as well as outdoor ambient conditions. Using this dataset, a well-performing architecture is identified, which provides accurate temperature predictions in the various rooms of the building for prediction horizons of 24 hours.

1. Introduction

Buildings are widely regarded as one of the major contributing sectors in terms of both energy consumption and CO_2 emissions. Furthermore, future energy systems with high fractions of Renewable Energy Sources (RES) depend on high demand-side flexibility. Therefore, there is a clear need for increasing not only the performance but also the flexibility of buildings. However, to achieve feasible and intelligent operation strategies for both cost minimization and flexibility services implementation without compromising the indoor comfort levels of buildings, reliable and accurate forecasting of building indoor thermal behavior is vital. In terms of indoor temperature forecasting, Artificial Neural Network (ANN) models have shown great potential in capturing the dynamics with high prediction accuracy (Alawadi, et al., 2022). In addition, these models can also be easily adapted and scaled up to different building cases.
This work presents an ANN-based approach that requires no prior specifications for the modeled building and can achieve accurate indoor temperature predictions for long prediction horizons of 24 hours or more. The models developed generalize well enough to be used for scenario planning and what-if analyses, e.g., to test the impact of custom setpoint and shading schedules on indoor temperature.

2. Case Definition

The building under consideration in this work is an 8500 m² highly energy-efficient university building from 2015. It is located in Denmark, and it primarily consists of space types such as classrooms, study zones, corridors, and offices. In each of these spaces, indoor air temperature T and CO_2 concentration C are measured through installed sensors. In addition, each space contains space heaters of specific capacities with equipped mechanical valves that control the water massflow. The position of these valves $u_v \in [0,1]$ is managed centrally by the Building Management System (BMS) with $u_v = 0$ meaning fully closed with no massflow and $u_v = 1$ meaning fully open with maximum massflow. The supply water temperature is kept constant at approximately 60 °C.

The building is also equipped with a weather station that measures outdoor air temperature T_o, longwave solar irradiance Φ_L, shortwave solar irradiance Φ_S, and wind speed. The supply air temperature setpoint is constant, at either 21-22 °C, depending on each space. The supply and exhaust airflows are controlled in each space by the supply and exhaust damper positions $u_d \in [0,1]$, with $u_d = 0$ meaning fully closed with no airflow, and $u_d = 1$ meaning fully open with maximum airflow. These damper positions are also managed through the BMS with Demand Controlled Ventilation (DCV), aiming at keeping the measured CO_2 concentration below 600 ppm. Finally, each space is also equipped with shades that are controlled by the BMS through a position parameter $u_{sh} \in [0,1]$, with $u_{sh} = 0$ meaning fully exposed with no shading, and $u_{sh} = 1$ meaning fully enclosed with maximum shading. The shades are controlled based on outdoor and indoor illuminance with a safety roll-up mechanism that sets $u_{sh} = 0$ at wind speeds higher than 15 m/s.

3. Methodology

3.1 Model Architecture

This work makes use of a specific type of ANNs called Recurrent Neural Networks (RNN) to model the transient temperature dynamics of a room. Specifically, Long Short-Term Memory (LSTM) networks were chosen due to their numerous demonstrations of adaptability and robustness in time-series black-box modeling, including indoor environment modeling (Fang et al., 2021; Mtibaa et al., 2020). LSTM models are a specific kind of RNN that were originally developed to deal with the vanishing and exploding gradient problem of traditional RNN models. A detailed explanation of the LSTM model is provided in the references (Hochreiter & Schmidhuber, 1997; Van Houdt et al., 2020).

To properly account for all phenomena that can significantly influence the energy balance of the room, it is very important to choose appropriate dynamic inputs for the model. In this work, the inputs are determined by considering the following energy transfer mechanisms:

- *Heat transfer by conduction through external surfaces* is considered by including indoor air temperature T, and outdoor temperature T_o as input.
- *Heat transfer by radiation* is considered by including longwave solar irradiance Φ_L, shortwave solar irradiance Φ_S, and the position of the shades u_{sh} in the model input.
- *Internal heat gains through occupancy* are included indirectly by including measured CO_2 concentration C, and damper position u_d. These inputs can, to a certain extent, represent occupancy due to the direct correlation between CO_2 concentration, ventilation airflow, and occupancy presence (Franco & Leccese, 2020).
- *Heat added by the space heater* is considered by adding the measured valve position u_v as input, which represents the water massflow. The supply water temperature is constant and does not therefore contribute as input.
- *Heat transfer by ventilation* is considered by adding the supply and exhaust damper positions u_d as inputs, which represent the airflow rates. The supply air temperature is constant and therefore does not contribute as input.

The model architecture is seen in Fig. 1 with inputs and outputs of the model. As shown, the model consists of two sequential LSTM models, A and B. All previously mentioned weather and sensor inputs from the previous timestep are fed to LSTM A. In addition, the LSTM also receives the cell state vector $c_{A,t-1} \in \mathbb{R}^n$ and hidden state vector $h_{A,t-1} \in [-1,1]^n$, where n is a hyperparameter that determines the size of these vectors. These two state vectors are an integral part of LSTM models. which essentially dictate the state of the system modeled during a given timestep. LSTM A outputs $c_{A,t}$ and $h_{A,t}$, which represents the updated state vectors.

LSTM B has $n = 1$ and is only given three inputs, the cell state $c_{B,t-1} \in \mathbb{R}$, the hidden state $h_{B,t-1} \in [-1,1]$, and the hidden state vector $h_{A,t}$. LSTM B outputs $c_{B,t}$ and $h_{B,t}$, which represent the updated state vectors of LSTM B. The training task is then to find an optimal set of parameters in LSTM A and B to minimize the error between $h_{B,t}$ and the chosen prediction target over multiple sequences of data.

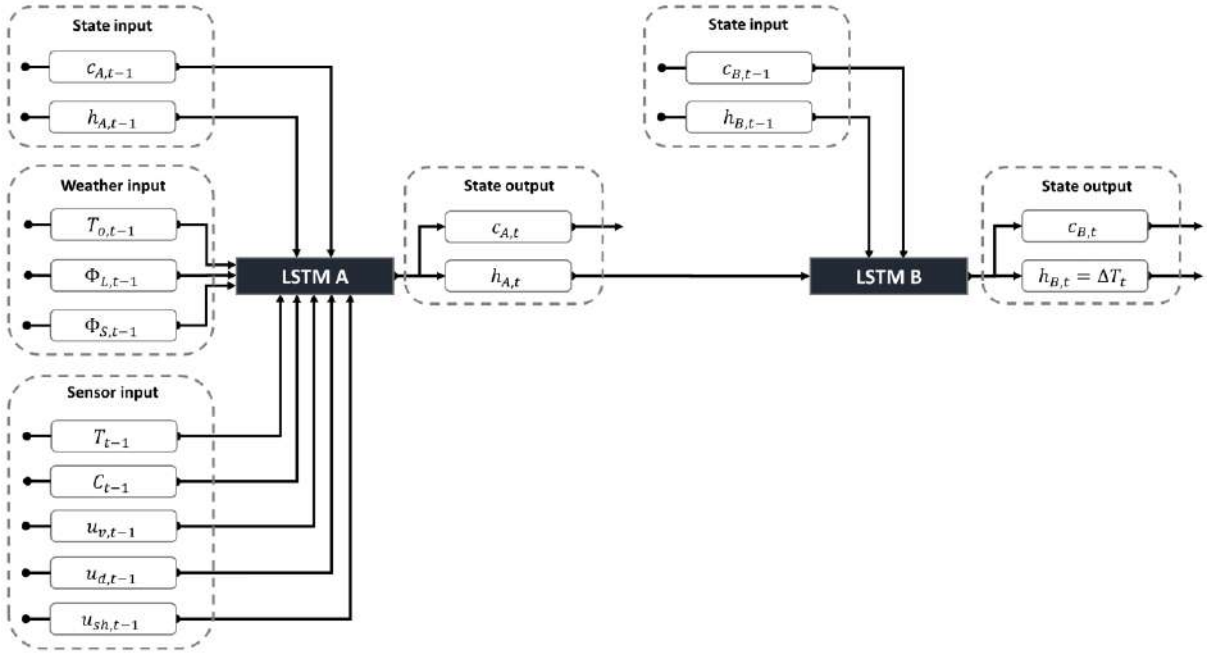

Fig. 1 – Model architecture with inputs and outputs of the sequential LSTM models, A and B

In the studies reviewed, the prediction target of the learning algorithms employed was indoor temperature in all cases. During initial testing, it was found that this configuration yielded good prediction results when testing with historical data as input. However, it was found that the models generalized poorly when fed with custom inputs instead of historical data, e.g., when using the model for setpoint control, as shown later in Section 4.2. When collecting operational data from a building, the actuation signals, e.g., valve positions, are typically directly correlated with indoor temperature through a thermostat with a simple control law, e.g., in the form of a Proportional (P) or Proportional Integral (PI) controller. Therefore, if the prediction target is temperature, the model will likely overfit the specific mode of operation that is reflected in the historical data used to train and test the model. We hypothesize that the model essentially learns to map the inverse control law of the thermostat instead of the actual thermal physics of the room. In this work, we are proposing that the model should predict the indoor temperature change ΔT instead of the actual temperature value, as this disrupts the direct correlation that is otherwise present between input and output.

3.2 Data Preprocessing

The dataset was constructed with all the weather and sensor readings introduced for 76 rooms in the case study building at a 10- minute interval for two years spanning January 1st 2018 to December 31st 2019. The raw data were pretreated and validated to ensure that proper and clean data were used. Following this, all inputs were min-max scaled between -1 and 1. After preparing the dataset, 24-hour sequences of 144 timesteps with no missing data were selected to form a collection of sequences for each space. In Fig. 2, the distribution of data sequences available among spaces is shown monthly. As shown, the number of sequences varies between rooms. The month with the most data is January, with a median of about 6000 sequences, while the month with the least data is August, with a median of about 3000 sequences.

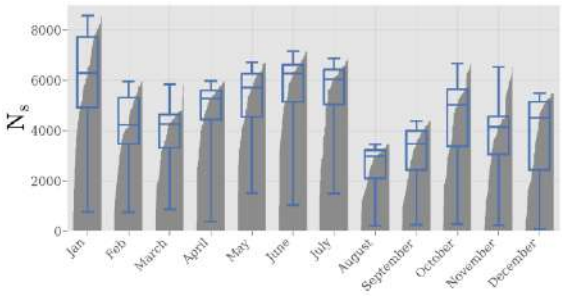

Fig. 2 – Number of sequences available per space for each month

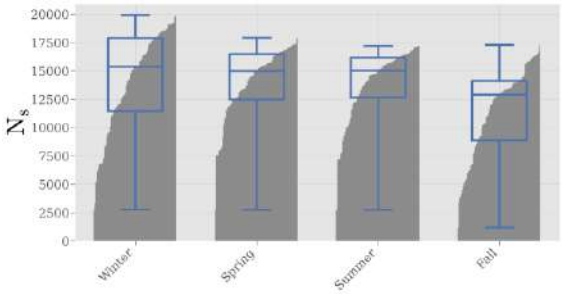

Fig. 3 – Number of sequences available per space for each season

In Fig. 3, the distribution is shown on a seasonal level. Here, the dataset generally appears to be more balanced with less variation. Hence, it is expected that the constructed datasets have enough diversity to cover most of the seasonal variance in the operation and thermal dynamics of the building.

3.3 Training and Testing Method

After preprocessing, the data is split into training, validation, and testing data sets with the splits [2/3, 1/6, 1/6], respectively. These data splits were carefully designed to ensure no overlap between sequences in the three data sets, while ensuring that seasonal and monthly variations are reflected in each dataset. For training, the machine-learning library Pytorch was used with Stochastic Gradient Descent (SDG) as optimizer, a momentum of 0.9, a batch size of 32, and a learning rate of 10^{-1}. The size n of cell state c_A and hidden state h_A was set to 20 for all space models.

During training, the model loss was evaluated on the validation dataset and saved at every 64th gradient update. At every 3000th gradient update, a copy of the model was saved, along with an average of the last 100 validation loss evaluations. After 100,000 gradient updates, the model with the lowest saved validation loss was selected. If the model had not converged after 100,000 gradient updates, the procedure was repeated up until 400,000 gradient updates. This approach was used to train models for all 76 spaces. To properly test the trained space models, two modes of operation were presented.

The first mode was aimed at assessing the prediction accuracy of the space models given historic inputs. Here, the developed models were employed in a closed-loop configuration, as shown in Fig. 4, where future temperature predictions were based on past predictions. Perfect forecasting was assumed by feeding historical data for all weather and sensor inputs, except for the indoor temperature.

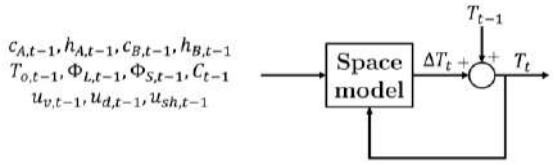

Fig. 4 – Closed-loop configuration designed to forecast indoor temperature for an arbitrary number of timesteps

The model then, for each timestep, predicted the temperature change to obtain the indoor temperature of the next time step, which was fed back to the model. This could be repeated as long as historical inputs were available. By repeating this for all timesteps in a simulation period, the produced temperature profile could then be compared with the actual measured temperature profile of the room to assess the prediction accuracy of the space model.

The second mode of operation was aimed at testing whether the developed space models generalize well enough to provide reasonable predictions under unseen operational conditions. Here, custom inputs were thus be fed to the model to observe the response. This was a very important property that made it possible to use the model for testing different operational strategies or what-if scenarios and their influence on indoor comfort in a safe environment.

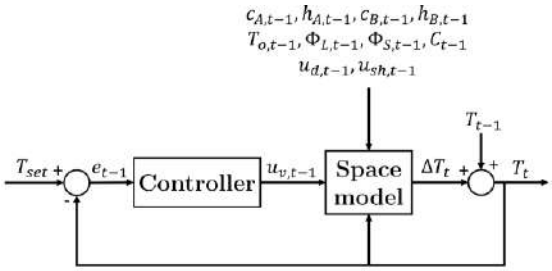

Fig. 5 – Closed-loop configuration designed for temperature setpoint control through the valve position of the space heater

In this work, two model inputs were considered for this purpose; u_v and u_{sh}. In one simulation, the space heater valve position input u_v was constructed by implementing the space models in a closed-loop configuration for temperature setpoint control, as shown in Fig. 5. Here, all inputs were historical except for u_v and temperature T. The implemented controller was a simple proportional controller that each timestep scales the input signal $u_{v,t-1}$ proportionally to the error $e_{t-1} = T_{set} - T_{t-1}$, where T_{set} was the temperature setpoint in the room. In another simulation, the shades position input u_{sh} was constructed by implementing a simple predetermined schedule that operates based on the time of the day. All inputs except for u_{sh} and T were thus historical.

4. Results and Discussion

4.1 Quantitative Performance Assessment

First, the quantitative model performance was evaluated by using the first mode of operation as described in Section 3.3. Here, the Mean Absolute Error (MAE) between measured indoor temperature and predicted temperature was calculated for each space model across all 24-hour sequences in the test dataset. Fig. 6 shows the performance of each trained space model. Specifically, it shows the relationship between MAE, Standard Deviation of prediction targets $\sigma(\Delta T)$, and number of sequences N_s. The three marked space models were used for a qualitative performance assessment in Section 4.2. As seen in the figure, most of the space models (~86 %) achieve MAE values below 0.5 °C, which is lower than the required measurement accuracy of temperature sensors of ± 0.5 °C (ISO, 1998).

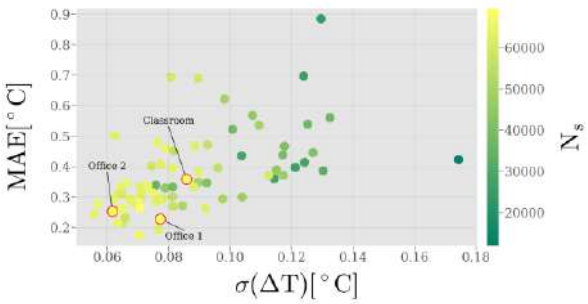

Fig. 6 – Relationship between Mean Absolute Error MAE, Standard Deviation of prediction targets $\sigma(\Delta T)$, and number of sequences N_s. The three space models chosen for qualitative assessment are marked

The best performing space model represents an office with $N_s = 66297$ and $\mathrm{MAE} = 0.17$, while the worst performing model is of a classroom with $N_s = 24210$ and $\mathrm{MAE} = 0.88$. As seen from the colormap in Fig. 6, there seems to be a negative correlation between the prediction error and the number of sequences available, agreeing with the general notion in machine-learning, that more data yields lower prediction error and better model generalization. Therefore, it is expected that the poor-performing space models could attain similar performance with more data. Furthermore, there seems to be a positive correlation between prediction error and the variation observed for the prediction target ΔT. This means that the prediction error will be higher for datasets that have a more fluctuating temperature profile. This is to be expected, as a fluctuating indoor temperature is generally harder to predict than a steady temperature.

4.2 Qualitative Performance Assessment And Applications

To provide a qualitative performance assessment of the models developed, three case study spaces were selected, one classroom and two offices, as also marked in Fig. 6. For each of these space models, a winter period and a summer period of 24 hours were chosen to evaluate how the space models perform under different ambient conditions. The models were first simulated for these periods using the first mode of operation, as explained in Section 3.3.

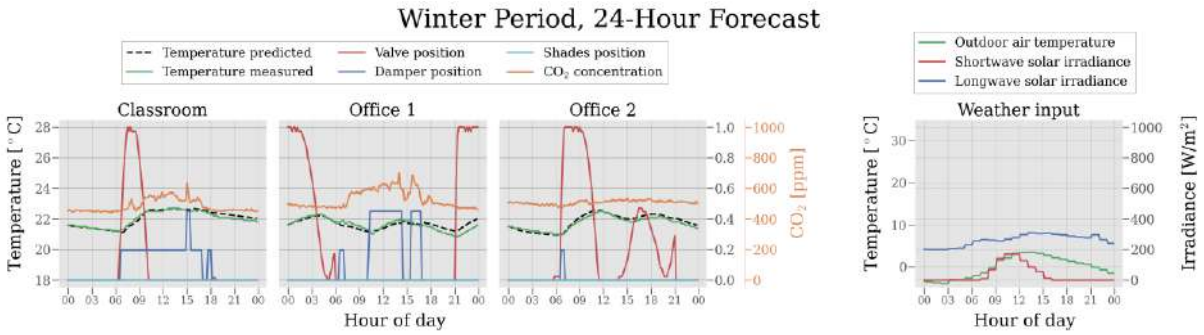

Fig. 7 – 24-hour temperature forecast in a winter month compared with actual measured temperature. The weather input is shown on the plot furthest to the right, while the individual inputs for the three selected space models are shown on the plots to the left

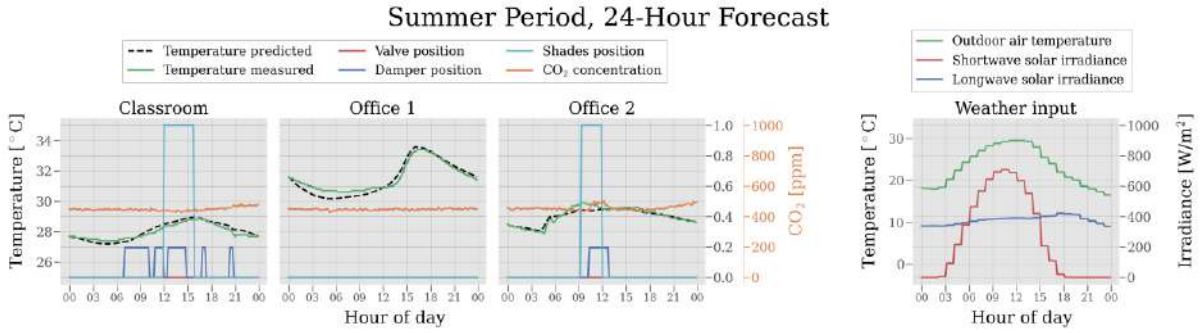

Fig. 8 – 24-hour temperature forecast in a summer month compared with actual measured temperature. The weather input is shown on the plot furthest to the right, while the individual inputs for the three selected space models are shown on the plots to the left

For the winter simulation, the results are shown in Fig. 7, with the weather inputs in the plot furthest to the right, while the results for each of the three chosen rooms can be seen on the left. As seen, all three space models accurately predict the indoor temperature, although Office 1 seems to slightly overestimate the temperature during the last 6 hours. The space heater valve position has a clear significance in all three spaces, where the general trend is that $u_v = 0$ results in decreasing room temperature, while $u_v > 0$ results in increasing room temperature. The models are also able to account for heat gains and heat losses associated with occupancy and ventilation. This is mostly seen in the Classroom and Office 1 in the period from 09:00 to 15:00, where the CO_2 concentration rises above 600 ppm and the dampers are positioned at around 50 %. Here, the model correctly predicts that the indoor temperature increases, although the space heater is not in operation. The shades are all rolled up ($u_{sh} = 0$) as they have no desirable effect during winter.

Moving to the simulation results for the summer period, the results are shown in Fig. 8. The weather data inputs are again seen on the plot furthest to the right, where the ambient temperature and irradiance levels are much higher compared with the winter period. As seen, this has a significant impact on the predicted and actual temperatures in the three spaces, especially for Office 1, where temperatures are above 30 °C during the whole 24 hour-period. The cause for large differences in both shape and peaks of the temperature profiles was different orientation, shading, and geometrical properties of the spaces. As seen, all three space models have learned to correctly account for these properties and provide accurate predictions for all 24 hours, although Office 1 slightly underestimates the temperature during the first 12 hours of the period. From the CO_2 levels, which have a very constant profile of around 450 ppm, the occupancy appears to be close to zero. However, this is expected during July and August, where the students are on summer leave. The shades are, to some extent, utilized in the Classroom and Office 2. However, it is expected that the high temperatures could be mitigated even more, by increasing the duration of the shades being rolled down ($u_{sh} = 1$). This will be investigated further in the following analysis.

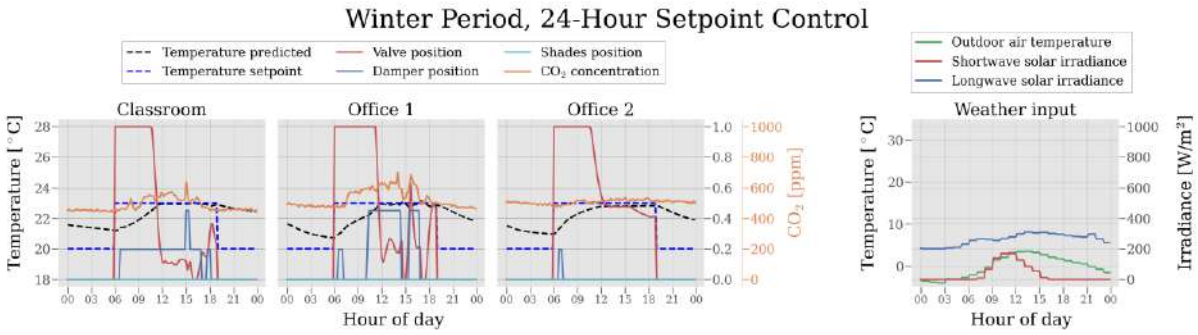

Fig. 9 – 24-hour setpoint control in a winter month. The weather input is shown on the plot furthest to the right, while the individual inputs for the three selected space models are shown on the plots to the left along with the predicted temperature and the setpoint

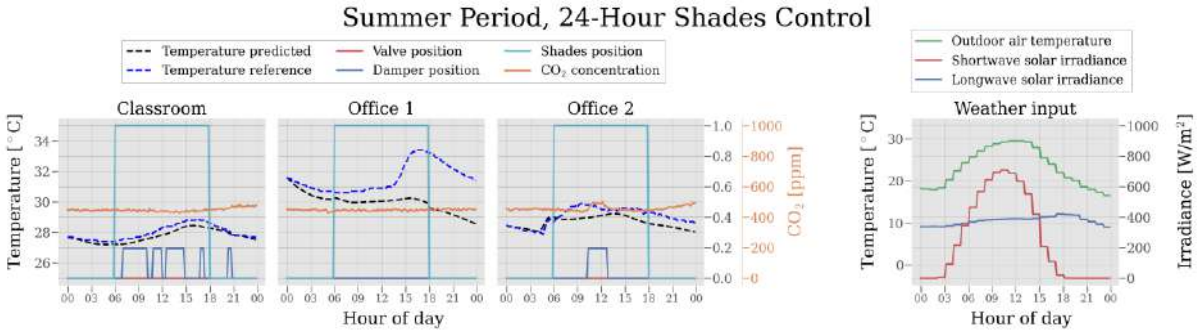

Fig. 10 – 24-hour shades control in a summer month. The weather input is shown on the plot furthest to the right, while the individual inputs for the three selected space models are shown on the plots to the left along with the predicted temperature. The original measured temperature in this period is shown as a reference

As just demonstrated, the models perform well when predicting temperatures under historical conditions. However, to demonstrate the applicability of the models, the second mode of operation, as presented in Section 3.3, was employed. The temperature setpoint control was implemented for the same winter period as shown in Fig. 7, while the shades control was implemented for the same summer period as shown in Fig. 8.

The results for the temperature setpoint control are shown in Fig. 9. As seen, the setpoint was varied, depending on the time of day. From 06:00 to 18:00, the setpoint was 23 °C, while from 18:00 to 06:00, the setpoint was 20 °C. The controller adapted to these setpoint signals by varying the valve position accordingly. For all three spaces, the valve was closed during the night, where the temperature was allowed to decrease. At 06:00, when the setpoint was raised to 23 °C, the valve was opened, and the indoor temperature increased until around 12:00, where the indoor temperature in all three rooms reached the specified setpoint. At this point, the valve position was operated between 0 and 1 in an attempt to keep the indoor temperature at the setpoint. For Office 2, it was noticed that the temperature and valve position profile was smoother compared to the Classroom and Office 1, which had small fluctuations in temperature. However, as seen, the Classroom and Office 1 also had more disturbances in the form of varying CO_2 levels and ventilation airflows. Despite these disturbances, the simple controllers managed to keep the temperature at 23 °C in all three space models until 18:00, where the setpoint was again decreased to 20 °C. Here, the valve was again shut, and the temperature started to decrease.

Moving on to shades control during the summer period, the results are shown in Fig. 10. Here, the shades were rolled down ($u_{sh} = 1$) from 06:00 to 18:00 and rolled up ($u_{sh} = 0$) from 18:00 to 06:00. This had a significant effect on the predicted indoor temperature when compared with the original measured temperature (temperature reference), where the duration of shading was very limited. The

effect was very clear for Office 1, where the peak at 17:00 shifted from around 33 °C to 30 °C. The Classroom and Office 2 also had a reduced temperature response, although not as significant as Office 1.

5. Conclusion

In this work, a fully automated and scalable approach for temperature forecasting in buildings was presented and assessed. The presented method relied on ANNs in the form of two sequential LSTM models to predict temperature change within a room, given weather data and sensor inputs such as space heater valve positions, damper positions, shades positions, and CO_2 concentration. Hence, the developed approach needed no prior information about the building such as geometry, material properties, design data, etc.

The methodology developed was implemented considering 76 rooms of an 8500 m^2 university building in Denmark with 86 % of the rooms achieving a Mean Squared Error of less than 0.5 for 24-hour forecasting. The difference in prediction performance between space models was explained by differences in the amount of data available. However, more work is needed to identify more robust criteria concerning the amount, type, and quality of data that is needed to obtain accurate space models. The applicability of the models was demonstrated by implementing three selected models in a closed-loop setpoint control configuration for a 24-hour winter period. Additionally, different shading schedules were also explored to show their impact during a 24-hour summer period.

In line with the emerging initiatives toward digitalization of the building sector, building digital twins has promising technical and economic impacts. In this context, a fully scalable and automated energy modeling approach is vital, so that these twins can provide a robust, generic, and effective solution for various applications in the building sector. The modeling approach proposed in this study serves as a core for future building digital twin development and could be used as a backbone for various automated services, including performance monitoring, scenario assessment, and operational management.

Acknowledgement

This work was carried out under the 'Twin4Build: A holistic Digital Twin platform for decision-making support over the whole building life cycle' project, funded by the Danish Energy Agency under the Energy Technology Development and Demonstration Program (EUDP), ID number: 64021-1009.

References

Alawadi, S., D. Mera, M. Fernández-Delgado, F. Alkhabbas, C. M. Olsson, and P. Davidsson. 2022. "A comparison of machine learning algorithms for forecasting indoor temperature in smart buildings." *Energy Systems* 13: 689–705. doi: https://doi.org/10.1007/s12667-020-00376-x

Fang, Z., N. Crimier, L. Scanu, A. Midelet, A. Alyafi,, and B. Delinchant. 2021. "Multi-zone indoor temperature prediction with LSTM-based sequence to sequence model." *Energy and Buildings* 245: 111053. doi: https://doi.org/10.1016/j.enbuild.2021.111053

Franco, A., and F. Leccese. 2020. "Measurement of CO2 concentration for occupancy estimation in educational buildings with energy efficiency purposes." *Journal of Building Engineering* 32: 101714. doi: https://doi.org/10.1016/j.jobe.2020.101714

Hochreiter, S., and J. Schmidhuber. 1997. "Long Short-term Memory." *Neural computation* 9(8): 1735-1780.

ISO. 1998. *ISO 7726 - Ergonomics of the Thermal Environment - Instruments for Measuring Physical Quantities*.

Mtibaa, F., K.-K. Nguyen, M. Azam, A. Papachristou, J.-S. Venne, and M. Cheriet. 2020. "LSTM-based indoor air temperature prediction framework for HVAC systems in smart buildings." *Neural Computing and Applications* 32: 17569–17585. doi: https://doi.org/10.1007/s00521-020-04926-3

Van Houdt, G., C. Mosquera, and G. Nápoles. 2020. "A Review on the Long Short-Term Memory Model." *Artificial Intelligence Review* 53(8): 5929-5955. doi: https://doi.org/10.1007/s10462-020-09838-1

Effects of Different Moisture Sorption Curves on Hygrothermal Simulations of Timber Buildings

Michele Libralato – University of Udine, Italy – michele.libralato@uniud.it
Maja Danovska – Free University of Bozen-Bolzano, Italy – maja.danovska@natec.unibz.it
Giovanni Pernigotto – Free University of Bozen-Bolzano, Italy – giovanni.pernigotto@unibz.it
Andrea Gasparella – Free University of Bozen-Bolzano, Italy – andrea.gasparella@unibz.it
Paolo Baggio – University of Trento, Italy – paolo.baggio@unitn.it
Paola D'Agaro – University of Udine, Italy – paola.dagaro@uniud.it
Giovanni Cortella – University of Udine, Italy– giovanni.cortella@uniud.it

Abstract

Building energy simulations are a key tool in designing high performance buildings capable of facing the future challenges and in helping emission reduction targets to be met. Currently, thermal properties of materials used in most building energy simulations are assumed to be constant and not dependent on moisture content and temperature. Heat and moisture dynamic transfer models allow a simulation of building envelope performance considering thermal resistance reduction due to moisture effects. These models are generally considered more accurate than the heat transfer models, and they could be used to simulate the heat transfer (increased by water vapor storage) and the moisture buffering effect on the indoor environment. For the simulation to be performed, hygrothermal material properties should be known as functions of moisture content. Nevertheless, hygrothermal material properties are rarely available and correlations from the literature have to be used. In this study, the moisture storage curves of CLT, OSB and two types of wood fibre insulation have been measured with a dynamic vapor sorption analyser. The other hygrothermal properties are estimated from values measured in previous studies or taken from the literature. The simulations of two small single room buildings in four Italian locations are performed with the software EnergyPlus, considering an ideal HVAC system, to calculate the heating and cooling needs of the building. The HAMT (heat and moisture transfer) module of EnergyPlus is used. With the results presented in this study, it is possible to evaluate how an approximated curve affects the results of a whole-building simulation in terms of wall average water content, indoor air relative humidity and heating/cooling loads.

1. Introduction

The energy required for heating and cooling buildings is a large fraction of the total consumption and therefore of greenhouse gas emissions. These emissions need to be reduced as soon as possible and Building Energy Simulation (*BES*) methods are essential for designing high performance buildings and predicting their energy needs. Researchers and practitioners are using dynamic detailed building energy models that consider the transient behavior of the building envelope and of the *HVAC* systems to minimize the carbon emissions and reduce the energy demands during both heating and cooling seasons. When the building envelopes are composed of porous materials, water vapor diffusion plays a significant role in heat transfer. The main effect on the materials is the increase of the value of thermal conductivity, which results in larger heat losses during the heating season and larger heat gains during the cooling one (Danovska et al., 2020a and 2020b). Using the appropriate software, it is possible to model whole buildings using heat, air and moisture transfer models (*HAMT*) for the building envelope, calculating the effects of moisture diffusion and storage in building materials (Libralato et al., 2021a and 2021b), as well as the moisture buffering effect on the air conditions of the thermal zones (Zu et al., 2020). 17 *BES* tools based on *HAMT* models (including EnergyPlus) are presented in Woloszyn and Rode (2008), defining a benchmarking process included in IEA EBCS Annex 41. All these models require advanced

hygrothermal material characterizations, which are possible with time-consuming testing activities. The thermal and hygroscopic properties of the materials have to be tested at different temperatures and moisture contents, often requiring months of conditioning in climatic chambers (depending on the size of the samples).

This research is focused on the comparison between Moisture Sorption Curves (*MSCs*) interpolation models (Fig. 1), commonly used for timber materials when few Equilibrium Moisture Content (*EMC*) values are available. The study is based on the *MSCs* of four wood-based materials, measured at the Thermal Systems Laboratory of the University of Udine, and the thermal conductivity of three of the same set of materials, previously measured at different moisture contents and temperatures at the Building Physics Laboratory of the Free University of Bozen-Bolzano (Danovska et al., 2020a and 2020b).

First, the points of the moisture curve are measured using a Dynamic Vapor Sorption (*DVS*) analyser. Then, a piece-wise linear curve is developed to represent a *MSC* starting from the measured points. At this stage, using only three *EMC* points from the measured ones, three commonly used *MSC* models are adopted to interpolate the values. Finally, two small single-zone buildings are simulated in four locations, using the 4 *MSC* modeling approaches and comparing the results. The simulation tool used is EnergyPlus (version 9.5).

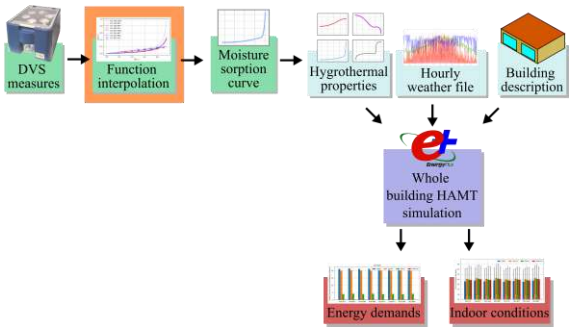

Fig. 1 – Study procedure scheme. In this study the effects of the choice of the function interpolation of *MSC* are quantified in terms of energy demands and indoor air conditions

The effect of *HAMT* models on *BES* energy consumption results has been already studied in the literature (Yang et al., 2015), finding differences of 5-10 % from the thermal simulations. The aim of this comparison is to assess to what extent an approximated sorption curve can alter the results of a whole-building hygrothermal simulation. Indeed, little information exists in the literature on the influence of different *MSCs* on *BES*.

The topic of the effects of *MSC* has been mainly tackled when considering moisture hysteresis in *HAMT* wall simulations for moisture-related risk analysis or for moisture buffering evaluations (Berger et al., 2020; Libralato et al., 2021a; Scheffler, 2008), comparing the effects of including hysteresis sorption models in the material sorption process. In this paper, hysteresis will not be considered, since EnergyPlus cannot model moisture hysteresis, but the adsorption and desorption curves of the materials will be taken into account separately.

2. Material Characterization

To perform heat and moisture transfer transient simulations, knowledge of several hygro-thermal material properties is required. In this study, the *MSCs* and thermal conductivities are obtained from measurements, while heat capacity and vapor permeability is taken from the literature. The study is limited to the hygroscopic range (under 95 % *RH*).

The *MSCs* of four materials were measured using the Proumid VSORP basic *DVS* analyser (Fig. 2). The instrument was set to perform gravimetric tests of the five samples every 20 minutes in a small climatic chamber with controlled dry bulb air temperature (*T*) and relative humidity (*RH*). *T* and *RH* being kept constant, and the samples are weighed until they reach equilibrium conditions. This procedure is performed automatically for every point of the *MSCs*. The environment was set to 23 °C and the relative humidity was set sequentially to 0 %, 30 %, 40 %, 50 %, 60 %, 70 %, 80 %, 90 %, 80 %, 70 %, 60 % and 50 % *RH*. The air *RH* is kept constant until the equilibrium condition is met by all the samples. The equilibrium condition is set to a mass change lower than 0.01 % in 350 minutes. The balance resolution is 0.1 mg. The whole test lasted approximately 42 days for a total of 12 *EMC* points.

The measurement procedure used differs from the standard ISO 12571 (CEN, 2021) on the following points:

- the sample's mass shall be at least of 10 g, and 100 mm x 100 mm if the material has a density lower than 300 kg/m³. Smaller samples can be used but it should be demonstrated that the result will not be affected;
- three samples shall be tested for each material;
- the equilibrium is reached when three consecutive weights, made 24 h apart, differ less than 0.1 % of the total mass;
- the starting point for the desorption curve should be at least 95 % *RH*.

Using the *DVS* analyser in place of the standard procedure removes the error caused by moving the sample from the controlled air environment to the scale, and reduces the time required by the test.

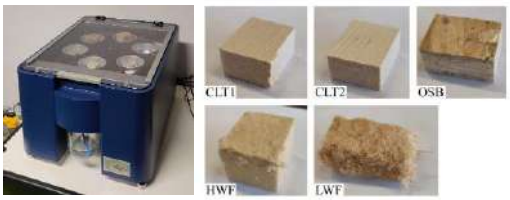

Fig. 2 – Experimental device (Vsorp Basic dynamic vapor sorption analyser) and studied samples of wood-based materials

The materials studied (Fig. 2) are spruce timber (used for Crossed Laminated Timber (*CLT*) panels), Orientated Standard Board (*OSB*), Low-density Wood Fibre (*LWF*) and High-density Wood Fibre (*HWF*). Since the instrument can measure 5 samples at the same time, two samples of *CLT* are tested and the *MSCs* used in the simulations is obtained averaging the two values.

The dry weight, volume, and free saturation moisture content of the samples are presented in Table 1. The dry weight is obtained after conditioning the samples at 0 % *RH* at 23 °C. The free saturation moisture contents of the five samples are obtained from the weight of the samples submerged in water until the weight variation is under the 0.1 %. A scale with 0.01 g resolution is used. The results of the sorption analysis are presented in Fig. 3. The *EMCs* of the five samples for the adsorption process are measured starting from the dry state up to the 90 % *RH*, and for the desorption process, starting at 90 % *RH* and back to 50 % *RH*.

Table 1 – Sample description

Sample ID	Dry weight [mg]	Volume [mm³]	Sat. M.C. [mg]
CLT1	7577.0	14570	13270
CLT2	7094.2	15850	14740
OSB	8632.1	18045	19890
LWF	2449.5	47740	41410
HWF	8654.5	80686	46390

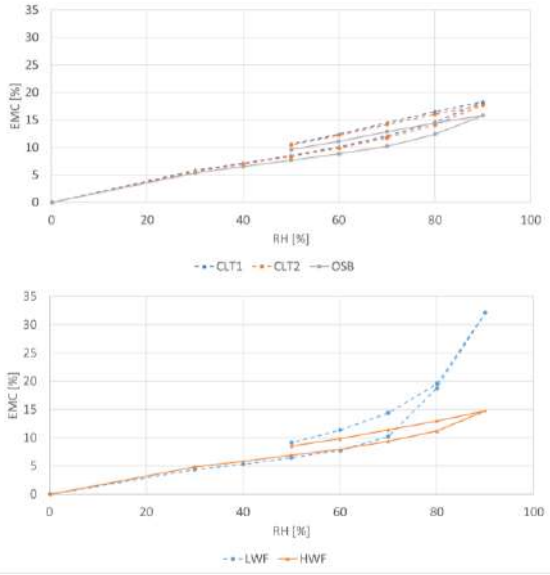

Fig. 3 – Adsorption and desorption curves measured for the five samples

2.1 Other Hygrothermal Properties

The thermal conductivity and specific heat values of the materials are taken from (Danovska et al., 2022), except for the *OSB* values which are obtained from the correlation reported in (Vololonorina et al., 2014) at 25 °C. The values of thermal conductivity are measured at different moisture contents and temperatures, but for this paper only the values at 20 °C with different moisture contents are considered. As an overall description of the materials, the hygrothermal properties are presented in Table 2. The values of permeability μ_{dry} and specific heat c_{dry} of the dry materials are taken from (Carbonari, 2010), except for *OSB*, which is from (Igaz et al., 2017).

Table 2 – Hygrothermal properties of the materials

Material	λ_{dry} [W m^{-1}K^{-1}]	ρ_{bulk} [kg m^{-3}]	c_{dry} [J kg^{-1} K^{-1}]	μ_{dry} [-]
CLT	0.104	467	1380	34
OSB	0.096	478	1287	46
LWF	0.039	51	2100	6
HWF	0.048	107	1380	6

The values of density ρ_{bulk} are calculated from Table 1. The values of μ used in the models are dependent on the moisture content and are described by linear piecewise functions connecting the values presented in (Vololonorina et al., 2014). The values of the vapor resistance factor at 0 % *RH*, μ_{dry} are presented in Table 2.

2.2 Moisture Sorption Curve Functions

In this study, four types of *MSC* interpolation are compared:

1 - Piecewise linear function (*PLF*)

2 - Brunauer–Emmett–Teller model (*BET*)

3 - Guggenheim-Anderson-de Boer model (*GAB*)

4 - Modified BET (*B80*)

The *PLF* case is obtained from the list of measured points. The interpolated *EMC* are calculated between the known points with a linear interpolation. The *BET* and the *GAB* model isotherm functions are considered in the form described in (Thybring et al., 2021) and they are used to obtain a correlation for the *MSC*s from three points of the measured *EMC* values series using the parabolic form presented also in (Thybring et al., 2021). The *B80* modified *BET* model is presented in (Künzel, 1995) and it is used in the WUFI software family to define the unknown *MSCs*. The parameters of the *B80* curve are defined by the *EMC* at 80 % *RH* and by the free water saturation point, set at 100 % *RH*, therefore it is the only function in this study that includes information on the over-hygroscopic range. The analytical curves obtained are used to define the sorption curve in EnergyPlus in the hygroscopic range for both adsorption and desorption curves. Fitting the values of *EMC* is commonly done when only few measured *EMC* are available. Therefore, to perform this situation, 3 *EMC* values are used to calculate the functions' parameters. The *GAB* and *BET* adsorption curves are fitted to the *EMC* values of 30 %, 50 % and 80 % *RH*, while the desorption curves are fitted to the 50 %, 70 % and 80 % *RH* points.

3. Simulations

To perform a simple comparison a modified version of the BESTEST Common Exercise 600 (Fig. 4) is used as test building (ANSI/ASHRAE, 2017).

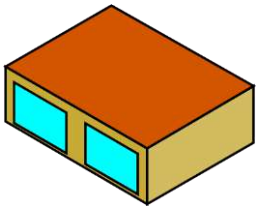

Fig. 4 – The BESTEST 600 geometrical model is used for the simulations. The model is a single room building with two large windows facing South

To evaluate the effects of the variation of the *MSC*s, the Heat Balance Algorithm is set to the Combined Heat and Moisture Finite Element model. Then the materials' *MSCs* are defined with 22 points (EnergyPlus allows a maximum of 25 points). The 22-point definition of the *MSCs GAB*, *BET* and *B80* is obtained from this subdivision of the *RH* range: every 10 % *RH* up to the 70 % *RH*, while from 72 % *RH* to 96 % every 2 %; the last point of the moisture curve is set at 100 % *RH* to the free water saturation point. The liquid conduction coefficients are set to 0 to avoid the over-hygroscopic moisture transport. Constant infiltration is set to 0.5 ACH and the internal sensible heat gains are set (as the BESTEST case) constantly to 200 W (60 % radiative, 40 % convective, 0 % latent). The weather files used are the ASHRAE IWEC (International Weather for Energy Calculation) files for the locations of Milan, Rome, Palermo and Venice. Annual average *T*, *RH* and total solar horizontal irradiation I_G of the weather files are presented in Table 3. The initial water content for every material is set to the *EMC* value correspondent to the 50 % *RH* value of the adsorption *PLF MSC*.

Table 3 – Weather files: average temperature and relative humidity, and total solar horizontal irradiation

Location	*T* [°C]	*RH* [%]	I_G [MWh/m²]
Milan	11.8	75	1.29
Palermo	18.8	74	1.69
Rome	15.8	78	1.46
Venice	13.2	77	1.15

Two construction types are set as external vertical walls (yellow walls in Fig.4): a *CLT* wall and a frame wall, while the floor and the roof constructions are the same for both cases. The build-ups of the two walls are described in Table 4.

Table 4 – Wall types

Wall type	Material layers	d [cm]
CLT wall U = 0.26 W/(m²K)	*OSB* (external layer)	2
	LWF	10
	CLT	10
Frame wall U = 0.37 W/(m²K)	*OSB* (external layer)	2
	HWF	10
	OSB	2
Floor and Roof U = 0.31 W/(m²K)	Barrier (external layer)	-
	HWF	10
	LT	10

A vapor barrier (S_d = 1500 m), not defined in the BESTEST, is added on the external side of the floor and of the roof, to remove the influence of the ground and of the roof. The floor external surface is set as adiabatic. An ideal heating and cooling system is set to maintain the internal temperatures between 20 °C and 27 °C, without air humidity control, and the heating and cooling demand is calculated. There are six warmup days required by EnergyPlus to reach convergence not reported in the results.

4. Results

In this section, first the *MSC* fitted curves are compared with the measured *PLF* curves, then the effects of using different *MSCs* in EnergyPlus *HAMT* whole building simulations are presented.

4.1 Fitting Evaluation

The curves fit the experimental points differently: from Fig. 5 it could be observed that the *GAB* model tends to follow the measured points, but it does not increase the *EMC* values after 90 % *RH*. Differently, the *BET* and *B80* curves always have lower *EMC* for values of *RH* lower than 80 %.

On one hand, the *B80* function is constrained at the *EMC* for 80 % *RH* and at 100 % *RH* and overestimates the values at 90 % *RH*. On the other hand, the *BET* curves overestimate also the 80 % *RH*. It should be also noted that the *LWF* adsorption *GAB* curve is above the desorption curve after the 80 % *RH*, being the only case where the *GAB* curve shows high moisture contents in the higher *RH* values.

Depending on the *RH* range used in the simulations, the material will have different moisture contents. In the cases studied, the room air *RH* is calculated to be between 30 % and 60 %, therefore, the representativeness is evaluated only up to 70 %. To evaluate the goodness-of-fit, the difference (in terms of moisture content) between the curves (*BES*, *GAB* and *B80*) and the *EMC* measured points (*PLF*) is calculated for each measured point of the desorption and adsorption curves, up to 70 %. The average of the differences is presented in Fig. 6. The *GAB* curves are the closest to the measured points, except for the *LWF* curve. The *BET* and *B80* curves have higher differences, therefore larger differences are expected in the simulation results. Despite the constraint at 80 % *RH*, the *B80* curves have larger average distances from the measured points.

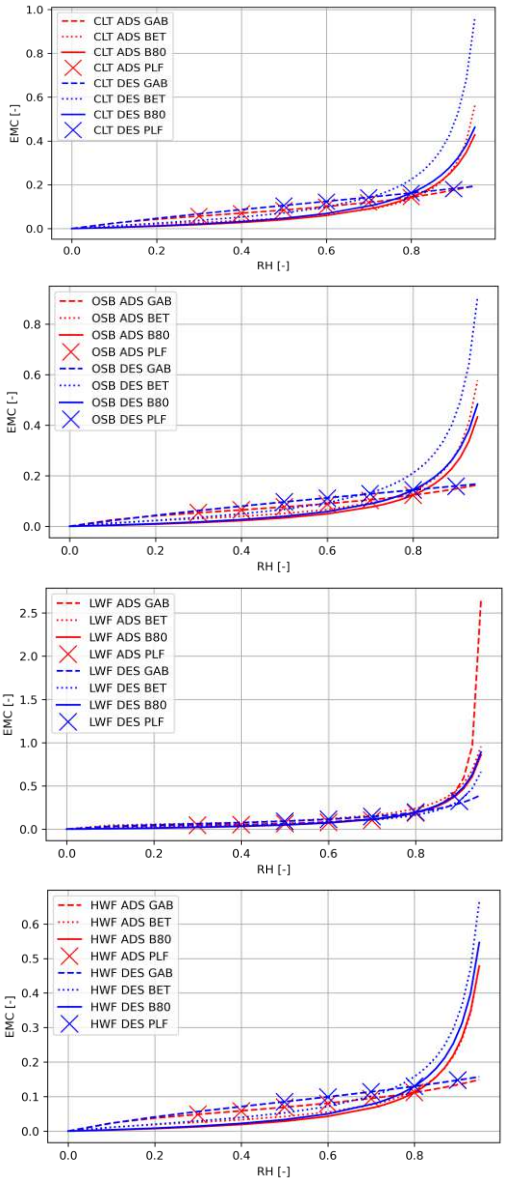

Fig. 5 – Measured (*PLF*) adsorption and desorption curves, *BET*, *GAB* and *B80* (adsorption and desorption) curves for the four considered materials

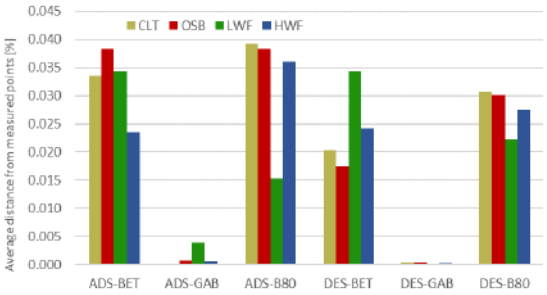

Fig. 6 –Absolute average distance from measured points of the *MSCs* considered. The differences are expressed in percentage mass/mass and the points from 0 % to 70 % *RH* are considered

4.2 Simulations

The results of the simulations follow the expectations of the differences presented in Fig. 6. The hourly values (Fig. 7) show that the moisture contents calculated with the measured curves are almost overlapping the values obtained using the *GAB* curve for both adsorption and desorption. The other results follow the order of the *CLT* sorption curves: *ADS-B80*, *DES-B80*, then *ADS-BET* and *DES-BET*, *ADS-GAB* and *ADS-PLF* (whose line is covered by the *ADS-GAB*), and, finally, *DES-GAB* and *DES-PLF*.

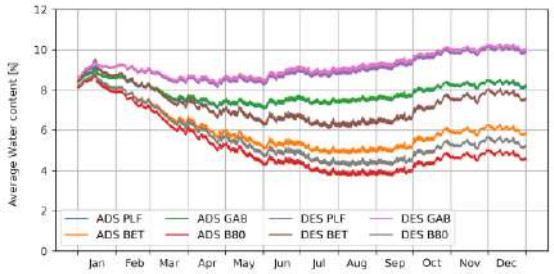

Fig. 7 – Hourly average water content of 1 m^2 of the North-facing wall for the *CLT* wall building simulation in the Milan weather file. The visualised values start after the 6-day warm-up period and are expressed in %kg_{water}/kg_{dry}

In Fig. 8, the annual mean values are reported for both wall typologies and for all the other climates considered. The relative positions of the *MSCs* seen in Fig. 6 are confirmed. Similar results with similar values are obtained for the Frame wall case (not reported here). When considering the heating and cooling demands, the simulations with *MSCs* with higher *EMC* values are expected to have larger values of energy needs, and lower energy needs for lower *EMC*, since the thermal conductivity is dependent on the moisture content of materials. Moreover, also the effects of latent heat transfer should be expected, especially when the effect of initial moisture content is present.

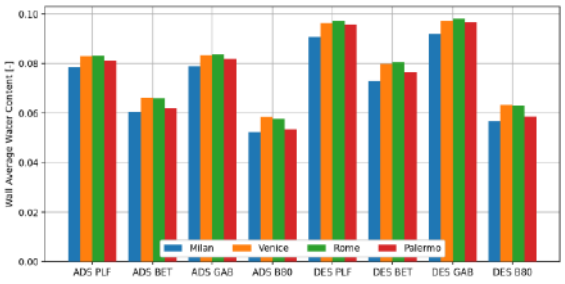

Fig. 8 – Annual mean water content of 1 m^2 of the North-facing wall for the *CLT* wall building simulation in the Milan weather file

Heating and cooling demands are also influenced by the latent loads due to the walls drying or adsorbing air moisture to reach *EMC*; this resulted in larger heating loads for the simulations with *MSCs* with lower *EMC* values and vice versa. The differences among the loads of the studied cases are the combination of the effect of the conductivity reduction and the effect of latent loads provided by the moisture migration from the walls. The results for the adsorption and desorption curves are presented as annual energy demands in Table 4 (*CLT* wall) and Table 5 (frame wall). In most of the cases, the energy demands values are higher for the adsorption curve results, except for the *CLT* cooling demands of Venice, Rome and Palermo, and the heating demands in Milan.

Table 4 – Annual heating and cooling demands calculated for the *CLT* wall with the adsorption and desorption *PLF MSC*

Location	**Heating demand [kWh/(m² yr)]**		**Cooling demand [kWh/(m² yr)]**	
	ADS	*DES*	*ADS*	*DES*
Milan	21.77	21.80	32.40	32.32
Venice	20.98	20.75	27.75	27.77
Rome	4.19	4.05	40.16	40.19
Palermo	0.17	0.16	56.45	56.61

Table 5 – Annual heating and cooling demands calculated for the frame wall with the adsorption and desorption *PLF MSC*

Location	**Heating demand [kWh/(m² yr)]**		**Cooling demand [kWh/(m² yr)]**	
	ADS	*DES*	*ADS*	*DES*
Milan	28.22	27.95	33.54	33.28
Venice	26.05	25.80	28.11	27.89
Rome	7.52	7.34	40.48	40.19
Palermo	0.69	0.65	56.03	55.90

The desorption curves have higher moisture contents, and this is expected to lead to higher demands, caused by higher thermal conductivity values of the envelope materials. However, when the loads due to the drying process are larger, the resulting effect is the opposite. The charts in Fig. 9 show the deviation from the adsorption and desorption results obtained using *MSC* fitting curves. In these charts the difference for the adsorption and desorption fitting curves is calculated from the results of the adsorption and desorption *PLF* curves, respectively. The calculated differences for the heating demands are all below 1.2 kWh/m², with Milan *CLT ADS-BET* having the highest corresponding to a deviation of 5 % from the *PLF* values. The higher relative deviations are found for Palermo *CLT DES-B80* (38 % of 0.16 kWh/(m² yr)) due to the very low heating loads. The cooling loads differences are below 1 kWh/m² (e.g., for Milan frame wall *DES-B80*), which is also the maximum relative difference (2.5 %). As expected, in every case, the *GAB* model produces the lowest differences, while the *B80* the largest. The negative values of the *CLT* wall cooling demands are caused by the drying process due to the initial moisture contents of the walls. To verify this, multi-year simulations have been performed (removing the dependence on the initial moisture content), obtaining positive differences in the last year of the simulations.

The effect of the *MSCs* on the internal environment for the *CLT* wall case is presented in Fig. 10. While the internal temperature values are controlled by the ideal heating and cooling system, the relative humidity is influenced by the constant air infiltration and by the moisture buffering effect of the building materials on the internal environment. The results show that the *MSCs* compared can also have an influence on the annual average moisture content. The variation due to the *MSC* of the average value is less than 2 % *RH*, while the maximum values have variations up to 4 % *RH*. The minimum annual average values are found for the *CLT ADS-B80* case (e.g., 41.3 % *RH* in Milan), while the maximum is found for *CLT DES-GAB* (e.g., 43.0 % *RH* in Milan). The *ADS* simulations have 1 % *RH* higher values than the respective *DES* simulations, and the *BET* and *B80* have higher values than *PLF* and *GAB*. Sorption curves with lower *EMC* obtained lower wall moisture contents (Fig. 8) and higher air *RH* values.

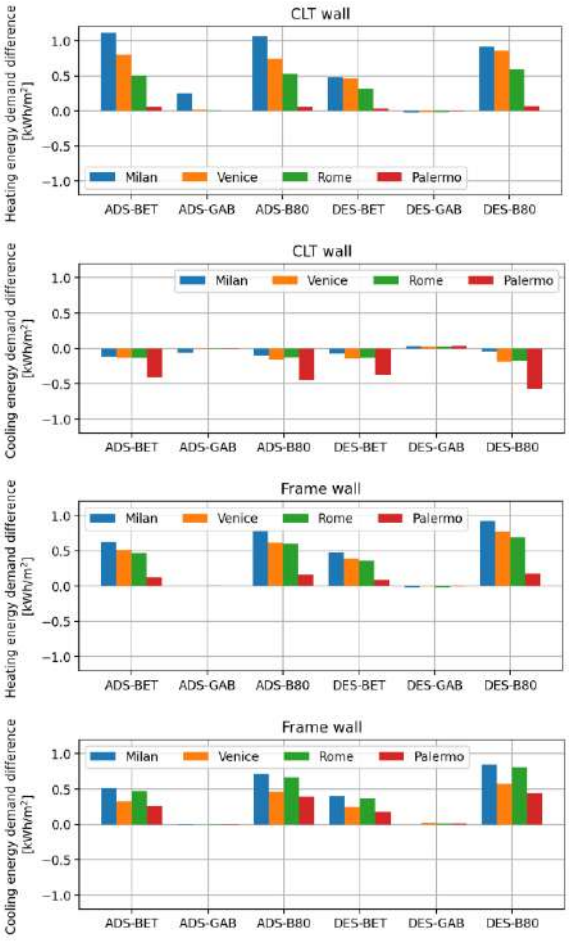

Fig. 9 Annual heating and cooling demands deviations. The differences of the *ADS* and *DES* fitting curves are calculated from the respective *ADS* and *DES PLF* curves (Table 5)

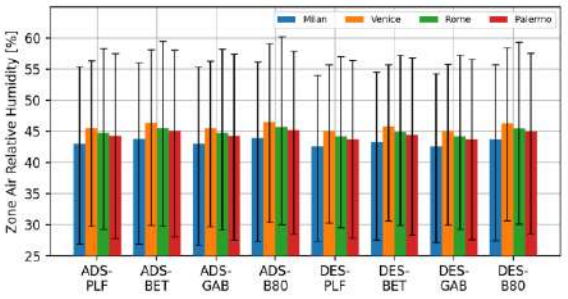

Fig. 10 – Annual average indoor air *RH* calculated with different *MSCs* at different locations. The error bars indicate the annual hourly maximum and minimum *RH* values

5. Conclusions

In this preliminary research the moisture adsorption and desorption curves of four wood-based building materials have been measured with a *DVS* analyser. The measured values have been compared with three commonly used fitting functions based on different *MSC* models. 64 simulations of a small building have been performed, with two different envelopes composed of the materials analysed, in four Italian locations, for four *MSC* fitting curves, for both adsorption and desorption curves. The simulations have been performed with the software EnergyPlus considering moisture dependent hygrothermal material properties.

The effects of every fitting function on the results of the simulation have been quantified in terms of heating and cooling annual demands, moisture content in walls and air relative humidity. The main findings are:

- The *GAB* function represents better the measured *EMC* in the hygroscopic range.
- For the studied cases, using the *BET* and *B80* functions in hygrothermal building energy simulations caused errors in the heating demand up to 1.2 kWh/(m² yr) (case of *CLT* simulation in Milan, with 5 % difference from the same *PLF* case) and 1 kWh/(m² yr) in cooling demands (Milan frame wall *DES-B80*, with 5 % difference from the same *PLF* case).
- When considering the internal annual average air relative humidity, the influence of the fitting function is found to be of 2 % *RH*, and of 4 % *RH* on the annual maximum values.

In conclusion, the differences are of a small order, and could be of interest when high precision results are required (for example, with high performance buildings, in risk evaluations, or in model calibration procedures). The desorption curves, as expected, led to the calculation of higher moisture contents and internal relative humidity values, and should be preferred to adsorption curves when conservative simulations are needed.

Further research is required to increase the accessibility of hygrothermal simulations. Future work will focus on extending the analysis on the other hygrothermal material properties and on the over-hygroscopic range, considering the effects of rain and extreme weather conditions. Occupants' comfort parameters and multi-year results will also be considered.

Acknowledgement

The research leading to these results has also received funding from the MIUR of Italy within the framework of the PRIN2017 project «The energy flexibility of enhanced heat pumps for the next generation of sustainable buildings (FLEXHEAT)», grant 2017KAAECT.

Libralato M. acknowledges fellowship funding from MUR (Ministero dell'Università e della Ricerca) under PON "Ricerca e Innovazione" 2014-2020 (D.M. 1062/2021).

This research was partially funded by the project "Klimahouse and Energy Production", in the framework of the programmatic-financial agreement with the Autonomous Province of Bozen-Bolzano of Research Capacity Building.

Nomenclature

Symbols

c_{dry}	Specific heat capacity ($J \cdot kg^{-1} K^{-1}$)
λ_{dry}	Thermal conductivity ($W \cdot m^{-1} K^{-1}$)
μ_{dry}	Water vapor resistance factor (-)
ρ_{bulk}	Density ($kg \cdot m^{-3}$)
U	Air-to-air thermal transmittance ($W \cdot m^{-2} K^{-1}$)

Abbreviations

ADS	Adsorption
B80	BET model with 80 % *RH* constraint
BES	Building Energy Simulation
BET	Brunauer–Emmett–Teller model
CLT	Cross-Laminated Timber
DES	Desorption
DVS	Dynamic Vapor Sorption analyser
EMC	Equilibrium Moisture Content
GAB	Guggenheim-Anderson-deBoer model
HAMT	Heat Air and Moisture Transfer
HWF	High-density Wood Fibre
LWF	Low-density Wood Fibre
MSC	Moisture Sorption curve
OSB	Oriented Strand Board
PLF	Piecewise Linear Function
RH	Relative Humidity

References

ANSI/ASHRAE. 2017. "Standard Method of Test for the Evaluation of Building Energy Analysis Computer Programs (ANSI/ASHRAE Standard 140)."

Berger J., T. Busser, T. Colinart, and D. Dutykh. 2020. "Critical assessment of a new mathematical model for hysteresis effects on heat and mass transfer in porous building material." *International Journal of Thermal Sciences* 151: 106275. doi: https://doi.org/10.1016/j.ijthermalsci.2020.106275

Carbonari, A. 2010. "Proprietà materiali edilizi." Lecture notes. Accessed on December 1, 2021 http://www.iuav.it/Ateneo1/docenti/architettu/docenti-st/Carbonari-/materiali-1/claSA-06-0/proprmat.pdf

CEN. 2021. EN ISO 12571:2021 – *Hygrothermal performance of building materials and products - Determination of hygroscopic sorption properties*. European Committee for Standardization.

Danovska, M., G. Pernigotto, P. Baggio, and A. Gasparella. 2022. "Simulation uncertainty in heat transfer across timber building components in the Italian climates: the role of thermal conductivity". *Energy and Buildings* 268: 112190. doi: https://doi.org/10.1016/j.enbuild.2022.112190

Danovska, M., G. Pernigotto, M. Baratieri, P. Baggio, and G. Gasparella. 2020a. "Influence of moisture content, temperature and absorbed solar radiation on the thermal performance of a spruce XLAM wall in the Italian climates." *Journal of Physics: Conference Series, 37th UIT Heat Transfer Conference*. doi: https://doi.org/10.1088/1742-6596/1599/1/012028

Danovska, M, M. Libralato, G. Pernigotto, A. De Angelis, O. Saro, P. Baggio, and A. Gasparella. 2020b. "Numerical and experimental study on the impact of humidity on the thermal behavior of insulated timber walls." *Proceedings of Building Simulation Applications BSA 2019*. doi: https://doi.org/10.13124/9788860461766

EnergyPlus. 2021. "Weather Data." National Renewable Energy Laboratory (NREL). Accessed Dec 1, https://energyplus.net/weather

Igaz, R., L. Krišťák, L. Ružiak, M. Gajtanska and M. Kučerka. 2017. "Thermophysical properties of OSB boards versus equilibrium moisture content." *BioResources* 12(4): 8106-8118.

Künzel, H.M. 1995. "Simultaneous heat and moisture transport in building components: One- and two-dimensional calculation using simple parameters." Fraunhofer-Institut für Bauphysik

Libralato, M., A. De Angelis, O. Saro, M. Qin, and C. Rode. 2021a. "Effects of considering moisture hysteresis on wood decay risk simulations of building envelopes." *Journal of Building Engineering* 42: 102444 doi: https://doi.org/10.1016/j.jobe.2021.102444

Libralato, M., A. De Angelis, G. Tornello, O. Saro, P. D'Agaro, and G. Cortella. 2021b. "Evaluation of Multiyear Weather Data Effects on Hygrothermal Building Energy Simulations Using WUFI Plus." *Energies.* doi: https://doi.org/10.3390/en14217157

Scheffler, G. A. 2008. "Validation of hygrothermal material modelling under consideration of the hysteresis of moisture storage." PhD Thesis. Dresden University of Technology.

Thybring, E. E., C. R. Boardman, S. L. Zelinka, and S. V. Glass. 2021 "Common sorption isotherm models are not physically valid for water in wood." *Colloids and Surfaces A: Physicochemical and Engineering Aspects* 627: 127214. doi: https://doi.org/10.1016/j.colsurfa.2021.127214

Vololonorina, O., M. Coutand, and B.Perrin. 2014. "Characterization of hygrothermal properties of wood–based products – Impact of moisture content and temperature." *Construction and Building Materials* 63: 223–233. doi: https://doi.org/10.1016/j.conbuildmat.2014.04.014

Woloszyn, M., and C. Rode. 2008. "Tools for performance simulation of heat, air and moisture conditions of whole buildings." *Building Simulation* 1: 5–24. doi: https://doi.org/10.1007/s12273-008-8106-z

Yang, J., H. Fu, and M. Qin. 2015. "Evaluation of Different Thermal Models in EnergyPlus for Calculating Moisture Effects on Building Energy Consumption in Different Climate Conditions" *Procedia Engineering* 121: 1635-1641 doi: https://doi.org/10.1016/j.proeng.2015.09.194

Zu, K., M. Qin, C. Rode, and M. Libralato. 2020. "Development of a moisture buffer value model (MBM) for indoor moisture prediction." *Applied Thermal Engineering* 171: 115096 doi: https://doi.org/10.1016/j.applthermaleng.2020.115096

Energy Performance Evaluation and Economical Analysis by Means of Simulation Activities for a Renovated Building Reaching Different Nzeb Definitions Targets

Riccardo Gazzin – EURAC Research, Italy – riccardo.gazzin@eurac.edu
Jennifer Adami – EURAC Research, Italy – jennifer.adami@eurac.edu
Mattia Dallapiccola – EURAC Research, Italy – mattia.dallapiccola@eurac.edu
Davide Brandolini – EURAC Research, Italy – davide.brandolini@eurac.edu
Miren Juaristi Gutierrez – EURAC Research, Italy – miren.juaristigutierrez@eurac.edu
Diego Tamburrini – EURAC Research, Italy– diego.tamburrini@eurac.edu
Paolo Bonato – EURAC Research, Italy – paolo.bonato@eurac.edu
Martino Gubert – EURAC Research, Italy – martino.gubert@eurac.edu
Stefano Avesani – EURAC Research, Italy – stefano.avesani@eurac.edu

Abstract

The nZEB target is increasingly becoming one of the main objectives in building renovation, but a unique nearly-Zero Energy Building definition is not explicitly available in the 31/2010 EU directive, the so-called "Energy performance of buildings directive". Nevertheless, the technical implementation of the nearly-Zero Energy Building concept into defined constraints and requisites is a determining factor for the consequences of energy-economic performance . In fact, in the renovation process of a building, different technical requirements lead to different design solutions that affect investment and operative costs, as well as energy performance. Through an optimization process based on dynamic simulations for energy and economic performance assessment, a comparison between different approaches for the nZEB building retrofit for a demo-case building has been performed. First, an energy target which is stricter than the nZEB standard is examined. In particular, the so-called "Positive Energy Building" approach, consisting of the design of a building that produces more energy than it consumes in the overall year, is evaluated. Then, the results of the Positive Energy Building target are compared to a nearly-Zero Energy Building approach in which self-sufficiency is promoted, instead of the energy production/consumption balance. Also, the nearly-Zero Energy Building target promoted by the Italian legislation has been evaluated, comparing the result of a plausible implementation with the other more stringent approaches. The simulation work has been aimed at comparing significant Key Performance Indexes, regarding both energetical and economical aspects. In particular, initial investment costs, expected net present value of the investment after 25 years and energy performance indexes have been evaluated. The discussion demonstrates that, according to the assumptions adopted for the investment and energy costs, the Positive Energy Building target is excessively economically inconvenient for a renovation intervention of this type. Moreover, designers should prioritize the self-sufficiency of the building energy system with respect to the production/consumption yearly ratio. Finally, the discussion demonstrates that a renovation design in accordance with the Italian nearly-Zero Energy Building target is economically sustainable but the PV system size to meet the minimum requirements could be non-optimal.

1. Introduction

1.1 Background

To achieve the goal of a strong reduction of building-related CO_2 emissions for the next decades in the EU, a significant contribution must come from acting on the existing residential building stock renovation. The target of nearly-Zero Energy Buildings (nZEB) for new buildings has been set by the EU Commission with the 31/2010 EU directive, the "Energy performance of buildings directive" (EPBD). Nevertheless, a unique approach for the definition of the technical requirements has not been defined,

since each country should take charge of the implementation of the directive (D'Agostino et al., 2021).
The nZEB as target performance also applies to major building renovation since 2021. Moroever, building deep retrofit is one of the key actions capable of decarbonizing the building sector to meet global targets to address climate change (D'Agostino et al., 2017). Reaching nZEB targets when renovating a building allows a greater reduction in fossil energy savings and greenhouse gas emissions compared with a traditional retrofit intervention (Holopainen et al., 2016). In the literature, cost-optimum calculations have been performed to identify which renovation interventions lead to the best economic benefits while meeting the nZEB target (Zangheri et al., 2018). Nevertheless, the renovation rate in Europe is around 1 % (A Renovation Wave for Europe, 2020) - still quite below the target of 2 %. In this framework, the trend of a prefabricated and industrialised retrofit is attracting more and more attention thanks to a set of research projects (D'Oca et al., 2018) and bottom-up national initiatives (e.g. EnergieSprong, ...). Prefabricated solutions could allow an increase of the annual renovation rate of the European building stock, also thanks to the integration of different functions and technologies in the same element (Pernetti et al., 2021; Pinotti, 2020).
After the introduction of the nZEB target, Positive Energy Buildings (PEBs) are somehow considered as the next phase for building sector sustainability. The requirements in terms of energy consumption efficiency are the same as the nZEB target, but a reinforcement of the building energy production is expected. Barriers and challenges in the Positive Energy Building implementation have been investigated by Ala-Juusela et al. (2021). PEBs also allow a significant contribution to the energy support of the local neighborhood, the so-called Positive Energy Neighborhood. Good et al. (2017), analysed this topic, highlighting its challenges and opportunities.

1.2 Italian Framework for nZEB Buildings

In the Italian framework, the implementation of the EU directive for nZEB buildings has been carried out by the "Decreto ministeriale 26/06/2015". In both cases of new construction or renovation, the decree requires that the project building is compared with a reference building.
The reference building is a fictitious building that has identical geometrical shape (same volume, floor areas, envelope surfaces etc.), climatic conditions, orientation, destination of use and surrounding situation. The differences from the project building lie in the thermal characteristics of the envelope and in the energy system characteristics. These values are reported in specific tables.
A series of indexes that indicate the quality of the envelope and the efficiency of the energy system are calculated both for the project building and the reference building. Then, a comparison is made to assess whether the building can be considered as nZEB or not, considering the reference building as the minimum standard to be achieved by the project case.
Specifically, the previously mentioned indexes are:

- H'_T, which is the overall average coefficient of heat transfer by transmission
- $A_{sol,est}$/ $A_{sup\ utile}$, which is the so-called equivalent summer solar area per useful area unit
- Solar transmission factor, also considering the shadings
- Thermal inertia properties, such as superficial mass (Ms) and periodic thermal transmittance (Y_{IE})
- Thermal transmittance of the internal partition walls and of the outward-facing structures of non-air-conditioned rooms.
- Useful thermal performance indexes for heating ($E_{PH,nd}$) and cooling ($E_{PC,nd}$)
- Energy performance indices for winter space heating (E_{PH}) and summer space cooling (E_{PC}) and overall building performance, in non-renewable and total primary energy (E_{Pgl})
- Seasonal average efficiency of the system for winter space heating (η_H), summer space cooling (η_C) and domestic hot water production (η_w).

In addition, the building must accomplish some requirements in terms of renewable energy production. These requisites are reported in the "Allegato 3, DLgs 3 marzo 2011 n. 28". The building must guarantee:

- production of electrical energy by means of systems from renewable sources (mandatory installed on or inside the building or in its out-buildings) with a power measured in kW calculated according to the following formula:

$$P = \frac{1}{k} \cdot S\ [kW]$$

where:

S is the floor area of the building at ground level, measured in m²; k s a coefficient that takes the value K = 50 m²/kW if the application for the authorization is submitted after 1 January 2017.

- Contemporary coverage, by means of renewable energy sources, of the 50 % of the domestic hot water, space heating and cooling demand, and the 50 % of domestic hot water. In case the building is public, these percentages must be increased by 10 %.

1.3 Aim and Research Objective

The ambitious target of nZEB to be achieved by a prefabricated solutions approach for the renovation of a building is still lacking a technical feasibility analysis. In other words, from the literature it is still not clear which technical features of a retrofit action are compliant with the nZEB definition. Moreover, a techno-economic comparison between different nZEB definitions to be achieved with prefabricated technologies has not been performed. Such research questions are national-dependent and will be discussed in this paper for a case study in Italy. The case study is a residential building undergoing an innovative renovation process. The renovation intervention consists of the installation of prefabricated multifunctional envelope modules (façade and roof) that might integrate the following available technologies depending on needs: building-integrated photovoltaic or solar thermal panels (BIPV and BIST), mechanical ventilation machine units and green façade modules. Coloured BIPV panels are taken into consideration to optimize the building integration from an aesthetic point of view.

For the support activities in the preliminary design phase, dynamic simulations have been performed to examine the relationship between possible different renovation scenarios and the fulfilment of the nZEB definitions. In particular, a preliminary design of the BIPV system, with the possibility of integrating a Battery Energy Storage System (BESS), has been carried out.

The whole analysis aims at investigating how different renovation building scenarios – all targeting the nZEB level, perform from a techno-economic point of view.

2. Methodology

The building to be renovated is located in Greve in Chianti (Florence), and consists of two heated floors, with four apartments overall. The renovation aims to convert the building energy system into a full-electric system, producing electricity on-site to cover the energy demand. The heating and cooling services are set to be provided by an electric air-to-air heat pump, which will be, at least partially, fed by the BIPV system.

To achieve the goal of evaluating different renovation scenarios and their impacts in terms of nZEB definitions, energy performance and costs, the following methodology has been defined. First, the target scenarios have been defined:

- Scenario 1, based on the Positive Energy Building (PEB) target d1, for which the building produces more energy than it consumes in a yearly balance. As a consequence, the BIPV system has been sized to cover more than 100 % of the building's electric demand.
- Scenario 2 assumes that the system has to guarantee a level of self-sufficiency equal to the one resulting in Scenario 1 while minimizing the cost per kWh produced (Levelized Cost Of Electricity, LCOE). It means the BIPV system is optimized in a way that a specified portion of the energy demand is covered by self-produced electricity, also considering the support of a battery storage system.
- Scenario 3 assumes that the system has to guarantee self-sufficiency equal to 30 %, i.e., a typical value achieved in residential applications (McKenna et al., 2017).
- Scenario 4 aims to meet the Italian nZEB target described in Section 1.2. Unlike in the previous scenarios, here the PV configuration is an input of the BIPV optimization tool, which is used in

simulation mode, and the building electric load is not taken into account for the sizing of the components. In particular, the PV nominal power is the result of a previous calculation (UNI/TS 11300 and "Allegato 3 del D. Lgs. 28/2011"), aimed at ensuring the minimum compliance with the Italian regulation; the PV module position is determined considering the most irradiated building surfaces, i.e., in this case, the south-facing roof pitch.

These scenarios are summarized in Table 1.

Table 1 - nZEB scenarios for the simulations

Scenario	nZEB approach	Energy target
1st scenario	Zero Energy Building	Energy produced is equal to energy consumed in a yearly balance
2nd scenario	Prioritization of self-sufficiency	Same self-sufficiency of the 1st scenario, but the Levelized Cost of Electricity is minimized
3rd scenario	Prioritization of self-sufficiency	Self-sufficiency is lower than in 2nd scenario, Levelized Cost of Electricity is still minimized
4th scenario	Italian nZEB standard	Requirements of the "Allegato 3 del D. Lgs. 28/2011" and other technical requisites

Then, the final Key Performance Indicators to compare the renovation scenarios against been defined as the following:

- Initial investment costs for the BIPV system (including the battery cost)
- Expected NPV (Net Present Value) after 25 years
- Self-sufficiency (i.e., the portion of building demand directly covered by self-consumed PV electricity)
- Self-consumption (i.e., the portion of PV-produced electricity directly consumed or stored in the building)
- Annual cumulative production – consumption rate

The electrical energy demand for the different renovated building scenarios has been calculated with an energy dynamic model (TRNSYS). After that, the electrical demand curve is considered as input in a "BIPV optimization tool", able to find optimal BIPV-battery configurations to meet the previously described requirement scenarios. The outcomes of the optimization are processed and evaluated in terms of energy and economic performance through the set of KPIs that have been previously described. Hence, the solutions suggested for the BIPV and battery system design are compared. Considerations regarding different nZEB approaches and requisites are also reported.

2.1 Electrical Energy Demand Calculation

For the purposes of this work, the dynamic energy modeling tool TRNSYS (Thermal Energy System Specialists) has been used to model and simulate the building thermal behavior, calculating the space heating and cooling energy demands, the indoor thermal comfort and the electrical energy consumption needed by the heating/cooling and ventilation systems (plug loads are not considered). The required input data are reported in Table 2. Specifically, a 3D model is produced to represent the geometry of the building (Fig. 1). Information regarding the actual thermal characteristics of the envelope, as well as the ones related to the energy system are retrieved from a previous building energy audit. The characteristics of the existing building are then crossed with the planned renovation project, defining the future building energy model. In fact, the thermal transmittance of the envelope-renovated portion is updated to the designed conditions and the new Heating, Ventilation and Cooling (HVAC) system is implemented, using a heat pump TRNSYS type developed at Eurac Research. This type has been developed as a grey-box model, in which the generated heat and the electrical consumption are

determined by developed algorithms out of performance maps provided by manufacturers. Generated heat and electrical consumption of the heat pump are calculated as a function of boundary conditions. After the boundary conditions of the simulation are set, together with the expected building occupants' behavior and the expected internal gains (SIA 2024:2015), the total electrical energy demand is calculated.

Table 2 - Input for the TRNSYS model

Input data	Source
Geometry of the building	SketchUp 3D model
Thermal properties of the building envelope	Energy audit report; thermal characteristics of the prefabricated panels and new windows
HVACS characteristics	Properties of the system that is expected to be installed during the renovation process; heat pump performance is simulated with a black-box model developed by EURAC Research
Boundary weather conditions	Typical meteorological year (TMY) of the building location
Occupancy schedule and internal gains	SIA 2024:2015

Simulating the behavior of the building in hourly time-steps, the electrical energy consumption is calculated in TRNSYS. This electricity curve is later used as input in the "BIPV optimization tool".

2.2 BIPV Optimization

For the BIPV system optimization, a Python-based tool (EnergyMatching) (Lovati et al., 2019) has been used.

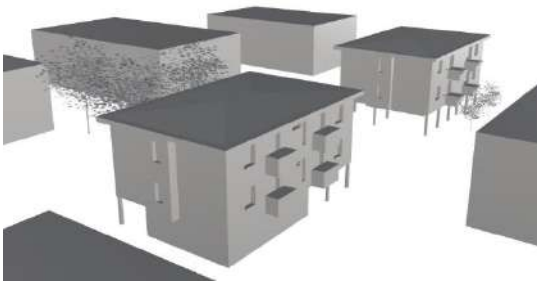

Fig. 1 - 3D model of the building case study

This has been developed by Eurac Research to support designers and other professionals who want to integrate a photovoltaic system in buildings or districts. The tool is based on a direct search algorithm applied to a minimization/maximization problem, which can be constrained or unconstrained, depending on the target function selected (minimization of the Levelized Cost of Electricity, Maximization of the Net Present Value, etc.). As a solution, it suggests the optimal BIPV configuration, i.e., how many PV modules and where to integrate them over the building envelope (on roofs, façades, shading devices, balustrades, etc.). It can also suggest including an electric storage system to increase the ratio of self-consumed energy. The BIPV configurations are optimized according to the specificities of the cases (building geometry, local weather, surrounding shade, unitary costs of the system and current benefits to produce electricity, sold or self-consumed), also considering how much energy is indeed needed by the building throughout the day and the seasons. Moreover, different target functions can be assigned to the tool, to achieve energy, economic and/or environment-related goals. Based on hourly time-step calculations that allow evaluation of the energy fluxes between the photovoltaic system, the battery, the load and the grid, the tool can provide a set of KPIs showing the expected performance of the photovoltaic system, from energy, economic and environmental points of view. Further information and details on the BIPV optimization tool calculation model are available in (EnergyMatching, 2022).

The assumptions and input data for the BIPV-BESS optimization are reported in Table 3. It has to be noted that the technology prices are higher than benchmark on-the-market PV modules because it refers to aesthetically appealing glass-glass BIPV

modules able to comply with the requirements of façade integration also in culturally preserved urban contexts.

Table 3 - Assumptions and input data for BIPV optimization

Price of electricity bought from the grid	0.215	[€/kWh]
Price of electricity sold to the grid	0.05	[€/kWh]
BIPV module efficiency	0.13	[%]
BIPV cost	2800	[€/kWp]
BESS cost	800	[€/kWh]

3. Results Analysis and Discussion

The results obtained for the four renovation scenarios considered are shown in Table 4 and discussed case-by-case in this section.

Table 4 - Results of BIPV optimization tool in the four scenarios

Scenarios	1	2	3	4
Suggested PV capacity [kWp]	15.7	11	5.4	4.4
Suggested electric storage capacity [kWh]	0	3.4	0	0
Investment costs [€]	44045	33533	14976	12333
Expected NPV after 25 years [€]	-18018	-10034	-60	571
Self-sufficiency [%]	48	48	30	27
Self-consumption [%]	46	66	86	91
Annual cumulative ratio production/consumption	1.03	0.73	0.36	0.29

Scenario 1: considering the design target of a ratio production/consumption (on a yearly basis) higher than one, the photovoltaic nominal power suggested by the BIPV optimization tool is the highest among the scenarios considered and is equal to 15.7 kWp. On the contrary, the electric storage capacity is 0 kWh, since it does not contribute towards achieving the design target. From an economic point of view, this solution is the less cost-effective, from both the investment and NPV perspective.

Scenario 2: results obtained show the same performance in terms of self-sufficiency as Scenario 1 (because it has been set as optimisation target for this scenario) but with lower investment costs and a better NPV, due to the presence of a battery storage. As the suggested PV capacity is lower, the annual ratio production/consumption decreases to 0.73.

Scenario 3: in this scenario, the annual cumulative ratio production/consumption is lower compared with Scenario 1 and 2 (below 0.4) but the investment payback is achieved during the system lifetime of 25 years considered. Self-sufficiency is only 30 %, meaning that the BIPV system contributes less compared with the previously described scenarios to cover the electricity demands of the building.

Scenario 4 achieves similar results in terms of annual balance and self-sufficiency compared with the ones obtained in Scenario 3.

The best BIPV configuration obtained for Scenario 1 turns out to be less cost-effective than the ones obtained with the other approaches from both the investment and NPV perspective.

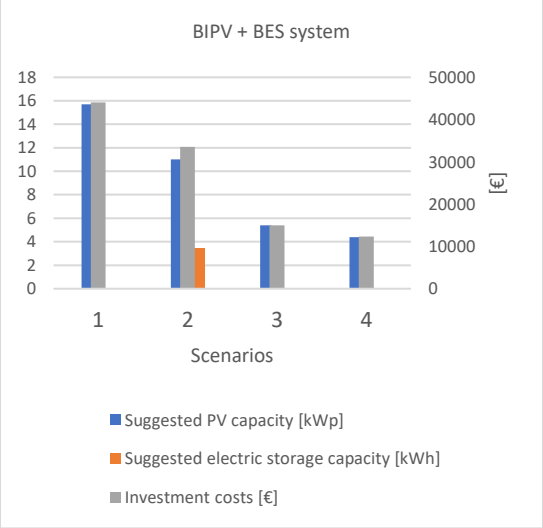

Fig. 2 - BIPV and BESS characteristics

Moreover, considering that the only design constraint is obtaining the target yearly energy production, the electric storage capacity is equal to 0, at the cost of a low self-consumption (46 %), as seen in

Fig. 3. On the contrary, results obtained for Scenario 2 confirm that the same self-sufficiency can be achieved by installing a more balanced system. This is confirmed by the self-consumption index (SC), which is increased to 66 % by decreasing the nominal power of the photovoltaic system and favoring the installation of an electric energy storage (3.4 kWh), as seen in Fig. 2. Also from an economic point of view, Scenario 2 can be considered a better approach, since the investment costs are decreased by 24 % and the NPV also improves. Due to the lower nominal power installed, the ratio consumption/production decreases to 0.73, meaning that, on an annual basis, the building does not produce the same electrical energy that is consumed.

Regarding Scenario 3, the annual cumulative ratio of production/consumption decreases significantly (below 0.4) but the payback of the system is achieved after 25 years. This is caused by the fact that a small system is installed and no battery is needed to meet the energy target. This is confirmed by the high value of self-consumption (86 %), meaning that most of the energy produced is directly self-consumed by the building. However, high values of self-consumption and low values of self-sufficiency mean that the system covers only a small fraction of the total energy consumption even if most of the energy produced is self-consumed. This usually indicates that the system is slightly undersized compared with the building energy consumption.

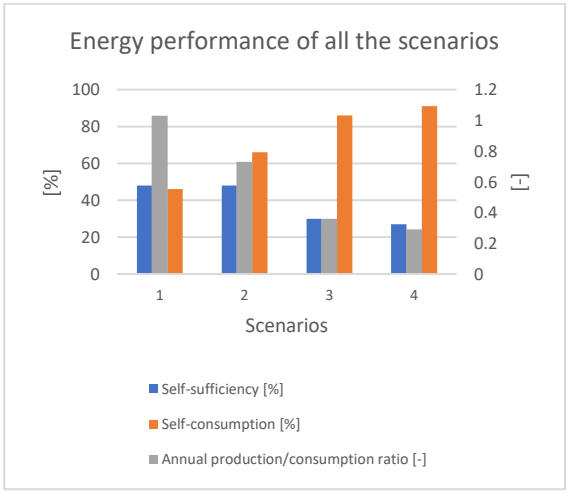

Fig. 3 - Self-sufficiency and self-consumption for the scenarios considered

For Scenario 4, the system was not optimized to obtain a specific target but designed to respect the Italian regulation for the installation of photovoltaic panels in nZEB buildings. Results obtained are similar to the ones obtained for Scenario 3 and the same considerations can be applied. However, the main limitation of this approach is that it suggests reasonable solutions only for a limited number of cases. In fact, as discussed in the paperwork by Lovati et al. (2020), the same photovoltaic nominal power is suggested for a fixed building gross area and it does not depend on the building floors (and as a consequence on the building energy consumption).

Numerical results can change if investment costs or if the price of electricity are different. There are important aesthetic advantages to the selected BIPV panels, but they lead to higher investment costs and lower efficiency compared with standard solutions. This means that the payback time of the investment is also longer.

All the analyzed have proved to be compliant with the nZEB Italian definition, which is the minimum required by law. Nevertheless, actual foreseen energy performances are very different among the scenarios and underline relevant discrepancies in the energy behavior. In particular, Scenario 1 can be called “yearly zero energy balance”, but requires the electric grid to perform the electric energy exchange and is the most expensive in terms of initial investment with the longest payback time. Scenario 2 can be considered a “low grid dependency” nZEB target. In fact, it prioritizes self-sufficiency, which considers the energy produced in situ, which is directly consumed (or stored) without exchange with the grid. This approach presents better economic results if compared with Scenario 1, having lower investment costs and shorter payback time. Decreasing the self-sufficiency target, in Scenario 3, the economic KPIs are improved and the Italian nZEB requisites are still accomplished.

4. Conclusions

Observing the results of the dynamic simulations, which assess the expected energy and economic consequences of renovating a building according to different nZEB approach targets, it is possible to assert that the implementation choice of the nZEB definition has a strong impact. Since the European guidelines are not very well defined in terms of technical requisites and energy performance targets, each EU Country has decision space to set its own technical requirements for the nearly-Zero Energy Building assessment. Because of the elevated number of factors that occur in the energy sector, identifying an optimal nZEB definition is not simple. Nevertheless, the authors consider that the renovation design for a nearly-Zero Energy Building should lead to an energy-efficient building, capable of supplying its own energy demands through the implementation of economically and environmentally sustainable solutions.

The simulation outcomes indicate that prioritizing the energy production/consumption yearly balance, having as the Positive Energy Building target as an objective, could lead to an oversized system in terms of energy generation and, consequently, to an excessive investment cost compared with the economic benefits over time. On the other hand, prioritizing the self-sufficiency of the building energy system could lead to the design of more balanced systems and a significant improvement in the energy and economic KPIs.

The current Italian nZEB target, which has also been examined, seems to be economically sustainable for this specific case-study, but it could lead to not-optimal designs in case of multi-floor buildings.

Prioritizing the self-sufficiency target instead of the yearly ratio production/consumption will become particularly relevant and crucial in the next years, when subsidies such as net billing and net metering will be abolished in many European countries. In this view, the results presented in this article should be considered when the requirements for the PEB and nZEB standards are updated.

The fluctuations of the electricity price and the increase of the cost of raw materials could have an impact on the results. It would be interesting to carry out further research regarding the impact of cost variability on the analysis considerations performed.

This paper is part of the research activities of the INFINITE project, funded by the European Union's Horizon 2020 research and innovation programme under grant agreement No 958397.

References

Ala-Juusela, M., H. u. Rehman, M. Hukkalainen, and F. Reda. 2021. "Positive Energy Building Definition with the Framework, Elements and Challenges of the Concept". *Energies* 14(19): 6260. doi: https://doi.org/10.3390/en14196260

Communication from the Commission to the European parliament, the council, the European economic and social committee and the committee of the regions, "A Renovation Wave for Europe - greening our buildings, creating jobs, improving lives", 2020

D'Agostino, D., S. Tsemekidi Tzeiranaki, P. Zangheri, and P. Bertoldi. 2021. "Assessing Nearly Zero Energy Buildings (NZEBs) development in Europe" *Energy Strategy Reviews* 36: 100680. doi: https://doi.org/10.1016/j.esr.2021.100680

D'Agostino, D., P. Zangheri, and L. Castellazzi. 2017. "Towards Nearly Zero Energy Buildings in Europe: A Focus on Retrofit in Non-Residential Buildings". *Energies* 10(1): 117. doi: https://doi.org/10.3390/en10010117

DIRECTIVE 2010/31/EU - Energy performance of buildings directive. "*Directive 2010/31/EU of the European Parliament and of the Council of 19 May 2010 on the energy performance of buildings*". EU commission. 2010.

D'Oca, S., A. Ferrante, C. Ferrer, R. Pernetti, A. Gralka, R. Sebastian, and P. Op 't Veld. 2018. "Technical, Financial, and Social Barriers and Challenges in Deep Building Renovation: Integration of Lessons Learned from the H2020 Cluster Projects". *Buildings* 8(12): 174. doi: https://doi.org/10.3390/buildings8120174

Energy Matching website. 2022. "Results". Energy Matching. Accessed April 5, 2022. https://www.energymatching.eu/results/?page=2

Good, N., E. A. Martínez Ceseña, P. Mancarella, A. Monti, D. Pesch, and K.A. Ellis. 2017. *Barriers, Challenges, and Recommendations Related to Development of Energy Positive Neighborhoods and Smart Energy Districts. Energy Positive Neighborhoods and Smart Energy Districts: Methods, Tools, and Experiences from the Field.* Elsevier BV. pp. 251-274. doi: https://doi.org/10.1016/B978-0-12-809951-3.00008-9

Holopainen, R., A. Milandru, H. Ahvenniemi and T. Häkkinen. 2016. "Feasibility Studies of Energy Retrofits – Case Studies of Nearly Zero-energy Building Renovation". *Energy Procedia* 96: 146-157. doi: https://doi.org/10.1016/j.egypro.2016.09.116

Lovati, M., M. Dallapiccola, J. Adami, P. Bonato, X. Zhang, and D. Moser. 2020. "Design of a residential photovoltaic system: the impact of the demand profile and the normative framework". *Renewable Energy* 160: 1458-1467. doi: https://doi.org/10.1016/j.renene.2020.07.153

Lovati, M., G. Salvalai, G. Fratus, L. Maturi, R. Albatici, and D. Moser. 2019. "New method for the early design of BIPV with electric storage: A case study in northern Italy". *Sustainable Cities and Society* 48: 101400. doi: https://doi.org/10.1016/j.scs.2018.12.028

McKenna, R., E. Merkel, and W. Fichtner. 2017. "Energy autonomy in residential buildings: A techno-economic model-based analysis of the scale effects". *Applied Energy* 189: 800-815. doi: https://doi.org/10.1016/j.apenergy.2016.03.062

Pernetti, R., R. Pinotti, and R. Lollini. 2021. "Repository of Deep Renovation Packages Based on Industrialized Solutions: Definition and Application". *Sustainability* 13(11): 6412. doi: https://doi.org/10.3390/su13116412

Pinotti, R. 2020. *Timber Prefabricated Multifunctional Facade: Approaches and Methods for a Feasibility Analysis, System Design and Testing*, PhD Thesis, Free University of Bozen-Bolzano, Italy.

Swiss society of engineers and architects. Raumnutzungsdaten für Energie- und Gebäudetechnik. SIA 2024:2015.

TRNSYS Software website. 2022. Thermal Energy System Specialists. Accessed 5 April, 2022. http://www.trnsys.com/index.html

Zangheri, P., R. Armani, M. Pietrobon and L. Pagliano. 2018. "Identification of cost-optimal and NZEB refurbishment levels for representative climates and building typologies across Europe". *Energy Efficiency* 11: 337–369. doi: https://doi.org/10.1007/s12053-017-9566-8

Preliminary CFD Parametric Simulations of Low- and Medium-Density Urban Layouts

Ritesh Wankhade – Free University of Bozen-Bolzano, Italy – riteshnarendra.wankhade@natec.unibz.it
Giovanni Pernigotto – Free University of Bozen-Bolzano, Italy – giovanni.pernigotto@unibz.it
Michele Larcher – Free University of Bozen-Bolzano, Italy – michele.larcher@unibz.it

Abstract

Most existing cities were not designed to exploit wind and air displacement phenomena to ensure pollutant dilution and enhance the effectiveness of natural ventilation of the built environment. Although this problem is well known in the literature, the majority of previous studies focused on real case studies or on parametric layouts often characterized by high-rise buildings, which are not typical for most Italian and European cities. In this framework, the goal of this research was to perform a preliminary CFD parametric study on street canyons with low- and medium-rise buildings, focusing on the different parameters impacting outdoor air displacement in an urban layout. Seven different configurations of street canyon were simulated with ANSYS Fluent, focusing on the air displacement around a low-, medium- or high-rise target building, located at the beginning, at the end, or in the middle of the street canyon, respectively. The velocity and pressure contour plots were analysed to understand the behavior of airflow around the buildings in the different configurations, discussing in such a way the natural ventilation potential.

1. Introduction

Advances in technology and facilities available in urban cities have caused rapid urbanization, leading to the transfer of the population from rural to urban areas in search of new opportunities. The United Nations estimates that, by the year 2030, 60 % of the population will live in urban areas with at least half a million inhabitants (United Nations, 2018). Compared to the current situation, this phenomenon will generate demand for the construction of new homes and buildings. As a result, concerns about urban environmental and human health issues, such as air quality, natural outdoor ventilation, and dilution of pollutants in the built environment will grow (Li et al., 2020). If not properly managed, these urbanization trends will bring increased urban density, with limited spaces among buildings (e.g., parks, parking lots, trees, etc.). This will further reduce air flows coming from surrounding areas, affecting air quality and pollutant dilution (Li et al., 2020; Song et al., 2018).

For this reason, there are many studies that have been conducted on the phenomena of urban ventilation and effectiveness of natural ventilation in cities. In particular, several studies focused on the impact of different urban parameters on natural ventilation, working on generic layouts, real city layouts, or both. Guo et al. (2015) selected a typical urban area in Dalian, China, to perform a comparative and simulative analysis about air displacement due to wind using CFD tools. King et al. (2017) presented a relationship between incident angle and ventilation rate, using an isolated cube and an array of irregular cubes representing generic buildings. Peng et al. (2017) ran CFD simulations of ten identical buildings forming a street canyon to investigate wind-driven natural ventilation and pollutant diffusion at pedestrian level.

When working with building layouts, there are some aspects to consider, such as the space between buildings, the size of buildings, doors and windows, and the width of the streets adjacent to them. These parameters are useful for understanding the relationship between buildings, cities, and natural ventilation potential. Some of the important parameters are, for instance, building height, building density *BD* (Ding & Lam, 2019), floor area ratio *FAR*, building site coverage *BSC*, and street aspect ratio AR_{street} (Yang et al., 2020). Park et al. (2020) and Cheng et al. (2009) investigated the flow characteristics around step-up street canyons and ventilation performance with different aspect ratios using

CFD. Peng et al. (2019) used the floor area ratio and the building site coverage to find the correlation between urban morphological parameters and ventilation performance. By keeping the floor area ratio constant and changing the building site coverage, they established nine idealized building configurations to find the correlation between these urban morphological parameters and ventilation performance. Street canyons and their size can also influence natural ventilation performance. For example, Yang et al. (2020) and Chatzimichailidis et al. (2019) underlined the importance of the street canyon aspect ratio characterizing indoor and outdoor ventilation and flow patterns.

As observed in the literature, CFD simulations have been used to compare and discuss in more detail the results obtained from experiments. For instance, Padilla-Marcos et al. (2017) performed their simulation with Ansys Fluent for a generic building layout, with the aim of studying ways to increase natural ventilation potential in buildings. However, the majority of these studies, and, in particular, those which evaluate natural ventilation in street canyons, primarily focus on high-density or populated cities. As an example, Yuan and Ng (2012) examined the pedestrian-level natural ventilation performance in the context of a regular street grid in the high urban density of Mong Kok in Hong Kong.

Despite the variety of research, most of this has paid particular attention only to high-rise buildings, with limited investigation into low-density cities and low or medium-rise buildings, which are more representative and typical of several countries in the European Union, such as Italy. Therefore, the aim of this study was to perform a preliminary CFD parametric analysis for low or medium-rise buildings, focusing on the different parameters impacting outdoor air displacement in this kind of urban layout, and to discuss if there is a potential for natural ventilation of buildings, considering relative height and position in a street canyon.

2. Methodology

2.1 Generic Urban Buildings Layout

In this work, a generic street canyon layout was chosen. The shape of each building considered is cuboidal with a cross-section equal to 20 m x 20 m. Each floor of the building has a gross height of 4 m, assuming the internal room height of 2.8 m. The height of the high, medium, and low-rise target buildings are 36 m, 24 m, and 12 m, respectively. 10 buildings are positioned in a 5 x 2 rectangular array, where the target building, i.e., the object of the investigation, can be in the front corner, in the middle of the side, or in the rear corner. Different to other studies in the literature (Ding & Lam, 2019; Ramponi et al., 2015), the distances between adjacent buildings along the street canyon are modeled as significantly less than the street's width, i.e., 5 m distance against 20 m of street width. Figs. 1 to 4 show the different configurations of the building arrangements.

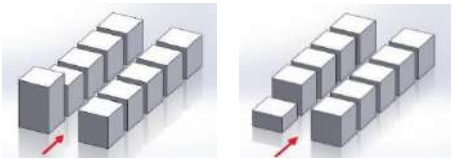

Fig. 1 – High-rise and low-rise building at corner (windward)

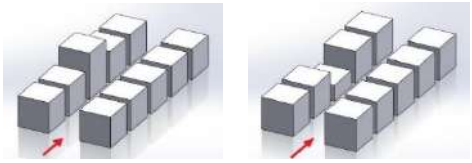

Fig. 2 – High-rise and low-rise building at side

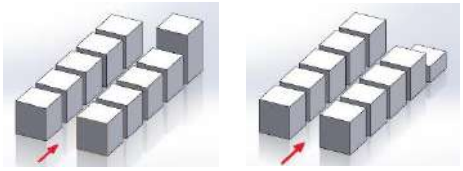

Fig. 3 – High-rise and low-rise building at corner (leeward)

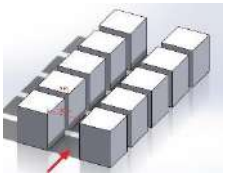

Fig. 4 – Buildings with same height

2.2 CFD Simulation

2.2.1 Computational Domain

The Ansys Fluent 19.0 simulation tool was used to simulate the cases mentioned in Section 2.1. The building geometries were drawn at full scale in Solidworks 2018 and then exported to Ansys Fluent.

The computational domain size was based on previous examples from the literature, such as (Ding & Lam, 2019) and (Park et al., 2020). Following the examples of (Ding and Lam, 2019), the computational domain was set with a downstream length of eight times the building height (*H*) 8*H*, an upstream length of 4*H*, a lateral length of 4*H* on both sides of the buildings, and a height of 4*H*. As a whole, the CFD domain size was set to 1560 m x 1020 m x 300 m (respectively, length, width, and height). The distance between the windward surface of the domain and the first building walls was equal to 450 m; both lateral distances between the surface of the domain and the walls of the building were 480 m; and the distance between the leeward surface of the domain and the wall surface of the rear building was equal to 930 m.

2.2.2 Meshing

Before setting up and running the CFD simulation, it was necessary to create a mesh. Following the literature (King et al., 2017), it was decided to use the hexahedral mesh for the entire domain in order to keep the resolution scheme simple. Fine meshing was applied on the buildings' walls in order to accurately capture the flow around them. The number of elements for the generic building layout cases ranged from 3 to 5.2 million.

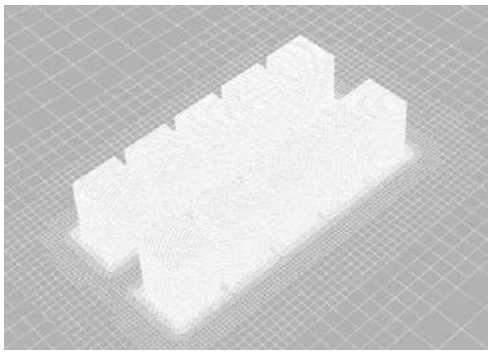

Fig. 5 – Mesh representation of generic building layout

2.2.3 Boundary Conditions and Numerical Setup

Choosing an appropriate boundary condition is an important step in CFD simulations. The windward surface of the domain was considered as the velocity inlet, and the lateral surfaces, the top surface, and the leeward surface of the domain as the pressure outlet. The velocity profile ($u(z)$) of inlet, the turbulent kinetic energy profile (k) and turbulent dissipation rate profile (ε) were calculated in agreement with the following equations (King et al., 2017):

$$u(z)= \frac{u^*}{\kappa}\ln\left(\frac{z+z_0}{z_0}\right) \quad (1)$$

$$k= \frac{u^*}{\sqrt{C_\mu}} \quad (2)$$

and

$$\varepsilon= \frac{u^{*3}}{\kappa(z+z_0)} \quad (3)$$

where u^*, z, z_0 are friction velocity (m/s), height coordinate (m), and roughness length (m), respectively. κ (=0.41) and $C\mu$ (=0.09) are von Karman constant and a model constant, respectively. Referring to the meteorological data of Bolzano (typical year according to the Comitato Termotecnico Italiano), an average wind velocity of 1 m/s was chosen.

Reynolds-averaged Navier-Stokes (*RANS*) and Large Eddy Simulation (*LES*) are the most commonly used turbulence models for urban ventilation assessment. The accuracy of the *LES* turbulence model is higher than the *RANS* turbulence models, but it is also more expensive compared with the computational cost of the *RANS* turbulence models (Peng et al., 2019). *RANS* turbulence models are appropriate because of their simplicity, reasonable ventilation assessment results and less expensive computing power (Padilla-Marcos et al., 2017; Peng et al., 2019). The standard k-ε turbulence model was used. The standard k-ε model is a semi-empirical model based on model transport equations for the turbulence kinetic energy (k) and its dissipation rate (ε). The governing equations that were solved during the simulation in case standard k-ε turbulence model are the following:

$$\frac{\partial}{\partial t}(\rho k)+\frac{\partial}{\partial x_i}(\rho k u_i)=\frac{\partial}{\partial x_j}\left[\left(\mu+\frac{\mu_t}{\sigma_k}\right)\frac{\partial k}{\partial x_j}\right]+G_k-\rho\epsilon-Y_M \quad (4)$$

$$\frac{\partial}{\partial t}(\rho \epsilon)+\frac{\partial}{\partial x_i}(\rho \epsilon u_i)=\frac{\partial}{\partial x_j}\left[\left(\mu+\frac{\mu_t}{\sigma_\epsilon}\right)\frac{\partial \epsilon}{\partial x_j}\right]+C_{1\epsilon}\frac{\epsilon}{k}G_k-C_{2\epsilon}\rho\frac{\epsilon^2}{k} \quad (5)$$

$$\mu_t=\rho C_\mu \frac{k^2}{\epsilon} \quad (6)$$

In these equations, G_k represents the generation of turbulence kinetic energy due to the mean velocity gradients. Y_M represents the contribution of the fluctuating dilatation in compressible turbulence to the overall dissipation rate. $C_{1\varepsilon}$ (=1.44), $C_{2\varepsilon}$ (=1.92) and μ_t (=0.09) are constants. σ_k (=1.0) and σ_ε (=1.3) are the turbulent Prandtl numbers for k and ε, respectively.

The pressure-velocity coupling used was SIMPLE, with final second order spatial discretization methods for pressure, momentum, turbulent kinetic energy (k), and turbulent dissipation rate (ε). The convergence criteria were set to 1 x 10^{-6} for all the residuals.

The simulation was initialized with the first order spatial discretization parameters and default under-relaxation factors (*URFs*) until the residuals' stabilization. Once the residual stability was achieved, the spatial discretization parameters were changed to second order upwind and the *URFs* to 0.15 for pressure and 0.4 for density, body forces, momentum, turbulent kinetic energy (k), turbulent dissipation rate (ε) and turbulent viscosity (μ_t).

3. Results and Discussions

The simulation results are presented as a function of geometry and position of the buildings, distinguishing cases with the same height, low and high-rise building cases (at side, corner windward, and corner leeward).

Due to the different shapes and sizes of the buildings, there was a variation in the magnitudes of the different parameters under consideration. There was also a change in flow direction at various points due to buildings, which caused a change in magnitude. The variations in the parameters' magnitudes help in understanding the feasibility of airflow and natural ventilation around buildings and street canyons. As specified in Section 2.1, the height of each floor of the building was 4 m. The reference plane for the analysis was set at 1.5 m above the ground of each floor. The airflow velocities and the corresponding static pressures at different locations in the reference planes can be viewed in the contour plots.

3.1 Contour Plot Presentation of the Cases

Fig. 6 shows the static pressure contour developed around the buildings due to airflow. The change in pressure gradient can be noticed from the first buildings (left in the figure) to the last buildings (right in the figure). As the first buildings are directly facing the incoming airflow, there is a maximum pressure on the walls facing the airflow and then it gradually decreases.

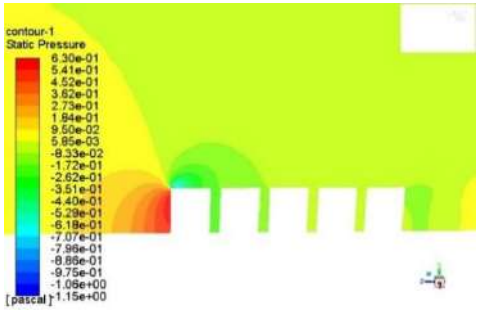

Fig. 6 – Static pressure contour for buildings with same height

Fig. 7 presents the contour plot of velocity around the reference plane on the side. The street aspect ratio (AR_{street}) for the case of buildings with the same height is 1.2 and the aspect ratio ($AR_{building\ gap}$), considering the gap between the buildings, is 4.8, which greatly affects the airflow behavior and natural ventilation around the buildings.

$$AR_{street} = \frac{H_{target\ building}}{Street\ width} \quad (7)$$

$$AR_{building\ gap} = \frac{H_{target\ building}}{Gap\ between\ buildings} \quad (8)$$

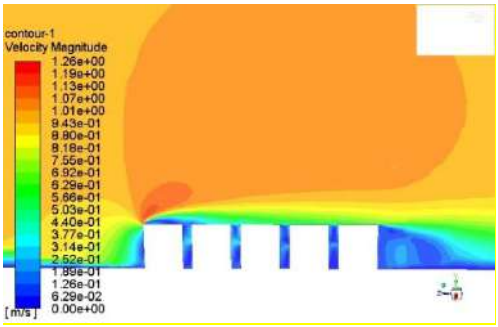

Fig. 7 – Velocity contour for buildings with same height

As mentioned in the literature, there are three main flow regimes: isolated roughness flow regime (*IRF*, $AR < 0.1$-0.125), wake interference flow regime (*WIF*, $0.1 < AR < 0.67$) and skimming flow regime with one main vortex (*SF*, $0.67 < AR < 1.67$) (Yang, et al., 2020).

However, in the configuration with buildings with same height, the $AR_{building\ gap}$ is 4.8, i.e., much higher than the skimming flow regime case. Indeed, two vortexes with low intensity can be observed in the gaps between the buildings (Figure 8).

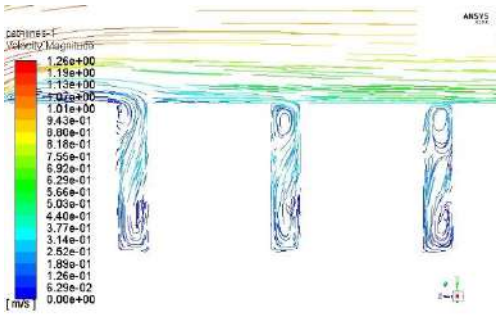

Fig. 8 – Velocity path lines for buildings with same height (side view)

The cases of high-rise and low-rise buildings represent the step-up and step-down canyon cases (Li et al., 2020; Park et al., 2020). The $AR_{building\ gap}$ for high-rise and low-rise buildings is 7.2 and 2.4, respectively. Depending on the location of the high-rise and low-rise buildings, step-up and step-down canyons were decided.

The pressure contours for different cases of high-rise and low-rise buildings indicate that there is a similar trend in the pressure distribution for different buildings configurations, as mentioned at the beginning of this section. This can be seen from Figures 9 to 14 for the high-rise building cases.

Figs. 15 to 20 represent velocity contour plots for low and high-rise building cases. Great variation in the velocity magnitude can be seen near building walls and around buildings, as illustrated by the velocity contour plots illustrate. In addition, as previously mentioned, there is an occurrence of vortexes in the gap between buildings which assist airflow around buildings. Flow has been diverted due to buildings being obstacles and there is a recirculation of the airflow at the top of the buildings. This also an essential condition to have an airflow around buildings and, in turn, suitable for natural ventilation around and inside the buildings.

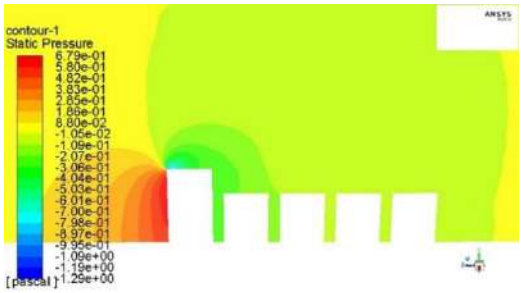

Fig. 9 – Pressure contour plot for high-rise building at windward position

Fig. 10 – Pressure contour plot for high-rise building at center-side position

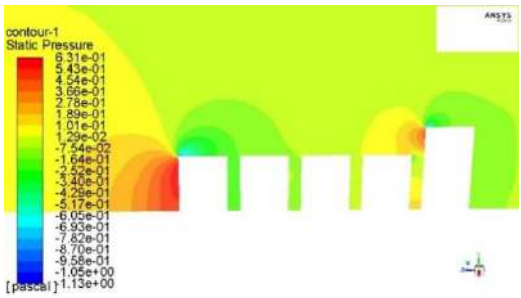

Fig. 11 – Pressure contour plot for high-rise building at leeward position

Fig. 12 – Pressure contour plot for low-rise building at windward position

Fig. 13 – Pressure contour plot for low-rise building at center-side position

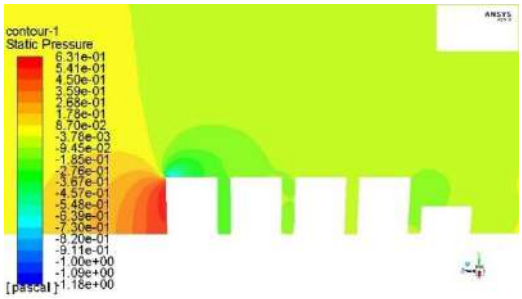

Fig. 14 – Pressure contour plot for low-rise building at leeward position

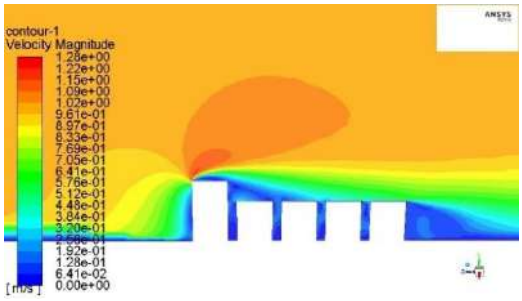

Fig. 15 – Velocity contour plot for high-rise building at windward position

Fig. 16 – Velocity contour plot for high-rise building at center-side position

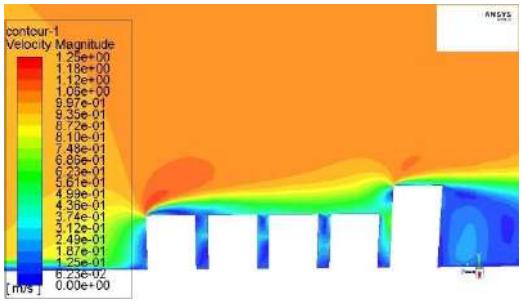

Fig. 17 – Velocity contour plot for high-rise building at leeward position

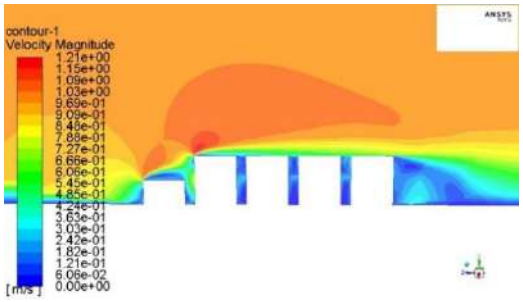

Fig. 18 – Velocity contour plot for low-rise building at windward position

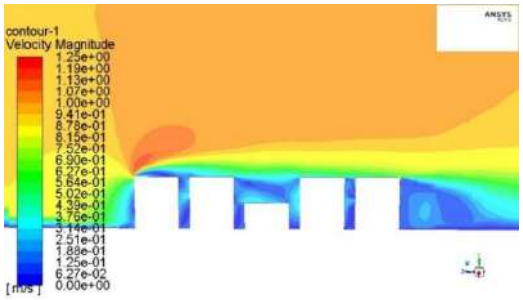

Fig. 19 – Velocity contour plot for low-rise building at center-side position

Fig. 20 – Velocity contour plot for low-rise building at leeward position

3.2 Graphical Representation of the Cases

The graphs in Figs. 21 to 24 illustrate the velocity and pressure plots determined at different heights at a distance of 1 m from the walls of the building facing the street. The vertical distance represented in the graphs is a normalized vertical distance, calculated as the ratio of the vertical distance of the point measured from the ground ($Y_{position}$) to the height of the target building (H). Similar criteria are set for the normalized velocity, which is the ratio of the velocity at the corresponding point (V_{mag}) to the reference velocity (V_{ref}) of 1 m/s.

It can be observed from Figs. 21 and 22 that the graphs for the high-rise buildings ($AR_{street,high\text{-}rise,1}$ = 1.8, $AR_{street,high\text{-}rise,2}$ = 1.2) in the center and leeward positions have a similar trend, while that is not true in case of the building in the windward position,

characterized by higher airflow velocities and pressures. This suggests higher potential of exploitation of natural solutions for the ventilation of the indoor environments of that building.

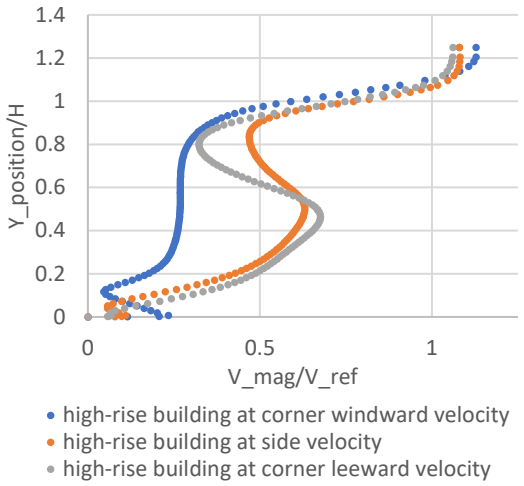

Fig. 21 – Velocity plot for high-rise buildings (1m from the wall facing the street)

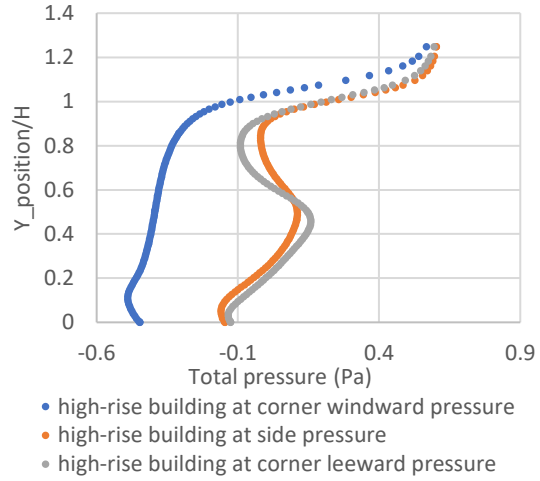

Fig. 22 – Total pressure plot for high-rise buildings (1m from the wall facing the street)

In the case of low-rise buildings ($AR_{street,low\text{-}rise,1}$ = 0.6, $AR_{street,low\text{-}rise,2}$ = 1.2) (Fig. 23 and 24), similar trends can be observed, with an increase in velocity and pressure magnitudes along the vertical distance of the target building. Low-rise windward buildings do not follow the same path as the other two low-rise building cases.

In the windward cases of both high- and low-rise buildings, the first buildings experience the decrease in velocity and pressure at ground floor level. This occurs because these buildings are directly facing the wind flow, which causes air recirculation (as it can be noticed from Figs. 15 to 20), resulting in the decreased velocity and pressure.

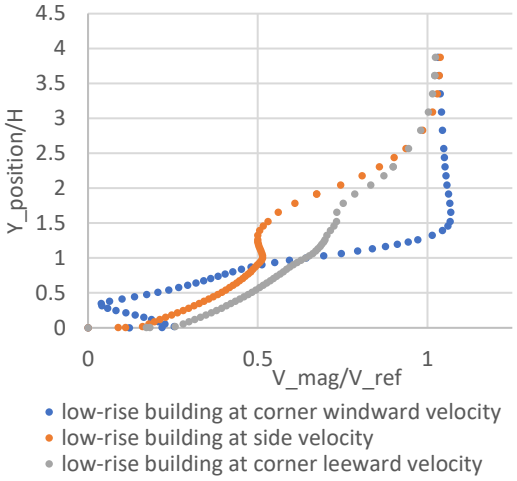

Fig. 23 – Velocity plot for low-rise buildings (1m from the wall facing the street)

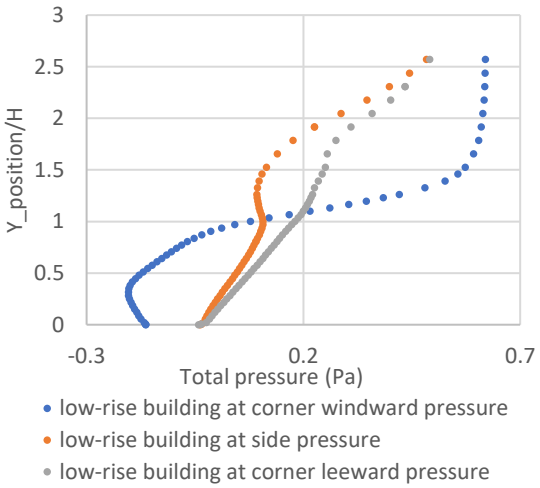

Fig. 24 – Total pressure plot for low-rise buildings (1m from the wall facing the street)

4. Conclusion

This work is a preliminary parametric CFD study about the behavior of airflow around the buildings in different configurations. The analysis focused on the generic building layout of street canyons, considering same-height buildings and different types of target building (high-rise, low-rise). Seven configurations were evaluated, each time focusing on the air displacement around a target building, located respectively at the beginning, at the end, or in the middle of the street canyon, and a case of same height building layout. Pressure and velocity variations were analyzed at different floors of the building façade, also with the help of CFD contour plots.

We observed that, considering the higher aspect ratio of the gaps between buildings in comparison with that of the street canyon, vortices can be easily generated, inducing a recirculation that could facilitate the exploitation of natural ventilation solutions at the different floors of the target building.

From the contour and graphic results, it can also be stated that specific building configurations and building positions (e.g., high-rise and low-rise building at the center and the leeward position in the street canyon) show higher potential for exploiting natural solutions for the ventilation of the indoor environments. On the contrary, the buildings in a windward position show a poorer performance.

Further developments of this preliminary research will address validation and generalization of the findings. First, the obtained results will be verified and validated against small-scale experimental tests. Then, multiple configurations of street canyons will be simulated, with the goal of developing a set of rules and simplified correlations useful to engineers, architects, and urban planners to discuss natural ventilation potential from the early stages of new building design or retrofitting of the existing ones.

References

Chatzimichailidis, A. E., C. D. Argyropoulos, M. J. Assael, and K. E. Kakosimos. 2019. "Implicit Definition of Flow Patterns in Street Canyons—Recirculation Zone—Using Exploratory Quantitative and Qualitative Methods." *Atmosphere* 10(12): 794. doi: https://doi.org/10.3390/atmos10120794

Cheng, W. C., C.-H. Liu, and D. Y. C. Leung. 2009. "On the comparison of the ventilation performance of street canyons of different aspect ratios and Richardson number." *Building Simulation* 2 (1): 53-61. doi: https://doi.org/10.1007/S12273-008-8332-4

CTI. 2016. Comitato Termotecnico Italiano Energia e Ambiente. www.cti2000.it

Ding, C., and K. P. Lam. 2019. "Data-driven model for cross ventilation potential in high-density cities based on coupled CFD simulation and machine learning." *Building and Environment* 165: 106394. doi: https://doi.org/10.1016/j.buildenv.2019.106394

Guo, F., Y. Fan, and H. Zhang. 2015. "Natural Ventilation Performance in a High Density Urban Area Based on CFD Numerical Simulations in Dalian." In *Proceedings of ICUC9 - 9th International Conference on Urban Climate jointly with 12th Symposium on the Urban Environment*.

King, M.-F., H. L. Gough, C. Halios, J. F. Barlow, A. Robertson, R. Hoxey, and C. J. Noakes. 2017. "Investigating the influence of neighbouring structures on natural ventilation potential of a full-scale cubical building using time-dependent CFD." *Journal of Wind Engineering and Industrial Aerodynamics* 169: 265-279. doi: https://doi.org/10.1016/j.jweia.2017.07.020

Li, Z., T. Shi, Y. Wu, H. Zhang, Y.-H. Juan, T. Ming, and N. Zhou. 2020. "Effect of traffic tidal flow on pollutant dispersion in various street canyons and corresponding mitigation strategies." *Energy and Built Environment* 1(3): 242-253. doi: https://doi.org/10.1016/j.enbenv.2020.02.002

Padilla-Marcos, M. Á., A. Meiss, and J. Feijó-Muñoz. 2017. "Proposal for a simplified CFD procedure for obtaining patterns of the age of air in outdoor spaces for the natural ventilation of buildings." *Energies* 10(9): 1252. doi: https://doi.org/10.3390/en10091252

Park, S.-J., J.-J. Kim, W. Choi, E.-R. Kim, C.-K. Song, and E. R. Pardyjak. 2020. "Flow Characteristics Around Step Up Street Canyons with Various Building Aspect Ratios." *Boundary-Layer Meteorology* 174(3): 411-431. doi: https://doi.org/10.1007/s10546-019-00494-9

Peng, Y., X. Ma, F. Zhao, C. Liu, and S. Mei. 2017. "Wind driven natural ventilation and pollutant dispersion in the dense street canyons: Wind Opening Percentage and its effects." *Procedia Engineering* 205: 415-422. doi: https://doi.org/10.1016/j.proeng.2017.10.392

Peng, Y., Z. Gao, R. Buccolieri, and W. Ding. 2019. "An Investigation of the Quantitative Correlation between Urban Morphology Parameters and Outdoor Ventilation Efficiency Indices." *Atmosphere* 10(1): 33. doi: https://doi.org/10.3390/atmos10010033

Ramponi, R., B. Blocken, L. B. de Coo, and W. D. Janssen. 2015. "CFD simulation of outdoor

ventilation of generic urban configurations with different urban densities and equal and unequal street widths." *Building and Environment* 92: 152-166. doi: https://doi.org/10.1016/j.buildenv.2015.04.018

Song, J., S. Fan, W. Lin, L. Mottet, H. Woodward, Davies M. Wykes, R. Arcucci, et al. 2018. "Natural ventilation in cities: the implications of fluid mechanics." *Building Research and Information* 46(8): 809-828. doi: https://doi.org/10.1080/09613218.2018.1468158

United Nations. 2018. "The World's Cities in 2018." https://www.un.org/en/events/citiesday/assets/pdf/the_worlds_cities_in_2018_data_booklet.pdf

Yang, X., Y. Zhang, J. Hang, Y. Lin, M. Mattsson, M. Sandberg, M. Zhang, and K. Wang. 2020. "Integrated assessment of indoor and outdoor ventilation in street canyons with naturally-ventilated buildings by various ventilation indexes." *Building and Environment* 169: 106528. doi: https://doi.org/10.1016/j.buildenv.2019.106528

Yuan, C., and E. Ng. 2012. "Building porosity for better urban ventilation in high-density cities - A computational parametric study." *Building and Environment* 50: 176-189. doi: https://doi.org/10.1016/j.buildenv.2011.10.023

Smart Sensors and Auditory Sensitivity: Acoustic Optimization of Dedicated Spaces for Autistic Individuals

Federica Bettarello – University of Trieste, Italy – fbettarello@units.it
Marco Caniato – Free University of Bozen-Bolzano, Italy – marco.caniato@unibz.it
Arianna Marzi – Free University of Bozen-Bolzano, Italy – arianna.marzi@natec.unibz.it
Giuseppina Scavuzzo – University of Trieste, Italy – gscavuzzo@units.it
Andrea Gasparella – Free University of Bozen-Bolzano, Italy – andrea.gasparella@unibz.it

Abstract

This work deals with the design of an indoor environment dedicated to autistic individuals, who may suffer from hypersensitivity to acoustic stimuli. Specifically, in this volume customized pieces of furniture are included, containing smart sensors, designed to help people with cognitive deficits to live an independent life. Among the indoor comfort aspects, the acoustic requirements have been investigated, in order to guarantee both the optimal functioning of the acoustic sensors and the acoustic occupants' well-being. The optimal indoor acoustic levels are based on a literature review. Measurements are performed in order to calibrate a 3D acoustic model. Then diverse scenarios are analysed, and an optimized configuration is proposed and realized. The model is then validated with the final acoustic measurements, which confirm the designed results.

1. Introduction

Many autistic individuals show particular sensitivity to noise disturbance, both indoors and outdoors, often to a greater extent than neurotypical people, thus exhibiting acoustic hypersensitivity (American Psychiatric Association, 2013).

In a recent study conducted in Canada involving 168 families with an autistic child (3-16 years old) 87 % of the respondents reported that their children were very sensitive to noise (Nagib & Williams, 2018). Specific studies carried out on school environments (Tronchin et al., 2018) with autistic children have shown that the application of interventions aimed at reducing noise coming from outside the classroom (from corridors, or neighboring classrooms), have permitted them to reduce behavioral temperaments (self-stimulatory behavior), such as obsessive behavior, specific for each child, including head-banging, biting their hands and rocking (Kanakri et al., 2017). These results are also confirmed by the first analysis of the SENSHome Interreg Project research, which features an investigation of Italian and Austrian families. In this case too, acoustics were found to be the greatest source of stress for autistic people and their relatives and caregivers. Many papers, institutional programs, manuals and documents related to acoustic individuals explained that acoustics are of paramount importance when designing dedicated spaces (Ahrentzen & Steele, 2015; Braddock & Rowell, 2011; Mostafa, 2014).

For all these reasons, during the construction and setting up of an environment dedicated to a full-scale reproduction of living environments for autistic people and their families, the acoustic aspect was analysed beforehand and verified on site. Specifically, the SENSHome environment is located inside the Building Physics Laboratory at the Free University of Bolzano. It hosts the furniture specifically designed for autistic people by the University of Trieste and integrated with the smart sensors system that make up the early warning system, specifically developed for the SENSHome project.

2. Setting Up The SENSHome Laboratory

As formerly pointed out, the determination of acoustic quality parameters is of paramount im-

portance (Tronchin, 2021). The reverberation time R_T, clarity C_{50} and definition D_{50} for environments dedicated to autistic people are the most commonly used parameters to qualify an indoor environment both for indoor comfort and for the use of microphone sensors (Griesinger, 2013; Marshall, 1994; Tsilfidis, 2013). These factors were then considered as reference for the acoustic optimisation of this environment.

Fig. 1 – Starting conditions of the building physics laboratory at UNIBZ

The interior design included a frame structure of vertical wooden panels and some fake windows covered with a white acoustic-transparent membrane (Fig. 2). Featuring this configuration, the space included three areas: an entrance, a kitchen and a living room (quiet space). Each area is then filled with furniture specifically designed for the project (Fig. 3).

Fig. 2 – Interior covering provided in the laboratory for the preparation of the SENSHome scenario. Vertical wooden panels

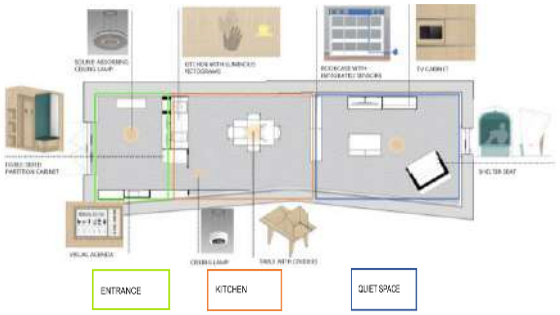

Fig. 3 – Layout of the internal distribution of spaces and location of various pieces of furniture

From an acoustic point of view, it was possible to act directly at the design phase, considering the issues related to indoor acoustic comfort described. Going into detail, many elements of the designed furniture were implemented with sound- absorbing materials (Fabbri et al., 2021) or systems. In particular, the coverings of the entrance furniture (Fig. 4a) and the quiet place armchair (refuge space, Fig. 4b) were produced using soft, sound-absorbing materials, (specifically a polyurethane foam), featuring a thickness of 5 cm.

Interestingly, inside the refuge space, both the high performance of the sound-absorbing interior coating and the huge presence of exposed surface area permitted a very special acoustic field for those sitting inside. This was highly appreciated by the autistic individuals, who liked this special feature of the refuge space, lying inside it many times and for significant time spans.

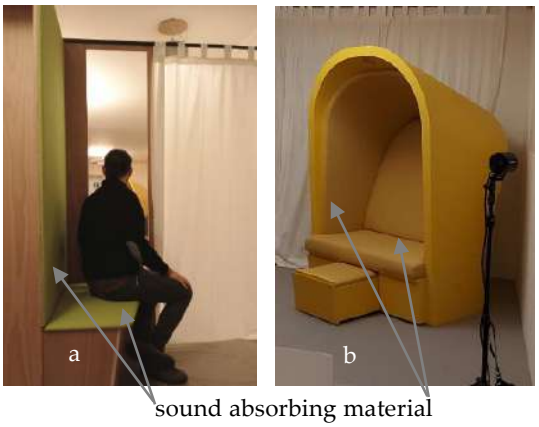

Fig. 4 – a) entrance furniture with sound-absorbing coating; b) dedicated armchair (refuge space) with sound absorbing coating

Another piece of furniture which included sound-absorbing characteristics is the kitchen table. It is equipped with special panels, which could be used to separate every single person sitting around it. Indeed, some autistic individuals cannot stand someone else's food or smell. For this reason, the panels include active carbon layers and sound-absorbing elements. This provides a customized local environment where an individual can experience her/his own personal requirements, but still maintain a social breakfast/lunch/dinner. In Fig. 5, the panels are shown. It is possible to detect the perforated internal surface, where both odors and noise could enter and be absorbed.

Moving onto the suspended ceiling lamps, 4 elements were included. Specifically, a round-shaped wood panel was used and filled with microphone sensors, LED strips and sound-absorbing polyurethane foam, 7 cm thick. The lamps are 65 cm in diameter and suspended where the highest noise levels are supposed to be. Accordingly, one was suspended over the lunch table (Fig. 5), another one over the sofa where the television is seen, a third one in the entrance were people gather before entering and the last one over the kitchen space.

Fig. 5 – Detail of the kitchen table with sound-absorbing dividers and ceiling lamps with sound-absorbing coating

In addition, between the wooden frame of the casing and the cladding, a hollow space is left to be filled with sound-absorbing panels, usable to reduce internal reverberation (Fig. 6).

Fig. 6 – Detail of the suspended sound-absorbing panels layered between the wooden structure and beyond the acoustic-transparent membrane

The sound-absorbing foam used to cover furniture complements and the sound-absorbing panels on the wall are characterized by the frequency sound absorption coefficients reported in Figs. 7 and 8. It is possible to notice how the two selected layers are characterized by a very good acoustic performance.

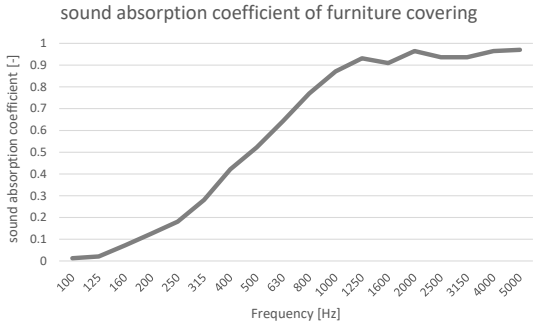

Fig. 7 - Sound absorption coefficient frequency trend of the cover furniture

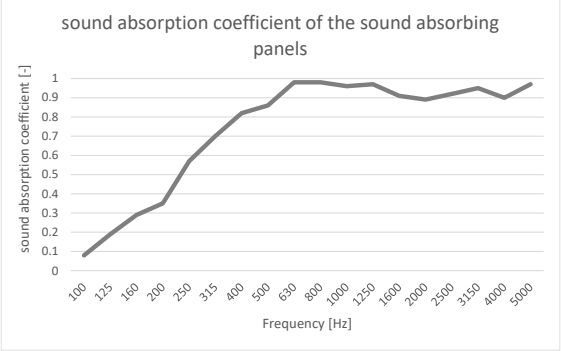

Fig. 8 - Sound absorption coefficient frequency trend of the internal panels

The main aim of the acoustic analysis was to obtain an indoor average reverberation value of between 0.5 and 0.7 s (Griesinger, 2013; Marshall, 1994; Tsilfidis, 2013). These values represent the right compromise for the achievement of optimal conditions both for the use of the environment by autistic people and for the use of the microphone sensors.

3. Acoustic Analysis of Various Scenarios

Since it is acknowledged that acoustic models should be calibrated using reverberation time (Karjalainen & Järveläinen, 2001; Suárez et al., 2005, Tronchin, 2005), only this parameter was considered in the following dissertation.

The general criteria of the ISO 3382-1 were considered when performing acoustic measurements. The microphone height was 1.6 m, while the source height was 1.9 m in all cases (Tronchin et al., 2021). The measurement was set by placing the source in 2 different positions and the 8 receivers all along the void space (Tronchin & Bevilacqua, 2022). The source played a sinusoidal sine sweep having a frequency of between 50 Hz and 12000 Hz and a duration of 20 seconds (Tronchin & Knight, 2016). Measurements were performed in an unoccupied configuration.

The average reverberation time of the laboratory in the empty condition was measured and was 3.5 s. The average was computed considering the range 500 Hz – 1000 Hz – 2000 Hz. Since the aim is to obtain an average reverberation time on the same frequency range of 0.5-0.7 seconds (Griesinger, 2013; Marshall, 1994; Tsilfidis, 2013), some actions should be considered.

Therefore, the correct amount of sound-absorbing panels had to be calculated in order to achieve the target reverberation values. For the acoustic optimisation of the laboratory environment, it was necessary to provide a quantity of sound-absorbing materials of approx. 45 m² (i.e., an amount equal to 22.5 % of the total reflective surface of the room). Figs. 8-10 show the virtual models of the three configurations of the laboratory analyzed: i) empty, ii) with furniture and iii) with furniture and sound-absorbing panels.

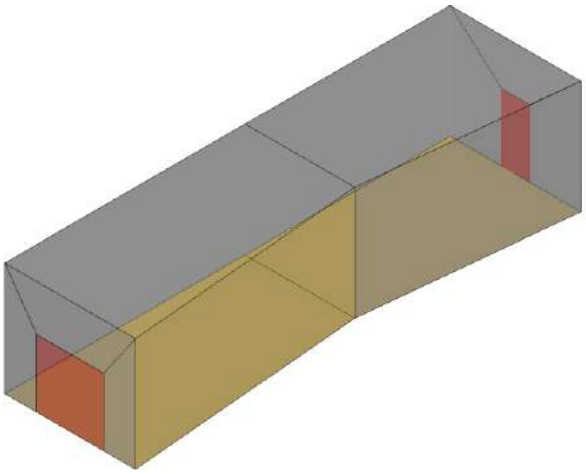

Fig. 8 – Virtual model of the laboratory: configuration i) empty

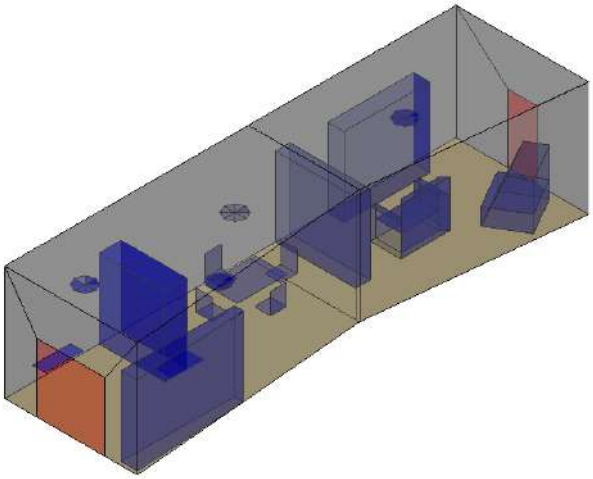

Fig. 9 – Virtual model of the laboratory: configuration ii) with furniture

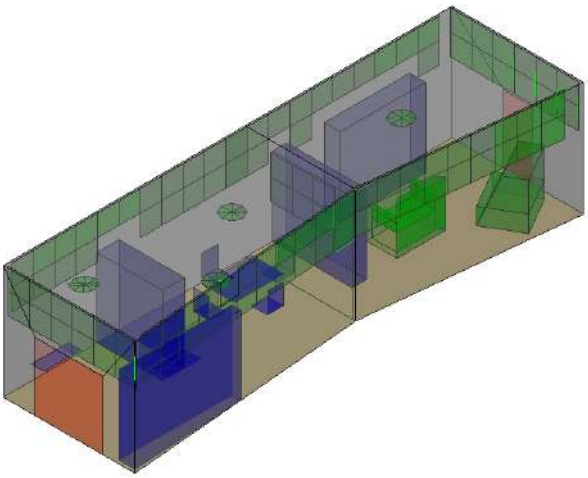

Fig. 10 – Virtual model of the laboratory: configuration iii) with furniture and sound-absorbing panels

In Table 1, we can see that, for the empty scenario, the simulation provides good results compared to the measured ones. In Fig. 11, the indoor sound field simulated at 1000 Hz is represented. It is interesting to notice how its distribution it is almost symmetrical. Since the calibration is positive, it is possible to proceed with the other two scenarios reported in Figs. 9 and 10.

Table 1 − Calculated averaged reverberation time for different scenarios

Lab configuration	Scenario (i)	Scenario (ii)	Scenario (iii)
Average reverberation time [s]	3.49	1.49	0.61

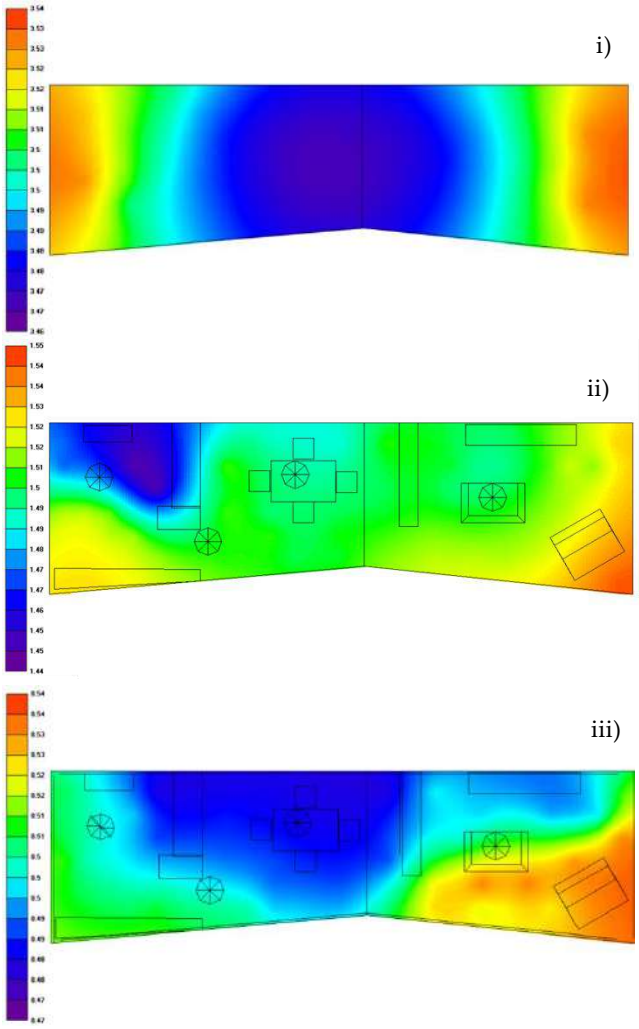

Fig. 11 − spatial reverberation time distribution for different scenarios: i) empty room, ii) furnished room and iii) furnished room with sound absorbing panels. Frequency plot: 1000 Hz

In Table 1, the average reverberation time values are reported, while in Figs. 12 and 13 the average reverberation time values at 1000 Hz are reported, for the analysed configurations.

4. Model Validation

The validation of the 3D model was developed when the SENSHome laboratory (scenario iii) had been set up (Fig. 12).

Fig. 12 − Two views of the SENSHome environment

The results obtained in terms of reverberation time agree strongly with the simulated ones. Indeed, the measured average reverberation time value is 0.63 seconds. Fig. 13 shows the frequency trend of measured results.

These values permit the next phase of the SENSHome laboratory to proceed, which concerns testing of the operation of the microphone sensors and the validation of the SENSHome scenario by hosting autistic individuals and their families and

caregivers within it. This will permit an understanding of the effectiveness of the indoor sound field designed.

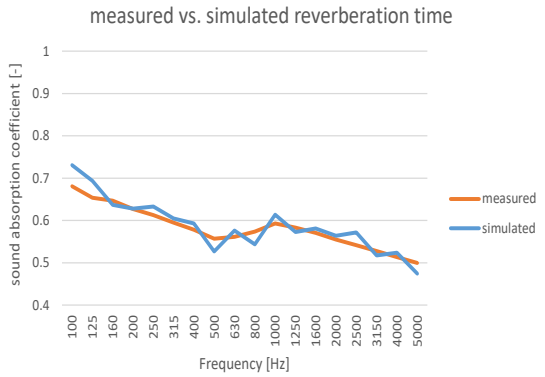

Fig. 13 − Reverberation time frequency trend of furnished room with sound-absorbing panels: in situ measurements

5. Conclusion

Acoustics are an indoor comfort aspect of paramount importance, especially for autistic people featuring auditory hypersensitivity. Taking care of the sound field of indoor environments could mean creating hospitable and non-discouraging living conditions. Using a robust procedure to design the SENSHome environment by means of measurements, 3D acoustic simulation and final validation also permitted the reverberation time of different scenarios to be optimised. This was also aimed at creating the best operating conditions for the microphone sensors that are part of the smart system included in the SENSHome environment. The acoustic properties of the sound-absorbing coverings were investigated. This led to the calculation of the surface area of the sound-absorbing panels to be used. The final measurements performed in the SENSHome environment built permitted an assessment of the effectiveness of the design developed. Future developments include validation of the microphone sensor operation conditions and of the internal acoustic quality perceived by autistic individuals, their relatives and caregivers.

Acknowledgement

This study was supported by the Interreg Italy-Austria project "SENSHome" ITAT 1088 CUP: I54I18000310006.

References

Ahrentzen, S., and K. Steele. 2015. *At Home with Autism. Designing Housing for the spectrum.* Bristol University Press.

Braddock, G., and J. Rowell. 2011. *Making Homes that Work: A Resource Guide for Families Living with Autism Spectrum Disorder and Co-occurring Behaviors* (p. 81). Creative Housing Solutions, Rowell Brokaw Architects.

Fabbri, K., L. Tronchin, and F. Barbieri. 2021. "Coconut fibre insulators: The hygrothermal behaviour in the case of green roofs". *Construction and building materials* 266: 1-9. doi: 10.1016/j.conbuildmat.2020.121026

Griesinger, D. 2013. "Physiologically based measures for clarity and engagement." *International Symposium on Room Acoustics*.

ISO. 2009. ISO 3382-1: 2009 Acoustics — Measurement of room acoustic parameters — Part 1: Performance spaces.

Kanakri, S. M., M. Shepley, J. W. Varni, and L. G. Tassinary. 2017. "Noise and autism spectrum disorder in children: An exploratory survey." *Research in Developmental Disabilities* 63: 85–94. doi: https://doi.org/10.1016/j.ridd.2017.02.004

Karjalainen, M, and H. Järveläinen. 2001. "More about this reverberation science: Perceptually good late reverberance." *The 111th Convention of the Audio Engineering Society*.

Marshall, L. G. 1994. "An acoustics measurement program for evaluating auditoriums based on the early/late sound energy ratio." *The Journal of the Acoustical Society of America* 96: 2251- 2261.

Mostafa, M. 2014. "Architecture for Autism: Autism ASPECTSS™ in School Design." *International Journal of Architectural Research* 8(1)

Nagib, W., and A. Williams. 2018. "Creating therapeutic landscapes at home: The experiences of families of children with autism." *Health and Place* 52: 46-54. doi:

https://doi.org/10.1016/j.healthplace.2018.05.001

Suárez, R., J. J. Sendra, J. Navarro, and A. L. León. 2005. "The sound of the cathedral-mosque of Córdoba." *Journal of Cultural Heritage* 6: 307–12. doi: https://doi.org/10.1016/j.culher.2005.03.005

Tronchin, L. 2005. "Modal analysis and intensity of acoustic radiation of the kettledrum". *The journal of the acoustical society of America* 117(2): 926-933: doi: https://doi.org/10.1121/1.1828552

Tronchin, L. 2021. "Variability of room acoustic parameters with thermo-hygrometric conditions". *Applied acoustics* 177: 1-14. doi: https://doi.org/10.1016/j.apacoust.2021.107933

Tronchin, L., and A. Bevilacqua. 2022. "Historically informed digital reconstruction of the Roman theatre of Verona. Unveiling the acoustics of the original shape". A*pplied acoustics* 185: 1-18. doi: https://doi.org/10.1016/j.apacoust.2021.108409

Tronchin, L., and D. J. Knight. 2016. "Revisiting Historic Buildings through the Senses. Visualising Aural and Obscured Aspects of San Vitale, Ravenna". *International journal of historical archaeology* 20: 127-145. doi: https://doi.org/10.1007/s10761-015-0325-2

Tronchin, L., K. Fabbri, and C. Bertolli. 2018. "Controlled Mechanical Ventilation in Buildings: A Comparison between Energy Use and Primary Energy among Twenty Different Devices". *Energies* 11: 1-20. doi: https://doi.org/10.3390/en11082123

Tronchin, L., F. Merli, and M. Dolci. 2021. „Virtual acoustic reconstruction of the Miners' Theatre in Idrija (Slovenia)". *Applied acoustics* 172: 1-9. doi: https://doi.org/10.1016/j.apacoust.2020.107595

Tsilfidis, A., I. Mporas, J. Mourjopoulos, and N. Fakotakis. 2013. "Automatic speech recognition performance in different room acoustic environments with and without dereverberation preprocessing." *Computer Speech & Language* 27(1): 380-395. doi: https://doi.org/10.1016/j.csl.2012.07.004

Simulation Application for the Assessment of the Energy Performance of a Building Renovated Using I-BEST System (Innovative Building Envelope through Smart Technology)

Cristina Carpino – University of Calabria, Italy – cristina.carpino@unical.it
Mario Maiolo – University of Calabria, Italy –mario.maiolo@unical.it
Patrizia Piro – University of Calabria, Italy – patrizia.piro@unical.it
Roberto Bruno – University of Calabria, Italy – roberto.bruno@unical.it
Natale Arcuri – University of Calabria, Italy – natale.arcuri@unical.it

Abstract

Energy renovation of existing buildings represents a fundamental action for achieving the objectives aimed at overcoming the climate crisis. However, several difficulties are encountered in building refurbishment. Among these are the high costs and long construction times, the invasiveness of interventions, which often prevent the usability of the building, and the impossibility of providing maintenance and verifying degradation of the underlying layers of the envelope. Regarding the systems, retrofit often causes substantial alterations to the building aesthetics, affecting its original character and defacing the surrounding environment. Furthermore, the integration of renewable sources is often hard to implement. The I-BEST system (Innovative Building Envelope through Smart Technology) is an innovative multifunction façade system for the redevelopment of the existing building stock, which aims to overcome these limits by offering a valid response to the growing demand for building "recladding". The system consists of sliding, modular and multi-functional panels, supported by a metal and light load-bearing structure fixed on the external wall and spaced from it to create a suitable cavity for containing plant ducts. The purpose of the present work is to evaluate, through dynamic simulation, the energy performance of a building renovated with the I-BEST system.

1. Introduction

Based on the Green Deal objectives, the European Union (EU) will have to achieve zero climate impact by 2050 (EU Commission). In the energy transition, a significant role is played by decarbonisation of the building stock, which accounts for 36 % of EU CO_2 emissions (United Nations Environment Programme, 2021). The European Commission has outlined a long-term restructuring strategy, using primarily the principle of energy efficiency, as well as evaluating the use of renewable energy. Consistently, each Member State has developed an Integrated National Plan for Energy and Climate to support the renovation of existing residential and non-residential buildings, both public and private, into nearly zero energy buildings, promoting cost-effective strategies. The renovation of buildings, which should take place at an average rate of 3 % per year, will make it possible to progressively increase the EU's energy independence, considering that each percentage point of increase in energy savings corresponds to a reduction in gas imports of 2.6 % (Directive (EU) 2018/844). In addition to energy inefficiency, existing buildings frequently show physical and formal degradation, which significantly alters the quality of the urban environment. Renovation actions often entail a series of problems that make it difficult to implement restructuring plans. The most common problems include: high costs and long construction times; the invasiveness of the interventions that usually require occupancy and work activities to be suspended; in the case of the application of external thermal insulation, the impossibility of periodic maintenance of the underlying elements and the inability to identify any cracks caused by earthquakes; the difficulty of integrating systems for the

production of energy from renewable sources; in the hypothesis of replacing the heating and cooling systems, the presence of pipes on the external façades that disfigure the appearance of the building. A potential solution to the aforementioned problems consists of the renovation of the building through systems that involve the application of a second skin from the outside. This technical solution has been proposed and analysed in various forms, characterized by different configurations and operating principles, and which have different effects on the energy performance of the buildings that they are applied to (Pomponi et al., 2016; Shameri et al., 2011). Generally, in the literature, the addition of a second layer on the external surface of the walls is defined as a "double skin" or, more properly when speaking of interventions on existing buildings, "recladding", meaning a coating with elements that can also be opaque. As stated by (Alberto et al., 2017), the double-skin system is strongly influenced by climatic conditions and the location of the building. The authors of this study developed a parametric analysis based on numerical simulation to evaluate the im-pact on the building's energy performance, of geometry, airflow path, cavity depth, openings area and type of glazing. The results showed that the most efficient solution leads to a 30 % saving in energy demand in a temperate climate and that the orientation of the façade (North or South) produces a difference in the results of 40 %. (Hamza, 2008) explored the possibilities of using the double façade in a hot and arid climate; in particular, the cooling loads were compared for a single skin base case against three possible changes to the physical properties of the external layer of the double skin façade. The simulation results showed that a reflective double façade can achieve higher energy savings than a reflective single façade. The research conducted by (Blanco et al., 2016) concerned the evaluation and optimization of perforated metal sheet double skin façades for a case study in Spain. Through simulation, the influence of different configurations on heating, cooling and artificial lighting loads was evaluated, and a methodology aimed at the optimization of design sustainability based on minimum energy consumption was developed. (Jankovic & Goia, 2021) presented a literature review on experimental and numerical studies of double-skin façades that investigates and evaluates the cause-and-effect connection between the construction characteristics and the thermo-physical phenomena occurring in the system. Simple links between construction properties and performance have been identified, but only when one parameter is analyzed at a time. However, the authors highlighted that the complex interaction between multiple variables is rarely investigated. The study developed by (Tao et al., 2021) proposes two new analytical models to determine the ventilation rate inside naturally ventilated double façades, depending on various factors and using simple in-puts. An adjustable double-skin façade mock-up placed into a climate simulator was used by (Jankovic et al., 2022), to investigate different double-skin façade configurations in combination with a wide range of boundary conditions. The authors provided an overview of several methods based on different types of experimental investigations with various levels of complexity to assess how different constructive features and boundary conditions affect the performance of double-skin façades. Recently, more advanced double-skin façade solutions have been tested. For example, (Alqaed, 2022) examined the use of different types of façades (simple façade, double-skin façade and double-skin façade filled with phase changing materials) based on different climatic conditions in Saudi Arabia. The results proved that the use of phase change materials in the double skin façade significantly reduces the energy demand for both heating and cooling. (Pérez et al., 2021) focused on the development of a method for creating the 3D characterization of an experi-mental double-skin green façade, using LiDAR technologies. The proposed methodology enabled the 3D reconstruction of the green façade's outer envelope, also allowing an evaluation of the temperature reduction obtainable on the external sur-face of the building and providing a 3D object to be used in Building Information Modeling (BIM).

In the present study, an innovative double-façade model, designed for the renovation of existing buildings, is presented and its effectiveness in reducing the heating energy demand is evaluated for a selected case study, with reference to Mediterra-

nean climatic conditions. The proposed system differs from the solutions currently available and discussed in the literature because: a) the façade is made up of opaque panels; b) the cavity of the double envelope is not ventilated; c) the system is multifunctional, in the sense that it is possible to adapt the cladding panels to different functions, according to the specific needs of the case in hand.

2. Methodology

2.1 Description of the I-BEST System (Innovative Building Envelope through Smart Technology)

I-BEST (Innovative Building Envelope through Smart Technology) is an innovative multifunction façade system developed for the refurbishment of existing buildings. This system is designed to implement integrated energy efficiency both in envelope and plant performance. Using the I-BEST system, in fact, it is possible to do the following: improve the energy efficiency of the building; enhance the aesthetic quality of the building and therefore of the surrounding urban environment; avoid the degradation phenomena affecting the materials of the building envelope; implement non-invasive interventions for the occupants of the building, who can continue to use the interior even during the renovation works. The I-BEST technology consists of a system of sliding, modular and multifunctional panels, supported by a metal and light load-bearing structure, which is fixed to the existing building from the outside, without structurally weighing on it. The application of the double skin creates a cavity that can be used to install plant ducts (air conditioning, electrical, water systems and the collection and drainage of rainwater). The design solution meets the growing demand from the recladding sector, which requires the replacement of façades, claddings and openings of aged buildings with new, modern, functional and high-performance components. Furthermore, the system offers a high potential in the construction market, thanks to its modularity, adaptability to different building types, and replicability in various climatic contexts, while maintaining low costs and reduced construction times. The main strength of the I-BEST system is its high flexibility. The multifunctional module-panels, in fact, can be used as a simple coating (also customizable on the surface), or they can include a layer of thermal insulation that varies according to the climate, incorporate solar modules for the production of renewable energy, integrate layers with vegetation to create green surfaces.

2.2 Presentation of the Case Study

For the evaluation of the I-BEST performance, its application to a building identified as a case study is considered. The building is part of the residential centre of the University of Calabria Campus. The location is characterized by a Mediterranean climate. The building consists of two adjacent blocks, slightly staggered in plan and two floors high. Each block includes two residential units, one on the ground floor and one on the first floor, with a net surface area of about 65.5 m^2. Overall, the building includes four apartments, with a total net area of 262.0 m^2. Fig. 1 shows the floor plan of the building. As regards the construction characteristics of the building, the external walls are made with a double layer of perforated bricks and a central cavity with thermal insulation, with thermal transmittance of 0.52 W/(m^2 K). Fig. 2 depicts the detailed stratigraphy of the external wall. The roof is flat, not insulated, with thermal transmittance equal to 1.35 W/(m^2 K).

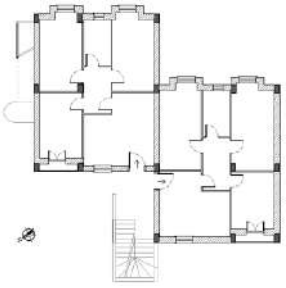

Fig. 1 – Floor plan of the case study building

The ground floor slab, also not insulated, is characterized by a U value of 1.55 W/(m^2 K). The windows have single glazing (U_{glass}=5.7 W/(m^2 K) and aluminum frames without thermal break (U_{frame}=5.9 W/(m^2 K)). Each apartment is equipped with a gas boiler for heating and DHW production.

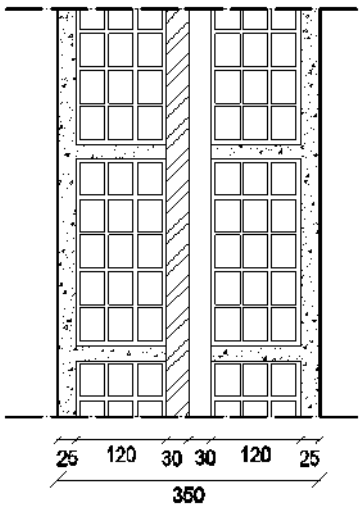

Fig. 2 – Stratigraphy of the external wall before renovation

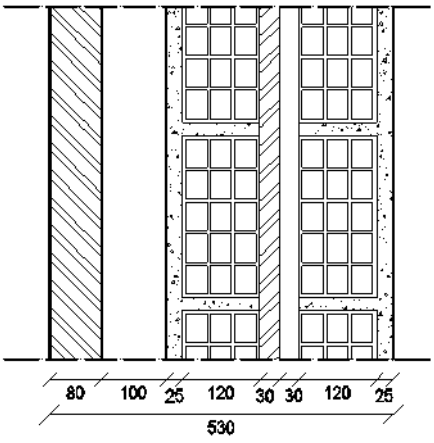

Fig. 2 – Stratigraphy of the external wall after renovation with the I-BEST system

2.3 Calculation Assumptions

In order to conduct a preliminary analysis, the energy model of the building was created using DesignBuilder software (DesignBuilder Software Ltd), a graphical interface of EnergyPlus (Energy Plus). The model was used to perform dynamic simulations and evaluate the effect of the introduction of the I-BEST system in the building, estimating the energy demand for heating before and after the installation of the double façade. The building was actually selected as a test building for the research project within which the innovative I-BEST system was developed, and it will therefore be renovated through the installation of the I-BEST modules on the external façades, in order to experimentally evaluate the performance of the proposed system. In this study, the effectiveness of the I-BEST system is evaluated exclusively by simulation and is limited to the analysis of the solution relating to the use of the I-BEST panel containing a layer of thermal insulation. Future studies will be aimed at exploring the effect produced by other solutions associated with the multi-functionality of the panel (integration of solar panels and green surfaces). Fig. 3 shows the stratigraphy of the external wall following the application of the I-BEST modules. Assuming the non-ventilated cavity, the thermal transmittance of the wall after the energy renovation with I-BEST is equal to 0.20 W/(m^2 K), complying with the minimum requirements set by law (D.M. 26 June 2015).

Hourly weather data provided by the Italian Thermotechnical Committee (CTI - Comitato Termotecnico Italiano) were used in the simulation. The location is classified within the climatic zone D (D.P.R. 412/93), with the heating period running from 1 November to 15 April. The heating setpoint temperature is set at 20 °C. Since no specific information on the occupancy is available, the internal gains have been quantified following the standard (UNI/TS 11300–1) and amount to 5.68 W/m2. Similarly, the natural ventilation rate has been estimated based on technical specification (UNI/TS 11300–1) and is equal to 0.3 ach. Dynamic simulation was conducted on an hourly basis in order to predict the thermal needs for heating and the primary energy required by the building at the current state and after the I-BEST renovation.

3. Results and Discussion

Fig. 3 shows the thermal heating requirement on a monthly basis, at present and after renovation with the I-BEST system. The results refer exclusively to the intervention on the external walls, in order to evaluate the impact of the proposed double façade system. For the purposes of this study, no other envelope efficiency measures were considered that would in any case be required to meet regulatory constraints (e.g., insulation of the roof and ground floor slab, replacement of the windows).

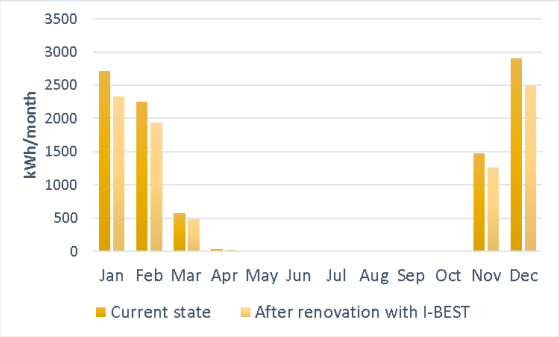

Fig. 3 – Thermal requirements for heating of the case study building before and after the renovation with I-BEST system

The installation of the I-BEST panels, including an appropriate layer of thermal insulation, allows a reduction in the monthly thermal requirement for heating varying from 14.0 % to 16.4 % to be obtained. Considering the whole heating season, the energy needs decrease from 38.08 kWh/(m²year) to 32.58 kWh/(m²year). The improvement in the energy performance of the external walls is also evident in the internal air temperature. Fig. 4 and Fig. 5 show the average daily air temperature corresponding to the coldest day of the year based on the weather file used, that is, February 2. On this day, the lowest outdoor air temperature occurs, equal to -2.8 °C.

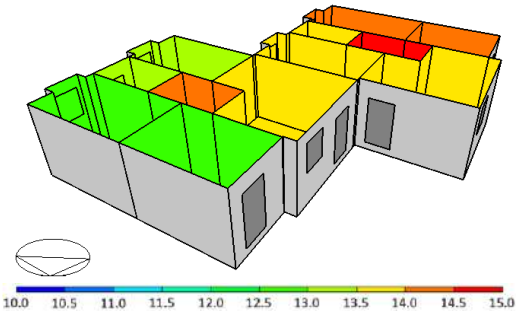

Fig. 4 – Average daily internal air temperature before renovation (free-floating simulation carried out for the coldest day of the year)

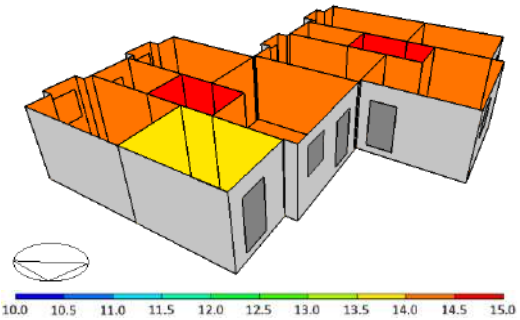

Fig. 5 – Average daily internal air temperature after renovation with I-BEST system (free-floating simulation carried out for the coldest day of the year)

The simulation is carried out in free-floating conditions, thus without considering the activation of the heating system. Therefore, the performance represented in the figures refers to the passive behavior of the envelope and only considers the energy efficiency measure applied on the external walls. The results are displayed based on a color graphic scale and are represented as an example for the ground floor of the building. From the figures, it can be noted that the use of the I-BEST modules produces an increase in the internal air temperature in all the areas of the housing units analyzed. This effect is due to the decrease in the thermal transmittance of the external walls after the addition of the I-BEST panels.

The assembly of the panels on the external façades allows a non-ventilated cavity, which acts as a thermal buffer between the internal and external environment, to be obtained. In fact, inside this cavity, the temperature values are higher than the external air temperature, creating a transition zone capable of mitigating heat dispersion. Fig. 6 shows the temperature trend for the coldest day (February 2), in free-floating operation. In particular, the external air temperature, the internal air temperature and the air temperature inside the cavity are displayed in the graph, with reference to a room on the ground floor.

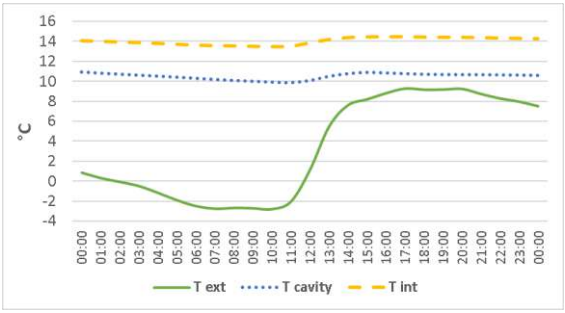

Fig. 6 – Hourly trend of the air temperature (external, internal and inside the cavity) obtained from simulation conducted in free-floating conditions for the coldest day of the year

However, the greatest potential of the I-BEST solution derives from the fact that it is an "integrated" renovation system which, in addition to improving the performance of the building envelope, allows renovation of the heating plant to be carried out easily and economically. The unvented cavity created by the installation of the double façade, in

fact, can be used to conveniently place the pipes of the heating system. Consequently, it is possible to assume the replacement of the existing heating plant consisting of gas boilers and radiators, with a more efficient system including an air-water heat pump (SCOP=3.5) supplying fan coils. Furthermore, this solution would also allow cooling in the summer. Thanks to the I-BEST technology, the new heating plant can be fitted quickly, without demolition work and excavations for the passage of the pipes, and without interfering with the use of the internal environment. At present, a gas supply of 11703 kWh is required. Considering the integrated restructuring of the envelope and heating plant, which involves the installation of the I-BEST system and the replacement of the boilers with an electric heat pump, electricity consumption of 2439 kWh is predicted.

To make a comparison, the energy supplied is converted into primary energy using the non-renewable primary energy conversion factors provided by the law (D. M. 26 Giugno 2015). Fig. 7 presents the monthly values of primary energy demand before and after renovation. A saving of 61 % is achieved for the heating season, with a reduction from 46.90 kWh/(m^{2}year) to 18.15 kWh/(m^{2}year).

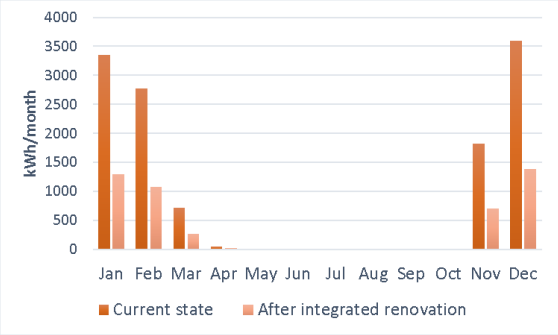

Fig. 7 – Comparison between the monthly primary energy demand for heating before and after integrated renovation, involving the installation of the I-BEST double façade and heat pump system

4. Conclusions

The analysis presented in this work concerned the evaluation using dynamic energy simulation of the energy performances offered by an innovative building renovation system, consisting of sliding and multifunctional modular panels (I-BEST system). The proposed technology allows for the creation of a double façade by realizing a non-ventilated cavity, which can be used to set up the pipes of the plants. This makes it possible to operate an integrated renovation of the building envelope and heating system in a short time, without demolition work and reducing costs. Since the I-BEST system is designed for the combined renovation of the heating system and external walls, its affordability is particularly evident when the following conditions occur: the need to install, complete or renovate the air conditioning system; the need to place scaffolding on public land to implement the work aimed at the thermal insulation of the envelope. In the first case, it would be very expensive to operate inside the house to build the air conditioning system, as this involves the demolition and reconstruction of the tracks where the pipes pass. With reference to the second hypothesis, the municipal charges to be paid for the occupation of public land are high, and a faster operation, such as that allowed by the I-BEST system can bring significant savings.

The modular and multifunction panels confer high flexibility to the system, in terms of adaptation to different contexts and functions performed (simple cladding, thermal insulation, solar façade, and green surfaces). In particular, the analysis developed in this study focused on the evaluation of the configuration designed for thermal insulation. A building was selected as a case study and the energy saving achievable following the integrated renovation was assessed, involving the application of the I-BEST system and the replacement of the heating plant. The results showed that the use of the I-BEST double façade allows for a reduction in the heating requirement of about 14 %. The enhanced performance of the walls allows an improvement of the internal conditions with regard to the passive behaviour of the envelope to be obtained, resulting in an increase in the internal air temperature. Considering the refurbishment of the heating system through the installation of a heat pump, it is possible to achieve a saving of 61 % in terms of primary energy. Future studies will be aimed at extending the analysis to evaluate the effect of the I-BEST technology also in the cooling period and to

explore the other possible alternative configurations of the I-BEST system (solar façade and green façade). Moreover, the implementation of the system on the building selected as test-case for the research project will also allow experimental analyses to be performed.

Acknowledgement

The study was developed as part of the I-BEST (Innovative Building Envelope through Smart Technology) Research Project funded by the PON Mise (Ministry of Economic Development) - H2020 program.
Identification number F/050234/01-0-2/X32

References

Alberto, A., N. M. M. Ramos, and R. M. S. F. Almeida. 2017. "Parametric Study of Double-Skin Façades Performance in Mild Climate Countries." *Journal of Building Engineering* 12: 87–98. doi: https://doi.org/10.1016/j.jobe.2017.05.013

Alqaed, S. 2022. "Effect of Annual Solar Radiation on Simple Façade, Double-Skin Façade and Double-Skin Façade Filled with Phase Change Materials for Saving Energy." *Sustainable Energy Technologies and Assessments* 51: 101928. doi: https://doi.org/10.1016/j.seta.2021.101928

Blanco, J. M., A. Buruaga, E. Rojí, J. Cuadrado, and B. Pelaz. 2016. "Energy Assessment and Optimization of Perforated Metal Sheet Double Skin Façades through Design Builder; A Case Study in Spain." *Energy and Buildings* 111: 326–36. doi: https://doi.org/10.1016/j.enbuild.2015.11.053

CTI - Comitato Termotecnico Italiano Https://Www.Cti2000.It/ (Accessed on 13 July 2021).

DesignBuilder Software Ltd, DesignBuilder Version 6, (2020). http://www.Designbuilder.Co.Uk (accessed on 13 July 2021).

EnergyPlus. n.d. https://energyplus.net/ (last access on 18 January 2022).

European Commission. EU Commission European Green Deal." https://ec.europa.eu/info/strategy/priorities-2019-2024/european-green-deal/

European Parliament And Council. 2018. *"Directive (Eu) 2018/844 of the European Parliament and of the Council of 30 May 2018 Amending Directive 2010/31/EU on the Energy Performance of Buildings and Directive 2012/27/EU on Energy Efficiency."*

Hamza, N.. 2008. "Double versus Single Skin Façades in Hot Arid Areas." *Energy and Buildings* 40(3): 240–48. doi: https://doi.org/10.1016/j.enbuild.2007.02.025

Italian Government. 2015. *D. M. 26 Giugno 2015 'Applicazione Delle Metodologie Di Calcolo Delle Prestazioni Energetiche e Definizione Delle Prescrizioni e Dei Requisiti Minimi Degli Edifici'.*

Jankovic, A., and F. Goia. 2021. "Impact of Double Skin Façade Constructional Features on Heat Transfer and Fluid Dynamic Behaviour." *Building and Environment* 196: 107796. doi: https://doi.org/10.1016/j.buildenv.2021.107796

Jankovic, A., M. S. Siddiqui, and F. Goia. 2022. "Laboratory Testbed and Methods for Flexible Characterization of Thermal and Fluid Dynamic Behaviour of Double Skin Façades." *Building and Environment* 210: 108700. doi: https://doi.org/10.1016/j.buildenv.2021.108700

Pérez, G., A. Escolà, J. R. Rosell-Polo, J. Coma, R. Arasanz, B. Marrero, L. F. Cabeza, and E. Gregorio. 2021. "3D Characterization of a Boston Ivy Double-Skin Green Building Façade Using a LiDAR System." *Building and Environment* 206. doi: https://doi.org/10.1016/j.buildenv.2021.108320

Pomponi, F., P. A.E. Piroozfar, R. Southall, P. Ashton, and E. R.P. Farr. 2016. "Energy Performance of Double-Skin Façades in Temperate Climates: A Systematic Review and Meta-Analysis." *Renewable and Sustainable Energy Reviews* 54: 1525–36. doi: https://doi.org/10.1016/j.rser.2015.10.075

President of the Italian Republic. 1993. *D.P.R. 412/93 'Regolamento Recante La Progettazione, l'installazione, l'esercizio e La Manutenzione Degli Impianti Termici Degli Edifici Ai Fini Del Contenimento Dei Consumi Di Energia, in Attuazione Dell'art. 4, Comma 4, Della L. 9 Gennaio 1991, n. 10.'*

Shameri, M. A., M. A. Alghoul, K. Sopian, M. Fauzi M. Zain, and O. Elayeb. 2011. "Perspectives of Double Skin Façade Systems in Buildings and Energy Saving." *Renewable and Sustainable Energy Reviews* 15(3): 1468–75. doi: https://doi.org/10.1016/j.rser.2010.10.016

Tao, Y., X. Fang, M. Yit Lin Chew, L. Zhang, J. Tu, and L. Shi. 2021. "Predicting Airflow in Naturally Ventilated Double-Skin Façades: Theoretical Analysis and Modelling." *Renewable Energy* 179: 1940–54. doi: https://doi.org/10.1016/j.renene.2021.07.135

UNI. 2014. *UNI/TS 11300–1. Building Energy Performance – Part 1: Evaluation of the Energy Need for Space Heating and Cooling* (in Italian).

United Nations Environment Programme. 2021. *Global Status Report for Buildings 2021,* Available at https://Globalabc.Org/Resources/Publications/2021-Global-Status-Report-Buildings-and-Construction (Last Access on 30/11/2021).

Modeling Occupants' Behavior to Improve the Building Performance Simulation of Classrooms

Federica Morandi – Free University of Bozen-Bolzano, Italy – federica.morandi@unibz.it
Julian Donges – Free University of Bozen-Bolzano, Italy – julian.donges@natec.unibz.it
Ilaria Pittana – IUAV University of Venice, Italy – ilaria.pittana@iuav.it
Alessandro Prada – University of Trento, Italy – alessandro.prada@unitn.it
Francesca Cappelletti – IUAV University of Venice, Italy – francesca.cappelletti@iuav.it
Andrea Gasparella – Free University of Bozen-Bolzano, Italy – andrea.gasparella@unibz.it

Abstract

Window operation in naturally ventilated classrooms is the only strategy for achieving proper air change rates. The modeling of the ventilation rate based on the window state implies knowledge of the window opening angle to evaluate the net exchange area. Nonetheless, the sensors most used to monitor window opening state are contact sensors, which allow only a binary state (i.e., open/close) to be devised. This work aims to investigate the effect that window opening information has on ventilation rates and building performance simulation by comparing the case in which window opening is described by the opening angle to the condition in which it is described as a binary I/O variable. A measurement campaign was conducted on six classrooms in a secondary school in Morlupo, Rome. Temperature, CO_2 concentration and relative humidity were monitored in the six classes, while temperature and relative humidity were monitored outdoors. During school time, a few students per class were asked to report information concerning the number of occupants and the opening state of windows and shutters on a discrete scale. From the data collected, an equivalent opening area was calculated, accounting for the combined opening of windows and shutters, being therefore representative of the net exchange area. Based on the original dataset, a second dataset was generated by considering binary window opening information both for windows and shutters. The two datasets were used, together with environmental data, to train behavioral models that were then fed into a building energy simulation model. The results of the simulations show that the simplified dataset causes an overestimation of the air changes and of the building energy need.

1. Introduction

Occupant behavior is commonly recognized as an influential factor when seeking explanations for the difference between the predicted performance of a building and its actual performance in post-occupancy conditions, the so-called performance gap (Shi et al., 2019).

Though most of the literature on occupant behavior focuses on residential and office buildings (Franceschini et al., 2022), the importance of studying people's behavior in educational buildings stems from the findings of the extensive literature regarding the role that ventilation plays in students' concentration, health, and performance (Bakó-Biró et al., 2012; Haverinen-Shaughnessy et al., 2015).

The drivers for human interaction with the envelope should be sought in a multi-domain approach. For instance, operating the shutters might be a consequence of glare or of direct solar radiation, and window operation might be triggered by air quality concerns, thermal comfort, or noise protection (Delzendeh et al., 2017). However, the drivers that are mostly used in occupant behavior modeling relate to the thermal and indoor air quality domains (Dai et al., 2020).

The interaction between occupants and the envelope is particularly relevant in naturally ventilated buildings, where window operation directly impacts on ventilation rates and, consequently, on indoor temperature, air quality, and finally on the building energy demand. In such buildings, the ventilation rate can be estimated from the indoor

and outdoor environmental conditions and the net exchange area (EN 16798), which can be derived by the combined state of windows and shutters.

Many sensors and technologies are available to detect the window state. The ones that are most often deployed, which are relatively cheap and require low implementation effort, are contact sensors, which report a binary status (Belafi et al., 2018; Naspi et al., 2018; Park et al., 2019). Nonetheless, monitoring the opening angle besides the state might be relevant, as different opening angles determine different net exchange areas. Window opening angle can be monitored, among other methods, using accelerometers (Andersen et al., 2013), by implementing image recognition algorithms (Sun et al., 2022), or assessed through the administration of questionnaires (Kim et al., 2019).

2. Aim And Method

In this paper, a naturally ventilated school building is used as a case study to develop behavioral models devoted to window opening to be used in building performance simulations. In particular, the focus is on the impact of detailed models able to predict the window opening angle as opposed to simpler binary models. The research question is: **To which extent does detailed information on window state affect the building energy demand compared to an I/O information?**

The methodology adopted to address such question can be summarized by the following steps:

1. **Collection of experimental data**. A measurement campaign was carried out in six classrooms of a high school in Morlupo, Rome. Environmental parameters were monitored and detailed information on the state of windows and roller shutters was reported by the students.
2. **Modeling occupant behaviour.** Data were preprocessed by calculating an equivalent opening area that takes into consideration the opening of the sashes and of the roller shutters. Then, a second dataset was created by attributing a binary status to sashes and shutters, i.e., simulating the dataset that would have been collected if contact sensors were used. Two behavioral models were trained on the two datasets based on classification trees, algorithms that split the data into branches based on impurity criteria and assign, following the tree-like structure built upon predictor variables, the probability of falling within a specific class of the response variable.
3. **Simulation of building performance.** Energy modeling of a reference building was carried out using the two different behavioral models to evaluate the effects of window state information on the ventilation rate, and the overall energy performance.

In the analysis proposed, only thermal and indoor air quality environmental variables are accounted for (air temperature, relative humidity, and CO_2 concentration), as these can be predicted by means of building energy simulations.

3. The Measurement Campaign

The measurement campaign took place between January and May 2022, for a total of 17 weeks. Six classrooms were involved in the reporting activities. Students participated in a training program organized jointly by the universities involved in the project and the high school.

The layout of the monitored classrooms is depicted in Fig. 1 and Fig. 2. The floor surface of each classroom is 50 m^2 approx. Classrooms are equipped with three two-sash windows and roller shutters.

The indoor environmental conditions were monitored using HoBO MX 1102 loggers (T, RH, CO_2 concentration), which were fixed on the walls, while outdoor conditions were monitored using a HOBO U23-001A data logger (T, RH). Data acquisition was carried out with a 10-min time resolution.

During the lecture, students were provided with printed spreadsheets in which they were asked to write down the condition of the room and the time at which any change in state occurred. The parameters that were monitored are:

- State of each window sash (0-0.5-1)
- State of each shutter (0-0.25-0.5-0.75-1)
- State of the door (0-1)
- Number of people in the classroom
- State of the lights (0-0.5-1).

(a) Ground floor

(a) First floor

(a) Second floor

Fig. 1 – Floor plans of the IIS "Margherita Hack" in Morlupo, Rome, with indication of the classrooms involved in the project (in gray color)

Fig. 2 – Internal view of one of the classrooms that participated in the project

Fig. 3 represents the physical meaning attributed to the values that represent the state of windows and shutters. Besides the state of these elements, students also had to report the motivation that led to the interaction with the environment, by choosing from a set of pre-determined questions, and to indicate whether the request for change came from a student or from the teacher.

Each classroom managed the organization of the data collection in a different manner. Students built shifts so that each component (e.g., windows, lights, shutters, etc) was controlled by one person at a time, to ease the work and not to distract them too much from their lesson.

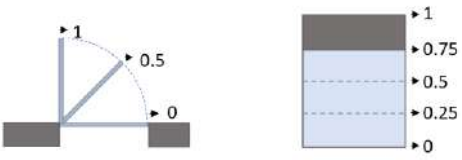

(a) window opening (b) shutter opening

Fig. 3 – Options available for the reporting of sashes (a) and shutters (b) status

After these paper-based sheets were collected, they were transferred to a digital archive in which the state was reported per each time step at which an environmental measure was available, i.e., every other 10 minutes.

4. Results

4.1 Data Pre-Processing

Data were filtered by presence, to exclude data that referred to unoccupied periods from the evaluation. Only complete datasets were included in this analysis, i.e., data was excluded from the selection, when even just the state of one sash was not reported.

Starting from the information on window and shutters status, an equivalent opening area was calculated by computing, for each window, the average opening of the two sashes and by multiplying that value by the opening of the shutter. In this manner, a situation in which window sashes are open and the shutter is closed would be represented by a null equivalent opening area. This dataset will be referred to in the following as "case 1".

From the original dataset, another equivalent opening area was calculated by considering that window sashes and shutters could only assume 1/0 values. In the case of windows, values of 0.5 were then converted into 1, while in the case of shutters, values of 0.25-0.5 and 0.75 were converted into 1. Then, the equivalent opening area was calculated again, following the procedure described above. This second dataset, referred to in the following as "case 2", is characterized by a less continuous distribution of values.

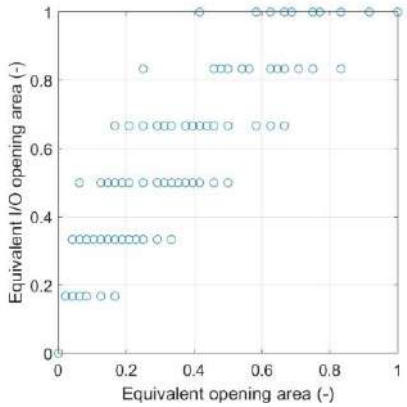

Fig. 4 – Equivalent opening areas calculated from the original dataset (case 1, x-axis) and from the modified dataset (case 2, y-axis)

The scatter plot of the equivalent opening areas calculated for case 1 and case 2 is reported in Fig. 4. The levels of equivalent opening area that are determined by the 1/0 discretization are clearly visible. As expected, in case 2 the equivalent opening area is much larger compared with the actual opening area.

4.2 Modeling Occupant Behavior

The two pre-processed datasets were then used to train behavioral models based on decision trees. To improve prediction accuracy, bagged tree classifiers were used. The equivalent opening area, binned at 25 % intervals, was assumed as the response variable, and the following predictors were used as input variables: indoor temperature, relative humidity and CO_2 concentration, outdoor temperature, and relative humidity. It is specified that the classes are very unbalanced, with a great number of occurrences related to the "closed" condition (0), and that no occurrence is found at fully open (1). This relates to the way the equivalent opening area is defined, as it is a multiplication between average opening of the window and of the shutters (which are hardly ever totally closed).

The importance of the predictors in estimating the models is reported in Fig. 5. The outdoor temperature has significant impact on both models, followed by indoor temperature and relative humidity. Outdoor humidity ranks the lowest predictor in terms of importance.

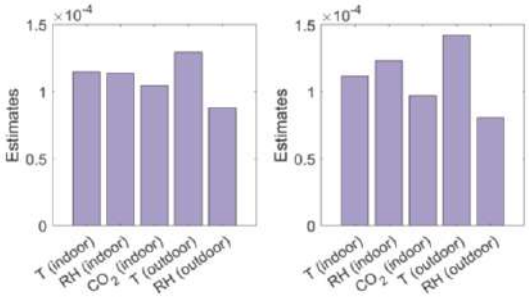

(a) Case 1 (original dataset) (b) Case 2 (I/O)

Fig. 5 – Importance of the predictors of the behavioral models

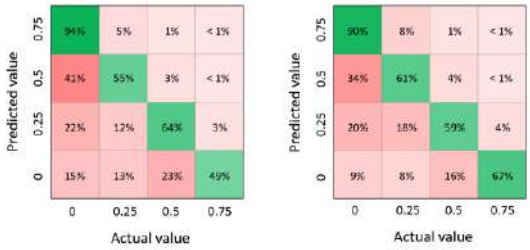

(a) Case 1 (b) Case 2

Fig. 6 – Confusion matrices of the behavioral models trained

The accuracy of the models is 81.9 % and 76.5 % for case 1 (original dataset) and case 2 (I/O dataset), respectively. The confusion matrices of the two trained models are reported in Fig. 6. Green diagonals show that most of the classes are correctly identified.

The relevant share of incorrect classifications displayed in the lower left part of the diagrams indicates a tendency of both models to underestimate the equivalent opening area.

4.3 Building Performance Simulations

The trained models were nested in the energy simulation of a school building located in Milan. The building consisted of two classrooms with a total surface of 100 m² and 3 m high, recalling the dimensions of the classrooms in which the training dataset was collected.

The typical reference year developed in (Pernigotto et al., 2014) was used. By looping TRNSYS with Matlab, the decision tree was used as a black box that, for each time step, would read the values of the predictors (i.e., indoor temperature, relative humidity and CO_2 concentration, and the outdoor temperature and relative humidity) and attribute a class to the response variable (i.e., equivalent open-

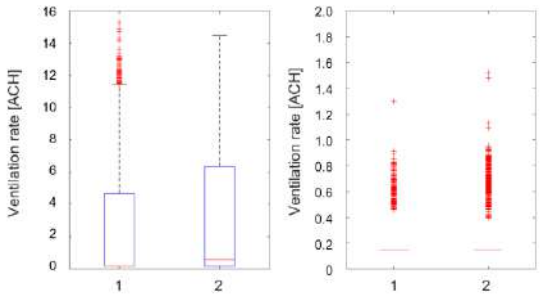

(a) summer season (b) winter season

Fig. 7 – Ventilation rate in the summer (a) and winter (b) season for case 1 and case 2

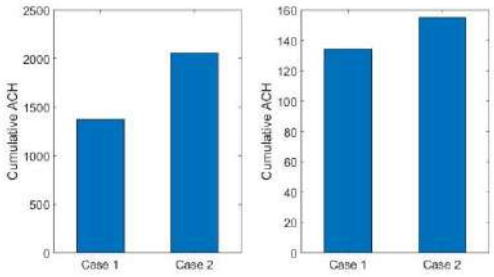

(a) Summer season (b) Winter season

Fig. 8 – Cumulative ACH calculated over the summer (a) and winter (b) season for case 1 and 2

ing area) based on a probabilistic approach. The information on window opening area was then used to estimate the ventilation rate based on the EN 16798 approach. A constant infiltration rate of 0.15 ACH was assumed in addition to natural ventilation to determine the overall air change rate.

All building characteristics were left unvaried in the two models (e.g., occupancy profiles, envelope characteristics, outdoor climate, etc), the different results generated by the twin simulations solely ascribable to the behavioral model called.

Fig. 7 provides a qualitative overview of the seasonal Air Changes per Hour (ACH) returned by the simulations. In the heating season (15th October-15th April), ventilation is governed by infiltration (almost no window opening). In summer, conversely, higher ventilation rates are predicted and differences among the two models arise – the number of air changes per hour being sensitively greater for case 2.

By summing up the ACH on a seasonal basis for case 1 and case 2 (Fig. 8), data displays a difference in ACH of 33 % in the summer season and a difference of 13 % in the winter season - case 2 leading to an overestimation of the ventilation rate in both cases.

Since air change rate related to infiltration is known (0.15 ACH), by data filtering it is possible to distinguish when the air change is related to infiltration or to window operation. These data are presented in Fig. 9, where the number of times in which ventilation could be attributed to infiltration or ventilation is represented as a percentage related to all observations. In case 2 (I/O opening), ventilation is generally triggered by window opening for a greater number of times compared to case 1.

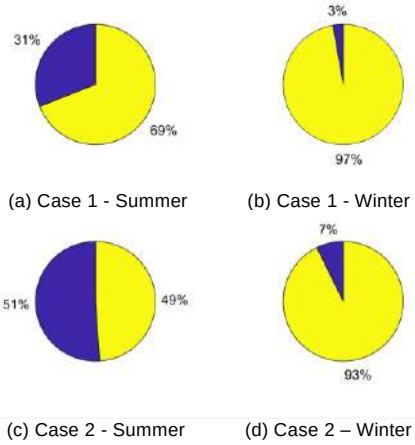

(a) Case 1 - Summer (b) Case 1 - Winter

(c) Case 2 - Summer (d) Case 2 – Winter

Fig. 9 – Share of ventilation rates occurrences related to window opening (in purple) and to infiltration (in yellow)

This effect is magnified in the summer season (51 % of occurrences related to window opening in case 2 vs 31 % in case 1).

This qualitative analysis might suffer from a bias related to the effectiveness of the window operation in the two models: in case 2, does the model predict fewer window openings because the air exchange is more effective?

The different estimates in ventilation rates affect the energy performance of the building. The energy demand in the winter season in case 1 corresponds to 1.93 MWh, while in case 2 it is 2.04 MWh, therefore indicating a 5 % increase in energy demand for case 2 in relation to case 1.

5. Discussion

The analysis carried out so far shows that there is a sensitive variation in the estimate of the air change rate when the actual window opening angle is

used. In relation to the individual steps of the method proposed, some points call for further comments:

- **Experiment bound**. Occupant behavior should be dealt with as a multi-domain-driven mechanism, as multiple factors contribute to determining the interaction of individuals with the envelope. In the present study, the environmental parameters considered refer to the thermal and air quality comfort domains, through the measurement of indoor and outdoor temperature and relative humidity, and indoor CO_2 concentration. This choice was made based on the consideration that these are the features that can be controlled in building performance simulations. Multi-domain simulation would allow for a proper integration of factors.
- **Data collection.** The information of window status was reported by students and is therefore subject to accuracy issues. Errors in reporting the window and shutter states should be random (one might forget to report a window opening as well as a window closing), and therefore it might contribute to the data noisiness. In any case, this should not affect the outcome of the present study, as a comparison is proposed between the two subsets, one of which is generated based on the other. Conversely, the accuracy of data reporting might affect the accuracy of the behavioral models trained. For this reason, some of the classrooms analyzed in the present study were equipped with a device to monitor the window opening angle; data will be used in further work to test the reliability of the data reported by students.
- **Behavioral models**. The behavioral models trained show high accuracy (82 % and 76 %, respectively), but the share of false negatives is not homogeneous among classes and shows a tendency of both models to underestimate the equivalent exchange area. That might be related to the fact that samples are unbalanced. Furthermore, an extension of the original dataset both in terms of monitored states and of environmental conditions would improve the model accuracy.
- **Building performance simulation.** The results of building performance simulations show a sensitive decrease in ventilation rate when actual opening angles are considered. For the case study analyzed, this translates into an underestimate of building energy consumption by 5 %. The magnitude of this effect might be biased by building, weather and systems-related factors and will be addressed in future work.

6. Conclusion

The research aimed at understanding the impact that window opening modeling has on energy performance simulation. An experimental campaign was carried out in which environmental parameters and the detailed states of windows and shutters were monitored. Two behavioral models were trained to account for I/O opening information and the discrete dataset.

Energy performance simulations show that ventilation rate is strongly affected by the detail with which the window opening information is provided. A I/O discretization would, in general, lead to an overestimate of the ventilation rate and of the overall energy demand of the building.

Future work will concern the improvement of behavioral models, the evaluation of the uncertainty brought by behavioral models into energy simulation, the evaluation of the reliability of the data reported by the students, and the inclusion of monitoring parameters affecting the other domains of comfort as drivers for the window opening.

Acknowledgement

The authors thankfully acknowledge Davide Michetti, Sonia Sgavicchia and Silvia D'Isidoro for their support for the project, Eleonora Righi for her support in the management of the experimental data of the monitoring campaign, and the students of Margherita Hack High School in Morlupo (classes 2D, 3B, 3C, 3D, 4A, 4B) for their active participation and dedication to the project.

References

Andersen, R., V. Fabi, J. Toftum, S. P. Corgnati, and B. W. Olesen. 2013. "Window opening behaviour modelled from measurements in Danish dwellings." *Building and Environment* 69: 101-113. doi: https://doi.org/10.1016/j.buildenv.2013.07.005

Bakó-Biró, Zs., D. J. Clements-Croome, N. Kochhar, H. B. Awbi, and M. J. Williams. 2012. "Ventilation rates in schools and pupils' performance." *Building and Environment* 48: 215-223. doi: https://doi.org/10.1016/j.buildenv.2011.08.018

Belafi, Z. D., F. Naspi, M. Arnesano, A. Reith and G. M. Revel. 2018. "Investigation on window opening and closing behavior in schools through measurements and surveys: A case study in Budapest." *Building and Environment* 143:523–531. doi: https://doi.org/10.1016/j.buildenv.2018.07.022

CEN. 2017. *EN 16798-7:2017. Energy performance of buildings - Ventilation for buildings - Part 7: Calculation methods for the determination of air flow rates in buildings including infiltration*. CEN, Brussels, 2017.

Dai, X., J. Liu, and X. Zhang. 2020. "A review of studies applying machine learning models to predict occupancy and window-opening behaviours in smart buildings." *Energy and Buildings* 223: 110159. doi: https://doi.org/10.1016/j.enbuild.2020.110159

Delzendeh, E., S. Wu, A. Lee, and Y. Zhou. 2017. "The impact of occupants' behaviours on building energy analysis: A research review." *Renewable and Sustainable Energy Reviews* 80: 1061-1071. doi: https://doi.org/10.1016/j.rser.2017.05.264

Franceschini, P. B., and L. Oliveira Neves. 2022. "A critical review on occupant behaviour modelling for building performance simulation of naturally ventilated school buildings and potential changes due to the COVID-19 pandemic." *Energy and Buildings* 258: 111831. doi: https://doi.org/10.1016/j.enbuild.2022.111831

Haverinen-Shaughnessy, U., R. J. Shaughnessy, E. C. Cole, O. Toyinbo, D. J. Moschandreas, 2015. "An assessment of indoor environmental quality in schools and its association with health and performance." *Building and Environment* 93(1): 35-40. doi: https://doi.org/10.1016/j.buildenv.2015.03.006

Kim, A., S. Wang, J. E. Kim, and D. Reed. 2019. "Indoor/outdoor environmental parameters and window-opening behavior: A structural equation modeling analysis." *Buildings* 9:94. doi: https://doi.org/10.3390/buildings9040094

MATLAB(R2019a). Natick, Massachusetts: The MathWorks Inc.

Naspi, F., M. Arnesano, L. Zampetti, F. Stazi, G. M. Revel and M. D'Orazio. 2018. "Experimental study on occupants' interaction with windows and lights in Mediterranean offices during the non-heating season." *Building and Environment* 127: 221–238. doi: https://doi.org/10.1016/j.buildenv.2017.11.009

Park, J., and C. S. Choi. 2019. "Modeling occupant behavior of the manual control of windows in residential buildings." *Indoor Air* 29(2): 242–251. doi: https://doi.org/10.1111/ina.12522

Pernigotto, G., A. Prada, D. Cóstola, A. Gasparella, J. L. M. Hensen. 2014. "Multi-year and reference year weather data for building energy labelling in north Italy climates." *Energy and Buildings* 72: 62–72. doi: https://doi.org/10.1016/j.enbuild.2013.12.012

Shi, X., B. Si, J. Zhao, Z. Tian, C. Wang, X. Jin, and X. Zhou. 2019. "Magnitude, Causes, and Solutions of the Performance Gap of Buildings: A Review." *Sustainability* 11: 937. doi: https://doi.org/10.3390/su11030937

Sun, C., X. Guo, T. Zhao, and Y. Han. 2022. "Real-time detection method of window opening behavior using deep learning-based image recognition in severe cold regions." *Energy and Buildings* 268: 112196. doi: https://doi.org/10.1016/j.enbuild.2022.112196

TRNSYS 18.02, Solar energy laboratory. A transient systems simulation program.

Modeling and Measurements in Natural Ventilation of Massive Buildings: A Case Study

Francesco Asdrubali – Roma Tre University, Italy – francesco.asdrubali@uniroma3.it
Luca Evangelisti – Roma Tre University, Italy – luca.evangelisti@uniroma3.it
Claudia Guattari – Roma Tre University, Italy – claudia.guattari@uniroma3.it
Marta Roncone – Roma Tre University, Italy – marta.roncone@uniroma3.it
Lucia Fontana – Roma Tre University, Italy – lucia.fontana@uniroma3.it
Ginevra Salerno – Roma Tre University, Italy – ginevra.salerno@uniroma3.it
Chiara Tonelli – Roma Tre University, Italy – chiara.tonelli@uniroma3.it
Valeria Vitale – Roma Tre University, Italy – valeria.vitale@uniroma3.it

Abstract

Numerical simulations are widely used to evaluate the thermal comfort and energy savings in the retrofit of historic buildings. In most cases, however, no detailed data are available on the materials and stratigraphy of the building envelopes, and on-site measurements can be expensive and time consuming.

The present work uses as a case study a university building characterized by a high thermal capacity in the city of Rome to verify whether the use of natural ventilation can be a practice of use in order to guarantee energy saving and natural comfort.

To this end, in the summer of 2020, an experimental campaign was carried out aimed at acquiring thermofluximetric measurements through the vertical walls, the air temperature inside and outside the analyzed environment and the air velocity. Measurements were conducted under three different usage protocols, including night ventilation and 24-hour continuous ventilation.

These measurements made it possible to identify the thermophysical characteristics of a wall considered "equivalent" to the real wall, allowing the realization of thermofluidodynamic computational models. In particular, in the study, 3 different stratigraphies were considered and compared, corresponding in the first case to the equivalent wall, in the second to that available from the Comsol software library, and, finally, in the third and last case, from literature data (Tabula project) for the building typology analyzed.

From the analysis, it emerged that the 3 groups of parameters do not have a significant impact in terms of variation of internal comfort, confirming the reliability of the use of the literature values for these types of modeling.

1. Introduction

Several findings in the literature highlight the significance of the aspects related to the indoor climatic control and the energy efficiency of historical buildings (Bay et al., 2016).

Natural ventilation of buildings is a good practice for the air quality of living and working environments and the well-being of the occupants. One of the significant effects of an adequate air change is the contribution given to the reduction of gas levels in buildings. The systems that are usually applied in heritage buildings are forced air coils and radiators based on hot water, since the initial investment is quite low compared with other solutions, and they have a short response time to cool/heat large volumes of indoor air. These two plant typologies adapt very well to the specific occupancy patterns and can be employed either discontinuously, targeting occupant thermal comfort satisfaction for a brief period of time, or uninterruptedly, to maintain constant hygrothermal conditions benefitting from the building's thermal mass (Bay et al. 2016; Bencs et al., 2007; Bratasz et al., 2007).

In buildings which are not designed to guarantee an adequate number of air changes, the ventilation obtained through the opening of windows does not allow high indoor thermal comfort level to be maintained, which inevitably returns within a few hours to levels similar to those present before ventilation.

An alternative to the ventilation obtained by simply opening windows can be obtained by equipping the building with an active ventilation system, obtained by means of ducts and aspirators that ensure an exchange of air between the external and internal environment.

This system guarantees greater continuity in the ventilation of the environment, not being linked to manual intervention, and can be carried out uninterrupted or cadenced over 24 hours, limiting the inconvenience of not being able to be used in the presence of wind. However, it should be emphasized that the use of active ventilation must be suitably sized, in order to avoid possible negative effects of a different nature.

In the presence of natural ventilation and high thermal masses, the use of passive and hybrid strategies based on natural ventilation and nocturnal thermal mass precooling can be crucial in terms of internal comfort and energy saving.

The aim of this work, taking as a case study a university building characterized by a high thermal capacity in the city of Rome, is to show the potential of CFD numerical models for quantifying the cooling effects and internal thermal comfort, analyzing different sets of thermophysical parameters assigned to the high thermal mass walls.

2. Material And Methods

This work presents a 2D model of Pavilion 2B (Fig. 1) of the *Ex-Mattatoio* (former abattoir) (Ersoch, 1891) in Rome, built using Computational Fluid Dynamics (CFD) software based on the finite element method (FEM). The transient simulations, as explained in a previous work (Vitale & Salerno, 2017), take the temporal variations and the interactions between internal and external thermal conditions into account, with the aim of evaluating different usage profiles and estimating the effects of passive cooling in the presence of natural ventilation and high thermal masses.

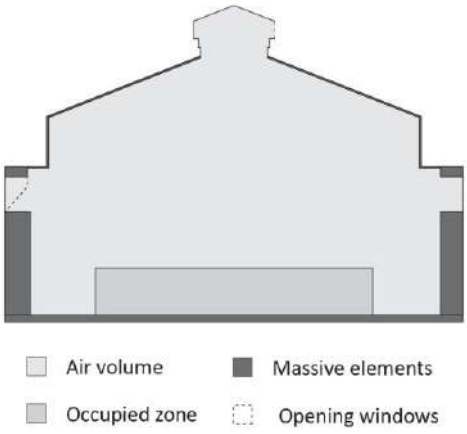

Fig. 1 – Cross section of the Pavilion 2B

The simulations were set up according to the following criteria:

- considering the variations in external conditions (temperature and solar radiation);
- without the use of HVAC systems;
- without occupancy load.

All simulations were carried out in three different usage profiles:

- with nocturnal and diurnal ventilation (24hV);
- with only nocturnal ventilation (10hV);
- without natural ventilation (Nov).

In addition to the three usage profiles, a parametric study was conducted using in each simulation three different sets of thermophysical parameters assigned for the wall (Table 1), determined as follows:

- COM: values from COMSOL Multiphysics library and literature (old simulations);
- SOS: values calculated with measured data and equivalent wall model;
- TAB: values from Tabula library, a report on Italian Building Typology realized by Turin Polytechnic as part of a European project and including the thermophysical characteristics of the most common building types in Italy from the 20th century onwards (Tabula project).

Table 1 – Thermophysical properties of the walls used for the simulations

Set	Thermal conductivity λ	Heat capacity c	Density ϱ
Unit	[W/(m·K)]	[J/(kg·K)]	[kg/m³]
COM	0,81	1512	1800
SOS	0,68	1200	2200
TAB	0,64	840	1681

In particular, Figs. 2 and 3 illustrate the plan of the pavilion selected for the experimentation (Fig. 2) and the measurement scheme of the instruments used for the acquisition of experimental data in the study room (Fig. 3) (Insula Architettura e Ingegneria), respectively.

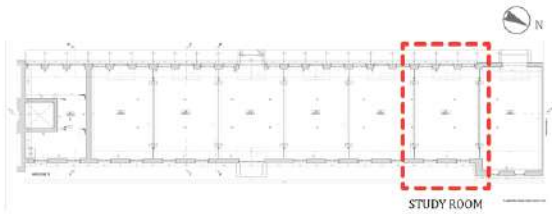

Fig. 2 – Plan of the pavilion analyzed with the delimitation of the study room

The experimental campaign took place in summer, in the period from 28 July 2020 to 7 September 2020, with the aim of acquiring data on the surface temperatures inside and outside the study wall, the heat flow through the wall, the temperatures of the air both inside and outside the study room, at the speed of the internal air (by placing a microclimatic control unit in the central position of the study room), and finally the surface temperature of the floor in the area near the microclimatic control unit. The uncertainty related to the measurement performed on the case study is equal to ±10 % (Evangelisti et al., 2022).

The data recorded allowed the study room to be characterized from a thermal point of view and made it possible to evaluate the equivalent thermal properties of the multilayer wall under study by coupling the simulations conducted with COMSOL Multiphysics software (COMSOL) on the experimental measurements (Evangelisti et al., 2022). By assimilating the multilayer wall to an "equivalent homogeneous wall" (Evangelisti et al., 2018.), thanks to a methodology already applied in several literature studies, its "equivalent thermophysical properties" were determined, thus obtaining a further set of data called "SOS" (Evangelisti et al., 2018; Gori et al., 2016).

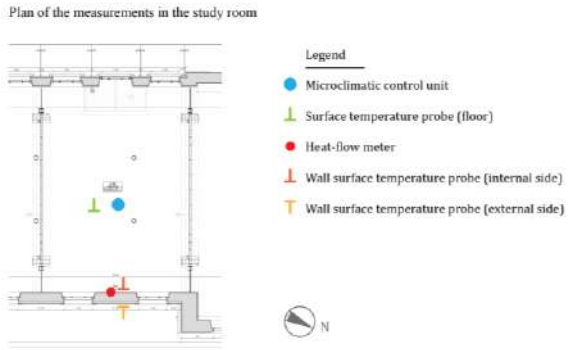

Fig. 3 – Plan of the study room with the measurement scheme of the instruments used in the experimental campaign

The main objective of this work is to show the potential of CFD numerical models for quantifying the incidence of different thermophysical characteristics on internal thermal comfort conditions in buildings with high inertia wall in different natural ventilation scenarios.

Figs. 4 and 5 show the air temperature trend (considering the average in the potentially occupied zone), the mean radiant temperature and the operative temperature for the three thermophysical sets with nocturnal and diurnal ventilation (24hV).

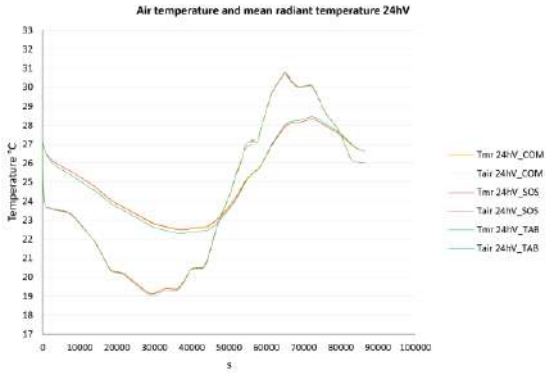

Fig. 4 – Air temperature and mean radiant temperature with diurnal and nocturnal ventilation (24hV)

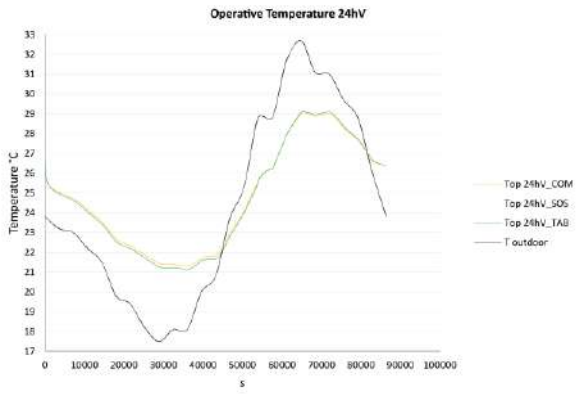

Fig. 5 – Operative temperature with diurnal and nocturnal ventilation (24hV)

In Figs. 6 and 7, the results for the three thermophysical sets with only nocturnal ventilation (10hV) are shown.

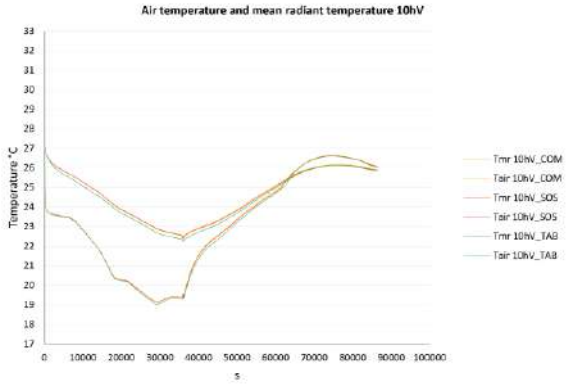

Fig. 6 – Air temperature and mean radiant temperature with only nocturnal ventilation (10hV)

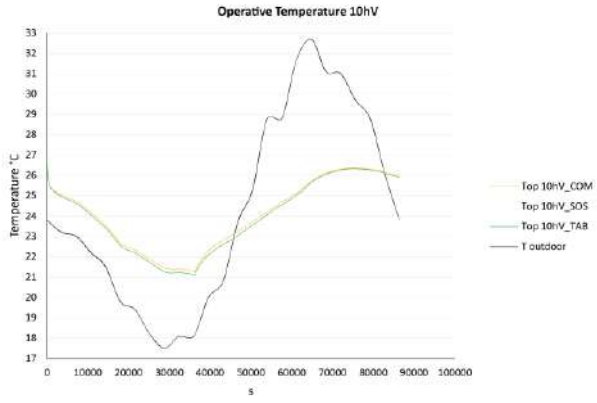

Fig. 7 – Operative temperature with only nocturnal ventilation (10hV)

In Figs. 8 and 9, the results for the three thermophysical sets without ventilation (NoV) are shown.

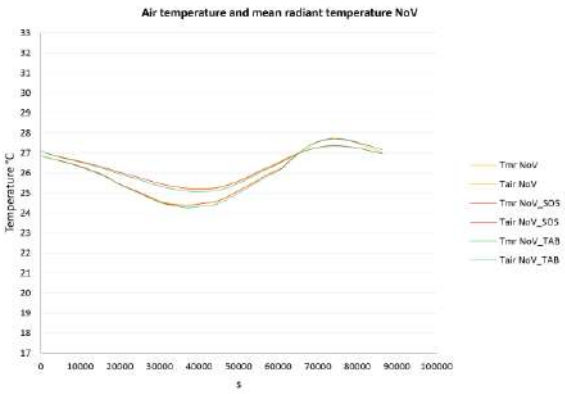

Fig. 8 – Air temperature and mean radiant temperature without ventilation (NoV)

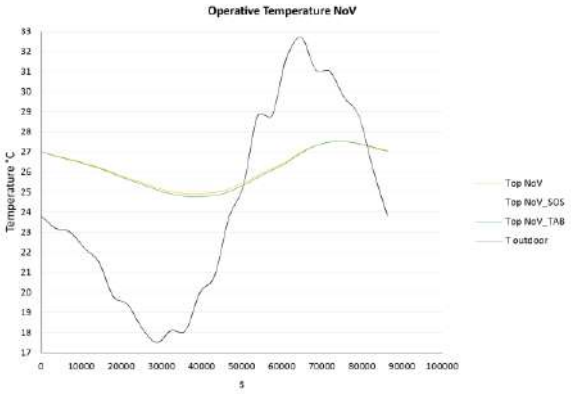

Fig. 9 – Operative temperature without ventilation (NoV)

Finally, Figs. 10, 11 and 12 show, for each ventilation scenario, the differences found between the results of the simulations, using the three sets of thermophysical parameters. The figures show the maximum, minimum and average difference of the mean radiant temperature (Tmr), the air temperature in the potentially occupied zone (Tair), and the operative temperature (Top).

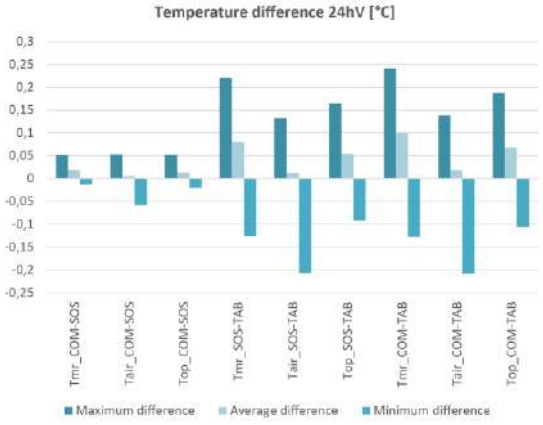

Fig. 10 – Temperature difference between thermophysical parameters sets with diurnal and nocturnal ventilation (24hV)

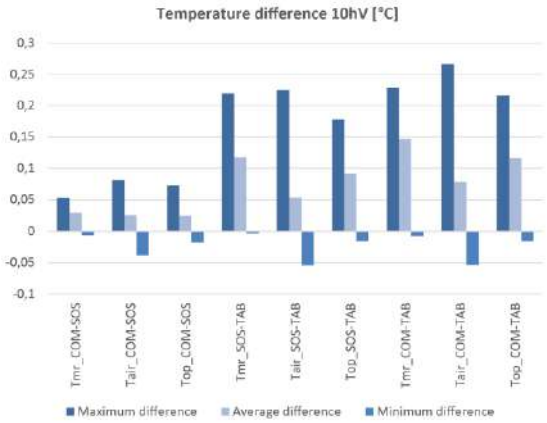

Fig. 11 – Temperature difference with only nocturnal ventilation (10hV)

By comparing temperature differences, we deduce that, in the three cases, although the parameter sets are different, their impact on internal condition is not so incisive.

It is interesting to note that the COM and SOS sets have more similar trends than the TAB set. Since the COM and SOS sets have more similar values of heat capacity while the SOS and TAB sets have more similar values of conductivity, it can be deduced that, in buildings with high thermal inertia under natural ventilation scenarios, the heat capacity value of the walls has a greater impact, in terms of internal comfort, than the thermal conductivity.

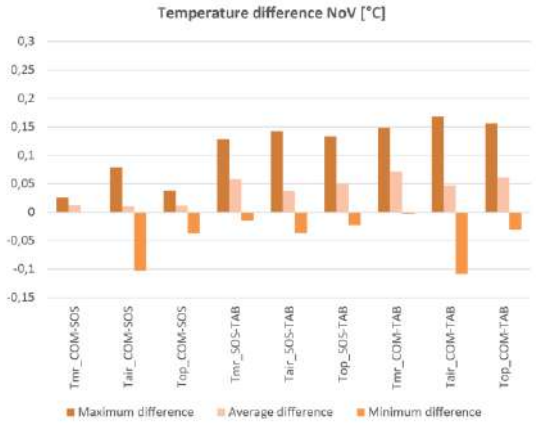

Fig. 12 – Temperature difference without ventilation (NoV)

This concept is reinforced by the fact that the NoV profile (without ventilation) is the one that reports the lowest differences between the three sets of thermophysical parameters.

3. Conclusions

In buildings characterized by high thermal masses, employing passive and hybrid strategies based on natural ventilation and nocturnal thermal mass precooling can be a critical issue for internal comfort and energy saving. With the aim of verifying whether the use of natural ventilation can be a practice of use to achieve energy saving and natural comfort, this work took a university building (in the city of Rome) characterized by high thermal capacity as a case study.

Different CFD numerical models were carried out to quantify the cooling effects and internal thermal comfort of different thermophysical parameters assigned to the walls and different natural ventilation scenarios (both nocturnal and diurnal).

It is worth noting that, when comparing the temperature differences among the three cases analyzed, although they have different thermophysical parameters, their impact on internal condition is not significant. Starting from the characteristics of the parameters sets considered, it can be observed that the internal comfort of buildings characterized by high thermal inertia, under natural ventilation conditions, are more influenced by the heat capacity value than by the thermal conductivity.

References

Bay, E., A. Martínez-Molina, I. Tort-Ausina, S. Cho, and J. L. Vivancos. 2016. "Energy Efficiency and Thermal Comfort in Historic Buildings: A Review". *Energy and Buildings* 61: 70-85. doi: https://doi.org/10.1016/j.rser.2016.03.018

Bencs, L., Z. Spolnik, D. Limpens-Neilen, H. L. Schellen, B. A. H. G Jutte, and R. Van Grieken. 2007. "Comparison of hot-air and low-radiant pew heating systems on the distribution and transport of gaseous air pollutants in the mountain church of Rocca Pietore from artwork conservation points of view". *Journal of Cultural Heritage* 8: 264–271. doi: https://doi.org/10.1016/j.culher.2007.05.001

Bratasz, Ł., R. Kozłowski, D. Camuffo, and E. Pagan. 2007. "Impact of indoor heating on painted wood monitoring the altar piece in the

church of santa maria Maddalena in rocca pietore, Italy". *Studies in Conservation* 52(3): 199–210. doi: https://doi.org/10.1179/sic.2007.52.3.199

COMSOL, Multiphysics 4.4, http://www.comsol.com

Ersoch, G. *Roma: il mattatoio e mercato del bestiame costruiti dal comune negli anni 1888-1891: descrizione e disegni, con progetto e direzione di Gioacchino Ersoch, Roma, 1891*.

Evangelisti, L., R. De Lieto Vollaro, and F. Asdrubali. 2022. "On the equivalent thermo-physical properties for modeling building walls with unknown stratigraphy". *Energy* 238: 121679. doi: https://doi.org/10.1016/j.energy.2021.121679

Evangelisti, L., C. Guattari, and F. Asdrubali. 2018. "Influence of heating systems on thermal transmittance evaluations: Simulations, experimental measurements and data post-processing". *Energy and Buildings* 168: 180-190. doi: https://doi.org/10.1016/j.enbuild.2018.03.032

Evangelisti, L., C. Guattari, P. Gori, and F. Asdrubali. 2018. "Assessment of equivalent thermal properties of multilayer building walls coupling simulations and experimental measurements". *Building and Environment* 127: 77–85. doi: https://doi.org/10.1016/j.buildenv.2017.10.038

Evangelisti, L., A. Scorza, R. De Lieto Vollaro, and S. A. Sciuto. 2022. "Comparison between Heat Flow Meter (HFM) and Thermometric (THM) Method for Building Wall Thermal Characterization: Latest Advances and Critical Review". *Sustainability* 14(2): 693. doi: https://doi.org/10.3390/su14020693

Gori, P., C. Guattari, L. Evangelisti, and F. Asdrubali. 2016. "Design criteria for improving insulation effectiveness of multilayer walls". *International Journal of Heat and Mass Transfer* 103: 349 – 3591. doi: https://doi.org/10.1016/j.ijheatmasstransfer.2016.07.077

Insula Architettura e Ingegneria, "Ex-Mattatoio al Testaccio, Roma, riconversione del Padiglione 2B in aulee universitarie", The Plan Webzine - Search engine for architecture. Available at: http://www.theplan.it/webzine/architettura-italiana/ex-mattatoio-al-testaccio-roma

Tabula, https://episcope.eu/fileadmin/tabula/public/docs/brochure/IT_TABULA_TypologyBrochure

Vitale, V., and G. Salerno. 2017. "A numerical prediction of the passive cooling effects on thermal comfort for a historical building in Rome". *Energy and Buildings* 157: 1-10. doi: https://doi.org/10.1016/j.enbuild.2017.06.049

Calibration of the Energy Simulation Model of a Library with a Meta-Model-Based Optimization Approach

Maja Danovska – University of Trento, Italy – maja.danovska@unitn.it
Alessandro Prada – University of Trento, Italy – alessandro.prada@unitn.it
Paolo Baggio – University of Trento, Italy – paolo.baggio@unitn.it

Abstract

Building simulations play a fundamental role both in applications like the design of new constructions and the optimization of building operation and control. This is quite relevant in the current energy framework, in which the energy consumption of buildings has increased over past decades. The reliability of the results' model does not depend only on the model itself, like the mathematical expression or the resolution process, but it is also related to the uncertainty that those parameters involve. This can cause discrepancies between the simulated and the real behavior of the building, causing a deviation from the expected one of the performance of a building. Hence, the calibration procedure of the model is a necessary process which allows more accurate results to be obtained and predictions that are closer to the real behavior of the building to be made, minimizing the discrepancy between predicted and actual performance by changing the values of the simulation parameters. When it comes to calibration of simulation models, many approaches are available in the literature, comprising manual and iterative ones, graphic comparative procedures, techniques based on specific tests, and many others. Among all possible approaches, optimization-based calibration is the most widely adopted in model calibration. However, this approach, which is usually based on evolutionary algorithms, has the disadvantage that it requires many expensive simulations to be run, especially when the number of parameters to be calibrated is high. This issue can be overcome by a preliminary sensitivity analysis that reduces the number of parameters to be calibrated and by an efficient optimization algorithm. For this reason, this work proposes a framework based on a sensitivity analysis designed to identify the most significant parameters separately on the energy budgets and other monitored environmental variables. The proposed calibration procedure is based on functional approximation models, which greatly increases the efficiency of the optimization algorithm. The case study is a university library placed in the municipality of Trento, Italy. The building was monitored in terms of indoor carbon dioxide, indoor temperature, and relative humidity. Results show how successful the proposed approach is in reducing the computational time required for calibration, especially when considering models with a high degree of complexity.

1. Introduction

Energy demand from buildings is still considered a significant share of the global energy consumptions, i.e., 36 % of the total energy demand (Santamouris & Vasilakopoulou, 2021). This means that measures in this sector must be taken to considerably reduce overall energy consumption. In this context, dynamic simulations of buildings are an extremely powerful tool, which can help in achieving such goals, not only from the point of view of assessing the energy efficiency of new constructions, but also for optimizing building operation and control. Nevertheless, dynamic and detailed models require a high number of both input data and parameters for describing the whole system. As reviewed by Chong et al. (2021), the building model requires input data which describe the physical model. If not directly measured or known, as in the case of new constructions, parameters must be assumed by the user. This assumption procedure brings uncertainty that has an unavoidable impact on the simulation output. Authors such as Karlsson et al. (2007), Scofield (2009) and Turner & Frankel (2008) reported how simulation results can differ significantly from monitored data. Hence, to adopt energy models that are as accu-

rate as possible, calibration procedures are becoming increasingly fundamental and are an unavoidable step in building simulation for closely matching simulated building behavior to reality (Coakley et al., 2014). When it comes to calibration of simulation models, many approaches are available in the literature, comprising manual and iterative ones, graphical comparative procedures, techniques based on specific tests and many others (Chong et al., 2021). Among all possible approaches, the optimization-based calibration is the most widely adopted in model calibration. However, this approach, which is usually based on evolutionary algorithms, has the disadvantage that it requires many expensive simulations to be run, especially when the number of parameters to be calibrated is high, as in detailed models. This issue can be overcome by a preliminary sensitivity analysis that reduces the number of parameters to be calibrated, and by an efficient optimization algorithm.

Thus, this research work proposes a framework based on a sensitivity analysis designed to identify the most significant parameters separately on the energy budgets, other monitored environmental variables and, after that, considering all the variables together. Then, a calibration procedure is performed based on functional approximation models, which greatly increases the efficiency of the optimization algorithm. The Root Mean Square Error (RMSE) was chosen as statistical indicator to be minimized, instead of the monitored variables. The case study is a university library located in the municipality of Trento, Italy. The building is constantly monitored in terms of indoor temperature (°C), relative humidity (%) and indoor carbon dioxide (ppm). The results show how successful the proposed approach is in reducing the computational time required for calibration, especially when considering models with a high degree of complexity.

2. Methodology

2.1 Monitored Case Study

To test the proposed calibration procedure, a real building was considered, specifically, a university library placed in Mesiano (46° 3' N, 11° 8' N), municipality of Trento, Italy.

Fig. 1 – Case study: University library *BUM*, University of Trento, Trento (Italy). The building was opened in 2021. Picture retrieved from http://www.weberwinterle.com

The construction was built in 2020, and it has a total floor area of 1533 m^2. It is a three-storey building composed of an underground basement , used as an archive and technical room, and two upper floors connected by internal stairs, where rooms are mainly used as offices and lecture halls. The generation system is composed of two heat pumps, one air-to-water and a ground source one. The hydronic heating/cooling system is based on a radiant floor panel system for the two upper floors, and a fan-coil system for the basement. The building is supplied with an air mechanical ventilation system coupled with an Air Handling Unit *AHU*, except for the basement.

Sensors are installed all over the library with the aim of monitoring the indoor conditions in terms of temperature *T*, relative humidity *RH*, and levels of CO_2 in each ambient. Additional sensors are also placed on the plant side (i.e., heat pump system and the Air Handling Unit). Since its construction, the building has been constantly monitored by means of the *Schneider Building Automation Server.* Fig. 2 shows the positions of the data loggers in the library. Red sensors record indoor temperature and relative humidity, and CO_2 levels, while the green ones only record the temperature. Data were recorded with time steps of 15 min. Table 1 lists the different sensors and the names of the different

zones.

Fig. 2 – Sensor locations with their identification numbers

Table 1 – Sensor list and their positioning

Sensor	Monitored quantity	Zone	Floor
1	T, RH, CO_2	Reading hall vs. Stairs	1st
2	T, RH, CO_2	Reading hall vs. Office	1st
3	T, RH, CO_2	Wardrobe	1st
4	T, RH, CO_2	Architecture hall	1st
5	T, RH, CO_2	Reading hall vs. Offices	GF
6	T, RH, CO_2	Reading hall vs. Toilets	GF
7	T, RH, CO_2	Architecture hall	GF
8	T, RH, CO_2	Conference room	GF
9	T, RH, CO_2	Archive	B
10	T	Office	1st
11	T	Meeting room	GF
12	T	Office 1	GF
13	T	Office 2	GF

2.2 Building Simulation Model

TRNSYS® (v18) software was adopted to model the building's performance.

At first, the geometry of the model was created through the TRNBUILD application in the SketchUp environment (https://www.sketchup.com/it), and then it was imported into the program through Multizone Building Modeling (*Type56*), where each thermal zone (35 in total) was defined in this subroutine, thermo-physical properties of materials adopted in the opaque components, glazing properties and so on were defined. In particular, those data were retrieved from technical datasheets of the construction company.

Weather data, in terms of external total solar radiation (W m^{-2}), external air temperature (°C), external air relative humidity (%) and wind speed (m s^{-1}), were taken from the weather station at Trento Laste (https://www.meteotrentino.it) with time steps of 1 h.

Solar radiation for each external tilted surface was modeled with the Perez Model (Perez et al., 1990) through *Type16*. The ground temperature was modeled with *Type77*. The external convective heat transfer coefficient h_{ce} was defined according to the Standard EN ISO 6946:2017 (CEN, 2017). Air infiltrations were calculated in accordance with the empirical method suggested by the ASHRAE K_1, K_2 and K_3 model (ASHRAE Handbook, 1989). Since the building is a new one, coefficients can be assumed equal to $K_1 = 0.1$, $K_2 = 0.011$ and $K_3 = 0.034$ (for tight constructions).

The light power density was taken from technical documentations and differentiated for each thermal zone. Three levels were considered, which are 20, 15 and 10 W m^{-2}, of which 60 % was accounted as thermal gain directly affecting the air node thermal balance. As regards thermal gains generated by the equipment, 7, 5 and 4 W m^{-2} power density levels were considered according to the ASHRAE Handbook (ASHRAE, 1989).

Schedules of lights, as well as of the external shading devices, were imported from an external file through *Type9*. These data come from the monitoring, since the building is also equipped with sensors giving information about the state of the lighting power in percentage terms and percentage value of the window shadings.

Since detailed occupancy schedules were not available, occupancy was assumed to follow Eq. (1).

$$occupancy_i = max\ people_i \cdot Schedule_i \quad (1)$$

The maximum number of people for each thermal zone was obtained with the help of on-site inspection by counting the number of available chairs, while the schedule of the reading hall, a value ranging from 0 to 1, was determined by analyzing the weekly occupancy rate supplied by Google (see Fig. 3) and available because of glocalization. As regards offices, a different schedule was considered.

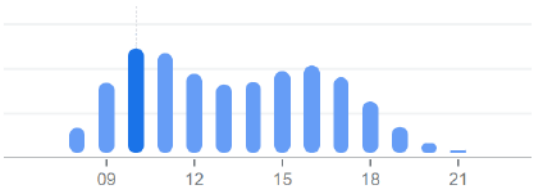

Fig. 3 – Example of occupancy rate of the library adopted as schedule for the reading hall. Profile retrieved from Google. Values range from 0 to 1. X-axis shows the time in hours

The Air Handling Unit was modeled as a black box, taking as input the monitored air temperature T_{supply} and relative humidity RH_{supply} of the supply air. In this way, composing devices were neglected. In the period monitored, the unit was working in *all-air* configuration due to COVID restrictions, thus no air recirculation was performed, and air was taken completely from the outside. Data about the supply air were passed through *Type9*. The air volume flow rate *VFR* introduced in each ventilated zone was defined as:

$$VFR = VFR_{design} \cdot Schedule_{VENT} \cdot Rg_{VENT} \quad (2)$$

where the design volume flow rate was taken from technical documentations, and the AHU schedule (expressed from 0 to 1) and the regulation of the supply ventilator expressed in percentage terms were retrieved from monitored data (through *Type9*).

The Radiant panels, adopted for both heating and cooling, were modeled through *Type1231 – Radiator* (TESS Libs 17 – HVAC Library Mathematical Reference). The general expression of the specific thermal output for a general radiator was characterized for the radiant floor system by setting a value of 1 for the exponent linked to the difference between surface temperature and air temperature. And a value of 0.2 was considered for calculating the altitude correction factor. Inlet water temperature to the radiant floor system was taken from monitored data (*Type9*) and the water mass flow rate expressed in kg hr^{-1} was defined as the product of the design water flow rate for each zone (retrieved from technical documentation) and the monitored signal relative to the functioning of the radiant floor system in that zone.

The evolution profiles of CO_2 concentrations were simulated as well. The levels of CO_2 in a room depend on the occupancy rate in that volume, the ventilation rate, and on the infiltrations. The model considered for the evolution in time of the indoor concentration accounts for the maximum value, at each time step, between the outdoor carbon dioxide $CO_{2,ext}$, considered equal to 400 ppm, and the expression in Eq. (3).

$$CO_{2\{i,m\}} = CO_{2\{i,m-1\}} + \{ INF \cdot (CO_{2,ext} - CO_{2\{i,m-1\}}) + \dots$$
$$\dots + VFR_i/V_i \cdot (CO_{2,ext} - CO_{2\{i,m-1\}}) + \dots$$
$$\dots + (k_{gen} \cdot 10^6 \cdot occupancy)/ V_i \cdot \} \cdot \Delta t \quad (3)$$

The generation term is equal to 0.017568 m^3 hr^{-1} $person^{-1}$. The three terms correspond to the infiltrations, ventilation system and the occupancy, respectively.

Beyond the thermal and the occupancy balance, also the moisture one was implemented by considering the moisture production of the people according to the ASHRAE Handbook (ASHRAE, 2017), where two different levels of activity were set, both sedentary and active.

2.3 Sensitivity Analysis

To identify the most dominant parameters affecting the model's outputs, a preliminary sensitivity analysis was performed. In particular, the methodology adopted is the one proposed by Sohier et al. (2014), which is a modified version of the qualitative *Morris method*, in which the significance threshold depends on the parameter with the highest elementary factor. This modification showed improvements in the estimation of the factors' impact with respect to the original one. The sensitivity analysis was applied separately to the three balances, and in particular:

(i) at first, on the thermal balance, by considering as objective function the RMSE for the indoor temperature *T*.

(ii) second, on the humidity balance, by considering the RMSE for the indoor absolute humidity *x*.

(iii) at the end, on the CO_2 balance, by considering the RMSE for the CO_2 concentration levels.

For each case, every parameter taken into consideration was varied in a specific range, then simula-

tions were run and the magnitude of the variation of the Root Mean Square Error RMSE, expressed in Eq. (4), was assessed.

$$RMSE_i = \sqrt{\frac{\sum_{m=1}^{N}\left(y_{i,m}^{mis} - y_{i,m}^{sim}\right)^2}{N-1}} \quad (4)$$

In particular, the *RMSE* relative to the individual variable, i.e., temperature, relative humidity, and CO_2 concentration, was calculated for each monitored zone and then averaged using the corresponding volume. The method was implemented in the MATLAB® environment, which allowed automatic link to the software TRNSYS.

2.4 Calibration Process

After the preliminary parameter screening, the calibration procedure was addressed. In particular, a meta-models-based optimization approach was adopted, which is described and discussed in detail in the work of Prada et al. (2018). Meta-models are, substantially, surrogate models that emulate building dynamics. Hence, instead of optimizing the initial building simulation code directly, an explicit expression of the code is constructed starting from the building simulation results and used together with the Genetic Algorithm *GA* for the optimization procedure. The main advantage of such meta-models is to filter out the variable domain regions with no eligible Pareto solutions, as stated by Prada et al. (2018). In particular, in this research, the surrogate model implemented is called Multivariate Adaptive Regression Splines (*MARS*) meta-model and it is based on piecewise cubic splines, which are adopted to approximate the cost function.

Such an approach aims at overcoming some issues related to the commonly adopted evolutionary algorithms, whose procedure is extremely time-consuming. The calibration was based on three monitored quantities, which are, firstly, the indoor air temperature of each zone, secondly, the absolute humidity for each ambient, except those related to sensors 10 to 13 (see Fig. 2) and, thirdly, regarding the CO_2 variable, all zones equipped with a CO_2 sensor were considered, except for the conference room and the basement (i.e., sensors 8 and 9), where the random component of the occupancy schedule was extremely significant and, thus, neglected. The objective function set for minimization is the RMSE (Eq. 4), defined separately for each monitored quantity, i.e., temperature, absolute humidity and CO_2, and normalized considering the initial case. Simulations were run considering a time-step of 15 min and a period from the 6th of November 2011 to the 12th of November 2011 (heating period). As for the sensitivity analysis, the procedure was implemented in the MATLAB® environment, which allowed an automatic link to the software TRNSYS.

3. Results and Discussion

In this section, results of the sensitivity analysis, as well as of the calibration procedure, are shown and discussed together. For instance, Table 2 shows the dominant parameters most affecting the model's output as a result of the sensitivity analysis. In particular, for each parameter, the magnitude of the influence (i.e., with numbers from 1 to 12) on each balance of temperature, of absolute humidity and of the CO_2 is specified. The term N/A is adopted when the model is not sensitive to that parameter.

The parameters most influencing the temperature variable are mainly related to material properties, i.e., specific heat capacity, infiltration rates and gains related to lights and equipment. However, gains related to occupancy and the volume flow rate of the ventilation system also have an impact on the temperature's output, as seen in Table 2. In terms of absolute humidity, the parameters affecting the balance the most are the occupancy rates and the volume flow rates of the environments where the ventilation system is installed. The same stands for the CO_2 balance, considering, in addition, the effect of the external levels of CO_2. Since parameters from no. 1 to no. 7 affect only the temperature, their calibration was performed only on the thermal balance and by considering a single objective function based on the indoor air temperature. On the other hand, the other parameters from no. 8 – 15 that have an influence either on absolute

humidity, CO_2 or both, were adjusted according to a two-objective function calibration, based on such variables. In this way, the calibration procedure was decoupled. As regards parameters related to occupancy rate and volume flow rates, which influence not only the absolute humidity and CO_2, but also the temperature (e.g., no. 8, 9, 10, 12 and 13), these were accounted for in the two-objective function calibration, since they are more dominant on such balances than on the thermal one. Once parameters no. 8, 9, 10, 12 and 13 were calibrated, they were changed in the thermal balance, and the calibration of the temperature was performed. Table 2 shows the calibration ranges of each parameter, where a variation of ± 20 % from the initial value was considered.

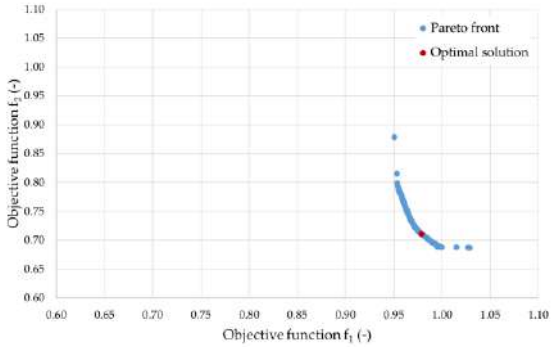

Fig. 4 – Pareto front (blue data) with the combinations of the objective functions f_1 and f_2 related to the absolute humidity AU (kg kg^{-1}) and CO_2 (ppm), respectively. The optimal solution is highlighted in red

Fig. 4 shows results of the optimization-based calibration on the absolute humidity and the CO_2, as combinations of the objective functions f_1 and f_2 expressed as the ratio between the current RMSE and the RMSE related to the initial case, both for the AU and the CO_2, respectively (see Eq. 5).

$$f_{1\ or\ 2} = \frac{RMSE_{AU\ or\ CO_2}}{RMSE_{0\ AU\ or\ CO_2}} \quad (5)$$

Results are placed on the Pareto front, as depicted in blue. By assessing the minimum distance of each solution from the origin, the optimal solution was selected and highlighted in red, as shown in Fig. 4. In particular, with this solution, only the CO_2 concentration was improved, instead of the absolute humidity, for instance, f_1 = 0.98 and f_2 = 0.71 (improvements equal to 2 % and 9 % compared with the initial case, respectively). This is because the prediction of humidity in environments was modeled with a simplified approach, which neglects some mechanisms like moisture buffering due to the building's opaque components. The values of the calibrated parameters related to this optimal solution are summarized in Table 2 from no. 8 to no. 15. Besides values of occupancy and volume flow rates of the ventilation system, the parameter which shows remarkable change with respect to the initial case is the external CO_2 concentration, which was not measured but assumed, and whose value influences the indoor CO_2 balance to a great extent, according to Eq. (3).

Results of the calibration on the thermal balance are reported in Table 2 from parameters no. 1 to 7, which refer to the minimum value of the objective function as expressed in Eq. 5, but only in terms of temperature. The obtained temperature objective function was equal to 0.90, which means a 10 % improvement compared with the initial case. In particular, parameters related to air infiltrations slightly decrease from the initial values, confirming the hypothesis of a highly airtight building, typical of new constructions.

Table 3 shows the computational effort of each calibration procedure (in h), the percentage improvement of the model with respect to the initial case expressed as 1- *f* and the calibration accuracy in terms of RMSE for each variable. In particular, three cases were reported: the initial one, the case after the decoupled calibration composed of *Cal 1* and *Cal 2*, which considered the joined AU and CO_2, and T, respectively. And, at the end, a third case based on a standard calibration procedure (*Cal 3*) taken only as a comparison. Specifically, the calibration considered all parameters of Table 2 and three objective functions for every variable implemented together. The computational time necessary for the decoupled calibration is about 32 h considering both Cal_1 and Cal_2. Clearly, Cal_1 is remarkably more time-consuming than Cal_2 (i.e., 30.8 h vs 1.2 h) because of the two objective functions. The improvement obtained after the decoupled procedure with respect to the initial case is 2 % for the absolute humidity, 29 % for the CO_2 and 10 % for the temperature. In terms of RMSE, it can be noticed that the variations with the initial case

are limited especially in terms of temperature and absolute humidity prediction. A more marked reduction in the RMSE(CO_2) is evident, i.e., from 88.3 ppm to 61.6 ppm. This is because the model was already robust at the beginning thanks to the reliability of the input data and parameters - a typical condition of new constructions. As regards the standard case, results in Table 3 show that the calibration procedure requires about 9 % more time than the decoupled case (i.e., 35 h vs 32 h) to get a comparable accuracy, or even slightly lower, when considering the CO_2 prediction. As before, the improvement is not greatly higher than the initial case because of the goodness of the initial model.

Table 2 – Parameters which influence the most the models' output obtained from the sensitivity analysis

Category	No.	Parameter	T	AU	CO2	Values range	Calibrated value
Material properties	1	*c* reinforced concrete [kJ kg^{-1} K^{-1}]	3rd	N/A	N/A	[0.704-1.056]	1.03
	2	*c* concrete - heated floor [kJ kg^{-1} K^{-1}]	11th	N/A	N/A	[0.704-1.056]	0.95
Infiltration rate	3	*K1* – INF [-]	5th	N/A	N/A	[0.08-0.12]	0.08
	4	*K2* – INF [-]	2nd	N/A	N/A	[0.088-0.0132]	0.009
Gains from lights and equipment	5	Light power density -1st level [kJ hr^{-1} m^{-2}]	1st	N/A	N/A	[58-86]	59
	6	Light power density – 2nd level [kJ hr^{-1} m^{-2}]	9th	N/A	N/A	[43-65]	63
	7	Equipment power density – 1st level [kJ hr^{-1} m^{-2}]	8th	N/A	N/A	[20-30]	20
Gains from people	8	Max *PPL* Reading hall vs. Stairs 1st [-]	4th	2nd	2nd	[50-74]	70
	9	Max *PPL* Reading hall vs. Offices 1st [-]	6th	1st	N/A	[6-10]	6
	10	Max *PPL* Reading hall vs. Offices GF [-]	12th	4th	N/A	[26-30]	26
	11	Max *PPL* Reading hall vs. Toilet GF [-]	N/A	N/A	3rd	[32-48]	32
Ventilation	12	*VFR* Reading hall vs. Stairs 1st [m3 hr^{-1}]	7th	3rd	N/A	[888-1332]	1024
	13	*VFR* Reading hall vs. Offices GF [m3 hr^{-1}]	10th	5th	5th	[435-653]	645
	14	*VFR* Reading hall vs. Toilet GF [m3 hr^{-1}]	N/A	N/A	4th	[544-816]	773
External environmental conditions	15	$CO_{2,ext}$ [ppm]	N/A	N/A	1st	[200-600]	514

Table 3 – Computational time, improvement and accuracy of the decoupled and standard calibration approach

	Initial case	Decoupled			Standard
		Cal 1		*Cal 2*	*Cal 3*
Calibration Time*	-	30.8 h		1.2 h	35 h
Improvement 1-*f*	-	2 % (AU)	29 % (CO_2)	10 % (T)	5 % (AU) 28 % (CO_2) 7 % (T)
$RMSE_T$	0.6 °C	0.6 °C			0.6 °C
$RMSE_{AU}$	0.3 g kg^{-1}	0.3 g kg^{-1}			0.3 g kg^{-1}
$RMSE_{CO2}$	88.3 ppm	61.6 ppm			63.6 ppm

* Processor: AMD Ryzen 9 5950X 16-Core – 3.40 GHz; Installed RAM: 32.0 GB.

4. Conclusions

In this work, a calibration of an energy simulation model based on the meta-model optimization approach was tested on a real case study. The methodology comprised a first sensitivity analysis designed to identify the most significant parameters on the energy budgets and other monitored environmental variables separately. Then, a calibration procedure based on functional approximation models was applied separately on the monitored variables, which are temperature, humidity and CO_2. The case study is a university library placed in the municipality of Trento, Italy. The building was monitored in terms of indoor carbon dioxide, indoor temperature, and relative humidity. Results show how the decoupled approach increases the efficiency of the optimization algorithm, especially in energy simulation codes with a high degree of complexity, thus with a high number of parameters. For instance, to obtain the same, or even slightly greater, accuracy than a standard calibration approach, the computational time required for this decoupled calibration is 9 % less than a standard approach, where no differentiation among monitored variables is performed. Hence, the adoption of the *MARS* model in calibration procedures of building simulation models can provide a contribution towards the optimization of both building refurbishment design, as well as building operation and control.

Nomenclature

Symbols

ACH	Air Changes per Hour (h^{-1})
AHU	Air Handing Unit
B	Basement
c	Specific heat capacity (kJ kg^{-1} K^{-1})
CO_2	Carbon Dioxide (ppm)
Δt	Simulation time step (hr)
GA	Genetic Algorithm
GF	Ground Floor
H/C	Heating/Cooling
h_{ce}	External convective heat transfer coefficient (kJ hr^{-1} m^{-2} K^{-1})
INF	Infiltration rate (h^{-1})
λ	Thermal conductivity (W m^{-1} K^{-1})
N	Number of simulation time steps
k_{gen}	Generation rate (m3 hr^{-1} $person^{-1}$)
PPL	People
Rg	Regulation
RH	Relative Humidity (%)
RMSE	Root Mean Square Error
T	Indoor air temperature (°C)
X	Absolute humidity (kg kg^{-1})
Y	Variable (either T, RH or CO_2)
VFR	Volume Flow Rate (m^3 hr^{-1})

Subscripts/Superscripts

ext	External
i	Of the ith thermal zone
mis	Measured
m	Of the current time step (-)
m-1	Of the previous time step (-)
sim	Simulated
supply	Of the supply air of the AHU
VENT	Of the supply ventilator

Acknowledgments

This research was funded by MIUR – the Italian Ministry of Education, Universities and Research (PRIN 2017) grant number 2017KAAECT in the framework of FLEXHEAT project "The energy FLEXibility of enhanced HEAT pumps for the next generation of sustainable buildings".

References

ASHRAE. 1989. *Handbook of Fundamentals: Ventilation and Infiltration*, Chapter 22.

ASHRAE. 2017. *Handbook Fundamentals, Nonresidential cooling and heating load calculations*, Chapter 18: 18.1-18.62.

Chong, A., Y. Gu, and H. Jia. 2021. "Calibrating building energy simulation models: A review of the basics to guide future work." *Energy and Buildings* 253: 111533. doi: https://doi.org/10.1016/j.enbuild.2021.111533

Coakley, D., P. Raftery, and M. Keane. 2014. "A review of methods to match building energy

simulation models to measured data." *Renewable and Sustainable Energy Reviews* 37: 123-141. doi: https://doi.org/10.1016/j.rser.2014.05.007

CEN European committee for Standardization. 2017. *EN 6946. Building components and building elements — Thermal resistance and thermal transmittance — Calculation methods.*

Karlsson, F., P. Rohdin, and M.-L. Persson. 2007. "Measured and predicted energy demand of a low energy building: important aspects when using Building Energy Simulation." *Building Services Engineering Research and Technology* 28(3): 223–235. doi: https://doi.org/10.1177/0143624407077393

Perez, R., P. Ineichen, R. Seals, J. Michalsky, and P. Stewart. 1990. "Modeling daylight availability and irradiance components from direct and global irradiance." *Solar Energy* 44:271–89. doi: https://doi.org/10.1016/0038-092X(90)90055-H

Prada, A., A. Gasparella, and P. Baggio. 2018. "On the performance of meta-models in building design optimization." *Applied Energy* 225: 814-826. doi: https://doi.org/10.1016/j.apenergy.2018.04.129

Santamouris, M., and K. Vasilakopoulou. 2021. "Present and future energy consumption of buildings: Challenges and opportunities towards decarbonization." *e-Prime-Advances in Electrical Engineering, Electronics and Energy* 1: 100002. doi: https://doi.org/10.1016/j.prime.2021.100002

Scofield, J. H. 2009. "Do LEED-certified buildings save energy? Not really…" *Energy and Buildings* 41(12): 1386-1390. doi: https://doi.org/10.1016/j.enbuild.2009.08.006

Sohier, H., J.-P. Farges, and H. Piet-Lahanier. 2014. "Improvement of the Representativity of the Morris Method for Air-Launch-to-Orbit Separation." In *IFAC Proceedings Volumes* 47(3): 7954-7959. doi: https://doi.org/10.3182/20140824-6-ZA-1003.01968

TESS Libs 17 – HVAC Library Mathematical Reference. Available online: http://www.trnsys.com/tess-libraries/

Turner, C., and M. Frankel. 2008. *Energy performance of LEED for new construction buildings*. New Buildings Institute, Washington, DC, US.

Development of a Detailed Model of Hybrid System Composed by Air-to-Water Heat Pump and Boiler

Erica Roccatello – University of Trento Italy – Erica.Roccatello@unitn.it
Alessandro Prada – University of Trento Italy – Alessandro.Prada@unitn.it
Marco Baratieri – Free University of Bozen-Bolzano, Italy – Marco.Baratieri@unibz.it
Paolo Baggio – University of Trento Italy – Paolo.Baggio@unitn.it

Abstract

Air-to-water heat pumps are one of the most promising and increasingly widespread solutions, despite some intrinsic drawbacks, such as their poor efficiency at low ambient temperatures and at high sink temperatures, e.g., in domestic hot water production. In this context, hybrid heat pump systems combining air-to-water heat pumps and boilers (HSs) have been proposed on the market, especially for the renovation of existing buildings, where high supply water temperatures are typically required. Even though HSs are off-the-shelf technology, the topic has recently gained interest in research. HSs consist of two generators, which must be designed with an integrated approach from the start. However, the performance improvement hinges on the availability of a detailed model able to accurately predict the HS performance. Most of the studies available in the literature use models based on performance maps that are not suitable for HS design. This study presents a new detailed model of a hybrid system, developed in the MATLAB environment. The model adopts a quasi-physical representation of the heat pump cycle and condensing boiler. The boiler model thermodynamically simulates the combustion process, using the Cantera solver and the Gri-Mech properties. The heat pump model simulates the thermodynamic cycle, using refrigerant properties obtained from CoolProp libraries. A detailed model for each main component of the system is developed. Component models are combined, thus allowing the user to consider the influence of single components or construction parameters on the overall HS performance. Individual component models were validated against software or performance data provided by manufacturers. The validation proved that the models of the single components can reproduce performance with high accuracy. Therefore, the model can be used for future studies involving HS design, to analyze the influence of construction choices on overall system efficiency.

1. Introduction

Hybrid systems (HSs) can be a promising solution for increasing the efficiency of heating systems, particularly for existing buildings that do not have as high levels of insulation as new buildings (Roccatello et al., 2022).

The way the two generators (boiler and heat pump) are combined is crucial for system efficiency. Therefore, the HS, consisting of two generators, must be designed with an integrated approach from the start. A detailed model of the system would be needed to study and develop a HS. This would allow the design of the individual components of the system to be optimized for their combination, to maximize the efficiency of the hybrid system under the chosen operating conditions.

Previous studies on the topic developed a HS model and used it to compare system performance with other solutions, e.g., monovalent systems with heat pump or boiler. Klein et al. (2014) applied a model of HS for simulating a building with different insulation levels, using TRNSYS software. They used a model of the hybrid system based on performance maps. Di Perna et al. (2015) adopted an experimentally derived HS model, for the comparison of HS performance with that of boiler or electric heaters. Bagarella et al. (2016) conducted simulations using TRNSYS to discuss the distribution between heat pump and boiler operation based on outdoor temperature. The HP model is based on the combination of performance map data for each component, while the evaporator was modeled using finned coil evaporator design software, which allows for estimation of the frost formation process on the evaporator. The boiler model ap-

plies numerical correlations for determination of the efficiency. Dongellini et al. (2021) analyzed the primary energy consumption due to the HS with different heat pump sizes. The model of the HS is based on performance data provided by manufacturers. Li & Du (2018) compared different hybrid system configurations by simulating system performance under certain operating conditions. They adopted a model based on performance maps for the heat pump, and an average efficiency for the boiler. Park et al. (2014) developed a detailed HP model, based on individual models of system components, and a boiler model based on experimental correlations.

The literature review shows that most of the hybrid system models are based on performance maps. These models, as already discussed, are well suited for application to building simulations, as they provide the real-life behavior of components already available on the market. However, they are not suitable to be used for a new design of the system itself, but rather to analyze the performance of a given system over a certain period of time.

The goal of the present work is to develop a semi-physical model of a HS. The model is primarily based on the physical laws describing the processes occurring in the individual components of the system.

The modeling involved the main components of the heat generators. The models of the individual components were combined into the overall model of the single generator. The HP and boiler models can be retrieved as subroutines from the overall HS model, which contains the hybrid system logic.

The heat pump and boiler model development are based on the currently most adopted systems in HSs. The heat pump considered for modeling is a modulating heat pump, equipped with a plate heat exchanger (HX) for the condenser, and a finned-coil HX for the evaporator. The boiler considered is a condensing, modulating, natural gas-fired boiler.

2. Methodology

The HS model consists of the logic that manages the interaction with the heating system – i.e., it determines whether a generator should operate and calculates the system setpoint – and decides which generator to operate based on the chosen control strategy. For a more detailed description of the logic of the HS model, the reader can refer to Roccatello et al. (2022). This paper presents a different type of HS model, in which the subroutines containing the heat pump and boiler models are not based on performance maps, but on semi-physical models of components. The generator models are developed as the union of the system components. The heat pump model is the combination of the component models of the air-refrigerant and water-refrigerant heat exchangers (evaporator and condenser), compressor, and expansion valve. The boiler is modeled as the union of the combustion chamber and the flue gas-water HX. Figs. 1 and 2 show the schematic of the heat pump and boiler models, respectively.

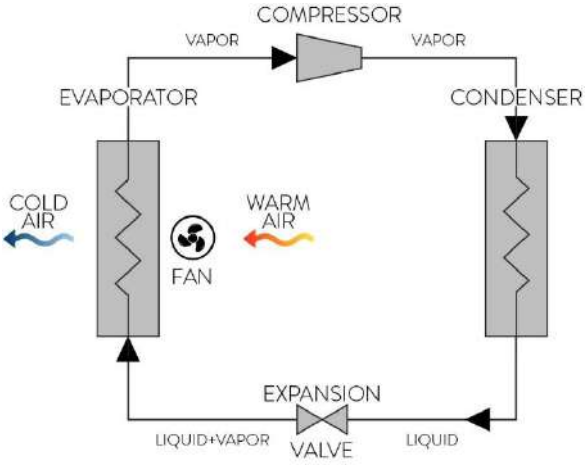

Fig. 1 – Schematic of heat pump model

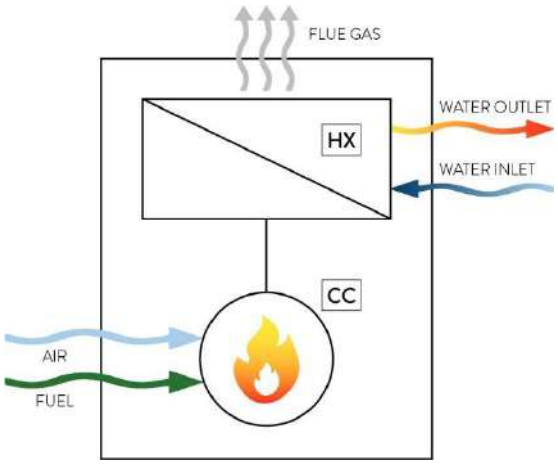

Fig. 2 – Schematic of boiler model

The following sections describe how the component models were developed, and subsequently combined, to generate the boiler and heat pump models.

2.1 Heat Pump Model

2.1.1 Condenser model

In this section, the heat transfer between refrigerant and water is modeled. The refrigerant exiting the compressor exchanges heat with water and undergoes condensation and subcooling. An example of a heat pump refrigerant cycle on a pressure/enthalpy diagram is shown in Fig. 3, in which the condensation process is highlighted.

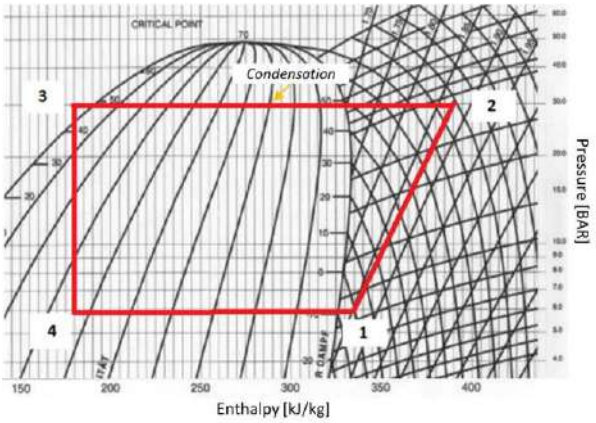

Fig. 3 – Condensation process represented on a pressure/enthalpy diagram

The condenser model refers to a plate HX, which is the most used type of exchanger for residential size heat pump systems.

Initially, a first guess of the value of the condensation temperature is estimated. The heat of condensation (Q_{cond}) can be calculated using the following equation, which considers the enthalpy state of the refrigerant entering and leaving the condenser.

$$Q_{cond} = m_{ref}(h_2 - h_3) \quad (1)$$

Subsequently, heat transfer correlations are implemented for determination of the global heat transfer coefficient (Bergman et al., 2017). The equation for the calculation of the global heat transfer coefficient of the condenser (U_c) is reported here below:

$$U_c = \frac{1}{\frac{1}{h_c} + \frac{1}{h_w}} \quad (2)$$

in which h_c is the heat transfer coefficient of refrigerant, and h_w is the water heat transfer coefficient in the condenser. The calculation of h_w is performed according to the following equation:

$$h_w = \frac{k_{wr} Nu_{wc}}{D_c} \quad (3)$$

D_c represents the hydraulic diameter, while Nu_{wc} is calculated according to the following equation:

$$Nu_{wc} = C_{wc}(Re_{wc})^{wn}(Pr_{wc})^{\frac{1}{3}} \quad (4)$$

in which:

- Re_{wc} and Pr_{wc}: Reynolds and Prandtl number
- μ_{wc}: viscosity of the water

The values of C_{wc} and wn are evaluated as follows:

$$C_{wc} = \begin{cases} 0.718 & Re_{wc} \le 10 \\ 0.348 & Re_{wc} > 10 \end{cases} \quad (5)$$

$$wn = \begin{cases} 0.349 & Re_{wc} \le 10 \\ 0.663 & Re_{wc} > 10 \end{cases} \quad (6)$$

The refrigerant heat transfer coefficient (h_c) is evaluated in a different way when the refrigerant is the vapor phase and when it is in the condensation phase. In the first case it is calculated as:

$$h_{sc} = \frac{k_{sc} Nu_{sc}}{D_c} \quad (7)$$

in which k_{sc} represents the thermal conductivity of refrigerant.

In the condensation process, the heat transfer coefficient of the refrigerant (h_{tc}) is calculated as follows:

$$h_{tc} = \frac{k_{tc} Nu_{tc}}{D_c} \quad (8)$$

in which k_{tc} is the thermal conductivity of the refrigerant and Nu_{tc} is calculated according to the following equation:

$$Nu_{tc} = 0.0125 \left(Re_{tc} \sqrt{\frac{\rho_{cl}}{\rho_{cv}}} \right)^{0.9} \left(\frac{x_c}{1-x_c} \right)^{0.1x_c+0.8} Pr_{cl}^{0.63} \quad (9)$$

- Re_{tc} is the Reynolds number of the refrigerant during condensation
- ϱ_{cl} and ϱ_{cv} are the refrigerant density of liquid and vapor
- x_c is the vapor quality
- Pr_{cl} is the Prandtl number of the refrigerant in the liquid-phase.

Finally, the calculation of the heat exchanged between the fluids in the condenser (Q_{cond}) is expressed by the equation:

$$Q_{cond} = U_c A_c \Delta T_c \quad (10)$$

where ΔT_c is the mean temperature difference between water and refrigerant, U_c the global heat transfer coefficient and A_c the condenser heat transfer area. The equation allows the adjustment of the value previously assumed for the condensation temperature.

2.1.2 Expansion valve

The process that the fluid undergoes after exiting the condenser is modeled as an isenthalpic expansion (Fig. 4). Hence, the following equation is obtained, which provides the input enthalpy conditions for the refrigerant evaporation phase.

$$h_3 = h_4 \quad (11)$$

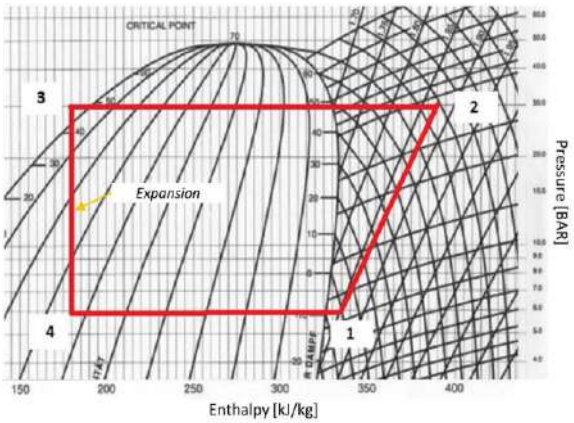

Fig. 4 – Expansion process represented on a pressure/enthalpy diagram

2.1.3 Evaporator

This section describes the modeling of heat transfer between air and refrigerant. The refrigerant process through the evaporator is shown in Fig. 5, on the pressure/enthalpy diagram. In the heat exchanger, the refrigerant undergoes an evaporation and a superheating. The type of HX considered is a finned-coil HX, which is widely used in air source heat pumps.

Initially, a first-guess value of evaporation temperature is assumed, which allows estimation of the heat exchanged during the evaporation process (Q_{ev}), hence the enthalpy difference between the outlet state and the inlet state at the evaporator. Referring to the diagram in Fig. 5, this can be expressed by the following equation:

$$Q_{ev} = m_{ref}(h_1 - h_4) \quad (12)$$

where m_{ref} represents the refrigerant mass flow rate.

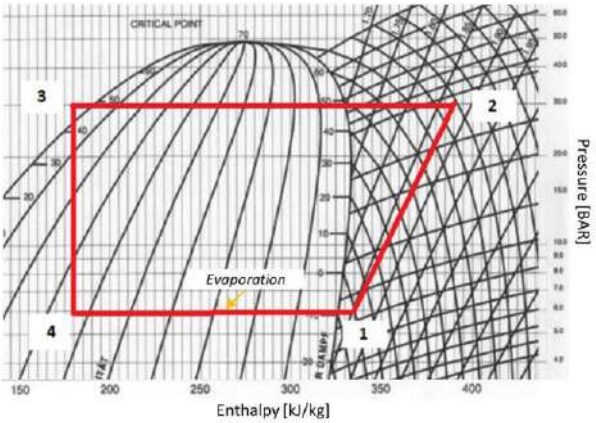

Fig. 5 – Evaporation process represented on a pressure/enthalpy diagram

Subsequently, the heat transfer correlations are implemented for the determination of the global heat transfer coefficient (Bergman et al., 2017).

h_a represents the air-side heat transfer coefficient:

$$h_a = \frac{j_a \rho_a u_m c_a}{Pr_a^{2/3}} \quad (13)$$

in which:

- is the density of the air
- is the specific heat of the air
- j_a is the heat transmission factor
- u_m is the maximum wind speed
- Pr_a is the Prandtl number of the air

j_a is calculated according to the following equation:

$$j_a = 0.0014 + 0.2618 Re_a^{-0.4} \left(\frac{A_{af}}{A_a} \right)^{-0.15} \quad (14)$$

in which:

- Re_a is the Reynolds number

- A_{af}/A_a is the ratio between the surface area of the tubes with and without fins.

The maximum wind speed (u_m) is calculated by Eqn. (15):

$$u_m = u_f \frac{s_h s_v}{(s_h - D_{te})(d_1 - d_2)} \quad (15)$$

where:

- u_f is the fan wind speed
- s_h is the tube spacings in the horizontal direction
- s_v is the tube spacings in the vertical direction
- D_{te} is the diameter of the tubes
- d_1 is the are the thickness of the fins
- d_2 is the spacing of the fins.

After that, the refrigerant heat transfer coefficient (h_e) is calculated. The value of the refrigerant heat transfer coefficient differs if the refrigerant is in the evaporation or in the superheating phase.

The refrigerant heat transfer coefficient in the superheating phase (h_{se}) is calculated as follows:

$$h_{se} = \frac{k_{se} Nu_{se}}{D_{te}} \quad (16)$$

in which k_{se} is the refrigerant thermal conductivity.

〖Nu〗_se is calculated as:

$$Nu_{se} = \frac{(f_{se}/8) Re_{se} Pr_{se}}{1.07 + 1.27\left(\frac{f_{se}}{8}\right)^{0.5} (Pr_{se}^{\frac{2}{3}} - 1)} \quad (17)$$

in which Re_{se} and Pr_{se} are the refrigerant Reynolds and Prandtl number, and f_{se} is the friction coefficient, calculated according to the equation:

$$f_{se} = (1.82 ln Re_{se} - 1.64)^{-2} \quad (18)$$

The heat transfer coefficient of the refrigerant in the condensation phase is calculated according to the following equation:

$$h_{te} = h_{el}\left\{\left[(1 - x_e) + 1.2 x_e^{0.4}(1 - x_e)^{0.01}\left(\frac{\rho_{el}}{\rho_{ev}}\right)^{0.37}\right]^{-2.2} + \left[\frac{h_{ev}}{h_{el}} x_e^{0.01}(1 + 8(1 - x_e)^{0.7}\left(\frac{\rho_{el}}{\rho_{ev}}\right)^{0.67})\right]^{-2}\right\}^{-0.5} \quad (19)$$

where:

- h_{el} is the heat transfer coefficient of the refrigerant liquid-phase
- h_{ev} is the heat transfer coefficient of the refrigerant vapor-phase
- ϱ_{el} is the density of the refrigerant liquid-phase
- ϱ_{ev} is the density of the refrigerant vapor-phase
- x_e is the vapor quality of the refrigerant.

Thus, the calculation of the evaporator global heat transfer coefficient (U_e) is performed according to the following equation:

$$U_e = \frac{1}{\frac{1}{h_e} + \frac{1}{h_a}} \quad (20)$$

Finally, the calculation of the heat exchanged between the fluids in the evaporator (Q_e) is expressed by the equation:

$$Q_{ev} = U_e A_e \Delta T_e \quad (21)$$

where ΔT_e is the mean temperature difference between air and refrigerant and A_e the evaporator heat transfer area.

2.1.4 Compressor

Given the geometric and operational complexity of the component, the compressor was modeled using performance data provided by the manufacturers, to avoid great inaccuracy of the heat pump model.

The compressor model adopts polynomial correlations, which allow for the estimation of the refrigerant mass flow rate and compressor power input, as a function of suction and discharge pressure, which correspond to the evaporating and condensing pressures in the heat pump model, if neglecting pressure drops.

In addition, the polynomial correlations are a function of the compressor frequency, i.e., they allow for the modeling of a variable-speed compressor, and thus for the development of a modulating heat pump model.

The correlations used in the model are reported here below (Copeland Select Software). The variable X represents either the refrigerant mass flow rate or the compressor power input. S and D are the evaporating and condensing temperatures, respectively, expressed in °C, while C0 – C9 are the specific coefficients for the compressor provided by the manufacturer.

$$X = C0 + C1*S + C2*D + C3*S\ ^2 + C4*S*D + C5*D^2 + C6*S\ ^3 + C7*D*S\ ^2 + C8*S*D^2 + C9*D^3 \quad (22)$$

2.1.5 Model development

The flow chart in Fig. 6 describes the rationale of the heat pump model. At the beginning, initial values of the evaporating and condensing temperatures are guessed. Based on these values, the com-

pressor model estimates the refrigerant mass flow rate and power input. These values are used as inputs by the condenser model, which estimates the heat exchanged in the condenser and adjusts the value of the condensing temperature. Similarly, the evaporator model allows for the adjustment of the first guess evaporating temperature value through an iterative procedure. Finally, the outputs of the model, i.e., heating capacity and power input, are released, allowing for the COP calculation.

2.2 Boiler Model

The boiler was modelled by subdividing the system into its major components, namely combustion chamber (CC) and HX.

The model of the CC is based on a thermodynamic equilibrium simulation of the combustion process carried out using the Cantera solver (Cantera). The inputs to the combustion chamber model are the fuel mass flow rate and air mass flow rate (or excess air). Through the modeling of the combustion process, the adiabatic flame temperature is calculated, i.e., the temperature that the gas mixture would ideally reach in the absence of heat loss. The model considers the heat losses of the combustion chamber (Q_{loss_cc}), based on information provided by the manufacturer. The outputs of the combustion chamber model are the temperature and mass flow rate of the flue gas.

These values are used as input for the model of the water-flue gas HX. An exchanger with unitary efficiency was considered, which is a good approximation, given the very high efficiency in recovering flue gas heat in the heat exchange process.

The value of flue gas outlet temperature determines whether condensation of water vapor in the flue gas occurs. If the flue gas outlet temperature is lower than the dew point, the condensation heat is recovered and transferred to the water. The logic adopted in the boiler model development is shown in Fig. 7.

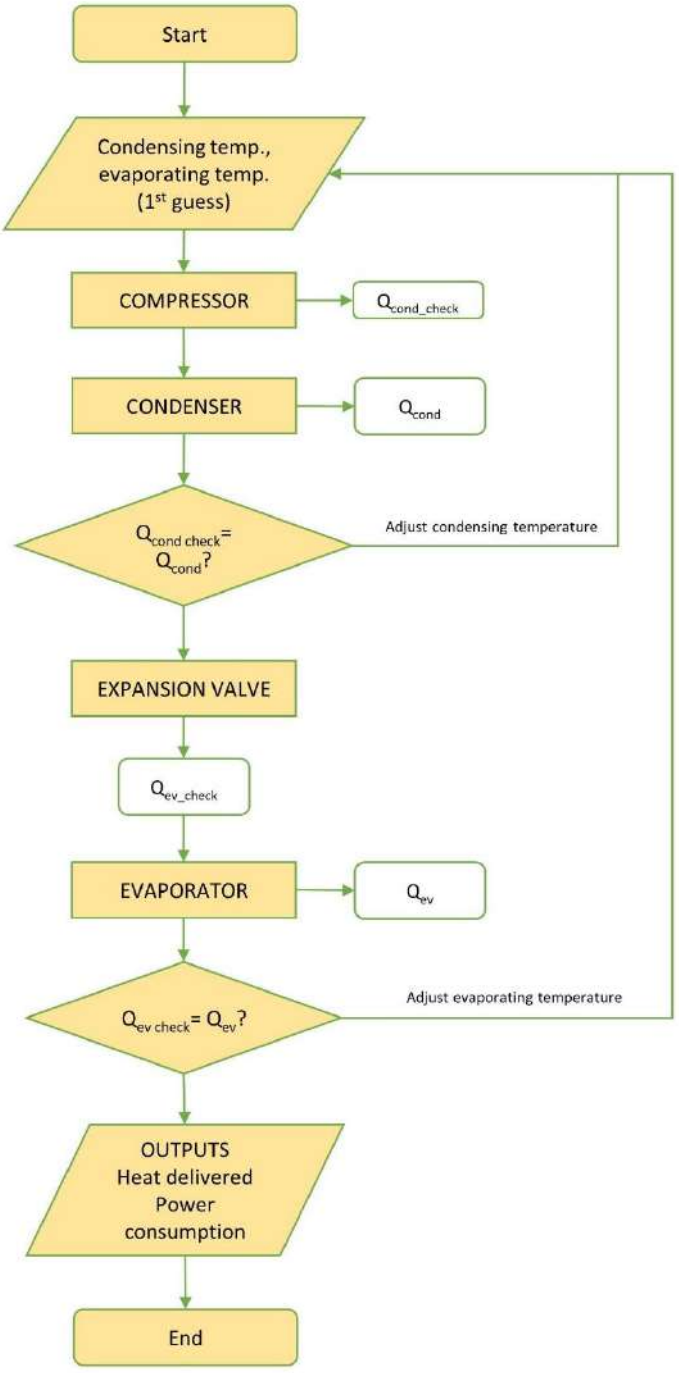

Fig. 6 – Heat pump model logic

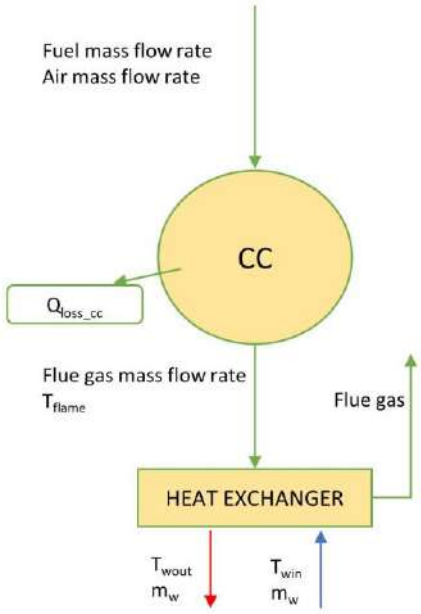

Fig. 7 – Boiler model logic

2.3 Model Validation

For the heat pump, validation of the HX models is presented, the compressor model being based on performance maps. The validation of the condenser model was carried out using the selection software provided by SWEP (SSP G8-SWEP), which provides the geometric parameters of the heat exchangers and allows the exchanged capacity to be evaluated by setting the operating conditions as input to the software.

The validation of the evaporator model was performed using performance data from a finned-coil HX obtained from NIST software (EVAP-COND). The software receives as input the geometric parameters and operating conditions and calculates the system performance in terms of exchanged capacity.

The validation of the boiler model was carried out using the data of heating capacity provided by the manufacturer, as a function of the fuel mass flow rate and water entering and leaving temperature.

3. Results And Discussion

In this section, the results of the validation of the component models are presented.

3.1 Condenser Model Validation

For a given heat exchanger, SWEP software returns the exchanged heating load by entering the operating condition data. The HX geometry and operating conditions are given as input to the model, which determines the overall heat transfer coefficient and heat load. Tables 1 and 2 show the geometrical and operating parameters related to the validation test carried out. Table 3 shows the results related to the heat exchanged between the fluids in the condenser obtained from the manufacturer's software and estimated using the model. It can be observed that the relative error in the estimate of the heat load is less than 5 %.

Table 1 – Input geometrical parameters used for validation test of plate heat exchanger model

Geometric parameters		
Total heat transfer area	m^2	1.57
Refrigerant channel volume	dm^3	0.0313
Water channel volume	dm^3	0.0301
Number of plates	units	58
Height	mm	324
Length	mm	94
Width	mm	90.7

Table 2 – Input operating parameters used for validation test of plate heat exchanger model

Operating parameters		
Operating parameters	°C	50
Condensing temperature	°C	56.2
Subcooling	°C	2
Condenser inlet temperature	°C	80
Refrigerant mass flow rate	kg/s	0.059
Water mass flow rate	kg/s	0.458

Table 3 – Heat load values provided by manufacturer and calculated by the model, and relative error, for validation test on plate heat exchanger model

Validation results		
Manufacturer's heat load	kW	9.6
Model heat load	kW	10.0
Relative error	%	4.7

3.2 Evaporator Model Validation

The model validation of the evaporator was performed, using EVAP-COND software, for a given finned-coil HX geometry. The heat exchanged between the two fluids calculated by the software was compared with the exchanged heat estimated by the model. The data for the finned-coil HX geometry considered for the validation are shown in Table 4 and the operating parameters used in the validation are reported in Table 5.

Table 4 – Evaporator geometric parameters

Geometric parameters		
Number of tubes	units	16
Number of rows	units	3
Tube length	mm	454
Inner diameter	mm	9.22
Outer diameter	mm	10.01
Tube pitch	mm	25.40
Depth row pitch	mm	22.23
Front area	mm	0.188
Heat transfer area	mm	3.8
Fin data		
Thickness	mm	0.2032
Pitch	mm	2.004

Table 5 – Evaporator operating parameters

Operating parameters		
Volumetric air flow rate	m^3/min	30
Evaporating temperature	°C	0
Superheating	°C	4.1
Air inlet temperature	°C	15
Inlet vapor quality	-	0.2
refrigerant mass flow rate	kg/h	0.0345

The results of the validation are shown in Table 6. The test shows a relative error below 10 % for the estimation of the heat exchanged between water and refrigerant in the evaporator.

Table 6 – Results of model validation

Validation results		
EVAP-COND heat load	kW	6.0
Model heat load	kW	6.5
Relative error	%	7.0

3.3 Boiler Model Validation

For the validation of the boiler model, the performance data of a commercial model of boiler manufactured by the Immergas S.p.A company were considered, for which certified performance data are available. These data show the useful heating capacity produced by the boiler as a function of fuel mass flow rate and water inlet and outlet temperatures. The manufacturer also indicates the value of excess air used by the boiler.

The model receives the fuel mass flow rate, excess air, return temperature, and water flow rate as inputs, and estimates the useful power delivered to the water. The validation was performed considering the conditions of inlet water at 30 °C and outlet water at 50 °C. In this case, water vapor condensation in the flue gas occurs. Validation was performed for fuel mass flow rates varying from min-

imum to maximum. The operating conditions used for validation are summarized in Table 7. The graph in Fig. 8 shows the results of the validation. It can be observed that the maximum relative error on the estimate of the useful boiler heating capacity does not exceed 10 % for each value of fuel mass flow rate.

Table 7 – Operating conditions for boiler model validation

Operating conditions		
Inlet water temperature	°C	30
Outlet water temperature	°C	50
Fuel mass flow rate (max-min)	kg/h	3.69–0.43

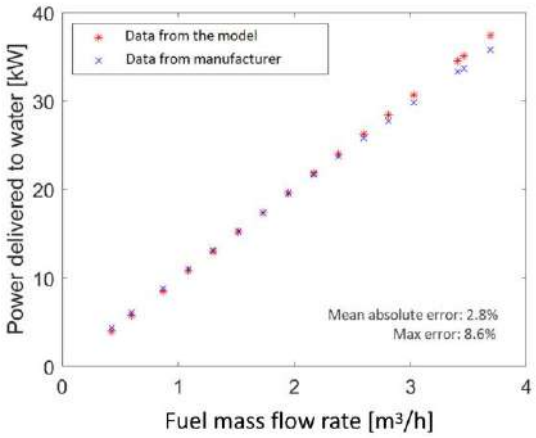

Fig. 8 – Validation results for the boiler model

3.4 Discussion

Regarding the validation of the heat pump components, the results presented show that the component models developed according to physical laws give results which are in line with the performance values declared by the manufacturers. Similarly, the validation of the boiler model showed how the physical model replicates with good accuracy the performance data provided by the manufacturer.

The heat pump and boiler models described can be used as subroutines of an overall HS model. Thus, this new model can be used to evaluate the influence that the choice of certain system components, or certain construction parameters, has on the overall efficiency of the hybrid system.

4. Conclusions

This paper presents the development of a new quasi-physical model of a hybrid system, based on the combination of the models of the individual components of the system. These models are based on physical laws, except for the compressor model, because of the high geometrical complexity of the component and the risk of introducing large errors by approximating its behavior with an analytical model.

For the heat pump, the evaporator and condenser model were developed using heat transfer correlations, which model the heat exchange between air and refrigerant, and water and refrigerant. The compressor model, on the other hand, is based on performance data provided by the manufacturers. The process occurring in the expansion valve is modeled as an isenthalpic expansion.

The boiler model is divided into a model of the combustion chamber and a model of the heat exchanger between flue gas and water. The combustion chamber model is based on the thermodynamic equilibrium simulation of the combustion process carried out using the Cantera solver.

After that, the validation of the models of the system components was presented, which provided results with acceptable accuracy to qualitatively estimate the behavior of a hybrid system.

Therefore, the model can be used for the detailed study of a hybrid system, and especially in the design process of the system itself. It will be possible to analyze the influence of the choice of certain components or construction parameters on the overall efficiency of the hybrid system.

Acknowledgement

This research was funded by the MIUR-Italian Ministry of Education, Universities and Research (PRIN 2017) grant number 2017KAAECT within the framework of FLEXHEAT project “The energy FLEXibility of enhanced HEAT pumps for the next generation of sustainable buildings”.

Nomenclature

CC	Combustion chamber
HS	Hybrid system
HX	Heat exchanger
Q_{loss_cc}	Heat losses in the combustion chamber
Q_{cond}	Heat exchanged in the condenser
Q_{ev}	Heat exchanged in the evaporator
m_{ref}	Refrigerant mass flow rate
m_w	Water mass flow rate
T_{win}	Inlet water temperature
T_{wout}	Outlet water temperature
T_{flame}	Temperature of flue gas exiting the combustion chamber

References

Bagarella, G., R. Lazzarin, and M. Noro. 2016. "Annual simulation, energy and economic analysis of hybrid heat pump systems for residential buildings." *Applied Thermal Engineering* 99: 485–494. doi: https://doi.org/10.1016/j.applthermaleng.2016.01.089

Bergman, T. L., A. Lavine, and F. P. Incropera, Fundamentals of heat and mass transfer. 2017.

Cantera. [Online]. Available: https://cantera.org/ [Accessed: 01-Feb-2022].

Copeland Select Software | Emerson IT. [Online]. Available: https://climate.emerson.com/en-it/tools-resources/copeland-select-software [Accessed: 01-Feb-2022].

Di Perna, C., G. Magri, G. Giuliani, and G. Serenelli. 2015. "Experimental assessment and dynamic analysis of a hybrid generator composed of an air source heat pump coupled with a condensing gas boiler in a residential building." *Applied Thermal Engineering* 76: 86–97. doi: https://doi.org/10.1016/j.applthermaleng.2014.10.007

Dongellini, M., C. Naldi, and G. L. Morini. 2021. "Influence of sizing strategy and control rules on the energy saving potential of heat pump hybrid systems in a residential building." *Energy Conversion and Management* 235: 114022. doi: https://doi.org/10.1016/j.enconman.2021.114022

EVAP-COND, Version 5.0 | NIST. [Online]. Available: https://www.nist.gov/services-resources/software/evap-cond-version-50 [Accessed: 01-Feb-2022].

Klein, K., K. Huchtemann, and D. Müller. 2014. "Numerical study on hybrid heat pump systems in existing buildings." *Energy and Buildings* 69: 193–201. doi: https://doi.org/10.1016/j.enbuild.2013.10.032

Li, G., and Y. Du. 2018. "Performance integration and economic benefits of new control strategies for heat pump-gas fired water heater hybrid system." *Applied Energy* 232: 101–118. doi: https://doi.org/10.1016/j.apenergy.2018.09.065

Park, H., K. Hwan Nam, G. Hyun Jang, and M. Soo Kim. 2014. "Performance investigation of heat pump-gas fired water heater hybrid system and its economic feasibility study." *Energy and Buildings* 80: 480–489. doi: https://doi.org/10.1016/j.enbuild.2014.05.052

Roccatello, E., A. Prada, P. Baggio, and M. Baratieri. 2022. "Analysis of the Influence of Control Strategy and Heating Loads on the Performance of Hybrid Heat Pump Systems for Residential Buildings." *Energies* 15(3). doi: https://doi.org/10.3390/en15030732

SSP G8 - SWEP. [Online]. Available: https://www.swep.net/support/ssp-calculation-software/ssp-g8/ [Accessed: 01-Feb-2022].

The Role of Ventilation in Indoor Spaces During the Covid-19 Pandemic: Comprehensive Analysis of ASHRAE Standard 62.1

Giovanni Francesco Giuzio – Università degli studi di Napoli Federico II, Italy – giovannifrancesco.giuzio@unina.it
Giovanni Barone – Università degli studi di Napoli Federico II, Italy – giovanni.barone@unina.it
Annamaria Buonomano – Università degli studi di Napoli Federico II, Italy – annamaria.buonomano@unina.it
Gianluca Del Papa – Università degli studi di Napoli Federico II, Italy – gianluca.delpapa@unina.it
Cesare Forzano – Università degli studi di Napoli Federico II, Italy – cesare.forzano@unina.it
Adolfo Palombo – Università degli studi di Napoli Federico II, Italy – adolfo.palombo@unina.it
Giuseppe Russo – Università degli studi di Napoli Federico II, Italy – giuseppe.russo9@unina.it

Abstract

The spread of COVID-19 has significantly increased attention focused on the air quality of indoor environments. All major international health organizations (e.g., World Health Organization, etc.) recognize the importance of ventilation in enclosed spaces in reducing pathogen concentrations and fighting the Corona virus, or future pandemics. In this context, the roadmap to ensure safer and healthier indoor environments, by also guaranteeing an adequate comfort level, involves the implementation of several measures leading to a not-negligible increase in buildings' energy consumption. Within this framework, the present paper aims to analyze the adequacy of the current Indoor Air Quality (IAQ) standards requirements, and to assess the impact of IAQ improving measures on end-use energy profiles to ensure occupants' comfort. Specifically, a dynamic simulation approach is adopted to estimate, for each building space typology defined by ASHRAE 62.1, both air contaminant concentration and zone energy consumption. Specifically, the risk to occupants of contracting the COVID-19 virus was assessed for different scenarios using a modified Wells-Riley model. The study confirms the urgent need for enhancing ventilation in enclosed spaces to exit the health emergency caused by COVID-19. In addition, the paper provides quantitative data on the resulting operating costs of HVAC systems.

1. Introduction

The diffusion of general pollutants, viruses, bio effluents, etc. in the indoor environment is kept under control by the ventilation system, whose key role is largely recognized and investigated in the scientific community (Emmerich et al., 2013; Risbeck et al. 2021; Shrubsole et al., 2019). Still, higher attention and interest has increased around this topic since the Covid-19 outbreak (Faulkner et al., 2021; Pan et al., 2021; Sun & Zhai, 2020; Zheng et al., 2021) and the vital need for reducing the infection risk (Agarwal et al., 2021; Li & Tang, 2021) by supplying outdoor air in adequate quantities (Guo et al., 2021; Sha et al., 2021). In this context, the aim of the present work is to analyze the existing connection between SARS-CoV-2 contagion risk and the fresh air rates per person, targeting a proposal of different solutions to reduce the contagion risk by also evaluating their energy impact to maintain adequate occupant comfort regarding indoor air quality and healthy conditions in indoor spaces (Castaldo et al., 2018).

Several studies in the literature investigate the risk of contagion of COVID-19 with increased mechanical ventilation in the indoor environment, such as classrooms (Schibuola & Tambani, 2021a; Xu et al., 2021), offices (Sha et al., 2021; Srivastava et al., 2021; Pavilonis et al., 2021), universities (Mokhtari & Jahangir, 2021), restaurants (Li et al., 2021), and hospitals (Li & Tang, 2021) etc. Among the works

stating the usefulness of adopting increased outdoor air ventilation rates in reducing the Covid-19 contagion risk, it is very difficult to find works quantitatively assessing the related energy impact, with the only exception of works reported in Balocco & Leoncini (2020) and Schibuola & Tambani (2021b). This is a large gap, given the great influence of ventilation systems on building energy demands. In addition, there is a lack of manuscripts investigating the Covid-19 contagion risk in a comprehensive way by assessing the analysis for a large group of space types, whereas it is more common to find works focusing on a specific case study. Such a lack implies the impossibility of determining unique design criteria and defining guidelines.

The aim of the present work is to fill the gap in knowledge identified above. Specifically, the Wells-Riley model (Miller et al., 2021; Riley et al., 1978), largely adopted in the literature to evaluate Covid-19 contagion risk, was implemented in a purpose - developed Matlab routine. By means of this tool, aiming at filling the lack of works examining a wide range of building types, all the building categories presented in the ANSI/ASHRAE Standard 62.1-2019 were studied by considering, for each space type, the related crowding indexes, the occupancy schedules, and the outdoor air ventilation rates suggested by the standard. By doing so, it was possible to assess Covid-19 contagion risk in the case of the presence of infected people for each of the investigated building typologies, as a function of diverse pivotal parameters (exposure time to virus, typology of the facial mask worn, etc.). To reduce the Covid-19 contagion risk associated with the investigated scenarios, and with the aim of providing useful insights and design criteria for ventilation system, higher outdoor air flow rates were tested by assessing their effect in terms of infection probability. Finally, by exploiting a dynamic simulation model, purposely developed by means of a Building Energy Modeling (BEM) approach, the energy implications of the proposed ventilation strategies were assessed. The mentioned analyses are presented in detail hereinafter.

2. Method and Mathematical Model

In the present paragraph, the method adopted to carry out the previously mentioned analyses is described. Specifically, in Fig. 1, a schematic diagram of the adopted workflow is presented. Specifically, to perform a parametric analysis of several building categories, a Matlab routine capable of both simulating energy performance of the examined room and assessing the probability of infection of the occupants was purposely developed. As shown in Fig. 1, the Matlab script is intended to manage either the inputs and outputs of the detailed simulation model of the building room or the infection risk calculation model.

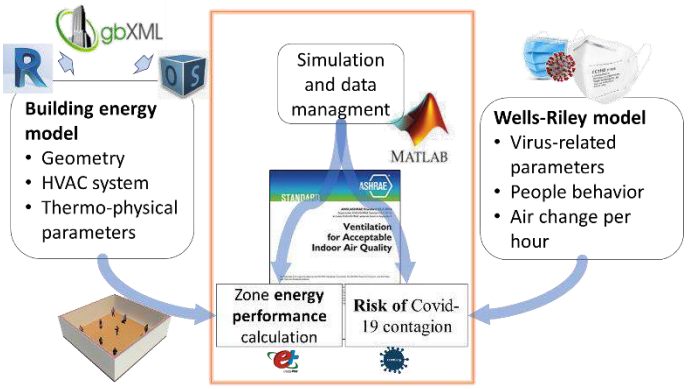

Fig. 1 - Schematic workflow of the methodology adopted (authors' illustration)

The building energy simulation relies on three different tools: Autodesk Revit, OpenStudio, and Energy Plus. Specifically, in Autodesk Revit, the building 3D model is developed in detail, by including building elements, as well as thermal zone data. The building model is then exported, by exploiting gbXML file, into OpenStudio suite, which is an energy-modeling software built on the EnergyPlus engine. At the same time, the assessment of Covid-19 contagion risk, for the same building and operating condition is also performed. This is conducted into a purposely developed Matlab subroutine, based on the Wells-Riley model. Both the energy consumption and Covid-19 contagion risk assessment methods will be described in detail in the following.

2.1 Building Energy Model

The energy model resulted in a well-mixed air single-zone building equipped with an ideal air loads systems capable of providing the exact thermal energy required to keep the temperature setpoints. An HVAC system like this also guarantees the minimum outdoor airflow rate (V_{bz}, breathing-zone ventilation), specified by means of Eq. (1), which depends on the number of people in the zone (N), the outdoor airflow rate per person (R_p), the net area of the zone (A_z), and the corresponding outdoor airflow rate required for unit of zone area (R_a).

$$V_{bz} = R_p \cdot N + R_a \cdot A_z \quad (1)$$

Furthermore, the influence of people, lighting and electrical equipment on the heat balance algorithm is accounted for by means of characteristic heat gain parameters, such as sensible and latent heat fraction per person ($g_{s,p}$ and $g_{l,p}$, *W/person*), lighting power load intensity (g_l, W/m^2) and electrical equipment power load intensity (g_{ee}, W/m^2). Appropriate schedules complete the model, taking into account the actual operating regime of the buildings under investigation. It is worth noticing that the ventilation rate necessary to ensure adequate IAQ is one of the key multi-physics factors that influences the occupants' comfort in indoor spaces; in this regard, complete multi-physics and multi-domain analysis aim at assessing thermo-hygrometric comfort, visual comfort, healthy conditions, and air quality.

2.2 Modified Wells-Riley Model

In order to assess the Covid-19 contagion risk, the Wells-Riley model (Miller et al., 2021; Peng & Jimenez, 2021; Peng et al., 2022; Riley et al., 1978) was adopted. This model is based on a standard aerosol Wells-Riley infection model, opportunely modified to consider the hypothesis of well mixed air volume. Following this model, the Covid-19 infection probability P can be expressed as:

$$P = 1 - e^{-n} \quad (2)$$

where n represents the inhaled "quanta", which is the concentration of infectious doses of the virus which are inhaled by a person. Note that a quanta is defined as the dose necessary to cause an infection in 63 % of the persons susceptible. The Covid-19 infection probability expressed by Eq. (2) is valid under certain hypothesis: i) the quanta emission rate from the infectious individual is constant, ii) no prior quanta are in the investigated environment, iii) the quanta aerosol is evenly distributed in the environment, iv) close-proximity infection is neglected. The number of quanta inhaled by a person is calculated as follow:

$$n = q_c \cdot b_r \cdot D \cdot (1 - \eta_{wm} \cdot \eta_{in}) \quad (3)$$

where η_{in} is the mean filtration efficiency of the face mask for inhalation, η_{wm} is the percentage of people wearing a facemask, D is the exposure time to the virus, b_r is the breathing rate, and q_c is the average quanta concentrations.

3. Case Study

The Wells-Riley model was adopted to investigate the effectiveness, in relation to Covid-19 contagion risk, of the ventilation rates proposed by ANSI/ASHRAE Standard 62.1-2019. To perform this analysis, a generic room (Fig. 2) characterized by a walkable area of 100 m^2 (10 m x 10 m), with a height of 3 m, for a total volume of 300 m^3, was considered. It is worth noticing that the investigated room was assumed as to be located in the core of a generic building. Consequently, all the walls were modeled as adiabatic. Note that such a hypothesis was made to provide results that were as little case-specific as possible, and take into account the sole effect of ventilation and internal heat gains on energy performance.

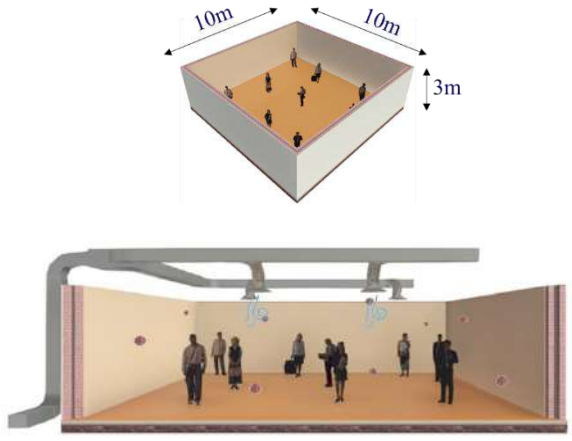

Fig. 2 – Investigated room

The investigated room was considered as alternatively belonging to all the 109 occupancy categories reported in the ANSI/ASHRAE Standard 62.1-2019, by taking into account the related outdoor air rates and occupancy density values. The 109 space typologies were grouped following the ANSI/ASHRAE Standard 62.1-2019, into 11 categories. The minimum and maximum outdoor air rates and occupancy density occurring within the group are reported in Table 1.

Note that the values reported in Table 1 represent the range limits of each building category group. However, each of the 109 spaces presented in the ANSI/ASHRAE Standard 62.1-2019 were simulated individually. For further details, please refer to the standard (ASHRAE, 2019). For each of the considered spaces, the Covid-19 contagion risk resulting from the adoption of the outdoor air ventilation rates suggested by the standard (calculated by means of Eq. 1) was assessed.

Table 1 – Outdoor ventilation rates, and occupant density for all the investigated categories

Occupancy Category	People Outdoor Air Rate *[L/s person]*		Area Outdoor Air Rate *[L/s person]*		Occupant Density *[persons/100m2]*	
	min	*max*	*min*	*max*	*min*	*max*
Animal Facilities	5	5	0.6	0.9	20	20
Correctional Facilities	2.5	3.8	0.3	0.6	15	50
Educational Facilities	2.5	5	0.3	0.9	10	100
Food and Beverage	2.5	3.8	0.3	0.9	2	100
Hotels, Motels, Resorts	2.5	3.8	0.3	0.6	10	120
Miscellaneous Spaces	2	5	0	0.9	0	100
Office Buildings	2.5	2.5	0.6	0.12	2	60
Outpatient Health Care	2.5	10	0.3	2.4	5	50
Public Assembly	2.5	3.8	0.3	0.6	10	150
Retail	3.8	10	0.3	2.4	7	150
Sports, Entertainment	3.8	10	0.3	2.4	7	150

The quanta exhalation rates, namely ER, used to evaluate the infection risk were gathered from the reference (Schibuola & Tambani, 2021a). Furthermore, in order to investigate diverse scenarios, five pivotal parameters were supposed to be variable as follows: i) three different Covid-19 variants were alternatively considered. The variant choice affects the quanta emission rate by means of a correction factor Q_{var}. Specifically, the three investigated variants are: original variant (Q_{var} = 1), Delta (Q_{var} = 2); and Omicron (Q_{var} = 2.5) (Burki, 2022; Campbell et al., 2021); ii) three different exposure times (D) were considered: 1 hour, 2 hours, 6 hours; iii) three different face mask scenarios, affecting inhalation and exhalation efficiency: no mask scenario, all people wearing chirurgical masks scenario, and all people wearing FFP2 masks scenario.

3.1 Proposed Solutions

The previously described case study, adopting the outdoor ventilation rates suggested by the ANSI/ASHRAE Standard 62.1-2019, was considered as Reference System (RS). To reduce Covid-19 contagion risk, the convenience of using increased outdoor air ventilation rates was investigated. Specifically, ventilation rates augmented three and ten times (Proposed System 1 – PS1, and Proposed System 2 – PS2, respectively) higher than those suggested by the standard were considered and tested. These values, which might seem quite high compared to those adopted in the case of RS, were selected in accordance with the data found in the existing literature, referenced in the literature review section. It should be considered that, as expected, the proposed outdoor rates will imply a substantial increase of the energy consumption for space heating and cooling due to the augmented ventilation loads. For this reason, both PS1 and PS2 systems were also tested by additionally considering a sensible heat recovery device equipped to reduce the ventilation load. The selected sensible heat recovery device is a commercial device with an average heat recovery efficiency equal to 75 %, and nominal pressure drops ranging from 100 to 300 Pa (depending on the elaborated airflow rate). Table 2 lists all the investigated systems.

Table 2 – Investigated case studies

System	Outdoor Ventilation Rates	Heat Recovery
RS	ANSI/ASHRAE Standard 62.1-2019	No
PS1	Ventilation x3	No
PS1.1	Ventilation x3	Yes
PS2	Ventilation x10	No
PS2.1	Ventilation x10	Yes

3.2 Energy Analysis

To assess the energy consumption associated with the selected ventilation strategies (both RS and proposed systems), the ANSI/ASHRAE Standard 90.1-2016 was taken into account for the following data: i) occupancy scheduling; ii) lighting load density and scheduling; iii) machinery load density and scheduling; iv) indoor air setpoints. Specifically, each of the investigated occupancy category spaces (see Table 1) was simulated by considering the corresponding values of the above-reported parameters. Concerning the HVAC system, the considered room space heating and cooling is ensured by an air source HPC (heat pump/chiller), sized on the maximum load, with a variable COP (Barone et al., 2016 and 2020).The energy consumption resulting from the conducted analysis is affected substantially by the climate zone, due to the different outdoor air temperature (it is worth noticing that the room is placed in the core of a conditioned building, so no transmission load is considered). Thus, aiming at assessing the energy impact of the proposed ventilation strategies for diverse climates, three different European weather zones were considered as representative of hot, mild, and cold weather (see Table 3).

Table 3 - Investigated weather zones

Climate	HDD	CDD	ISR
	[K d]		[kWh/(m²y)]
Almeria	763	982	1664
Rome	1475	730	1529
Berlin	3394	262	1001

4. Result and Discussion

In this paragraph, the results of the analyses carried out are provided. Specifically, the Covid-19 results will be presented first, then the energy implications will be discussed.

4.1 Covid-19 Analysis

In this section, the results of the Covid-19 analysis, in term of contagion probability, are presented. Specifically, in Fig. 3, the Covid-19 contagion risk is reported for all the occupancy categories investigated, in the case of two different face mask scenarios (no mask, on the left, surgical mask on the right), and in the case of three different exposure times (one hour in blue, two hours in red, and six hours in yellow). Note that the FFP2 mask results are not presented, since in this case the resulting Covid-19 contagion risk was already remarkably low. Numerical results obtained (probability of infection) are reported as boxplots in Fig. 3. Specifically, the distribution of the set of data, the minimum and maximum values (whiskers), as well as the 1st and 3rd quartiles (boxes), and the median are depicted for each of the occupancy category groups.

The infection probability, in case of people not wearing a mask and for an exposure time of one hour, almost always turns out to be higher than 1 % (considered in the literature as a "safe" value), while remaining quite close to it. Higher risk occurs in the case of 2 hours, with infection probability rising to 4 %. Finally, the highest infection probability in the case of no masks worn is obtained for 6 hours of exposure time, with contagion risk values rising to 12-14 %

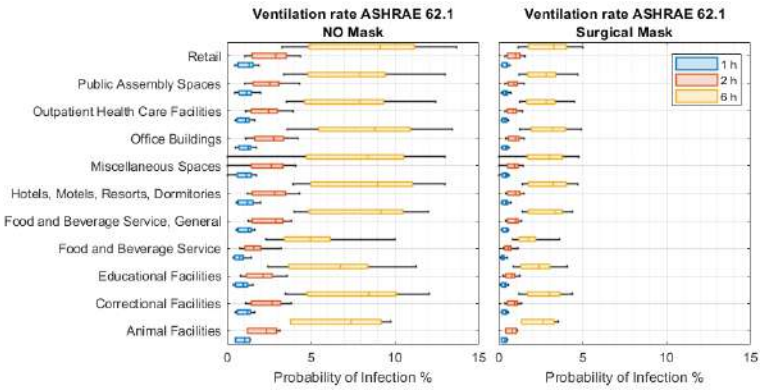

Fig. 3 – Covid-19 infection probability for all the investigated case studies (standard ventilation)

By using surgical masks (right-hand diagram in Fig. 3, it is possible to notice that, in the case of both 1 hour and 2 hours of exposure time, the infection probability is almost always below the 1 % value. Nevertheless, in the case of 6 hours, the risk is still higher than the threshold value. The reported results show that the ventilation rates suggested by the ANSI/ASHRAE Standard 62.1-2019 are adequate to control the Covid-19 contagion risk only in the case of all the occupants wearing an FFP2 mask, whereas a higher risk occurs in the case of surgical masks, and no mask worn. To reduce the estimated

contagion risk, the ventilation rates suggested by the standard were augmented 3 times, and the related contagion risk results are shown in Fig. 4. Here, it is possible to notice that, in the case of the no mask scenario, the contagion risk in the case of 1 hour exposure time is almost always below 1 %, ensuring occupant safety. Also, the contagion risks relative to 2 hours of attendance time drop. However, many cases return infection probabilities still higher than the safe threshold. The contagion risk connected to six hours exposure time is also reduced regarding the standard ventilation base case. Still, very high values are reached. A different situation occurs in the case of surgical masks worn. In this case, both 1 hour and 2 hours' exposure time return contagion risks lower than 1 %, whereas the 6-hour case returns a contagion risk higher than the safe threshold, but remarkably reduced compared with the base case.

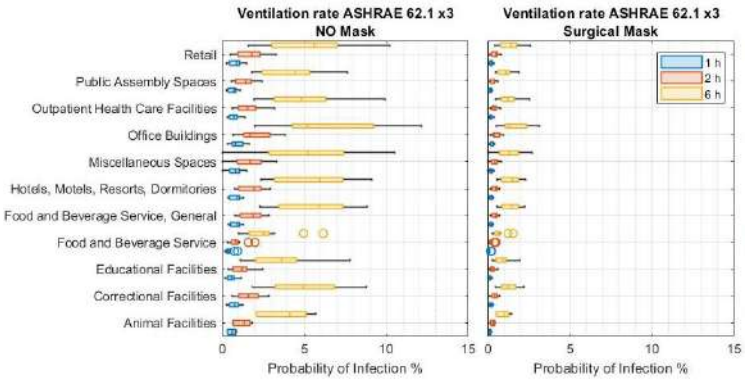

Fig. 4 – Covid-19 infection probability for all the investigated case studies (x3 ventilation)

In order to further reduce the contagion risk, ten-times-increased standard ventilation was also tested, and the related results are reported in Fig. 5. Here, it is possible to notice that, in the case of surgical mask worn, the contagion risk probability is lower than the threshold value for almost all the investigated scenarios and exposure times. On the contrary, in the case of no masks worn, one and two-hours residency time turns out to be still safe.

It is worth noticing that the absolute values shown in the previously reported figures are subject to uncertainty. This is mainly due to the adopted number of quanta, whose value is still under discussion in the scientific community. For this reason, relative results are also presented.

Specifically, the average relative contagion risk reduction, for all the mask configurations and exposure time, is presented in Fig. 6. From the figure it is possible to notice that, beside the absolute contagion risk value, the contagion risk percentage reduction ranges from 30 to 50 % in the case of x3 ventilation, and from 65 to 80 % in the case of x10 ventilation. Such results help in understanding the great effect that outdoor ventilation rates have on Covid-19 contagion risk reduction.

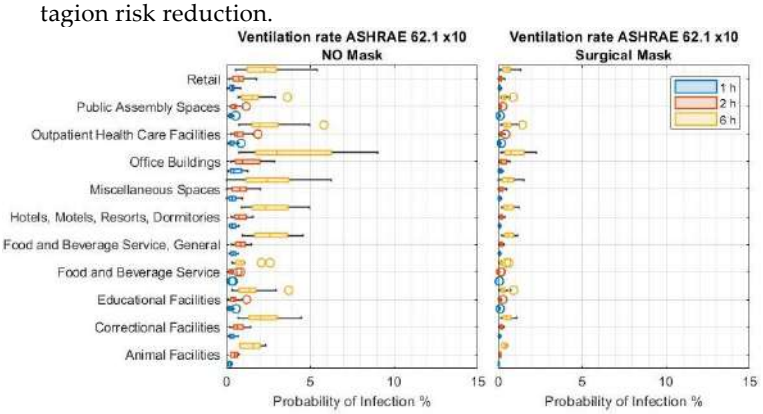

Fig. 5 – Covid-19 infection probability for all the investigated case studies (x10 ventilation)

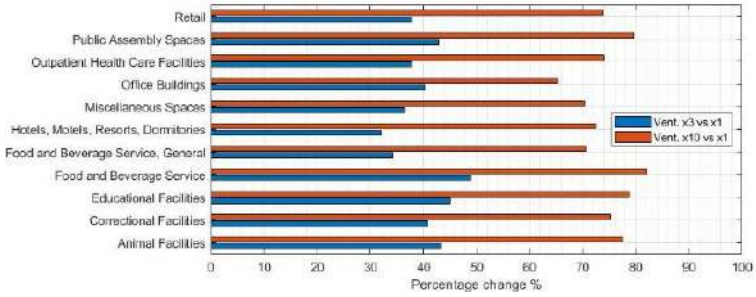

Fig. 6 – Average relative contagion risk reduction for all the face mask configurations

The higher ventilation rates proposed also entail a much higher dilution of indoor pollutants and lower level of carbon dioxide within the spaces. The indoor air quality significantly improves, so that the required comfort level by the occupants can be fully satisfied with the proposed ventilation rates (ASHRAE 62.1 x3 and ASHRAE 62.1 x10) as demonstrated by Fig. 7. The figure refers to an auditorium seating area with high occupancy (about 150 people). With the current standard (ASHRAE 62.1),the CO_2 concentration rises to 1800 ppm, leading to a discomfort level perceived by the occupants due to poor air. In contrast, both the proposed ventilation rates adopted to reduce the Covid contagion risk

keep the CO_2 concentration within the acceptable range suggested by OHSA (Occupation Health & Safety Administration) for well ventilated indoor spaces.

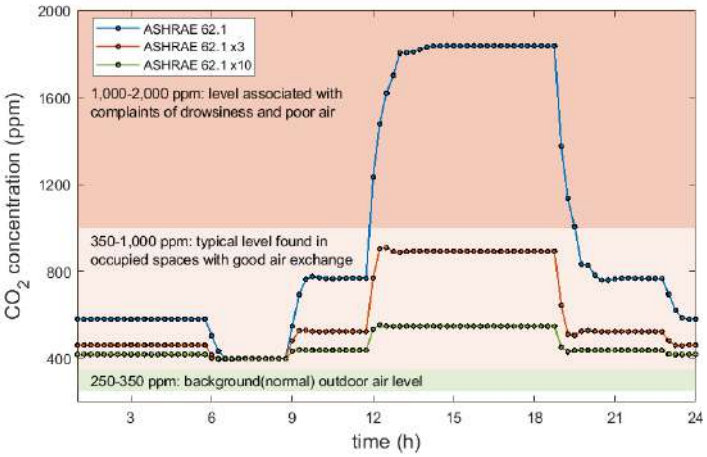

Fig. 7 – CO_2 concentration in the auditorium space and related comfort range for occupants

4.2 Energy Analysis

The previously described ventilation strategies, while reducing Covid-19 contagion risk, also increase the energy consumption of the building for space heating and cooling due to the augmented ventilation load. Furthermore, more air treated leads to higher handling costs. As an example of this increase, the space heating thermal energy demand for representative space typologies (selected from each category) are presented in Fig. 8 in the case of the building located in Berlin. From the figure, as expected, it is possible to notice that the adoption of x3 (PS1) and x10 (PS2) ventilation flow rates (red and light blue bars) always implies a remarkably higher energy demand compared with the RS scenario (blue bar). Different results are, on the other hand, achieved in the case of adoption of Heat Recovery (HR) device (orange – PS1.1 - and green – PS2.1 - bars in Fig. 8). Here, it is possible to notice that the energy demand increase is remarkably lower than those occurring without the HR adoption. It worth noticing that, in some cases, the PS1.1 energy demand (orange bars) is comparable with the RS one (blue bars).

Similar outcomes can be detected in the case of the thermal energy demand for space cooling, as shown in Fig. 9, where the results in the case of the building located in Almeria are presented. Nevertheless, by analyzing Fig. 9, it is possible to notice that, in the case of x3 ventilation, lower energy demands for space cooling are obtained also without HR (PS1 - orange bars). Such an occurrence is due to the free cooling effect played, in some cases, by the augmented flow rate. The same effect is not noticeable in the case of x10 ventilation (PS2 – light blue bars), since the positive effects connected with the free cooling are overwhelmed by the negative ones occurring in the other hours. However, it worth noticing that the overall weight of cooling need increase is remarkably lower than that of heating (the y-axis scale of Fig. 9 is different to that of Fig. 8). In addition, also the benefits of the HR are lower due to lower temperature difference between the outdoor air and the zone temperature during the summer season.

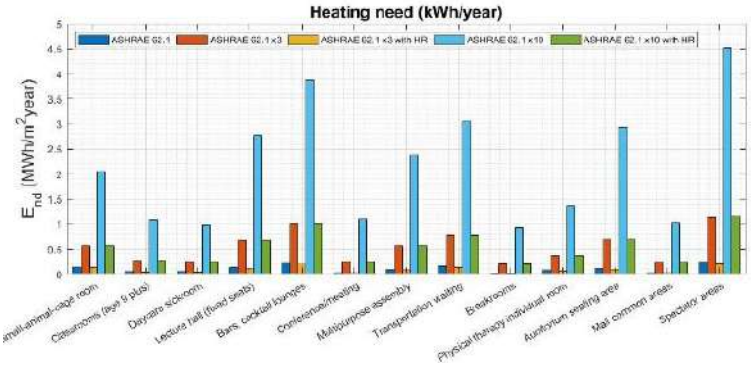

Fig. 8 – Space heating needs for all the case studies investigated for the building located in Berlin

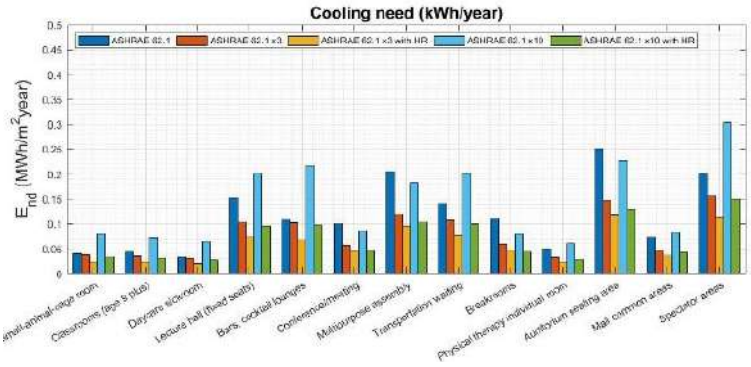

Fig. 9 – Space cooling needs for all the case studies investigated for the building located in Almeria

The thermal energy demand variations presented in Fig. 8 and Fig. 9 imply a variation of the considered room electricity consumption. Specifically, in Fig. 10, the distribution of electricity consumption is presented for all the investigated case studies. It is

worth noticing that, differently to Fig. 8 and Fig. 9, which report only the influence of the diverse ventilation strategies on the space heating and cooling thermal energy demand, the electricity results presented in Fig. 10 also take the electricity consumption of the fans into account. Referring to the median values of the set of data in Fig. 10, as expected, the adoption of PS1 (red boxes) and PS2 (purple boxes) systems always presents higher electricity demand vs the RS (blue boxes).

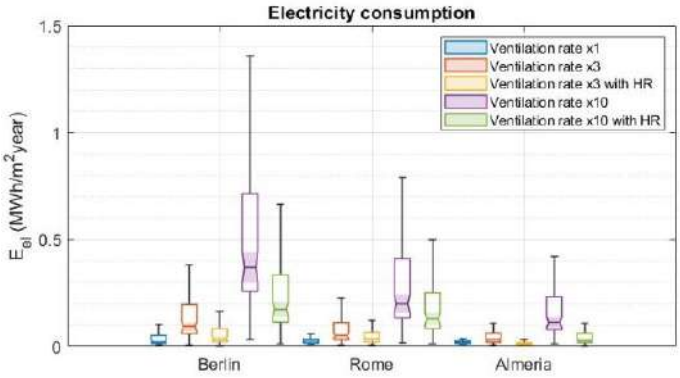

Fig. 10 – Electricity needs for all the case studies investigated

The benefits achieved during the cooling season, due to the free cooling effect, as shown in Fig. 9, are, in fact, counterbalanced by the highest consumption during the heating season. Lower electricity consumption increases are, on the other hand, detected in the case of adoption of PS1.1 (yellow bars) and PS2.1 (green bars). These reductions are smaller in magnitude with respect to those shown in the case of Fig. 7 and Fig. 8, due to the higher consumption of the fans connected to the HR adoption (higher duct system pressure drops).

5. Conclusions

In the present manuscript, the effectiveness of the ventilation rates proposed by the current ANSI/ASHRAE Standard 62.1-2019 in dealing with the Covid-19 contagion risk is investigated. To carry out this analysis, the Wells-Riley model (Riley, et al., 1978), largely adopted in the literature to evaluate the Covid-19 contagion risk, was implemented in a purpose -developed MATLAB routine. By means of this tool, all the building categories presented in the ANSI/ASHRAE Standard 62.1-2019, applied to a purpose -conceived case study, were studied by considering, for each space type, the related crowding indexes, the occupancy schedules, and the outdoor air ventilation rates suggested by the standard. By doing so, it was possible to assess the Covid-19 contagion risk in the case of the presence of infected people in the room for each of the investigated building typologies, as a function of diverse pivotal parameters (exposure time to virus, typology of the facial mask worn, etc.). Aiming at reducing the Covid-19 contagion risk associated with the scenarios investigated, and with the aim of providing useful insights and design criteria for ventilation systems, higher outdoor air flow rates were tested by assessing their effect in terms of infection probability. Finally, by exploiting a dynamic simulation model, purposely developed by means of a Building Energy Modeling (BEM) approach, the energy implications of the proposed ventilation strategies were assessed. From the analyses carried out, the key considerations are:

- The ventilation rates values proposed in the current ANSI/ASHRAE Standard 62.1-2019 are not capable of ensuring a safe indoor environment in the case of no face mask worn. Specifically, an infection risk probability higher than 1 % (value considered as safe) is almost always reached by the analysis conducted, regardless of the considered exposure time. The same is true for surgical mask adoption, which gives lower infection risk probability, but is very often still higher than the safe threshold.
- The current standard adoption returns a very low contagion risk probability only in the case of all occupants wearing a FFP2 mask.
- The adoption of higher ventilation rates (x3 and x10) always returns interesting infection risk reductions, ranging from between 30 to 50 % and 65 to 80 %, respectively. Nevertheless, x3 ventilation is viable only for an exposure time to the virus of 1 hour, whereas in the case of 2 and 6 hours, the resulting contagion risk is always higher than 1 %.
- Ten times augmented ventilation vs. ANSI/ASHRAE Standard 62.1-2019 values reduces the contagion risk below 1 % for both 1- and 2-hour exposure times, whereas 6 hours is often still too high.

- By increasing ventilation, it is possible to reduce the Covid-19 risk to under 1 %, without wearing face masks only for 1- and 2- hour attendance times, whereas, in the case of 6 hours, this is not possible. Consequently, in the case of certain space types characterized by long occupancy times (e.g., classrooms), further solutions should be adopted.
- From the energy point of view, the proposed ventilation strategies return remarkable electricity demand increases. In this framework, x3 ventilation proves to be the best trade-off solution.
- The adoption of a heat recovery device allows for a remarkable reduction of the energy impact of the proposed ventilation strategies, making both x3 and x10 ventilations more feasible than the same solutions without the HR.

From the results obtained, it is possible to conclude that the existing normative does not provide an adequate amount of outdoor air to ensure a low Covid-19 contagion risk in enclosed spaces for the wellbeing and comfort of occupants. In this framework, the augmentation of the outdoor air flowrate is proven to be a good solution to adopt. Nonetheless, such an action is highly energy- consuming, requiring the adoption of heat recovery devices. Otherwise, it would be unviable from an energy and economic point of view.

Acknowledgement

This research has been co-founded by the Italian Ministry of Research through the NEXT. COM (Prot. 20172FSCH4) "Towards the NEXT generation of Multiphysics and multidomain environmental COMfort models: theory elaboration and validation experiment" project, within the PRIN 2017 program. The authors wish to thank their project colleagues for their constructive feedback and collaboration.

Nomenclature

A_z	Net area of the zone
BEM	Building Energy Modeling
b_r	Breathing rate
D	Exposure time to the virus
ER	Quanta emission Rate
g_{ee}	Electrical equipment power load
g_l	Lighting power load intensity
$g_{l,p}$	Latent heat gain per person
$g_{s,p}$	Sensible heat gain per person
n	Inhaled quanta
N	Number of people in the room
P	Infection Probability
PS	Proposed System
q_c	Average quanta concentration
R_a	Outdoor airflow rate per area
R_p	Outdoor airflow rate per person
RS	Reference System
V	Room Volume
V_{bz}	Breathing-zone ventilation
V_{out}	Outdoor air ventilation flow rate

References

Agarwal, N., C. S. Meena, B. P. Raj, L. Saini, A. Kumar, N. Gopalakrishnan, A. Kumar, N. B. Balam, T. Alam, N. R. Kapoor, and V. Aggarwal. 2021. "Indoor air quality improvement in COVID-19 pandemic: Review." S*ustainable Cities and Society* 70: 102942. doi: https://doi.org/10.1016/j.scs.2021.102942

ASHRAE. 2019. *ASHRAE Standard 62.1-2019 Ventilation for Acceptable Indoor Air Quality*.

Balocco, C., and L. Leoncini. 2020. "Energy Cost for Effective Ventilation and Air Quality for Healthy Buildings: Plant Proposals for a Historic Building School Reopening in the Covid-19 Era." *Sustainability* 12(20): 8737. doi: https://doi.org/10.3390/su12208737

Barone, G., A. Buonomano, C. Forzano, and A. Palombo. 2016. "WLHP Systems in Commercial Buildings: A Case Study Analysis Based on a Dynamic Simulation Approach." *American Journal of Engineering and Applied Sciences* 9(3): 659-668. doi: https://doi.org/10.3844/ajeassp.2016.659.668

Barone, G., A. Buonomano, C. Forzano, G. F. Giuzio, and A. Palombo. 2020. "Passive and active performance assessment of building integrated hybrid solar photovoltaic/thermal collector prototypes: Energy, comfort, and economic analyses." *Energy* 209: 118435. doi: https://doi.org/10.1016/j.energy.2020.118435

Burki, T. K. 2022. "Omicron variant and booster COVID-19 vaccines." *The Lancet Respiratory Medicine* 10: e17. doi: https://doi.org/ 10.1016/S2213-2600(21)00559-2

Campbell, F., B. Archer, H. Laurenson-Schafer, Y. Jinnai, F. Konings, N. Batra, B. Pavlin, K. Vandemaele, M. D Van Kerkhove, T. Jombart, O. Morgan, and O. le Polain de Waroux. 2021. "Increased transmissibility and global spread of SARS-CoV-2 variants of concern as at June 2021." *Eurosurveillance* 26(24): 2100509.

Castaldo, V. L., I. Pigliautile, F. Rosso, F. Cotana, F. De Giorgio, and A. L. Pisello. 2018. "How subjective and non-physical parameters affect occupants' environmental comfort perception." *Energy and Buildings* 178: 107-29. doi: https://doi.org/10.1016/j.enbuild.2018.08.020

Emmerich, S. J., D. Heinzerling, J.-I. Choi, and A. K. Persily. 2013. "Multizone modeling of strategies to reduce the spread of airborne infectious agents in healthcare facilities." *Building and Environment* 60: 105-15. doi: https://doi.org/10.1016/j.buildenv.2012.11.013

Faulkner, C. A., J. E. Castellini, W. Zuo, D. M. Lorenzetti, and M. D. Sohn. 2021. "Investigation of HVAC operation strategies for office buildings during COVID-19 pandemic." *Building and Environment* 207B: 108519. doi: https://doi.org/10.1016/j.buildenv.2021.108519

Guo, M., P. Xu, T. Xiao, R. He, M. Dai, and S. L. Miller. 2021. "Review and comparison of HVAC operation guidelines in different countries during the COVID-19 pandemic." *Building and Environment* 187: 107368. doi: https://doi.org/10.1016/j.buildenv.2020.107368

Li, C., and H. Tang. 2021. "Study on ventilation rates and assessment of infection risks of COVID-19 in an outpatient building." *Journal of Building Engineering* 42: 103090. doi: https://doi.org/10.1016/j.jobe.2021.103090

Li, Y., H. Qian, J. Hang, X. Chen, P. Cheng, H. Ling, S. Wang, P. Liang, J. Li, S. Xiao, J. Wei, L. Liu, B. J. Cowling, and M. Kang. 2021. "Probable airborne transmission of SARS-CoV-2 in a poorly ventilated restaurant." *Building and Environment* 196: 107788. doi: https://doi.org/10.1016/j.buildenv.2021.107788

Miller, S. L., W. W. Nazaroff, J. L. Jimenez, A. Boerstra, G. Buonanno, S. J. Dancer, J. Kurnitski, L. C. Marr, L. Morawska, and C. Noakes. 2021. "Transmission of SARS-CoV-2 by inhalation of respiratory aerosol in the Skagit Valley Chorale superspreading event." *Indoor Air* 31: 314-23. doi: https://doi.org/10.1111/ina.12751

Mokhtari, R., and M. Hossein Jahangir. 2021. "The effect of occupant distribution on energy consumption and COVID-19 infection in buildings: A case study of university building." *Building and Environment* 190: 107561. doi: https://doi.org/10.1016/j.buildenv.2020.107561

Pan, Y., C. Du, Z. Fu, and M. Fu. 2021. "Re-thinking of engineering operation solutions to HVAC systems under the emerging COVID-19 pandemic." *Journal of Building Engineering* 43: 102889. doi: https://doi.org/10.1016/j.jobe.2021.102889

Pavilonis, B., A. M. Ierardi, L. Levine, F. Mirer, and E. A. Kelvin. 2021. "Estimating aerosol transmission risk of SARS-CoV-2 in New York City public schools during reopening." *Environmental Research* 195: 110805. doi: https://doi.org/10.1016/j.envres.2021.110805

Peng, Z., A. L. Pineda Rojas, E. Kropff, W. Bahnfleth, G. Buonanno, S. J. Dancer, J. Kurnitski, Y. Li, M. G. L. C. Loomans, L. C. Marr, L. Morawska, W. Nazaroff, C. Noakes, X. Querol, C. Sekhar, R. Tellier, T. Greenhalgh, L. Bourouiba, A. Boerstra, J. W. Tang, S. L. Miller, and J. L. Jimenez. 2022. "Practical Indicators for Risk of Airborne Transmission in Shared Indoor Environments and Their Application to COVID-19 Outbreaks." *Environmental Science & Technology* 56: 1125-37. doi: https://doi.org/10.1021/acs.est.1c06531

Peng, Z., and J. L. Jimenez. 2021. "Exhaled CO2 as a COVID-19 Infection Risk Proxy for Different Indoor Environments and Activities." *Environmental Science & Technology Letters*.

Riley, E. C., G. Murphy, and R. L. Riley. 1978. "Airborne spread of measles in a suburban elementary school." *American Journal of Epidemiology* 107: 421-32. doi: https://doi.org/10.1093/oxfordjournals.aje.a112560.

Risbeck, M. J., M. Z. Bazant, Z. Jiang, Y. M. Lee, K. H. Drees, and J. D. Douglas. 2021. "Modeling and multiobjective optimization of indoor airborne disease transmission risk and associated energy consumption for building HVAC systems." *Energy and Buildings* 253: 111497. doi: https://doi.org/10.1016/j.enbuild.2021.111497

Schibuola, L., and C. Tambani. 2021a. "High energy efficiency ventilation to limit COVID-19 contagion in school environments." *Energy and Buildings* 240: 110882. doi: https://doi.org/10.1016/j.enbuild.2021.110882

Schibuola, L., and C. Tambani. 2021b. "Performance comparison of heat recovery systems to reduce viral contagion in indoor environments." *Applied Thermal Engineering* 190: 116843. doi: https://doi.org/10.1016/j.applthermaleng.2021.116843

Sha, H., X. Zhang, and D. Qi. 2021. "Optimal control of high-rise building mechanical ventilation system for achieving low risk of COVID-19 transmission and ventilative cooling." *Sustainable Cities and Society* 74: 103256. doi: https://doi.org/10.1016/j.scs.2021.103256

Shrubsole, C., S. Dimitroulopoulou, K. Foxall, B. Gadeberg, and A. Doutsi. 2019. "IAQ guidelines for selected volatile organic compounds (VOCs) in the UK." *Building and Environment* 165: 106382. doi: https://doi.org/10.1016/j.buildenv.2019.106382

Srivastava, S., X. Zhao, A. Manay, and Q. Chen. 2021. "Effective ventilation and air disinfection system for reducing coronavirus disease 2019 (COVID-19) infection risk in office buildings." *Sustainable Cities and Society* 75: 103408. doi: https://doi.org/10.1016/j.scs.2021.103408

Sun, C., and Z. Zhai. 2020. "The efficacy of social distance and ventilation effectiveness in preventing COVID-19 transmission." *Sustainable Cities and Society* 62: 102390. doi: https://doi.org/10.1016/j.scs.2020.102390

Xu, Y., J. Cai, S. Li, Q. He, and S. Zhu. 2021. "Airborne infection risks of SARS-CoV-2 in U.S. schools and impacts of different intervention strategies." *Sustainable Cities and Society* 74: 103188. https://doi.org/10.1016/j.scs.2021.103188

Zheng, W., J. Hu, Z. Wang, J. Li, Z. Fu, H. Li, J. Jurasz, S. K. Chou, and J. Yan. 2021. "COVID-19 Impact on Operation and Energy Consumption of Heating, Ventilation and Air-Conditioning (HVAC) Systems." *Advances in Applied Energy* 3: 100040. doi: https://doi.org/10.1016/j.adapen.2021.100040

Design of Energy-Neutral Smart Buildings: An Ontological Framework to Integrate LCA, BIM and PLM

Tarun Kumar – CPDM, Indian Institute of Science, Bangalore, India – tarunkumar@iisc.ac.in
Monto Mani – CST & CPDM, Indian Institute of Science, Bangalore, India – monto@iisc.ac.in

Abstract

The smart built environment (SBE) exhibits a dynamic integration between the physical and digital environment, where the physical elements, such as spaces, walls, windows, doors, roof, and floor, interact with the digital sensing elements, such as sensors, actuators, control systems, and networking systems. Energy neutrality is a concept dealing with the lifecycle energy performance of energy-saving sensing devices integrated into the SBE, such as the smart sensor-actuator system (SSAS). Ontology is a concept of representing and organising information (and their inter-relationships) about a specific domain with the intention of managing complexity, enhancing understanding, and promoting problem-solving skills. Employing semantic web technologies, a framework for designing and simulating energy-neutral, sensor-embedded smart buildings is proposed, which exhibits an ontological integration of Lifecycle Assessment (LCA), Building Information Modelling (BIM), and Product Lifecycle Management (PLM). A preliminary implementation of the proposed framework is demonstrated using OWL (Ontological Web Language) in Protégé software. After that, a design interaction matrix between buildings (and their components), building designers, product designers, and lifecycle practitioners is developed to provide efficiency, optimisation, and sustainability in the design process. This integration framework would streamline the design process, providing a collaborative simulation platform for cross-field designers to enhance the environmental performance of the SBE. In the future, this framework could be employed to create a robust real-time integrated IoT-based platform for designing and modelling energy-neutral smart buildings.

1. Introduction

The design and modelling of smart buildings is a complex process compared to conventional buildings (Kumar & Mani, 2019; Panteli et al., 2020). The smart built environment dynamically integrates the physical and digital environments, with physical elements—such as spaces, walls, windows, doors, roofs, floors, lights, HVAC and so on—interacting with digital sensing elements such as sensors, actuators, control systems, and networking systems (Dasgupta, 2018; Kumar et al., 2022). The challenges in this interactive relationship stem from the need for a real-time information exchange between physical and digital environments, emphasising the importance of decisions made during the early stages of building design. For example, luminaire technology (LED/CFL), integrated occupancy sensors, and real-time interactions (or feedback) are critical for occupant comfort, well-being, and energy efficiency in the lighting subsystem of smart buildings (Khanna et al., 2019; Kumar et al., 2018; Nair et al., 2018 and 2019). Despite recent advances in information technology and computational intel-ligence, the architecture, engineering, construction, and operations (AECO) industry manifests a sub-stantial digital divide in technology adoption (Ayinla & Adamu, 2018; Saka et al., 2022). The computing industry's technical know-how, such as semantic web technologies, could be leveraged in the AECO industry to bridge this burgeoning gap (Pauwels et al., 2017).

Smart building design (SBD) is a cross-functional domain involving multiple stakeholders, including building designers (architects, civil engineers, structural engineers), computer and electronic engineers, sensor designers, control engineers, LCA practitioners, interaction designers and data scientists (Kumar & Mani, 2017a). As a result, incorporating smart sensor-actuator systems (SSAS) into the construction, information, operation, and control systems of smart buildings takes time and resources. The SBD requires a constant knowledge exchange and

information feedback from cross-functional domains to optimise performance. LCA, BIM, and PLM are domains involved in various SBD stages but are fragmented in process/data integration and stakeholder management, resulting in data redundancy, complexity, and inefficiency.

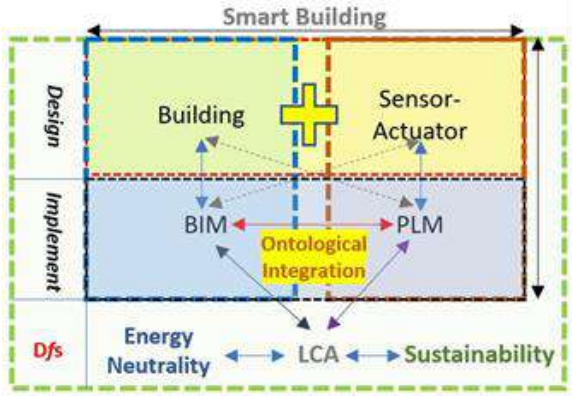

Fig. 1 – Design of energy-neutral smart buildings: conceptual structure of the research study integrating LCA, BIM and PLM

This paper proposes a framework for designing and modelling energy-neutral, sensor-embedded smart buildings using an ontological integration of LCA, BIM and PLM employing semantic web technologies. Fig. 1 presents the conceptual structure of the study.

Integrating collaborative knowledge of various designers and domains—at the early design phase of a smart building—is critical for synchronising the different design methodologies adopted by each stakeholder. Stakeholders (designers and modellers) use field-specific design and implementation methodologies from their respective domains at various stages of the design process. As a result, a comprehensive framework defining the criteria for combining data from multiple fields into a single collaborative platform that supports the inter-accessibility of data from all stakeholders involved in designing and modelling a smart building is needed. Such a framework reduces the limitations of disconnected data by creating an ontology-based linked data model for smart building design using semantic web technologies.

1.1 Energy Neutrality in Smart Buildings

Energy Neutrality is a concept dealing with energy payback associated with energy-saving sensing devices such as smart sensor-actuator systems (SSAS) over their lifecycle (Kumar & Mani, 2017b). Often, the energy involved over the lifecycle of an SSAS could be more than the energy-saving it yields, depending on the connected load (Kumar & Mani, 2017a). Smart buildings are those integrated with SSAS aimed at improving the productivity of the building occupants, saving energy, and information management. With smart buildings becoming increasingly complex, energy neutrality computations can provide an insight into the appropriate design and integration of smart sensor-actuator systems. Earlier studies into energy neutrality have revealed that the design of the SSAS in its entirety (electronics, housing, fixtures, wiring) has a significant impact on its total embodied energy (Kumar & Mani, 2017a and 2017b). The SSAS could be viewed as products integrated into buildings, with their lifecycle design influencing their effective integration in buildings, which ultimately affects the sustainability performance of smart buildings.

1.2 Lifecycle Assessment

Lifecycle assessment (LCA) is a method to assess the environmental impacts of a product (such as SSAS) throughout its lifecycle, including extraction, manufacturing, use/operation, and end-of-life stages (ISO, 2006). LCA methodology is one of the industry-accepted and scientific methods to assess the sustainability of a product (Jensen et al., 1997; Röck et al., 2018). It considers the inflow and outflow of mass, energy, and emissions through various product lifecycle stages. ISO 14040-14044 is the international standard that describes the framework and guidelines for conducting an LCA. The different phases according to ISO 14040:2006 are: 'Goal and scope definition', 'Lifecycle inventory analysis (LCI)', 'Lifecycle impact assessment (LCIA)', 'Interpretation phase' and 'Reporting and review phase' (ISO, 2006). The definition of 'system boundary' and 'functional units' are essential steps to conduct an LCA of any product. The databases used are Ecoinvent, GaBi, USDA, ELCD, Agri-footprint, etc. The prominent software used is Gabi, SimaPro, Umberto, openLCA, and so on.

1.3 Building Information Modelling

Widely used in the AECO industry, Building Information Modelling (BIM) is an integrated infrastructural data management process that shares and increases the transparency of building data in its designing, construction, and management (Ghaffarianhoseini et al., 2017; Volk et al., 2014). BIM is a three-dimensional model-ling process for developing a built environment as a digital representation of physical built elements and spaces (Ghaffarianhoseini et al., 2017). Moreover, BIM actively supports design and management decision-making at all phases of the building lifecycle, including planning, design, construction, and management stages, thus providing a collaborative platform for all the stakeholders by enhancing the information flow. The software tools for conducting BIM are Autodesk Revit, ArchiCAD, NavisWorks, Trimble Connect, and VectorWorks Architect.

Table 1 – A brief comparison of LCA, BIM and PLM

	LCA	BIM	PLM
Industry	Sustainability assessment	AECO industry	Manufacturing industry
Goal	Interested in environmental impacts	Building design construction and management	Product lifecycle management
Model & data	Lifecycle model & database	3D virtual models & BIM data	3D Product model & CAD data
Stakeholders	LCA practitioners, compliance authorities, designers & researchers	Shared repository between architects, engineers, and managers	Designers, engineers, manufacturers, researchers

1.4 Product Lifecycle Management

Product Lifecycle Management (PLM) is an extensive data management system for managing the entire life of a product. It is a collaborative activity that integrates product management and stakeholders across its lifecycle (Lämmer & Theiss, 2015). The product's data flows through initial design conception to detailed engineering design, manufacturing, packaging, distribution, usage, service (maintenance), and end-of-life phases. It is critical to centralise a product's information throughout its lifecycle to facilitate cross-domain knowledge exchange. The approach adopted in PLM primarily focuses on improving product efficiency in its design, economic value, environmental impact, and social outreach to promote the decision-making process, especially during early design decisions. Table 1 compares LCA, BIM, and PLM and lays the conceptual foundation for their integration.

1.5 Ontology and Semantics

Ontology is a machine-readable (formal) specification of conceptualisation for representing and organising information in a specific domain to manage complexity, improve understanding, and promote problem-solving ability (W3C, 2004). By converting complex systems into simple processes, ontology creates a shared and collaborative platform in the information sciences, allowing knowledge to be used in widespread cross-domain functionality that can be searched and queried via the internet. It also explicitly manages knowledge bases by systematically organising their specification—in terms of concepts, classes, properties, relations, definition, function, constraints, axiom, rules, and categories—and displaying logical reasoning and web semantics in data description and structural layout (for example, knowledge graph).

The family of ontologies (formal knowledge representation languages) are created in Web Ontology Language (OWL), based on the Semantic Web domain (Antoniou & Van Harmelen, 2004; W3C, 2004). The design of OWL is a build-up version of the Resource Description Framework (RDF). Semantic web technologies (OWL and RDF) promote mapping and analysis of data to create meaningful knowledge-bases and promote information interoperability across domains. In general terms, the primary function of semantic web technologies is the creation of an interlinkage (of language with different formats) that integrates different frameworks adopted from cross-functional fields and data collected from multiple sources in varied (non-standardised) protocols. Hence, ontologies authored in formal languages (such as OWL) are the connecting bridges across multiple data formats to extract common (and unambiguous) meaningful information, characterising the knowledge in class, objects, and

their inter-relativity, functions, attributes, and hierarchies. From the semiotic perspective, any language (machine-readable or English) consists of three distinct fields: a) syntactics (objective: the set of rules and grammatical structure), b) semantics (subjective: the arrangement of vocabulary in a structured format to generate its meaning and expression), and c) pragmatics (contextual implicature: inference and implication, context-dependent). Similarly, semantic web technologies have triples for knowledge management and modelling semantic data. The semantic triples consist of three entities which are as follows: (a) subject (entity); (b) predicate (attribute); and (c) object (value-model) to compose a common machine-interpretable statement about the semantic database. Therefore, this makes ontological languages (e.g., OWL) an integration layer to standardise the cross-functional knowledge-base. For the effective design of smart buildings, the integration of LCA, BIM, and PLM is necessitated. The 'smart building design' domain could benefit immensely by leveraging the power of ontology and semantics to integrate SSAS into buildings, thereby making them more sustainable. Hence, Ontology and semantic web technologies provide an appropriate collaborative platform for such a cross-domain integration.

2. Integrated Ontological Framework

An integrated ontological framework is proposed in Fig. 2 to integrate LCA, BIM and PLM at various levels, i.e., L1-data integration layer, L2-data exchange layer, L3-software implementation layer, L4-design implementation layer, L5-stakeholder integration layer, and L6-domain integration layer. An ontological knowledge integration framework across these layers (L1-L6) provides a consolidated framework for the collaborative design of energy-neutral smart buildings. The three vertices of the triangular layers represent the LCA (sustainability domain), the BIM (building domain), and the PLM (product design domain), respectively. In the L1 layer, LCA data is integrated with product and building data. In layer L2, LCA, BIM and PLM exchange formats are consolidated to form a machine-interpretable, formal, and explicit data layer. Then, these data are fed into an integrated software environment that combines the LCA, BIM and PLM capabilities (L3).

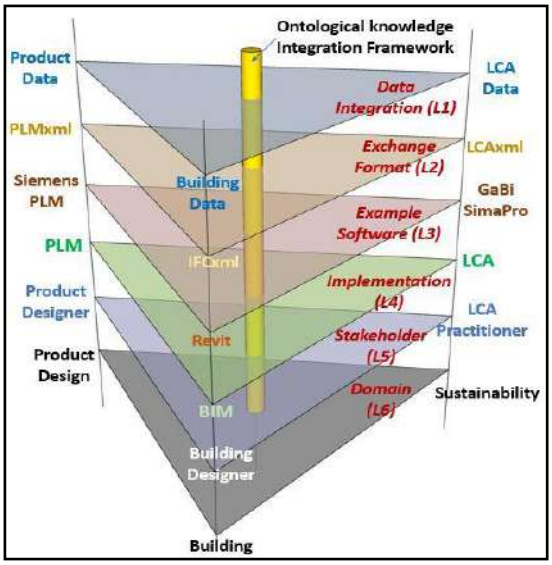

Fig. 2 – A model framework for the ontological integration of BIM, PLM and LCA for the design of energy-neutral smart buildings

After that, a design implementation layer (L4) is envisaged with data processing and knowledge integration capabilities. The L4 layer leads to a collaborative design platform(L5) comprising subject experts, i.e., LCA practitioners, architects and product designers. A single cross-functional design team may replace these designers in the future. Finally, the domain level integration of sustainability, building design, and product design is completed at layer L6, resulting in an inter-disciplinary domain for smart building design.

3. Implementation in Protégé

This preliminary framework for LCA-BIM-PLM integration is modelled on Protégé software using the ontological web language (OWL). The XML version used for the data integration is XML version 1.0. The data modelling vocabulary used is RDFS (Resource Description Framework Schema). The model framework structure comprises: - 'Entity', 'Classes', 'Object properties', 'Annotation properties', 'Data properties' and 'Individual by class'. 'Design_Smart_Buildings' is the main class in 'Owl: Things', and 'LCA', 'BIM', and 'PLM' are subclasses, as shown in Fig. 3.

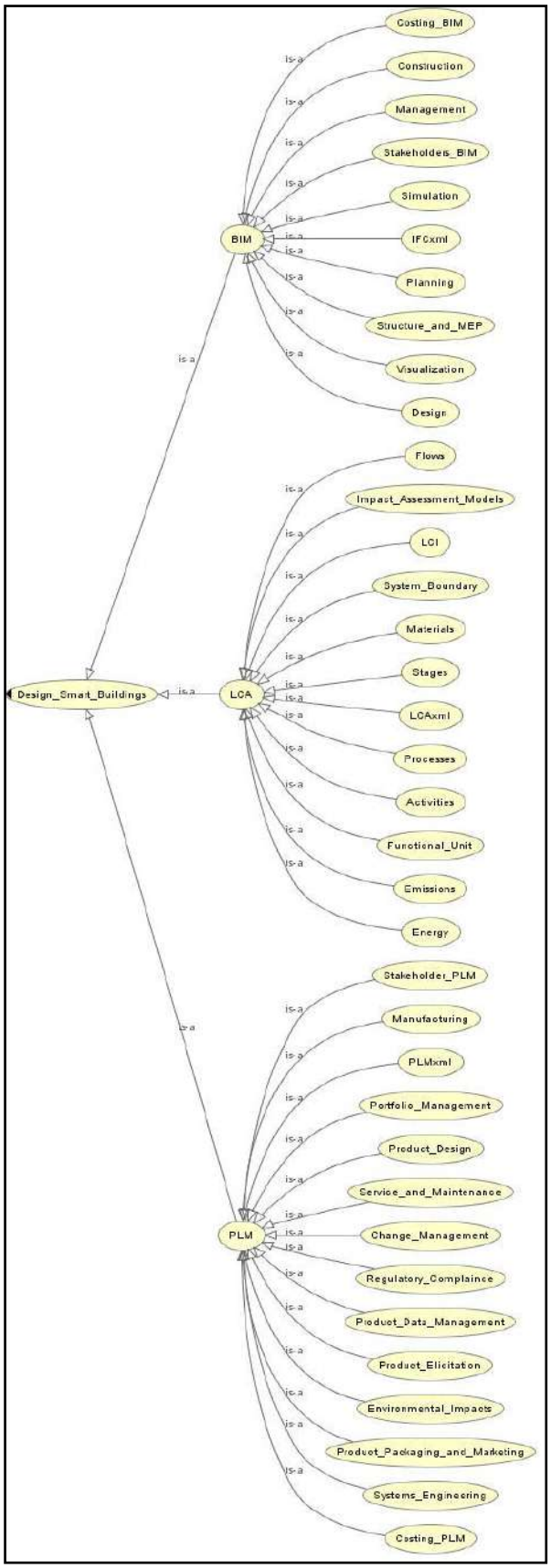

Fig. 3 – Preliminary implementation of the Model LCA-BIM-PLM framework for the design of smart buildings in Protégé Software

This framework schema can be saved in RDF/XML syntax, Turtle syntax, OWL/XML syntax, OBO syntax, Manchester/OWL syntax, OWL functional syntax, and LaTeX JSON-LD syntax. The 'reasoner' used for querying is ELK 0.4.3. 'OWLviz' is used for visualisation, while 'OntoGraf' is used for creating the graph. DL query and SPARQL 1.1 semantic query languages are used to access, retrieve, and manipulate data in RDFS. A Java code is generated to interface, translate, and bridge the sematic web ontology with the logic programming domain.

Each class/subclass can have their object, data, and annotation properties connected by relationships. Each instance in this framework can be designed as a standalone smart building with all the above-mentioned characteristics. These unique instances of smart buildings could be accessed via the web and would form a smart building database known as the 'Internet of Buildings' (IoB).

4. Discussions

As shown in Table 2, column V1 represents the lifecycle of data through 'data', 'information', 'knowledge', 'insight and wisdom' and 'design and optimisation' stages. The rows represent the integration between LCA, BIM and PLM domains.

Table 2 – OWL-based ontological integration framework for LCA, BIM and PLM to design energy-neutral smart buildings

V1	V2	V3	V4	V5
		LCA	BIM	PLM
H1	Data	ILCD	IFC	JT
	Processing and Apply Syntax	LCA XML	IFC XML	PLM XML
H2	Information	Integrate Data Format		
	Meaning and Semantics	Ontological Integration by OWL		
H3	Knowledge	Standardise Meaning		
	Cross Domain Integration	LCA K_n1	BIM K_n2	PLM K_n3
H4	Insight and Wisdom	Knowledge Integration		
	New Knowledge Generation	Shared Conceptualisation		
H5	Design and Optimisation	Creative Innovations		
	Smart Buildings	Resource Efficient and Energy-Neutral Design		

Feedback

It should be noted that appropriate transformations are applied to each stage. H1 represents the data processing and application of syntax for data integration. Existing data in the LCA, BIM and PLM industries are fragmented. Recently, work on standardising data formats within the domains has started, e.g., ILCD format in LCA, IFC data format in BIM, and JT format in PLM. The inter-operability of such cross-domain datasets is low due to multiple formats, multiple software platforms and different protocols. The eXtended Markup Language (XML) can solve this problem by applying user-defined specific rule sets (Syntax) to make it machine-interpretable and independent of software and hardware platforms. In this framework, the LCA, BIM and PLM data are converted to XML format, ready to be processed and queried.

Once the cross-domain data is syntactic and formal (machine-interpretable), the question of data semantics (meaning of such data) arises. In the H2 stage, the ontological web language (OWL) is used to semantically integrate this data and reduce ambiguity in its meaning. The processing of cross-functional data with semantic web tools would transform the data into chunks of useful information, which is still far away from a consolidated knowledge stage. In the H3 stage, when these chunks of information are integrated vertically in their respective domain, it becomes knowledge (e.g., Kn1 in LCA, Kn2 in BIM, Kn3 in PLM). In the next stage (H4), these knowledge sets are integrated through an ontological knowledge-integration framework to form a consolidated design knowledge set that provides valuable insights into smart building design and modelling. This acquired wisdom backed by empirical and integrated data, constitutes the breeding ground for 'shared conceptualisation' and 'new' knowledge. The designer (of smart buildings) would use this 'new knowledge' to improve designs, create innovations and provide optimisations for energy-neutrality in the H5 stage. Moreover, the design and optimisation (H5) stage would provide a feedback loop for the data stage (H1), further improving the data requirements, new data collection, data filtering and data integration processes. The capability of the H5 stage to provide a reinforcement feedback loop is not only limited to H1 stage, but it can also give feedback to H2, H3, H4 and H5 stage.

This framework facilitates multi-variate assessment of smart building performance in terms of energy, functionality, and operability before finalising the design by creating a 'design schema' as a transitional framework between the building's physical and digital (geo-spatial and energy-related) information. Additionally, this meta-framework comprehensively characterises a smart built environment integrated with a sensing system, allowing designers (and stakeholders) to evaluate the design using a hybrid simulation platform, and then make necessary early-design decisions regarding building performance, sensor-actuator integration, energy efficiency, and human-building interactions (HBI).

4.1 Design Implications

This ontological integration framework provides for the interactions (and feedback) between various designers, researchers and stakeholders involved in designing energy-neutral smart buildings. A design interaction matrix captures the interactions between buildings (and their functional components), and designers (of building, products, and sustainability) are captured by a design interaction matrix, as shown in Table 3. B(i) and B(j) represent smart buildings. B(i) is the superset containing elements from individual building components to the whole building system. 'Building designer' set D(B) consists of architects, civil engineers, structural engineers, and various consultants involved in the BIM process. Whereas D(P) represents the product designer set of smart sensor-actuator systems and energy-saving appliances.

Table 3 – Design interaction matrix for the ontological integration of BIM, PLM and LCA for energy-neutral smart buildings

$B(i) \rightarrow B(j)$ $\forall B(i) \subseteq B(j)$	**B(j)**	**D(B)**	**D(P)**	**S(L)**
B(j)	B(j) → B(j)	B(j) → D(B)	B(j) → D(P)	B(j) → S(L)
D(B)	D(B) → B(j)	D(B) → D(B)	D(B) → D(P)	D(P) → S(L)
D(P)	D(P) → B(j)	D(P) → D(B)	D(P) → D(P)	D(P) → S(L)
S(L)	S(L) → B(j)	S(L) → D(B)	S(L) → D(P)	S(L) → S(L)

To add the sustainability layer to the smart building design, S(L) indicates the LCA practitioners who perform the sustainability assessment of the system.

The diagonal of this matrix is the self-interactions in the B(j), D(B), D(P) and S(L). The first cell represents the interaction between buildings B(i) and B(j), which opens the possibilities of inter-building communication and smart city integration. This matrix is skew-symmetric, as the D(B)→B(j) interaction is not the same as B(j)→D(B) interaction, but rather is opposite in direction.

The ontological integration framework can assist these interactions between stakeholders in designing better smart buildings. In future, these interactions can be automated, and the D(B), D(P) and S(L) designers can be integrated to form one single set of designers, known as 'Smart Building Designers'. Such cross-platform designers would further improve the design framework, resulting in smart buildings that are both energy- and resource-efficient.

5. Conclusions

Based on the ontological integration of the three participating domains, this LCA-BIM-PLM integrated framework provides a plausible solution for designing an energy-neutral smart building system. A preliminary implementation of this ontological framework is demonstrated in Protégé software with the help of OWL. Furthermore, a design interaction matrix is created between buildings (and their components), building designers, product designers, and lifecycle practitioners, allowing for increased efficiency, optimisation, and sustainability in the building design and simulation process, which is further enhanced by reinforcing feedback loops.

The proposed framework would improve the environmental performance of smart buildings by streamlining the design and simulation process, providing a collaborative platform for cross-field designers. In the future, a robust real-time platform for designing and modelling energy-neutral smart built environments could be developed using this framework as its foundation.

References

Antoniou, G., and F. Van Harmelen. 2004. "Web Ontology Language: Owl." In *Handbook on Ontologies*: 67–92. Springer.

Ayinla, K. O., and Z. Adamu. 2018. "Bridging the Digital Divide Gap in BIM Technology Adoption." *Engineering, Construction and Architectural Management* 25(10): 1398–1416. doi: https://doi.org/10.1108/ECAM-05-2017-0091

Dasgupta, A. 2018. *Towards a Unified Framework for Smart Built Environment Design: An Architectural Perspective*. Virginia Tech.

Ghaffarianhoseini, A., J. Tookey, A. Ghaffarianhoseini, N. Naismith, S. Azhar, O. Efimova, and K. Raahemifar. 2017. "Building Information Modelling (BIM) Uptake: Clear Benefits, Understanding Its Implementation, Risks and Challenges." *Renewable and Sustainable Energy Reviews* 75: 1046-1053. doi: https://doi.org/10.1016/j.rser.2016.11.083

ISO. 2006. *ISO 14040: Environmental Management–Life Cycle Assessment—Principles and Framework*. International Organization for Standardization.

Jensen, A A, J. Elkington, K. Christiansen, L. Hoffmann, B. T. Moller, and A. Schmidt. 1997. "Life-Cycle Assessment (LCA)-a Guide to Approaches." *European Communities*. https://www.eea.europa.eu/publications/GH-07-97-595-EN-C/Issue-report-No-6.pdf

Khanna, A., S. Arora, A. Chhabra, K. K. Bhardwaj, and D. Kumar Sharma. 2019. "IoT Architecture for Preventive Energy Conservation of Smart Buildings BT - Energy Conservation for IoT Devices : Concepts, Paradigms and Solutions." edited by Mamta Mittal, Sudeep Tanwar, Basant Agarwal, and Lalit Mohan Goyal, 179–208. Singapore: Springer Singapore. doi: https://doi.org/10.1007/978-981-13-7399-2_8

Kumar, T., and M. Mani. 2017a. "An Energy-Neutrality Based Evaluation into the Effectiveness of Occupancy Sensors in Buildings: An Integrated Life-Cycle Study." In *Design to Thrive Proceedings* PLEA 2017, 2:2579–86. NCEUB 2017

Kumar, T., and M. Mani. 2017b. "Life Cycle Assessment (LCA) to Assess Energy Neutrality in Occupancy Sensors." In *Research into Design for Communities*: 105–16. doi: https://doi.org/10.1007/978-981-10-3521-0_9

Kumar, T., and M. Mani. 2019. "Discerning Occupant Psychosocial Behaviour in Smart Built Environment and Its Design." In *Proceedings of the 1st ACM International Workshop on Urban Building Energy Sensing, Controls, Big Data Analysis, and Visualization - UrbSys'19*: 69–76. doi: https://doi.org/10.1145/3363459.3363534

Kumar, T., R. R. Rao, P. C. Ramamurthy, and M. Mani. 2018. "Safety of Light Emitting Diode (LED) Based Domestic Lighting in Rural Context." In *2018 15th IEEE India Council International Conference (INDICON)*: 1–5. Doi: https://doi.org/10.1109/INDICON45594.2018.8987093

Kumar, T., R. Srinivasan, and M. Mani. 2022. "An Emergy-Based Approach to Evaluate the Effectiveness of Integrating IoT-Based Sensing Systems into Smart Buildings." *Sustainable Energy Technologies and Assessments* 52: 102225. doi: https://doi.org/https://doi.org/10.1016/j.seta.2022.102225

Lämmer, L., and M. Theiss. 2015. "Product Lifecycle Management." In *Concurrent Engineering in the 21st Century: Foundations, Developments and Challenges*. doi: https://doi.org/10.1007/978-3-319-13776-6_16

Nair, S., R. Rao, T. Kumar, G. G. Prasad, M. Kumar, P. K. Henna, A. Saifudeen, and M. Mani. 2019. "Design of a Do-It-Yourself (DIY) Based Solar-Powered LED Lighting System for Training and Empowering Rural Youth." In *ICoRD 2019:* 451–60. doi: https://doi.org/10.1007/978-981-13-5974-3_39

Nair, S., R. R. Rao, T. Kumar, G. G. Prasad, M. Kumar, P K. Henna, A. Saifudeen, and M. Mani. 2018. "'Roshini' - Developing a DIY Rural Solar Light: Utilizing Products at End-of-Life (EoL) Stage." In *2018 IEEE Global Humanitarian Technology Conference (GHTC)*: 1–6. doi: https://doi.org/10.1109/GHTC.2018.8601891

Panteli, C., A. Kylili, and P. A Fokaides. 2020. "Building Information Modelling Applications in Smart Buildings: From Design to Commissioning and beyond A Critical Review." *Journal of Cleaner Production* 265: 121766. doi: https://doi.org/https://doi.org/10.1016/j.jclepro.2020.121766

Pauwels, P., S. Zhang, and Y.-C. Lee. 2017. "Semantic Web Technologies in AEC Industry: A Literature Overview." *Automation in Construction* 73: 145–65. doi: https://doi.org/https://doi.org/10.1016/j.autcon.2016.10.003

Röck, M., A. Hollberg, G. Habert, and A. Passer. 2018. "LCA and BIM: Visualization of Environmental Potentials in Building Construction at Early Design Stages." *Building and Environment* 140: 153–61. doi: https://doi.org/https://doi.org/10.1016/j.buildenv.2018.05.006

Saka, A. B., D. W. M. Chan, and A.-M. Mahamadu. 2022. "Rethinking the Digital Divide of BIM Adoption in the AEC Industry." *Journal of Management in Engineering* 38(2): 4021092.

Volk, R., J. Stengel, and F. Schultmann. 2014. "Building Information Modeling (BIM) for Existing Buildings—Literature Review and Future Needs." *Automation in Construction* 38: 109–27.

W3C. 2004. "OWL Web Ontology Language Semantics and Abstract Syntax." Edited by P. Patel-Schneider, P. Hayes, and I. Horrocks. W3C. https://www.w3.org/TR/owl-semantics/semantics-all.html

Assessing the Performance of a Simplification Algorithm for Urban Building Energy Modeling in Multi-Objective Optimization

Federico Battini – Free University of Bozen-Bolzano, Italy – federico.battini@natec.unibz.it
Giovanni Pernigotto – Free University of Bozen-Bolzano, Italy – giovanni.pernigotto@unibz.it
Andrea Gasparella – Free University of Bozen-Bolzano, Italy – andrea.gasparella@unibz.it

Abstract

Urban Building Energy Modeling and Multi-Objective Optimization are two very computationally intensive applications of Building Performance Simulation. In this research, a simplification algorithm developed to speed up thermal simulations at urban scale was tested to assess its performance in optimization studies. Since the algorithm showed good accuracy at the individual building level, it was applied to standalone buildings, considering a set of energy efficiency measures and all the possible combinations of four objectives, i.e., heating and cooling needs, thermal comfort and costs. The algorithm showed adequate performance in finding the optima with the same inputs for most of the considered buildings and combinations of objectives in different climatic conditions, allowing the simulation time to be reduced to one third.

1. Introduction

In 1965, Gordon E. Moore stated that the number of transistors on an integrated circuit would have increased at a rate of roughly a factor of two per year, at least over ten years (Moore, 1965). Nowadays, such a prediction, known as Moore's law, is still true, and it means that the power of computers is approximately doubling every couple of years. Thanks to such exponential increases in computing resources, two fields of Building Performance Simulation *BPS* have been gaining more and more interest in recent years: Multi-Objective Optimization *MOO* and Urban Building Energy Modeling *UBEM*. Rather than offering a one-design solution, *MOO* provides the flexibility of choosing from a set of optimal solutions with a more realistic decision-making process (Costa-Carrapiço et al., 2020). On the other hand, *UBEM* aims at finding an aggregated and simplified way of estimating the operational energy needs of groups of buildings, overcoming the limitations of single building modeling (Reinhart & Davila, 2015).

The major computational cost of *MOO* and *UBEM* is the main drawback that they have in common. Regardless of other technical aspects, such as the modeler's skills and knowledge, being too computationally demanding is the first hurdle preventing their widespread employment in common practice. In addition, it is also the main reason why most of the *UBEM* studies present in the literature investigate retrofit or design scenarios (Ang et al., 2020) rather than performing *MOO*. Haneef et al. (2021) carried out one of the few studies combining *UBEM* and *MOO*. Considering a residential district of around a hundred buildings, they examined different sets of renovation measures for the building envelope and found the Pareto front with regarding three objectives, i.e., energy, economic and sustainability performances.

In a previous work (Battini et al., 2021), we proposed a simplification algorithm for *UBEM* to speed up the simulation time limiting the accuracy loss at hourly and building scale. The algorithm simplifies any arbitrarily shaped building into a representative shoebox to estimate the building's indoor temperatures and thermal loads. Since the procedure showed good precision in assessing the building's performance at individual level, it could also be used to expedite other aspects of *BPS*, such as *MOO*. Given these premises, the aim of the present work is to assess the capabilities of the simplification in performing *MOO*. A batch of standalone buildings were selected to test the procedure and they were simulated in three climates. The optimization was carried out considering energy efficiency measures

pertaining only the building envelope respect to up to four objectives, i.e., heating needs, cooling needs, indoor thermal comfort, and economic performance. The objectives were considered one, two, three and four at a time, in order to evaluate the algorithm's reliability with all possible target combinations.

2. Methodology

2.1 Simplification Algorithm

The simplification, or "shoeboxing", algorithm is capable of converting a building of any shape into a shoebox. Thus, from a detailed or starting model, a simplified or shoebox model is obtained. The process to be employed for simplifying each building present in an urban model into its representative shoebox has three steps:

1. *Shoebox generation*: by solving a non-linear system of three equations in three unknowns, the dimensions of the shoebox are found from the starting building geometry.
2. *Radiation modeling*: opaque surfaces are placed on a portion of each window of the simplified model, in order to reduce the amount of incoming radiation and reproduce the effect of the contextual and self-shadings simulated in the detailed model. To size such equivalent shading surfaces, a radiation analysis is performed on both models to compute obstruction ratios for each orientation and floor.
3. *Building adjacency*: adiabatic surfaces are used to account for adjacent buildings.

A more in-depth description of the shoeboxing process can be found in a previous work by the authors (Battini et al., 2021). Once obtained, detailed and simplified models are characterized by the same non-geometrical features.

The procedure does not depend on specific tools to be developed, hence it can be reproduced with any software having the right capabilities. In this work, Rhinoceros and Grasshopper were employed for the geometrical conversion, Ladybug Tools SDK was used for creating the energy models, and EnergyPlus was utilized as *BPS* tool. The programs were coupled by automating the entire process thanks to custom-made Python scripts.

2.2 Multi-Objective Optimization

2.2.1 Buildings selection for testing

The simplification algorithm developed was first tested on 3072 buildings of complex shape built out of polyominoes (Golomb, 1994) to guarantee complex and non-repetitive shapes. Moreover, to assess its prediction capabilities under different boundary conditions, every building geometry obtained and its related simplified model were simulated in three climates, i.e., Bolzano and Messina, Italy, and Denver, US.

Since performing a *MOO* is already largely computationally and time-consuming, a set of buildings were chosen from the ones already generated. Fig. 1 reports the boxplots for the relative annual differences between detailed and simplified models in the three climates. The results are reported as a function of the number of floors of each building and show how, for both targets, the simplified model prediction always falls within ± 20 % difference. Five buildings for each target (i.e., heating and cooling) were chosen for each climate, thus thirty building were used in the *MOO*. In order to employ representative buildings in this work, starting from the relative annual differences obtained by the previous study, buildings corresponding to the minimum, first quartile, median, third quartile and maximum difference were selected. In this way, it was possible to study buildings whose performances are different but also representative of the batch which they were picked from. Among the starting 3072 possibilities, Fig. 2 reports the buildings selected for the analysis. Instead of simulating all buildings in the three climates, each building was simulated in the same climate from which it was selected. Thus, ten buildings were simulated per each climatic condition.

2.2.2 Optimization

The aim of the present optimization is to test whether the detailed and simplified building models' non-dominated solutions match in terms of inputs. Thus, the optima found should have the same values for the inputs rather than the outputs.

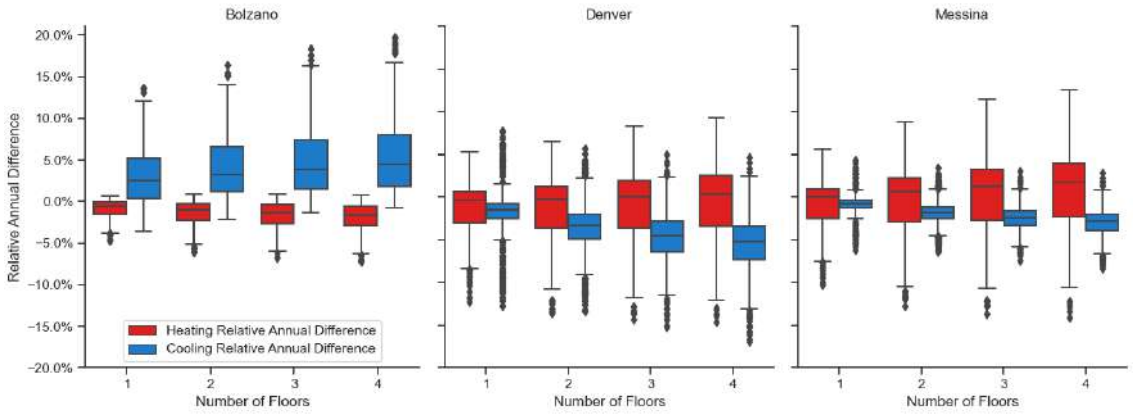

Fig. 1 – Boxplots for annual heating and cooling needs relative differences depending on buildings' number of floors for the entire building

Since the algorithm was developed for urban scale applications, the variables considered in this first study only focus on the envelope. Since in *UBEM*, the information regarding the systems is usually not available, retrofit or design scenarios mainly pertain to the buildings' envelope. Thus, three variables were considered:

- insulation type: all external opaque surfaces are characterized by the same composition, three types of insulation were selected, i.e., XPS, mineral wool, and cellulose fiber.
- insulation thickness: the thickness of the type of insulation varied from 2 to 20 cm with a step of 2 cm.
- type of window: five different types of windows were chosen, such as double glazing with air filling, double glazing with argon filling and high solar factor, double glazing with argon filling and low solar factor, triple glazing with argon filling and high solar factor, and triple glazing with argon filling and low solar factor.

In Table 1, the variables considered are reported along with their properties and related investment costs. As far as insulation is concerned, the investment cost per square meter was computed in function of the thickness s according to the formulas reported for each type of material. The investment costs considered in this study for the opaque and transparent envelope are the same as those employed by Haneef et al. (2021) and Pernigotto et al. (2017). Given the low number of combinations, a full factorial analysis was carried out and all possibilities were simulated.

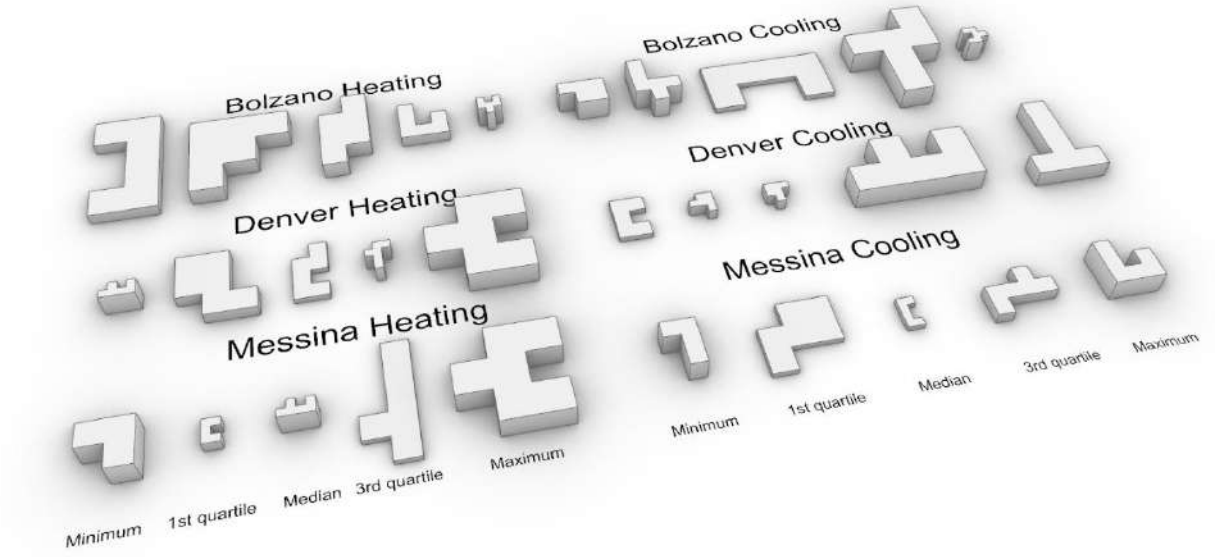

Fig. 2 – Selection of buildings for each target and climate

Table 1 – Variables for *MOO*

Insulation				
Insulation	Thermal conductivity [W m^{-1} K^{-1}]	Density [kg m^{-3}]	Specific heat [J kg^{-1} K^{-1}]	Investment cost [€ m^{-2}]
XPS	0.035	30	1450	112.5 · s + 55.6
Mineral wool	0.038	130	1030	213.6 · s + 70.2
Cellulose fiber	0.045	160	2000	363.7 · s + 74.6
Windows				
Window		Glass transmittance [W m^{-2}K^{-1}]	SHGC [-]	Investment cost [€ m^{-2}]
Double glazing air filling		2.72	0.76	247.30
Double glazing argon filling high SHGC		1.14	0.61	404.33
Double glazing argon filling low SHGC		1.10	0.35	439.06
Triple glazing air filling high SHGC		0.61	0.58	477.65
Triple glazing air filling low SHGC		0.60	0.34	454.49

Thus, the real Pareto solutions were found, since no optimization algorithm was used.

To test the simplification capabilities as broadly as possible, the heating demand, cooling demand, thermal comfort and economic performance were considered as the objectives to be minimized. The heating and cooling needs were accounted as annual energy needs expressed in megawatt hour by summing up the hourly needs. Thermal comfort was evaluated as the annual average of the hourly results for the Predicted Percentage of Dissatisfied *PPD*, since it is one of the suggested methods by UNI EN ISO 7730 (UNI, 2006) for long-term evaluations of comfort conditions. The costs were considered by computing the Net Present Value *NPV* of the building by means of an economic analysis with a lifespan of 30 years according to UNI EN 15459-1 (UNI, 2018). The optimal solutions were found for all the possible combinations of objectives, thus from one at a time to all four together, resulting in 15 combinations. In this way, it was possible to assess the performance of the procedure with a variable number of objectives and non-dominated solutions.

For each case, the optimal solutions found for the detailed and simplified models were compared. First, the total number of optima was counted. Then, it was checked for the presence of non-matching solutions as follows: (i) the solutions that were found as optima for the detailed model which were dominated for the simplified one were counted as optima not found, (ii) the solutions that were labeled as non-dominated for the simplified model that were not optima for the detailed one were considered as wrongly found optima. On top of these two absolute values, for each combination of objectives, the error rate in performing a right choice or a wrong choice with respect to the total number of real optima was computed.

3. Results and Discussion

Even though the aim of this work is to assess if the detailed and simplified models result in having the same input values for the optimal solutions, the simulation outputs for heating and cooling needs, and the *PPD* for the detailed and simplified models were visually compared.

Fig. 3 and Fig. 4 show that the simplified models tend to underestimate the heating needs and overestimate the cooling ones. Such behavior was present also in the previous work from which the buildings were selected. However, since prior to this research the algorithm was tested focusing mainly on the buildings' shape rather than varying the thermophysical properties of the envelope, it was not possible to state that such a tendency could be true in all cases. Fig. 5 reports the boxplots with the *PPD* distribution for all the combinations for the buildings considered. Compared with the thermal needs, the distributions of the annual average *PPDs* for the simplified and detailed models are much more similar.

From Figs. 3, 4 and 5, it is clear that the differences between detailed and shoebox models are independent of the starting building's shape. Thus, to be consistent with previous research, the results for the optimization were compared in the three climates to assess the procedures' weaknesses more in detail.

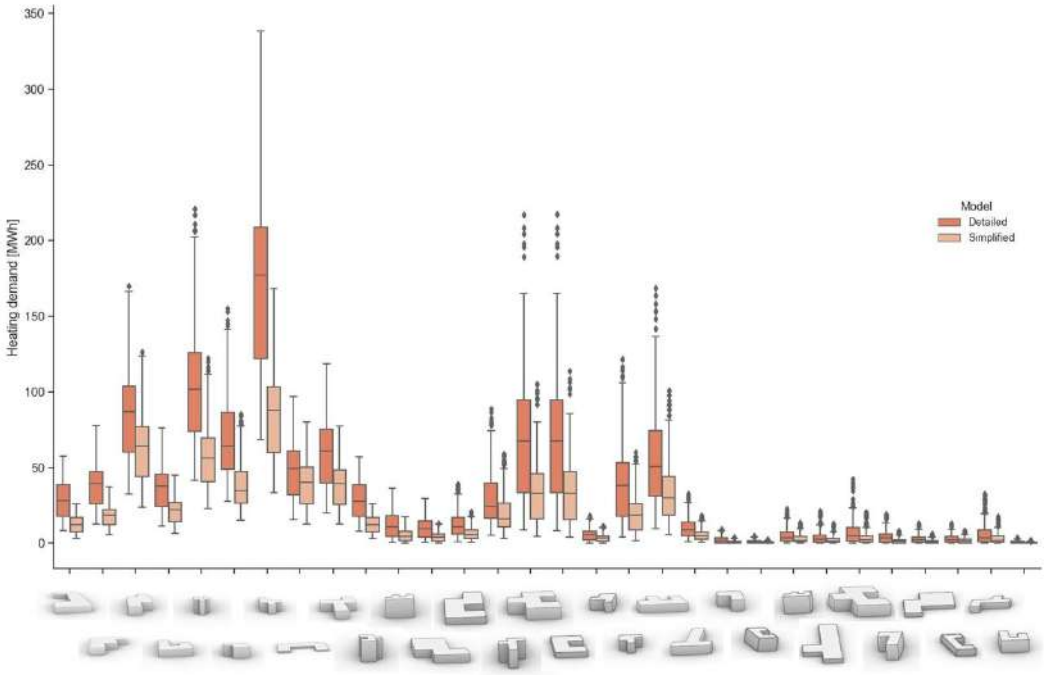

Fig. 3 – Annual heating needs boxplots for detailed and simplified models of each building for all input combinations

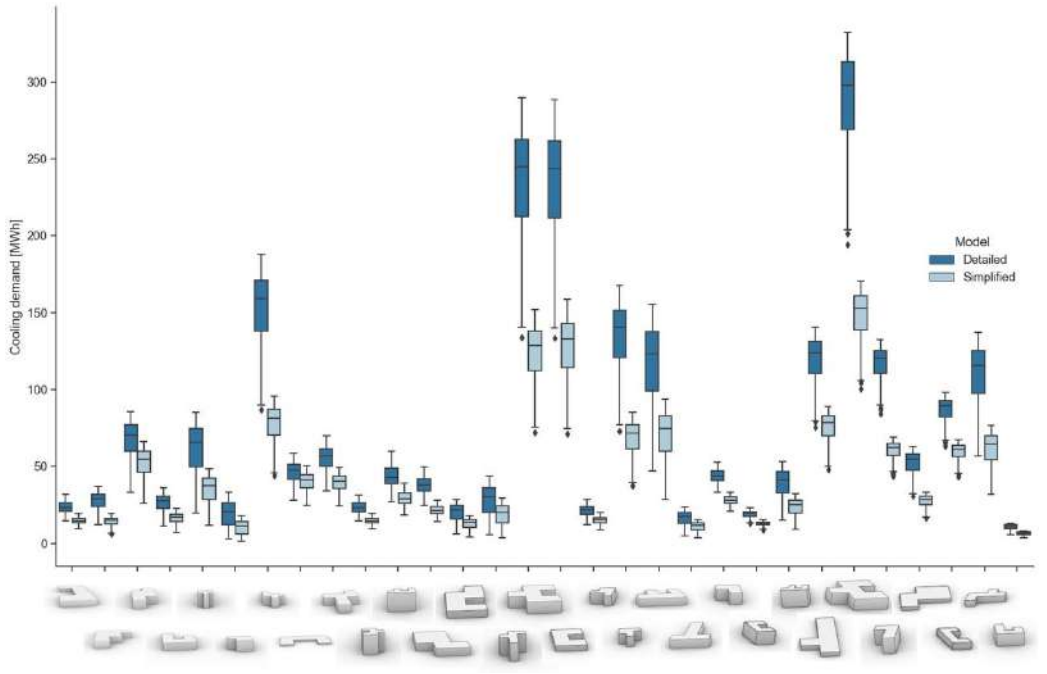

Fig. 4 – Annual cooling needs boxplots for detailed and simplified models of each building for all input combinations

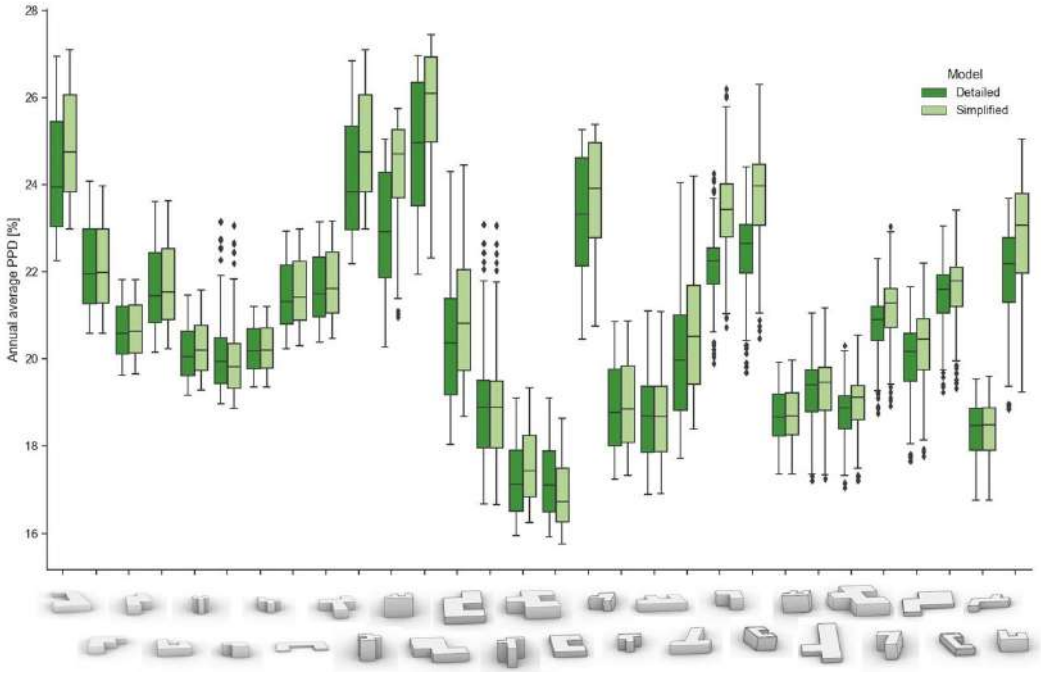

Fig. 5 – *PPD* boxplots for detailed and simplified models of each building for all input combinations

Table 2 reports the results for all combinations of objectives in the three climates. To visually understand in which cases the algorithm is performing better, the cells reporting the objectives considered were color-coded according to the right or wrong error rates. The combinations of objectives were colored in green if both error rates were lower or equal to 10 %, yellow if at least one of them was larger than 10 % and lower or equal to 20 %, and red if at least one of the two errors was greater than 20 %. In this way, it is possible to have a quick understanding of the reported tabular results.

The number of optimal solutions found for the detailed models is greatly affected not only by the number of objectives but also by the type of objectives considered. When antagonist objectives such as heating and cooling are in the same optimization problem, the number of optimal solutions increases much more compared with other cases. Since the *NPV* is related to both heating and cooling annual needs, including the economic performance leads to an increase of optima as well. Even though from Fig. 5 it seems that, for detailed and simplified models, the distributions for the annual average thermal comfort could be similar, Table 2 reports higher error rates when thermal comfort is included among the objectives, mainly for the climates of Bolzano and Denver. Generally, in all climates, low error rates are reported when having one, three or four objectives. Thus, the algorithm's performance in finding the right optimal solutions is more accurate when there is a unique solution (i.e., one objective) or the number of optima is very large.

In the climate of Bolzano, the higher error rates occur when the economic and comfort objectives are optimized. When they are coupled with the cooling needs for the simplified models, not every optimum is found. On the other hand, coupling them with the heating needs leads to mainly wrongly labeled optima. As far as the climate of Denver is concerned, the results obtained are very similar to those of Bolzano. Even though thermal comfort and costs still yield the least accurate outcomes, there is an overall reduction of the error rates, except for the analysis with thermal comfort as sole objective.

Finally, the climate of Messina is the one yielding the most accurate optimization predictions, even for the heating demand, which is not a target output for this type of climate. Overall, for standalone buildings, the algorithm is three times faster in performing energy simulations for the buildings considered. Thus, the time required to run an optimization for each of these buildings was cut to one third. Even though, in some cases, the errors are still not negligible, the algorithm's performance in finding a set of optimal solutions is adequate for the purpose.

Table 2 – Optimal solutions comparison in the three climates

Objectives	Total real optima	Total not found optima	Total wrongly labeled optima	Right choice error [%]	Wrong choice error [%]	Average number of optima
Bolzano						
Heating	10	0	0	0.00	0.00	1.00
Cooling	10	0	0	0.00	0.00	1.00
Costs	10	0	0	0.00	0.00	1.00
Comfort	10	4	4	40.00	40.00	1.00
Comfort-Costs	115	36	28	31.30	24.35	11.50
Cooling-Comfort	101	19	0	18.81	0.00	10.10
Cooling-Costs	169	13	0	7.69	0.00	16.90
Heating-Comfort	99	2	50	2.02	50.51	9.90
Heating-Cooling	289	0	0	0.00	0.00	28.90
Heating-Costs	353	1	42	0.28	11.90	35.30
Cooling-Comfort-Costs	403	52	0	12.90	0.00	40.30
Heating-Cooling-Comfort	299	0	1	0.00	0.33	29.90
Heating-Cooling-Costs	1025	5	0	0.49	0.00	102.50
Heating-Comfort-Costs	503	0	52	0.00	10.34	50.30
Heating-Cooling-Comfort-Costs	1047	5	1	0.48	0.10	104.70
Denver						
Heating	10	1	1	10.00	10.00	1.00
Cooling	10	0	0	0.00	0.00	1.00
Costs	10	2	2	20.00	20.00	1.00
Comfort	10	4	4	40.00	40.00	1.00
Comfort-Costs	332	50	17	15.06	5.12	33.20
Cooling-Comfort	153	16	1	10.46	0.65	15.30
Cooling-Costs	80	5	0	6.25	0.00	8.00
Heating-Comfort	87	5	16	5.75	18.39	8.70
Heating-Cooling	256	8	2	3.13	0.78	25.60
Heating-Costs	405	8	14	1.98	3.46	40.50
Cooling-Comfort-Costs	477	56	1	11.74	0.21	47.70
Heating-Cooling-Comfort	259	8	3	3.09	1.16	25.90
Heating-Cooling-Costs	912	13	3	1.43	0.33	91.20
Heating-Comfort-Costs	578	9	31	1.56	5.36	57.80
Heating-Cooling-Comfort-Costs	918	13	3	1.42	0.33	91.80
Messina						
Heating	10	0	0	0.00	0.00	1.00
Cooling	10	1	1	10.00	10.00	1.00
Costs	10	0	0	0.00	0.00	1.00
Comfort	10	0	0	0.00	0.00	1.00
Comfort-Costs	38	0	0	0.00	0.00	3.80
Cooling-Comfort	15	0	1	0.00	6.67	1.50
Cooling-Costs	30	2	0	6.67	0.00	3.00
Heating-Comfort	284	1	1	0.35	0.35	28.40
Heating-Cooling	290	1	3	0.34	1.03	29.00
Heating-Costs	615	5	7	0.81	1.14	61.50
Cooling-Comfort-Costs	38	0	0	0.00	0.00	3.80
Heating-Cooling-Comfort	297	0	1	0.00	0.34	29.70
Heating-Cooling-Costs	1014	6	7	0.59	0.69	101.40
Heating-Comfort-Costs	1067	4	6	0.37	0.56	106.70
Heating-Cooling-Comfort-Costs	1081	3	4	0.28	0.37	108.10

4. Conclusion

In this work, the performance of a simplification algorithm developed for *UBEM* was tested in order to speed up the simulation time of building-level *MOO*. From a previous study, a group of buildings was chosen to perform a *MOO*, and energy efficiency measures and four objectives were selected. Heating and cooling needs, thermal comfort and investment costs were considered as objectives. To test the capabilities of the simplification in finding the right optimal solutions, all possible combinations of objectives were counted, and the buildings were simulated in three different climates.

Overall, it was possible to reduce to one third the thermal simulation time, obtaining adequate results for almost all combinations of objectives, regardless of the climatic condition considered. More specifically, the error rates in choosing the right optima were lower than 10 % for more than half of the combinations of objectives considered. Except for four cases, it was always possible to limit the error rate to maximum 20 %. Nonetheless, since the optimal solutions are related to the prediction accuracy of the algorithm, improving the precision of the simplification procedure will lead to more exact solutions. For this reason, a new configuration of the algorithm modeling the incoming radiation on a monthly basis is under development by the authors.

Acknowledgement

This research has been partially developed in the framework of the Internal Project of the Free University of Bozen-Bolzano TESES-Urb ("Techno-economic methodologies to investigate sustainable energy scenarios at urban level", CUP: I54I19001130005)

References

Ang, Y. Q., Z. M. Berzolla, and C. F. Reinhart. 2020. "From concept to application: A review of use cases in urban building energy modeling." *Applied Energy* 279: 115738. doi: https://doi.org/10.1016/j.apenergy.2020.115738

Battini, F., G. Pernigotto, and A. Gasparella. 2021. "Development of a shoeboxing approach for Urban Building Energy Modeling." In *Proceedings of the VI International High Performance Buildings Conference at Purdue*, West Lafayette, IN, US.

Costa-Carrapiço, I., R. Raslan, and J. N. González. 2020. "A systematic review of genetic algorithm-based multi-objective optimisation for building retrofitting strategies towards energy efficiency." *Energy and Buildings* 210: 109690. doi: https://doi.org/10.1016/j.enbuild.2019.109690

Ente Nazionale Italiano di Normazione (UNI). 2006. *EN ISO 7730 - Ergonomia degli ambienti termici - Determinazione analitica e interpretazione del benessere termico mediante il calcolo degli indici PMV e PPD e dei criteri di benessere termico locale.*

Ente Nazionale Italiano di Unificazione (UNI). 2018. *UNI EN 15459-1 - Energy performance of buildings - Economic evaluation procedure for energy systems in buildings - Part 1: Calculation procedures, Module M1-14.*

Golomb, S. W. 1994. *Polyominoes: Puzzles, Patterns, Problems, and Packings*. Princeton, New Jersey: Princeton University Press.

Haneef, F., G. Pernigotto, A. Gasparella, and J. H. Kämpf. 2021. "Application of Urban Scale Energy Modelling and Multi-Objective Optimization Techniques for Building Energy Renovation at District Scale." *Sustainability* 13(20): 11554. doi: https://doi.org/10.3390/su132011554

Moore, G. E. 1965. "Cramming more components onto integrated circuits." *Electronics* 38(8).

Pernigotto, G., A. Prada, F. Cappelletti, and A. Gasparella. 2017. "Impact of Reference Years on the Outcome of Multi-Objective Optimization for Building Energy Refurbishment." *Energies* 10(11): 1925. doi: https://doi.org/10.3390/en10111925

Reinhart, C., and C. Davila. 2015. "Urban building energy modeling - A review of a nascent field." *Building and Environment* 97: 196-202. doi: https://doi.org/10.1016/j.buildenv.2015.12.001

Application of a Simplification Algorithm for Urban Building Energy Modeling to Complex-Shaped Educational Buildings

Matteo Merli – Free University of Bozen-Bolzano, Italy – matteo.merli@stud-extra.unibz.it
Federico Battini – Free University of Bozen-Bolzano, Italy – federico.battini@natec.unibz.it
Giovanni Pernigotto – Free University of Bozen-Bolzano, Italy – giovanni.pernigotto@unibz.it
Andrea Gasparella – Free University of Bozen-Bolzano, Italy – andrea.gasparella@unibz.it

Abstract

To reduce greenhouse gases emissions related to the building sector and to make informed decisions about sustainable building design and urban planning, building energy simulation should be adopted as a supporting tool by designers and policy makers. However, since building simulation is extremely time-consuming, its application is limited in daily design work. This research aims at testing a new simplification algorithm proposed for Urban Building Energy Modeling to reduce the computational complexity of thermal models in favor of the simulation speed without compromising accuracy. The procedure was applied on two educational buildings of complex shapes located in Bolzano, Italy. Results show that the simplified models reduced the simulation time up to 135 times, with building level relative annual deviations lower than 6 %.

1. Introduction

In the building professional sector, Building Energy Modeling *BEM* can serve to design an energy efficient building or to verify its compliance with local, regional or national energy codes, as well as the actual energy performance. The former requires the use of *BEM* as an early design tool to support design tasks aiming at finding the best cost-effective solutions. At this stage of the design process, standard inputs and boundary conditions are conventionally used and a short calculation time is essential to compare multiple alternatives. The latter bypasses the analysis of different scenarios and focuses on the final simulation output, comparing it to a reference benchmark. In this case, the models are prepared in accordance with codes or technical standards, and a high degree of calculation accuracy is expected.

Overall, since accurate modeling procedures and iterative design processes require a large amount of time and computational resources, simplification workflows can be employed to speed up these kinds of simulations. However, most of the simplification techniques present in the literature have been developed for Urban Building Energy Modeling, *UBEM,* rather than *BEM*. Indeed, since *UBEM* is very computationally intensive, it is necessary to introduce such methods in order to perform urban scale simulations.

Even though *UBEM* is a relatively new field of study aiming at designing and optimizing urban energy systems and planning urban development, several tools, such as CitySim, SimStadt, umi, CityBES, URBANopt and TEASER, have already been released. Nonetheless, in recent years, different types of simplification algorithms intended to ease *UBEM* computing resources have been proposed. Different to the tools listed above, which fully comprise the *UBEM* workflow, these algorithms are only meant to replace the simulation stage.

In 2013, Dogan and Reinhart developed a fully automated and accelerated method capable of abstracting building massing into a meaningful group of simplified box-unit (shoebox) thermal models (Dogan & Reinhart, 2013), which they later named Shoeboxer (Dogan & Reinhart, 2017). In 2019, inspired by the idea of the Shoeboxer, Zhu et al. (2019) developed the Building Blocks Energy Estimation *BBEE* method for assessing building thermal demand at the district level by combining a *BBEE* algorithm and energy databases.

In this work, a new algorithm, developed by Battini et al. (2021b), which simplifies every building energy model into a representative simplified shoe-

box, was tested at the individual building level. The aim is to evaluate the algorithm's performance in estimating the energy use and accelerating the simulation of complex-shape buildings by applying it to two educational buildings in Bolzano, Italy.

2. Methodology

The process followed in order to assess the performance of the shoeboxing algorithm on the buildings considered is made of several steps. (i) case study introduction and data gathering, (ii) detailed geometry and energy modeling, (iii) calibration against monitored temperature profiles, (iv) application of the algorithm, and (v) model simulation and comparison.

2.1 Case Study

The two case studies are two educational buildings located in Bolzano, Italy. The first one is a kindergarten, called "Positano", built in 2009, while the second one is a primary school, called "Langer", built in 2014. Fig. 1 shows the location of the two buildings in the city of Bolzano. As reflected in their year of construction, both buildings are located in the western part of the city, in which new neighborhoods have been built over the past few decades. Positano kindergarten is a three-storey building, one of which is underground, and it is located in a district in which it is surrounded by residential buildings of up to 6 floors in height.

Fig. 1 – Locations of the two buildings in Bolzano, Italy

On the other hand, Langer primary school, which has three floors above ground and one underground, faces high residential buildings from North-East to South and open agricultural areas to the west.

2.2 Detailed Building Energy Modeling

Rhinoceros3D and Grasshopper were used to model the buildings' geometry in compliance with the technical floorplan drawings provided by the Municipality of Bolzano, allowing a characterization of the outer shell with windows and external fixed shades, as well as the subdivision of the internal spaces into different zones. Multi-zonal building energy models were prepared according to two main factors: construction assemblies and use of space. Adjacent spaces with similar properties were merged into a single zone, i.e., a single massing model with no internal partitions. Since each level includes spaces with similar functions, Positano was modeled with one thermal zone per floor. On the other hand, Langer school was subdivided into 12 thermal zones, according to the different functions and shapes of the school.

To model the urban context, the geometries of surrounding buildings' up to 200 m distance away have been imported into Rhinoceros3D with the aid of Gismo, a Grasshopper plug-in which enables automatic generation of urban environment and terrain geometry through a connection with the OpenStreetMap website.

The conversion from massing models to thermal zones was conducted using Ladybug Tools, an open-source suite of plug-ins for Grasshopper, and the characterization of the energy models was automated thanks to eppy, a Python scripting language for EnergyPlus which allows rapid and selective modification of EnergyPlus input files.

The energy certifications provided by the Municipality of Bolzano were used to define the construction elements (opaque and transparent) making up the envelope of the buildings. Occupancy profiles, people density, plug loads and lighting power densities were provided by the school administrations or obtained during in-situ surveys. Since the city of Bolzano belongs to the climate zone E, the heating period was set from the 15th of October to the 15th of

April, in accordance with Italian law. For Positano, the heating setpoint was set to 21 °C, based on the real temperature data available. On the other hand, for Langer primary school, the heating setpoint was set equal to 22 °C, in accordance with the information received by the school administration. The daily schedules of occupancy were determined combining information from the schools' administration and suggestions based on technical standards, such as UNI CEN/TR 16798-6 (2018) and ASHRAE 90.1 (2013). The density of people per square meter was estimated using the technical standard UNI 10339 (1995). The infiltration rates were set equal to 0.17 ach, according to the results of a previous experimental study in which indoor conditions were monitored in a classroom at Positano kindergarten (Dugaria et al., 2021). The ventilation rates were initially estimated by means of the calculation proposed in the technical standard UNI 10339 (1995), while the ventilation schedules were obtained by estimating the window openings depending on the variation of CO_2 concentration detected by dedicated sensors. Thanks to already-performed monitoring campaigns, it was possible to have data from one sensor in one classroom for the ground and first floors in Positano and one sensor in one classroom in Langer. Moreover, in the primary school, all the thermal zones, except the classrooms and the hallway, are equipped with a controlled mechanical ventilation system. Thus, for these thermal zones, a decision was made to use the design ventilation rates and schedules reported in the energy certification. Finally, as regards the shades, a dynamic solar based control with a setpoint of 300 W/m^2 was hypothesized, in accordance with what was found by Roberts et al. (2022), limiting their activation to the period from February 15th to October 31st in both buildings. The values for the internal loads and controls for all the zones of both buildings are reported in Table 1.

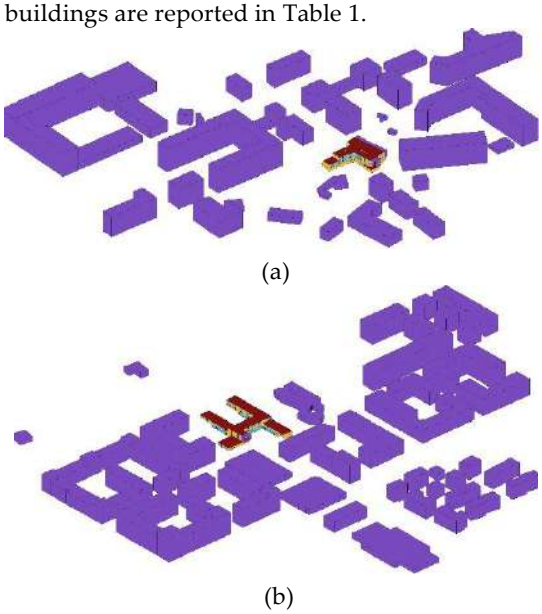

(a) (b)

Fig. 2 – 3D geometrical models of the buildings with context: (a) Positano kindergarten and (b) Langer primary school

Table 1 – Internal loads, HVAC system controls and shading control settings for type of zone in the two buildings

	Zone	Lighting power [W/m^2]	People [people/m^2]	Ventilation rate [ach]	Infiltration rate [ach]	Heating setpoint [°C]	Shading setpoint [W/m^2]
Positano	Underground	5.71	0.1	2.82	0.17	21	–
	Ground	4.25	0.17	1.72	0.17	21	300
	First	5.24	0.26	1.86	0.17	21	300
Langer	Basement	1.5	0.08	1.5	0.17	22	–
	Hallway	2.65	0.12	1.64	0.17	22	300
	Canteen	2.55	0.6	3.36	0.17	22	300
	Classrooms	3.8	0.3	2.42	0.17	22	300
	Library	3.95	0.3	3.03	0.17	22	300
	Gym	2.4	0.2	2.87	0.17	22	300
	Auditorium	5	0.6	1.83	0.17	22	300

2.3 Calibration

Both models were calibrated against the real indoor air temperature data available for two kindergarten classrooms for the whole year 2019 for Positano and of one classroom from 11th April 2019 for Langer. The calibration was performed using the weather file of Bolzano from the year 2019 only on the zones for which data were available. For Positano, the ground and first floor were calibrated, while for Langer, the zone in which the monitored classroom is present. For the primary school, the result of the calibration was then applied to the other zones without mechanical ventilation.

The models were calibrated considering as variables the ventilation rate and people density. Both variables ranged from -50 % to +50 %, with a step of 10 %, starting from the nominal values computed according to standards. Table 2 reports all the values employed for the calibration for the zones considered. For each zone, a full factorial calibration was carried out, resulting in 121 simulated models for each case. The hourly Root Mean Square Error *RMSE* was computed between the simulated and monitored temperature during the period of interest for the calibration, i.e., the heating season, from the 15th of October to the 15th of April. Since for Langer no data were available for the first period of the year, the school's classroom was calibrated only considering the last months of the year.

In the present study, since no data were available about the heating system and its rated power, an ideal heating system characterized by an unlimited power was employed. For this reason, the simulated temperatures will always be greater or equal to the setpoint, even though the monitored temperature profiles can be lower. In order to cope with such discrepancies and to pick the most suitable combination of inputs from the calibration, the minimum seasonal *RMSE* was found. Then, all the combinations yielding a *RMSE* within 5 % difference from the minimum were considered. Among these combinations, the one with the lowest *RMSE* closest to the nominal ventilation rate was selected. In this way, it was possible to prevent choosing a combination with too low or too high a ventilation rate, which could undermine annual prediction accuracy for the heating demand. Indeed, since the simulated temperatures cannot be below the setpoint, changing the ventilation rate can lead to very limited improvements in the *RMSEs* of the temperature profiles, while having a huge impact on the heating demand.

2.4 Application of the Simplification Algorithm

Once the detailed building energy models were calibrated, the simplification algorithm was used to obtain as many shoebox energy models as the number of thermal zones making up the detailed models.

Table 2 – Ranges and values for calibration per zone

	-50 %	-40 %	-30 %	-20 %	-10 %	0 %	10 %	20 %	30 %	40 %	50 %
Positano – Ground Floor											
Ventilation rate [ach]	0.86	1.05	1.25	1.44	1.63	1.72	1.82	2.01	2.2	2.4	2.59
People [people/m²]	0.08	0.1	0.12	0.14	0.16	0.17	0.18	0.19	0.2	0.21	0.22
Positano – First Floor											
Ventilation rate [ach]	0.93	1.13	1.34	1.55	1.75	1.86	1.96	2.17	2.37	2.58	2.78
People [people/m²]	0.13	0.16	0.19	0.22	0.25	0.26	0.27	0.3	0.33	0.36	0.39
Langer – Classroom											
Ventilation rate [ach]	1.21	1.48	1.75	2.02	2.29	2.42	2.56	2.83	3.09	3.36	3.63
People [people/m²]	0.15	0.18	0.22	0.25	0.28	0.3	0.32	0.35	0.38	0.42	0.45

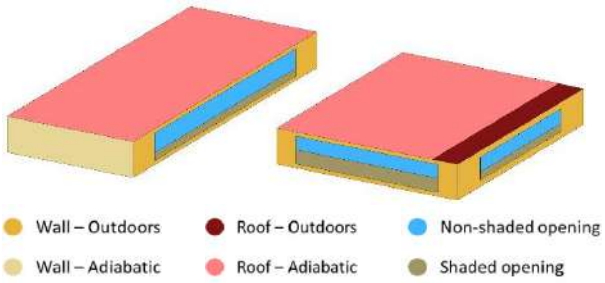

Fig. 3 – Example of shoebox models with boundary conditions

A comprehensive overview of the operations executed by the algorithm can be found in the work by Battini et al. (2021b). Nonetheless, the main steps can be summarized as follows:

1. Incident radiation analysis on the windows of the detailed energy model, subdivided for each cardinal direction by considering a ± 45° tolerance range. The ratio between the annual incident radiation on each façade and the one calculated for a reference box unit is set as shading factor in order to take into account the share of radiation obstructed by self-shading and external objects.
2. Shoebox generation based on three geometrical indicators employed to solve a system of equations, in which the three dimensions of the shoebox are the unknowns. The shoebox's apertures are generated according to the same window-to-wall ratio calculated for each orientation of the related thermal zones (± 45° tolerance range).
3. Calculation of the adjacent surface area portions for each thermal zone that are in contact with other thermal zones. Since the algorithm generates freestanding buildings, the inter-building partitions are treated as adiabatic surfaces, assuming no heat flow between touching thermal zones.
4. Shoebox aperture surface reduction according to the shading factor that was calculated for each orientation. The reduction is implemented by substituting a part of transparent surface with an opaque element having the same thermophysical properties of the window.

Once the shoeboxes were obtained, the same non-geometrical properties of the starting thermal zone were assigned to the related shoebox.

2.5 Detailed and Simplified Model Comparison

Different to the procedure followed in the calibration process, in which temperatures were used to compare the monitored and simulated profiles, the comparison between detailed and simplified models was performed on the heating needs. Although energy simulations commonly adopt Typical Meteorological Year (TMY) weather files, the same weather file with the climatic data of Bolzano for the year 2019 employed for the calibration was utilized to assess the algorithm's performance.

As regards heating needs, the comparison metrics selected for this purpose are: (i) the absolute difference of the annual energy needs, (ii) the relative difference of the annual energy needs and (iii) the *RMSE*, calculated with a time step of 1 hour. Since shoeboxes are generally smaller than the starting geometry, their heating demand was multiplied by a scaling factor to take into account the reduction of floor area that is part of the simplification process.

3. Results and Discussion

3.1 Calibration

Table 3 reports the outcomes of the calibration, in which people densities do not correspond to the ones computed from the standards, while the values for ventilation rates are the same. This is because, even though the lowest *RMSEs* obtained were the ones with the greatest ventilation rates, as stated in Section 2.5, values closer to the ones computed following the standards would have been chosen if within 5 % difference.

Table 3 – Calibration results

	Ventilation rate [ach]	People density [people/m^2]
Positano – Ground floor	1.72	0.08
Positano – First floor	1.86	0.16
Langer – Classroom	2.42	0.25

Indeed, the *RMSEs* showed differences in the order of hundredths or thousandths of degree, hence negligible. The combination of inputs obtained from the calibration process was also used in the simplified models for the comparison.

3.2 Simplification Results

The annual energy demands for space heating are reported in Table 4.

For Positano kindergarten, the simplified model's total annual heating demand is equal to 30.13 MWh, 1.69 MWh more compared with the detailed model's results. In relative terms, the total deviation of the detailed model is equal to -5.62 % compared with the simplified one.

Regarding each thermal zone, the underground floor shoebox underestimates the heating demand, although only slightly, while the ground and first floor shoeboxes overestimate it by a deviation that does not exceed 2.06 MWh. As regards *RMSEs*, even though they are low for all floors, the underground floor shoebox shows the best performance in terms of hourly deviation from the detailed thermal zone's heating demand prediction.

For Langer primary school, the simplified model's total annual heating demand prediction is equal to 153.21 MWh, which is 7.05 MWh greater than the detailed model's predicted results. In relative terms, the total deviation is equal to +4.60%. Analyzing the results for each thermal zone, only the basement and the canteen underestimate the heating demand, while the rest of the shoeboxes overestimate the annual heating demand by a deviation that varies for each zone. Classrooms, gym and auditorium shoeboxes show the best performances, overestimating no more than 13.10 % in relative terms, or 0.88 MWh in absolute terms. The library's ground floor shoebox overestimates the predicted heating demand of the detailed model by 27.30 %, which is, however, one of the lowest heating needs (only 4.89 MWh). On the other hand, although the library's first floor heating demand is below average, it is characterized by a deviation of 6.20 %.

Table 4 – Heating needs prediction comparison

		Detailed - Heating [MWh]	Simplified - Heating [MWh]	Absolute difference [MWh]	Relative difference [%]	RMSE [kWh]
Positano	Underground	7.41	6.91	0.49	-7.16%	0.08
	Ground	9.05	9.18	-0.13	1.40%	0.79
	First	11.97	14.03	-2.06	14.68%	0.42
	TOTAL	28.43	30.13	-1.69	5.62%	0.89
Langer	Basement	19.91	17.97	1.95	-10.80%	0.33
	Hallway	33.03	36.25	-3.22	8.90%	0.61
	Canteen	10.71	10.62	0.08	-0.80%	0.31
	First Floor Classroom1	10.46	11.34	-0.88	7.80%	0.19
	First Floor Classroom2	8.15	8.42	-0.28	3.30%	0.06
	First Floor Classroom3	2.69	2.98	-0.29	9.80%	0.06
	Second Floor Classroom1	9.80	10.00	-0.20	2.00%	0.04
	Second Floor Classroom2	3.02	3.47	-0.45	13.10%	0.09
	Library Ground Floor	4.89	6.73	-1.83	27.30%	0.42
	Library First Floor	8.96	9.56	-0.59	6.20%	0.12
	Gym	22.29	22.92	-0.63	2.70%	0.25
	Auditorium	12.26	12.94	-0.69	5.30%	0.16
	TOTAL	146.16	153.21	-7.05	4.60%	1.38

Table 5 – Recorded simulation time and comparison

			Simulation time [s]	
Positano	Underground		4.01	
	Ground floor		5.16	
	First Floor		5.43	
	Simplified	Total	14.60	134.78x faster
	Detailed		1967.64	
Langer	Basement		3.97	
	Hallway		5.18	
	Canteen		4.83	
	First Floor Classroom1		4.83	
	First Floor Classroom2		4.85	
	First Floor Classroom3		4.51	
	Second Floor Classroom1		4.85	
	Second Floor Classroom2		4.79	
	Library Ground Floor		4.80	
	Library First Floor		4.88	
	Gym		5.19	
	Auditorium		4.83	
	Simplified	Total	53.54	8.18x faster
	Detailed		438.14	

The results of both case studies showed that shoeboxes can predict fairly well the heating needs of the detailed thermal zones. Moreover, for both buildings, the sum of the shoeboxes' predictions achieves high accuracy in estimating the global annual heating demand of the buildings detailed.

Even though results about temperatures have not been reported, the temperature profiles of the simplified models are generally underestimated throughout the entire year (i.e., leading to larger heating needs), with larger discrepancies in the summer period. This is mainly because, in general, the shoeboxing procedure leads to smaller thermal zones having a lower thermal capacity and it models the incoming radiation starting from a fixed obstruction ratio for the whole year. Indeed, in order to yield even more accurate results, the modeling of the external shadings should be improved since the surrounding context has a different impact on the air node heat balance during the year, i.e., it has a greater influence in summer (Battini et al., 2021a).

Table 5 reports the simulation runtime of detailed and simplified models. Regardless of the building considered, the shoebox simulation time takes between 3 and 5 seconds. Summing up the time required by the simplified models for each building and considering the simulation time of the whole building models, the simplified building models reduced the computing time of the energy simulation by 134.78 and 8.18 times for Positano and Langer, respectively. Such discrepancies in time reduction are due to the time required for the detailed models to be simulated. Indeed, the speed of the detailed model's simulation mostly depends on the shape of the thermal zones and the external shading objects. Even though Positano kindergarten is composed of only three thermal zones, all of them are characterized by a complex shape, while Langer primary school is mostly composed of parallelepiped-shaped thermal zones. Moreover, the number of surfaces representing the urban context in Positano is approximately 3.5 times the one in Langer.

4. Conclusion

In this work, a new simplification algorithm capable of properly estimating the energy use of complex-shape buildings reducing the simulation time was tested. The algorithm can convert every building of whatever shape and geometry into a representative shoebox energy model. The conversion involves the simplification of the building geometry, apertures and adjacencies, and the transformation of the buildings' obstructions into shading opaque elements.

To test the procedure at the individual building level, two educational buildings of complex shape located in Bolzano, Italy, were studied, i.e., Positano kindergarten and Langer primary school. Firstly, both buildings were modeled in detail in terms of geometry, construction assemblies, internal loads, schedules and surrounding context. Then, they were calibrated thanks to monitored indoor temperature data of the schools' classrooms considering the two variables characterized by the largest uncertainty: ventilation rates and people densities. Afterwards, the simplification algorithm was applied to obtain shoeboxes from the detailed thermal zones. Finally, detailed and simplified models were simulated in EnergyPlus using the same weather file and

the simulation results were analyzed and compared. The comparison highlighted that, in both case studies, the simplification algorithm is able to convert complex-shape building thermal zones into shoeboxes that can predict their annual heating demand with high accuracy and through significantly faster energy simulations. In general, the heating needs are slightly overestimated by the shoeboxes, leading to total overestimates equal to 5.62 % and 4.60 %, for Positano kindergarten and Langer school, respectively. Since shoeboxes have proven to be more capable of predicting thermal behavior of the detailed building model in winter rather than in summer, the implementation of new solutions for managing the incoming radiation is needed as further research.

In terms of computing time, the simplified models' energy simulations were 135 and 8 times faster compared with the detailed ones for Positano and Langer, respectively.

The significantly faster simulations achieved by the shoeboxes, together with their high accuracy in predicting the detailed model's energy performance, allow this simplification algorithm for building level applications to be used.

Acknowledgement

This research was developed thanks to the Geology, Civil Protection and Energy Office of the Municipality of Bozen-Bolzano, within the framework of the Project IndAIR-Edu – "Indoor Air Quality and Ventilation Effectiveness in Educational Buildings" (CUP: I56C18000180005; Free University of Bozen-Bolzano, Faculty of Science and Technology, RTD call 2018).

References

ASHRAE 2013. *ASHRAE 90.1-2013. Standard energy standard for buildings except low-rise residential buildings.*

Battini, F., G. Pernigotto, and A. Gasparella. 2021a. "A parametric analysis of the impact of thermophysical, geometry and urban features on the energy demand of a simplified building shoebox model." In *Proceedings of Building Simulation 2021*, Bruges, Belgium

Battini, F., G. Pernigotto, and A. Gasparella. 2021b. "Development of a shoeboxing approach for Urban Building Energy Modeling." In *Proceedings of the VI International High Performance Buildings Conference at Purdue*, West Lafayette, IN, US.

Dogan, T., and C. Reinhart. 2013. "Automated conversion of architectural massing models into thermal 'shoebox' models." In *Proceedings of Building Simulation 2013*, Chambéry, France.

Dogan, T., and C. Reinhart. 2017. "Shoeboxer: An algorithm for abstracted rapid multi-zone building energy model generation and simulation." *Energy and Buildings* 140: 140-153. doi: https://doi.org/10.1016/j.enbuild.2017.01.030

Dugaria, S., G. Pernigotto, and A. Gasparella. 2021. "Indoor conditions in educational buildings: the case of Bolzano schools." In *ASHRAE Topical Conference Proceedings*, Athens, Greece.

Roberts, J. A., G. De Michele, G. Pernigotto, A. Gasparella, and S. Avesani. 2022. "Impact of active façade control parameters and sensor network complexity on comfort and efficiency: A residential Italian case-study." *Energy and Buildings* 255: 111650. doi: https://doi.org/10.1016/j.enbuild.2021.111650

UNI. 1995. *UNI 10339:1995. Air-conditioning systems for thermal comfort in buildings: general, classification and requirements. offer, order and supply specifications.*

UNI. 2018. *UNI CEN/TR 16798-6:2018. (2018). Energy performance of buildings - ventilation for buildings - part 6: Interpretation of the requirements in en 16798-5 -1 and en 16798-5-2 - calculation methods for energy requirements of ventilation and air conditioning systems.*

Zhu, P., D. Yan, H. Sun, J. An, and Y. Huang. 2019. "Building Blocks Energy Estimation (BBEE): A method for building energy estimation on district level." *Energy and Buildings* 185: 137-147. https://doi.org/10.1016/j.enbuild.2018.12.031

Numerical Investigation of Radiation Efficiency of a Cross-Laminated Timber Floor

Marco Caniato – Free University of Bozen-Bolzano, Italy – marco.caniato@unibz.it
Nicola Granzotto – Free University of Bozen-Bolzano, Italy – nicolagranzotto74@gmail.com
Federica Bettarello – University of Trieste, Italy – fbettarello@units.it
Arianna Marzi – Free University of Bozen-Bolzano, Italy – arianna.marzi@natec.unibz.it
Paolo Bonfiglio – Materiacustica srl, Italy – paolo.bonfiglio@materiacustica.it
Andrea Gasparella – Free University of Bozen-Bolzano, Italy – andrea.gasparella@unibz.it

Abstract

Cross-Laminated Timber (CLT) is a building technology that is becoming increasingly popular due to its sustainability and availability. Nevertheless, CLT structures present some challenges, especially in terms of both structure-borne and airborne insulation. In this paper, a 200 -mm CLT floor was characterized in the laboratory, according to ISO standards, by using a standard tapping machine in order to understand its vibro-acoustic behavior in terms of radiation efficiency for structural excitation. In particular, experimental tests were compared to analytical prediction models available in the literature to check the accuracy of simulation methods in the prediction of the radiation capability of CLT structures.

1. Introduction

In recent years, the use of timber as a construction material in the building sector has been increasing. Sustainable edifices made exclusively with timber or refurbishment of conventional heavyweight houses using new timber structures are common in most cities. In view of this, the use of wooden components and, in particular, Cross Laminated Timber (CLT) elements has greatly increased in the past decade. Timber has a number of advantages: it is an eco-friendly material, well suited for thermal comfort and a fast-track on-site construction process, featuring the possibility of implementing existing structures thanks to its reduced weight.

However, its acoustic simulations lack a complete description, since the literature does not always provide reliable methods capable of predicting reliable values as regards acoustic performance. From this perspective, further studies are needed to develop and improve prediction models of CLT floor sound and vibrational behavior (Yang et al., 2021; Zhang et al., 2020). Among all available parameters, one worthy of investigation is represented by radiation efficiency. Indeed, the sound radiation index is of paramount importance for understanding and simulating the behavior of these elements (Kohrmann, 2017).

A recent study (Jansson, 2021) has shown how the use of software and calculation models, currently available for the study of the characteristics of multilayer systems, are not reliable when wooden structures are used. For this reason, it is of paramount importance not only to know the characteristics of the materials, but also their radiation efficiency.

However, the study of this parameter, in relation to the characterization of CLT floors, is still partially incomplete.

Hence, to design CLT structures with good acoustic insulation, there is the need to characterize the sound radiation of the vibrating elements.

The radiation efficiency can be computed using dedicated equations or simulated using Finite Elements Methods. In this paper, this latter approach is used to verify if, with reference CLT floor, the method can be used and if it could provide reliable and robust results.

2. Material and Methods

2.1 Description of Investigated CLT Floor

This paper presents the results of a numerical investigation of the radiation efficiency of a CLT floor with a thickness of 200 mm and a size of 4155 mm x 3000 mm, measured in a laboratory built in accordance with the ISO 10140 series standards, using a standardized tapping machine (B&K 3297) as mechanical source (Fig. 1).

Fig. 1 – Investigated CLT floor mechanically excited using a standardized tapping machine

The laboratory was built to minimize flanking transmission and, in particular, it features a volume of transmitting room of 50.9 m^3 and a volume of the receiving room of 60.63 m^3.

Fig. 2 – Picture of the available acoustic facility

A grid of accelerometers was used to monitor the acceleration levels. Precisely, the measurement pattern is described in Fig. 3.

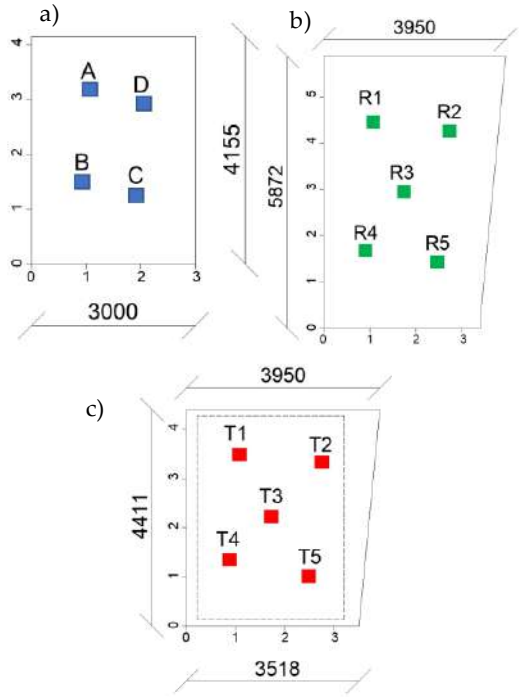

Fig. 3 –Tapping machine positions (a); microphone positions in the receiving room; (b) accelerometer position in the receiving room (c)

The radiation efficiency was measured using following expression:

$$\sigma_{rad} = \frac{W_{rad}}{\rho_0 c_0 S \langle v^2 \rangle_{S,t}} \quad (1)$$

where W_{rad} [W] is the radiation power, ρ_0 [kg/m^3] is the air density, c_0 [m/s] is the speed of sound, S [m^2] is the floor surface, $\langle v^2 \rangle_{S,t}$ is the average square vibration velocity on the receiving side. The radiation power was evaluated using the average sound pressure level (Svantek 958) and the reverberation time in the receiving room. The averaged squared velocity was measured using accelerometers (Dytran 3023) mounted on the bottom side of the CLT floor.

2.2 Description of Numerical Approaches

As previously described , CLT floor is made of five layers (having a thickness of 4 cm each and density of around 420 kg/m^3). It is well known in the literature that each layer is an orthotropic solid and a comprehensive analysis requires the knowledge of 9 independent parameters (3 Young's modulus, 3 shear modulus and three Poisson's ratio). Table 1 summarizes values of mechanical parameters utilized as input data of investigated numerical approaches.

Parameters in Table 1 were used for layers 1, 3 and 5. Layers 2 and 4 were modeled using the same parameters in a 90-degree- rotated coordinate system. In the following sessions, two different numerical approached will be described.

Table 1 – Mechanical properties of each CLT layer

E [GPa]	G [GPa]	ν [-]	η [-]
E1=11	G12=0.69	0.14	0.01
E2=0.37	G13=0.069	0.33	0.01
E3=0.37	G23=0.69	0.14	0.01

2.2.1 Hybrid FEM-Analytical model I

A statistical radiation efficiency model was implemented, based on the modal-average formulations, using frequency-dependent stiffness properties as input data. Such a statistical approach requires some additional assumptions: (a) high modal density and modal overlap over the entire frequency range (b) the sound power is only radiated by resonant modes; (c) the resonant modes are uncorrelated; (d) equipartition of modal energy can be applied. The radiation efficiency can be calculated as:

$$\sigma_{\text{ortho}}(\omega) = \frac{L_x L_y}{\pi^2 n_d} \int_0^{\pi/2} \sigma(\omega,\phi) k_B \frac{\partial k_B}{\partial \omega} d\phi. \quad (2)$$

where L_x and L_y are the lateral size of the CLT floor, $\sigma(\omega,\phi)$ the radiation efficiency calculated using Leppington's formulation (Leppington et al., 1982), η_d the plate modal density and k_B the structural bending wave propagating in the plate. At any propagation angle ϕ, the direction-dependent bending wavenumber can be estimated from the wavenumber components along the principal directions k_{Bx} and k_{By}, by applying a well-established orthotropic elliptic model.

To summarize, if the wavenumber components, along with the principal directions kBx and kBy are known together with the size and the plate density, the radiation efficiency can be calculated.

In the present research, the wavenumbers k_{Bx} and k_{By} were determined using a simplified finite element model (implemented in Comsol Multiphysics) and the Inhomogeneous Wave Correlation (IWC). In particular, two finite element models of freely suspended CLT beams (1 m long) in x and y directions are solved when a unit force in z direction is exerted on a side of the beam.

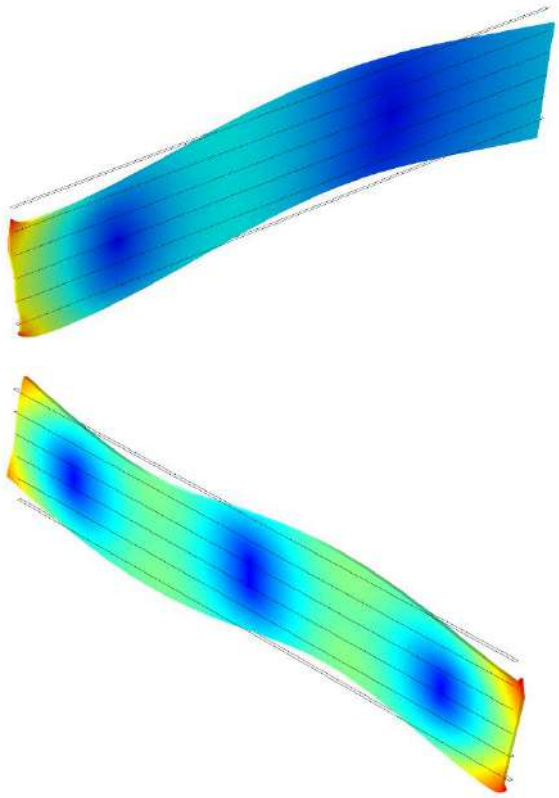

Fig. 4 – FEM models of CLT beams for the extraction of the structural wavenumbers along the principal directions

Once each model is solved, the z direction complex displacement is computed along each beam on a set of equally spaced points (1cm of spacing has been considered). By applying the IWC method, it is possible to determine the dispersion relation (the wavenumber as a function of the frequency) in both principal directions (Fig. 5).

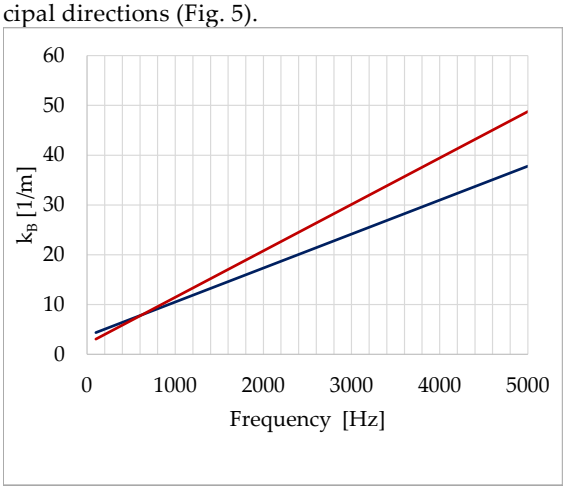

Fig. 5 – Computed structural wave numbers along the principal directions

2.2.2 Hybrid FEM-Analytical model II

The second hybrid method requires a two-step procedure:

1. A FEM model of the entire floor is solved for a mechanical point excitation. In this case, the three different simulations were considered according to the positions of the tapping machine during experimental.
2. Once the model is solved, the z direction complex velocity is computed on a grid of equally spaced points (5 cm of spacing was considered). The mean-squared velocity in Eq. 1 can be directly calculated as the average of the squared velocity, while radiated power of Eq. 1 has been computed using the Discrete Calculation Method (DCM) (Santoni et al., 2019):

$$W_{\text{rad}} = \sum_i \left[\text{Re}(Z_{ii}) |v_i|^2 + \sum_j \text{Re}\left(Z_{ij} v_i v_j^* \right) \right]. \quad (3)$$

where Z_{ii} and Z_{ij} are the self- and cross-radiation impedances, respectively.

2.2.3 Accuracy

In order to estimate the quality of the fit, a standard deviation is calculated by taking into consideration the measured values as the average data (μ) for each of n frequency bands (1/3 octave) and the calculated values as experimental ones (Eq. 3):

$$\sigma_{dev} = \sqrt{\frac{1}{N} \sum_{i=1}^{n} (x_i - \mu)^2} \quad (3)$$

In addition, the mean difference is computed (Eq. 4):

$$\Delta_{mean} = \frac{1}{N} \sum_{i=1}^{n} |x_i - \mu| \quad (4)$$

3. Results

Experimental radiated sound power and structural velocity levels are shown in Fig. 6.

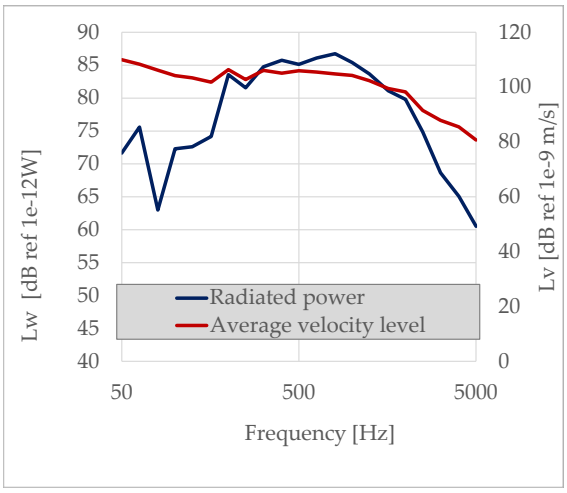

Fig. 6 – Experimental radiated sound power and structural velocity levels

The comparison between experimental values and numerical models of the radiation efficiency is shown in Fig. 7.

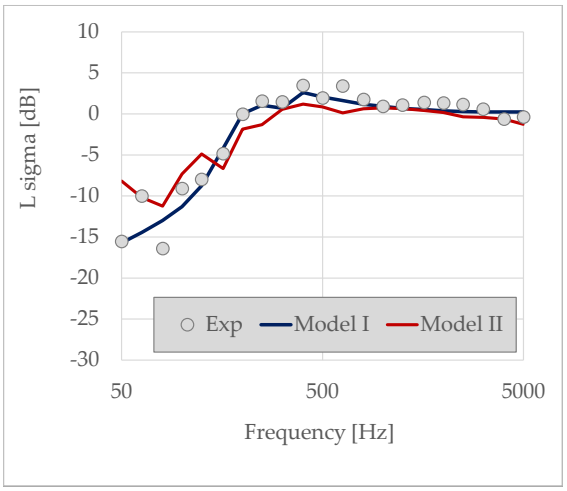

Fig. 7 – Radiation efficiency. Comparison between different simulation approaches

From the curves in the previous graph, it is possible to observe satisfactory accuracy of both simulation techniques. The average absolute differences are equal to 1 dB and 1.8 dB for Model I and Model II when compared with experimental tests. In particular, model II is able to investigate modal behavior of the plate. Fig. 8 depicts the modal resonances of the full floor at frequencies of up to around 150 Hz.

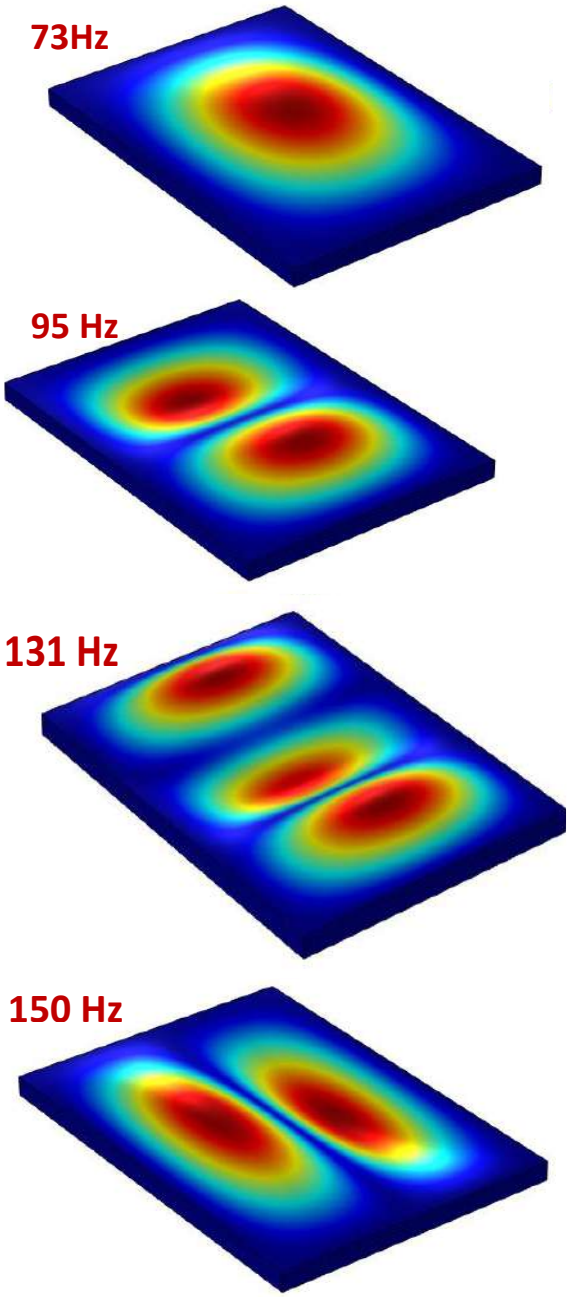

Fig. 8 – Model eigenfrequencies determined using a full 3D FEM model

Furthermore, deviations (i.e., arithmetic differences) between experimental data and numerical simulations are depicted in Fig. 9. From the comparison, it is possible to observe a better capability of Model I to simulate the radiation efficiency of the CLT structure, while both methodologies show higher deviations at frequencies lower than 125 Hz, which is the frequency region governed by resonant modes of the floor and it is highly dependent on boundary conditions, generally difficult to implement in simplified numerical models.

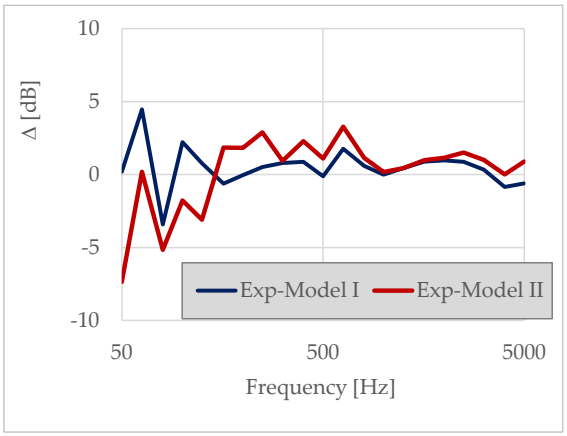

Fig. 9 – Deviations between experimental data and numerical simulations

In Table 2, the simulation accuracy is reported. It can be noticed that model I presents better values than model II, mostly because of low frequency values differences reported in Fig. 9.

Table 2 – Accuracy for different numerical methods

Numerical method	*Dev.st*	Δ_{mean}
Model I	0.91	0.74
Model II	1.72	1.47

4. Conclusion

In this paper, two different numerical approaches were utilized for the prediction of the radiation efficiency of a Cross-Laminated Timber frame for building constructions. Results were compared with experimental tests carried out in a dedicated laboratory. The accuracy of proposed methodologies was proved to be between 1 and 2 dB in terms of average radiation efficiency level. The implementation of both methodologies is straightforward and requires knowledge of the mechanical properties of the orthotropic timber material. Future work will be devoted to extension of the proposed numerical formulations to different acoustic and mechanical excitations.

Acknowledgement

This work was financed by the European Interreg BIGWOOD project, IT AT 1081 CUP: I54I18000300006.

Nomenclature

Symbols

W_{rad}	radiation power (W)
ρ_0	air density (kg/m^3)
c_0	speed of sound (m/s)
S	floor surface (m^2)
$\langle v_2 \rangle_{S,t}$	is the average square vibration velocity on the receiving side (m/s)
E	Young's modulus (GPa)
G	Shear modulus (GPa)
ν	Poissino ratio (-)
η	Loss factor (-)
L_x	dimension (m)
L_y	y-direction size dimension (m)
$\sigma(\omega,\phi)$	radiation efficiency (-)
η_d	plate modal density (-)
k_B	structural bending wave propagating in the plate (m^{-1})
ϕ	propagation angle (rad)
Z	radiation impedances (rayls)

Subscripts/Superscripts

x	x-direction
y	y-direction

References

ISO. 2021. *ISO 10140-3:2021; Acoustics—Laboratory Measurement of Sound Insulation of Building Elements—Part 3: Measurement of Impact Sound Insulation*..

Jansson, L. 2021. "Estimating Impact Noise through Cross Laminated Timber Floors Using the Transfer Matrix Method". *In Proceedings of the INTER-NOISE 2021*.

Kohrmann, M. 2017. *Numerical Methods for the Vibro-Acoustic Assessment of Timber Floor Constructions*. Technische Universität München: München, Germany.

Leppington, F. G., E. G. Broadbent, and K. H. Heron. 1982. "The acoustic radiation efficiency of rectangular panels". *Proceedings of the Royal Society of London A: Mathematical, Physical and Engineering Sciences* 82: 245–71.

Yang, Y., C. Fenemore, M. J. Kingan, and B. R. Mace. 2021. "Analysis of the vibroacoustic characteristics of cross laminated timber panels using a wave and finite element method". *Journal of Sound and Vibration* 494: 115842.

Zhang, X.; X. Hu, H. Gong, J. Zhang, and Z. Lv, and W. Hong. 2020. "Experimental study on the impact sound insulation of cross laminated timber and timber-concrete composite floors". *Applied Acoustic* 161: 107173.

Assessment of Contagion Risk due to Covid-19 for a Multi-Zone Building Model of Offices

Riccardo Albertin – Free University of Bozen-Bolzano, Italy – riccardo.albertin@natec.unibz.it
Alessandro Pernici – Free University of Bozen-Bolzano, Italy – alessandro.pernici@natec.unibz.it
Giovanni Pernigotto – Free University of Bozen-Bolzano, Italy – giovanni.pernigotto.unibz.it
Andrea Gasparella – Free University of Bozen-Bolzano, Italy – andrea.gasparella.unibz.it

Abstract

In this research, a probabilistic model was applied to a building model of a public building located in Bolzano, Italy, for the assessment of the airborne contagion risk due to Covid-19. Different ventilation strategies were investigated in terms of risk reduction, as well as the effectiveness of the Pfizer vaccine. TRNSYS and TRNFLOW models of the public building were created to evaluate the internal airflows, necessary to calculate Covid-19 concentrations in the offices. Both building and airflow models were calibrated against measurement data collected with temperature sensors located in some of the building offices and hallways, prior to coupling with a Monte Carlo model for the risk assessment process. The results were reported in terms of infection risk, both for occupants located in the same office, as well as for occupants in adjacent spaces. It was observed that the current operational modes of both natural and mechanical ventilation are able to limit the spread of Covid-19 only in case of vaccination coverage presence and if the Delta variant is considered. If vaccination coverage is not present or if the Omicron variant is concerned, a higher frequency of windows opening, and a schedule based on occupancy profiles for mechanical ventilation should be adopted.

1. Introduction

In the literature, some references about airborne contagion risk assessment due to Covid-19 are available. One example is given by the work of Buonanno et al. (2020a), on which the "Airborne Infection Risk Calculator" (AIRC) is based, for risk

Fig. 1 – Case study building located in Bolzano, Italy

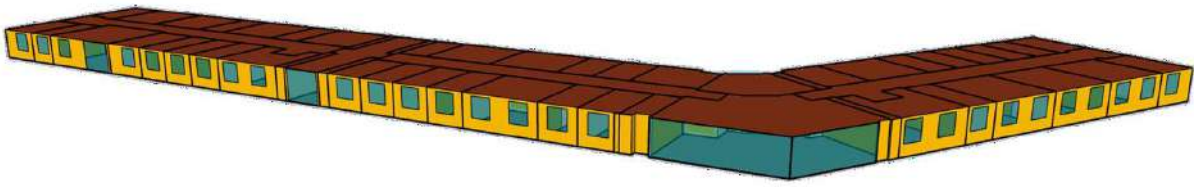

Fig. 2 – 3D model of the second floor of the case study building

assessment due to airborne diseases, including Covid-19. The AIRC tool, as well as other works regarding risk assessment for airborne contagion due to Covid-19, have some limitations. Firstly, it is possible to perform risk assessment only for one room at a time, not considering in this way potential infections in adjacent rooms due to the spread of the Covid-19 virus through doors, or ducts in the mechanical ventilation system. Secondly, one of the major assumptions needed to perform risk assessment is static conditions. For this reason, in Albertin et al. (2022a), a Monte Carlo model was developed to overcome the aforementioned limitations. The probabilistic method proposed is based on the coupling of TRNSYS and TRNFLOW, a building simulation software and a plugin for the evaluation of airflows and infiltrations, respectively, and an algorithm based on the AIRC tool developed in MATLAB® environment. The airflows evaluated with the building and airflow models were utilized for the calculation of Covid-19 concentrations in the internal zones of the building. Then, a Monte Carlo model was used to evaluate the risk of infection for the occupants under different environmental conditions by simulating several scenarios 1000 times each. The whole process was subsequently enhanced in Albertin et al. (2022b), giving the possibility of also considering different Covid-19 variants (Alpha, Delta, Omicron), vaccines (AstraZeneca, Pfizer, Moderna), air purifiers and other features.

In this work, the enhanced version of the probabilistic model is further expanded with the Page algorithm for the randomized creation of occupancy profiles for each occupant and applied to a public building containing offices.

2. Case Study

The case study selected for this work is part of the second floor of a public office (Fig. 1) located in via

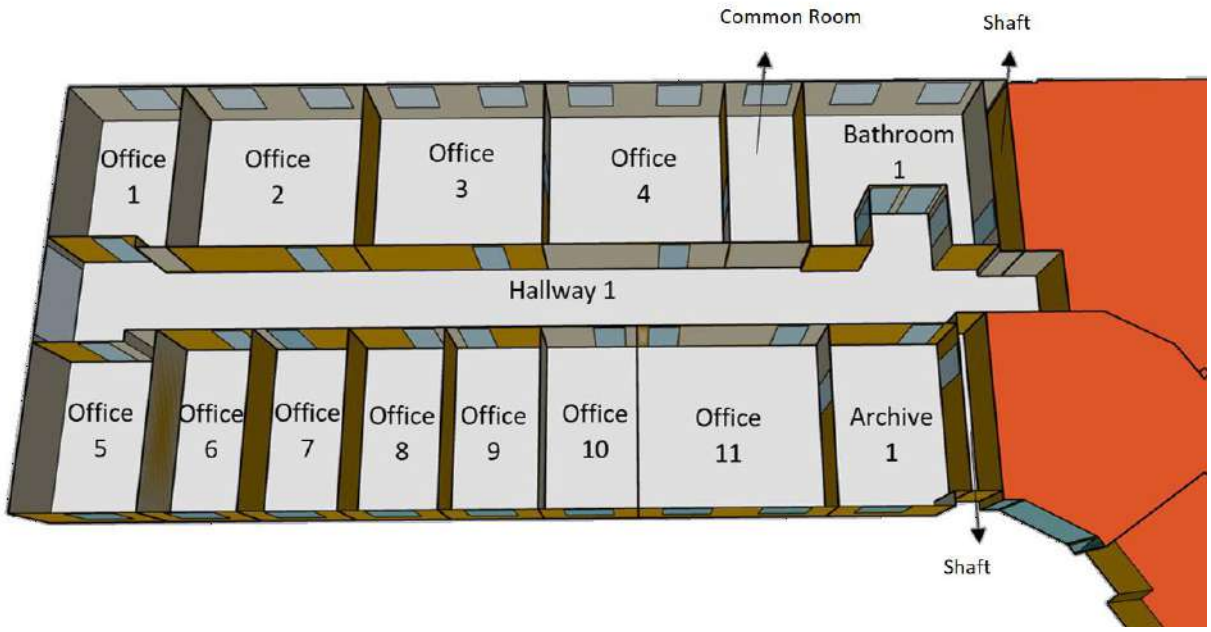

Fig. 3 – Highlight of the second floor of the office block selected for the risk assessment

Vincenzo Lancia, Bolzano, Italy. The second floor is composed of three blocks, and the one selected for the risk assessment is represented in detail in Fig. 3. The surface area of the block is about 564 m^2, for an internal height of 2.7 m and, therefore, a total internal volume of 1523 m^3.

Different ventilation systems are installed for each block, with a low air-flow velocity setting, integrated dehumidification system and crossflow heat recovery unit. However, it has been observed that the mechanical ventilation system is not utilized during working hours, especially in summer, due to issues regarding thermal comfort. For this reason, mechanical ventilation is operative only early in the morning, during lunch hours and in the evening after 6 pm.

All the office windows are composed of a double-glazed glass and an aluminium frame. Given their large dimension and proximity to a busy street, a source of air pollution and acoustic discomfort, it has been observed that the windows are rarely opened and just for short periods of time.

Temperature, relative humidity, and CO_2 sensors are present in three different offices to monitor the environmental parameters (offices 4, 8 and 9 in Fig. 3), and only temperature sensors are present in the relative adjacent rooms for calibration and validation purposes. The sensors used are ONSET HOBO MX1102A for the three offices and ONSET HOBO U12-013 for the adjacent rooms.

3. Model Development

3.1 Building Model

An existing model of the case study building developed in TRNYS was adapted for the calculation of the internal airflows and infiltrations prior to coupling with the probabilistic model. While, in the original model, several rooms were characterized in detail, including offices, bathrooms, hallways, archives, etc. (Fig. 2), in the model used for the risk assessment, only one of the three blocks of the building was considered (Fig. 3). In the selected block, eleven offices, one archive, a hallway, one bathroom, a common room and two shafts are located. As mentioned before, CO_2 was monitored in three offices (offices 4-8-9), while the temperature was also monitored in some adjacent spaces (offices 3-7-10, the hallway and the common room). The data collected from the adjacent rooms was used to set the boundary conditions of the three main offices during the calibration process. The period selected for calibration goes from November 30th to December 15th, 2021, while the validation was carried out in the period starting from December 15th to December 24th of the same year. Calibration and validation were performed on the measured temperature.

The occupancy profiles were randomly determined with the Page stochastic algorithm, based on the occupancy probability profiles proposed by ASHRAE standards. An occupancy profile was created in this way for each occupant of the block, considering in the process the day of the week (weekday, Saturday, Sunday) and the hour of the day. With the Page algorithm, it was possible to account for short moment of absence from the office, as well as long periods of absence usually related to sickness or holidays.

The airflow evaluation was carried out with TRNFLOW, a plugin for TRNSYS, based on the software COMIS. Two external nodes were added to the TRNFLOW model (a.k.a. airflow network, or AFN), one for each external side where windows are present. Pressure coefficients were chosen accordingly to the TRNFLOW manual for a semi-sheltered building. Infiltrations were modeled with the *crack* component, both for closed windows and for doors, while internal and external airflows (present in the case of an open window and/or door), with the *large opening* component. Four different opening profiles for the opening and closing of the windows were extrapolated from the data collected in the monitored offices, and then assigned to all the internal spaces. Finally, the *test data* component was used to model the mechanical ventilation, with a constant rate of fresh air supply when active.

3 design variables were considered during the calibration process, and these are related to each component: for the *crack* component, the air mass flow coefficient, the discharge coefficient for the *large opening* component and the ventilation efficacy for the *test data* component were considered. After

calibration, the AFN was used to evaluate both infiltrations and airflows in the block considered for risk assessment.

3.2 Occupancy Scenarios

Some hypotheses regarding the occupancy of the offices were formulated. Firstly, it was supposed that all the occupants of the building were susceptible subjects (i.e., people that can be infected by Covid-19). Only one person was infected and contagious at the start of the risk assessment process: an occupant of office 3 (Fig. 3). In all offices, only one person was present at a time, with the exception of offices 2-3-4, where 2 persons could be present at the same moment according to their occupancy profiles. In total, during occupancy hours, 15 people could be simultaneously present in the block considered for risk assessment. Occupancy hours were scheduled to be from 8 am to 12 pm in the morning, and then from 1 pm to 5 pm in the afternoon. The occupants of the offices did not move from one space to another: whenever an office was scheduled to be empty, the occupants were supposed to be outside the block.

Doors were considered usually closed and briefly open only whenever a change in the occupancy status of a given office occurred (i.e., an occupant entered/left the office according to its occupancy profile). Windows were also observed to be usually closed. Since the expected state of the windows when open was the tilted position, an opening fraction of 30 % was considered for the windows when open. This was necessary to limit the airflows evaluated by the *large opening* component of the AFN, avoiding an overestimation of the air change rate for the internal spaces.

4. Monte Carlo Analysis

The Monte Carlo model used for the risk assessment analysis was based on a previous model, developed for a set of three university classrooms in the Free University of Bozen-Bolzano (Albertin et al., 2022a), where it was used to evaluate the airborne risk of contagion for the students and professors of the classrooms for different scenarios. Some ventilation strategies were investigated in terms of risk reduction, as well as the effect of mask utilization. The probabilistic model was subsequently enhanced in Albertin et al. (2022b), to consider different Covid-19 variants (Delta and Omicron), vaccines (AstraZeneca, Pfizer and Moderna), and the effect of air purifiers, as well. In this work, the Monte Carlo model was adapted to the office building and further enhanced with the Page algorithm for the creation of randomized occupancy profiles for each occupant. The probabilistic nature of the Page algorithm could be fully exploited within the Monte Carlo method, whose simplified schematic is represented in Fig. 4.

The process started with the definition of a scenario, by selecting the ventilation strategy, the presence of vaccine coverage, Covid-19 variants, etc. Then, each scenario was evaluated 1000 times, in this work referred as *iterations*. An iteration consists of a series of simulations, each one representing a day. During the simulations, the airflow database was used to calculate the concentration of Covid-19 in the offices, and, thus, the dose received by the occupants (Buonanno et al., 2020b). Thanks to the dose, it was possible to account on a day-to-day basis for newly infected occupants, who would contribute towards increasing Covid-19 concentrations in the block in the next simulations. The simulations stopped when it was not possible to have new infections, meaning that the infected occupants were either no longer contagious or kept outside the block.

In this chapter, the risk assessment model is described in detail, highlighting the differences with respect to previous works.

4.1 Scenario Definition

The risk assessment process begins with the definition of the scenario. The ventilation strategies considered for the given scenario were automatically implemented in the TRNSYS model, as well as in the AFN, changing the parameters used for the evaluation of both infiltrations and airflows. The building model was then used to create a database of airflows under different conditions (windows and/or door opened or closed). The database was used during the simulation phase to dynamically

evaluate the concentrations for each office, necessary for calculating the dose received by the occupants, and thus, to identify new infections.

4.2 Scenario Evaluation Process

Each scenario was evaluated with 1000 iterations. An iteration started with a random process for assigning a quanta emission rate value (QR, where a quantum is defined as "*the dose of airborne droplet nuclei required to cause infection in 63 % of susceptible persons*" in Buonanno et al., 2020b) to each occupant. The process was also carried out for the occupants that were not infected to save computational time. During a simulation, if a subject was not infected, his or her QR was considered to be zero. The QR was then switched to the value assigned only for those occupants that were infected during a simulation. The QR values were randomly selected with a lognormal distribution curve whose parameters depended on the activity performed by each occupant (Buonanno et al., 2020b). The activities were subdivided into primary and secondary activity.

The time allocated to the secondary activity was randomly chosen with a Gaussian distribution, with a process ensuring that the primary activity was carried out at least 70 % of the time. Two values of QR were then randomly extracted for the occupants, one for each activity, and subsequently weighted with the time allocated to the respective activities, and finally added up.

In a similar process, two other values were randomly assigned to all the occupants during the initial phase of an iteration: asymptomatic status and vaccination status.

Asymptomatic status was determined once again for all the occupants, infected or not. Early categorization was performed randomly with a normal distribution curve whose parameters were set according to Ma et al. (2021). Those occupants categorized as asymptomatic and who would get infected during a simulation would increase the Covid-19 concentrations in the block during the whole contagious period, without ever being kept outside the building.

Table 1 – List of activities with relative parameters for the log-normal distribution curve

Activity	Log Mean	Log Standard Deviation	Type
Resting-breathing	-0.43	0.73	Primary
Standing-speaking	1.08	0.72	Secondary

Finally, vaccination status was randomly extracted. All the occupants were categorized in this way as fully vaccinated (2 doses received), partially vaccinated (1 dose received) or not vaccinated. The number of occupants in each category was automatically assigned to match the vaccination coverage according to the global database of Covid-19 vaccinations (Mathieu et al., 2021). The vaccination

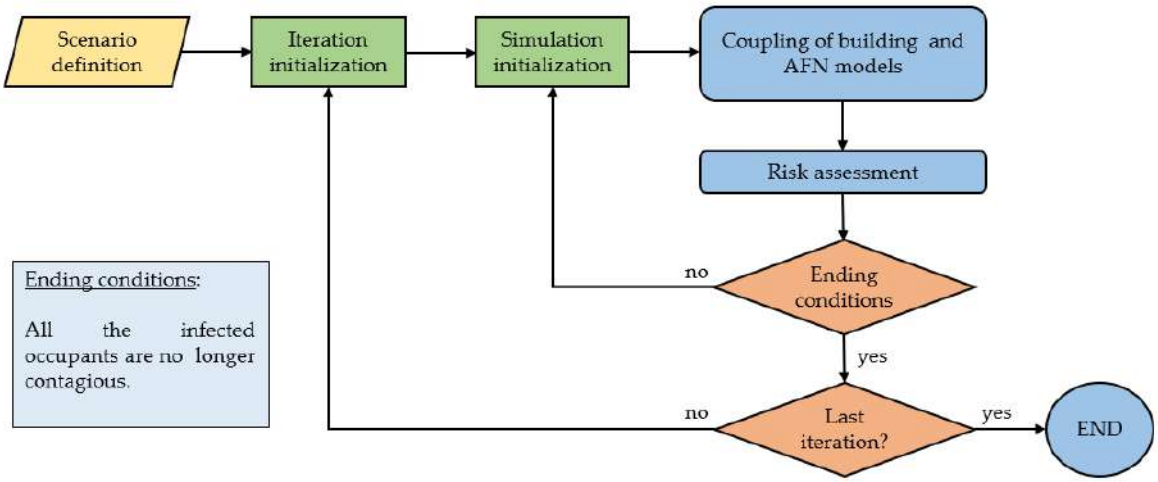

Fig. 4 – Scheme of the Monte Carlo model utilized for the risk assessment process

coverage selected represents the situation in Italy on November 1st, 2021, with 72 % fully vaccinated, 5.8 % partially vaccinated and 22.2 % not vaccinated. Furthermore, the effectiveness of each vaccination category depends on the typology of Covid-19 variants considered, and on the vaccine selected: Pfizer, Moderna, AstraZeneca (Andrews et al., 2022). The effectiveness of the vaccine selected can then vary from occupant to occupant, and it was used to randomly select the subjects who were immune to airborne contagion due to Covid-19 for a given iteration. For example, a fully vaccinated occupant with 2 doses of Moderna had a higher probability of being immune to the Delta variant compared with an occupant with only one dose of AstraZeneca.

Before the start of the simulations, some hypotheses were formulated: all the occupants were not infected and were susceptible to Covid-19 contagion, except for one occupant in office 3, who was already infected, asymptomatic, and contagious. The initial concentrations of Covid-19 in all the internal spaces of the block were equal to zero.

At this stage, the simulations started and were performed until the ending condition is met, which signified the end of the iteration. At the end of each iteration, the number of infected occupants in office 3 and in the whole block were counted, obtaining a distribution of 1000 values. It was then possible to calculate the likelihood of having one or more infected subjects both for the office where the first infected was located (office 3) and for the other offices of the block. The distinction was important, since having new infections in adjacent spaces meant that it was possible for the Covid-19 virus to spread from one room to another, increasing the chances of unacceptable outcomes.

4.3 Risk Assessment

During a simulation, the airflows evaluated with the AFN were utilized to dynamically calculate Covid-19 concentrations in all the internal environments of the block considered. Then, at the end of each day, the dose received by the occupants was calculated, taking into consideration the occupancy profile of each subject and Covid-19 concentration in the respective office. Finally, with the dose received it was possible to calculate the probability of infection for each occupant (Buonanno et al., 2020a), and thus, to randomly account for new infections at the end of each day. Those occupants that were selected as not infectable during the assessment of the vaccination status always had a probability of infection equal to zero for the given iteration.

For each newly infected occupant, the contagious period was randomly determined, as well as the symptom onset day. The process is reported in detail in Albertin et al. (2022b). The occupants that were infected and that were outside the contagious period cannot be infected again during an iteration. The simulations were repeated until all the occupants were no longer contagious. At this stage, the final number of infected occupants was computed for each office and the iteration came to an end.

5. Simulation Plan

A total of 27 scenarios were evaluated with the Monte Carlo model by considering different natural and mechanical ventilation strategies, Covid-19 variants, and the presence of vaccination coverage with the Pfizer vaccine.

There were 3 natural ventilation strategies considered for the scenarios: (1) all the windows were always closed; (2) the opening of the windows was set by profiles based on measured data; (3) the windows were open for 10 minutes every hour and during the lunch break. There were also 3 mechanical ventilation strategies: (1) always inactive; (2) active outside occupancy hours as observed during the monitoring period (7 – 8 am, 12 – 13 pm, 5 – 6 pm); (3) active during occupancy hours (8 am – 12 pm, 1 – 5 pm). Two Covid-19 variants were considered, (a) Delta and (b) Omicron, respectively. Finally, the efficacy of vaccines was investigated by comparing the case where (a) all the people were not vaccinated or (b) with vaccination coverage, performed with the Pfizer vaccine. Cases were coded, with a sequence of two numbers, both in range 1-3, representing respectively the natural and mechanical ventilation strategy considered, followed by a letter D or O, respectively, for the Delta and Omicron variants, or O/D if the case was

valid for both variants. Finally, the last member of the sequence was a number: 1 when vaccination coverage was present, and 0 when not. As, for example, code 13O1 represents the case with windows always closed (natural ventilation strategy number 1), mechanical ventilation active during occupancy hours (mechanical ventilation strategy number 3), Omicron variant and vaccination coverage present.

6. Results

The results were reported as the likelihood of having a specific number of newly infected subjects by considering all offices:

- L0, refers to the likelihood of not having new infections,
- L1, refers to the likelihood of having exactly one new infection,
- L2, refers to the likelihood of having exactly two new infections,
- L2+, refers to the likelihood of having more than two new infections.

Furthermore, the likelihood values were colored in shades of red and green, where red represents the lower value, and green the highest value for L0. The colours were inverted for the metrics L1, L2, L2+. In this way, it was easily possible to identify the scenarios with the best and worst possible outcome thanks to the colors of each row in Table 2.

To this end, it was possible to identify the worst-case scenario as 11D/O0. In this case, the windows are always closed, allowing only a small amount of fresh air (infiltrations) to enter the building through the cracks and small openings, since the mechanical ventilation is always inactive, too. Furthermore, in this case, vaccination coverage is not present. The result is a likelihood of 50 % of having a new infection in the block. Most of the time, the infection will occur inside the same office (L1 ~ 27 %) but it can also happen in other rooms, too (L2 ~ 9 %; L2+ ~ 14 %). By taking into consideration the case that represents the actual conditions of the block regarding both mechanical and natural ventilation strategies, in the case of vaccine coverage not being present (22D/O0), the results are similar to the worst-case scenario, with a probability of 42 % of having at least one new infection. The coupling of mechanical and natural ventilation is able to reduce the probability of infection in adjacent rooms from ca. 23 % to 17 %. In the case of windows being opened often, and the mechanical ventilation being active during occupancy hours (case 33D/O0), it is possible to reduce the probability of new infection even further to 25 % (half with respect to the worst-case scenario), and the probability of new infections in adjacent offices to 7 %. The efficacy of vaccination coverage strongly depends on the Covid-19 variant considered. By looking at the table, it is possible to observe how vaccinations are a valid substitute for the optimal ventilation strategies (i.e., strategy number 3 for both mechanical and natural ventilation) when the Delta variant is considered. In fact, the scenario with windows always closed and mechanical ventilation always inactive (11D1) is comparable with the best-case scenario without vaccination coverage (33D/O0). If all the possible counter measures are taken (scenario 33D1), it is possible to reduce the probability of new infections to 10 %, and the probability of having new infections in adjacent rooms to almost 0 %. For the Omicron variant, the considered vaccines are not as effective as for the Delta variant. In this case, the results are slightly better if compared with the scenarios without vaccination coverage.

7. Conclusion

In this work, a Monte Carlo method for the assessment of airborne contagion risk due to Covid-19 was applied to some offices contained in a public building, taking into consideration different ventilation strategies, two Covid-19 variants, and the presence of vaccine coverage. It was observed that the current strategies regarding both window utilization and mechanical ventilation are not able to prevent the spread of Covid-19 virus from office to office. Vaccination coverage alone is able to reduce the risk of contagion due to Covid-19 to acceptable values only when it is a case of the Delta variant.

Table 2 – Likelihood of having exactly 0 (L0), 1 (L1), 2 (L2), or more (L2+) newly-infected occupants for each scenario

Scenario Code	L0 (%)	L1 (%)	L2 (%)	L2+ (%)
11D/O0	50	27	9	14
12D/O0	56	29	7	8
13D/O0	65	24	8	4
21D/O0	54	29	9	9
22D/O0	58	26	9	8
23D/O0	65	21	8	6
31D/O0	70	20	6	4
32D/O0	73	21	4	2
33D/O0	75	19	5	2
11D1	74	19	4	2
12D1	79	18	3	1
13D1	85	13	2	0
21D1	81	16	2	1
22D1	77	18	3	2
23D1	86	12	2	0
31D1	87	12	1	0
32D1	88	11	1	0
33D1	90	8	1	0
11O1	60	25	8	7
12O1	62	25	8	6
13O1	70	21	6	3
21O1	62	24	7	7
22O1	65	24	6	5
23O1	73	21	3	3
31O1	72	21	5	3
32O1	73	21	5	2
33O1	82	14	3	2

In fact, if the Omicron variant is considered instead, the only proper way to contain the spread of the virus is to combine vaccination coverage with an increase in opening frequency of windows, and to adopt an appropriate schedule for mechanical ventilation, preferably based on occupancy profiles.

Acknowledgement

This study was funded by the Free University of Bolzano-Bozen within the "Ventilation and Indoor Air Quality in Offices: Monitoring and Improvement" project (CUP: I55F21002050005) and performed with the support of the Geology, Civil Protection and Energy Office of the Municipality of Bozen-Bolzano.

References

Albertin, R., G. Pernigotto, and A. Gasparella. 2022a. "Assessment Of The Covid-19 Contagion Risk In University Classrooms With TRNSYS And TRNFLOW Simulations." *Proceedings of IAQ 2020*, May 4-6, 2022, Athens, Greece.

Albertin, R., G. Pernigotto, and A. Gasparella. 2022b. "Contagion Risk Assessment For COVID-19 Variants With A Dynamic Approach For A Multizone Building Model Of University Classrooms." *Proceedings of Herrick Conferences*, July 10-14, 2022, West Lafayette, United States.

Andrews, N., J. Stowe, F. Kirsebom, S. Toffa, T. Rickeard, E. Gallagher, C. Gower, M. Kall, N. Groves, A. M. O'Connell, D. Simons, P. B. Blomquist, A. Zaidi, S. Nash, N. Iwani Binti Abdul Aziz, S. Thelwall, G. Dabrera, R. Myers, G. Amirthalingam, S. Gharbia, … J. Lopez Bernal. 2022. "Covid-19 Vaccine Effectiveness against the Omicron (B.1.1.529) Variant." *The New England journal of medicine*, NEJMoa2119451. doi: https://doi.org/10.1056/NEJMoa2119451

Buonanno, G., L. Morawska, and L. Stabile. 2020a. "Quantitative assessment of the risk of airborne transmission of SARS-CoV-2 infection: Prospective and retrospective applications." *Environ-*

ment international 145: 106112. doi: https://doi.org/10.1016/j.envint.2020.106112

Buonanno, G., L. Stabile, and L. Morawska. 2020b. "Estimation of airborne viral emission: Quanta emission rate of SARS-CoV-2 for infection risk assessment." *Environment international* 141: 105794. doi: https://doi.org/10.1016/j.envint.2020.105794

Ma, Q., J. Liu, Q. Liu, L. Kang, R. Liu, W. Jing, Y. Wu, and M. Liu. 2021. "Global Percentage of Asymptomatic SARS-CoV-2 Infections Among the Tested Population and Individuals with Confirmed COVID-19 Diagnosis: A Systematic Review and Meta-analysis." *JAMA network open* 4(12): e2137257. doi: https://doi.org/10.1001/jamanetworkopen.2021.37257

Mathieu, E., H. Ritchie, E. Ortiz-Ospina, M. Roser, J. Hasell, C. Appel, C. Giattino, and L. Rodés-Guirao. 2021. "A global database of COVID-19 vaccinations." *Nature human behaviour* 5(7): 947–953. doi: https://doi.org/10.1038/s41562-021-01122-8

Impact of Visual, Thermal, and Indoor Air Quality Conditions on Students' Wellbeing and Learning Performance in a Primary School of Bolzano, Italy

Giovanni Demozzi – Free University of Bozen-Bolzano, Italy – giovanni.demozzi@gmail.com
Luca Zaniboni – University of Trento & Free University of Bozen-Bolzano, Italy – luca.zaniboni@unitn.it
Giovanni Pernigotto – Free University of Bozen-Bolzano, Italy – giovanni.pernigotto@unibz.it
Andrea Gasparella – Free University of Bozen-Bolzano; Italy – andrea.gasparella@unibz.it

Abstract

Poor Indoor Environmental Quality *IEQ* conditions, defined by the four environmental comfort domains (thermo-hygrometric, visual, Indoor Air Quality *IAQ* and acoustic), can cause not only discomfort to building occupants, but also lack of concentration, and harmful and unhealthy status. In this work, visual, thermal and *IAQ* conditions in a primary school located in Bolzano, Italy, were analysed to assess their impact on students' learning performance. After a survey in the school, which included measurements of illuminance, luminance, optical properties of materials, air temperature and CO_2 concentration, some simulation models were developed. Through a Radiance model, daylight metrics (e.g., Daylight Factor and Daylight Autonomy) and glare metrics (e.g., Daylight Glare Index and Daylight Glare Probability) were calculated. Furthermore, the melanopic illuminance was simulated to evaluate the non-visual effects of light on children's circadian cycles. In addition to that, EnergyPlus simulations allowed an evaluation of the long-term indoor air quality and thermal comfort conditions, which were used to estimate the students' potential performance loss according to some models in the literature. Interventions on shading devices and *HVAC* system controls were suggested, in order to optimize *IEQ*, with a minimization of performance loss and energy consumption.

1. Introduction

Indoor Environmental Quality *IEQ*, defined by the combination of the four environmental comfort domains (thermo-hygrometric, visual, Indoor Air Quality *IAQ*, and acoustic), must be carefully guaranteed in places such as schools, where people spend a considerable amount of their lifetime. In fact, poor environmental conditions can lead to discomfort in the occupants, and even to poor learning and work performance (UNI EN 15251:2007, UNI EN 16798-1:2019). Furthermore, recent studies in the literature suggest taking comfort from a multi-domain point of view into account (Schweiker et al., 2020; Toftum, 2002; Torresin et al., 2018).

As regards visual comfort, several studies in the literature found this fundamental for indoor wellbeing, since it also affects psychological and psychophysical conditions, as well as circadian rhythms and people's performance (Aries et al., 2010; Cajochen et al., 2005; Khanie et al., 2016; Stevens & Rea, 2001; Webb, 2006; Zaniboni et al., 2022).

As far as the circadian rhythms are concerned, the first models of sensitivity to circadian light were defined in 2001 by Brainard et al. (2001) and Thapan et al. (2001). Later, Rea et al. (2005; 2011) proposed an empirical model of human circadian response based on the neuroanatomy and neurophysiology of the retina and on the results of psychophysical studies. In this model, the concept of Circadian Stimulus *CS*, which represents the relative effectiveness of circadian light, was introduced. According to Rea et al. (2005; 2011), a *CS* of 0.3 in the morning is suitable for the promotion of a good circadian cycle.

Figueiro et al. (2016) highlighted that, in order to stimulate the circadian rhythm, a high circadian stimulus with bright, bluish-white light must be received in the morning, while a low circadian sti-

mulus with dim, yellowish-white light is preferable in the evening. In this way, both levels of alertness and sleep quality are improved. Nevertheless, as Figueiro et al. (2016) discovered, several aspects must be taken into careful consideration to have a correct *CS* trend during the day:

1. spectral power distribution of light sources has to be characterized, not relying exclusively on Correlated Colour Temperatures *CCTs*;
2. both vertical illuminance E_v and only horizontal illuminance E_h on the work plane have to be considered;
3. the fact that illuminance level influences *CS* more than *CCT* has to be remembered.

As regards *IAQ*, CO_2 concentration is the main parameter usually monitored. In fact, even if CO_2 is not classified as a pollutant by the World Health Organization, it can be considered a good proxy of the Indoor Air Quality (López et al., 2021). As Bakó-Biró et al. (2012) stated, large CO_2 concentrations have been proven to reduce pupils' attention and vigilance, thus negatively affecting memory and concentration.

Similar effects can be generated by thermal discomfort. Indeed, as observed by Porras-Salazar et al. (2018), thermal discomfort in classrooms can reduce the ability of students to perform typical school tasks, and has an impact on their performance scores.

Given these premises, this study aimed to discuss the impact of visual and thermal aspects and *IAQ* on students' wellbeing and learning performance. The structure of the research was two-fold. The first part focused on the visual and non-visual effects of light on learning performance of students. The second part, on the other hand, concerned thermal comfort and *IAQ*, quantifying the pupils' expected performance loss in agreement with the models by Porras-Salazar et al. (2018) and Wargocki et al. (2019).

2. Case Study

This study features a primary school located in Bolzano, Italy. The building, opened in 2014, has a simple and linear architectural form, with a fully glazed atrium on a central square, a place of meeting and social gathering for the neighborhood community. The structure is organized into two sectors connected by a central element.

Fifteen classrooms, each with an area of about 50 m^2, are on the first and second floors. Classrooms are illuminated by large windows equipped with internal light curtains, and with ceiling tube LED lamps. This analysis focused on three classrooms, north, south and east-oriented.

Fig. 1 – Internal northern classroom view

3. Photopic and Melanopic Analysis

3.1 Survey and Building Model

During the survey, performed on October 23rd, 2019, the following information was collected:

- every surface's color, with reflected luminous fluxes, incident luminous fluxes, reflectance, and chromatic coordinate (Yxy), obtained by means of a portable spectrophotometer;
- illuminance values on students' task area, measured with a luxmeter;
- luminance and luminance maps considering students' typical viewpoints, measured with a spot luminance meter and a calibrated digital camera.

These data were used as inputs for the development of Radiance models.

3.2 Photopic Simulation Model

The Radiance models were developed using Rhinoceros and Grasshopper, with the Ladybug and Honeybee plugins. Urban and natural contexts were imported using Blender. A 2019 actual meteorological year was employed first to compare the simulated results with the measurements, and then for annual simulations.

The following analyses were performed:

a) *Image-based point-in-time simulations to detect glare risks for students and teacher and validate the model against measured data.*
The pupils are supposed to change frequently their view, looking at the desk or at the teacher alternatively. Thus, the selected visual task area was not limited to the desk, but also included the frontal view. Furthermore, the teacher's view of the classroom was included as well. 15 comparisons between simulated Daylight Glare Probability *DGP* values and those calculated from the luminance maps collected with the calibrated digital camera were carried out.

b) *Calculation of daylight metrics:* assessment of the *Daylight Factor DF*, with CIE overcast sky, and of *dynamic daylight metrics*, such as Daylight Autonomy *DA*, continuous Daylight Autonomy *cDA*, Useful Daylight Illuminance *UDI*, and spatial Daylight Autonomy *sDA*. In both cases, a 210-point squared grid (0.5 m x 0.5 m x 0.7 m) on the task area of seated students was used, in agreement with the EN 12464-1.

c) *Annual calculation of eDGP*, in particular, considering students looking at the window.

d) *Annual shading and lighting switch profiles*, suggesting, respectively, if venetian blinds need to be adopted or not and whether lights need to be turned on during the year and at which intensity level.

3.2.1 Results

The following figures show some of the results obtained through the simulations described in Section 3.2. Fig. 2 and Fig. 3 show a comparison between the *DGP* calculated from a *HDR* camera luminance map and the simulated one in the eastern classroom. As can be noticed, both gave a value of 0.20, demonstrating the accuracy of the developed Radiance model.

Table 1 shows the Daylight Factors for the three classrooms considered. Except for the south-oriented classroom, it can be noticed that DF is larger than 4 %, in agreement with the current requirements set by Italian law for these types of buildings.

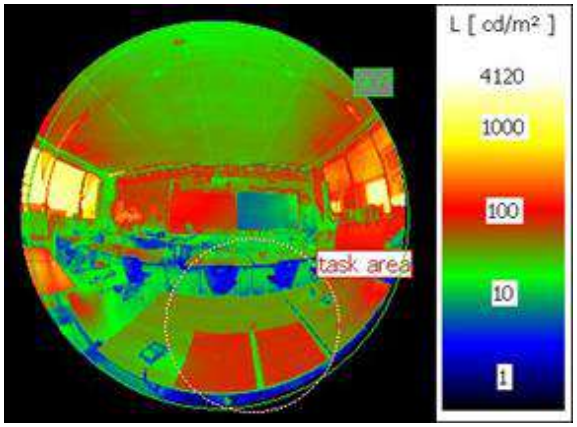

Fig. 2 – Eastern classroom – measured luminance map and student's view DGP = 0.20

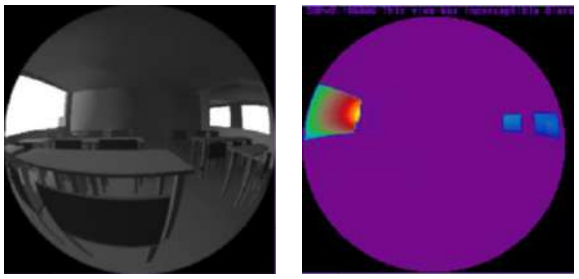

Fig. 3 – Eastern classroom – simulated luminance map and student's view *DGP* = 0.20

Table 1 – Daylight factor

	Northern classroom	Southern classroom	Eastern classroom
$DF_{average}$	4.4 %	3.2 %	4.2 %

Figs. 4-6 show the values of *DA*, *cDA* and *UDI* for the east-oriented classrooms. As can be noticed, the portion of the room closer to the windows shows a large value of *DA* and *cDA*; however, the natural illuminance can be excessive, as can be observed considering the *UDI* shown in Fig. 6.

Table 2 summarizes the dynamic daylight metrics for all three classrooms. The eastern classroom shows the highest values of *DA*, *cDA* and *sDA*, while the south-oriented one is characterized by the minimum ones. This is due to the exposure, the effects of reflectance of nearby buildings and the absence of high obstacles.

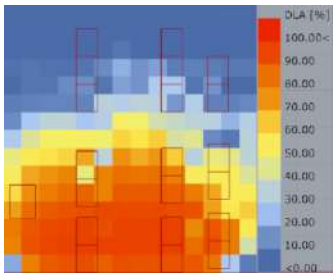

Fig. 4 – Eastern classroom – *DA*

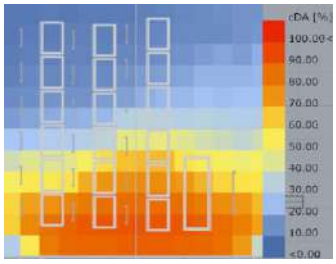

Fig. 5 – Eastern classroom – *cDA*

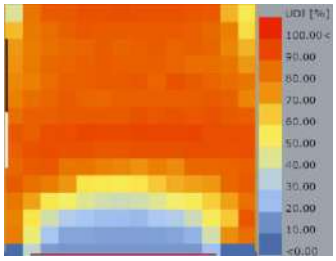

Fig. 6 – Eastern classroom – *UDI*

Table 2 – Dynamic daylight metrics

	Northern classroom	Southern classroom	Eastern classroom
$DA_{average}$	30.9 %	20.9 %	40.1 %
$cDA_{average}$	60.3 %	40.1 %	63.8 %
$UDI_{average100\text{-}2000lx}$	85.0 %	47.9 %	70.8 %
sDA	31.6 %	22.6 %	40.9 %

Finally, Figs. 7-9 represent the annual distribution of *eDGP* calculated for the view of a student in the centre of the room, recommended usage of shading devices and light switch for the eastern classroom. As can be noticed, the risk of glare is frequently encountered, in particular, during autumn and spring. Therefore, the presence of shadings is here recommended. The same applies to the south-oriented classroom.

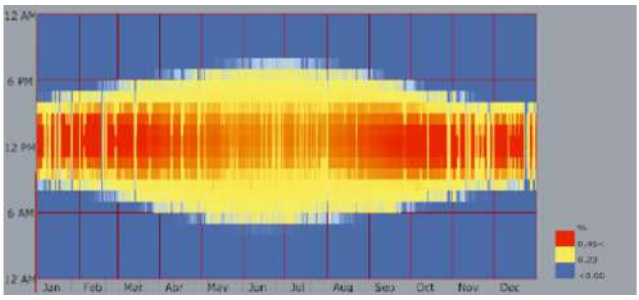

Fig. 7 – Eastern classroom annual DGP

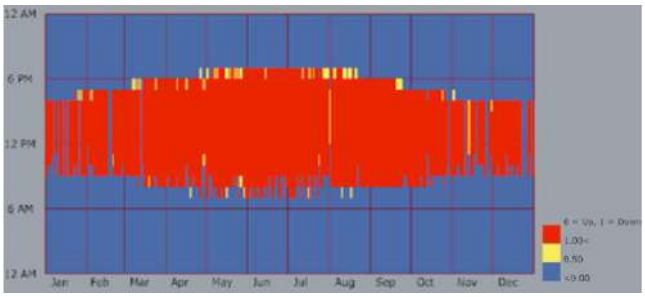

Fig. 8 – Eastern classroom annual shadings device

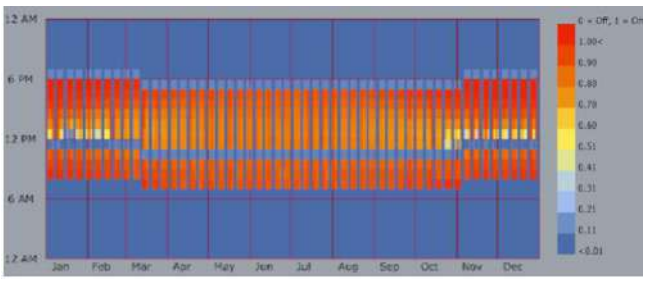

Fig. 9 – Eastern classroom annual lighting switch

3.3 Melanopic Simulation Model

The melanopic illuminance was computed using Lark, a Grasshopper plugin released by Inanici et al. (2015). In order to perform a simplified monthly calculation, a representative day for each month was considered, in accordance with Klein (1976). For the sake of comparison, the analysis was performed using both a CIE clear sky and a climate-based sky.

Within this computation, the light stimulus was evaluated vertically (e.g., in the direction of gaze) by means of six virtual sensors placed across a regularly spaced analysis grid of nine points, at a height of 1.2 m (seated person eye level). All the simulations were set with the same hourly time intervals during the occupational period, i.e., from 8 am to 4 pm.

After the calculation of Rea's melanopic illuminance, the three classrooms were analyzed, verifying if a *CS* value of 0.3 was achievable for at least 1 h in the early part of the day.

3.3.1 Results

In all three classrooms, melanopic illuminance was unevenly distributed and quite low. This was particularly true for the positions far away from windows and during winter months, as shown in Fig. 10 and Fig. 11 for the eastern classroom. This condition risks not allowing a shift in the biological clock of the occupants. Results from annual calculations indicated that roughly 1/2 of the area in the northern classroom, 1/2 of the area in the southern classroom, and 1/3 of the area in the eastern classroom did not benefit from melanopic illuminance all year long.

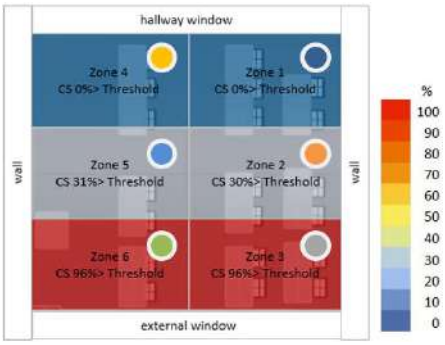

Fig. 10 – Eastern classroom sensor position and percentage of threshold exceedance over the year

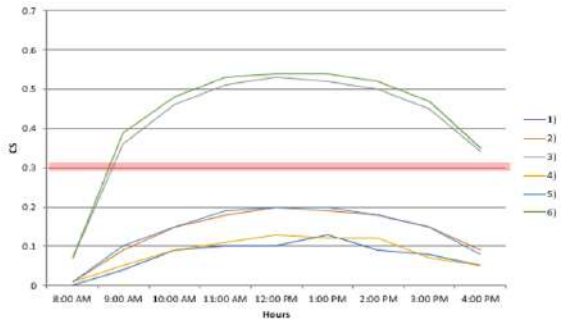

Fig. 11 – Eastern classroom *CS* trend on January 17th

4. CO_2 and Thermal Analysis

4.1 Survey and Building Model

A monitoring campaign was performed in one of the three classrooms, specifically the southern one, measuring air temperatures and CO_2 concentrations from November to December 2019, with a 10-minute time step.

An EnergyPlus model was developed using a 2019 actual meteorological year and including the surrounding urban context. The thermophysical properties of the building envelope (material thermal conductivity, thickness, density and specific heat capacity) were taken from the technical report and the CasaClima building energy certificate. As regards the glazing system, double glazed low-e windows were modeled with WINDOW by the Lawrence Berkeley National Laboratory (LBNL), considering a window gap of 0.016 m, with a mixture of 90 % argon and 10 % air.

Internal gains were estimated considering the 9 luminaires of 166 W each installed, the presence of 100-W electric equipment (laptop and beamer), and occupants (ASHRAE Handbook of Fundamentals), with a metabolic rate of 1.2 met (as suggested in EN ISO 7730 for sedentary activities), clothing of 1 clo, and in agreement with the school official occupancy schedules. An overall CO_2 generation rate of 0.00002 m^3/s was set, and a reference of 400 ppm CO_2 concentration.

Infiltration and ventilation rates were set according to Table 3. Specifically, typical opening schedules of windows were simulated according to the information given by school teachers. Similarly, the control of the shading devices was set in agreement with the typical behavior communicated by school teachers, also considering lowering the shadings when the direct radiation incident on the window is larger than 150 W.

The model calibration was performed manually, varying the infiltration rate, the carbon dioxide generation and the optic properties of obstacles and internal shadings.

4.2 Simulated Configurations and Outputs

The EnergyPlus simulations were computed with four different controls for the HVAC systems:

- *Standard*: simulation of the heating period with heating setpoint of 20 °C and natural ventilation;
- *VAR1*: simulation of the same *Standard* configuration with an additional cooling system with a cooling setpoint of 26 °C;
- *VAR2*: simulation of the same *Standard* configuration with the addition of a Mechanical Ventilation System *MVS* supplying 5 h^{-1} (i.e., 11 l/s/person during hours of occupation);
- *VAR3*: the combination of *VAR1* + *VAR2*.

Table 3 – Natural and mechanical ventilation in the different configurations

	Standard	VAR1	VAR2	VAR3
Infiltration (Always present)	0.05 h^{-1}	0.05 h^{-1}	0.05 h^{-1}	0.05 h^{-1}
Tilt open (Occupancy period)	0.1 h^{-1}	0.1 h^{-1}	-	-
Windows completely open (Lunch break, after lessons)	5 h^{-1}	5 h^{-1}	-	-
MVS (Occupancy period)	-	-	5 h^{-1}	5 h^{-1}

Simulated CO_2 concentrations and Fanger PMVs were correlated to pupils' performance loss according to the model developed by Porras-Salazar et al. (2018) and Wargocki et al. (2019). Diverse learning activities were considered, including typical schoolwork tasks, such as arithmetical calculations, reading and comprehension exercises, psychological tests measuring cognitive skills and the abilities needed to perform schoolwork (i.e., tests measuring concentration, memory and response time, results of aptitude and national tests examining progress in learning, results of midterm and final exams and end-of-year grades). Short-term sick leave rates were evaluated as well.

4.2.1 Results

As may be observed in Fig. 12, if no mechanical ventilation is used (as in the *Standard* and *VAR1* configurations), the level of CO_2 concentration exceeds those recommended in EN 16798-1:2019 for school environments (i.e., category I). As reported in Table 4, this issue led to important losses, especially in "*speed and reaction time*" and "*national and aptitude tests and exams*" scores.

On the whole, simulations revealed that the main performance loss of pupils in all the four configurations is due to thermal discomfort, up to 20 %. This result is consistent with Sarbu et al. (2015), who reported that occupants are more sensitive to temperature variations than to CO_2 concentration variations.

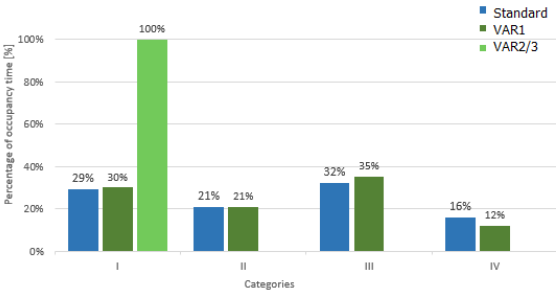

Fig.12 – Share of occupied time in the different *IAQ* categories in accordance with EN 16798-1:2019

Table 4 – Different configurations and maximum performance losses

max % performance losses	Standard	VAR1	VAR2	VAR3
Speed or reaction time	12 %	12 %	0 %	0 %
Accuracy	2 %	2 %	0 %	0 %
National and aptitude tests and exams	16 %	16 %	0 %	0 %
Daily attendance	4 %	4 %	0 %	0 %
Thermal discomfort	22 %	21 %	16 %	16 %

5. Discussion and Conclusion

This study uses experimental monitoring and dynamic simulation to assess *IEQ* in three classrooms of a case study school in Bolzano, evaluating the impact on students' wellbeing and learning performance.

In the first part of the study, related to the visual and non-visual analysis of classroom lighting conditions, several issues were identified. In fact, not all environments were well illuminated by daylight (due to the building configuration and to the presence of nearby buildings and mountains), and the risk of glare occurred all year round in east and south-oriented classrooms. For this reason, it was found advisable to adopt shading devices and dimmed daylight systems controlled by a photosensor in order to solve issues of glare and lack of daylight. Also, timed control artificial lighting, compensating for the lack of daylight, could be beneficial. These recommendations can be considered to be in agreement with what has been suggested in other works in the literature (e.g., Akashi et al., 2013; Choi et al., 2020).

As regards the non-visual effects of light, it was found that in all three classrooms, melanopic illuminance was unevenly distributed and quite low, especially for the east-oriented classroom, with the risk of not allowing a proper shift in the biological clock of the occupants.

The second part of the study revealed that the main performance loss (from 16 % to 22 %) of the pupils is due to thermal discomfort. In this respect, a potential measure could be the adoption of a local thermostat for controlling the room temperature, avoiding typical problems of overheating in winter months, with positive effects on the energy consumption and pupil performance.

Furthermore, mechanical ventilation was found necessary to ensure good *IAQ* conditions for students. In this framework, an integrated control of the *HVAC* system could be helpful to further improve both environmental quality and energy performance.

Acknowledgement

This thesis was partially developed in the framework of the internal project "IndAIR-Edu – Indoor Air Quality and Ventilation Effectiveness in Educational Buildings" of the Free University of Bozen-Bolzano. The authors kindly thank the Geology, Civil Protection and Energy Office of the Municipality of Bolzano, in particular the engineer Francesca Roberti, for supporting this research, and the management team of A. Langer school.

References

Akashi, Y., and J. Neches. 2013. "Detectability and acceptability of illuminance reduction for load shedding." *Journal of the Illuminating Engineering Society: 3-13.* doi: https://doi.org/10.1080/00994480.2004.10748422

Aries, M. B., J. A Veitch, and G. R. Newsham. 2010. "Windows, view, and office characteristics predict physical and psychological discomfort." *Journal of environmental psychology* 30(4): 533-541. https://doi.org/10.1016/j.jenvp.2009.12.004

ASHRAE. 2017. ASHRAE Handbook-Fundamentals.

Bakó-Biró, Z., D. J. Clements-Croome, N. Kochhar, H. B. Awbi, and M. J. Williams. 2012. "Ventilation rates in schools and pupils' performance." *Building and Environment* 48. doi: https://doi.org/10.1016/j.buildenv.2011.08.018

Brainard, G. C., J. P. Hanifin, J. M. Greeson, B. Byrne, G. Glickman, E. Gerner, and M. D. Rollag. 2001. "Action Spectrum for Melatonin Regulation in Humans: Evidence for a Novel Circadian Photoreceptor." *Journal of Neuroscience* 21(16): 6405-6412. doi: https://doi.org/10.1523/JNEUROSCI.21-16-06405.2001

Cajochen, C., M. Munch, S. Kobialka, K. Krauchi, R. Steiner, P. Oelhafen, S. Orgul, and A. Wirz-Justice. 2005. "High sensitivity of human melatonin, alertness, thermoregulation, and heart rate to short wavelength light". *The journal of clinical endocrinology & metabolism* 90(3): 1311-1316. doi: https://doi.org/10.1210/jc.2004-0957

Choi, K., and H. J. Suk. 2020. "The gradual transition from blue-enriched to neutral white light for creating a supportive learning environment." *Building and Environment* 180: 107046. doi: https://doi.org/10.1016/j.buildenv.2020.107046

EnergyPlus. 2019. "Weather data". EnergyPlus website (https://energyplus.net/weather), accessed on June 2019.

European Committee for Standardization. 2005. *EN ISO 7730. Ergonomics of the Thermal Environment - Analytical Determination and Interpretation of Thermal Comfort Using Calculation of the PMV and PPD Indices and Local Thermal Comfort Criteria.* Belgium: Brussels.

European Committee for Standardization. 2007. *EN 15251. Indoor environmental input parameters for design and assessment of energy performance of buildings addressing indoor air quality, thermal environment, lighting and acoustics.* Belgium: Brussels

European Committee for Standardization. 2011. *EN 12464-1. Light and lighting - Lighting of work places - Part 1: Indoor work places.* Belgium: Brussels

European Committee for Standardization. 2019. *EN 16798-1. Energy performance of buildings - Ventilation for buildings - Part 1: Indoor environmental input parameters for design and assessment of energy performance of buildings addressing indoor air quality, thermal environment, lighting and acoustics*. Belgium: Brussels

Figueiro, M. G., K. Gonzales, and D. Pedler. 2016. "Designing With Circadian Stimulus." *Lighting Design and Application*: 31–33.

Klein. S. A. 1977. "Calculation of monthly average insolation on tilted surfaces." *Solar energy* 19(4): 325-329. doi: https://doi.org/10.1016/0038-092X(77)90001-9

López, M. J. R., G. Guyot, B. Golly, M. Ondarts, F. Wurtz, and E. Gonze. 2021. "Relevance of CO2-based IAQ indicators: Feedback from long-term monitoring of three nearly zero-energy houses." *Journal of Building Engineering* 44: 103350. doi: https://doi.org/10.1016/j.jobe.2021.103350

Porras-Salazar, J. A., D. P. Wyon, B. Piderit-Moreno, S. Contreras-Espinoza, and P. Wargocki. 2018. "Reducing classroom temperature in a tropical climate improved the thermal comfort and the performance of elementary school pupils." *Indoor Air* 28. doi: https://doi.org/10.1111/ina.12501

Rea, M. S., M. G. Figueiro, A. Bierman, and R. Hamner. 2011. "Modelling the spectral sensitivity of the human circadian system." *Lighting Research and Technology*. doi: https://doi.org/10.1177/1477153511430474

Rea, M. S., M. G. Figueiro, J. D. Bullough, and A. Bierman. 2005. "A model of phototransduction by the human circadian system." *Brain Research Reviews* 50(2): 213-228. doi: https://doi.org/10.1016/j.brainresrev.2005.07.002

Sarbu, I., and C. Pacurar. 2015. "Experimental and numerical research to assess indoor environment quality and schoolwork performance in university classrooms." *Building and Environment.* doi: https://doi.org/10.1016/j.buildenv.2015.06.022

Sarey Khanie, M., J. Stoll, W. Einhaeuser, J. Wienold, and M. Andersen. 2016. "Gaze responsive visual comfort: New findings on gaze behaviour in a daylit office space in relation to glare"(No. CONF, pp. 373-384). *Cie Central Bureau.*

Schweiker, M., E. Ampatzi, M.S. Andargie, R. K. Andersen, E. Azar, V. M Barthelmes, and S. Zhang. 2020. "Review of multi-domain approaches to indoor environmental perception and behaviour." *Building and Environment* 176: 106804. doi: https://doi.org/10.1016/j.buildenv.2020.106804

Stevens, R. G., and M. S. Rea. 2001. "Light in the built environment: potential role of circadian disruption in endocrine disruption and breast cancer." *Cancer Causes & Control* 12(3): 279-287. doi: https://doi.org/10.1023/A:1011237000609

Thapan, K., J. Arendt, and D. J. Skene. 2001. "An action spectrum for melatonin suppression: evidence for a novel non-rod, non-cone photoreceptor system in humans." *Journal of Physiology*. doi: https://doi.org/10.1111/j.1469-7793.2001.t01-1-00261

Toftum, J. 2002. "Human response to combined indoor environment exposures." *Energy and*

buildings 34(6): 601-606. doi: https://doi.org/10.1016/S0378-7788(02)00010-5

Torresin, S., G. Pernigotto, F. Cappelletti, and A. Gasparella. 2018. "Combined effects of environmental factors on human perception and objective performance: A review of experimental laboratory works." *Indoor air* 28(4): 525-538. doi: https://doi.org/10.1111/ina.12457

Wargocki, P., J. A. Porras-Salazara, S. Contreras-Espinozad. 2019. "The relationship between classroom temperature and children's performance in school." *Building and Environment* 157: 197-204. doi: https://doi.org/10.1016/j.buildenv.2019.04.046 157

Webb, A. R., 2006. "Considerations for lighting in the built environment: Non-visual effects of light." *Energy and Buildings* 38(7): 721-727. doi: https://doi.org/10.1016/j.enbuild.2006.03.004

Zaniboni, L., M. Sarey Khanie, G. Pernigotto, J. Toftum, A. Gasparella, and B.W. Olesen. 2022. "Lighting conditions in physiotherapy centres: A comparative field study." *Lighting Research & Technology*: 14771535211046521. doi: https://doi.org/10.1177%2F14771535211046521

Performance Simulation of Desiccant Wheel under Dynamic Conditions: Comparison between Detailed and Simplified Models

Simone Dugaria – Free University of Bozen-Bolzano, Italy – simone.dugaria@unibz.it
Andrea Gasparella – Free University of Bozen-Bolzano, Italy – andrea.gasparella@unibz.it

Abstract

In the last few decades, European countries have been facing an increasing demand for active air-conditioning (cooling and dehumidification) in the summer period. As a good alternative to energy demanding vapor compression cooling-based air dehumidification, building HVAC systems integrating desiccant-based dehumidification has drawn increasing attention. These technologies offer the possibility to significantly reduce the energy requirement for air dehumidification and post-heating due to excessive cooling. In fact, air-conditioning systems that use solid or liquid desiccant offer the interesting capacity of separating dehumidification and sensible cooling of air and realizing high-energy-efficiency systems. However, the complexity perceived by technicians towards the design of air-conditioning systems based on these technologies actually limits their adoption in HVAC systems, mainly due to the difficulties in predicting the performance of the desiccant devices, which is the crucial component of the system. On the one hand, many simplified approaches commonly adopted to simulate and optimize the dehumidification performance are based on steady-state models and their reliability under unsteady conditions is questionable; on the other hand, accurate detailed models available for the design and development of components do not turn out to be particularly suitable for simulation of energy systems, due to their high computational cost. The present work focuses on desiccant wheels, whose performance is not only directly related to the properties of the sorption material, but also depends strongly on operating conditions, such as rotational speed, regeneration temperature and inlet air conditions, which are typically non-stationary in real application. In this context, the purpose of this paper is to assess the reliability of a simplified model to predict the behavior of a desiccant wheel under dynamic conditions. To do so, a detailed model of a desiccant wheel is developed and validated against experimental data available in the literature. Finally, a comparison between the developed detailed model and the simplified model under dynamic conditions is carried out.

1. Introduction

The adoption of new and efficient dehumidification technologies as an alternative to condensation is attracting increasing interest, both in civil application and industrial production. Compared with the traditional vapor compression dehumidification method, the absorption dehumidification method can save up to 40 % energy (Du & Lin, 2020) and make full use of renewable energy sources. Moreover, adsorption dehumidification systems allow improved control of systems with advantages for occupants' thermohygrometric comfort. As clearly discussed in many review papers (Ge et al., 2014; Daou et al., 2006; Sultan et al., 2015), desiccant wheel systems are attracting increasing interest because they offer advantages over other air conditioning systems, such as the possibility of:

i) using water as a natural refrigerant and other environmentally-friendly desiccant materials (such as silica gel and zeolites);
ii) making energy-efficient cooling systems that work with the sensitive and latent loads, the application of which is possible under different environmental conditions;
iii) meeting the requirements of miniaturization and being less subject to corrosion compared with the liquid desiccant system (in which the liquid and air directly interact);
iv) integrating low-grade heat sources (such as solar energy, geothermic energy and waste heat), hence significantly reducing the operating costs;

v) overcoming the discontinuous problem of the fixed-bed desiccant cooling system.

The rotary desiccant wheel is a relatively mature technology, yet its wide application is still limited due to the complexity perceived by technicians towards the design of air-conditioning systems based on this technology. The design of HVAC systems based on this technology is quite complex because of the difficulties in predicting the performance of the desiccant wheel, which is the crucial component of the system. In fact, the performance of the desiccant wheel is critical to the capability, size and cost of the whole system (De Antonellis et al., 2010). Desiccant wheel performance strongly depends on regeneration temperature on the revolution speed, inlet airflow conditions (temperature, humidity and flow rate) and on the coupled heat and mass transfer within the desiccant. These aspects greatly complicate the development of models which can accurately predict the performance of a desiccant wheel under non-stationary conditions without incurring in high computational load and complexity. On the one hand, many detailed desiccant wheels models have been based on a detailed physical approach and they are particularly suitable for the development and design of components (Ge et al., 2008); on the other hand, simplified approaches based on practical correlations (Angrisani et al., 2012; De Antonellis et al., 2015; Jurinak, 1982; Panaras et al., 2010) are commonly used to simulate and optimize the dehumidification performance, but their reliability under unsteady conditions is questionable. The purpose of this work is to assess the reliability of simplified models to predict the behavior of a desiccant wheel under dynamic conditions. The rotary desiccant dehumidifier model contained in the TESS Component Libraries for Trnsys18™ was chosen to represent the simplified models based on the correlations. A detailed model of a desiccant wheel was developed and validated against experimental data available in the literature and, finally, a comparison between these two models was carried out.

A desiccant wheel is a cylindrical rotating device generally consisting of a structure of several channels. The channels run in the axial direction of the wheel and are parallel to each other. Depending on the manufacturing process, they can have usually a rectangular, triangular or sinusoidal shape. The structure is made by supporting material impregnated with an adsorbent substance (desiccant) in a typical content f of 70–80 %. The most widespread support materials are paper, aluminium, synthetic fibers or plastic, while common adsorbents are silica gel, zeolite and activated alumina (De Antonellis et al., 2015).

In its basic configuration, the wheel is divided into two sections, where the air streams are arranged in counter-flow. In the process section, the air stream is dehumidified and undergoes heating. In the regeneration section, an air stream is heated before passing through the wheel to increase its moisture-holding capacity; the regeneration air stream passing through the wheel removes vapor from the desiccant material and exits cooled and humidified. A diagram of a desiccant wheel is shown in Fig. 1.

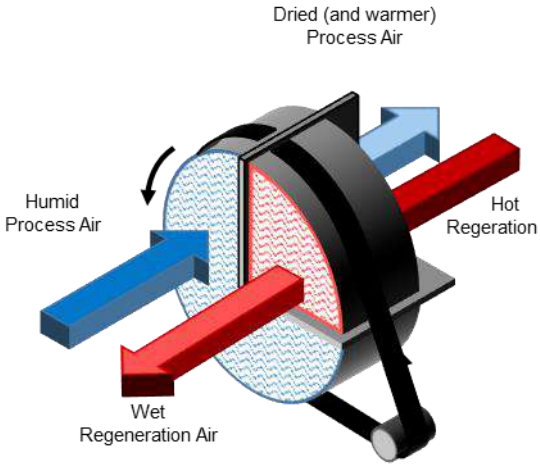

Fig. 1 – Diagram of a desiccant wheel

2. Model Description

Two models were considered in this paper to simulate the performance of a desiccant wheel such as the one shown in Fig. 1. In the first defined detailed model, the coupled heat and mass transfer within the wheel is modeled in detail. The simplified model is a correlation-based model that can immediately provide output conditions without the need to specify detailed parameters of the desiccant wheel.

In the detailed model, to reflect the actual transfer processes occurring in the desiccant wheel, a gas and solid side resistance was applied, where also the solid side heat conduction and mass diffusion

resistances were considered. Compared with only gas-side resistance models, gas and solid side resistance models are more related to the actual process in the desiccant wheel (Ge et al., 2008). However, the diffusion and adsorption processes inside the desiccant are lumped into the mass and heat transfer coefficients. The precision of these models is considered satisfactory because the desiccant layer is rather thin (Ge et al., 2008). The model also takes also into account heat and mass transfer from the desiccant to the air stream and the developing temperature and velocity profiles along the desiccant wheel channels.

The numerical analysis is based on the following assumptions:

a) Heat and mass transfer from the wheel to the surroundings are negligible;
b) The channels are considered identical and uniformly distributed throughout the wheel;
c) Supporting and desiccant materials are evenly distributed in the layer.
d) The properties of the dry desiccant material, as well as of the supporting material are constant;
e) Heat and mass transfer between adjacent channel are negligible: temperature and moisture content gradients in circumferential and radial directions are not considered;
f) The hygroscopic capacity of supporting material is negligible compared with the adsorbent;
g) The inlet air conditions are uniform and the air flow is one-dimensional;
h) Air leakages between the two streams are negligible;
i) Heat conduction in humid air is negligible;
j) Pressure loss of the air stream is negligible for heat and mass transfer processes (the thermodynamic properties are unaffected)
k) Axial heat conduction and mass diffusion in the air are small compared with convective processes;
l) The vapor enters the pores, diffuses in the pores, and, meanwhile, is adsorbed.
m) The influence of the pressure drop in axial direction on heat and mass transfer is neglected;
n) The heat of adsorption is set free in the layer immediately when the vapor enters the porous layer and is partially convected into air stream.

The schematics of a channel segment in the desiccant wheel is shown in Fig. 2.

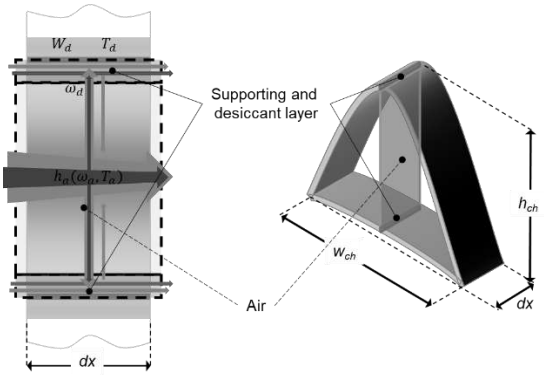

Fig. 2 – Schematic of the control volume in a channel segment (right) and mass and energy transfers in a control volume (left)

In the detailed model, one channel segment with an infinitesimal length dx is selected as the control volume (Fig. 2 - left). The control volume is separated into two nodes, one is the humid air in the channel and the other is the layer composed of supporting and desiccant materials (Fig. 2 - right). The layer of supporting and desiccant material is shared by two channels: therefore, the thickness of the layer in one control volume is half of its actual value and the middle of this layer is considered to be adiabatic.

Referring to Fig. 2, the following laws were applied to the infinitesimal control volume.

Mass balance of water in the desiccant material and adsorbed water:

$$\begin{aligned}\rho_a \varepsilon A_{ch}(1-f)\frac{\partial \omega_d}{\partial t} + \rho_d(1-\varepsilon)A_{ch}(1-f)\varphi\frac{\partial W}{\partial t} \\ = \rho_a \varepsilon A_{ch}(1-f)D_{eff}\frac{\partial^2 \omega_d}{\partial x^2} \\ + \rho_d A_{ch}(1-f)D_s\frac{\partial^2 W}{\partial x^2} \\ + h_m P_{ch}(\omega_d - \omega_a)\end{aligned} \quad (1)$$

Energy balance for the desiccant material, supporting material and adsorbed water:

$$\begin{aligned}\rho_s(1-\varepsilon)A_{ch}(1-f)c_{p,s}(1-\varphi)\frac{\partial T_d}{\partial t} \\ + \rho_d(1-\varepsilon)A_{ch}(1 \\ - f)c_{p,d}\varphi\left(\frac{\partial T_d}{\partial t} - \frac{\lambda_d}{\rho_d c_{p,d}}\frac{\partial^2 T_d}{\partial x^2}\right) \\ = h_{th}P_{ch}(T_a - T_d) \\ + h_m P_{ch}(\omega_a - \omega_d)c_{p,v}(T_a - T_d) \\ - h_m P_{ch}(\omega_a - \omega_d)(1-\eta)i_{ad}\end{aligned} \quad (2)$$

Mass balance of water in the air stream:

$$\rho_a f A_{ch}\left(\frac{\partial \omega_a}{\partial t}+u\frac{\partial \omega_a}{\partial x}\right)=h_m P_{ch}(\omega_d-\omega_a) \quad (3)$$

Energy balance in the air stream:

$$\begin{aligned}\rho_a f A_{ch}\left(c_{p,a}+\omega_a c_{p,v}\right)\left(\frac{\partial T_a}{\partial t}+u\frac{\partial T_a}{\partial x}\right)&\\ =h_{th}P_{ch}(T_d-T_a)&\\ +h_m P_{ch}(\omega_d-\omega_a)c_{p,v}(T_d-T_a)&\\ -h_m P_{ch}(\omega_d-\omega_a)\eta i_{ad}&\end{aligned} \quad (4)$$

To solve the system of partial differential equations, a set of boundary and initial conditions is needed. Assuming adiabatic and impermeable boundaries at the entrance and exit flow channel leads to a negligible error: according to Simonson and Besant (1997), the transfer area at the inlet and outlet of the wheel correspond to less than 0.1 %. Therefore, the following relationships apply for the support and desiccant layer:

$$\begin{aligned}\left.\frac{\partial T_d}{\partial x}\right|_{x=0}&=\left.\frac{\partial T_d}{\partial x}\right|_{x=L}=0\\ \left.\frac{\partial \omega_d}{\partial x}\right|_{x=0}&=\left.\frac{\partial \omega_d}{\partial x}\right|_{x=L}=0\end{aligned} \quad (5)$$

The temperature, humidity ratio and velocity boundary conditions for the air are given by Dirichlet boundary conditions periodically switching between process and regeneration air stream:

$$\begin{aligned}T_a(0,t)&=\begin{cases}T_{p,inlet}\\T_{r,inlet}\end{cases}\\ \omega_a(0,t)&=\begin{cases}\omega_{p,inlet}\\\omega_{r,inlet}\end{cases}\\ u_a(0,t)&=\begin{cases}u_{p,inlet}\\u_{r,inlet}\end{cases}\end{aligned} \quad (6)$$

Assuming uniform initial temperature and humidity ratio of the air and of the support and desiccant, we have:

$$\begin{aligned}T_a(x,0)&=T_{a0}\\ \omega_a(x,0)&=\omega_{a0}\\ T_d(x,0)&=T_{d0}\\ \omega_d(x,0)&=\omega_{d0}\\ W(x,0)&=W_0\end{aligned} \quad (7)$$

Additional equations are needed to solve the initial-boundary-value problem.

The equilibrium water uptake in the desiccant material can be expressed by a general sorption curve that directly links the water uptake *W* to the relative humidity.

The isosteric heat of adsorption i_{ad} of silica gel calculate using the equation recommended by San (1993). The effective diffusion coefficient D_{eff} accounts for both molecular diffusion and Knudsen diffusion. However, as reported by Pesaran and Mills (1987), since most of the pores of silica gel are less than 100 10^{-10} m, ordinary diffusion can be ignored in usual silica gel applications. The surface diffusion *Ds* is evaluated with the relationship proposed by Pesaran and Mills (1987).

The heat transfer coefficient h_{th} is derived from the local Nusselt, calculated following equation of Niu and Zhang (2002). Assuming a sinusoidal geometry for the channel, the Nusselt number for the fully developed flow and the equivalent diameter were calculated through the correlations proposed by Kakaç et al. (1987). The mass transfer coefficient h_m was derived from the Sherwood number.

Given the initial and boundary condition, the partial differential equations system of the four non-linear and coupled heat and mass transfer equations is implemented and solved in Matlab™ environment.

In the simplified model developed by Howe (1983) and based on the original work of Jurinak (1982), the outlet air conditions (humidity ratio and temperature) are provided through two combined potentials *F1* and *F2* for a silica gel desiccant defined in the following way:

$$F1=\frac{-2865}{T^{1.490}}+4.344\,\omega^{0.8624} \quad (8)$$

$$F2=\frac{T^{1.490}}{6360}+1.127\omega^{0.07969} \quad (9)$$

In order to obtain the process air outlet condition, Eqs. (8) and (9) should be numerically solved to get the corresponding values of temperature and humidity ratio. The model computes the values of *F1* and *F2* for a given set of design conditions of both the process and regeneration streams, then uses an iterative process to guess and then converge to the values of the outlet conditions.

3. Validation and Model Comparison

To validate the models, the model results were compared with the experimental data of a commercial desiccant wheel produced by the Japanese manufacturer Seibu Giken Co. Ltd. (Kodama et al., 1993) available in the literature. The supporting layer of the wheel in consideration is made of ceramic porous fiber paper, impregnated with silica gel. The constant thermophysical properties and geometrical parameters of the wheel are listed in Table 1.

Table 1 – Thermophysical and geometrical parameters assumed for the simulation

Angle of regeneration	90°
Desiccant material	Silica gel type A
Porosity	0.4
Volume ratio of desiccant in the layer	0.7
Supporting material	Ceramic fiber sheets
Channel pitch (w x h)	3.2 x 1.8 mm
Wheel diameter	320 mm
Wheel length	200 mm
Rotation speed	6 rph

The structure contains between 70 % and 80 % type A silica gel. The regeneration zone occupies a quarter of the frontal area of the wheel, while the remaining area is dedicated to process air dehumidification. There is 20 mm of brass between the two zone with no air flow. However, the presence of these two separators was not considered in the detailed model. All three experimental series were obtained at the optimum wheel speed, equal to 6 rph.
Table 2 reports the experimental data used in the comparison for the inlet process air conditions. For the inlet regeneration conditions, the same humidity ratio of the process air and a constant regeneration temperature of 140°C is assumed.

Table 2 – Experimental inlet conditions for the process air (Kodama et al., 1993)

	Series 1	Series 2	Series 3
Temperature	24.4 °C	23.7 °C	23.3 °C
Humidity ratio	14.2 g/kg	8.9 g/kg	7.3 g/kg

The *F1* and *F2* potentials of the simplified model were calculated by taking as reference the outlet conditions for process and regeneration air from another series of data of the same experiments taken under similar conditions (Kodama et al., 1993). Then, these potentials were used to evaluate the output conditions for the three series considered here.
The two models were compared under dynamic conditions with varying inlet air temperature and humidity. The other model inputs (regeneration temperature, rotation speed, air flow rate) were kept constant, as were the characteristics of the desiccant wheel. In order to provide a representative input for a real application, inlet temperature and humidity ratio are generated from a monitoring data set obtained from a weather station installed at the Free University of Bozen-Bolzano. The sampling time is 1 minute.

4. Results and Discussion

Fig. 3 and Fig. 4 show the outlet process air humidity ratio and temperature as a function of the angular position. These figures provide a graphical comparison of the experimental and simulated outlet conditions as function of the angle. The data depicted in these figures refer to Series 1 (in blue) Series 2 (in red) and Series 3 (in green). The experimental angular values are plotted with markers, the dashed line is the angular distributions obtained from the detailed model, while the dotted lines refer to the outputs of the simplified model. It has to be mentioned that the plotted angular distributions of the detailed model are those obtained once the transient period has ended and the outlet conditions have reached stable values.

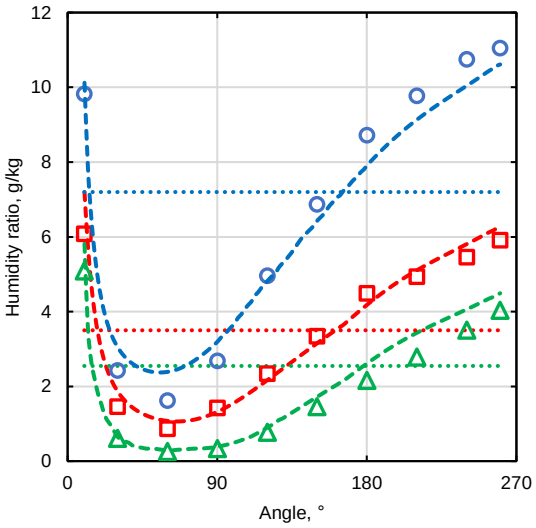

Fig. 3 – Angular distribution of the humidity ratio of processed air at the outlet

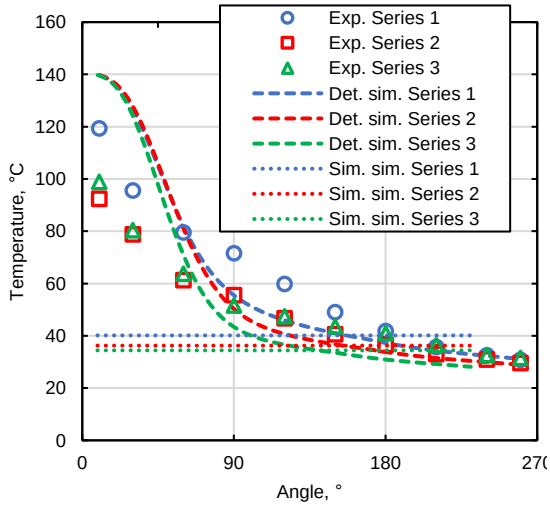

Fig. 4 – Angular distribution of the temperature of process air at the outlet

The detailed model is able to capture the physics of the problem and reproduce with fidelity the angular distribution of the outlet humidity ratio; however, the errors obtained for the single angular values of the humidity ratio may be significant (up to 47 %). The angular distribution of the outlet temperature differs more from the experimental data than does the humidity ratio. The largest differences between simulated and experimental values occur at the first angular positions where the transition between regeneration and process has just occurred. For all the experimental series, the detailed model underestimates the average temperature and humidity ratio of the outlet process air (calculated as the average of the angular values). The difference in the process air average outlet conditions between simulated and the experimental values is always below 12 % (largest error for Series 1) for the humidity ratio and 10 % for the temperature (largest error for Series 2).

Regarding the simplified model, as shown in Fig. 3 and Fig. 4, this cannot provide the angular distribution of temperature and humidity ratio, but only a constant value corresponding to the average outlet conditions of the process air leaving the desiccant wheel. Comparing the values provided by the simplified model against the experimental data for Series 1 and Series 3, we have an overestimation of the output humidity ratio, with an error of 5 % and 21 %, respectively, while for Series 2, the model overestimates the dehumidification capacity of the wheel (difference in the outlet humidity ratio equal to 4 %). The temperature in the outlet process air is always underestimated by the simplified model with an error ranging between 31 % and 36 %.

The two models were compared under dynamic conditions with varying inlet air temperature and humidity. The other model inputs (regeneration temperature, rotation speed, air flow rate) were kept constant, as were the characteristics of the desiccant wheel. The humidity ratio profile obtained from the two models of the are shown in Fig. 5.

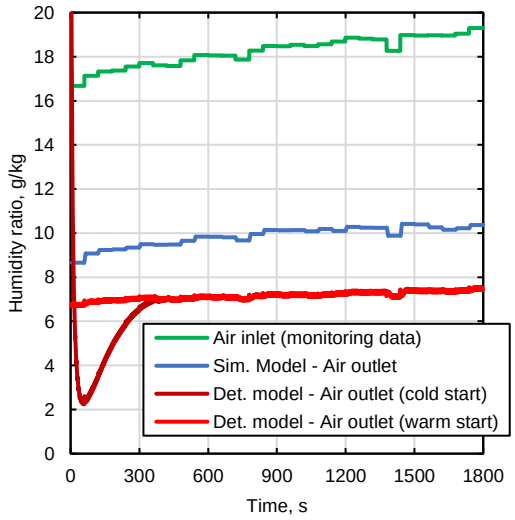

Fig. 5 – Inlet and outlet humidity ratio under dynamic conditions

Although involving a significant difference in terms of absolute values, simplified and detailed model (warm start) return similar trends for outlet air conditions. This is true when the initial wheel state in the detailed model is derived from an earlier operation state (warm start). On the other hand, if a cold start is considered (the initial state of the wheel is assumed to be in equilibrium with the environment), the detailed model reproduces typical transient trends and, once exhausted (after about 400 s), it leads to the reconciliation of the profiles with those obtained with the warm start.

5. Conclusion

A detailed and a simplified model of a desiccant wheel were implemented. The performance of the desiccant wheel simulated by the two models was compared against experimental data. Both models are able to provide the humidity of the air leaving the wheel with small errors. Within the limits of the conditions considered in this study, the simplified model presents larger errors in simulating the outlet temperature in comparison with the detailed model. Comparison under dynamic conditions shows that the simplified model cannot reproduce any transient regime of the desiccant wheel. This limitation may lead to errors in the prediction of output conditions, especially in the cold start case, as evidenced by the simulations conducted. However, once the steady state condition is reached, the simplified model returns results with trends similar to the detailed model with significant computational cost savings.

The main limitations of the simplified model considered in this study are related to the fact that it must be initialized with reference conditions that are bound to rotational speed of the wheel, regeneration conditions and air flow rate. This implies that the simplified model can return reliable results only when the simulated conditions are similar to the reference conditions under consideration.

Acknowledgement

This study was funded by the Free University of Bolzano-Bozen within the Ventilation and Indoor Air Quality in Offices: Monitoring and Improvement" project (CUP: I55F21002050005).

Nomenclature

Symbols

A_{ch}	Cross sectional area of the channel (m^2)
c_p	Isobaric specific heat ($J\ kg^{-1}\ K^{-1}$)
D_{eff}	Effective diffusivity ($m^2\ s^{-1}$)
D_s	Surface diffusivity ($m^2\ s^{-1}$)
f	Area ratio of flow passage in the channel
h_m	Mass convection coefficient ($kg\ m^{-2}\ s^{-1}$)
h_{th}	Heat convection coefficient ($W\ m^{-2}\ K^{-1}$)
i_{ad}	Isosteric heat of adsorption ($J\ kg^{-1}$)
P_{ch}	Perimeter of the flow passage (m)
t	Time (s)
T	Temperature (K)
u	Air velocity in the flow passage ($m\ s^{-1}$)
W	Water uptake in the desiccant ($kg_w\ kg_d^{-1}$)
x	Axial coordinate
ε	Porosity
η	Fraction of ads. heat convected to air
λ	Thermal conductivity ($W\ m^{-1}\ K^{-1}$)
ρ	Mass density ($kg\ m^{-3}$)
ω	Humidity ratio ($kg_v\ kg_{da}^{-1}$)

Subscripts/Superscripts

a	Air
d	Desiccant material
s	Supporting material
v	Water vapor

References

Angrisani, G., C. Roselli, and M. Sasso. 2012. "Experimental Validation of Constant Efficiency Models for the Subsystems of an Unconventional Desiccant-Based Air Handling Unit and Investigation of Its Performance." *Applied Thermal Engineering* 33–34: 100–108. doi: https://doi.org/10.1016/j.applthermaleng.2011.09.018

Daou, K., R. Wang, and Z. Xia. 2006. "Desiccant Cooling Air Conditioning: A Review." *Renewable and Sustainable Energy Reviews* 10(2): 55–77. doi: https://doi.org/10.1016/j.rser.2004.09.010

De Antonellis, S., M. Intini, and C. M. Joppolo. 2015. "Desiccant Wheels Effectiveness Parameters: Correlations Based on Experimental Data." *Energy and Buildings* 103: 296–306. doi: https://doi.org/10.1016/j.enbuild.2015.06.041

De Antonellis, S., C. M. Joppolo, and L. Molinaroli. 2010. "Simulation, Performance Analysis and Optimization of Desiccant Wheels." *Energy and Buildings* 42(9): 1386–93. doi: https://doi.org/10.1016/j.enbuild.2010.03.007

Du, Z., and X. Lin. 2020. "Research Progress of Rotary Desiccant Wheel Optimization Technology." *IOP Conference Series: Earth and Environmental Science* 512(1): 012181. doi: https://doi.org/10.1088/1755-1315/512/1/012181

Ge, T. S., Y. J. Dai, and R. Z. Wang. 2014. "Review on Solar Powered Rotary Desiccant Wheel Cooling System." *Renewable and Sustainable Energy Reviews* 39: 476–97. doi: https://doi.org/10.1016/j.rser.2014.07.121

Ge, T. S., Y. Li, R. Z. Wang, and Y. J. Dai. 2008. "A Review of the Mathematical Models for Predicting Rotary Desiccant Wheel." *Renewable and Sustainable Energy Reviews* 12(6): 1485–1528. doi: https://doi.org/10.1016/j.rser.2007.01.012

Howe, R. R. 1983. "Model and Performance Characteristics of a Commercially-Sized Hybrid Air Conditioning System Which Utilizes a Rotary Desiccant Dehumidifier." Madison: University of Wisconsin--Madison.

Jurinak, J. J. 1982. "Open Cycle Desiccant Cooling—Component Models and System Simulations." PhD Thesis, Madison ProQuest Dissertations Publishing.

Kakaç, S., R. K. Shah, R. K. Shah, and W. Aung. 1987. *Handbook of Single-Phase Convective Heat Transfer.* A Wiley-Interscience Publication. Wiley.

Kodama, A., M. Goto, T. Hirose, and T. Kuma. 1993. "Experimental Study of Optimal Operation for a Honeycomb Adsorber Operated with Thermal Swing." *Journal of Chemical Engineering of Japan* 26(5): 530–35. doi: https://doi.org/10.1252/jcej.26.530

Niu, J. L., and L. Z. Zhang. 2002. "Heat Transfer and Friction Coefficients in Corrugated Ducts Confined by Sinusoidal and Arc Curves." *International Journal of Heat and Mass Transfer* 45(3): 571–78. doi: https://doi.org/10.1016/S0017-9310(01)00177-6

Panaras, G., E. Mathioulakis, V. Belessiotis, and N. Kyriakis. 2010. "Experimental Validation of a Simplified Approach for a Desiccant Wheel Model." *Energy and Buildings* 42(10): 1719–25. doi:https://doi.org/10.1016/j.enbuild.2010.05.006

Pesaran, A. A., and A. F. Mills. 1987. "Moisture Transport in Silica Gel Packed Beds—Theoretical Study." *International Journal of Heat and Mass Transfer* 30(6): 1037–49. doi:https://doi.org/10.1016/0017-9310(87)90034-2

San, J.-Y. 1993. "Heat and Mass Transfer in a Two-Dimensional Cross-Flow Regenerator with a Solid Conduction Effect." *International Journal of Heat and Mass Transfer* 36(3): 633–43. doi: https://doi.org/10.1016/0017-9310(93)80039-W

Simonson, C., and R. Besant. 1997. "Heat and Moisture Transfer in Desiccant Coated Rotary Energy Exchangers: Part I. Numerical Model." *HVAC&R Research* 3(4): 325–50. doi: https://doi.org/10.1080/10789669.1997.10391381

Sultan, M., I.I. El-Sharkawy, T. Miyazaki, B. Baran Saha, and S. Koyama. 2015. "An Overview of Solid Desiccant Dehumidification and Air Conditioning Systems." *Renewable and Sustainable Energy Reviews* 46: 16–29. doi: https://doi.org/10.1016/j.rser.2015.02.038

BIM and Mixed Reality for Visualizing Building Energy Data

Dietmar Siegele – Fraunhofer Italia, Italy – dietmar.siegele@fraunhofer.it
Paola Penna – Fraunhofer Italia, Italy – paola.penna@fraunhofer.it
Ilaria Di Blasio – Fraunhofer Italia, Italy – ilaria.diblasio@fraunhofer.it
Michael Riedl – Fraunhofer Italia, Italy – michael.riedl@fraunhofer.it

Abstract

The visualization of building energy data is an open topic, intuitive approaches are rare and new concepts are required to handle big data collected by more and more sensors or even derived from energy simulation results. The interpretation of data, either derived from a monitoring system or from building simulation analysis, can be difficult to handle. Combining geometrical data and energy data into a visualization interface could be a promising way to help designers and facility managers to better understand the use of different spaces, enabling a higher efficiency of building management. In this paper, an application for visualizing monitoring data or simulation results by means of Mixed Reality and BIM is presented. For the purpose, a doll's house concept (third-person observer) has been adopted as a container for the visualization of energy data in a geometrical context. Time-series based interactive diagrams, derived from monitoring system or simulation results, are integrated into geometrical holograms of buildings or parts of buildings (like floors) and they allow intuitive working. Moreover, multi-user scenarios applying cloud anchors are supported. The geometrical models are retrieved by applying Building Information Modelling (BIM).

1. Introduction

One of the main challenges in modern Building Energy Management Systems (BEMS) is related to the visualization of measurement data (Ramelan et al., 2021). Internet of Things (IoT) initiatives produce a large amount of collected data that have become difficult to handle because of the difficulties related to the interpretation of the data and moreover to their visualization before interpretation can take place. In addition, the visualization of simulation results can be difficult to interpret if not connected directly to a geometrical context. Thus, in the area of BEMS, combining geometrical data and measurement or simulation data into one interface is a main research topic. Integrating real time collection of occupancy data, such as location and behavior, into a BIM model could help facility management (FM) to better understand the use of different spaces, enabling a higher efficiency of building management. Mixed Reality (MR) can be even more useful because it allows virtual information to be displayed in real world, making data interpretation easier. In recent literature, several works deal with new approaches for visualizing monitoring or simulation data in a more intuitive ways, mainly using BIM as a container for information (Gerrish et al., 2017; Marzouk et al., 2014; Truong et al., 2017) as well as using augmented reality (AR) and scanning a QR-code for displaying on-site sensor data (Mylonas et al., 2019). This paper proposes a new approach for visualizing energy or indoor comfort data in a geometrical context, imported from BIM, by combining a doll's house concept (third-person observer) with a real-world concept that was initially proposed in (Siegele et al., 2021). This concept does not only allow a very intuitive exploration of data, but it paves the way for a multi-user interface approach, where several users, at the same place or distributed, can explore data together on-site or off-site. Moreover, in the case of a monitoring infrastructure, by using QR-code scanning, it is possible to check the data of specific sensors on-site directly.

Mixed Reality (MR) has already been applied in different areas of building construction. Most of the time the classical approach for visualization is used: information is overlaid on real world geometry, like by (Riexinger et al., 2018) or

(Schweigkofler et al., 2018). The benefits of using MR and Augmented Reality (AR) have been proved to be efficient for supporting the most critical working phase on the building site. Indeed, this has been tested by several Horizon projects, such as BIM4EEB (BIM4EEB, 2022) and BIMplement (BIMplement Project H2020, 2022). Another interesting application of AR is for supporting the design phase, by visualizing the simulation results in a more intuitive way. (Fukuda et al., 2019) developed a new AR-based methodology for intuitively visualizing indoor thermal environment benefits leads by different renovation design alternatives, based on computational fluid dynamics simulation results. (Carneiro et al., 2019) presented an approach for guiding occupant behavior by visualizing the effects of their preferences on light distribution and energy consumption in an office space by means of virtual reality (VR).

The use of MR and AR for visualizing time-series based data in order to overcome the difficulties of handling a large amount of data derived from the IoT infrastructure has been slightly investigated. Such a concept was presented by (Jang et al., 2019), who used a time-series graph like on a screen. However, this does not allow interaction with the data. Moreover, in a multi-user scenario this approach is non-intuitive. Another concept was proposed by (Aftab et al., 2017). They overlaid shading areas or lines on the geometry (floors, walls) to visualize real-time information about the building. Today's IoT-approaches focus on single-point measurement. Another interesting approach is presented by (Dave et al., 2018). The authors developed a platform that integrates the built environment data with IoT sensors and BIM, which provides information about energy usage, occupancy and user comfort. In this context, multi-point measurement (like thermal imaging) is rarely used and only these kinds of measurements benefit from such an approach. This is likely also the reason why (Aftab et al., 2017) only presented a concept without results of a real use case. It is also very difficult from a technical point of view to reach the necessary accuracy of indoor positioning to achieve this with AR devices (Minneci et al., 2019; Siegele et al., 2020). Other approaches, related to the different possibilities of visualizing energy efficiency concepts by means of Virtual Reality (VR), were proposed by (Häfner et al., 2014). They used interactive charts to visualize time-series-based data. However, it was only presented in VR and the representation of the building structure was rudimentary. Applications for MR-devices (like HoloLens), are rare.

An application for studying the improvement of HVAC systems in learning factories was proposed by (Czarski et al., 2020). However, no time-series data was visualized in that context. A third-person perspective on-site was presented by (Liu et al., 2020) for visualizing data of a thermal imaging camera that measures the temperature of a façade (and thus the energy efficiency). However, this concept was not based on MR, but on AR by using a tablet.

To visualize measurement data with BIM models, several approaches are available. In the literature they are mainly defined as Digital Twins, even if usually not the complete features of a Digital Twin are proposed. The process for integrating indoor comfort data collected by a monitoring system through the application of a BIM-based model was described by (Penna et al., 2019).

The present work tries to overcome the limitations of time-series data visualization by proposing a digital multi-user interface realized by means of MR for localizing measurement data in a geometrical context, realized through BIM. Moreover, this approach also allows the visualization of the results coming from energy simulation software (i.e., IDA ICE, TRNSYS; EnergyPlus etc.). The approach shows a concept of exploring and analyzing monitoring and simulation data in an intuitive way and, at the same time, of giving the possibility to several users to visualize the data off-site and on-site.

This research is structured as follows: first, we present the adopted method by describing the software used, the proposed software architecture and the implemented features. Second, in the Results section, we describe how the application is working and what can be done with it. Consequently, in the Discussion section, we discuss the impact of our proposed software architecture. Moreover, we discuss how the software architecture can be extended and we propose how industrial standards (IFC, OpenXR) must move to provide such inter-

faces in a more general way applicable to a broader audience.

2. Materials And Methods

The application, which we developed for visualizing sensors and simulation data into a geometrical context, is based on the implementation of a proxy, which represents a data hub. An open API using REST is implemented, with which the gap between data and Mixed Reality is closed. The software architecture of our application is shown in Fig. 1.

As shown in Fig. 1, either the data derived from sensors or from energy simulation analysis are stored and saved in a time-series database. Regarding the monitoring infrastructure, we use LoRaWAN technology, because it allows the use of battery-driven sensors and it has a high coverage. In the same way, building energy simulation data can be evaluated by means of any simulation platform (i.e., Energyplus, TRNSYS, IDA ICE etc.) and results are stored in a time-series database. We used the time-series database *InfluxDB* (InfluxDB, 2022). In general, all kind of time-series databases, if they provide an API, can be used after implementing it into the proxy. We use the REST interface provided by *InfluxDB* to query the data from the database.

We use Unity (Unity Real-Time Development Platform, 2022) to develop the Mixed Reality (MR) application that is based on the Microsoft Mixed Reality Toolkit (MRTK 2.7) (MRTK-Unity Developer Documentation, 2022) and is designed by means of the OpenXR architecture (OpenXR Overview, 2022). Thus, it can also be used on other XR-compatible devices.

We get the models for different environments from BIM models by using the FBX file format, which is a proprietary file format owned by Autodesk. FBX is not a standard format when using BIM. We did not use the industrial file standard IFC, which is usually used for data exchange when working with BIM, because it has some significant disadvantages when used in a non-BIM environment like Unity. A main issue is that textures are not stored in the file, but also information on how e.g., two walls are connected, is not explicitly stored in the file. This makes it very difficult to use the IFC file format to exchange visual information. Moreover, also the FBX format allows us to store metadata with the model.

This aspect has high relevance for visualizing monitoring data, as in the BIM model, where the unique identifiers (ID) of the sensors are stored as metadata. With this ID, a link between the model and the database is created. In this way, it is easy to assign sensor data in Unity to the corresponding geometry. The ID consists of abbreviations that include the city, the street, the street number, the building part/lot, the floor, the room, and an incremental sensor number.

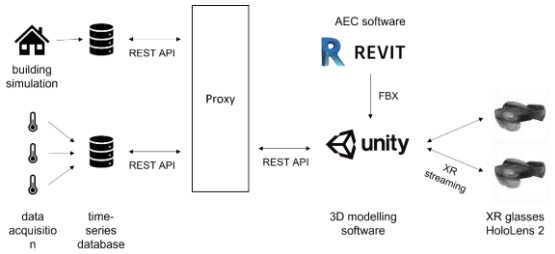

Fig. 1 – Software architecture

To catch specific data from a sensor in an on-site environment, QR-codes are used. *OpenCV for Unity* asset (OpenCv for Unity, 2022) is used to realize this feature. The QR-codes are generated from the ID introduced above.

For visualizing the time-series data in Unity we use Asset *Graph and Chart* (Graph and Chart, 2022). It enables us to visualize real-time data by adding data streams in a programmatic way.

The application itself can run stand-online on a XR-device, like the Microsoft HoloLens 2. However, for better graphics (shading) and better performance, we apply XR streaming. Multiple devices can be operated at the same time, while using the concept of persisting virtual content in the real-world. We share the actual position and orientation of the doll's house model by applying *Azure Spatial Anchors*. The position is stored in a *CosmosDB* database. On the XR device, a localization process is carried out, where the MRTK supports a coarse localization by using Wi-Fi and BLE signatures. The localization itself is realized by matching landmarks.

In the XR application several features are implemented:
Doll's house view of BIM-imported model with display of real-time data and time-series-based interactive diagram, derived from monitoring system or simulation results, as part of the hologram. In the model, values like temperature, humidity or CO_2 concentration are shown as numbers. Occupancy can be displayed with avatars.
Scanning of QR-codes in an on-site environment for reading data of a specific sensor (real-time and time-series-based diagram) and localization of the sensor in the doll's house-view of the model.
Multi-user sessions for the doll's house view for interactive sessions with several persons.

3. Results

The application is run on a Microsoft HoloLens 2 and the result of the developed XR application is shown in Fig. 2. This is the doll's house mode, where a flat within a building is visible. In each room, indoor air quality (IAQ) sensors are installed, whose real-time values can be visualized as tooltips based on the MRTK. The tooltips change their orientation and size according to the position of the viewer and allow an intuitive and clear view of the data. Occupancy can be visualized with avatars in the corresponding rooms. Not only IAQ data can be visualized, but any kind of data measured in the selected rooms or simulated by means of energy simulation software. At the moment, our concept concentrates all data measured from different sensors in one room to a single tooltip. A set of buttons allows control of the model, and the doll's houses are freely scalable and rotatable through the vertical axis. In the future, also a concept of zones will be added to visualize bigger models without dedicated rooms, i.e., shopping centers.

Fig. 2 – View of doll's house with real-time values

In Fig. 3 we show a screenshot of the XR application with a time-series-based diagram. It can be interactively controlled by using finger gestures. Sliding backwards and forwards in time is enabled by this feature. In the future, these diagrams will be enhanced by adding i.e., shading colors to visualize comfort or safety areas. E.g., the CO_2 output can be assisted by using traffic light colors to quickly identify critical rooms or zones and time ranges. co

Fig. 3 – View of doll's house with time-series-based diagrams

The user can also change the building, as shown in Fig. 4, where we visualize the floor of an office building.

Fig. 4 – View of doll's house of a different building

When on-site, the feature of Fig. 5 can be used by a facility manager. Scanning a QR-code assigned with the ID of the sensors allows an additional hologram with the time-series based interactive diagram to appear. In addition, in the geometrical model the position of the sensor is highlighted as a tooltip, which is not visible in the figure presented. On-site orientation for the user is significantly improved by this feature. To allow free movement on-site, the hologram shown in Fig. 3 can also be detached and follows the user automatically. Moreover, an arrow always shows the position of the doll's house, if it is not in the field of view of the user.

Fig. 5 – Time-series-based diagram assigned to a sensor

4. Discussion

Displaying time-based data in MR devices provides a very intuitive option of showing data in an interactive way. In the multi-user mode people can use the application, e.g., in a workshop to discuss aspects on data collected.

By this paper we want to present the principal concept of displaying time-series-based data in MR devices. There is a need to implement several additional features before it can be tested in a real-world scenario, like in the facility management. The diagram to display data must be improved. For now, it is not possible to choose different timestep sizes or to scale the diagram on the time axis. Here, we need also to develop new ways to apply e.g., hand gestures or speech recognition for activating these advanced features. For now, it is also not possible to load a BIM model dynamically into the application. This must be done manually in Unity. It is also necessary to manually export the BIM model into the FBX file format. This aspect can be particularly problematic: developing complex interfaces, which would be necessary for these tasks, is very difficult in MR. There is, so far, no common guideline available, as to how such a task – which, using a PC and a mouse, may take a matter of minutes – can be carried out on an MR device.

Additional features for a real application should include comments and drawings. In the future, a real-time coupling with the BIM model should also be achieved. However, implementing these features requires XR streaming and a server-based software architecture.

5. Conclusion

In this paper, we presented a concept of an XR application for visualizing data in building energy management systems. Using time-series-based interactive diagrams integrated into a geometrical hologram of a zone can help to improve the usability of such applications. Using time-series-based databases allows fast querying of data, and thus provides a seamless integration into the overall experience.

In the further development, we want to get rid of the QR-codes on the sensors by implementing a BIM-based navigation algorithm for pre-positioning in combination with cloud anchors (based on landscapes) for an accurate positioning

within a room (the same approach we use for robotic applications (Follini et al., 2020). This will allow even better immersion and usability. In addition to the time-series based diagrams, we will add additional diagram types. We want to add additional features for visualization, like better visibility of sensors with sprites and surface shading for multi-point data or simulation data. In the long term, we want to achieve a close-to-real-time import of the BIM model, where we target a server-based solution as an application on its own (automatic conversion from Revit-files or IFC to FBX or similar).

Acknowledgement

The research leading to these results has received funding from the European Regional Development Fund (Fondo Europeo di Sviluppo Regionale FESR Alto Adige 2014-2020) under the Grant Agreement n. FESR1141 CUP B54E20002030001.

References

Aftab, M., S. Chi-Kin Chau, and M. Khonji. 2017. "Enabling Self-Aware Smart Buildings by Augmented Reality." In *Proceedings of ACM International Conference on Future Energy Systems (e-Energy) 2018*.

BIM4EEB. "BIM4EEB: BIM Based Toolkit for Efficient rEnovation in Buildings." Accessed January 2022. https://www.bim4eeb-project.eu/

BIMplement Project H2020. "Towards a Learning Building Sector by Setting up a Large-Scale and Flexible Qualification Methodology Integrating Technical, Cross-Craft and BIM Related Skills and Competence." Accessed January 2022. https://www.bimplement-project.eu/

Carneiro, J.P., A. Aryal, and B. Bacerik-Gerber. 2019. "Influencing Occupant's Choices by Using Spatiotemporal Information Visualization in Immersive Virtual Environments." *Building and Environment* 150: 330-338. doi: https://doi.org/10.1016/j.buildenv.2019.01.024

Czarski, M., Y. T. Ng, M. Vogt, M. Juraschek, B. Thiede, P.S. Tan, S. Thiede, and C. Herrmann. 2020. "A Mixed Reality Application for Studying the Improvement of HVAC Systems in Learning Factories." *Building and Environment* 150: 330-338. doi: https://doi.org/10.1016/j.promfg.2020.04.039

Dave, B., A. Buda, A. Nurminen, and K. Främling. 2018. "A Framework for Integrating BIM and IoT through Open Standards." *Automation in Construction* 95: 35-45. doi: https://doi.org/10.1016/j.autcon.2018.07.022

Follini, C., V. Magnago, K. Freitag, M. Terzer, C. Marcher, M. Riedl, A. Giusti, and D. T. Matt. 2020. "BIM-Integrated Collaborative Robotics for Application in Building Construction and Maintenance." *Robotics* 10: 2. doi: https://doi.org/10.3390/robotics10010002

Fukuda, T., K. Yokoi, N. Yabuki, and A. Motamedi. 2019. "An Indoor Thermal Environment Design System for Renovation Using Augmented Reality." *Journal of Computational Design and Engineering* 6: 179-188. doi: https://doi.org/10.1016/j.jcde.2018.05.007

Gerrish, T., K. Ruikar, M. Cook, M. Johnson, M. Phillip and C. Lowry. 2017. "BIM Application to Building Energy Performance Visualisation and Management: Challenges and Potential." *Energy and Buildings* 144: 218-228. doi: https://doi.org/10.1016/j.enbuild.2017.03.032

Graph And Chart. Unity Asset Store. Accessed January 2022. https://assetstore.unity.com/packages/tools/gui/graph-and-chart-78488

Häfner, P., J. Seeßle, J. Dücker, M. Zienthek, and F. Szeliga. 2014. "Interactive Visualization of Energy Efficiency Concepts Using Virtual Reality." In *Proceedings of Conference and Exhibition of the European Association of Virtual and Augmented Reality 2014*. doi: http://dx.doi.org/10.2312/eurovr.20141346

InfluxDB. "InfluxDB: Open-Source Time Series Database ". InfluxData. Accessed January 2022. https://www.influxdata.com/

Jang, H., M. Choi, S. Lee, J. Lee, and S. Park. 2019. "Building Energy Management System Based on Mixed Reality for Intuitive Interface." In *Proceedings of the 2019 2nd International Conference on Electronics Technology ICET 2019*, 483-486.

Liu, F., T. Jonsson, and S. Seipel. 2020. "Evaluation of Augmented Reality-Based Building Diagnostics Using Third Person Perspective." *ISPRS International Journal of Geo-Information* 9: 53. doi: https://doi.org/10.3390/ijgi9010053

Marzouk, M., and A. Abdelaty. 2014. "Monitoring Thermal Comfort in Subways Using Building Information Modeling." *Energy and Buildings* 84: 252–257. doi: https://doi.org/10.1016/j.enbuild.2014.08.006

Minneci, G., A. Schweigkofler, C. Marcher, G. Pasetti Monizza, T. Tillo, and D. Matt. 2019. "Computer Vision Approach for Indoor Location Recognition Within an Augmented Reality Mobile Application." In *Proceedings of the Lecture Notes in Computer Science (including subseries Lecture Notes in Artificial Intelligence and Lecture Notes in Bioinformatics)* 11792: 45-53.

MRTK-Unity Developer Documentation. Mixed Reality Toolkit. Accessed January 2022. https://docs.microsoft.com/en-us/windows/mixed-reality/mrtk-unity/?view=mrtkunity-2021-05

Mylonas, G., C. Triantafyllis, and D. Amaxilatis. 2019. "An Augmented Reality Prototype for Supporting IoT-Based Educational Activities for Energy-Efficient School Buildings." *Electronic Notes Theoretical Computer Science* 343: 89–101. doi: https://doi.org/10.1016/j.entcs.2019.04.012

OpenXR Overview. The Khronos Group. Accessed January 2022. https://www.khronos.org/openxr/

OpenCV for Unity. Unity Asset Store. Accessed January 2022. https://assetstore.unity.com/packages/tools/integration/opencv-for-unity-21088

Penna, P., G. L. Regis, A. Schweigkofler, C. Marcher, and D. Matt. 2019. "From Sensors to BIM: Monitoring Comfort Conditions of Social Housing with the KlimaKit Model." In *Proceedings of the Lecture Notes in Computer Science (including subseries Lecture Notes in Artificial Intelligence and Lecture Notes in Bioinformatics)*, 11792: 108-115.

Ramelan, A., F. Adriyanto, C. Hermanu, M. H. Ibrahim, J. S. Saputro, and O. Setiawan. 2021. "IoT Based Building Energy Monitoring and Controlling System Using LoRa Modulation and MQTT Protocol". *IOP Conference Series: Materials Science and Engineering* 1096: 012069. doi: https://doi.org/10.1088/1757-899x/1096/1/012069

Riexinger, G., A. Kluth, M. Olbrich, J.-D. Braun, and T. Bauernhansl. 2018. "Mixed Reality for On-Site Self-Instruction and Self-Inspection with Building Information Models." In *Proceedings of the Procedia CIRP*, 72: 1124-1129.

Schweigkofler, A., G. Pasetti Monizza, E. Domi, A. Popescu, J. Ratajczak, C. Marcher, M. Riedl, and D. Matt. 2018. "Development of a Digital Platform Based on the Integration of Augmented Reality and BIM for the Management of Information in Construction Processes." In *IFIP Advances in Information and Communication Technology*, 540: 46-55.

Siegele, D., U. Di Staso, M. Piovano, C. Marcher, and D. T. Matt. 2020. "State of the Art of Non-Vision-Based Localization Technologies for AR in Facility Management." *Lecture Notes in Computer Science* 12242: 255–272. doi: https://doi.org/10.1007/978-3-030-58465-8_20

Siegele, D., P. Penna, and M. Riedl. 2021. "Visualizing Building Energy Measurement Data in Mixed Reality Applying B.I.M." *Lecture Notes in Computer Science* 12980: 255–272. doi: https://doi.org/10.1007/978-3-030-87595-4_18

Truong, H., A. Francisco, A. Khosrowpour, J. E. Taylor, and N. Mohammadi. 2017. "Method for Visualizing Energy Use in Building Information Models." *Energy Procedia* 142: 2541–2546. doi: https://doi.org/10.1016/j.egypro.2017.12.089

Impact of Solar Radiation Modelling on the Simulated Building Energy Performance in the Climate of Bolzano, Italy

Giovanni Pernigotto – Free University of Bozen-Bolzano, Italy – giovanni.pernigotto@unibz.it
Alessandro Prada – University of Trento, Italy – alessandro.prada@unibz.it
Aleksandr Gevorgian – Free University of Bozen-Bolzano, Italy – aleksandr.gevorgian@natec.unibz.it
Andrea Gasparella – Free University of Bozen-Bolzano, Italy – andrea.gasparella@unibz.it

Abstract

We can mainly identify two groups of models in the literature to calculate solar irradiance incident on building envelope surfaces: *horizontal diffuse irradiance models*, to distinguish beam and diffuse horizontal components and *irradiance models for tilted surfaces*, to determine the irradiance incident on inclined surfaces. Due to the fact that solar irradiance data are different depending on location, climatic condition and topographic factors, there is no uniform solar irradiance model that can provide the same level of accuracy worldwide. Furthermore, this is even more critical in mountain areas, characterized by terrain complexity and the presence of specific local climatic conditions affecting solar radiation distribution.

In this research, the performance of 22 horizontal diffuse irradiance models and 12 irradiance models for tilted surfaces was assessed to check their suitability for application in mountain regions. The analysis was carried out in the Italian Alps, specifically, in the city of Bolzano, using as a reference the global solar irradiance data collected for both horizontal and vertical surfaces. Moreover, the energy needs for space heating and cooling of 48 simplified building configurations were simulated to quantify the impact of solar irradiance models on the simulated building energy performance.

1. Introduction

Nowadays, architects and engineers increasingly rely on building energy simulation tools to design more and more energy-efficient buildings. In this context, precise modeling of solar irradiance on building components is crucial, especially when simulating the thermal behavior of buildings. Various mathematical and empirical models have been developed and proposed in the literature in the last few decades, for both the subdivision of global horizontal solar irradiance into beam and diffuse components (horizontal diffuse irradiance models) and for estimating solar irradiance on tilted surfaces (irradiance models for tilted surfaces). Examples include isotropic models, as cited by (Duffie & Beckman, 1991), and anisotropic models (Gueymard, 1987; Klucher, 1979; Muneer & Kinghorn, 1997; Perez et al., 1990; Robledo & Soler, 1998). Comparisons and modifications to these models and their application to specific regions have also been undertaken (Behr, 1997; Remund et al., 2003).

Despite the availability of many models, these were primarily derived from flat regions, and their results are to some extent location-dependent. Indeed, accuracy issues might be found when these irradiance models are used in a mountain region, where orographic complexity may cause a wide variety of inclines, introduce shades and reflections influencing meteorological parameters and contributing to the formation of local climate conditions. In this case, the success in providing adequate solar irradiance information would depend on the model's accuracy and reliability of input parameters. As a consequence, these models should be validated in each location by comparing experimental data with the predicted ones (Loutzenhiser et al., 2007). Validation is indeed essential for quantifying output uncertainty, whose propagation in building performance simulation models can also depend on the building's characteristics (Prada et al., 2015).

In this research, the accuracy of solar irradiance models on simulated building energy performance was investigated for a mountain climate, i.e., Bolzano, Italy. Specifically, 22 horizontal diffuse irradi-

ance models were coupled with 12 irradiance models for tilted surfaces, obtaining 264 combinations. The different profiles of calculated solar irradiance incident on the building envelope surfaces were used as input in TRNSYS 18 for the simulation of the energy performances of a dataset of 48 simplified residential buildings. This set was defined by changing insulation level and thermal inertia of opaque components, window surface and orientation, and kind of glazing system, focusing on their solar heat gain coefficient (*SHGC*). Finally, minimum and maximum monthly and annual deviations in heating and cooling needs for the simulated dataset of 48 buildings were discussed, employing statistical analysis to correlate the differences in energy performance prediction to the building envelope features.

2. Case Study

2.1 Location and Weather Station

Bolzano is a municipality in the Italian Alpine region (46.500° N, 11.350° E), located specifically in a basin where the Sarntal Valley, the Eisacktal Valley, and the Adige Valley meet. Almost 110,000 people live in this city on an area of about 30 km^2. Although the city centre is located at an altitude of 268 m, the municipality spreads from 232 m to more than 1600 m above sea level.

The weather station considered in this study is installed on the flat roof of the A2 Building at NOI TechPark in Bolzano (46.479° N, 11.331° E, about 25 m high), in the southern and industrial neighborhood of the city (Fig. 1).

As shown in Fig. 2, the weather station is equipped with 5 Delta-T SPN1 Sunshine Pyranometers able to measure both global and diffuse irradiance - one installed horizontally and four installed vertically towards the main cardinal directions. Furthermore, the weather station includes 5 LiCor Photometric Sensors (1 horizontal + 4 vertical, as for the SPN1 Sunshine Pyranometers) and an EKO ASI 16 sky camera (not used in this work). The 5 SPN1 Sunshine Pyranometers collect solar data with a 1-minute time discretization and the period considered in this analysis ranges from April 2021 to March 2022.

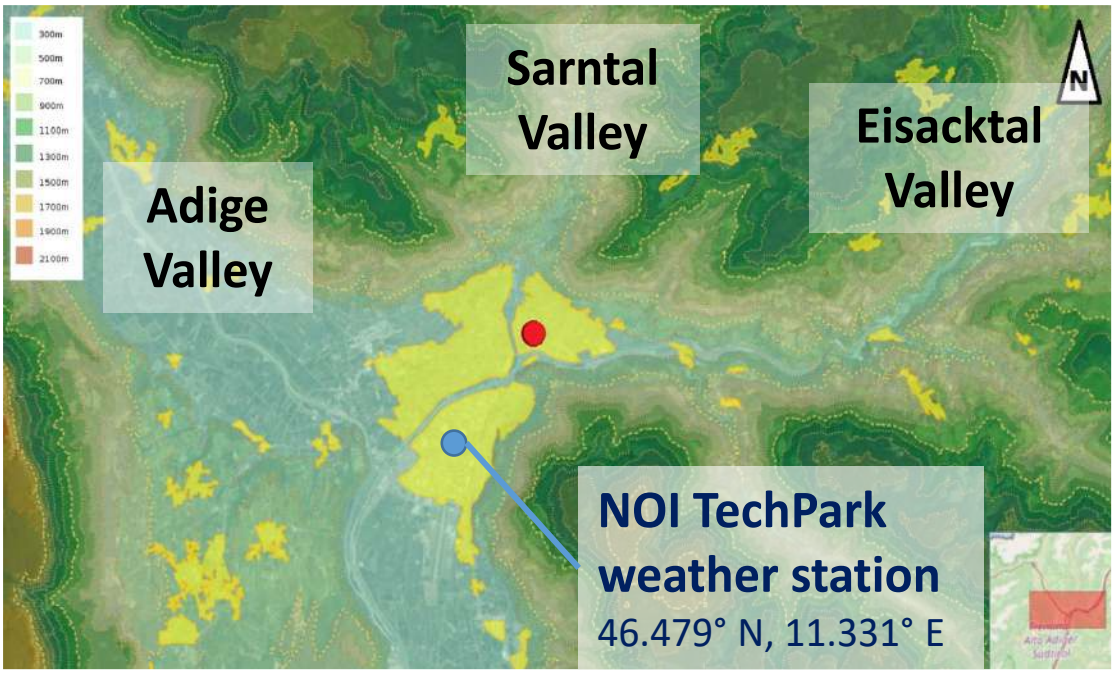

Fig. 1 – Basin of Bolzano: the different colors (light green to brown) indicate the altitude, while the yellow indicates the urban areas (map developed starting from Geobrowser Maps by the Autonomous Province of Bolzano). The red dot in the picture on the left indicates the University campus, while the blue dot highlights the position of the weather station at NOI TechPark considered in this research.

Table 1 – Solar irradiance models

ID	Horizontal diffuse irradiance models	ID	Irradiance models for tilted surfaces
1	Erbs et al. (1982)	A	Liu & Jordan (1960)
2	Orgill & Hollands (1977)	B	Burgler (1977)
3	Reindl et al. (1990a) – Model 1	C	Temps & Coulson (1977)
4	Reindl et al. (1990a) – Model 2	D	Klucher (1978)
5	Reindl et al. (1990a) – Model 3	E	Hay & Davies (1980)
6	Lam & Li (1996)	F	Ma & Iqbal (1983)
7	Boland et al. (2008)	G	Skartveit & Olseth (1986)
8	Hawlader (1984)	H	Gueymard (1986)
9	De Miguel et al. (2001)	I	Reindl et al. (1990b)
10	Karatasou et al. (2003)	J	Perez et al. (1990)
11	Chandrasekaran & Kumar (1994)	K	Muneer (2006) – Model 1
12	Oliveira et al. (2002)	L	Muneer (2006) – Model 2
13	Soares et al. (2004)		
14	Muneer et al. (1984)		
15	Spencer (1982)		
16	Chendo & Maduekwe (1994) – Model 1		
17	Chendo & Maduekwe (1994) – Model 2		
18	Skartveit & Olseth (1987)		
19	Maxwell (1987)		
20	Perez et al. (1992) – Model 1		
21	Perez et al. (1992) – Model 2		
22	Perez et al. (1992) – Model 3		

Fig. 2 – Weather station installed at NOI TechPark in Bolzano

3. Simulation

3.1 Solar Irradiance Models

As a follow-up to previous research on this topic (Pernigotto et al., 2015, 2016 and 2022; Prada et al., 2014a and 2014b), we focused on the same set of 22 horizontal diffuse irradiance models and 12 irradiance models for tilted surfaces previously analyzed (Table 1). The two groups of irradiance models were combined, for a total of 264 alternatives.

3.2 Dataset of 48 Building Configurations

48 simplified buildings were used for the assessment of the impact of the solar irradiance models on the simulated energy needs for space heating and space cooling. All 48 configurations are characterized by the same geometry and have a single thermal zone, with a square floor area of 100 m^2, an internal height of 3 m, and the façades oriented towards the main cardinal directions. In each building, all windows are positioned on the same façade. Both sides of the vertical walls and the internal side of the roof have a solar absorptance of 0.3, while the external side of the roof and the internal side of the floor have 0.6.

All opaque components are made of a two-layer structure with insulating polystyrene on the external side and an internal massive layer, whose thermal resistance is about 0.8 m^2 K W^{-1}. The polystyrene has a thermal conductivity of 0.04 W m^{-1} K^{-1}, a density of 40 kg m^{-3}, and a specific heat capacity of 1470 J kg^{-1} K^{-1}. The massive layer can be either timber (thickness: 0.10 m; thermal conductivity: 0.13 W m^{-1} K^{-1}; density: 399 kg m^{-3}; specific heat capacity: 1880 J kg^{-1} K^{-1}) or concrete (thickness: 0.30 m; thermal conductivity: 0.37 W m^{-1} K^{-1}; density: 1190 kg m^{-3}; specific heat capacity: 840 J kg^{-1} K^{-1}). The window systems are composed of double-pane glazing with a U-value of 1.1 W m^{-2} K^{-1} and a timber frame (20 % of the window area) with a U-value of 1.2 W m^{-2} K^{-1}.

Internal gains and ventilation rate are kept constant, with values representative of residential buildings (UNI, 2014) and equal, respectively, to 4 W m^{-2}, half radiative and half convective, and to 0.3 air changes per hour (ACH). An ideal system maintains the internal air temperature between 20 °C and 26 °C, i.e., the heating and the cooling setpoints. Conventional limits of heating and cooling seasons for the climate of Bolzano were neglected, assuming ideal space heating and cooling available all year.

A summary of the variables considered in the set of 48 buildings is reported in Table 2. Further details about this dataset of buildings can be found in (Pernigotto et al., 2021).

Table 2 – Variables describing the buildings in the dataset

Insulation thickness and U-value	Materials and thermal inertia c	Window size and WWR ratio	Window SHGC	Window orientation
5 cm	Timber	14.5 m^2	0.35	East
(U = 0.45 W m^{-2} K^{-1})	(c = 75 kJ m^{-2} K^{-1})	(WWR = 48.5 %)		
15 cm	Concrete	29.1 m^2	0.61	South
(U = 0.21 W m^{-2} K^{-1})	(c = 300 kJ m^{-2} K^{-1})	(WWR = 97.1 %)		
				West

3.3 Methodology

As a first step, focus was placed on the data collected by the SNP1 Sunshine Pyranometers of NOI TechPark weather station, performing a quality check to identify missing entries and outliers (e.g., values exceeding the solar constant and positive values before dawn and after dusk). Post-processed solar data, still with 1-minute time discretization, were further manipulated to obtain hourly profiles of solar irradiation, expressed in watt-hours per square meter in agreement with the typical convention adopted in weather data for building performance simulation (e.g., the EnergyPlus *.epw* weather files). Minor missing entries (i.e., one or few hours of missing solar irradiation data) were fixed by either linear or cyclic interpolation, depending on the length of the missing data series. Missing data entries longer than a day, on the other hand, were not fixed and simply discarded from the analysis.

In the second step, the capabilities of the 264 pairs of solar irradiance models were assessed using the measured solar data as a reference. Specifically, for each one of the 264 combinations of horizontal diffuse irradiance models and irradiance models for tilted surfaces, the hourly profiles of global solar horizontal irradiation of the selected period (April 2021 - March 2022) were used as inputs to determine the global and the diffuse solar irradiation on four vertical surfaces oriented towards the main cardinal directions. These estimated hourly profiles of global and diffuse solar irradiation were then compared to the measured ones, calculating for each orientation the Mean Absolute Error (*MAE*) in order to identify the best and the worst-performing pairs of models.

As regards the last step, the energy performances of the 48 reference building configurations were simulated in TRNSYS 18, using the best and the worst-performing pairs of solar irradiance models as inputs.

4. Result Analysis and Discussion

4.1 Step 1 – Quality Check on the Dataset of Solar Irradiation Measurements

Thanks to the quality check performed, it was found that, for the analyzed period (April 2021 – March 2022), the missing and wrong 1-minute entries had only minor impacts on the annual series, without continuous gaps longer than 1 hour. This ensured a robust basis for the comparisons performed in the next steps.

4.2 Step 2 – Comparison Between Simulated and Measured Solar Irradiation Values

4.2.1 Accuracy in the prediction of vertical diffuse solar irradiance

Table 3 shows the best and the worst-performing pairs of irradiance models, determined for each orientation according to the Mean Absolute Error (*MAE*) for the diffuse vertical irradiance values. It can be noticed that each orientation has a given pair of models optimizing the prediction of the diffuse vertical irradiance. Specifically, the pairs A10 (Liu & Jordan + Karatasou models) for the south orientation, A15 (Liu & Jordan + Spencer models) for the east one, H6 (Gueymard + Lam & Li models) for the north one, and B8 (Burgler + Hawlader models). The largest *MAE*s are found for east and west orientations, as expected, considering the geography of the location (Fig. 1). As regards the worst-performing pairs of models, for south and east orientations, the largest errors are found with the pair F20 (Ma & Iqbal + Perez Model 1) while D20 (Klucher + Perez Model 1) is the worst-performing pair for north and west orientations. *MAE* values are lower than about 15 Wh m^{-2} in case of the best-performing pairs and even larger than 70 Wh m^{-2} for the worst-performing ones.

Analyzing the horizontal diffuse irradiance models, which are most frequently found among the best-performing ones, we can list the Soares model for the south orientation, the Perez Model 1 for the east and the west orientations, and the Muneer model for the north. Some of these models, optimal for a given orientation, are the worst-performing ones for another. For instance, the Perez model 1 is the worst-performing for south and north orientations, the Soares model is the worst-performing model for the east one, and the Spencer model gives the worst estimates of vertical diffuse irradiance for the west orientation.

4.2.2 Accuracy in the prediction of vertical global solar irradiance

Table 4 shows the same analysis as in Section 4.2.1 considering *MAEs* calculated for the global solar irradiation on the vertical surfaces. As regards the best-performing models, G16 (Skartveit & Olseth + Chendo & Manduekwe Model 1), B20 (Burgler + Perez Model 1), H14 (Gueymard + Muneer) and B20 (Burgler + Perez Model 1) were identified, respectively, for south, east, north and west orientations. The pairs of worst-performing solar irradiance models were, instead, C20 (Temps & Coulson + Perez Model 1) for the south-oriented surface, F13 (Ma & Iqbal + Soares) for the east-oriented one, D20 (Klucher + Perez Model 1) for the north one, and F15 (Ma & Iqbal + Spencer) for the west one. As can be noted, when global solar irradiance is considered, the best- and worst-performing models are different to those found for the diffuse solar irradiance. Looking at the *MAEs*, larger values are generally observed compared to the previous analysis on the diffuse solar irradiance. Focusing on the best-performing models in global irradiance analysis, it can be seen that slightly larger *MAEs* are found for south and north-oriented vertical surfaces (i.e., respectively 24.8 versus 12.7 Wh m^{-2} and 9.8 versus 7.9 Wh m^{-2}). On the contrary, very large errors are observed for east and west orientations, with *MAEs* larger than 120 and 150 Wh m^{-2}. The same trends can be identified analyzing the results of the worst-performing models, with *MAEs* similar to those observed in the diffuse irradiance analysis for south and north orientations (i.e., 61.9 versus 75 Wh m^{-2} and 57.5 versus 61.6 Wh m^{-2}) and much larger for the east and west ones (i.e., 184.1 versus 71.8 Wh m^{-2} and 207.9 versus 58.6 Wh m^{-2}). On the whole, it can be concluded that a good level of accuracy can be obtained in the estimation of the incident global irradiance for south and north-oriented vertical walls,

while larger errors are more frequently found for east and west orientations due to the presence of close natural obstacles.

As regards irradiance models for tilted surfaces, the Liu & Jordan model (south orientation), the Burgler Model (east and west orientations), and the Perez model (north orientation) can be seen as the most frequently found among the best-performing ones. Regardless of orientation, the worst-performing model most frequently encountered is the Ma & Iqbal model.

4.2.3 Comparison with another weather station

Table 5 reports the main findings of a former analysis (Pernigotto et al., 2022) focusing on another Bolzano weather station installed on top of one of the buildings of the university campus in the city center (46.498° N, 11.349° E) and performed over a three-year period (2018, 2019 and 2021). By comparing the *MAEs* reported in Table 4 with those in Table 5, it can be commented that larger errors are generally encountered in the prediction of solar irradiance in the location of the city center weather station. This is true for all vertical orientations except the eastern one. Indeed, studying the natural obstacles in the two locations, it can be seen that they are taller for the NOI TechPark weather station as far as the east orientation is concerned, while for the university weather station in the city center, they are more relevant for the west one. Again, each orientation has specific best and worst-performing pairs of solar irradiance models, which are typically different from those identified for the NOI TechPark weather station, except for the best-performing models for the west orientation and the worst-performing one for the north one.

Table 3 – Best and worst-performing pairs of solar irradiance models: diffuse irradiance

Best-performing pairs of irradiance models MAEs (Wh m^{-2})				Worst-performing pairs of irradiance models MAEs (Wh m^{-2})			
South	East	North	West	South	East	North	West
A10 Liu & Jordan + Karatasou	A15 Liu & Jordan + Spencer	H6 Gueymard + Lam & Li	B8 Burgler + Hawlader	F20 Ma & Iqbal + Perez Model 1	F20 Ma & Iqbal + Perez Model 1	D20 Klucher + Perez Model 1	D20 Klucher + Perez Model 1
12.7	15.1	7.9	14.8	75.0	71.8	66.1	58.6

Table 4 – Best and worst-performing pairs of solar irradiance models: global irradiance

Best-performing pairs of irradiance models MAEs (Wh m^{-2})				Worst-performing pairs of irradiance models MAEs (Wh m^{-2})			
South	East	North	West	South	East	North	West
G16 Skartveit & Olseth + Chendo & Manduekwe Model 1	B20 Burgler + Perez Model 1	H14 Gueymard + Muneer	B20 Burgler + Perez Model 1	C20 Temps & Coulson + Perez Model 1	F13 Ma & Iqbal + Soares	D20 Klucher + Perez Model 1	F15 Ma & Iqbal + Spencer
24.8	121.7	9.8	150.2	61.9	184.1	57.5	207.9

Table 5 – Best and worst-performing pairs of solar irradiance models: global irradiance. Comparison with the analysis performed in Pernigotto et al. (2022) with respect to the UNIBZ weather station (46.498° N, 11.349° E) for the years 2018, 2019 and 2021

Best-performing pairs of irradiance models MAEs (Wh m^{-2})				Worst-performing pairs of irradiance models MAEs (Wh m^{-2})			
South	East	North	West	South	East	North	West
H18 Gueymard + Skartveit & Olseth	C20 Temps & Coulson + Perez Model 1	J18 Perez et al. + Skartveit & Olseth	B20 Burgler + Perez Model 1	I15 Reindl et al. + Spencer	F15 Ma & Iqbal + Spencer	D20 Klucher + Perez Model 1	F18 Ma & Iqbal + Skartveit & Olseth
43.8	79.3	26.1	165.3	67.4	130.6	79.9	384.1

4.3 Step 3 – Analysis of Building Energy Performance

Table 6 reports the minimum and the maximum deviations found by simulating the energy performances for the considered dataset of buildings with the different pairs of solar irradiance models. Specifically, considering the results described in Section 4.2, the following 7 pairs of models were selected for this analysis:

1. Burgler + Perez Model 1 (B20)
2. Temps & Coulson + Perez Model 1 (C20)
3. Klucher + Perez Model 1 (D20)
4. Ma & Iqbal + Soares (F13)
5. Ma & Iqbal + Spencer (F15)
6. Skartveit & Olseth + Chendo & Manduekwe Model 1 (G16)
7. Gueymard + Muneer (H14)

The largest heating need deviations are within 5 kWh m^{-2} m^{-1} and are registered in the coldest months of the year (i.e., January, December), as expected. As regards the whole simulated period, the largest heating need deviations range from 1.4 to 17.7 kWh m^{-2} a^{-1}. Higher sensitivity to the choice of solar irradiance models is often found in those configurations with poorly insulated massive walls (i.e., concrete structures with 5 centimeters of insulation), and large south-oriented windows with high *SHGC*.

The cooling needs are characterized by monthly deviations within or around 4 kWh m^{-2} m^{-1}, usually occurring during the summer (i.e., June). Considering the whole simulated period, cooling needs deviations range from 3 to 23 kWh m^{-2} a^{-1}. This time, the largest deviation occurs for building configuration with well-insulated lightweight walls (i.e., timber walls with 15 centimeters of insulation), and large west-oriented windows with high *SHGC*.

Table 6 – Minimum and maximum monthly deviations of heating and cooling needs for the simulated dataset of 48 buildings

	Heating need deviations [kWh m^{-2}]		Cooling need deviations [kWh m^{-2}]	
Time	min	max	Min	max
Jan 2022	0.3	4.8	0.0	3.8
Feb 2022	0.3	3.2	0.0	3.5
Mar 2022	0.0	1.8	0.0	3.3
Apr 2021	0.0	0.7	0.0	2.0
May 2021	0.0	0.1	0.0	3.4
Jun 2021	0.0	0.0	1.1	4.2
Jul 2021	0.0	0.0	0.9	3.9
Aug 2021	0.0	0.0	0.7	3.0
Sep 2021	0.0	0.0	0.3	2.3
Oct 2021	0.0	1.3	0.0	4.1
Nov 2021	0.2	3.5	0.0	2.3
Dec 2021	0.3	4.9	0.0	1.5
Period	1.4	17.7	3.1	22.9

Fig. 3 depicts the cumulative distribution functions of the annual energy needs for space heating and cooling simulated for the 48 buildings. As can be seen, a larger variability of the findings is recorded for the cooling needs, especially when the horizontal diffuse irradiance model 20 (i.e., the Perez Model 1) is involved.

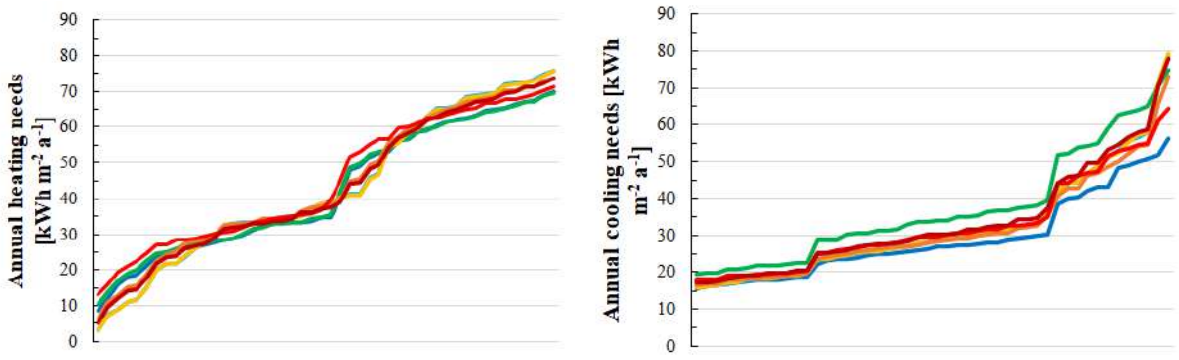

Fig. 3 - Cumulative distribution functions of the annual heating and cooling energy needs simulated for the 48 buildings with the following solar irradiance models: **B20** (Burgler + Perez Model 1), **C20** (Temps & Coulson + Perez Model 1), **D20** (Klucher + Perez Model 1), **F13** (Ma & Iqbal + Soares), **F15** (Ma & Iqbal + Spencer), **G16** (Skartveit & Olseth + Chendo & Manduekwe Model 1), and **H14** (Gueymard + Muneer)

5. Conclusion

This research assessed the capabilities of 22 horizontal diffuse irradiance models and 12 irradiance models for tilted surfaces for the calculation of the solar irradiance incident on the building envelope in mountain environments, which are characterized by complex irradiation patterns depending on the orography and the multiple terrain reflections. Solar irradiance calculated by all combinations of horizontal diffuse irradiance models and irradiance models for tilted surfaces were compared with diffuse and global irradiance measured in the Alpine location of Bolzano, Italy, during the period between April 2021 – March 2022 on four vertical surfaces oriented towards the main cardinal directions. Through the analysis of hourly Mean Absolute Errors, the best and the worst-performing pairs of models were first identified for each orientation and then used in TRNSYS simulations determine the energy needs for space heating and cooling for a dataset of 48 simplified buildings.

We found that:

- The performances of the pairs of solar irradiance models can be very different, depending on the orientation considered. In particular, the east and west orientations were found to be the most critical ones for the case study considered. Furthermore, varying accuracy can be expected for different locations in the same mountain valley or basin.
- None of the models in the literature was found able to ensure the same level of accuracy for all the four vertical cardinal orientations.
- The impact of the selection of solar irradiance models on the simulated energy performance is affected by the building's features.

Taking into consideration the main findings listed above, further developments of this research will involve testing potential modifications of the studied solar irradiance models to increase their capabilities when applied in mountain environments, in particular in the considered case study location of Bolzano, Italy.

Acknowledgement

This research was funded by the internal project of the Free University of Bozen-Bolzano "SOMNE - Bolzano Solar Irradiance Monitoring Network" (CUP: I56C18000930005; CRC Call 2018).

References

Behr, H. D. 1997. "Solar radiation on tilted south oriented surfaces: Validation of transfer-models." *Solar Energy* 61(6): 399-413. doi: https://doi.org/10.1016/S0038-092X(97)00081-9

Duffie, A. J., and W. A. Beckman. 1991. *Solar Engineering of Thermal Processes (*4th ed.). Wiley, Hoboken.

Gueymard, C. 1987. "An Anisotropic Solar Irradiance Model for Tilted Surfaces and Its Comparison with Selected Engineering Algorithms." *Solar Energy* 38(5): 367-386. doi: https://doi.org/10.1016/0038-092X(87)90009-0

Klucher, T. M. 1979. "Evaluation of models to predict insolation on tilted surfaces." *Solar Energy* 23(2): 111-114. doi: https://doi.org/10.1016/0038-092X(79)90110-5

Loutzenhiser, P. G., H. Manz, C. Felsmann, P. A. Strachan, T. Frank, and G. M. Maxwell. 2007. "Empirical validation of models to compute solar irradiance on inclined surfaces for building energy simulation." *Solar Energy* 81(2): 254-267. doi: https://doi.org/10.1016/j.solener.2006.03.009

Muneer, T., and D. Kinghorn. 1997. "Luminous efficacy of solar irradiance: Improved models." *International Journal of Lighting Research and Technology* 29(4): 185-191. doi: https://doi.org/10.1177/14771535970290040401

Perez, R., P. Ineichen, R. Seals, J. Michalsky, and R. Stewart. 1990. "Modeling Daylight Availability And Irradiance Components From Direct And Global Irradiance." *Solar Energy* 44(5): 271–289. doi: https://doi.org/10.1016/0038-092X(90)90055-H

Pernigotto, G., A. Prada, P. Baggio, A. Gasparella, and A. Mahdavi. 2015. "Impact of solar irradiation models on simulated hourly energy performance of buildings." In *Proceedings of Building Simulation 2015*, Hyderabad, India.

Pernigotto, G., A. Prada, P. Baggio, A. Gasparella, and A. Mahdavi. 2016. "Solar irradiance modelling and uncertainty on building hourly profiles of heating and cooling energy needs." In *Proceedings of the IV International High Performance Buildings Conference at Purdue*, West Lafayette, IN, U.S.

Pernigotto, G., A. Gasparella, and J.L.M. Hensen, 2021. "Assessment of a weather-based climate classification with building energy simulation." In *Proceedings of Building Simulation 2021*, Bruges, Belgium.

Pernigotto, G., A. Prada, and A. Gasparella, 2022. "Assessment Of The Accuracy Of Solar Irradiance Models In Mountain Locations: The Case Of Bolzano, Italy." In *Proceedings of the VII International High Performance Buildings Conference at Purdue*, West Lafayette, IN, U.S.

Prada, A., G. Pernigotto, A. Gasparella, and A. Mahdavi. 2014a. "Combined effects of diffuse fraction and tilted surface radiation models." In *Proceedings of ECPPM 2014 - 10th European Conference on Product & Process Modelling*, Vienna, Austria.

Prada, A., G. Pernigotto, P. Baggio, A. Gasparella, and A. Mahdavi. 2014b. "Effect of Solar Radiation Model on the Predicted Energy Performance of Buildings." In *Proceedings of the III International High Performance Buildings Conference at Purdue*, West Lafayette, IN, U.S.

Prada, A., G. Pernigotto, F. Cappelletti, and A. Gasparella. 2015. "Impact of solar irradiation models on building refurbishment measures from multi-objective optimization." In Proceedings of Building Simulation 2015, Hyderabad, India.

Robledo, L., and A. Soler. 1998. "Modeling Irradiance on Inclined Planes with an Anisotropic Model." *Energy* 23(3): 193-201. doi: https://doi.org/10.1016/S0360-5442(97)00083-2

Remund, J., W. Lucien, and J. Page. 2003. "Chain of algorithms to calculate advanced radiation parameters." In *Proceedings of ISES Solar World Congress*, Goteborg, Sweden.

UNI (Ente Nazionale Italiano di Normazione). 2014. *UNI/TS 11300-1:2014 – Energy performance of buildings Part 1: Evaluation of energy need for space heating and cooling*, Milan, Italy: UNI.

Effect of the Time Interval Base on the Calculation of the Renewable Quota of Building in an Alpine Context

Margherita Povolato – University of Trento, Italy – margherita.povolato@unitn.it
Alessandro Prada – University of Trento, Italy – alessandro.prada@unitn.it
Paolo Baggio – University of Trento, Italy – paolo.baggio@unitn.it

Abstract

The European goal of decarbonization drives design toward high-performance buildings that maximize the use of renewable sources. Hence, the European RED II Directive (EU, 2018) and the Italian decree (DL 8/11/2021) raise the minimum renewable share in new buildings and major renovations. In this framework, an air-source heat pump (ASHP) combined with an on-site photovoltaic system (PV) is one of the most popular solutions. However, the effectiveness of this heating system in mountainous contexts is not taken for granted, since the harsh climate induces both an increase in heating requirements and a deterioration of heat pump performance. For these reasons, energy simulation is a useful tool for understanding energy behavior and evaluate strategies to ensure the best energy savings. Currently, the renewable quota verification involves a quasi-steady state calculation on a monthly basis. However, this implies the use of the national grid as a battery through the net metering mechanism. The actual share of renewable coverage in the absence of expensive electric storage will necessarily be lower. This work analyzes the actual renewable share achievable in a new building in a mountainous area. Five representative locations in the province of Trento were initially identified through a cluster analysis. The renewable share was evaluated through a coupled dynamic simulation of the building and the energy systems. The results show how the calculated renewable share in this building changes according to the time interval used to close the balance with the grid. The evaluation of the renewable quota (QR) was carried out not only closing the balance by the hour or sub-hour but also by the month.

1. Introduction

Despite the recent increase in efficiency investment, the International Energy Agency (IEA, 2021) states that buildings' lifecycles are responsible, directly and indirectly, for about 37 % of global energy and process-related CO_2 emissions. According to the European Directive 2018/2001 (EU, 2018) and to Legislative Decree n.199/2021 (DL 8/11/2021), heat pump and renewable equipment deployment seems to be one of the most effective and the most economical solutions for reducing buildings' carbon footprint.

In the absence of electric batteries, a certain level of the renewable share is assured by the direct use of the PV production for heat pump operation. Nevertheless, the mismatch between the solar availability (during the day) and the building energy demand (mostly during the evening) is one of the main challenges to reach a high renewable share. Different solutions have been studied in the literature to increase the renewable quota of the system, such as energy storage and control strategies to match the building load to the solar availability (Fisher et al., 2017; Luthander et al., 2015). In (Pinamonti et al., 2020) the authors showed how the use of simple rule-based controls can lead to the reduction of up to 17 % of the energy withdrawn from the grid. Similarly, in (Franzoi et al., 2021a), the benefit of renewable energy communities in self-consumption of PV production emerges. What is not yet clear is whether the mandatory limits on renewable quotas are achievable without these measures. Moreover, the regulation currently provides for the calculation based on balance closure on a monthly basis, thus ensuring within the month the possibility of balancing between the

energy delivered in the central hours of the day and that withdrawn during the night, in a net metering scheme. Another research question therefore involves how much the real self-consumption of renewable energy of buildings that comply with the regulatory constraint in the absence of net metering and expensive electric batteries is.

This work therefore focuses on the analysis of a new residential building equipped with a low temperature heating system, thermal storage and a heat pump coupled with a PV system.

The single-family building (MF) analyzed represents a typical Italian building (Capozza et al., 2014), whose thermal properties meet mandatory constraints for new construction or major renovations.

2. Methodology

This paper studies the energy behavior of the MF building, to estimate the renewable quota. The goal is to verify whether the minimum share (DL 8/11/2021) of total primary energy covered by renewable primary energy is also achievable in a mountain context. The building and the HVAC systems are modeled in (TRNSYS v.17), as shown in the figure below.

2.1 Climate Conditions

The paper specifically analyzes the Alpine climate context of northern Italy. Five municipalities were selected by (Ceccolini et al., 2020), as a result of a clustering of the climate data of the municipalities of Trentino, in northern Italy (Fig. 2). Trento is located in the Italian climatic zone E, with heating degree days from 2101 Kd to 3000 Kd; while the other municipalities are in zone F, with heating degree days over 3001 Kd (DPR 412/93).

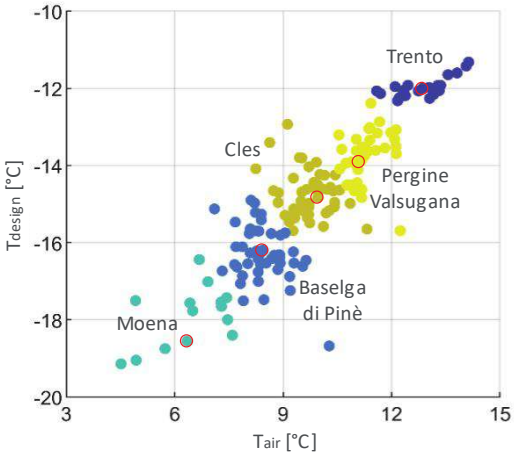

Fig. 2 – Identification of the 5 clusters of Trentino municipalities from the analysis of the average annual temperature and of the design temperature

Climate data are those of UNI 10349-1:2016 standard (UNI, 2016a), but for locations not included in the list, the solar irradiation of the nearest main city is assumed. Pergine Valsugana and Baselga di Pinè are related to Trento, whereas Cles and Moena are nearest to Bolzano.

Table 1 – Climatic data for the 5 municipalities of Trentino

Cluster	Municipalities	Lat	Alt	T_{design}	T_{air}
1	Trento	46.04	194	-12	12.9
2	Pergine V.	46.04	482	-14	11.4
3	Cles	46.22	658	-15	10.1
4	Baselga di Pinè	46.08	964	-16	8.8
5	Moena	46.23	1184	-18	6.4

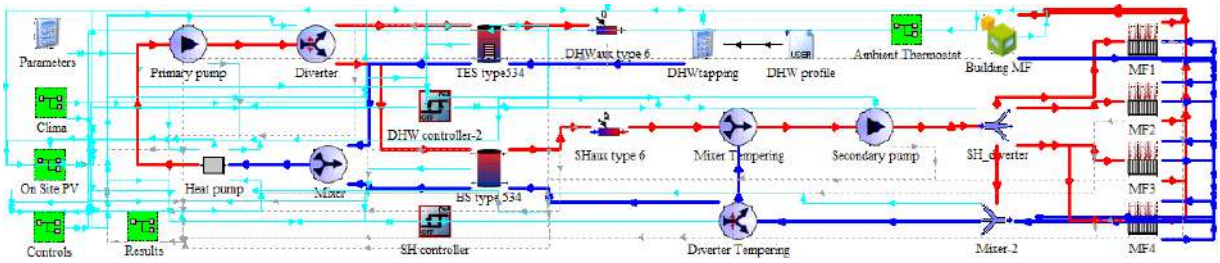

Fig. 1 – Layout of the developed TRSNYS model

2.2 Case Study Building

The MF building is composed of 2 floors, each with an area of around 88 m². The thermal characteristics are close to the limits of transmittance required by the current local legislation (DPP 13/07/2009). To reach a high-performance level, the building has 15 cm of extruded polystyrene (EPS) insulation on the external walls, 12 cm on the roof and well-insulated windows. The 4 thermal zones, 44 m² each, are identified by splitting the building along the west to the east axis in order to have uniform solar gains in the zone.

Table 2 presents the geometrical characteristics and the thermal properties of the building.

Table 2 – Geometrical characteristics and thermal properties of the single-family building

Geometrical characteristics		MF
Floors	/	2
Apartments	/	1
A_{FloorL}	m²	104.86
A_{FloorN}	m²	87.99
VolumeN	m³	527.91
$A_{w,N}$	m²	8.4
$A_{w,S}$	m²	8.4
$A_{w,E-W}$	m²	8.4
Height/$_{1\ floor}$	m	3
Thermal properties		**MF**
U_{foor}	$Wm^{-2}K^{-1}$	0.366
U_{wall}	$Wm^{-2}K^{-1}$	0.183
U_{roof}	$Wm^{-2}K^{-1}$	0.225
U_{window}	$Wm^{-2}K^{-1}$	0.8

2.3 HVAC System

The HVAC system (Fig. 3) consists of an inverter-driven heat pump (HP), a buffer storage tank (BS) for space heating (SH), and one for thermal energy storage (TES) for domestic hot water (DHW) preparation. The heat pump has a rated capacity of 7.18 kW for source temperature 7 °C and sink 35 °C. The emission terminals for SH are radiant panels fed with an inlet temperature of the hot water of 35 °C in the design conditions. The supply temperature to the radiant panels, as well as the BS and the HP setpoint temperatures, are controlled by an outdoor reset control. The setpoint temperature of the TES is 50 °C. The temperatures of the BS and TES determine the activation of the heat pump and are controlled by a proportional control.

The building is also provided with a photovoltaic system, inclined 20° on the south pitch of the roof. There are 7 modules connected in series, resulting in a peak power of 2.94 kW and an overall area of 12 m² (i.e., roughly 12.5 % of the roof surface).

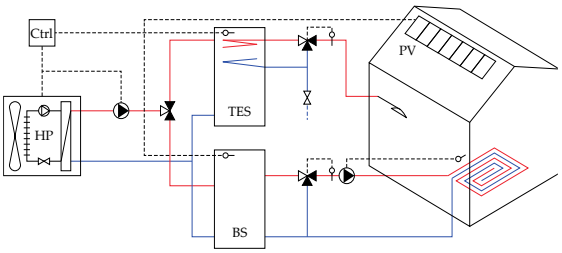

Fig. 3 – Heating system

2.4 Control Strategy

The single-family building is analyzed with and without self-consumption (SC) maximization strategies.

In the first scenario (*bas*), there is no advanced control strategy. A basic control is used, whereby the thermal storages are fully charged when a temperature set-point change occurs.

In the second scenario (*enh*), a rule-based control strategy (RBC) is adopted to maximize the SC of PV generation. The BS and TES set-points are raised, in case of PV energy surplus. This strategy, for inverter-driven air-to-water heat pump, was proposed by (Pinamonti et al., 2020).

2.5 Renewable Primary Energy Quota

Although the dynamic energy simulation uses a time step of 1 minute, the calculation of the renewable energy quota is performed closing the balance on a monthly basis (Eq. 1), according to the Italian standard (UNI 2016b). In addition, Eq. 2 and Eq. 3 show the calculation of the renewable quota closing the balance on an hourly basis, according to the current net metering scheme, and on the minute (i.e., the time step), respectively.

$$QR_{mo.} = \frac{\sum_{months} \min(\int_{mo.} Load ; \int_{mo.} PV)}{\sum_{months} \int_{mo.} Load} \quad (1)$$

$$QR_{ho.} = \frac{\sum_{hours} \min(\int_{ho.} Load ; \int_{ho.} PV)}{\sum_{hours} \int_{ho.} Load} \quad (2)$$

$$QR_{mi.} = \frac{\sum_{minutes} \min(\int_{mi.} Load\,;\, \int_{mi.} PV)}{\sum_{minutes} \int_{mi.} Load} \quad (3)$$

3. Results and Discussion

This section presents the results of the dynamic simulation, for both scenarios. The analysis performed allows an understanding of the extent to which the different interval affects the QR. Furthermore, the results are represented according to the different site elevations, thus showing the role of climate severity.

3.1 Annual Renewable Quota (*bas*)

The calculated quota of renewable energy over the total primary energy increases by 12 % ÷ 17 % in the 5 locations, changing the balance closure interval from a minute to a month (Fig. 4). This shows how the regulatory constraint of 60 % (monthly basis), with no storage batteries, corresponds to an actual renewable share of about 50 %.

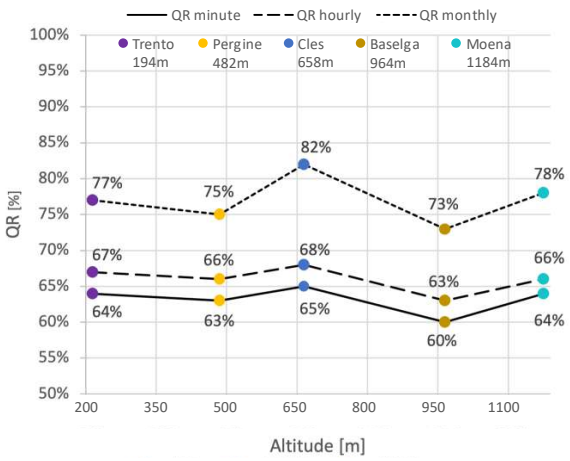

Fig. 4 – Annual values of QR minute, QR hourly and QR monthly: TRNSYS results for the MF building (*bas*)

The hourly and minute calculation has almost similar values with less marked deviations. The differences are much more evident if QRminute or QRhourly is compared with QRmonthly. Between the monthly renewable share and the minute one there is an average difference of about 13 %. The greatest difference is in Cles, Baselga and Moena, the municipalities with a harsher climate.

The renewable share calculated on a monthly basis is obviously greater than that on a minute basis, because the assumed on-site exchange allows the grid to be used as a virtual battery (within the month).

It can be noted that the percentage of QR decreases as the altitude of the municipalities increases, and, consequently, the design and the outdoor air temperature is lower. However, two anomalous behaviors are found for Cles and Moena. This is due to the higher solar radiation (UNI, 2016a).

3.2 Self-Consumption (*bas*)

Figs. 5 to 9 present the comparison between the monthly load profile (blue bars) and PV generation (orange bars) and the self-consumed energy based on a one-minute balance (yellow bars). The representation is made for each climate analyzed. In addition, the graphs show the self-consumption factor (SCF) and load coverage factor (LCF). The former is defined as the ratio of self-consumed PV energy vs the total PV energy generated. LCF, on the other hand, represents the fraction of PV energy used over the electricity absorbed by the HP and auxiliary systems. The LCF index differs from QRminute because it estimates only the renewable electricity share, neglecting both the renewable electricity taken from the grid, as well as the air source energy of the HP.

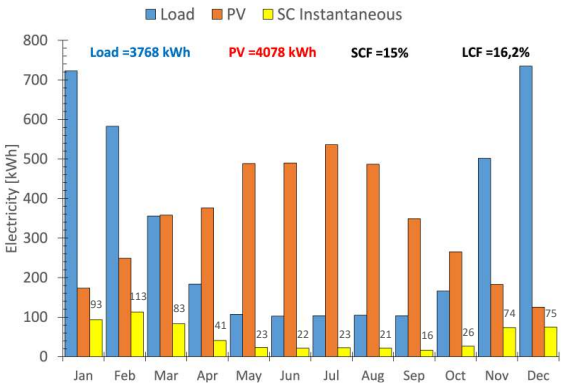

Fig. 5 – Energy profiles and SC minute based on Trento (*bas*)

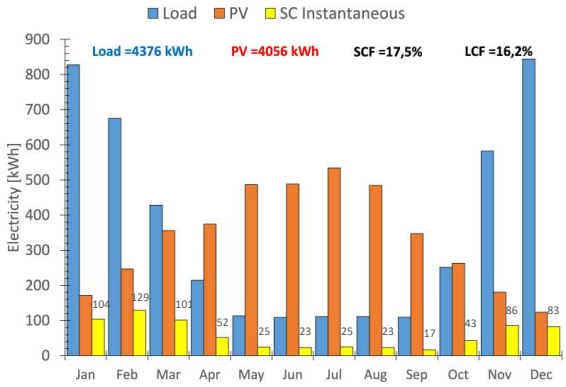

Fig. 6 – Energy profiles and SC minute based on Pergine (*bas*)

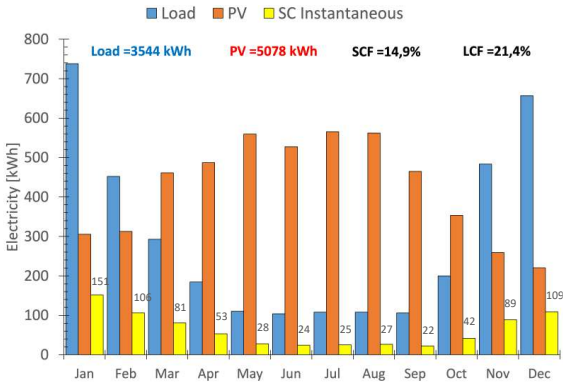

Fig. 7 – Energy profiles and SC minute based on Cles (*bas*)

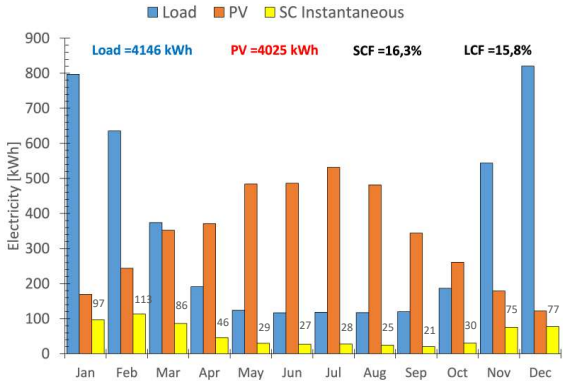

Fig. 8 – Energy profiles and SC minute based on Baselga (*bas*)

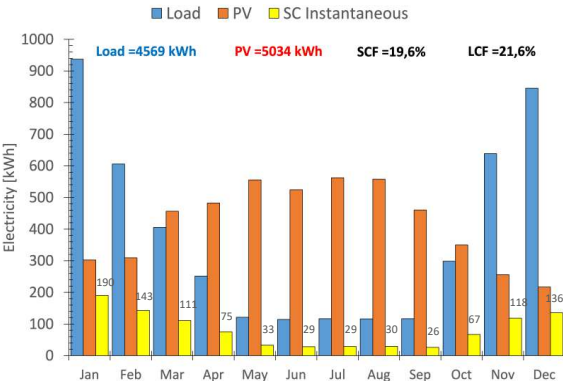

Fig. 9 – Energy profiles and SC minute based on Moena (*bas*)

Obviously, the load profile does not coincide with that of PV production. The largest gains from PV are during the summer period and during the daytime. This contrasts with the monthly demand profile and the daily habits of households, which consume more in the evening hours.

If self-consumption based on a monthly balance were shown, in summer, the yellow bar would coincide with the blue bar (self-consumption equal to load) and, in winter, with the orange one (self-consumption equal to PV generation). As already mentioned, closing the balance with an interval of a month implies balancing between the energy injected into the network in the central hours and that taken during the night in a net-metering scheme, that is, exploiting the grid as a virtual battery, albeit with the constraint of using all the stored energy within the month.

By calculating the actual SC of renewable energy, in the absence of net-metering and electric batteries, lower renewable quotas would be achieved.

As shown in the graphs, SCF ranges from a minimum of 15 % to a maximum of 20 % (17 % average), while LCF ranges from 16 % to 22 % (18 % average). The highest values are obtained in Moena. High LCF and SCF values mean that the electricity load is mostly covered by PV panels.

3.3 Annual Renewable Quota (*enh*)

To increase the SC, in the second scenario, the rule-based control strategy is applied. Comparing the results in Fig. 10 with those in Fig. 4, QRminute and QRhourly increase, while QRmonthly decreases.

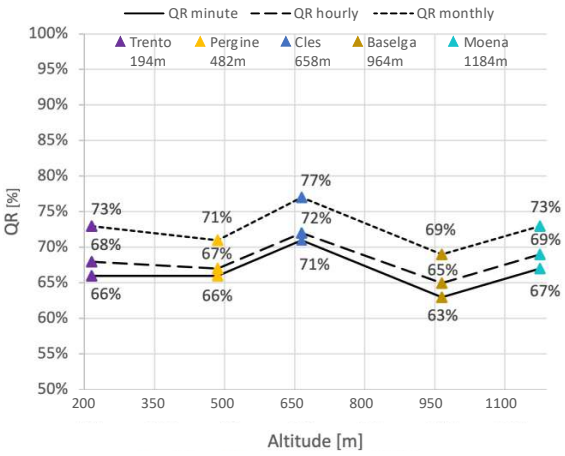

Fig. 10 – Annual values of QR minute, QR hourly and QR monthly: TRNSYS results for the MF building (*enh*)

The graph firstly highlights a lower variability (5 % ÷ 7 %) between the QR evaluated on a monthly basis compared with the minute-evaluated QR. This demonstrates the ability of the adopted control in optimizing the use of the PV generation.
QRminute improves by about 3 % because the instantaneous consumption of PV energy rises, and grid withdrawal decreases by about 4 %. In contrast, the QRmonthly decreases as rule-based control results in an increased load (Figure 11). However, in the monthly balance calculation all the PV production was already self-consumed also in the *bas* scenario, since the grid acts as a battery. Therefore, the higher load of the rule-based control corresponds to a higher withdrawal from the grid and, consequently, to a QR decrement.
Summing up, the difference between the instantaneous values and the monthly one is lower. In the first scenario, the gap is about 13 %, while in the second one, it is about 6 %.

3.4 Self-Consumption (*enh*)

Figure 11 shows the effects of the enhanced control strategy (*enh*) for the municipality of Trento. Compared with the *bas* scenario (Fig. 5), the profile of instantaneous self-consumption changes.

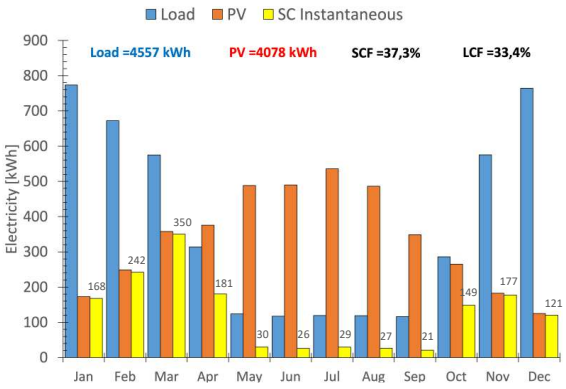

Fig. 11 – Energy profiles and SC minute based on Trento (enh)

The PV generation remains the same, since the system has not been upgraded, but improved. On the other hand, consumption increases slightly (from 3768 kWh to 4557 kWh) due to the control system. The demand profile rises simultaneously with the increase in self-consumption of the energy produced. With the basic control strategy, SCF and LCF are 15 % and 16,2 %; while with the rule-based control are 37.3 % and 33.4 %. This then demonstrates the capability of the control to directly use the PV production, reducing power exchange with the grid.

3.5 Discussion

As the results show, the interval used for balance closure greatly affects QR value. This is especially true if enhanced control strategies aimed at maximizing self-consumption are not employed. However, these enhanced controls are not (currently!) rewarded by the calculation method adopted by Italian law. However, the ongoing changes on the billing scheme for electric power that will soon introduce the hourly based balance calculation will undoubtedly reward the enhanced control scheme with a reduced energy cost.
Looking at both scenarios (*bas* and *enh*), the QR limit of 60 % is easily reached even in the harsh climates analyzed.
The building is close to being a zero-energy building on an annual basis at all locations investigated, as demonstrated by the energy matching chart (Luthander et al., 2015). The solid line in Fig. 12 connects all points where SCF is equal to LCF, implying that annual PV production is equal to annual load. A point above the bisector means that the annual PV generation is greater than the annual consumption of the building.

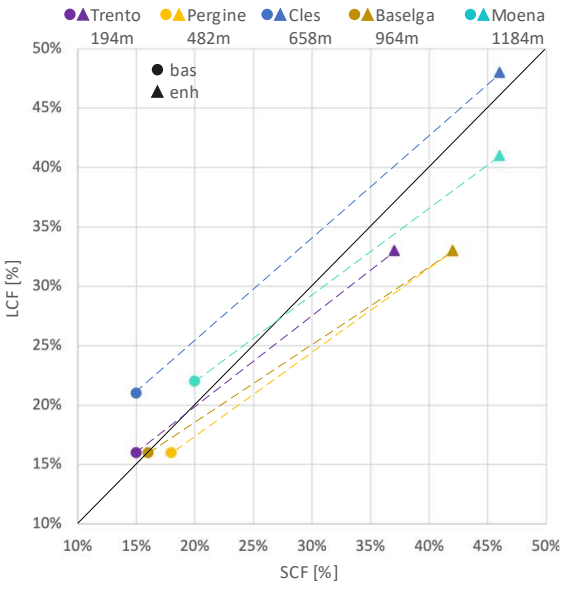

Fig. 12 – Comparison between bas (circle) and enh (triangle) through matching chart

The graph then shows how the control simultaneously increases SCF and LCF. However, there is a tendency for SCF to increase more than LCF, due to the slight increase in consumption. However, it should be emphasized how this is done by installing a cheap controller. A higher performance is achievable with (more expensive) batteries, which allow a better match of the building load to the solar availability.

4. Conclusions

The results show that 60 % renewable share is easily achieved in a new building, even in the mountainous areas analyzed.

If no control strategies aimed at maximizing self-consumption are employed, achieving a monthly QR of 60 % means an actual renewable share of about 13 % less, whereas, using an enhanced control strategy, the actual renewable share is about 6 % less than the monthly balance.

By closing the balance on a monthly basis, advanced control strategies are not rewarded. In fact, the pursuit of self-consumption often leads to an increase in energy demand, which, by closing the budget on a monthly basis, can lead to a reduction in the renewable share.

These controls, however, are beneficial in terms of reduced exchanges with the grid. In Trento, there is a 22.3 % increase in PV self-consumption and a 17.2 % increase in PV coverage of electricity consumption if the balance is closed on a minute or hourly basis. Taking all 5 municipalities into consideration, SCF rises by about 26 % and LCF by about 19 %.

Acknowledgement

This research was funded by the MIUR-Italian Ministry of Education, Universities and Research (PRIN 2017) grant number 2017KAAECT within the framework of FLEXHEAT project "The energy FLEXibility of enhanced HEAT pumps for the next generation of sustainable buildings".

Nomenclature

Symbols

A	Surface (m^2)
$A_{Floor}L$	Gross surface (m^2)
$A_{Floor}N$	Net surface (m^2)
ASHP	Air-Source Heat Pump
BAS	Base control strategy
BS	Buffer Storage
ENH	Enhanced Control Strategy
HP	Heat Pump
LCF	Load Cover Factor
MF	Single-family
PV	Photovoltaic
QR	Quota of renewable primary energy
SC	Self-Consumption
SCF	Supply Cover Factor
T_{air}	Air-dry bulb temperature (°C)
T_{design}	Design temperature (°C)
TES	Thermal Energy Storage
U	Thermal transmittance ($Wm^{-2}K^{-1}$)
V	Volume (m^3)

Subscripts/Superscripts

ho.	Hour
mi.	Minute
mo.	Month
w,E-W	East and West-oriented windows
w,N	North-oriented windows
w,S	South-oriented windows

References

Capozza, A., F. Carrara, M. Gobbi, F. Madonna, and F. Ravasio. 2014. *Analisi tecnico-economica di interventi di riqualificazione*.

Ceccolini, C., N. Franzoi, A. Prada, and P. Baggio. 2020. *Scenario di penetrazione delle pompe di calore per il riscaldamento e la produzione acqua calda sanitaria.*

European Parliament (EU). 2018. *Renewable Energy Directive (RED II), Directive (EU) 2018/2001 of the European Parliament and of the Council of 11 December 2018 on the promotion of the use of energy from renewable sources.*

Fisher, D., and H. Madani. 2017. "On heat pumps in smart grids: A review." *Renewable and*

Sustainable Energy Reviews 70: 342–357. doi: https://doi.org/10.1016/j.rser.2016.11.182.

Franzoi, N., A. Prada, S. Verones, and P. Baggio. 2021. "Enhancing PV Self-Consumption through Energy Communities in Heating-Dominated Climates." *Energies* 14: 4165. doi: https://doi.org/10.3390/en14144165

Italian Government. 2021. *DL 8/11/2021. Decreto legislativo 8 novembre 2021, n. 199. Attuazione della direttiva (UE) 2018/2001 del Parlamento europeo e del Consiglio, dell'11 dicembre 2018, sulla promozione dell'uso dell'energia da fonti rinnovabili.*

International Energy Agency (IEA). 2021. *Tracking Buildings 2021; Tracking Report;* IEA, Paris, France. Accessed March 30, 2022. https://www.iea.org/reports/tracking-buildings-2021

Luthander, R., J. Widén, D. Nilsson, and J. Palm. 2015. "Photovoltaic self-consumption in buildings: A review." *Applied Energy* 142: 80–94. doi: https://doi.org/10.1016/j.apenergy.2014.12.028

Pinamonti, M., A. Prada, and P. Baggio. 2020. "Rule-Based Control Strategy to Increase Photovoltaic Self-Consumption of a Modulating Heat Pump Using Water Storages and Building Mass Activation." *Energies* 13: 6282. doi: https://doi.org/10.3390/en13236282

President of the Italian Republic. 1993. *DPR 412/93. Decreto del presidente della Repubblica 412/93 – Regolamento recante norme per la progettazione, l'installazione, l'esercizio e la manutenzione degli impianti termici degli edifici ai fini del contenimento dei consumi di energia.*

Province of Trento. 2009. *DPP 13 13/07/2009. Decreto del presidente della provincia 13 luglio 2009, n. 11-13/Leg - Disposizioni regolamentari in materia di edilizia sostenibile in attuazione del titolo IV della legge provinciale 4 marzo 2008, n.1 (Pianificazione urbanistica e governo del territorio).*

TRNSYS Version 17. Madison, U.S.A.: Solar Energy Laboratory, University of Wisconsin-Madison. Accessed February-3, 2022. https://www.trnsys.com

UNI (Ente italiano di unificazione). 2016a. *UNI 10349-1 – Riscaldamento e raffrescamento degli edifici - Dati climatici - Parte 1: Medie mensili per la valutazione della prestazione termo-energetica dell'edificio e metodi per ripartire l'irradianza solare nella frazione diretta e diffusa e per calcolare l'irradianza solare su di una superficie inclinata.*

UNI (Ente italiano di unificazione). 2016b. *UNI TS 11300-4 – Prestazioni energetiche degli edifici - Parte 5: Calcolo dell'energia primaria e della quota di energia da fonti rinnovabili.*

Innovative Approaches for Teaching BPS: First Implementations of Business Game-Like Activities

Andrea Gasparella – Free University of Bozen-Bolzano, Italy – andrea.gasparella@unibz.it

Abstract

Experiential Learning (ExL) has long been considered a useful and necessary tool in educational courses in several different fields, including engineering. Nevertheless, traditional didactical approaches have prevailed, in particular, in Bachelor and Master Engineering programs, at least in Italy.

This implies the focus is kept more on theoretical aspects even for disciplines in which practical activities and learning by doing could provide the necessary competence for students to enter the job market promptly. Futhermore, ExL is recognized as providing a more immersive educational environment, capable of increasing participation and motivation in students.

One of the techniques introduced by the ExL consists of roleplaygames, some of which in the form of business games. This work reports about the main outcomes from an initial implementation of a business game-like approach to train perspective building envelope and energy systems designers. In particular, the game is intended to train students in the use of building simulation, showing what the potential and the peculiarities of the job can be when approaching the market. In addition, since it is commonly recognized that, while BPS is widely used in teaching and research, it is not widespread among practitioners, the game was also conceived to promote BPS use in practice.

The main features, including constraints and critical points, of the implementations within a university course in an Energy Engineering study program are described together with some suggestions for future improvements.

1. Introduction

Experiential Learning (ExL) is commonly defined as a teaching approach based on learning from experience, as opposed to a more traditional and formal education, which is mostly focused on the presentation of somehow abstract concepts by the teacher. Indeed, the relevant difference does not refer to the abstraction, rather than to the approach, which requires the learner to assume an active role in the learning process.

Even if it is indisputable that ExL can contribute to filling the gap between theoretical knowledge and practical skills and competences that is so often observed in many higher educational programs, the focus is more on the process of creating and acquiring knowledge.

Nevertheless, the experience itself, which is often included in many study programs at least in the form of traineeships and internships, is not enough. As introduced through the foundational theories of experiential learning by Dewey, Freire, James, Lewin, and Rogers, a transformation of the experience is required.

In the Experiential Learning Theory, introduced by Kolb and Kolb (2009, 2017), two dialectically related modes of grasping experience—Concrete Experience (CE) and Abstract Conceptualization (AC)— as well as two dialectically related modes of transforming experience—Reflective Observation (RO) and Active Experimentation (AE) - are combined in a cyclic and iterative process.

In this respect, the theoretical concepts provided by the teacher in the traditional model are still required to support knowledge development, even if it emerges more and more from an interactive relation between teacher and learners, and between reflection and experience.

This also leads to some extent to a larger engagement of the learner. In addition, due to the constructivist nature of the learning process, learning outcomes are the result of a personal interpretation by the learner.

Finally, this is compatible with a more recursive interaction between theory and practice, and compatible with a process of gradual development

of knowledge, in which foundational concepts are not necessarily provided prior to the practical experimentation.

It seems there is a general consensus towards the broad effectiveness of ExL in achieving all learning outcomes, namely knowledge, skills and competences (or responsibility/autonomy, according to the definition of the European Qualification Network). In educational areas and levels, such as Bachelor and Master Engineering programs, where it is important the student be trained to not only to acquire theoretical skills but also to take a more practical attitude towards problem solving, design, decision making, etc., this appears of crucial importance.

However, in many cases, only some of the tools proposed by the ExL are implemented. As an example, Baker et al. (2012) confirm that, despite the robust use of experiential learning in fields such as agricultural education, "experiential learning" and "experiential education" have mainly been used to describe teaching approaches such as field work experiences, internships, outdoor education, adventure education, vocational education, lab work, simulations, and games (Itin, 1999).

In this framework, the implementation of ExL concepts in courses dealing with Building Physics and Building Performance Simulation is described as necessary by Beausoleil-Morrison et al. (2015), to "develop the necessary knowledge and skills to effectively apply BPS tools", to the point that "this must be recognized in the way we teach the discipline".

The above reasons led to the adoption of ExL practices within a course in Building Physics and Building Energy Simulation in a Master program in Energy Engineering at the Free University of Bolzano (Gasparella, 2017). Not only was BPS awareness and competence improved through the implementation of numerical solutions to the theoretical governing equations, but the learning of the theoretical foundations of BP itself was enhanced by the development of the solution approaches with the use of a spreadsheet, instead of working with already available simulation tools. This allowed combining experientially the application of the concepts with introducing the students to the use and understanding of BPS. The students were also asked to apply BPS in small groups and develop a project to be presented and discussed at the final exam.

Although BPS is a powerful tool for designing, operating, and renovating buildings, its use in professional design practice seems to be less common than expected and to lack professionals able to work with it, independently of the efforts put into simplifying interfaces and integrating functionalities within the most common design tools (Soebarto et al., 2015).

With the additional goal of increasing the awareness and readiness of graduates to use BPS tools once entering the job market, it made sense to extend and rationalize the use of ExL techniques, turning the project work into a business game, or at least to start moving in that direction.

Business simulation games are roleplay games introduced in the 1950s to train students in business schools. As reported by Jackson (1959), they derived from the war games used in Germany in mid-19th century and later in Japan, in preparation for World War II. Business games are generally based on strategic decisions that imply some consequences for the players, providing direct feedback for their decisions and actions. In addition, detailed rules and realistic complexity are required to mirror real applicative contexts. Competition among teams is often included to engage participants and improve interactions within the groups. Specialized games can focus only on some areas of business management. Faria (1990) reported a rapid spread of the tools in the US in the thirty years from 1960 and 1990, even if a wide expansion potential was still present.

The use of business game-like tools in the field of BP and BPS, as in other engineering and technical areas is not well documented.

IBPSA, the International Building Performance Simulation Association, has introduced a Student Modeling Competition taking place within the biennial Building Simulation conference, since 2013. So far, five competitions have taken place (namely in 2013, 2015, 2017, 2019 and 2021). In the 2013 edition, the students were asked to use simulation to design an energy-positive house, limiting only the building geometry and focusing

on energy, under constraints on comfort and IAQ. In 2015, the focus was on an office building, and on designing and testing a mixed-mode ventilation strategy. In 2019, a more structured case was proposed, considering an existing historical building, with peculiar constraints limiting the possible interventions, and asking the students to undergo a 5-step approach (simulation pentathlon) from simulating the existing building to optimize the overall building performance (including multi-objective optimization). The 2021 edition focused on low-tech buildings and on the use of simulation to improve comfort, while preserving the energy efficiency.

In this work, a preliminary report is presented on the attempt to implement a business game-like task in the above-mentioned course in Building Physics and Building Energy Simulation in the Master program in Energy Engineering at the Free University of Bolzano. The existing project work was reorganized and proposed in the form of a game, with small groups competing and comparing their solutions in public presentations during the course.

The game focused on the renovation of a residential building. It was organized into four phases, asking the students to refine the project through the introduction of additional and contrasting objectives, and building on top of the results of a preliminary evaluation of the baseline configuration.

The activity required the students to use a BPS tool, with only basic preliminary knowledge, while theoretical foundations related to BP and to the numerical solutions of the governing equations were provided in parallel, considering further applications of the ExL approach, as described in Gasparella (2017).

2. Methods

2.1 Experiential Learning Experiences

An ExL integrated teaching method for a course dealing with Building Physics and Building Performance Simulation within a Master program in Energy Engineering had been under development and testing for ten years at the time of writing this paper. In approximately 90 hours, the fundamentals of building physics and modeling are presented, together with the main aspects of thermal comfort and indoor air quality. The course starts illustrating the thermodynamic balance of the indoor air volume, according to the model called “air node balance”.

The definition of the boundary conditions for solving the balance requires characterizing the unsteady thermal conduction in the envelope components, which in turn can be determined only through the surface balances, so through the analysis of convection, long and short wave radiation interactions at the external and internal surfaces for opaque and transparent envelope elements, and so on.

For each of the mentioned processes (i.e., conduction, convection, radiation), the main controlling equations are defined and their numerical or analytical solutions discussed, to end with a step-by-step implementation of a detailed model in a general productivity spreadsheet environment. As a result, at the end of the course, the students are able to develop a comprehensive simulation tool that, despite the limitations in the computational efficiency proper of a spreadsheet, can compare favorably to the most widespread tools available on the market in terms of both detail and accuracy.

In short, the student has the opportunity of applying the theoretical foundations, experiencing through simulation the behavior and relevance of each different process, and its contribution to the overall performance, observing the outcomes, conceptualizing the findings and actively interacting with the experimental environment, while understanding the inner operation of BPS tools.

The learning circle encompassing the four phases of Concrete Experience (CE), Reflective Observation (RO), Abstract conceptualization (AC), Active experimentation (AE) is therefore entirely implemented and repeated iteratively while progressing with the analysis of the different aspects.

2.2 Towards a Business Game

A business game is a roleplay game in which the player/learner has to perform tasks and obtain

results/feedback typical in professional practice, generally in the managerial field. In particular, the learner is expected to apply knowledge, skills and capabilities to evaluate alternatives and make decisions.

In the case of graduate students in Energy Engineering with a focus on Building Physics and Building Energy Systems, it is likely that in their professional activities they have to contribute to or directly perform the design of buildings, analyzing energy-related aspects, optimizing investment, and maximizing comfort conditions. They are expected to deploy the skills and competences necessary to (i) simulate performance, (ii) verify reliability of results, (iii) analyze outcomes and evaluate their sensitivity to the design parameters, (iv) optimize contrasting objectives, (v) make sensible proposals and find trade-offs, (vi) present and discuss with clients or other consultants, (vii) manage time and resources devoted to the analysis, understanding costs and benefits, in the different design phases.

To this aim, the project originally included in the exam assignments has been redesigned to serve as a sort of roleplay game.

The students had to start working on an assigned project in small teams of 3-4 persons, as if they were a design studio in charge of renovating an existing residential building and giving advice to a client. Students in a team could have different roles but also discuss ideas and methods.

A simulation tool was shortly introduced during the first weeks of the course and students got familiar with it through a guided example presented by some teaching assistants, who had been former students in the same course.

One of a couple of different buildings (Fig. 1) were randomly assigned to each of the nine teams.

Both buildings were detached houses, with two storeys for a three-person family. The envelope was typical of the '60s, therefore lacking any insulation and adopting single pane glazing. The buildings had different internal layouts, different orientations (main axis East to West or North to South), and different locations (Bolzano, Italy – cold winter and warm to hot summer, or Graz, Austria – with colder winter and slightly milder summer as in Fig. 2).

Shade cast from nearby buildings is also included in the evaluation in order to promote careful analysis of the context.

Even if non-thermal energy performances were not considered**,** students were encouraged to maximise daylight as a preference from the owner. While guaranteeing minimum access to daylight through the prescription of a minimum WWR was requested, increasing window size, changing their position and redefining the internal layout was allowed.

Students were asked to proceed to the following steps:

(i) Analysis of the baseline case,
(ii) Assessment of the energy impact of intervention measures,
(iii) Definition of cost-effective solutions, and
(iv) Assessment and improvement of thermal comfort and indoor air quality.

Data to perform the economic analysis (costs for the different interventions, including windows resizing and repositioning, layout redesign and shades installation) were provided after phase (ii). Input and requisites for the comfort analysis were provided after the cost-effective optimization in phase (iii).

At the end of phases (ii), (iii) and (iv), the teams were asked to give a short presentation (10-15 minutes) to the other groups (three times in total), receiving comments and answering questions. This represented a novelty compared with the original project work, which was mainly discussed at the end of the course and only with the examiner.

In two rounds after the second and third presentations, all teams were also asked to evaluate each other's work, selecting the best one for each of four categories (i) presentation; (ii) innovation; (iii) comprehensiveness; (iv) performance. From the preferences expressed in the two rounds, a ranking list was formed for each of the evaluation categories, and updated with the teacher and teaching assistants' evaluations. Four teams were commended as the best in one of the categories and one as overall winner for the game.

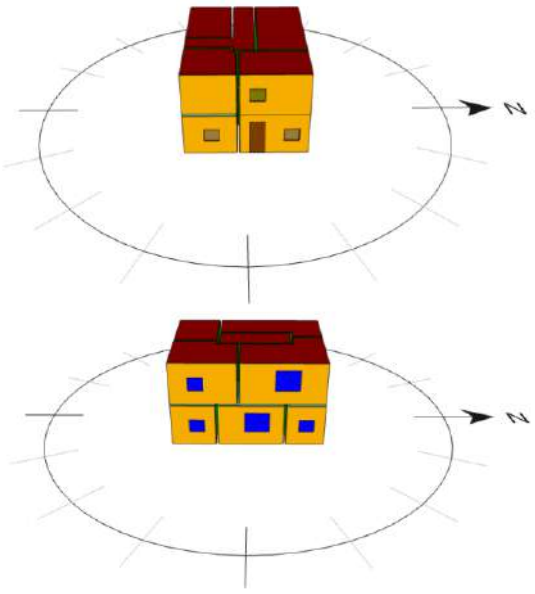

Fig. 1 – Residential buildings for the business game. The cases of Bolzano (above) and Graz (below)

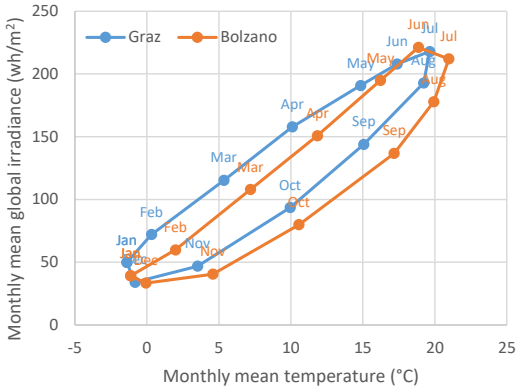

Fig. 2 – Reference climatic conditions (air temperature and global irradiance on the horizontal) in Bolzano and Graz

3. Results and Discussion

As for the outcomes of the adoption of the game, an initial evaluation concerns the students' behavior and strategies. In particular, some interesting techniques were observed among those implemented to overcome limitations in the calculation capabilities and minimize the required efforts.

Most of the groups developed a customized approach to assessing the combined effect of different intervention measures and to adding optimization objectives in an efficient way.

Some of noticeable strategies adopted in the different phases are reported below:

(i) The preliminary analysis of the baseline configuration was generally conducted through a multi-zone simulation. One of the teams, however, ran free-floating simulations considering individual rooms, to point out specific critical points from peculiar temperature profiles. Some teams also included daylight evaluation, even if not explicitly requested.

(ii) Most of the teams decided to redefine the layout and window position, to optimize both the distribution of spaces and the access to solar gains and daylight. In many cases, preliminary parametric evaluations were performed with different window sizes.

(iii) Some teams minimized the cost of a full sensitivity analysis on each of the intervention measures, establishing a preference order. They selected the most influential interventions, adopting parametrically the most extreme levels allowed for each. They then kept the order in the optimization steps. Some others increased the level of each intervention at a time (such as the insulation thickness), stopping when the marginal improvement was reduced to below a certain percentage, and moving to the next with the same approach.

(iv) Energy optimization followed generally from either the simple combination of the preferred levels of the different intervention measures, or a sequential approach. That foresaw the optimization of the most impacting intervention, adding on top of it the second best, and so on. In some cases, students seemed more aware of the possible non-linear interaction effects, so solutions related to the previous intervention level were explored again after adopting the new one.

(v) Cost optimization was mostly based on the evaluation of the economic performance (simple payback period) of the energy optimized configurations. Subsequently a reduction in the investment cost and so in the payback was attempted through the decrease or removal of some of the interventions, such as of the reduction of the insulation thickness or moving back to single or double pane glazing from double or triple, respectively. Some

groups decided to cap the economic indicators.

(vi) Comfort (thermal and IAQ) was generally only assessed verifying the compatibility of the renovated configuration(s) with the prescribed comfort category. In some cases, when overheating issues were highlighted, some control strategies dealing with increased natural ventilation or with some refined assumptions about the occupant's behavior and presence were considered. Somewhat surprisingly, some of the teams simply decided to adopt air conditioning.

Presentations deserve a special mention. Presentations proved to be a good tool not only to engage the participation and practice some soft skills, such as communication strategies, but also to self-assess the quality of the work. Reiteration led to an increased quality level: some groups were motivated to increase the number of simulations, explore different solutions, use different approaches, and in general to verify their own results, and refine the presentation strategy. Overall, presenting and discussing among peers and with the support of the teacher and assistants proved to be effective in reinforcing, together with the game itself, the effectiveness of the different steps in the learning cycle, and improving the overall outcomes of the course.

Some general pros and cons can be listed as follows. As concerns the positive aspects:

(i) A simulation tool was learned through its direct use, with little need for training but some hours to develop a guided test case together with the students;

(ii) A more competitive context and an early start was able to increase collaboration and team working within groups with respect to the original project work. Some level of specialization of the members of a group was observed;

(iii) The business game promoted a more practical mind-set, more aware of real-life limitations and more sensitive to a client's perspective, forcing students to consider aspects they would not be fully aware of otherwise;

(iv) Multi-objective optimization without the availability of optimization tools, which could have been considered detrimental, turned out to be quite beneficial. It forced the students to develop empirical approaches to assess sensitivity and refine solutions;

(v) Public discussion and multi-step development allowed the comparison of the intermediate achievements of the groups, stimulating students to improve their approaches and recognize the limitations of the proposals.

Some negative outcomes or aspects to improve on have that have been identified are:

(i) The game had to start even earlier than the theoretical lessons to be able to provide adequate insight into the involved phenomena. That is accepted in ExL but would require deepening the phase of abstract conceptualization and the support for the teams and students;

(ii) Some of knowledge and skills required to develop the project are partially missing, such as those related with the economic evaluation. This could require in the future a multi-disciplinary approach in which the business game encompasses different courses;

(iii) A significant amount of time had to be allocated during the course, in particular for autonomous work, which might lead to compression of some parts and overloading of the students;

(iv) MOO without reliance on optimization tools led to sub-optimal solutions and possibly to inconsistencies between the findings of different groups;

(v) The structure of the business game still needs to be refined, and some dynamics and roles/ responsibilities introduced more clearly.

(vi) The evaluation grid needs to be improved to support the conceptualization phase and generate more competition among groups.

4. Conclusion

This work reports on the implementation of a business game-like task in a university course in Building Physics and Building Energy Simulation

for a Master program in Energy Engineering at the Free University of Bolzano. The course had already been designed and organized to take advantage of some ExL techniques. In particular, BP and BES concepts and competences were already developed in a learning cycle approach, implementing and experimenting on the theoretical foundations presented in class through the development of a simulation spreadsheet including all the relevant aspects contributing to the building dynamic energy behaviour.

In this framework, a project work was designed in the form of a business game, with small groups competing and comparing the solutions proposed in a series of presentations to the class. The game focused on the renovation of a small residential building. It was organized into four phases, asking the students to refine the project by adding progressively contrasting objectives, such as energy, costs, and comfort.

The activity required the students to use a BPS tool, with only basic preliminary knowledge, while theoretical foundations related to BP and to the numerical solutions of the governing equations were still being provided in parallel, as described in Gasparella (2017).

Overall, the attempt improved the quality of the experiential learning approach proposed in the course, stimulating greater participation and promoting a deeper awareness of the main concepts, skills and competences required in the field. The business game represented a step forward regarding the usual project work, in particular because of its structured approach, the focus on a couple of reference cases only, the presentations and interactions occurring after each phase and the discussion within and among the groups.

There is still a significant amount of work to do in order to:

(i) Provide more structured rules and roles, to make the game more realistic and engaging.
(ii) Consolidate the features of the case studies in order to facilitate the development of some parts which would have needed more information and to simplify the verification.
(iii) Involve professionals in the definition of the case study (to make them more realistic as from point i) and possibly also in the discussion and evaluation of the results
(iv) Extend the game to other universities and introduce "finals" levels involving the best groups from each university

Acknowledgements

The activities described in the paper could not have been developed without the passionate and tireless contribution of Federico Battini and Riccardo Albertin, former students in the course and PhD candidates at the time of the implementation of the business game-like approach described in this work, who also served as teaching assistants.

References

Baker, M. A., J. S. Robinson, and D. A. Kolb. 2012, "Aligning Kolb's Experiential Learning Theory with a Comprehensive Agricultural Education Model." *Journal of Agricultural Education* 53(4): 1–16. doi: https://doi.org/10.5032/jae.2012.04001

Beausoleil-Morrison, I., C. J. Hopfe, D. Crawley, and R. Rawal. 2015. "Teaching Building Performance Simulation through a Continuous Learning Cycle." Proceedings of Building Simulation 2015 - 14th Conference of International Building Performance Simulation Association, Hyderabad, India, December 7-9.

Faria, A. J. 1990. "Business Simulation Games after Thirty Years: Current Usage Levels in the United States." *Guide to Business Gaming and Experiential Learning*.

Gasparella, A. 2017. "Building Physics and Building Simulation: An Integrated Approach to Educational Programs." *Applied Mechanics and Materials* 887: 117–128. doi: https://doi.org/10.4028/www.scientific.net/amm.887.117

Itin, C. M. 1999. "Reasserting the philosophy of experiential education as a vehicle for change in the 21st century." *The Journal of Experiential Education* 22(2): 91-98. doi: https://doi.org/10.1177/105382599902200206

Jackson, J. R. 1959. "Learning from Experience in Business Decision Games." *California Management Review* 1(2): 92-107. doi: https://doi.org/10.2307/41165351

Kolb, A. Y., and D. A. Kolb. 2009: "The Learning way: Meta–Cognitive Aspects of Experiential Learning." *Simulation Gaming* 40: 297–327. doi: https://doi.org/10.1177/1046878108325713

Kolb, A. Y., and D. A. Kolb. 2017. "Experiential Learning Theory as a Guide for Experiential Educators in Higher Education." *ELTHE: A Journal for Engaged Educators* 1 (1): 7–44.

Soebarto, V., C. J. Hopfe, D. Crawley, and R. Rawal. 2015. "Capturing the Views of Architects about Building Performance Simulation to be used During Design Processes." Proceedings of Building Simulation 2015 - 14th Conference of International Building Performance Simulation Association, Hyderabad, India, December 7-9.